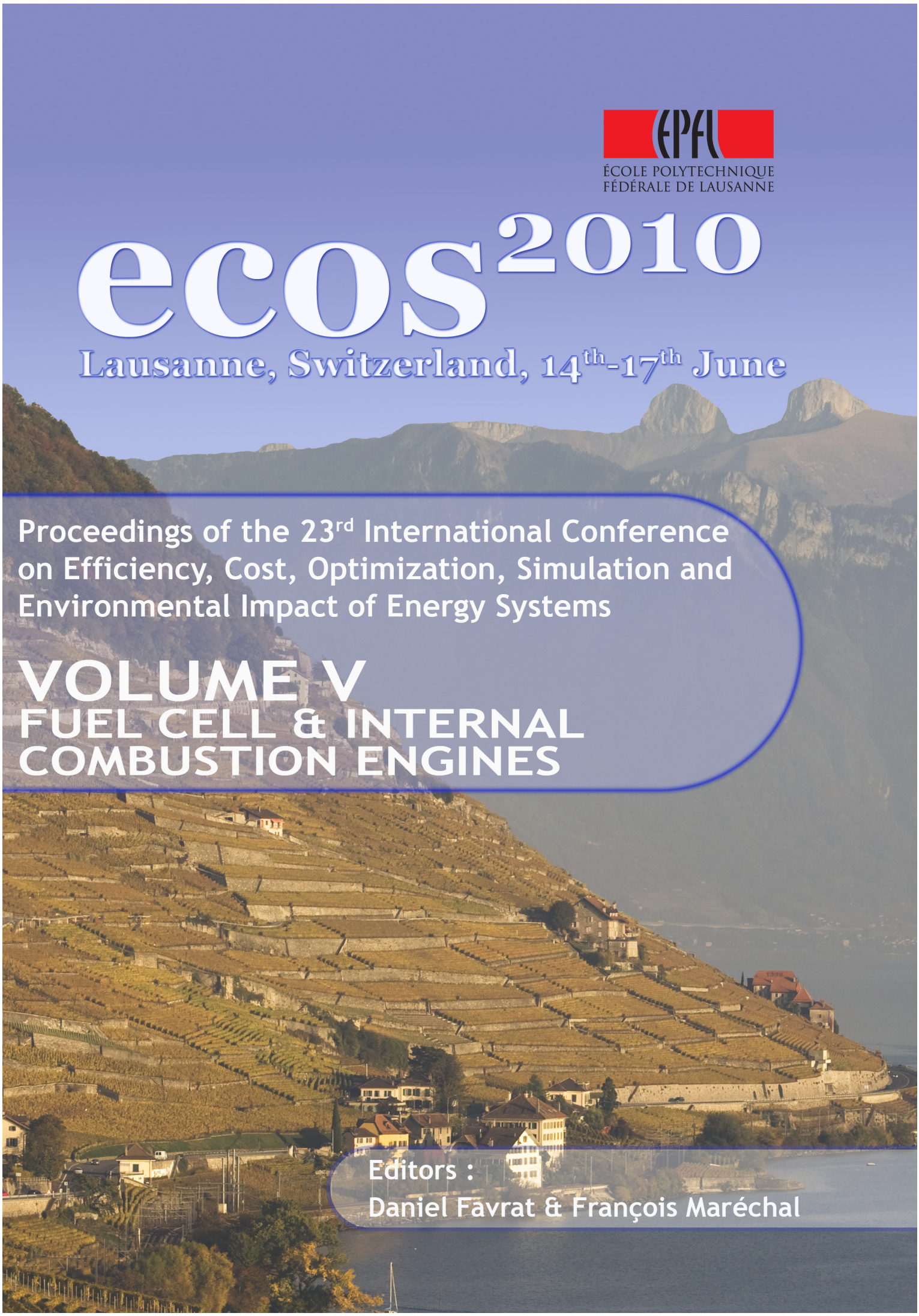
ÉCOLE POLYTECHNIQUE
FÉDÉRALE DE LAUSANNE
ecos2010
Lausanne, Switzerland, 14th-17th June
Proceedings of the 23rd International Conference on Efficiency, Cost, Optimization, Simulation and Environmental Impact of Energy Systems
VOLUME V
FUEL CELL & INTERNAL COMBUSTION ENGINES
Editors :
Daniel Favrat & François Maréchal

ecos2010

Proceedings of the 23rd International Conference on
Efficiency, Cost, Optimization, Simulation,
and Environmental Impact of Energy Systems

Lausanne, Switzerland
June 14-17, 2010

Volume V
Fuel cell &
Internal combustion engines

Editors
Daniel Favrat and François Maréchal

Organised by
Laboratoire d'Énergétique Industrielle (LENI)
École Polytechnique Fédérale de Lausanne (EPFL)

Official Website of the conference
www.ecos2010.ch

Corresponding e-mail
ecos2010@epfl.ch

Corresponding address
EPFL / LENI – ISE - STI
Bat. ME A2
Station 9
CH-1015 Lausanne
Switzerland

Book creation
Nicolas BORBOËN, Yannick BRAVO

PREFACE

Energy plays a major role in human societies. The supply of energy services is also a major contributor to the global and, too often, local environmental problems the World is facing. According to the International Energy Agency, actions to target future CO_2 concentrations in atmosphere below either 550ppm, or even below 450ppm, will have to be primarily focused on efficiency. A broader use of renewable, nuclear power and perhaps carbon sequestration will also contribute. To maintain a viable economic development these actions will have to be cost effective while globally reducing all emissions and caring about energy and material resources. A systemic approach is therefore essential to get a holistic vision, design better systems and optimize money and resources utilization.

The ECOS conferences have a long tradition in fostering the key aspects and the scientific knowledge that are essential for the engineers. The organizers of this 23rd edition are proud to acknowledge one of the largest participation ever with many original and high quality papers.

Our thanks go to the authors who accepted to travel from all continents and meet in Lausanne to present and share their scientific contributions. Many thanks also to all reviewers and members of the scientific committee who contributed to the quality of these proceedings. The conference chairmen are also grateful to the local organizing team including in particular, Nicolas Borboën, Stina Zufferey, Brigitte Gabioud, Yannick Bravo, Suzanne Zahnd and Irène Laroche. Many thanks also to the other members of the Industrial Energy Systems Laboratory of EPFL, the MEDIACOM EPFL team and the sponsors who greatly helped the organization of this fruitful event.

Daniel Favrat & François Maréchal

ORGANISING COMMITTEE

Prof. Daniel Favrat (chairman)
François Maréchal (chairman)

Nicolas Borboën, Yannick Bravo, Brigitte Gabioud,
Irène Laroche, Suzanne Zahnd, Stina Zufferey

INTERNATIONAL ADVISORY BOARD

Ozer Arnas, United States
Christos A. Frangopoulos, Greece
George Tsatsaronis, Germany

SCIENTIFIC COMMITTEE

Monika Axel, Sweden
Rangan Banerjee, India
Adrian Bejan, United States
Thore Berntsson, Sweden
Asfaw Beyene, United States
Paolo Bosshard, Italy
Denis Clodic, France
Stephen R. Connors, United States
R.L Cornelissen, Netherlands
Michel Feidt, France
Carl-Johan Fogelholm, Finland
Richard Gaggioli, United States
Yalçın A. Göğüş, Turkey
Gershon Grossman, Israel
Simon Harvey, Sweden
Abel Hernandez-Guerrero, Mexico
Gerard Hirs, Netherlands
Andrew Forbes Alexander Hoadley, Australia
Koichi Ito, Japan
Hervé Jeanmart, Belgium
Signe Kjelstrup, Norway
Jiri Klemes, Hungary
Zygmunt Kolenda, Poland
Andrea Lazzaretto, Italy
Noam Lior, United States
Sylvie Lorente, France
Giampaolo Manfrida, Italy
Philippe Mathieu, Belgium
Alberto Mirandola, Italy
Michael Moran, United States
Zhang Na, China
Silvia Azucena Nebra, Brazil
Eduardo de Oliveira Fernandes, Portugal
Silvio de Oliveira Júnior, Brazil
Ricardo Rivero, Mexico
Marc A. Rosen, Canada
Dominick A. Sama, United States
Peter Schossig, Germany
Enrico Sciubba, Italy
Luis M. Serra, Spain
Samuel Stucki, Switzerland
Pascal Terrien, France
Jules Thibault, Canada
Daniel Tondeur, France
Vittorio Verda, Italy
Laura Vanoli, Italy
Michael R. von Spakovsky, United States
Carl-Jochen Winter, Germany
Li Zheng, China
Andrzej Ziębik, Poland
Ron Zevenhoven, Finland

Innovative Hybrid Cycle Solid Oxide Fuel Cell- Inverted Gas Turbine with CO_2 Separation

Emanuele Facchinetti[a], *Daniel Favrat*[a], *François Marechal*[a]

[a] *Ecole Polytechnique Federale de Lausanne, EPFL, Lausanne, Switzerland*

Abstract: Decentralized power generation and cogeneration of heat and power is an attractive way toward a more rational conversion of fossil or bio fuel. In small scale power production fuel cell – gas turbine hybrid cycles are an emerging candidate to reach higher or comparable efficiency than large scale power plants. In spite of the advantages of this hybrid technology, many technical barriers have to be overcome to develop a highly efficient system. The present contribution introduces an innovative concept of hybrid cycle that allows to reach high efficiency maintaining the fuel cell operating under atmospheric condition and thus avoiding fuel cell pressurization technical problems. Carbon dioxide separation represents an additional advantage. A thermodynamic optimization approach, based on the system energy integration, is used to analyse several design options. The methodology proceeds in two steps: modelling the system for a set of decision variables and optimizing their values. The innovative system is analyzed and compared with state of the art fuel cell - gas turbine hybrid cycle. Exergy analysis has been performed. Optimization results prove the existence of designs that, neglecting the pressure drops, achieve exergy efficiency higher than 75%.

Keywords: Hybrid Cycle, Solid Oxide Fuel Cell, Gas Turbine, Inverted Brayton-Joule, CO_2 separation.

1. Introduction

The rising demand for electrical power and the necessity to decrease fossil fuel consumption push for development of new power generation systems, with higher efficiencies and reduced environmental impacts. An attractive way to reach a more rational energy conversion of fossil or bio fuels is the decentralized power generation and cogeneration of heat and power. Among major weaknesses of existing small systems at the building level, consisting mainly of internal combustion or Stirling engines, are low electrical efficiency, high maintenance costs, together with noise and vibration. Recently introduced mini gas turbines in the range of 40 to 120 kWel have reduced the three latter problems however at an even lower efficiency. Moreover they are not available in the smaller power range typical of many multi-family houses. Molten Carbon Fuel Cells (MCFC) and Solid Oxide Fuel Cells (SOFC) are emerging as major candidates to alleviate all the above mentioned drawbacks. However the fuel cannot be entirely converted electrochemically in the fuel cell alone and part of it is combusted downstream of the fuel cell with low energy efficiency. One existing approach suggests to further improve the electrical efficiency by combining the fuel cell with a gas turbine in a hybrid system.

In the last years the research demonstrated potential and limits of this technology. Many studies have assessed the feasibility and operating condition of a variety of integrated high efficiency design options. Those alternatives are usually classified either in pressurized systems, if the fuel cell is operating under pressurized conditions, or in atmospheric systems. So far the studies showed that the pressurized systems reach the highest efficiencies. Palsonn [1] showed the possibility to reach in a pressurized system, also with a low pressure ratio, more than 65 % of efficiency. Massardo [2] analyzed pressurized and atmospheric systems with efficiencies up to 75%. Autissier [3] performed a thermo-economic analysis demonstrating the possibility to reach 70% efficiency for an estimated 6700 $/kW with a 50 kW pressurized system. Tsujikawa [4, 5] proposed an interesting way to fully integrate a gas turbine driven in an inverted Brayton-Joule cycle with a fuel cell operating under atmospheric conditions. The inverted Brayton-Joule cycle, which has been fully detailed by Wilson [6], is characterized by the expansion in the turbine before the compression.

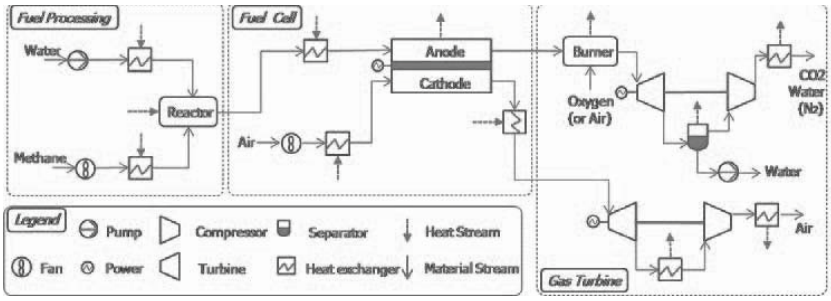

Fig. 1 Innovative hybrid cycle flow-chart

Despite the high potential, so far the experimental applications of fully integrated highly efficient hybrid systems remain limited to a small number of cases. The world's first demonstration of the SOFC-gas turbine hybrid concept, including a pressurized tubular SOFC module integrated with a micro gas turbine, was delivered to Southern California Edison for operation at the Irvine's National Fuel Cell Research Center. This system reached 53% electric efficiency for 220 kW [7]. A few other experimental applications have been developed, but all are restricted to the bulky tubular SOFC stacks. SOFCs are available in two different typologies: tubular geometry and planar geometry. The latter are more effective, compact and globally less material intensive than the tubular geometry based, but even more challenging to operate under pressurized conditions. Only recently, Lim [8] operated for a few hours a pressurized hybrid cycle with a 25 kW micro gas turbine and a 5 kW class planar SOFC, originally designed to work under atmospheric conditions.

So far the fuel cell pressurization remains a major challenge to overcome and represents a limit to the hybrid cycle development. The present paper introduces an innovative concept of atmospheric hybrid cycle capable of reaching higher or comparable efficiencies to the state of the art, whilst avoiding fuel cell pressurization technical problems. An additional advantage offered by the system is the carbon dioxide separation. This innovative system is compared to the state of the art hybrid cycle. A thermodynamic optimization approach, based on the system energy integration, is used to investigate several design options. The exergy analysis is performed to compare the energy conversion efficiency of the systems.

2. System and model description

An innovative concept of SOFC-gas turbine hybrid cycle is introduced, described and compared with the state of the art hybrid cycle. The developed system model is detailed underneath.

2.1. Innovative hybrid cycle

The innovative concept is based on a planar SOFC operating under atmospheric pressure integrated with two gas turbines driven in an inverted Brayton-Joule cycles. One embodiment of the system is presented in Fig. 1.

The idea is to capitalize on the intrinsic oxygen-nitrogen separation characteristic of the fuel cell electrolyte by sending separately to the relative gas turbines the cathodic flow and the anodic flow, which is free of nitrogen.

The cathodic flow, consisting in air impoverished in oxygen at the fuel cell outlet temperature, could be additionally heated up before passing through the sub-atmospheric gas turbine and to be exhausted. The anodic flow coming out of the fuel cell contains a part of unconverted fuel depending on the fuel utilization factor of the fuel cell. This remaining fuel is oxidized in a combustion chamber. If the oxidizer used is pure oxygen, the anodic flow passing through the turbine consists of only carbon dioxide and water. The water can easily be condensed and separated in the cooling process between the turbine and the compressor. The latter mainly compresses carbon dioxide whereas the water is pumped up separately. Carbon dioxide can be stored for other uses or can be compressed to a compatible state for transportation and sequestration. As gas compression is much more demanding in terms of mechanic power than liquid pumping, the reduced gas flow leads to savings of power with respect to traditional systems. To benefit as much as possible

from this gain, supplementary steam can be injected in the fuel processing unit. As a consequence, the anodic flow steam injection rate is another degree of freedom and is usually increased in comparison with the standard hybrid fuel cell-gas turbine system.
The advantages of the carbon dioxide separation and the compressor power reduction, although reduced, are maintained when the post combustion is realized with air instead of pure oxygen. This is due to the fact that post combustion concerns only a small part of the total fuel conversion in the system. In this case carbon dioxide and nitrogen have to be recompressed and separated afterwards if carbon dioxide collecting and storage is required.
Analyses have been performed on both cases, with pure oxygen injection and with air injection.
Since the innovative concept can be applied in any range of power, the system analysis performed is size independent.

2.2. Model Description

A steady-state model of the innovative hybrid cycle has been developed. The system model is subdivided into three sub-systems: fuel processing, fuel cell and gas turbines. Each sub-system includes a energy flow model computing the thermodynamic performance and the energy requirement. The models have been developed using a commercial process modeling software, BELSIM-VALI [9].

2.2.1. Fuel Processing

To simplify, the fuel feeding the system is methane, which is the major component of natural gas or of some biogas. The fuel processing is based on steam reforming, which can partially be internal. An appropriate excess of steam is guaranteed to avoid the formation of soot, which is an important cause of degradation. A carbon deposition risk model has been developed and integrated into the energy model. Pressure drops are neglected. The auxiliary devices needed, including pumps and blowers, are driven by the electrical power provided by the system.

2.2.2. Fuel Cell

The partially reformed fuel coming from the fuel processing unit feeds the anode of a planar SOFC operating under atmospheric pressure. Although not absolutely necessary in steady state operation, a blower, electrically driven by the system, provides the required air flow to the cathode.

The fuel cell model is based on the model for planar technology developed by Van herle et al. [10]. Anode supported cells, composite LSCF cathode and metallic interconnectors are assumed. The electrochemical model includes diffusion losses at the anode and cathode, as well as other polarization and ohmic losses. Possibility of internal reforming is included. The cell potential is a function of inlet gases composition, current density and fuel utilization. The inlet temperature is limited in the range between 973 K and 1073 K. To avoid cracks, the thermal gradient across the stack is maintained to under 100 K by removing the eventual extra energy through a heat exchanger. Pressure drops are neglected.
The model has been calibrated using experimental results presented by Wuillemin [11].

2.2.3. Gas Turbines

The anodic flow coming out the SOFC is mixed with an oxidizer in the combustion chamber in order to realize a stoichiometric and complete combustion. Post combustion hot gases have to be cooled down to the turbine inlet temperature (TIT).
Considering the characteristic of the system and the size-independent aspect of the analysis, the parameters characterizing the turbomachinery have been chosen so as to cover applications in different power ranges. The isentropic efficiency is supposed constant and equal to 0.85. The maximum pressure ratio considered is 6. Pressure drops are neglected. The analysis is performed for two different TIT limits: 1173 K and 1573 K.

2.3. State of the art hybrid cycle

A flow-chart of the state of the art hybrid cycle, used as reference, is presented in Fig. 2.

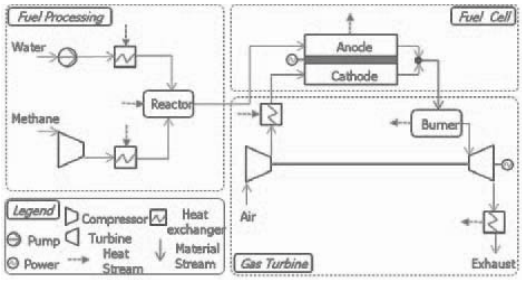

Fig. 2 State of the art hybrid cycle flow-chart

The system is based on a pressurized planar SOFC coupled with a gas turbine. A fuel processing unit, analog to the one described for the innovative

layout, feeds the anode with partially reformed methane at the operating pressure. A compressor supplies compressed air at the cathode. The cathode and the anode flows are combined downstream of the SOFC. This mixture is sent to the combustion chamber where the unconsumed fuel is completely oxidized. Following this, the hot gases expand in the turbine and are ejected as exhaust gases.
The model of each sub-system is corresponding to the model descriptions concerning the innovative system mentioned previously.

3. Thermodynamic optimization

A thermodynamic optimization approach is used to evaluate several design options. The methodology consists in two phases: to model the system defining a set of decisional variables and to optimize their values. This approach, described hereafter, is integrated into OSMOSE, a software under development at LENI [12] for design and optimization of integrated energy systems.

3.1. System modeling

The aim of the system modeling is to represent the impact of the design choices on the performances. The system's state and performances are expressed by variables divided in two categories: the decision variables provided as input, and the dependant variables computed as output.
The system modeling is organized in three sub-models (Fig. 3): the energy flow model, the heat and power integration model and the performance evaluation model.

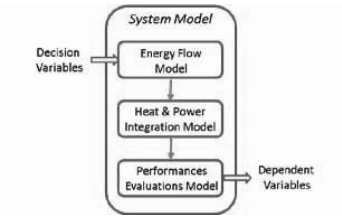

Fig.3 System Model Layout

The energy flow model has been previously introduced and detailed in section 2.2.

The heat and power integration model solve the heat cascade and the energy balance of the plant maximizing the combined production of heat and power. This identifies the minimum energy requirement and sets the basis for the heat exchanger network design, based on the exergy losses minimization. The heat exchange is assumed with a minimum temperature difference ($T_{\min}$) of 10 K.

The performance evaluation model allows to evaluate the system performances taking into account the energy flow model and the energy integration results. First Law efficiency and exergy efficiency are both estimated. The First Law efficiency (1) is defined as the ratio between the electrical power output and the power provided to the system in terms of fuel and, eventually, as separated oxygen. The electrical power output is the sum of the fuel cell power output, E_{FC} , and the net power output of the gas turbines (turbines power minus compressor and auxiliaries powers), E_{GT} . The energetic cost of the oxygen separation is considered equal to the ideal diffusion work of the pure component to its partial pressure in the atmosphere, which is the diffusion exergy [13].

$$\frac{E_{FC} \quad E_{GT}}{M_F \quad h_{i\,F}^{0} \quad M_{O_2} \quad e_{sO_2}}, \tag{1}$$

According with the general definition and following the formalism proposed by Favrat [13, 14], the exergy efficiency is defined as the ratio between the exergy rate delivered by the system and the exergy rate received by the system. The exergy rate delivered by the system consists in the electrical power output and in the diffusion exergy of the separated carbon dioxide. The exergy rate received by the system is reduced to the transformation exergy received (2).

$$\frac{E_{FC} \quad E_{GT} \quad M_{CO_2} \quad e_{s\,CO_2}}{M_F \quad k_{F}^{0} \quad M_{O_2} \quad e_{sO_2}} \tag{2}$$

3.2. Optimization

The objective of the optimization is to choose the design options that maximize the system efficiency. The influence of the decision variables on the system efficiency can be also investigated.
The optimisation is performed using MOO, a Multi - Objective Optimizer which is described in [15]. Evolutionary Algorithms are heuristic methods that base the optimization procedure on the exploration of the search space, thus allowing to optimize a non-linear and non-continuous system of equations. The search space is defined by the decision variables and their bounds. The multi-objective optimization solution is a set of

points in the decision variables space that define the possible trade-off between the objectives. The Pareto frontier expresses this compromise delimiting the unfeasible domain from the feasible but sub-optimal one.

4. Results

Three systems are compared in the results: the new system firstly with pure oxygen as oxidizer in the combustion chamber (HCox), and secondly with air (HCair), and the state of the art system (HCP).
The decision variables and their range are presented in Table 1.

Table 1. Decision Variables

Variable	Range	Variables	Range
ξ_{sc} [-]	[0.7 - 3.5]	i [A/cm^2]	[0.3 - 0.6]
T_{sr} [K]	[973-1073]	μ [-]	[0.5 - 0.8]
T_{fc} [K]	[973-1073]	π [-]	[2.5-6]
λ [-]	[2 - 10]	T_{ic} [K]	[298 - 343]

The fuel cell allows a more efficient energy conversion compared to the gas turbine. For this reason in all the optimization performed the fuel cell fuel utilization is maximized to the upper limit of its allowable range. Higher fuel cell efficiency can be achieved with a lower current density. A lower current density means larger fuel cell dimensions. Since the approach used does not consider any constraints on the fuel cell size, in all the optimization performed the current density has been minimized to the lower limit of the range.

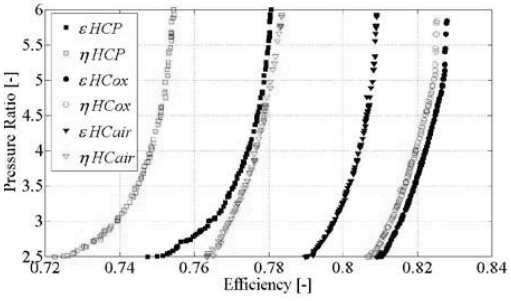

Fig.4 Efficiency vs. pressure ratio with max TIT=1573K.

The relation between First Law efficiency, exergy efficiency and pressure ratio is presented in the form of Pareto curves for the case of maximum TIT equal to 1573 K in Fig. 4. For HCox and HCair the pressure ratio reference is that of the anodic side. The system efficiency increases with the pressure ratio, although the increase becomes less important toward high pressure ratios. At low pressure ratios the performances of HCP are more sensitive to the pressure ratio variation. HCox is the most performing system. Considering the First Law efficiency HCox is between 1.5% and 2% more effective than HCair.
The gain with respect to HCP is around 5%. Those results are due to the reduction in compressor power and in exergy losses enabled by the new hybrid cycle concept. The gain is more important in HCox than in HCair, since avoiding the presence of nitrogen a higher amount of water can be condensed and pumped up.
However the First Law efficiency does not consider the carbon dioxide separation value and in general is not an adequate indicator of energy conversion performance. The exergy efficiency is the most appropriate performance indicator to estimate the thermodynamic quality of an energy conversion system. In terms of exergy analysis the advantage of HCox is higher: the analysis proves that HCox is about 4% more effective than HCair and around 7% more effective than HCP.
Fig. 5 illustrates how the system power output is distributed between the gas turbines and the fuel cell. The gas turbines power output is limited between 25 and 35% of the total power output. The reduced compression work enables HCox having the highest rate of power supplied by the gas turbines.

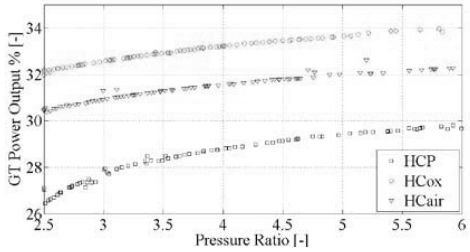

Fig.5 Pressure ratio vs. gas turbines power output percentage with max TIT=1573K.

Fig. 6 shows the relation between the steam to carbon ratio and the pressure ratio. The optimum HCox and HCair rate of water are higher than for HCP.
The optimal air excess in the fuel cell slightly decreases with the pressure ratio for all three systems, as illustrated in Fig. 7.
The pressure ratio of the cathodic turbine remains nearly constant for HCox while decreases for HCair with respect to the anodic pressure ratio (Fig.8).

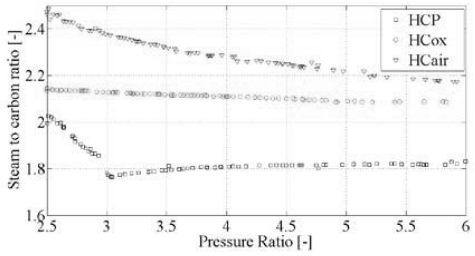

Fig.6 Pressure ratio vs. steam to carbon ratio with max TIT=1573K.

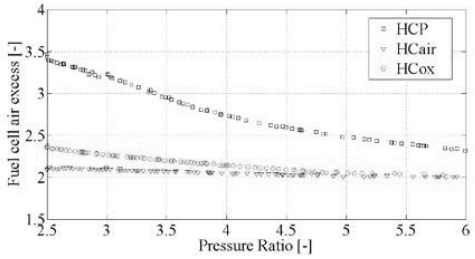

Fig.7 Pressure ratio vs. fuel cell air excess with max TIT=1573K.

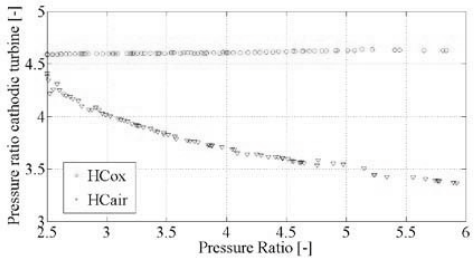

Fig.8 Pressure ratio vs. cathodic turbine pressure ratio with max TIT=1573K.

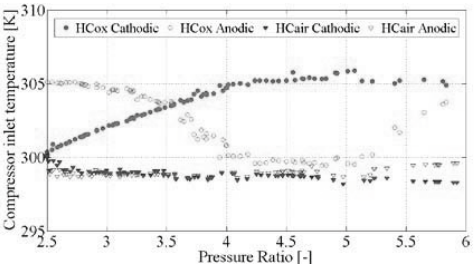

Fig.9 Pressure ratio vs. compressor inlet temperature with max TIT=1573K.

Figure 9 displays the relation between the pressure ratio and the anodic and cathodic compressor inlet temperatures. Anodic and cathodic compressor inlet temperatures of HCair are minimized in order to reduce the compression work. The compressor inlet temperatures of HCox are slightly higher than the lower limit of the range. This is due to the low temperature heat load required by the system energy integration.

Corrected composite curves of optimal solutions, characterized by the same pressure ratio, are compared in Fig. 10. The decision variables describing those solutions are presented in table 2. The corrected composite curves represent the relation between corrected temperature ($T \pm (\Delta T_{\min}/2)$) and the heat load specific to the power output. The cold curve represents the heat requirements of the cooling water utility, the water and the fuel supplied to the fuel process unit, the air provided to the cathode and the steam reforming reactor. The hot curve represents the heat extracted to limit the TIT, to cool down the fuel cell and the turbine outlets.

Three pinch points are created in HCox and HCair: at low temperature by the steam production for the fuel processing, at intermediate temperature by the steam reforming and at high temperature by the additional heating of the cathodic turbine inlet. HCP has only the pinch point at low temperature created by the steam production.

The heat load of the two atmospheric systems is higher with respect to that of the pressurized system. Two contributes explain this difference: the water condensation presents in HCox and HCair and the different air excess in the fuel cell. An important amount of heat is extracted in the low temperature zone of HCox and HCair for the water condensation in the anodic flow. The largest part of this heat is evacuated by the cooling water utility. In HCP the water is evacuated as steam in the exhausted gases. The different air excess explains the residual difference of the heat load: if the air excess is higher more air is heated up in the fuel processor unit and more heat is recuperated before the cathodic compressor. The heat exchanged between the incoming cold air and the outgoing hot air represents the main fraction of the heat exchanged in the intermediate temperature zone. In this region HCox and HCair are characterized by lower exergy losses with respect to HCP. The possibility to differentiate the cathodic and anodic pressure ratios enables a reduction in exergy losses, especially in this intermediate temperature zone. On the contrary in the high temperature zone, HCP has lower exergy losses. The high air excess characterizing the combustion in HCP maintains low the temperature at the turbine inlet, thus reducing the exergy losses. For the same reason the exergy losses are

more significant for HCox than for HCair, in which the nitrogen injected in the combustor contributes to cool down the flow.

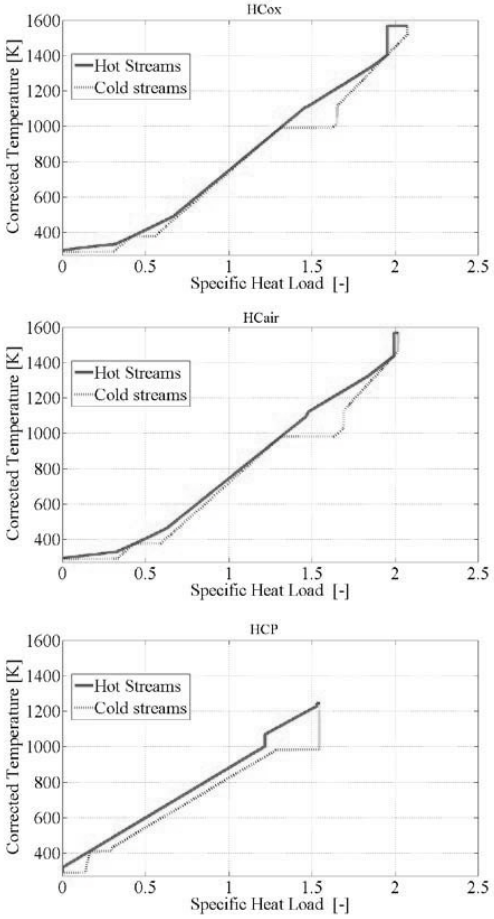

Fig.10 Composite curves for optimal solutions with π=3 and max TIT=1573K.

Table 2. Decision Variables for optimal solutions π=3 and max TIT=1573K.

Variable	HCox	HCair	HCP
ξ_{sc} [-]	2.13	2.37	1.77
T_{sr} [K]	985	976	979
T_{fc} [K]	1009	1026	979
λ [-]	2.3	2.1	3.2
μ [-]	0.8	0.8	0.8
i [A/cm^2]	0.3	0.3	0.3
π [-]	3	3	3
$\pi_{cathode}$ [-]	4.6	4.00	-
$T_{ic\ cathode}$[K]	302	299	-
$T_{ic\ anode}$ [K]	304	299	-

In conclusion the influence of a lower TIT is investigated. The Pareto frontiers obtained considering 1173 K as TIT limit are shown in Fig.11. The influence of the pressure ratio on the efficiency appears less important than in the case of TIT limit 1573 K. The expected decrease in efficiency is between 2.5% and 3% for HCox, between 2% and 2.5% for HCair and no more than 1% for HCP, in the whole pressure ratio range. The performance of HCox and HCair are more sensitive to the TIT variation.

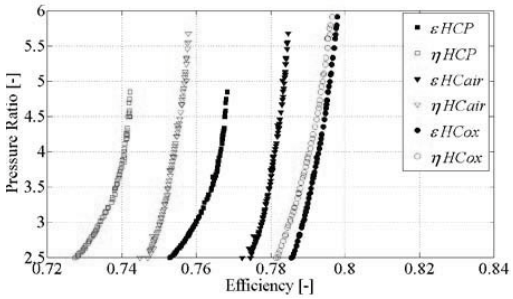

Fig.11 Efficiency vs. pressure ratio with max TIT=1173K.

5. Conclusions

A new concept of hybrid cycle integrating a Solid Oxide Fuel Cell, operating under atmospheric pressure, and a gas turbine, based on an inverted Brayton-Joule cycle, is introduced. A model of the system has been developed. Process integration techniques have been used to investigate several design options and estimate the integrated system performance. A size-independent analysis has been carried out to compare the innovative system with the state of the art, represented by a hybrid cycle based on a pressurized fuel cell integrated with a gas turbine.

Despite the more challenging system regulations and heat exchangers network definition, due to the integration of two gas turbines, the advantages offered by the innovative hybrid cycle with respect to the state of the art, are substantial.

Fuel cell pressurization technical problems are avoided, as the fuel cell operates under atmospheric pressure.

The new system enables the carbon dioxide separation.

The energy conversion efficiency is higher. Results demonstrate that the innovative system can achieve 83% First Law efficiency with a pressure ratio of 6. The gain with respect the state of the art is about 5%. However the value of the carbon dioxide separation cannot be evaluated by the First Law efficiency. The exergy analysis proves that

the gain in terms of exergy efficiency with respect to the state of the art is about 7%. The new system can achieves around 82.5% of exergy efficiency with a pressure ratio of 6. Further performance improvement could be expected with an intercooled compressor of the anodic gas turbine.

Nomenclature

$()^+$	Convention positive into the system
$()^-$	Convention positive out of the system
Δh_i^0	Specific lower heating value, kJ/kg
Δk^0	Specific exergy value, kJ/kg
e_s	Specific diffusion exergy, W/kg
$\dot{E}$	Exergy of mechanical work/electricity, W
$\dot{M}$	Mass flow, kg/s
i	Current Density, A/cm^2
T_{fc}	Fuel cell inlet temperature, K
T_{ic}	Compressor inlet temperature, K
T_{sr}	Steam reforming temperature, K

Greek symbols

ε	First Law efficiency
ξ_{sc}	Steam to carbon ratio
η	Exergy efficiency
λ	Fuel cell air excess
μ	Fuel cell fuel utilisation
π	Pressure ratio

Subscripts and superscripts

F	Fuel
FC	Fuel cell
GT	Gas turbine

References

[1] Palsson, J., et al., Combined solid oxide fuel cell and gas turbine systems for efficient power and heat generation, Journal of Power Sources, vol.86, Issue: 1-2, 2000.

[2] Massardo, A.F., et al., Internal reforming solid oxide fuel cell gas turbine combined cycles (IRSOFC-GT) Part A - Cell model and cycle thermodynamic analysis, Journal of Engineering for Gas Turbines and Power - Transactions of the ASME, vol.122, Issue: 1, 2003.

[3] Autissier, N., et al., Thermo-economic optimization of a solid oxide fuel cell, gas turbine hybrid system, Journal of Fuel Cell Science and Technology, vol.4, Issue: 2, 2007.

[4] Tsujikawa, Y., et al., Proposal of the Atmospheric Pressure Turbine (APT) and High Temperature Fuel Cell Hybrid System, JSME International Journal Series B, vol.47, 2004.

[5] Tsujikawa, Y., et al., Performance analysis of APT (atmospheric pressure turbine)-molten carbonate fuel cell hybrid system, Proceedings of the ASME Turbo Expo 2006, Vol. 4, 2006.

[6] Wilson, D.G., *The Design of High-Efficiency Turbomachinery and Gas Turbines*, MIT Press, 1993.

[7] Vejo, S.L., et al., Tubular Solid Oxide Fuel Cell/Gas Turbine Hybrid Cycle Power Systems: Status, Journal of Engineering for Gas Turbines and Power, vol.124, 2002.

[8] Lym, T.H., et al., Operating characteristics of a 5 kW class anode-supported planar SOFC stack for a fuel cell/gas turbine hybrid system, International Journal of Hydrogen Energy, vol.33, Issue: 3, 2008.

[9] Belsim SA, VALI IV, 2009, www.belsim.com

[10] Van herle, J., et al., Energy balance model of a SOFC cogenerator operated with biogas, Journal of Power Sources 118, 2003.

[11] Wuillemin, Z., Experimental and modeling investigations on local performance and local degradation in solid oxide fuel cells, PhD Thesis Ecole Polytechnique Federale de Lausanne, 2009.

[12] Marechal, F., et al., Thermo-economic modeling and optimization of fuel cell systems, Fuel Cells: From Fundamentals to Systems, 2004.

[13] Borel L., Favrat, D., *Thermodynamic and Energy System Analysis*, EPFL Press, 2010.

[14] Favrat, D., et al.,The challenge of introducing an exergy indicator in a local law on energy, Energy, vol.33, 2008.

[15] Molyneaux, A., et al., Environomic multi-objective optimization of a district heating network considering centralized and decentralized heat pumps , Energy, vol.35, 2009.

Performance Investigation of a SOFC-GT Hybrid System Based on Thermodynamic Optimization Strategies

Yingru Zhao[a], Nilay Shah[b] and Nigel Brandon[a]

[a] *Department of Earth Science Engineering, Imperial College London, London SW7 2AZ, UK*
[b] *Department of Chemical Engineering, Imperial College London, London SW7 2AZ, UK*

Abstract: A thermodynamic optimization methodology is developed to model, analyze, and predict the system behaviour of a combined SOFC-GT cycle. The system efficiency and power output are used as a basis to optimize the whole hybrid power plant. The optimized performance characteristics are presented and discussed in detail through a parametric analysis. Simulations of the effects that various design and operating parameters have on system performance have led to some interesting results. This study can be considered as a preliminary investigation of more complex fuel cell and gas turbine hybrid systems incorporating additional practical irreversible losses.

Keywords: Solid Oxide Fuel cell, Gas Turbine, Hybrid System, Thermodynamic Optimization.

1. Introduction

The combination of a solid oxide fuel cell (SOFC) and gas turbine (GT) has been identified as a promising innovative technology, superior to many other options due to its high energy conversion efficiency, fuel flexibility, and environmentally friendly characteristics. In such a hybrid configuration, high quality exhaust gases from the SOFC are used to drive a bottoming gas turbine cycle and provide supplementary power.

Experimental investigation of the interrelated parameters governing a hybrid system is sometimes difficult and expensive, therefore various modeling and simulation methods have emerged to reveal the inherent mechanisms of such energy conversion. Accordingly, the purpose of this study is to present a methodological optimization procedure to model, analyze, and predict the system behavior of an ambient pressure SOFC-GT hybrid power plant based on a previously developed SOFC model [1-3]. This hybrid system is simulated and analyzed with major irreversible losses due to electrochemical reaction, electric resistances, finite-rate heat transfer, and heat loss to the environment being specified and considered. Optimum strategies are determined as a realistic measure for the potential of improving the performance of each system component. The thermal efficiency, as well as the power output are identified and used as a basis to optimize the hybrid system. A parametric analysis is carried out in order to evaluate the influence of a wide range of important design parameters and operational variables on the system performance. This approach is expected to provide guidelines for the investigation of more complex fuel cell and gas turbine combined cycles incorporating additional irreversibilities.

2. A model SOFC-GT hybrid system

The high efficiencies developed by some of the fuel cell hybrids are of great interest, yet the optimum system configurations for the generation of power may remain to be determined. An ambient pressure system has several advantages, the most prominent of which is selection of the GT pressure independently of the fuel cell pressure [4]. Since this setup would require less integration of the SOFC and gas turbine, it also has the potential to be simpler to develop and could accommodate a wider variety of gas turbines [5]. Accordingly, an ambient pressure hybrid system is examined in the present study as a representative layout for integrating a fuel cell and gas turbine, as depicted schematically in Figure 1, where the fuel cell acts as the high-temperature heat reservoir of the gas turbine for the further production of power.

As described in Figure 1, there is no mass exchange between the fuel cell and gas turbine and only heat is transferred between subsystems. The gas turbine is modeled as a compressor and turbine mechanically linked via a common shaft, and thermodynamically coupled to the fuel cell via a primary heat exchanger, where the air leaving the compressor is heated up by the high-temperature exhaust gas of the fuel cell. This hot air enters

Corresponding Author: Nigel Brandon, Email: n.brandon@imperial.ac.uk

directly into the turbine and expands to produce power. A second heat exchanger is adopted following the primary one, recovering heat from the exhaust gas of the primary heat exchanger, and preheating the inlet air and fuel before entering the fuel cell.

2.1. System description

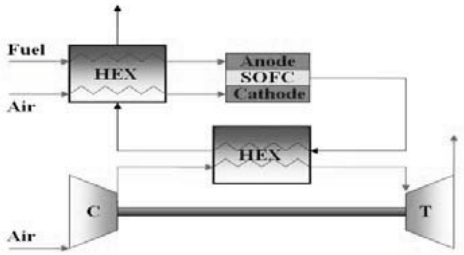

Fig. 1. The schematic diagram of a SOFC-GT system.

To develop a mathematical model representing the complex electrochemical and thermodynamic characteristics of each component of the system, the following simplifications and assumptions are made [1-3]: (1) both the fuel cell and gas turbine are assumed to be operated under steady-state conditions; (2) all gases are treated as ideal; (3) gas leakage is negligible; (4) complete chemical reactions are considered for the fuel cell; (5) operating temperature and pressure are uniform and constant for the fuel cell domain including the inlet reactants and outlet products.

2.1.1. An irreversible model for SOFC

As a starting point for the present work, a previously developed SOFC model [1-3], which is based on a planar solid oxide fuel cell using hydrogen as fuel and air as oxidant, is used. The overall electrochemical reaction is summarized as $H_2+½O_2 \rightarrow H_2O+\text{Heat}+\text{Electricity}$.

The maximum electrical work obtainable in a fuel cell, operating at constant temperature (T) and pressure (p_0=1atm), is given by the change in Gibb's free energy ($-\Delta \dot{G}$) of the electrochemical reaction. The relationship between the Gibb's free energy and the reaction enthalpy is known to be $-\Delta \dot{H}=-\Delta \dot{G}-T\Delta \dot{S}$, where $-\Delta \dot{H}$ corresponds to the total thermal energy available in the system, $\Delta \dot{S}$ denotes the change in entropy and $-T\Delta \dot{S}$ represents the amount of heat generated by a fuel cell operating reversibly. The enthalpy change and Gibbs free energy change between the products and the reactants of the global electrochemical reaction at temperature T can be, respectively, expressed as

$$\Delta \dot{H} = \frac{iA}{n_e F}\Delta h \tag{1}$$

$$\Delta \dot{G} = \frac{iA}{n_e F}\Delta g(T, p) \tag{2}$$

where $\Delta h = \sum_j \nu_j h_j$, $\Delta g(T, p) = \sum_j \nu_j \mu_j(T, p)$, subscript j represents the j^{th} species of the reaction, n_e is the number of electrons transferred in the reaction, i is the current density, A is the surface area of the interconnect plate (assuming the interconnect plates have the same area), F=96,485Cmol^{-1} is Faraday's constant, h is the molar enthalpy, μ is the partial molar Gibbs free energy of species, and ν is the stoichiometric coefficient. In particular, $\Delta g(T, p) = \Delta g^\circ(T) - RT\ln\left(p_{H_2} p_{O_2}^{1/2} / p_{H_2O}\right)$ denotes the molar Gibbs free energy change for the fuel cell reaction, where R=8.314Jmol^{-1}K^{-1} is the universal gas constant, p_{H_2}, p_{O_2}, and p_{H_2O} are the partial pressures of reactants H_2, O_2, and H_2O, respectively. It is noteworthy that $\Delta g^\circ(T)=\Delta h^\circ - T\Delta s^\circ$ is the molar Gibbs free energy change at p_0=1 atm, which also depends on temperature, and that the calculation of $\Delta g^\circ(T)$ is based on the tabulated values [6] at operating temperature T.

Although the Gibbs free energy change is a measure of the maximum electrical energy obtainable from an electrochemical reaction, this energy component is never completely utilized in a practical fuel cell because of various thermodynamic and electrochemical irreversibilities [7,8]. For example, the output voltage of the fuel cell is always less than its reversible voltage because there exist irreversible losses originating primarily from activation overpotential (V_{act}), ohmic overpotential (V_{ohm}), and concentration overpotential (V_{conc}) [9,10]. Besides the overpotential irreversibilities, another irreversible loss can be electronic current leakage through the electrolyte [1-3] and/or gas leakage from inadequate sealing. In practical systems the the measured open-circuit potential in a practical fuel cell can be lower than its ideal reversible potential, and therefore a leakage resistance can be introduced. The terminal voltage of an operating

cell can thus be generically derived by considering a cell as many small elements in series, including a reversible voltage determined by the Nernst equation, an internal resistance (R_{int}) made up by the sum of three overpotential contributions, and a leakage resistance (R_{leak}) in parallel with the load.

Entropy can be used to calculate the theoretical limits to energy conversion. According to [11-13], minimum irreversibility or entropy generation means maximum efficiency of the system. Combining those irreversibilities yields the rate of the total entropy production of an irreversible SOFC, which includes the entropy production rate resulting from the internal resistance and leakage resistance as:

$$\dot{S}_{tot} = I_{int}^2 R_{int} / T_0 + I_{leak}^2 R_{leak} / T_0 \quad (3)$$

where T_0 is the ambient temperature, and I_{int} and I_{leak} represent the corresponding electric currents through the equivalent resistances R_{int} and R_{leak}, respectively.

Considering all the irreversibilities discussed in the above analysis, the power output of the SOFC subsystem can be deduced as a function of current density, temperature, partial pressures, chemical composition, and geometric/material characteristics [1-3]:

$$P_{fc} = -\Delta\dot{G} - T_0\dot{S}_{tot} = \frac{iA}{n_e F}\left[d_2 - RTd_1 - \frac{k}{RTd_1}(d_2 - RTd_1)^2\right] \quad (4)$$

where

$$d_1 = 2n_c \sinh^{-1}\left(\frac{i}{2i_{0,a}}\right) + 2n_c \sinh^{-1}\left(\frac{i}{2i_{0,c}}\right) - \ln\left(1-\frac{i}{i_{L,a}}\right) - \ln\left(1-\frac{i}{i_{L,c}}\right) + \frac{in_e FL_{el}}{\sigma_0 R}\exp\left(\frac{E_{el}}{RT}\right)$$

, $k = R_{int} / R_{leak}$, and $d_2 = -\Delta h^\circ + T\Delta s^\circ + RT\ln\left(\frac{p_{H_2} p_{O_2}^{1/2}}{p_{H_2O}}\right)$. The thermal efficiency of the SOFC can thus be calculated from Eq.(4) as

$$\eta_{fc} = \frac{P_{fc}}{-\Delta\dot{H}} = \frac{P_{fc}}{-\frac{iA}{n_e F}\Delta h^\circ} = \frac{1}{-\Delta h^\circ}\left[d_2 - RTd_1 - \frac{k}{RTd_1}(d_2 - RTd_1)^2\right] \quad (5)$$

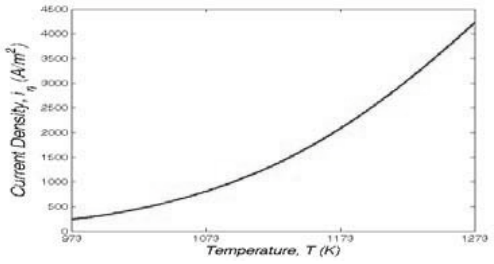

Fig. 2. The relationship between the optimized current density i_η and the fuel cell temperature T.

According to our previous study [1], results show that there exists a maximum efficiency for the proposed SOFC model when its current density is varied. Using Eq. (5) and its extremal condition, i.e., $\partial\eta_{fc}/\partial i=0$, it can be proved that when the efficiency attains its maximum value, the corresponding current density of the fuel cell, i.e., i_η, is determined by

$$-RTd_3 + 2kd_3(d_2 - RTd_4)/d_4 + kd_3(d_2 - RTd_4)^2/(RTd_4^2) = 0 \quad (6)$$

where

$$d_3 = \frac{2n_e}{i_{0a}\left(4+\frac{i_\eta^2}{i_{0a}^2}\right)^{1/2}} + \frac{2n_e}{i_{0c}\left(4+\frac{i_\eta^2}{i_{0c}^2}\right)^{1/2}} + \frac{1}{i_{la}\left(1-\frac{i_\eta}{i_{la}}\right)} + \frac{1}{i_{lc}\left(1-\frac{i_\eta}{i_{lc}}\right)} + \frac{n_e FL_{el}}{\sigma_0 R}\exp\left(\frac{E_{el}}{RT}\right)$$

$$d_4 = 2n_e \sinh^{-1}\left(\frac{i_\eta}{2i_{0a}}\right) + 2n_e \sinh^{-1}\left(\frac{i_\eta}{2i_{0c}}\right) - \ln\left(1-\frac{i_\eta}{i_{la}}\right) - \ln\left(1-\frac{i_\eta}{i_{lc}}\right) + \frac{i_\eta n_e FL_{el}}{\sigma_0 R}\exp\left(\frac{E_{el}}{RT}\right)$$

Solving Eq. (6) enables us to generate the curve of the optimized current density i_η varying with T as shown in Fig. 2. It is clearly seen that i_η is a monotonically increasing function of the SOFC operating temperature for other given parameters. Substituting the solution of Eq. (6) into Eqs. (4) and (5), one can further obtain the maximum fuel cell efficiency and the corresponding optimal power output.

2.1.2. An endoreversible model for gas turbines

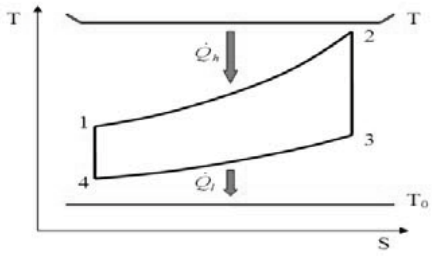

Fig. 3. The T-S diagram of an endoreversible Brayton cycle.

The basic thermodynamic cycle on which the gas turbine is based is known as the Brayton cycle. A steady-flow endoreversible Brayton cycle (assuming no changes in kinetic and potential energy) is shown in Fig. 3 as a temperature-entropy (T-S) diagram, where the processes 1-2 and 3-4 are isobaric heat addition from the SOFC and isobaric heat release to the environment respectively, the process 4-1 is an isentropic compression representing the power used by the compressor, and process 2-3 is an isentropic expansion representing the power output from the

turbine. T_i(i=1,2,3,4) are the temperatures of the working substance in the gas turbine at state points 1, 2, 3, and 4, and $\dot{Q}_h$ and $\dot{Q}_l$ denote the rates of heat flow transferred from SOFC to GT at T and from GT to the surroundings at T_0, respectively.

As a main source of irreversibility, the irreversible loss caused by the finite-rate heat transfer in the primary heat exchanger between the SOFC and GT subsystems is considered. Once the finite-rate heat transfer is taken into account, the performance of the gas turbine is closely dependent on heat-transfer laws. According to Newtonian heat-transfer [14] and the expression of log mean temperature difference (LMTD) [15], $\dot{Q}_h$ and $\dot{Q}_l$ can be, respectively, expressed as

$$\dot{Q}_h = \dot{m}c_p(T_2 - T_2x^{-1}) = \frac{U_1A_1(T_2 - T_2x^{-1})}{\ln u} \quad (7)$$

$$\dot{Q}_l = \dot{m}c_p(T_3 - T_4) = \frac{U_2A_2(T_4x - T_4)}{\ln v} \quad (8)$$

where $u=(T-T_2/x)/(T-T_2)$, $v=(xT_4-T_0)/(T_4-T_0)$, $x=T_2/T_1=T_3/T_4$ is the temperature ratio of the isobaric processes, $\dot{m}$ and c_p are, respectively, the mass flow rate and the heat capacity at constant pressure of the working fluid in the gas turbine, U_1 and U_2 are the heat transfer coefficients between the gas turbine and the high- and low-temperature reservoirs, A_1 and A_2 denote the corresponding heat transfer areas, and the total heat transfer area of the gas turbine cycle A_h=A_1+A_2. Using Eqs. (7) and (8), the relationship between A_1, A_2, and A_h can be deduced as

$$A_1 = \frac{A_h}{1+U_1\ln v/(U_2\ln u)} \quad (9)$$

$$A_2 = \frac{A_h}{1+U_2\ln u/(U_1\ln v)} \quad (10)$$

Inevitably, part of the thermal energy produced in the SOFC is directly released as a heat loss to the environment [1-3], which can be expressed as:

$$\dot{Q}_{loss} = KA_l(T - T_0) \quad (11)$$

where K represents the convective and/or conductive heat-leak coefficient, and A_l denotes the effective heat-transfer area. Combining the previous analysis and equations yields the heat flow rate transferred from SOFC to GT as

$$\dot{Q}_h = -\Delta\dot{H} - P_{fc} - \dot{Q}_{loss} = -\Delta\dot{H}(1-\eta_{fc}) - KA_l(T - T_0) \quad (12)$$

The efficiency of the GT cycle can thus be calculated using Eqs. (7)-(12) as

$$\eta_{gt} = 1 - \frac{T_4}{T_2}x \quad (13)$$

or

$$\eta_{gt} = 1 - T_4(x-1)\frac{U_2}{U_1\ln v}\left[\frac{U_1A_h}{\dot{Q}_h} - \frac{\ln u}{T_2(1-x^{-1})}\right] \quad (14)$$

Comparing Eq. (13) with Eq. (14) yields the following relation:

$$\frac{U_2}{U_1\ln v}\left[\frac{U_1A_h}{\dot{Q}_h}T_2(1-x^{-1}) - \ln u\right] = 1 \quad (15)$$

Eq. (15) indicates that T_4 is a function of T_2 when $\dot{Q}_h$, the amount of heat released from the fuel cell to the gas turbine, is kept as fixed. Furthermore, by using the solution of T_4 in Eq. (15), T_4 can be eliminated from Eqs. (13) and (14). Therefore, it is clear that the gas turbine efficiency is only a function of T_2 and $\dot{Q}_h$ with other given parameters, i.e., $\eta_{gt} = \eta_{gt}(T_2,\ \dot{Q}_h)$.

For a given $\dot{Q}_h$, using Eqs. (13) and (14) and their extremal condition $(\partial\eta_{gt}/\partial T_2)_{\dot{Q}_h} = 0$, it can be proved that when the efficiency of the gas turbine attains its maximum, T_2 is determined by the following two equations:

$$(\partial T_4/\partial T_2)_{\dot{Q}_h} = T_4/T_2 \quad (16)$$

$$(\partial T_4/\partial T_2)_{\dot{Q}_h} = \left\{\left[\frac{T(1-1/x)}{(T-T_2/x)(T-T_2)} - \frac{\ln u}{T_2}\right]\times\frac{U_2}{U_1} + \frac{\ln v}{T_2}\right\}\times\frac{T_4(x-1)(T_4-T_0)}{T_4 - xT_0} \quad (17)$$

Thus the relationship between T_2 and T_4 when the gas turbine works with maximum efficiency can be easily deduced from Eqs. (16) and (17) as:

$$\left\{\left[\frac{T(1-1/x)}{(T-T_2/x)(T-T_2)} - \frac{\ln u}{T_2}\right]\times\frac{U_2}{U_1} + \frac{\ln v}{T_2}\right\}\times\frac{T_2(x-1)(T_4-T_0)}{T_4 - xT_0} = 1 \quad (18)$$

Substituting the solution of T_4 from Eq. (15) into Eq. (18) enables us to generate the curves of the

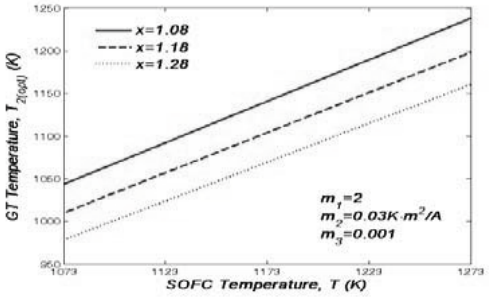

Fig. 4. The relationship between the optimized GT temperature T_2 and the fuel cell temperature T.

optimized T_2 varying with T as shown in Fig. 4, where the parameters m_1, m_2 and m_3 are three expressions given in the following analysis. From Fig. 4 it is clearly seen that the optimized value of T_2 is a monotonically increasing function of temperature T (the operating temperature of SOFC) for other given parameters.

Following the above procedure, the optimized GT efficiency, i.e., η_{gt}, becomes only a function of the fuel cell temperature T for a set of given parameters. Combining the above equations yields the optimum efficiency and power output of the gas turbine as:

$$\eta_{gt} = 1 - \frac{\dot{Q}_l}{\dot{Q}_h} = 1 - \frac{T_4(x-1)}{m_1 \ln v}\left[\frac{1}{im_2(1-\eta_{fc}) - m_3(T-T_0)} - \frac{\ln u}{T_2(1-x^{-1})}\right] \quad (19)$$

$$P_{gt} = \dot{Q}_h \eta_{gt} = A\left[-\frac{i\Delta h^\circ}{n_e F}(1-\eta_{fc}) + \frac{\Delta h^\circ m_3}{n_e F m_2}(T-T_0)\right] \times \left\{1 - \frac{T_4(x-1)}{m_1 \ln v}\left[\frac{1}{im_2(1-\eta_{fc}) - m_3(T-T_0)} - \frac{\ln u}{T_2(1-x^{-1})}\right]\right\} \quad (20)$$

where $m_1 = U_1/U_2$, $m_2 = -A\Delta h^\circ/(n_e F U_1 A_h)$, $m_3 = KA_l/(U_1 A_h)$, and the temperatures T_2 and T_4 are determined by simultaneously solving Eqs. (15) and (18). Eqs. (19) and (20) show clearly that the optimized efficiency and power output of the SOFC-driven gas turbine are closely dependent on the design and operation parameters of the fuel cell.

2.2 System efficiency and power output

Combining Eqs. (12)-(14), (19), and(20) yields the following expressions of the efficiency and power output for the SOFC-GT hybrid system:

$$\eta_{hybrid} = \frac{P_{hybrid}}{\dot{Q}_{in}} = \frac{P_{fc} + P_{gt}}{-\Delta \dot{H}} = \eta_{fc} + \frac{\dot{Q}_h}{-\Delta \dot{H}} \cdot \eta_{gt} \quad (21)$$

$$= \eta_{fc} + \left[1 - \eta_{fc} - \frac{m_3(T-T_0)}{m_2 i}\right] \times \left\{1 - \frac{T_4(x-1)}{m_1 \ln v}\left[\frac{1}{im_2(1-\eta_{fc}) - m_3(T-T_0)} - \frac{\ln u}{T_2(1-x^{-1})}\right]\right\}$$

$$P_{hybrid} = \dot{Q}_{in}\eta_{hybrid} = P_{fc} + P_{gt} = -\frac{iA\Delta h^\circ}{n_e F}\left\langle \eta_{fc} + \left[1 - \eta_{fc} - \frac{m_3(T-T_0)}{m_2 i}\right] \times \left\{1 - \frac{T_4(x-1)}{m_1 \ln v}\left[\frac{1}{im_2(1-\eta_{fc}) - m_3(T-T_0)} - \frac{\ln u}{T_2(1-x^{-1})}\right]\right\}\right\rangle \quad (22)$$

From Eqs. (21) and (22), it is clearly seen that the efficiency and power output of the SOFC-GT system are closely dependent on the parameters related to the various irreversible losses, which include the irreversibilities within the fuel cell itself, and those originating from heat transfer due to convection/conduction in the combined SOFC-GT power plant.

3. Performance characteristics and parametric optimization analysis

Knowledge of the performance and operating limits of the system leads to the development of optimization strategies and the determination of the realizable system and component potential. In this section, numerical calculations are performed to explore the optimum system operation based on the parameters adopted from data available in previous work [1-3]. Values of those parameters are used for all analysis as constants unless mentioned specifically. For example, the fuel composition at the SOFC inlet is taken as 97% H_2 + 3% H_2O, and the typical oxygen composition in ambient air, i.e., 21% O_2 + 79% N_2, is used as oxidant. Moreover, the enthalpy and entropy of reaction are generally not strong functions of temperature, which has been justified by the numerical examples for the hydrogen-oxygen reaction [1-3]. Thus, we can invoke the assumption that the changes in enthalpy and entropy across the fuel cell reaction are independent of temperature.

Since the prime motivation for the hybrid technology is to achieve a high thermal efficiency, the system parameters of the present model are chosen specifically to ensure not only the SOFC and GT subsystems, but also the entire hybrid cycle, works optimally at maximum efficiency. Therefore, the performance curves in the figures are all generated based on an optimized fuel cell current density, i.e., i_η. The sensitivity of the overall system performance to typical cycle parameters such as the operating temperature (T) of the SOFC, the temperature ratio (x) and the heat transfer coefficients ratio (m_1) of the gas turbine cycle, as well as the parameters related to the heat transfer between the subsystems and the heat leak to the surroundings, i.e., m_2 and m_3, will be explored in this section.

3.1. Effect of SOFC operating temperature

As briefly introduced in the previous discussion, the operating temperature of the fuel cell (T) affects the whole SOFC-GT cycle performance. Use of Eqs. (6), (21), and (22), as well as the solutions of T_2 and T_4 which are determined by the simultaneous Eqs. (15) and (18), enables us to plot

the curves of system efficiency and power density versus fuel cell temperature, as illustrated in Fig. 5, where the parameters $i=i_\eta$, x=1.08, m_1=2 and m_2=0.03K·m^2/A are chosen, and the power density $P^*_{hybrid}=P_{hybrid}/A$. The curves are generated based on a temperature range of 1073-1273K because a conventional high-temperature SOFC generally operates between 800˚C and 1000˚C.

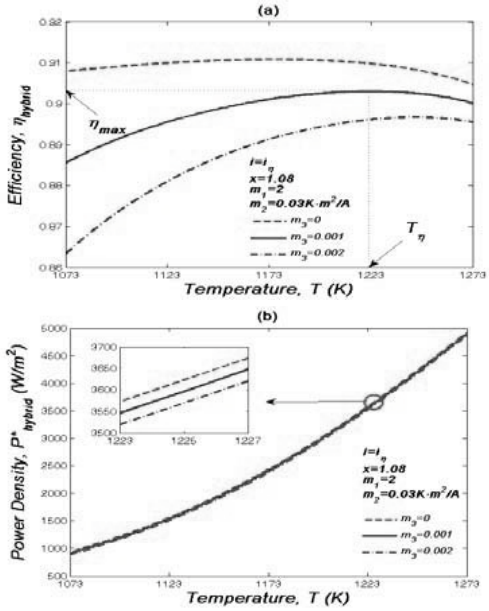

Fig. 5. The curves of the system efficiency (a) and power density (b) varying with the fuel cell operating temperature, where T_η is the temperature at which the system efficiency attains its maximum.

As clearly seen in Fig. 5(a), there exists a maximum efficiency η_{max} as the SOFC temperature is varied between 1073K and 1273K, with T_η denoting the corresponding temperature when the efficiency attains its maximum. On the other hand, the power density of the hybrid system increases monotonically when the SOFC temperature is increased, as presented by the curves in Fig. 5(b). This is due to many reasons. Firstly, increasing the fuel cell temperature enables a greater SOFC power and efficiency, as described by Eqs. (4) and (5). On the other hand, as shown clearly in Fig. 4, the highest temperature of the optimized GT cycle is directly increased by increasing the fuel cell temperature, which in turn results in an increase of the GT efficiency, as can be readily proved from Eq. (13). In addition, a growth in the optimized fuel cell current density can be detected when the SOFC temperature increases according to Fig. 2, thereby leading to an increase in the overall energy input of the hybrid system as illustrated by Eq. (21). However, a larger amount of heat loss from the SOFC to the environment can be expected when the fuel cell temperature increases based on Eq. (11). Conclusively, a higher fuel cell temperature provides not only larger SOFC power but also larger GT power, and thus enables higher system power output.

3.2. Influence of finite-rate heat transfer

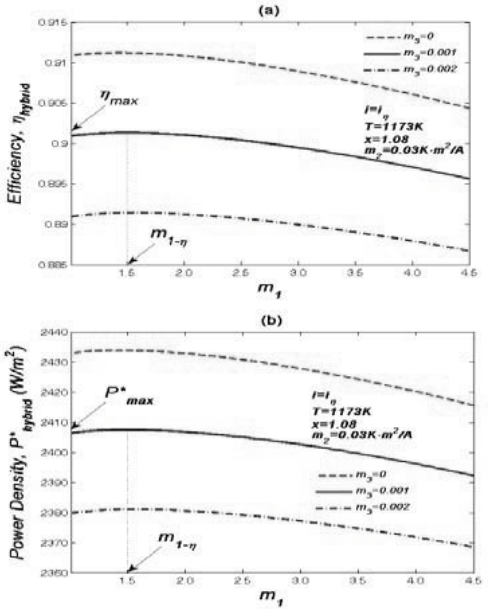

Fig. 6. The curves of system efficiency (a) and power density (b) varying with m_1, where $m_{1-\eta}$ is the value of m_1 at which both the system power output and efficiency attain their maxima.

The effect of irreversibilities due to finite-rate heat transfer on the system performance can be best explained by two parameters, m_1 and m_2. As the ratio of heat transfer coefficients between the gas turbine and the high- and low-temperature reservoirs, $m_1=U_1/U_2$ is a parameter to measure the performance of the GT cycle and is independent of the SOFC subsystem. Fig. 6 shows clearly the effect of m_1 on the power output and efficiency of the hybrid system. Eqs. (21) and (22) enable us to prove that there is a common extremal condition of $\partial\eta_{hybrid}/\partial m_1=\partial P_{hybrid}/\partial m_1=0$ for the hybrid system when Δh° is assumed to be independent of temperature. It implies the fact that there is a

common optimum $m_{1-\eta}$ at which both the power output and efficiency of the hybrid system attain their maxima, as illustrated in Fig. 6.

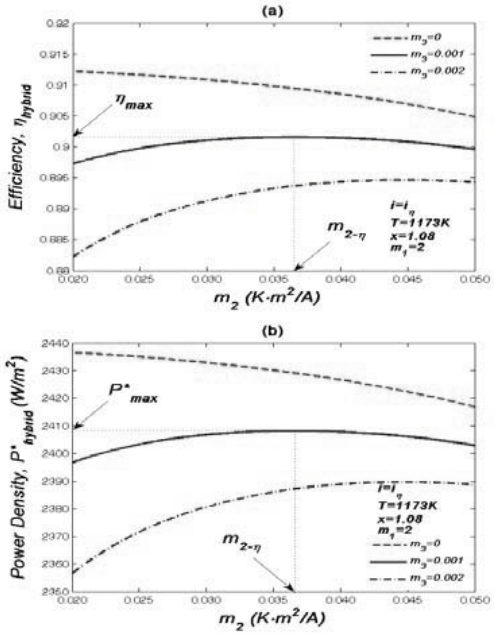

Fig. 7. The curves of system efficiency (a) and power density (b) varying with m_2, where $m_{2-\eta}$ is the value of m_2 at which both the system power output and efficiency attain their maxima.

On the other hand, Fig. 7 shows the variation in the system efficiency and power density with the parameter m_2, which is a synthetic parameter to measure the irreversibility of finite-rate heat transfer in the GT cycle. From Eqs. (21) and (22), it may be easily elucidated that there is a common extremal condition of $\partial\eta_{hybrid}/\partial m_2=\partial P_{hybrid}/\partial m_2=0$ for the hybrid system, which implies a common $m_{2-\eta}$ for the power output and efficiency of the hybrid system. This characteristic is illustrated clearly by the curves in Fig. 7.

3.3. Influence of GT cycle temperature ratio

According to Eqs. (21) and (22), we can further determine the effect of x, which is the temperature ratio of the isobaric processes in the GT cycle, on the system performance. Since the highest temperature of the optimized GT cycle is related to the fuel cell temperature, the variation of the temperature ratio of the GT cycle certainly affects the $T_{2(opt)} \sim T$ curves as illustrated in Fig. 4. It is found that the decrease of x leads to a higher $T_{2(opt)}$. Furthermore, as described in Fig. 8, there is a common optimum x_η at which both the system power output and efficiency attain their maxima, this is due to the existence of the common extremal condition of $\partial\eta_{hybrid}/\partial x=\partial P_{hybrid}/\partial x=0$ for the hybrid system when other parameters are given, as can be proved by using Eqs. (21) and (22).

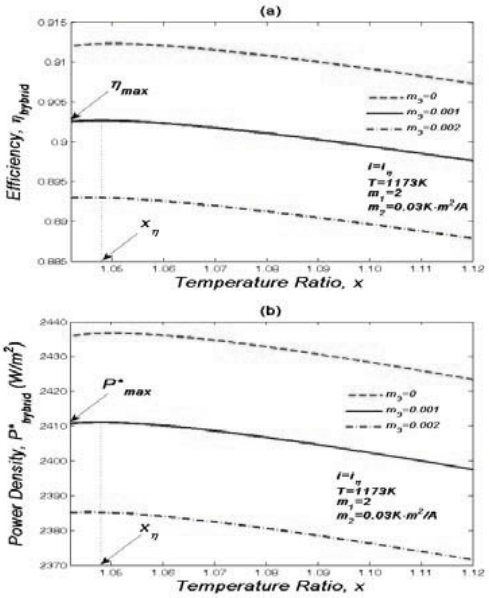

Fig. 8. The curves of system efficiency (a) and power density (b) varying with x, where x_η is the value of x at which both the system power output and efficiency attain their maxima.

3.4. Influence of heat loss

As a synthesized parameter to measure the heat loss irreversibility from the fuel cell to the surroundings and the heat transfer irreversibility in the gas turbine cycle, m_3 can be used to determine the effect of heat loss on system performance. From Eqs. (21) and (22), it can be proved that the power output and efficiency of the hybrid system are monotonically decreasing functions of m_3, as observed from Figs. 5-8. The reason is quite clear. A smaller value of the parameter KA_l and a larger value of the parameter U_1A_h imply the smaller heat loss irreversibility of the SOFC and the heat transfer irreversibility in the GT cycle, thus leads to a smaller value of m_3, and consequently enables a better hybrid performance. Accordingly, different values of m_3 correspond to different quantities of energy released by the system as heat loss to the environment. Therefore the hybrid

systems should be manufactured with the aim of reducing heat loss to achieve better performance.

More conclusions about the effect of heat loss on the system performance characteristics can be made based upon the curves of Figs. 5-8. For example, it is found from Fig. 5(a) that the maximum system efficiency (η_{max}) will increase with the decrease of m_3, while the corresponding SOFC temperature (T_η) will decrease when m_3 is decreased. Moreover, according to Figs. 6 and 7, the maximum efficiency and power output (η_{max} and P_{max}) will increase when m_3 is decreased, and the corresponding parameters $m_{1-\eta}$ and $m_{2-\eta}$ will increase as m_3 is increased. In addition, as shown in Fig. 8, not only η_{max} and P_{max} but also the corresponding x_η will decrease with the increase of m_3. In a word, the system performance depends closely on the heat loss.

Specifically, when the heat loss to the environment is negligible, i.e., $KA_l \to 0$, $m_3 \to 0$, we can obtain a simple system model, and consequently the results obtained above can be simplified. For example, Eqs. (21) and (22) can be further simplified as

$$\eta_{hybrid} = \eta_{fc} + (1-\eta_{fc}) \times \left\{ 1 - \frac{T_4(x-1)}{m_1 \ln v} \left[\frac{1}{im_2(1-\eta_{fc})} - \frac{\ln u}{T_2(1-x^{-1})} \right] \right\} \quad (23)$$

$$P_{hybrid} = -\frac{iA\Delta h^o}{n_e F} \left\langle \eta_{fc} + (1-\eta_{fc}) \times \left\{ 1 - \frac{T_4(x-1)}{m_1 \ln v} \left[\frac{1}{im_2(1-\eta_{fc})} - \frac{\ln u}{T_2(1-x^{-1})} \right] \right\} \right\rangle \quad (24)$$

In such a case, the power output of the system will remain a monotonically increasing function of the fuel cell temperature and there still exists a maximum value for the system efficiency with the increase of temperature as shown by the dotted curves in Fig. 5, while both the system efficiency and power output will become monotonically decreasing functions of the parameter m_2 as described by the dotted curves in Fig. 7. In addition, there still exist maximum values for the system efficiency and power output when the parameter m_1 or x is varied, as shown by the dotted curves in Figs. 6 and 8.

In summary, the parametric study identifies a number of important performance characteristics which became evident after the integration and development of the total system configurations. It is quite necessary to choose the appropriate design and control parameters based on the results obtained to improve the system performance.

4. Conclusions

A theoretical approach is presented to describe and optimize the performance of a SOFC-GT hybrid cycle by means of thermodynamic system modeling and numerical simulation. The model allows the investigation of the important system/component parameters to gain insight into the understanding of their impact on the performance characteristics of the hybrid system. This methodology is also valid for other fuel cell hybrid systems to develop irreversible models suitable for the investigation and optimization of similar energy conversion settings and electrochemistry systems.

The high efficiency predicted in the present paper demonstrates the benefit of such optimization strategy. However, further issues still need to be investigated to determine if such a system is practically feasible, and a more in-depth analysis of the multi-irreversibilities should be performed to see if a better optimization strategy can be found. In addition, more complex system models should be analyzed, considering a larger number of decision variables than actually considered in the present study, and new hybrid configurations will also be explored in our future work.

References

[1] Zhao, Y., Ou, C., Chen, J., 2008, International Journal of Hydrogen Energy, 33, pp. 4161.
[2] Zhao, Y., Chen, J., 2009, Journal of Power Sources, 186, pp. 96.
[3] Y. Zhao, N. Shah, N. Brandon, 2010, Fuel Cells, 10, pp. 181.
[4] Park, S. K., Oh, K. S., Kim, T. S., 2007, Journal of Power Sources, 170, pp. 130.
[5] Park, S. K., Kim, T. S., 2006, Journal of Power Sources, 163, pp. 490.
[6] Barin, I., Knacke, O., 1997, Thermochemical Properties of Inorganic Substances, Springer, Berlin, Germany.
[7] Wang, S., et al., 2007, Journal of Power Sources, 169, pp. 338.
[8] Zhang, L. H., et al., 2006, Journal of Power Sources, 162, pp. 1165.
[9] Campanari, S., Iora, P., 2005, Fuel Cells, 5, pp. 34.
[10] Khan, M. J., Iqbal, M. T., 2005, Fuel Cells, 5, pp. 463.
[11] Bejan, A., 1996, Entropy generation minimization, CRC Press, New York.
[12] Andresen, B., Rubln, M. H., Berry, R. S., 1983, Journal of Physical Chemistry, 87, pp. 2704.
[13] Salamon, P., et al., 2001, Journal of Non-Equilibrium Thermodynamics, 26, pp. 73.
[14] Durmayaz, A., et al., 2004, Progress in Energy and Combustion Science, 30, pp. 175.
[15] Arsalis, A., 2008, Journal of Power Sources, 181, pp. 313.

Acknowledgments: The authors are grateful to the UK Engineering and Physical Sciences Research Council, who supported this work through grant number EP/C522788/2, "Decentralised polygeneration of energy: Cross-disciplinary research at Imperial College London"

The Optimized Fuel cell for Combined Heat & Power Generation (CHP)

Mohammad Ameri[*]*, Mohammad Moulod*

Energy Engineering Department, Power & Water University of Technology (PWUT), Tehran, Iran

Abstract: By optimization of a CHP fuel cell, the cost of electricity production will be reduced significantly. In this paper, the grid connected CHP fuel cell for supplying electrical and thermal loads of Farhangian town located in Boukan city of West Azarbaijan state of Iran is studied as a distributed generation system (DG). With respect to cost of electricity production, the fuel cell can purchase the electrical energy from the grid or it can produce more electrical energy and sell it to the grid if its cost is economical. Moreover, an additional peak load gas heater supports the heat production if the heat from the fuel cell is not sufficient. The amount of electricity transfer between the fuel cell and grid depends on the production costs of electricity and thermal energy in addition to cost of purchased and sold electricity to/from the grid. An objective function has been presented for optimization of this problem. The optimization method is subjected to the some constrains. Some fuel cells in range of 2000-3500 kW have been assumed. The results show that all cases have suitable attractive rate of return and they are economically feasible. Therefore, one can conclude that supplying electrical and thermal loads by fuel cell for that town is a very suitable and economical alternative.

Keywords: Fuel cell, electrical load, thermal load, optimization.

1. Introduction

A fuel cell is an electrochemical "device" that continuously converts chemical energy into electrical energy and heat as long as fuel and oxidant are supplied. In this reaction there is no combustion and thermodynamically fuel cells aren't limited by Carnot efficiency. Thus, they don't produce pollution and they are much more efficient in comparison with an internal combustion engine.

The electricity from renewable energy sources such as wind, solar, hydro and geothermal can be used to produce hydrogen for the fuel cells. Fuel cells have some benefits. For example they are modular. In fact, installation of these units can warrant energy demand as they are reliable, quiet, easy to maintain and safe [1].

In this paper a high temperature solid oxide fuel cell (SOFC) has been used as distributed generation system for supplying electrical and thermal load of 600 home in Farhangian town of Boukan located in West Azarbaijan state of Iran. This type of fuel cell has the characteristic of high performance. It works at high temperature (1000 ˚C). Therefore, it can generate plenty of heat. It can reform fuel internally and therefore the natural gas, as fuel source, can be used for them [2]. Thus, solid oxide fuel cells are very suitable for CHP (combined heat and power) applications [2].

In the next sections an economical model has been presented and it has been solved subject to some constraints. Seven fuel cells in range of 2000-3500kW have been assumed and the model has been solved for all of them. Please note that these fuel cells are not off-the-shelf and the data is not from real units. In order to perform the optimization procedure, the fuel cells in this problem can produce more electrical energy than the demand electrical load. They sell the surplus amount to the electricity grid if it is economic. Also, the fuel cells can produce a portion of total electrical load and purchase the remaining load from the grid if it is economically feasible. The price of purchased electrical energy has been defined as a function of electrical load demand. Fuel cells also produce a lot of thermal energy that is wasted. However, this energy can be used for supplying thermal load, if the produced thermal energy by the fuel cell is lower than thermal load of this 600 home. The natural gas from gas grid can be purchased for supplying thermal load of these homes. The annual income, the rate of return and the payback period have been calculated.

Corresponding Author: Mohammad Ameri, Email: ameri_m@yahoo.com

Based on these data, the best case for supplying electrical and thermal load can be selected.

2. Modelling

In this section a mathematical model for optimization has been defined.

Some factors are economically effective on the model. For example, the amount of produced electrical energy by the fuel cell and subsequently the amount of produced thermal energy, the price of selling and purchasing electrical energy and the price of natural gas will affect the result of model. All of these factors have been formulated in the next section.

2.1 Objective function

In this model, the cost of producing electrical power by fuel cell in each time interval has been calculated as it follows:

$$Co_{pr} = Cn_1 T \sum_j \frac{P_j - P_a}{\eta} \quad (1)$$

The cost of purchasing electrical power from the grid is calculated by the following term:

$$Co_{pu} = C_{el,p} T \sum_j \max(L_{el.j} - P_j, 0) \quad (2)$$

If the electrical energy is more than demand in a time interval, the income of selling electrical energy to the grid can be calculated as the following:

$$In_s = C_{el,s} T \sum_j \max(P_j - L_{el.j}, 0) \quad (3)$$

However, if the produced thermal power by fuel cell is not sufficient to supply the thermal demand, the cost of purchased gas from the gas grid for residential loads will be calculated as it follows:

$$Co_{pg} = Cn_2 T \sum_j \frac{\max(L_{th.j} - P_{th,j}, 0)}{\eta_{th,h}} \quad (4)$$

In this model, the goal is to minimize the variable cost of supplying electrical and thermal loads of these homes. Thus, according to the defined factors, the objective function for optimization of this problem has been estimated:

$$obj = \min(\sum_j \cos t_j - \sum_j Income_j) \quad (5)$$

In this objective function, the target is to minimize the costs of supplying electrical and thermal loads. Therefore, the factors that reduce costs are categorized as income. Moreover, selling surplus electricity to the grid can be classified as income.

2.2 System constraints

The objective function is constrained by fuel cell capacity, ramp rate, minimum up time, minimum down time and maximum number of fuel cell start-stop cycles.

2.3 Model for optimization

This model has been adopted from [3,4]. However, some factors have been changed. For example, the total fuel cell investment cost has been included in the production electricity cost. Also, the income from selling electricity and cost of purchasing natural gas for direct use such as heating, have been accounted in the economical analysis. Moreover, the least rate of return and the attractive rate of return have been calculated.

The model, i.e. the objective function, can be introduced as the following:

$$obj = Cn_1 T \sum_j \frac{P_j - P_a}{\eta} + C_{el,p} T \sum_j \max(L_{el.j} - P_j, 0) - C_{el,s} T \sum_j \max(P_j - L_{el.j}, 0) + Cn_2 T \sum_j \max(L_{th.j} - P_{th,j}, 0) + OM \quad (6)$$

It is subjected to the following constraints:

$$P^{\min} \le P_j \le P^{\max}, \quad (7)$$

$$P_j - P_{j-1} \le \Delta P_U, \quad (8)$$

$$P_{j-1} - P_j \le \Delta P_D, \quad (9)$$

$$(T_{j-1}^{on} - MUT)(U_{j-1} - U_j) \ge 0, \quad (10)$$

$$(T_{j-1}^{off} - MDT)(U_j - U_{j-1}) \ge 0, \quad (11)$$

$$N_{start-stop} \le N^{\max}. \quad (12)$$

For solving this model, the mixed integer nonlinear programming (MINLP) method has been used and the optimization has been performed according to the related code.

3. Case study

In this study the Farhangian town of Boukan in West Azarbaijan state of Iran has been studied. This town has 600 homes and the electrical and

thermal load for these homes has been adopted form Tavanir [5] and National Gas Center of Iran [6] for cold zones respectively. In these references, the per capita consumption of electrical and thermal energy for cold zones has been presented. Based on these data and population of this town, the corresponding loads have been adopted.

For selection of the optimum fuel cell, several fuel cells with different power schemes in range of 2000-3500 kW have been studied and the objective function has been solved for them.

The electrical and estimated thermal loads as a sample data for a typical day (22/09/2008) have been showed in Figs.1 to 2.

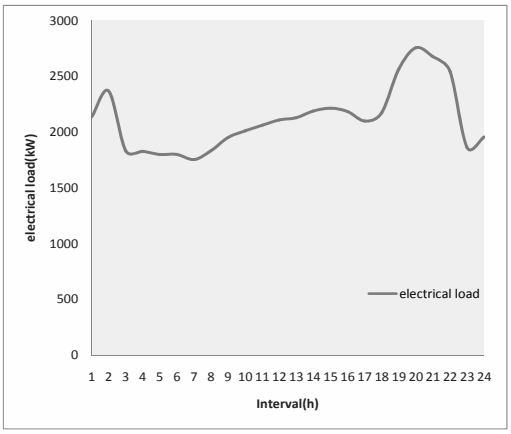

Fig. 1. Electrical load variation for Farhangian town of Boukan city in 22/09/2008 .

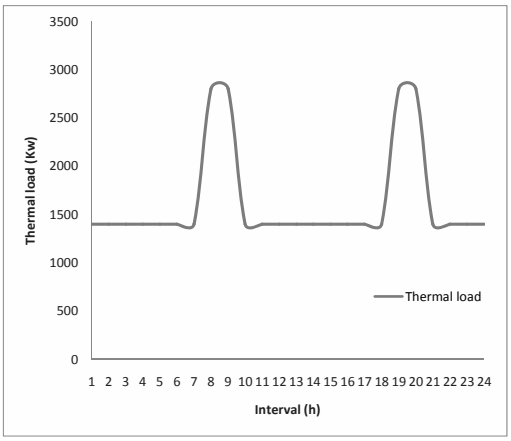

Fig. 2 The estimated thermal load variation for Farhangian town of Boukan city in 22/09/2008.

4. Input data

The input data to solve the model has been prepared in table 1.

The tariff for purchasing electricity is variable and has been assumed as a function of electrical load in order to optimize the electrical energy consumption. This tariff has been assumed as:

$$C_{el,p} = \left[100 + \left(round\left[\frac{L_{el}(T)}{50}\right]\right)\right]/1000. \qquad (13)$$

The tariff for selling electricity is the same tariff that has been promulgated by the energy ministry of Iran for purchasing renewable energy. In this tariff the price for purchasing electricity by energy ministry for peak times is 0.13 US$ and for off-peak times is 0.09 US$ [5].

Table 1. Input data.

Maximum limit of generating power, Pmax (kW)	FC capacity
Minimum limit of generating power, Pmin (kW)	0
Length of time interval, T (h)	1
limit for the ramp rate when increasing, ΔPU (kW/h)	200
limit for the ramp rate when decreasing, ΔPD(kW/h)	300
Price of natural gas for FCPP, Cn_1 (US$/kWh)	0.017
Price of Natural gas, Cn_2 (US$/kWh)	0.017
Minimum up-time, MUT (number of interval)	2
Minimum down-time, MDT (number of interval)	2
Maximum number of start-stop, Nmax	5
Number of intervals	24
Tariff for purchasing electricity, $C_{el,p}$ (US$/kWh)	Eq. 13
Tariff for selling electricity at off peak times, $C_{el,s}$ (US$/kWh)	0.09
Tariff for selling electricity at peak times, $C_{el,s}$ (US$/kWh)	0.13
Operating & maintenance cost, OM (US$/day)	77
η_{th}	30%

In table 1 the Thermal efficiency has been adopted from [2].

5. Results

In this section the result of optimization has been discussed. This model has been solved for the first

sW “TfWh A“uth Wis T‘x.fCfu T fI vfII. lu xWicf “T), Flth), slTIfxfuvf lu vWdWlh[T‘xdx‘s'vh“u “TfIfvbdlvWd“F fx

ahf A“sfI sfhfxAluf. thWb h“F A'vh fIfvbdlvW d“F fx vWi Uf dx‘s'vfs U[T fI vfII Wis h“F A'vh fIfvbdlvWd“F fx.h“' Is Uf d'xvhWfs T‘A cxls Eu .“Af vWf. lb F lII dx‘s'vf A'vh A“xf fIfvbdlvW d“F fx thWi thf fIfvbdlvW I“Ws sfAWis Eu thWb vWf lb F lII .fII thf Wsslh“uW fIfvbdlvWd“F fx b‘ thf cxls

ahf WA“' ub“TfIfvbdlvlh[bxWi.TfxUfhF ffu thf T fI vfII Wis cxls sfdfus. “u thf dx‘s'vh“u v“.b “T fIfvbdlvlh[Wis thfxAW fufxc[lu Wsslh“u b‘ v“.b “Td'xvhWfs Wis .“Is fIfvbdlvlh[b‘ T‘A thf cxls

ahf .WAdIf xf.' Ib T‘x Wh[dlvW sW hWCf Uffu .h“F u lu thf ufqbTlc' xf.

lc .h“F. thWb lu thl. sW thf T fI vfII .' ddIlfs WA“.b thf F h“If fIfvbdlvW I“Ws sfAWis Wis .“Af fIfvbdlvlh[hW Uffu .“Is b‘ thf cxls *“F fCfx .“Af fIfvbdlvlh[hW Uffu d'xvhWfs T‘A thf fIfvbdlvlh[cxls lu .“Af lubfxCW.

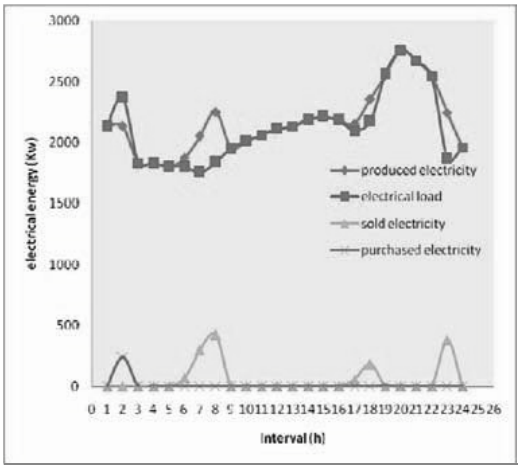

lo eCcGmOsbt nt gHI lNpHt h nt c GsCPfclPps st pT t n La nOCs PCss lh

lc dxf.fub thf thfxAW I“Ws dx‘s'vfs thfxAW fufxc[U[T fI vfII Wis thf WA“' ub“Td'xvhWfs uWb xWcW T‘A thf cW cxls

Eu thl. sW thf thfxAW I“Ws l. A“xf thWi dx‘s'vfs thfxAW fufxc[U[T fI vfII ahfxfT‘xf .“Af uWb xW cW F lII Uf d'xvhWfs T‘A thf cxls T‘x slxfvb'.f hfWluc lu thf.f h“Af. Wis .' ddI[luc thfxAW I“Ws

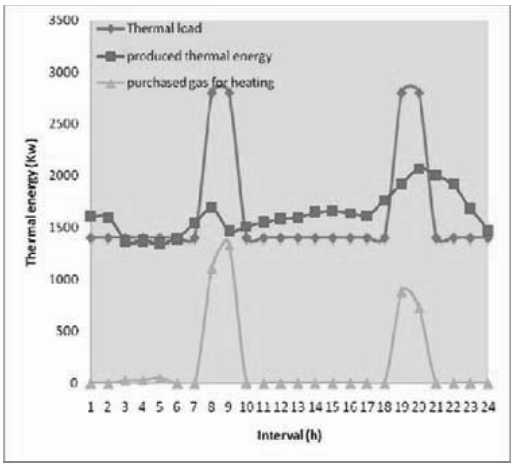

lo eCcGmOsbt nt gHI lNpHt h nt c beCcI ps st pT t n La nOCs PCss lh

lc .h“F. thf v“AdWl.“u “T dx‘s'vluc Wis d'xvhWluc v“.b “T fIfvbdlvW fufxc[Wis luv“Af “T.fIIluc fIfvbdlvW fufxc[lc dxf.fub thf b‘bW v“.b “T.' ddI[luc fIfvbdlvW F lth v“AdWl.“u F lth thf b‘bW v“.b “TthfxAW I“Ws

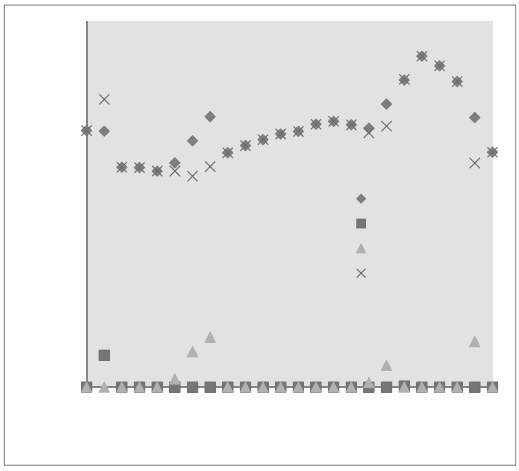

lo eCPt I gpclmt h t nbeCgct TOPHt h GsCPfclPHf Pt mb beCgOcPepmlho GsCPfclPHf Pt mb beClhPt I C nct I mOssIho GsCPfclPHf phT ht lps Pt mbt n mOggsf lho GsCPfclPps st pT

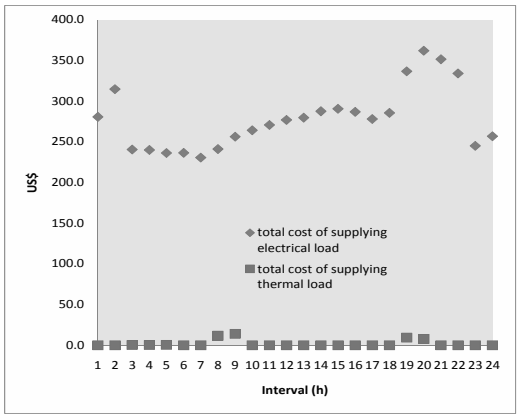

Fig. 6. The total cost of purchasing natural gas from the grid for heating homes in comparison with total cost of supplying electrical load.

6. Economical analysis

Table 2 presents the economical results for a 3500 kW fuel cell before and after optimization for this day (22/09/2008).

Table 2. Results for 3500 kW FC at 2008/09/22 before and after optimization.

Total cost without optimization (US$)	7655
Total cost with optimization (US$)	6802
Net total cost reduction with optimization (US$)	853

The result shows that only for this day it is possible to reduce the cost of supplying electrical and thermal loads by 853US$.

The consumers have to pay for consuming the electrical and thermal energy by the following tariffs:

$$tariff\ \ for\ electrical\ energy = 0.072\,\$/kW \text{ , [5]} \quad (14)$$

$$tariff\ \ for\ thermal\ energy = 0.069\ \$/M^3 \text{ , [6]} \quad (15)$$

Therefore, the total income from selling electrical and thermal energy to the consumers by a 3500 kW fuel cell application at 2008/09/22 can be estimated:

$$total\ income\ at\ 2008/09/22 = 3661\$ \quad (16)$$

The total income and economizing (revenue) from optimization procedure, for the first day of any month, has been calculated and prepared in the table 3. These calculations have been performed for one year as well.

Table 3. Total amount of estimated income plus economizing (revenue) for the application of a 3500 kW FC for one year.

date	Total income + total economizing for first day (US$)	total income + total optimization for any month (US$)
2008/03/20	3516	108987
2008/04/20	3986	123571
2008/05/21	4156	128836
2008/06/21	4494	139315
2008/07/22	4830	149725
2008/08/22	4683	145182
2008/09/22	4514	135411
2008/10/22	4170	125105
2008/11/21	3908	117226
2008/12/21	3972	119166
2009/01/20	4092	122768
2009/02/19	4113	119291
Total income for one year		1534582

In the same way the total annual income plus economizing from optimization for all fuel cells in range of 2000-3500 kW have been calculated and the results have been displayed in table 4.

Table 4. The result of income plus economizing for different fuel cell sizes.

Fuel cell (kW)	Yearly income + economizing (US$)
2000	1277750
2250	1303900
2500	1341532
2750	1387769
3000	1436503
3250	1485676
3500	1534582

Table 5 shows total investment [2], [7] and salvage value for all fuel cell sizes.

Table 5. Economical analysis results for all FC sizes.

FC (kW)	Total investment (US$)	Salvage value (US$)
2000	3640000	364000
2250	4095000	409500
2500	4550000	455000
2750	5005000	500500
3000	5460000	546000
3250	5915000	591500
3500	6370000	637000

By using the data of table 5, the internal rate of return, rate of return and payback period for all cases have been calculated and the results for various fuel cell sizes are given in the table 6.

Table 6. The rate of return and payback period for all fuel cell sizes.

Fuel cell (kW)	IRR	ROR	Pay back period (year)
2000	0.223	0.39	2.564
2250	0.178	0.354	2.83
2500	0.145	0.327	3.05
2750	0.106	0.308	3.25
3000	0.100	0.292	3.42
3250	0.081	0.279	3.58
3500	0.065	0.268	3.74

According to the results in table 6 (rate of return and pay back period) and decelerated inflation rate (12%), the attractive rate of return (AROR) is calculated in table 7.

$$AROR = ROR - Bank\ Interest \quad (17)$$

In year 2008, the bank interest rate is 12% in Iran.

Table 7. Attractive rate of return for all fuel cell sizes.

Fuel cell (kW)	Attractive rate of return
2000	0.27
2250	0.234
2500	0.207
2750	0.188
3000	0.172
3250	0.159
3500	0.148

These results show that all cases have suitable attractive rate of return and all of them are economically feasible.

7. Conclusions

By application of modeling and optimization of the grid connected CHP fuel cell for supplying electrical and thermal loads for Farhangian town of Boukan, the total cost for supplying electrical and thermal load of those homes has been reduced significantly. Several hypothetical fuel cells with different power scheme in range of 2000-3500 kW with the same efficiency and investment cost have been assumed and optimization has been performed for all of them. The total investment cost for all fuel cells including the installation, operating and maintenance, will be paid back in a period from 1.6 to 2.53 years. These results show that supplying electrical and thermal load by fuel cell for those homes is a very suitable and economical alternative. In comparison with the other CHP systems such as gas engine, it is notable that the other CHP systems offer less electric efficiency but lower investment cost rather than fuel cell systems. However, fuel cell systems also have special benefits that were mentioned before. Moreover, it will be an environmental friendly solution as it has a very high efficiency and reduces CO2 emission.

Nomenclature

ΔP_D Limit for the ramp rate when decreasing, (kW/h)

ΔP_U Limit for the ramp rate when increasing, (kW/h)

$C_{el,p}$ Tariff for purchasing electricity, (US$/kW)

$C_{el,s}$ Tariff for selling electricity, (US$/kW)

C_{n1} Price of natural gas for fuel cell, (US$/kW)

C_{n2} Price of natural gas for heating, (US$/kW)

Co_{pr} Cost of producing electrical power, (US$/h)

Co_{pu} Cost of purchasing electrical power from the grid, (US$/h)

Co_{pg} Cost of purchased gas for direct use in houses (i.e. heating), (US$/h)

In_s Income of selling electricity, (US$/h)

$L_{el,j}$ Electrical load demand in interval J, (kW)

$L_{th,j}$ Thermal load demand in interval J, (kW)

MUT Minimum up-time, (number of intervals)

MDT Minimum down-time, (number of intervals)

N^{max} Maximum number of start-stop (number of intervals)

OM Operating and maintenance cost, (US$)

P_a Power of the auxiliary devices in FC stack, (kW)

P_j Produced electrical power in interval j, (kW)

$P_{th,j}$ Produced thermal power in interval j, (kW)

P^{max} Maximum limit of generating power, (kW)

P^{min} Minimum limit of generating power, (kW)

SU Start up cost, (US$)

T^{on} Number of intervals that fuel cell has been on in previous interval, (h)

T^{off} Number of intervals that fuel cell has been off in previous interval, (h)

U On-off status of fuel cell, U=1 stands for running & U=0 stands for stopping.

Greek symbols

η electrical efficiency of fuel cell

$\eta_{th,h}$ Thermal efficiency of heater

$\eta_{th,fc}$ Thermal efficiency of fuel cell

Subscripts and superscripts

AROR Attractive rate of return

FC Fuel cell

IRR Internal rate of return

ROR Rate of return

SOFC Solid oxide fuel cell

References

[1] EG&G technical services, Inc, November 2004, *Fuel Cell Handbook (seventh edition)*, under contract No. DE-AM26-99FT40575, U.S. Department of Energy.

[2] Singhal, S.C. and K. Kendall, eds., 2003, *High Temperature Solid Oxide Fuel Cells: Fundamentals, Design and applications, 1st ed.*, Elsevier Ltd.

[3] M.Y. El-sharkh and A. Rahman and M.S. Alam, 2005, Evolutionary Programming-Based on Methodology for Economical Output Power for PEM Fuel cell for Micro-grid Application, J. Power Sources, vol. 139, No. 1-2, PP. 165-169.

[4] M.Y. El-Sharkh and M. Tanrioven, and A. Rahman and M.S. Alam, 2006, As Study of Cost-Optimized Operation of a Grid-Parallel PEM Fuel Cell Power Plant, IEE Transactions on Power systems, Vol. 21, No. 3.

[5] www.tavanir.org.ir

[6] www.nigc.ir

[7] http://www.netl.doe.gov/publications/press/2009/09018-Fuel_Cell_Exceeds_Goals.html

Optimal Sizing of Residential SOFC Cogeneration Unit for Power Interchange Operation from Energy-saving Viewpoint

Tetsuya Wakui[a] *and Ryohei Yokoyama*[a]

[a] *Department of Mechanical Engineering, Osaka Prefecture University, Osaka, Japan*

Abstract: A power interchange operation, in which electricity generated by multiple residential solid oxide fuel cell (SOFC) cogeneration units is shared among the residences in a housing complex without a reverse power flow to a commercial electric power system, has a high energy-saving effect as compared with stand-alone operations of individual units. In order to further improve its energy-saving effect, the optimal sizing of the SOFC cogeneration unit for the power interchange operation is discussed from the energy-saving viewpoint by conducting optimal operational planning based on mixed-integer linear programming. The analysis for a housing complex with 20 residences located in Japan reveals that the power interchange operation has an advantage over the stand-alone operation in the term of the energy saving for any scale of the SOFC cogeneration unit investigated in this study. Furthermore, its optimal scale for the power interchange operation is determined.

Keywords: Cogeneration, SOFC, Power Interchange, Optimal Sizing, Operational Planning

1. Introduction

Recently, cogeneration applications to improve the efficiency in saving energy have been extended to ordinary residences because small-scale prime movers with high performance, including fuel cells, gas engines, and Stirling engines, have been developed [1]. In particular, fuel cells have attracted attention due to their high electricity generating efficiencies. A residential cogeneration that uses a polymer electrolyte fuel cell (PEFC) has been released [2], and that using a solid oxide fuel cell (SOFC) is being developed [3]. An SOFC, in comparison to a PEFC, has a high electricity generating efficiency and can generate high temperature recovery heat.

The energy-saving effect obtained by utilizing a residential SOFC cogeneration unit (abbr. R-FCGU) has been studied. Cockroft and Kelly clarified the performance level of an R-FCGU required to reduce the CO_2 emission by means of a numerical analysis on dwellings in UK [4]. Alanne et al. examined the financial feasibility of R-FCGUs of 1 to 5 kW in single-family dwellings in Canada [5]. Furthermore, Hawkes and Leach reported the reduction effect of the CO_2 emission obtained by conducting the optimal operational planning for a 2-kW R-FCGU [6]. These studies premise that R-FCGUs can reverse surplus electricity to commercial electric power systems; thus, they can be operated in response to variations in demand for heat. However, in Japan, the reverse power flow by residential cogenerations is prohibited. Therefore, R-FCGUs in Japan must be downsized and operated in response to variations in demand for electricity. This means that R-FCGUs in Japan are often operated at partial loads with low electricity generating efficiencies. Moreover, R-FCGUs have the following operational restrictions: a continuous operation due to a long warm-up time for a high operating temperature and a minimum electric output for its stable operation. These restrictions force surplus electricity to be consumed as heat. Hence, the actual energy-saving effects of R-FCGUs used in Japan might fail to reach their potential.

On the basis of this background, the authors focus on a power interchange operation of multiple R-FCGUs in a housing complex (abbr. IC). In the IC, electricity generated by R-FCGUs is shared among the residences in a housing complex without a reverse power flow to a commercial electric power system. Because the surplus electricity generated at residences with a low demand for electricity can be transmitted to other residences that have a higher demand for electricity, the load factor of the R-FCGUs can be improved. Our feasibility study on the IC using the R-FCGUs with the rated electric output of 0.7 kW [7] has revealed that an operational strategy to meet total electric demand in a housing complex by the electric output of the R-FCGUs as much as possible is suitable from the energy-saving viewpoint.

Corresponding Author: Tetsuya Wakui, Email: wakui@ese.me.osakafu-u.ac.jp

In this further feasibility study, the optimal sizing of the R-FCGU for the IC, which adopts the aforementioned operational strategy, is discussed from the energy-saving viewpoint. The energy-saving effect of the IC for various scales of the R-FCGU is analyzed by conducting optimal operational planning based on mixed-integer linear programming. The analysis for a housing complex with 20 residences located in Japan on the representative day of each month reveals a high energy-saving effect of the IC as compared with the stand-alone operation for any scale of the R-FCGU investigated in this study and its optimal scale for the IC.

2. System configurations

A schematic of the IC is shown in Fig. 1. Each residence in a housing complex has the R-FCGU, an electric water heater (abbr. EH), a storage tank (abbr. ST), a radiator (abbr. RD), and a gas-fired water heater (abbr. GH). Electricity and hot water are considered to be the energy demands of the residences because space cooling and heating are supplied by electric air conditioners installed in each residence. The following analysis premises that the same-scale R-FCGU is installed at any residence.

Electricity generated by the R-FCGUs is shared among the residences without a reverse power flow to a commercial electric power system. Thus, electricity is supplied to the residences by operating the R-FCGUs and by purchasing electricity from an electric power company. Exhaust heat from the SOFC is recovered in the form of hot water and then stored in the ST. Surplus electricity is utilized at the EH; the hot water generated by the EH is also stored in the ST. The hot water in each ST is independently consumed at each residence. Since the R-FCGUs are continuously operated, surplus hot water is wasted at the RD when the ST is full. The shortage of hot water supply from the ST is compensated for by the supply of the hot water from the GH.

Furthermore, two additional residential energy supply configurations are considered to evaluate the energy-saving effect of the IC. The first is a stand-alone operation of individual R-FCGU without a power interchange among the residences and without the reverse power flow (abbr. SA); this is the only permissible operation method of residential cogenerations in Japan. The second is a conventional energy supply system without the R-FCGU (abbr. CO); at each residence, electricity is purchased from the electric power company, and hot water is supplied from the GH.

3. Optimal operational planning problem for various system scales

In order to discuss the optimal sizing of the R-FCGU for the IC from the energy-saving viewpoint, the optimal operational planning problem based on mixed-integer linear programming, which has been developed in [7], is applied to various scales of the R-FCGU. The optimal operation patterns including operation statuses of the system components, energy flow rates, and stored heat are determined to minimize primary energy consumption subject to the satisfaction of energy demand requirements. Since the details of the optimal operational planning problem have been described in [7], only its summary is provided here.

3.1. Mathematical formulation

The intended housing complex has N residences; the index for the residences is designated by n, i.e.,

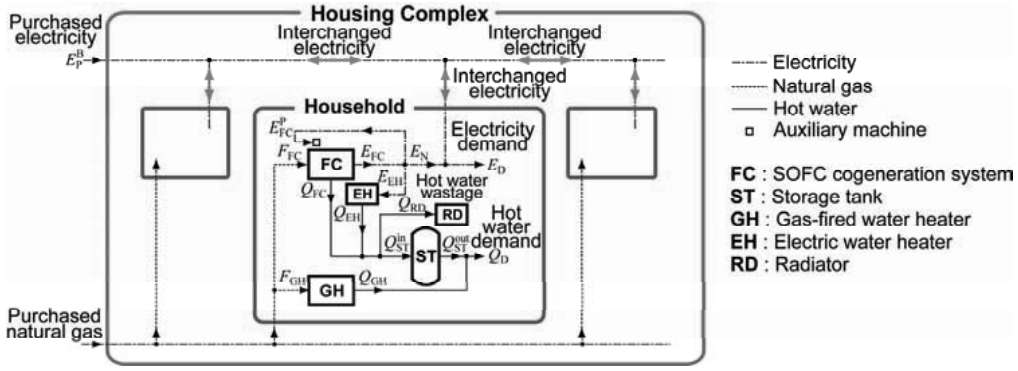

Fig. 1. Schematic of power interchange operation using multiple R-FCGUs in housing complex.

n = 1, 2, ···, N. To consider the seasonal and hourly changes in the energy demands, a typical year is divided into M representative days; the index for the representative days is designated by m, i.e., m = 1, 2, ···, M. Moreover, each representative day is divided into K sampling times with a period of Δt, i.e., $\Delta t = 24/K$; the index for the sampling times is designated by k, i.e., k = 1, 2, ···, K. The optimal operation pattern of an R-FCGU and ST cannot be determined independently for each sampling time. Thus, a daily cyclic operation, assuming that the energy demands change cyclically with a period of 24 h on each representative day, is considered.

3.1.1. Decision variables

The decision variables are composed of binary and continuous variables. The binary variables express the on-off status of the system components. The continuous variables express the energy flow rates of the input and output of the system components and the heat stored in the ST.

3.1.2. Objective function

From the energy-saving viewpoint, the objective function to be minimized is the total daily primary energy consumption of the intended residences on each representative day. The definition of the total daily primary energy consumption depends on the energy supply configurations. For the IC, the objective function, J_{IC}, on the mth representative day is expressed by the following equation:

$$J_{IC}(m) = \varphi_E \sum_{k=1}^{K} E_P^B(k,m)\Delta t + \varphi_G \sum_{k=1}^{K}\left\{\sum_{n=1}^{N} F_{FC}(n,k,m) + \sum_{n=1}^{N} F_{GH}(n,k,m)\right\}\Delta t \quad (m = 1,2,\cdots,M) \quad (1)$$

where φ_E and φ_G denote the conversion factors for the primary energy of purchased electricity and natural gas, respectively; F_{FC} and F_{GH} denote the natural gas consumption of the R-FCGU and GH, respectively; and E_P^B denotes the electricity purchased in bulk. For the SA, the objective function, J_{SA}, on the mth representative day is expressed by the following equation:

$$J_{SA}(m) = \varphi_E \sum_{k=1}^{K}\sum_{n=1}^{N} E_P^I(n,k,m)\Delta t + \varphi_G \sum_{k=1}^{K}\left\{\sum_{n=1}^{N} F_{FC}(n,k,m) + \sum_{n=1}^{N} F_{GH}(n,k,m)\right\}\Delta t \quad (m = 1,2,\cdots,M) \quad (2)$$

where E_P^I denotes the electricity purchased individually at each residence. For the CO, the objective function, J_{CO}, on the mth representative day is expressed by the following equation:

$$J_{CO}(m) = \varphi_E \sum_{k=1}^{K}\sum_{n=1}^{N} E_P^I(n,k,m)\Delta t + \varphi_G \sum_{k=1}^{K}\sum_{n=1}^{N} F_{GH}(n,k,m)\Delta t \quad (m = 1,2,\cdots,M) \quad (3)$$

3.1.3. Constraints

The constraints in this optimal operational planning problem consist of the performance characteristics of the system components and the energy balance and supply-demand relationships. These constraints are expressed by linear equations.

First, the performance characteristics of the system components are summarized. The input-output relationships of the R-FCGU and GH, which can operate at partial loads, are formulated by considering their minimum and maximum outputs. Moreover, the on-off statuses of the EH and RD are expressed by the binary variables. For the ST, the heat balance relationship including the heat loss is considered by the difference equation between two consecutive sampling times. The capacity of the ST is also considered. Further, based on the assumption of the daily cyclic operation, the heat stored in the initial state of a residence is considered to be equal to that stored in the terminal state on each representative day.

Second, the energy balance and supply-demand relationships for electricity and hot water are considered. Those for electricity depend on the energy supply configurations [8]. For the IC, they are considered in the housing complex; for the SA and CO, they are considered at each residence. On the other hand, for hot water, they are considered at each residence in any energy supply configuration.

3.2. Solution method

The optimal operational planning problem formulated in the previous section results in a mixed-integer linear programming problem. This is solved by the GAMS (General Algebraic Modeling System)/CPLEX solver [9], which is a general-purpose solver that combines the branch and bound method with the simplex method for large-sized problems.

4. Numerical Study

The input data for the aforementioned problem are described. Then, the energy-saving effect of the IC for various scales of the R-FCGU is analyzed by conducting the optimal operational planning.

4.1. Input data

4.1.1. Performance characteristic values of system components

The scale of the R-FCGU is represented by its rated electric output. In this study, it is assumed that the rated electric output of the R-FCGU is proportional to the number of the stacks connected in parallel. As a result, the electricity generating and heat recovery efficiencies can be considered to be constant at any rated electric output. At the rated load, the electricity generating and heat recovery efficiencies calculated by using the lower heating value of natural gas (LHV) are 43% and 33%, respectively [7]; the minimum electric output is 28 % of the rated one. The R-FCGUs with the rated electric output ranging from 0.2 kW to 1.5 kW are investigated. The capacity of the ST (30 MJ), the heating efficiency of the EH (90%), and the thermal efficiency of the GH calculated by using the LHV (88%) are constant at any rated electric output of the R-FCGU.

4.1.2. Residential energy demands

The investigated housing complex is located in the Kansai region of Japan, and it has 20 residences, i.e., N = 20. The demands for electricity and hot water of the 20 residences have been measured by Tsuji et al. [10]. The energy demands are estimated at 24 sampling times for a representative day of each month, i.e., M = 12, K = 24, and Δt = 1 h. The characteristics of the energy demands are summarized as follows [8]: the energy demands are less than those for typical detached houses in Japan; the hourly demand for electricity is increased in the morning and nighttime at any residence, although the maximum electricity demands differ widely among 20 residences; and the hourly demand for hot water is concentrated in the nighttime at any residence.

The authors consider the total daily heat to power demand ratio of the intended residences, *THPR,* to be the dominant characteristic of the residential energy demands that affects the energy-saving effect of the IC [8]. The total daily heat to power demand ratio on the mth representative day is defined by the following equation:

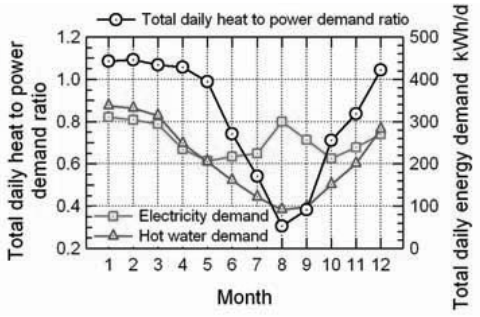

Fig. 2. Residential energy demand characteristics on representative day of each month.

$$THPR(m)=\frac{\sum_{k=1}^{K}\sum_{n=1}^{N}Q_{\mathrm{D}}(n,k,m)\Delta t}{\sum_{k=1}^{K}\sum_{n=1}^{N}E_{\mathrm{D}}(n,k,m)\Delta t}\quad (m=1,2,\cdots,M),(4)$$

where E_{D} and Q_{D} denote the demands for electricity and hot water, respectively. Fig. 2 shows the total daily heat to power demand ratio and total daily demands for electricity and hot water of the 20 residences on the representative day of each month. The detail analysis focuses on the representative days for the following three months: August with the lowest total daily heat to power demand ratio (*THPR* = 0.3); November with a medium one (*THPR* = 0.85), which is almost equal to its annual mean value; and February with the highest one (*THPR* = 1.1).

4.1.3. Conversion factors for primary energy

The conversion factors for the primary energy of purchased electricity and natural gas are listed in Table 1. For purchased electricity, the thermal power average conversion factor defined in the Law Concerning the Rational Use of Energy of Japan is introduced; this is calculated by considering thermal power generations as power regulator to load variations in commercial electric power systems.

Table 1. Conversion factors for primary energy.

Energy source	Value
Purchased electricity	φ_{E} = 9.83 MJ/kWh
Natural gas [11]	φ_{G} = 45.0 MJ/m^3

4.2. Results and discussion

4.2.1. Scale effect of R-FCGU on energy saving on three representative days

The energy-saving effect of the IC on the various scales of the R-FCGU is analyzed. By considering

the SA and CO as reference cases, the reduction rate of the total daily primary energy consumption of the intended residences from the CO to the IC (hereafter referred to as CO-to-IC reduction rate), $\alpha_{IC/CO}$, and that from the SA to the IC (hereafter referred to as SA-to-IC reduction rate), $\alpha_{IC/SA}$, on the mth representative day are defined as follows:

$$\alpha_{IC/CO}(m)=\frac{J_{CO}(m)-J_{IC}(m)}{J_{CO}(m)} \quad (m=1,2,\cdots,M), \quad (5)$$

$$\alpha_{IC/SA}(m)=\frac{J_{SA}(m)-J_{IC}(m)}{J_{SA}(m)} \quad (m=1,2,\cdots,M). \quad (6)$$

A positive reduction rate indicates that energy is saved by the IC. The relationship between the rated electric output of the R-FCGU and the two reduction rates of the total daily primary energy consumption of the 20 residences on the three representative days is shown in Fig. 3.

First, the CO-to-IC reduction rate has a maximum value on any representative day. The rated electric output that shows the maximum CO-to-IC reduction rate increases in the following order: August (0.4 kW), November (0.6 kW), and February (0.8 kW). The maximum CO-to-IC reduction rates on the representative days of November and February are almost the same value, while that on the representative day of August is much smaller than those on the representative days of November and February. Second, the SA-to-IC reduction rate has a positive value at any rated electric output on any representative day; this result shows the advantage of the IC over the SA in terms of the energy saving. Moreover, in small-scale R-FCGUs, the SA-to-IC reduction rate is increased with the rated electric output on any representative day; however, the increase in the SA-to-IC reduction rate saturates at the rated electric output larger than 0.6 kW and 0.7 kW on the representative day of August and February, respectively. On the other hand, the SA-to-IC reduction rate on the representative day of November has the maximum value at the rated electric output of 0.7 kW.

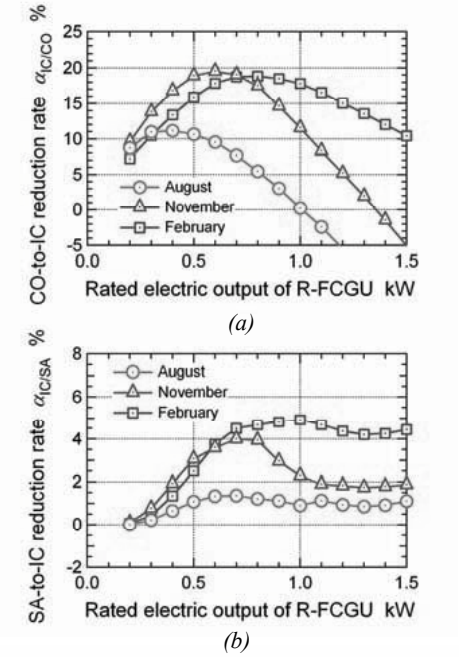

Fig. 3. Scale effect of R-FCGU on two reduction rates of total daily primary energy consumption on three representative days: a) CO-to-IC reduction rate, b) SA-to-IC reduction rate

4.2.2. Dominant factor of scale effect of CO-to-IC reduction rate

In order to clarify the dominant factor of the scale effect of the CO-to-IC reduction rate shown in Fig. 3(a), the following four performance criteria for the R-FCGUs under the IC on the mth representative day are focused on: an electric load factor, U_E, electric supply proportion, P_E, hot water utilization efficiency, η_Q, and hot water supply proportion, P_Q. They are defined as follows:

$$U_E(m)=\frac{\sum_{n=1}^{N}\sum_{k=1}^{K}E_{FC}(n,k,m)\Delta t}{NK\overline{E}_{FC}\Delta t} \quad (m=1,2,\cdots,M), \quad (7)$$

$$P_E(m)=\frac{\sum_{n=1}^{N}\sum_{k=1}^{K}E_N(n,k,m)\Delta t}{\sum_{k=1}^{N}\sum_{k=1}^{K}E_D(n,k,m)\Delta t} \quad (m=1,2,\cdots,M), \quad (8)$$

$$\eta_Q(m)=\frac{\sum_{n=1}^{N}\sum_{k=1}^{K}\{Q_{FC}(n,k,m)-Q_{RD}(n,k,m)\}\Delta t}{\sum_{k=1}^{N}\sum_{k=1}^{K}Q_{FC}(n,k,m)\Delta t} \quad (m=1,2,\cdots,M), \quad (9)$$

$$P_Q(m)=\frac{\sum_{n=1}^{N}\sum_{k=1}^{K}Q_{ST}^{out}(n,k,m)\Delta t}{\sum_{k=1}^{N}\sum_{k=1}^{K}Q_D(n,k,m)\Delta t} \quad (m=1,2,\cdots,M), \quad (10)$$

where E_{FC}, E_N, and $\overline{E}_{FC}$ denote the electric output, net electric output subtracting the electricity consumed at the EH and water pump, and rated

electric output of the R-FCGU, respectively; and Q_{FC}, Q_{RD}, and Q_{ST}^{out} denote the hot water output of the R-FCGU, heat flow rate of hot water wasted at the RD, and hot water output from the ST, respectively. The relationship between the rated electric output of the R-FCGU and the four performance criteria on the three representative days is shown in Fig. 4.

On any representative day, P_E and P_Q are increased with the rated electric output; this means that the purchased electricity and hot water supply from the GH are reduced in large-scale R-FCGUs. As a result, in small-scale R-FCGUs, the CO-to-IC reduction rate is increased with the rated electric output. On the other hand, in large-scale R-FCGUs, U_E is decreased with the increase in the rated electric output due to their partial load operations. η_Q is also decreased due to the wastage of the surplus hot water on the representative days of August and November. These results decrease the CO-to-IC reduction rate in large-scale R-FCGUs. Since the scale effect of the four performance criteria varies according to the representative day, the rated electric output that shows the maximum value of the CO-to-IC reduction rate depends on the representative day.

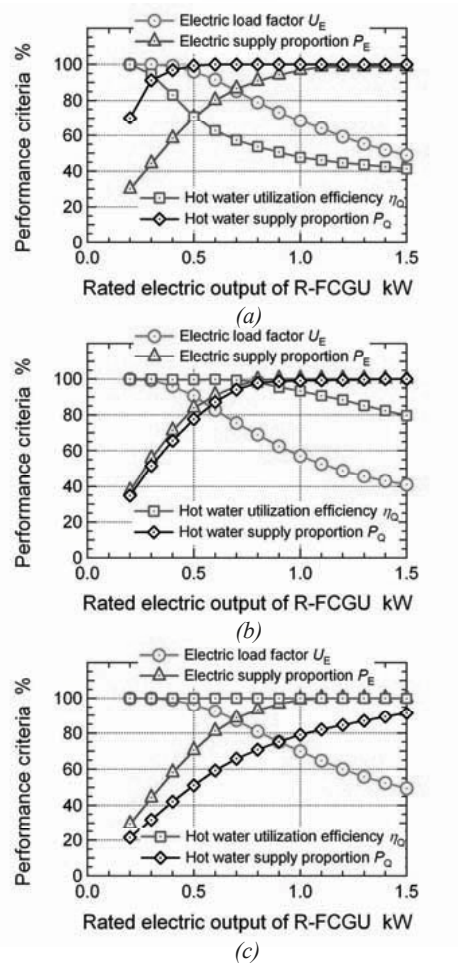

Fig. 4. Scale effect of R-FCGU on performance criteria on three representative days: a) August, b) November, c) February

On the representative day of August where the total daily heat to power demand ratio is smaller than the heat to power supply ratio of the R-FCGU (0.767), P_Q becomes 100% at the rated electric output of 0.5 kW; this means that all the demand for hot water can be met by the hot water output of the R-FCGU. However, η_Q remains at 70%. Thus, the R-FCGU with the rated electric output of 0.4 kW, at which P_Q is slightly smaller than 100% but η_Q becomes over 80%, has the maximum CO-to-IC reduction rate.

On the representative day of November, the total daily heat to power demand ratio is close to the heat to power supply ratio of the R-FCGU. Thus, both P_E and P_Q become 100% at the rated electric output of 0.8 kW. Moreover, on the representative day of February where the total daily heat to power demand ratio is larger than the heat to power supply ratio of the R-FCGU, P_E becomes 100% at the rated electric output of 1.0 kW. However, at those rated electric outputs, U_E remains at 70%. Thus, the R-FCGUs with the rated electric output of 0.6 kW and 0.8 kW, at which P_E and P_Q are smaller than 100% but U_E becomes over 80%, have the maximum CO-to-IC reduction rates on the representative day of November and February, respectively.

4.2.3. Dominant factor of scale effect of SA-to-IC reduction rate

In order to clarify the dominant factor of the scale effect of the SA-to-IC reduction rate shown in Fig. 3(b), the performance criteria ratios for the electric load factor, U_E^*, hot water utilization efficiency, η_Q^*, and hot water supply proportion, P_Q^*, are focused on; they are defined as the ratio of the results for the IC to those for the SA. Fig. 5 shows the relationship between the rated electric output of the R-FCGU and the three performance criteria ratio on the three representative days.

First, U_E^* has the maximum value at the rated electric output of 0.6 kW, 0.5 kW, and 0.7 kW on

the representative day of August, November, and February, respectively. The increase in U_E^* is due to the increase in the operating time of the R-FCGUs at their partial loads under the SA; this result increases the SA-to-IC reduction rate with the rated electric output in small-scale R-FCGUs. On the other hand, the decrease in U_E^* is because large-scale R-FCGUs under the IC also operate at their partial loads.

On the representative day of August, η_Q^* is decreased with the increase in U_E^* in small-scale R-FCGUs; however, the SA-to-IC reduction rate is increased with the rated electric output. This is because the energy saved due to the increase in U_E^* surpasses the energy increased due to the decrease in η_Q^*. In the R-FCGUs with the rated electric output larger than 0.6 kW, η_Q^* is increased due to the increase in the wastage of the surplus hot water of the R-FCGUs under the SA as compared with that under the IC. Since the energy saving due to the increase in η_Q^* counterbalances the energy increase due to the decrease in U_E^*, the SA-to-IC reduction rate has almost the same value at the rated electric output larger than 0.6 kW.

As shown in Fig. 3(b), the increase in the SA-to-IC reduction rate on the representative day of February also saturates at the rated electric output of 0.7 kW due to the same reason as on the representative day of August. However, the saturated value of the SA-to-IC reduction rate on the representative day of February is much higher than that on the representative day of August. This is because η_Q^* on the representative day of February is larger than unity at any rated electric output unlike the result on the representative day of August.

On the representative day of November, P_Q^* is decreased in the R-FCGUs with the rated electric output larger than 0.7 kW. This is because in the large-scale R-FCGUs, P_Q of the IC becomes 100% but P_Q of the SA is still increased. The decrease in both U_E^* and P_Q^* causes the decrease in the SA-to-IC reduction rate in the large-scale R-FCGUs.

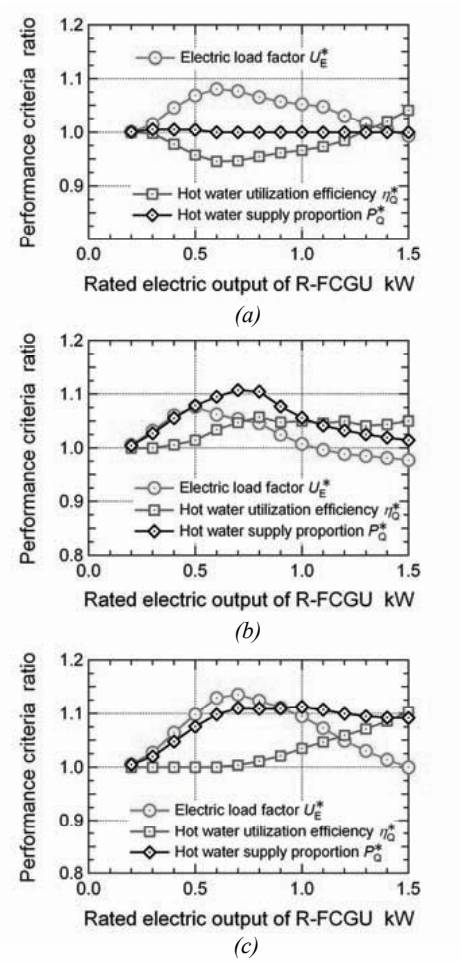

Fig. 5 Scale effect of R-FCGU on performance criteria ratio on three representative days: a) August, b) November, c) February

4.2.4. Scale effect of R-FCGU on energy saving for a year

Finally, the scale effect of the R-FCGU on the energy saving for a year is discussed. Fig. 6 shows the relationship between the rated electric output of the R-FCGU and the two reduction rates of annual primary energy consumption, which is defined as the total primary energy consumption of the 12 representative days.

First, the CO-to-IC reduction rate has the maximum value of 17% at the rated electric output of 0.6 kW. The optimal scale of the R-FCGU derived from the result for the year coincides with

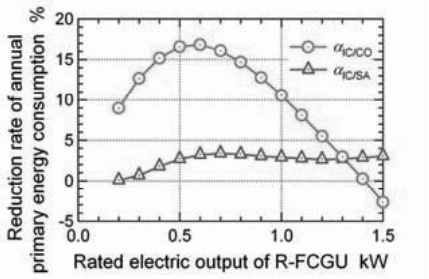

Fig. 6. Scale effect of R-FCGU on two reduction rates of annual primary energy consumption.

that derived from the result on the representative day of November because both the total heat to power demand ratios are almost equal as described in subsection 4.1.2. Second, the SA-to-IC reduction rate has a positive value at any rated electric output and its increase reaches the ceiling of around 3% at the rated electric output of 0.7 kW. This rated electric output coincides with that with the maximum value of the SA-to-IC reduction rate on the representative day of November. The saturation of the increase in the SA-to-IC reduction rate in the large-scale R-FCGUs is affected by the results on the other representative days including August and February.

5. Conclusion

To discuss the optimal sizing of the R-FCGU for the IC from the energy-saving viewpoint, the optimal operational planning based on mixed-integer linear programming has been carried out for various scales of the R-FCGU. The results obtained through the analysis for a housing complex with 20 residences located in Japan on the representative day of each month are summarized as follows:

- In small-scale R-FCGUs, the energy-saving effect of the IC to the CO depends on the proportions of the generated electricity and hot water to their total demands, whereas in large-scale R-FCGUs, it is dominated by the electric load factor and wastage of the surplus hot water.
- The energy-saving effect of the IC to the SA is governed by the electric load factor and wastage of the surplus hot water. It should also be noted that large-scale R-FCGUs under the IC reduce the wastage of the surplus hot water as compared with those under the SA.

By considering these scale effects of the R-FCGUs on the energy saving, the following conclusions are derived:

- The IC has an advantage over the SA at any scale; however, this advantage saturates in large-scale R-FCGUs.
- The R-FCGU with the rated electric output of 0.6 kW is the optimal scale for the IC in terms of the energy saving.

The rated electric output of the R-FCGU that is currently under development in Japan is 0.7 kW [3]; however, there is little difference from the energy-saving effect of the optimal scale R-FCGU derived in this study. Thus, the R-FCGU under development is also effective for the IC.

References

[1] Paepe, M.D., et al., 2006, Micro-CHP systems for residential applications, Energy Conversion and Management, 47(18-19), pp. 3435-3446.

[2] Tokyo Gas Co., 2004, Press release. URL: http://www.tokyo-gas.co.jp/Press_e/20041206-2e.pdf

[3] Kyocera Corporation, 2007, Press release. URL: http://global.kyocera.com/news/2007/0201.htm

[4] Cockroft, J., and Kelly, N., 2006, A comparative assessment of future heat and power sources for the UK domestic sector, Energy Conversion and Management, 47(15-16), pp. 2349-2360.

[5] Alanne, K., et al., 2006, The financial viability of an SOFC cogeneration system in single-family dwelling, Journal of Power Source, 158(1), pp. 403-416.

[6] Hawkes, A. D., and Leach, M. A., 2007, Cost-effective operating strategy for residential micro-combined heat and power, Energy, 32(5), pp. 711-723.

[7] Wakui, T., Yokoyama, R., and Shimizu, K., 2010 Suitable operational strategy for power interchange operation using multiple residential SOFC cogeneration systems, Energy, 35(2), pp. 740-750.

[8] Wakui, T., et al., 2008, Feasibility study on power interchange operation of multiple household gas engine cogeneration units by an optimization approach, Journal of environment and Engineering, 3(2), pp. 272-284.

[9] GAMS/CPLEX, 2008, Software package, Ver. 22.9, GAMS Development Corp., Washington, D.C.

[10] Tsuji Laboratory, 2007, Monitored Energy Data for Residential Houses in Kansai Region 1998-2005, Technical report, Osaka University, Japan.

[11] Tokyo Gas Co., 2004, Environmental performance data. URL: http://www.tokyo-gas.co.jp/csr/report_e/environment/pdf/performancedata.pdf

Acknowledgments: This study has been conducted on the basis of the achievement of the collaborative project with Osaka Gas Co., Ltd. in 2005 and 2006.

Entropy Generation Minimization for the Optimal Design of the Fluid Distribution System in a Circular MCFC

Adriano Sciacovelli[a], *Vittorio Verda*[a]

[a] *Politecnico di Torino Dip. Energetica, Torino, Italy*

Abstract: In this paper, the prototype of a circular Molten Carbonate Fuel Cell (MCFC) built in the laboratories of Fabbricazioni Nucleari (FN) is analyzed using a tridimensional computational fluid dynamic (CFD) model. This model considers heat, mass and current transfer as well as chemical and electrochemical reactions. The results show that some inhomogeneous distributions in the reactants, causing non optimal use of the reactant surfaces, take place.
An effective way to improve the distribution in current density consists in tracing tree shaped channels on the surface onto the distribution porous medium. A preliminary study on the effectiveness of such technical solution is investigated considering a network model of the fluid flow in the porous medium and the channels. Then the optimal shape of distribution channels is investigated considering some geometrical parameters identifying their topology and length as the independent design variables. Minimum entropy generation is considered as the objective function.
The results show that significant improvements in the current density can be achieved.

Keywords: Molten Carbonate Fuel Cell, Entropy Generation, Optimization.

1. Introduction

Among high temperature fuel cells, Molten Carbonate Fuel Cells (MCFC) have reached nowadays an advanced industrial development. In particular, the integration of this technology with microturbines, which represents a major option for future distributed generation, has been already obtained in various full scale demonstration plants [1]. Despite these results, large efforts are still required to improve performances and reliability and to reduce costs.
This paper is focused on the fuel cell performance improvements through re-design of the fuel distribution, with the aim of maximizing the homogeneity of the reactants concentration on the active surfaces. The analysis is conducted using a CFD model and is applied to a circular shaped fuel cell prototype. The model results are presented for the current design of the distribution system in order to show the inefficiencies and to define possible ways to improve it. The optimization is then conducted by modifying the configuration of the distribution system inside the cell. A fluid network model is used to select the configuration, then the system optimization is conducted using the CFD model. The entropy generation analysis is used as the tool for system optimization.

2. Nomenclature

$D_{i,eff}$	Effective binary diffusivity
E	Total energy (J/kg)
h	Specific enthalpy (J kg^{-1})
i	Current density (A/m^2)
$\vec{J}_i$	Diffusive flux of species *i* (kg m^{-2} s^{-1})
$\vec{J}_q$	Heat flux (W m^{-2})
K	Permeability (m^2)
k	Thermal conductivity (W m^{-1} K^{-1})
p	Pressure (Pa)
R	Universal gas constant (W mol^{-1} K^{-1})
S_i	Species source term (kg m^{-3} s^{-1})
S_h	Heat source term (W m^{-3} s^{-1})
s_i	Specific entropy of species *i*
g_p	Entropy generation per unit volume (W m^{-3} K^{-1})
T	Temperature (K)
$\vec{V}$	Velocity vector (m s^{-1})
V	Voltage (V)
Greek symbols	
Φ	
β	
Δ	Strain tensor (s^{-1})
ε	porosity
μ	Viscosity (m s^{-2})
μ_i	Chemical potential of species *i*
ρ	Density (kg m^{-3})
σ	Electric conductivity (Ω^{-1} m^{-1})
$\vec{\sigma}$	Entropy flux
ω_i	Mass fraction of species *i*
Subscripts	
μ	Fluid friction entropy generation
h	Heat transfer entropy generation
m	Mass transfer entropy generation
c	Heat – mass transfer entropy generation

3. System geometry

Figure 1 shows a schematic of FN circular shaped fuel cell. A cross section (A-A) is shown in Figure 2. The cell consists of an external supporting structure in stainless steel, where axial stack distribution channels are obtained, and the fuel cell. 16 distribution channels are used to supply reactants to the cell (4 channels for fuel supply and 4 channels for air supply) and to evacuate the corresponding exhaust flows (4 channels for depleted fuel evacuation and 4 channels for exhaust air evacuation). The fuel cell consists of 9 functional layers plus 2 external supporting layers in stainless steel. Starting from the top, the first functional layer is a porous distribution channel where fuel enters from four radial holes at 90°.
This fluid distribution system allows one to create stacks by simply laying the desired number of cells upon.

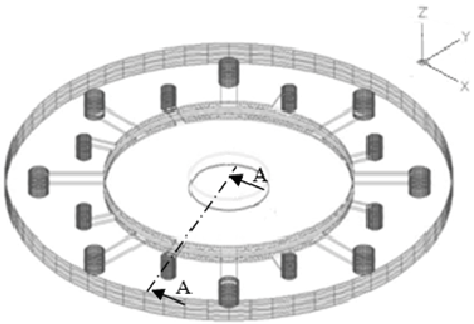

Figure 1. Schematic of a single fuel cell

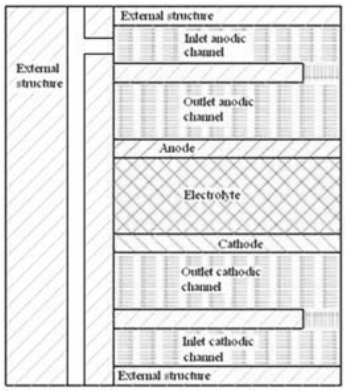

Figure 2. Cross section A-A of the fuel cell.

The fuel in this layer flows from the periphery towards the center. The second layer is a stainless steel plate; some axial holes are obtained in the central part in order to allow the fuel to flow through and reach the lower layer. In the third layer, named as outlet anodic channel in Figure 2, fuel flows from the center towards the periphery and permeates the porous anode (fourth layer). As the thickness of the outlet channel is larger than the inlet channel, here the average velocity is smaller. The four outlet holes are at 22.5° with respect to the inlet holes.
The air distribution is operated in a similar way on the other side of the fuel cell. The air inlet and outlet holes are at 45° with respect to the inlet and outlet fuel holes.
From physical viewpoint, the only function of inlet channels, both anodic and cathodic, is to convey fuel and air from the peripheral longitudinal ducts toward the center of the fuel cell. Here the gases reverse their direction and flow through the outlet channels providing the reactants to the electrochemical reactions. These reactions take place at the three-phase boundary (TPB): an interface between the porous electrode, where fluid and electrons are transferred, and the electrolyte, where ions are transferred. Gas composition significantly varies along the outlet channels, since the mass source terms are different than zero in the TPB. Accordingly, there are significant heat sources in the TPB.
These features allows one to simplify the complex geometry of Figure 2 in CFD models, when single cells are considered. The simplified geometry represented in Figure 3 and Figure 4 can be analyzed. The central part of the cell, corresponding to the inner edge of the stainless-steel plate separating inlet channel from outlet channel can be neglected. This simplification is possible since the active area of the central part of the fuel cell is relatively small if compared with the remaining portion. With this assumption a further simplification can be adopted: the inlet channels can be substituted by proper boundary conditions on the inlet sections of the anodic and cathodic channels. Since gas composition does not vary along the inlet channel, mass flow rate and species concentrations can be fixed at the inlet sections. Similarly, when a single cell is studied, the representation of the external structure of Fig. 2 can be avoided. Again, proper boundary conditions must be applied. In this case, ambient pressure can be specified on the outlet sections. Finally, from Figure 1 it comes that geometry has a periodic structure, specifically the fuel cell presents a repeating geometrical sector of 90°. So the fuel cell is fully characterized by this portion

of the entire geometry.

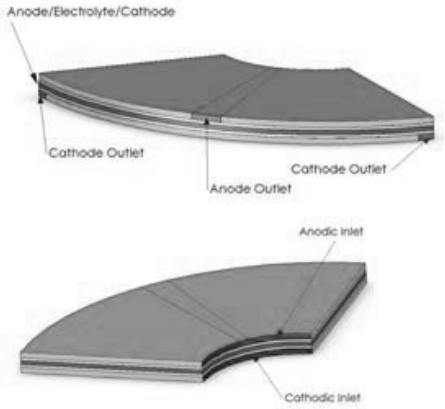

Figure 3. Computational domain.

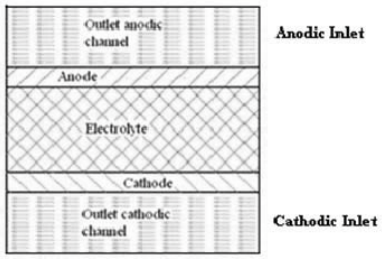

Figure 4. Cross section of the computational domain.

4. Fuel cell model

The electrolyte of a Molten Carbonate Fuel Cell (MCFC) is constituted of a ceramic matrix filled with sodium and potassium carbonates. At the cathodic side, the porous electrode is permeated by oxidizing gas species, i.e. oxygen and carbon dioxide. Carbonate ions are produced on the active surface according with the electrochemical semi-reaction:

$$\frac{1}{2}O_2 + CO_2 + 2e^- \rightarrow CO_3^{--} \qquad (1)$$

Ions migrate through the electrolyte to the anodic side. The anode is feed by hydrogen which reacts with the carbonate ions coming from the cathode, generating water:

$$H_2 + CO_3^{--} \rightarrow H_2O + CO_2 + 2e^- \qquad (2)$$

The model here presented consists of a set of partial differential equations taking in account the different transport phenomena: fluid flow, mass transfer, heat transfer, charge transfer, and electrochemical reactions. The model has been developed accordingly to the following assumptions:

1. Steady state conditions.
2. Gas mixtures are considered as ideal gases.
3. Fluid flow is laminar and incompressible.
4. Porous electrodes are homogeneous and isotropic with uniform morphology properties such as porosity, tortuosity and permeability.

Fluid flow and pressure field are governed by mass and momentum conservation. These two principles can be mathematically expressed by the continuity equation (3) and, under the preceding assumptions, by Navier-Stokes equation (4):

$$\nabla \cdot \rho\vec{V} = 0 \qquad (3)$$

$$\rho(\vec{V} \cdot \nabla)\vec{V} = -\nabla p + \mu\nabla^2\vec{V} \qquad (4)$$

The ideal gas state equation can be applied to determine the density in the previous equation.

When porous media such as anode and cathode are considered, it is necessary to take in account the presence of the solid matrix. In particular the momentum equation must be properly modified; in this paper the Brinkman equation (5) is adopted:

$$\rho(\vec{V} \cdot \nabla)\vec{V} = -\nabla p + \mu\nabla^2\vec{V} - \frac{\mu}{K}\vec{V} \qquad (5)$$

where K is the permeability of the porous media and $\vec{V}$ must be interpreted as the filtration velocity also known as Darcy velocity. The term $\rho(\vec{V} \cdot \nabla)\vec{V}$ is maintained since it facilitates to match solutions in a porous media and in an adjacent viscous flow [2].

The chemical species involved in the MCFC electrochemical reactions are: H_2, CO, CO_2, H_2O on the anode side and O_2, CO_2, N_2 on the cathode side. The conservation of each species is expressed by a proper balance equation:

$$\nabla \cdot (\rho\omega_i\vec{V}) = -\nabla \cdot \vec{J}_i + S_i \qquad (6)$$

in which ω_i is the mass fraction of the i-th species, $\vec{J}_i$ is the diffusive flux and must be computed in order to take in account bulk and Knudsen diffusion [3]. The flux for the i-th species is expressed through the following equation:

$$\vec{J}_i = -\rho D_{i,eff}\nabla\omega_i + \frac{\rho\omega_i}{M} - M\sum_j D_{i,eff}\nabla\omega_j - \nabla M\sum_j D_{j,eff}\nabla\omega_j \qquad (7)$$

The first term on the right-hand side represents the Fick diffusion due to concentration gradients. The last three terms are the corrections to enforce the Stefan-Maxwell equations for multi-component diffusion term [4]. The coefficient $D_{i,eff}$ is the effective binary diffusivity to account for reduced

mass flux due to solid structure of the porous medium. The generation/destruction of species due to electrochemical reaction is taken in account through proper boundary conditions instead of volumetric source term, therefore S_i is zero in Eq. (6). This boundary condition is expressed as a flux through Faraday law [5].

Heat transfer is solved by means of the energy equation, where the viscous effects have been neglected:

$$\nabla\cdot\left(\nabla\cdot\left(\vec{V}(\rho E+p)\right)\right)=\nabla\cdot\left(k_{eff}\nabla T-\sum_{\alpha}h_{\alpha}\vec{J}_{\alpha}\right)+S_h \quad (8)$$

where k_{eff} is an average thermal conductivity of the coexisting solid and gas phases. In the porous matrix the local thermal equilibrium hypothesis is assumed, so that a single temperature is used to describe the gas phase and the solid phase. In the electrodes the volumetric heat source term is due to Joule heating effect and is formulated as

$$S_h = \sigma\nabla\phi\cdot\nabla\phi \quad (9)$$

in which ϕ is the electric potential and σ is the electrical conductivity. Reversible heat associated with chemical reaction and activation loss associated with the electrochemical reactions are accounted through proper boundary conditions on the surfaces between the electrolyte and electrodes. In the electrolyte, only the source term (9) due to Ohmic heating survives.

To solve the electrical problem current density and electric potential must be found. Ohm's law can be used to relate the current density $\vec{\imath}$ to the electric potential:

$$\vec{\imath} = -\sigma\nabla\phi \quad (10)$$

The potential field throughout the conductive regions is calculated based on the conservation of charge:

$$\nabla\cdot\vec{\imath} = \begin{cases} j & \text{in the TPB} \\ 0 & \text{elsewhere} \end{cases} \quad (11)$$

where j is the current generation rate, produced at the TPB. This is assumed as coincident with the surface between the electrolyte and the electrodes. The current source is expressed by the Butler–Volmer equation:

$$i = i_0\left\{e^{\left[\frac{\beta z F\eta_{act}}{RT}\right]} - e^{\left[-\frac{(1-\beta)zF\eta_{act}}{RT}\right]}\right\} \quad (12)$$

where η_{act} is the electrode overpotential which is related with the reversible potential (Nernst's potential) and the ohmic losses through the following equation:

$$\eta_{act} = V_{rev} - \left|\eta_{electrode} - \eta_{electrolyte}\right| \quad (13)$$

5. Model results

The momentum equation, transport equations and boundary conditions are solved using a finite volume method to obtain velocity field, temperature and mass fractions in the fuel cell. The local current density is then computed so that the source term and boundary conditions for species and energy equation are determined. This procedure is repeated until convergence is reached.

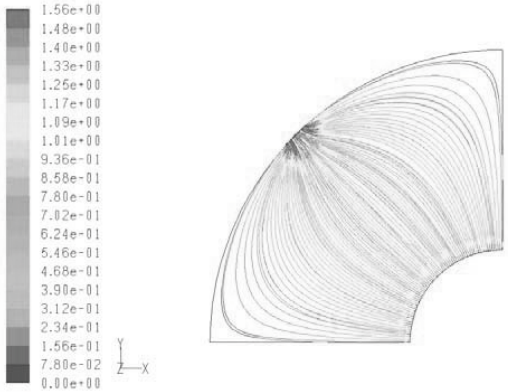

Figure 5. Pathlines in the anodic outlet channel (m/s).

Convective terms are computed by second order upwind scheme while the diffusive terms are computed by the central difference scheme. The numerical solution procedure adopts the semi-implicit SIMPLE algorithm. The detailed numerical procedure is available in [6].

Simulations have been performed considering mass flow rates of 3·10-6 kg/s at the anode (the mass fraction of constituents are 0.3 H_2, 0.4 CO_2, 0.3 H_2O) and 1·10-5 kg/s at the cathode (the mass fraction of constituents are 0.23 O_2, 0.23 CO_2, 0.54 N_2) and an inlet temperature of 823 K.

The velocity field in the anodic outlet channel is represented in Figure 5. Velocity is purely radial in the proximity of the inner radius of the computational domain. As far the fluid particles move toward the periphery of the cell they assume a circumferential velocity component due to the presence of outlet section. This component is particularly accentuate for the gas particles moving close to the outer wall of the fuel cell; here the flow field assumes a pure tangential configuration. Moreover, the fuel does not feed the cell uniformly since the fluid velocity magnitude is not homogenously distributed, as shown in the figure. An analogous velocity field occurs in the

cathodic compartment.
Both in the anodic and cathodic outlet channels there are areas were the velocity is very small. This affects the chemical species distribution: hydrogen, oxygen and carbon dioxide mass fractions are small in the areas between the outlet sections.
Hydrogen mass fraction is shown in Figure 6. The largest concentration occurs in the central area, in correspondence of the fuel inlet section. The concentration decreases towards the outlet section because of the fuel consumption associated with the electrochemical reaction. However the decrease of H_2 mass fraction is accentuated where the gas velocity is lower, since there regions are reached by a smaller amount of fuel.

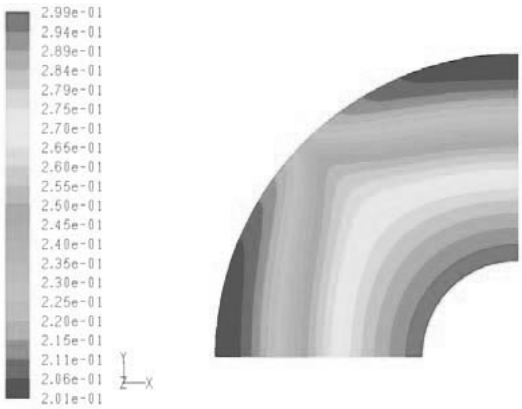

Figure 6. Hydrogen mass fraction.

Accordingly to the electrochemical reaction (2) water and CO_2 are produced at the anodic side of the cell. The corresponding mass fractions increase from the center toward the periphery of the fuel cell. Figure 7 shows the water mass fraction.

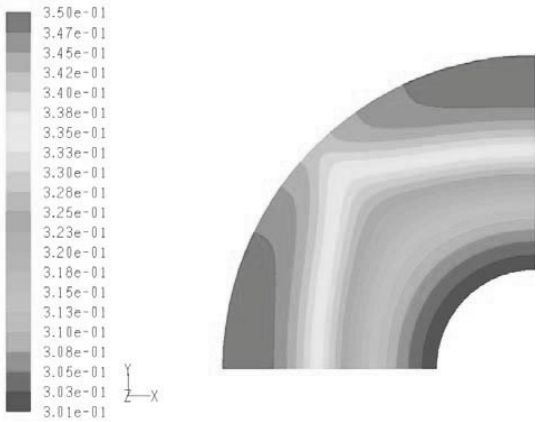

Figure 7. Water mass fraction in the anode.

The non-uniformities of the velocity field also affect H_2O and CO_2 concentration distribution: where the velocity is higher this species are quickly conveyed toward the outlet; consequently, mass fractions are lower. In the stagnation areas there are higher concentrations of these species.
Oxygen mass fraction decrease at the cathodic side of the fuel cell because carbonate ions are produced according with reaction (1). The fuel cell is fed by an higher oxidant mass flow rate compared to fuel mass flow rate; for this reason the decrease of O_2 concentration is limited. Oxygen mass fraction is shown in Figure 8.

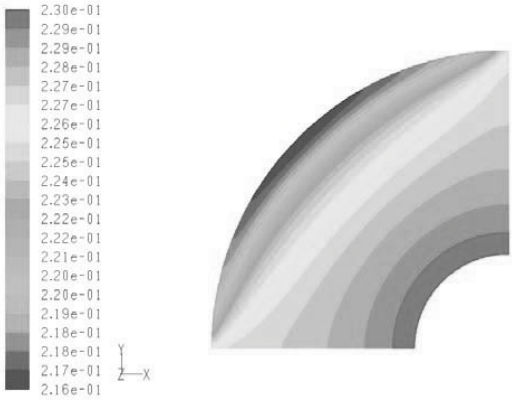

Figure 8. Oxygen mass fraction.

The current density distribution on the surface between anode and electrolyte is shown in Figure 9. This figure shows that the utilization of the active area rapidly decreases from the center to the periphery because of the decreasing concentration of hydrogen and oxygen.
Results of the presented model have been validated in [7] using some experimental results available from FN corresponding with a stack of 15 cells [8].

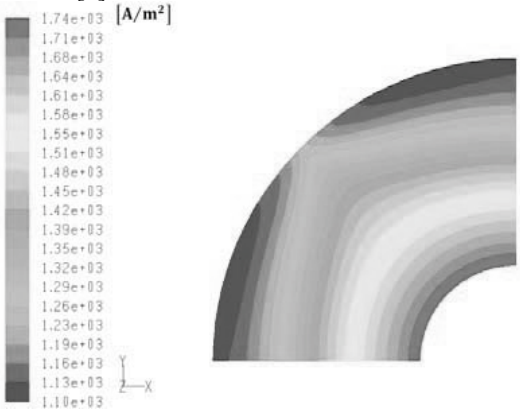

Figure 9. Current density distribution.

6. Network analysis for design improvement

To improve the utilization of the active area two main changes in the distribution system can be operated: 1) the number of outlet channels can be increased in order to make the outlet fluid velocity more homogeneous; 2) radial distribution channels can be traced in order to distribute fresh reactants to a wide area. The first design change involves changes at stack level, and this option is not considered in the present work. Instead, three shaped channels between the metallic structure and the outer part of the anodic and cathodic outlet channels are considered. As the CFD analysis and optimization of the fuel cell geometry plus these structures involve large computational load, a preliminary design improvement is performed using a fluid dynamic network model.

Porous media are discretized in nodes. One-dimensional branches connecting adjacent nodes are considered. Similarly radial channels are represented as one-dimensional branches connecting nodes [9]. Although this scheme can be used to solve all the phenomena presented in the previous section, here only the fluid dynamics is considered.

Momentum equation for a steady state incompressible flow in a general branch is

$$J \cdot l_a + J \cdot \frac{p_2 - p_1}{\rho} = 0 \qquad (14)$$

where J *is* the mass flow rate, l_a the unit mass friction loss and p the static pressure in the initial and final nodes. Kinetic and potential energy differences are considered as negligible. In channels, friction losses are expressed as the summation of distributed and local losses. In both cases the loss can be expressed as the function of the square of the average velocity, or of the square of the mass flow rate, namely:

$$l_a = l_{ad} + l_{ac} = R_h \cdot J^2 \qquad (15)$$

where R_h is a resistance coefficient. Pressure drop can be obtained from equation (15) as

$$\Delta p = p_1 - p_2 = \rho \cdot R_h \cdot J^2 = s_{12} \cdot R_p \cdot J^2 \qquad (16)$$

The coefficient s_{12} can have the values +1 and –1 and it takes the true (not arbitrary) verse of the flow into account. Equation (16) can be rewritten:

$$J = \frac{p_1 - p_2}{R_p^{0.5} \cdot |\Delta p|^{0.5}} = Y_{12} \cdot (p_1 - p_2) \qquad (17)$$

being Y_{12} the flow conductance of the branch. In the case of the porous medium, the flow conductance is constant and is obtained from Darcy equation.

To solve the complete network, the momentum equation must be written for all the branches. In addition, the continuity equation must be written for all the nodes. The continuity equation for a node is written

$$-\sum_{i=1}^{n_{in}} J_i + \sum_{i=1}^{n_{out}} J_i + J_{ex} = 0 \qquad (18)$$

where n_{in} is the number of flows entering the node from branches, n_{out} is the number of flows exiting the node and entering branches (n_{in}+n_{out} is equal to the number of branches having the node as initial or final end) and J_{ex} is the mass flow rate exiting the node to the ambient. This term is negative if the flow enters the node from the ambient. The conventional verse of the branches is used to set the equation.

Continuity equation can be written for the whole network in a matrix form. The incidence matrix, **A**, (see for example [10]) can be adopted to express the network topology. This is characterised by as many rows as the number of nodes (n) and as many columns as the number of branches (n). The element A_{ij} is 1 if the branch j exits the node i, -1 if the branch j enters the node i and 0 if the node i and the branch j are not related. The continuity equation is written as

$$\mathbf{A} \cdot \mathbf{J} + \mathbf{J}_{ex} = \mathbf{0} \qquad (19)$$

where **J** is the vector (m rows) of the mass flow rates in the branches and $\mathbf{J}_{ex}$ the vector (n rows) of the mass flow rate exiting the nodes to the ambient. Equation (19) can be rearranged by substituting the expression of mass flow rate in the branches obtained from the momentum equation. To do so, a matrix expression must be derived. The pressure difference in all the branches can be expressed as

$$\mathbf{\Delta P} = \mathbf{A}^{\mathbf{T}}\,\mathbf{P} \qquad (20)$$

where **P** is the vector (n rows) of the pressure in the nodes. A diagonal matrix **Y** ($m \times m$) is introduced, whose term Y_{jj} is the flow conductance of the j^{th} branch. The mass flow rate in the branches can be expressed as

$$\mathbf{J} = \mathbf{Y} \cdot \mathbf{\Delta P} = \mathbf{Y} \cdot \mathbf{A}^{\mathbf{T}} \cdot \mathbf{P} \qquad (21)$$

and then, substituting in (19)

$$\left[\mathbf{A} \cdot \mathbf{Y} \cdot \mathbf{A}^{\mathbf{T}}\right] \cdot \mathbf{P} + \mathbf{J}_{\mathbf{ex}} = \mathbf{0} \qquad (22)$$

To solve the set of non-linear equations (22) boundary conditions must be set. In this work, the inlet mass flow rate is fixed while a constant pressure is imposed on the active surface.
Two architectures are considered, the first one characterized with a single bifurcation level and the second one with two bifurcation levels [11]. These architectures are shown in Figure 10. The design parameters of three shaped channels, the angles and lengths of ducts, are progressively modified in order to maximise the angular momentum associated with fluid reaching the active surface. The reason for such objective function is that we are interested in increasing as much as possible the use of external area. The analysis is conducted considering the total surface covered by the ducts as constant. In addition, only symmetrical configurations are considered.

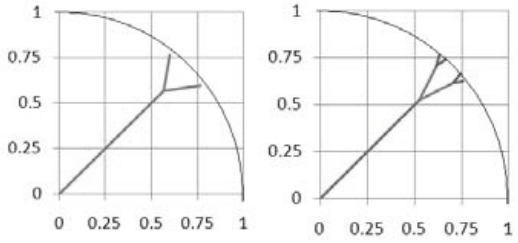

Figure 10. Selected architectures of the three shaped channels.

The results corresponding with the analysis of 100 configurations is presented in Figure 11.

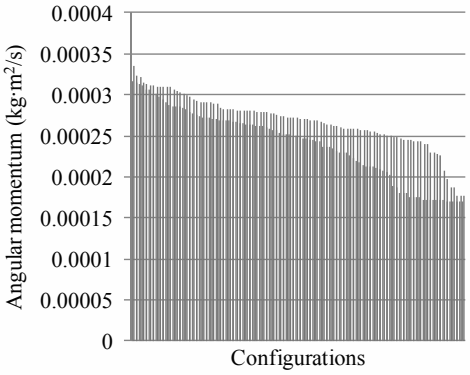

Figure 11. Angular momentum of fluid using three shaped distributed channels.
These configurations corresponds to 10 values of the ratio between channel length and 10 values of the bifurcation angle. Blue bars refers to single level bifurcations, while red bars to double level bifurcations. The latter allows better flow distribution as the angular momentum is larger. On average, the difference between the two architectures is about 11.5%, while the optimal configurations differs of only 5.8%. For this reason, system optimization is conducted considering the single bifurcation architecture.

7. Geometry optimization

The problem of optimal fluid distribution inside a given physical system has been tackled by a large number of researchers; typical examples in engineering are heat exchangers, pipe networks and cooling devices [12,13]. Similar studies have been also carried out for different typology of fuel cells. In this case is necessary to exploit a given amount reactants in the most effective way, that is obtain the highest possible electric power [14]. The entropy generation rate is one of the possible indicators for choosing the optimal design of an energy system. This quantity can be used to express the objective function in the optimization, but also to select the design parameters through analysis of the distribution of the entropy generation terms [15].
As discussed in the previous section, a Y-shaped inlet channel in the anodic compartment is considered. Similar conclusions can be drawn for the cathodic compartment.

The new geometry of the computational domain is shown in Figure 12.

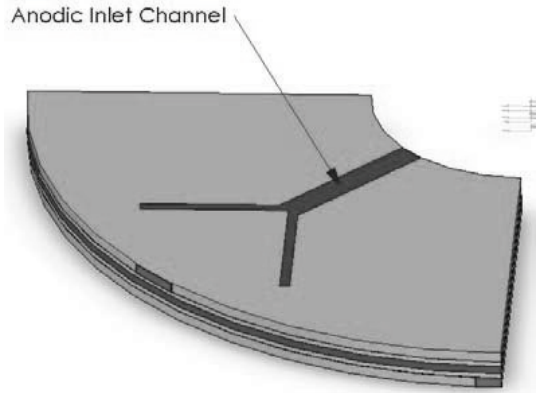

Figure 12. Modified MCFC geometry.

The effect of the Y-shaped channel on the fuel cell performance can be maximized by modifying the dimensions and orientation of the branches. Two antagonistic factors influence the optimal design of gas distribution inside the fuel cell: the

maximum electrical power and the maximum efficiency.

In a fuel cell the departure from ideal conditions is due to the so-called polarization losses. These effects are strictly related to the irreversible transport phenomena occurring in the system. Thus, the rate of entropy generation is a proper physical quantity that can be utilized to identify what are the major causes of irreversibility and efficiency decrease.

Entropy generation can be expressed in term of fluxes and the corresponding gradients of physical quantities; this equation is obtained from the entropy balance written for an infinitesimal volume, that is:

$$\rho\frac{\mathrm{Ds}}{\mathrm{Dt}} = -\nabla\cdot\vec{\sigma} + \mathrm{g_p} \qquad (23)$$

where s is the entropy per unit mass, $\vec{\sigma}$ is the entropy-flux vector and g_p is the rate of entropy generation per unit volume. To obtain $\vec{\sigma}$ and g_p we can assume local thermodynamic equilibrium, it follows that s is a well defined function of the various properties necessary to define the macroscopic state of the system. This can be expressed by the fact that the total differential of s is given by the Gibbs relation:

$$\mathrm{du} = \mathrm{Tds} - \mathrm{pd}\left(\frac{1}{\rho}\right) + \sum_i \mu_i \mathrm{d}\omega_i \qquad (24)$$

Differentials can be expressed using energy equation, the conservation of species and the fluid flow equation. After some rearrangement is possible to show that:

$$\vec{\sigma} = \frac{1}{\mathrm{T}}\left(\vec{\mathrm{J}}_\mathrm{q} + \sum_i \mu_i \vec{\mathrm{J}}_\mathrm{i}\right) \qquad (25)$$

The local rate of entropy generation can be split in four main contribution, each strictly correlate to a specific physical phenomenon:

$$\mathrm{g_p} = \mathrm{g_\mu} + \mathrm{g_h} + \mathrm{g_m} + \mathrm{g_c} \qquad (26)$$

The first term at the right-hand side of (26) is connected to the gradients of the velocity field, giving rise to viscous flow, the second arises from heat conduction, the third from mass transfer, and the fourth term is due to coupling between heat and mass transfer (convective term). The structure of the expression is that of a bilinear form: it is the summation of a flow quantity times the gradient of an intensive state variable driving that flow:

$$\mathrm{g_p} = \frac{1}{\mathrm{T}}\Delta{:}\,\tau + \frac{1}{\mathrm{T}^2}\left(-\mathrm{J_q}\cdot\nabla\mathrm{T}\right) + \frac{1}{\mathrm{T}}\left(\sum_i -\vec{\mathrm{J}_\mathrm{i}}\cdot\nabla\mu_\mathrm{i}\right) + \frac{1}{\mathrm{T}}\left(\sum_i -\mathrm{s_i}\,\vec{\mathrm{J}_\mathrm{i}}\cdot\nabla\mathrm{T}\right) \qquad (27)$$

in which Δ and τ are the strain and stress tensor. For a Newtonian fluid they can be expressed in terms of viscosity and fluid velocity gradient. In the case of a fuel cell, an additional term must be considered in equation (26). This term is associated with the entropy generation due to ohmic losses:

$$\mathrm{g_{ohm}} = \frac{1}{\mathrm{T}}\sigma\nabla\varphi\cdot\nabla\varphi \qquad (28)$$

The previous term is present only in conductive regions, that is electrodes and electrolyte.

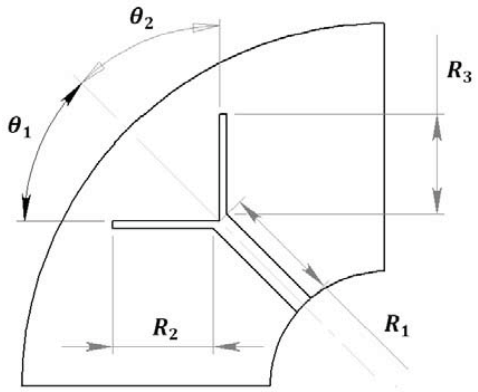

Figure 12. Parameterized MCFC geometry.

Since we are interested in the optimal configuration of the anodic inlet channel, it is necessary to properly parameterize the MCFC geometry in order to define the design variables free to vary. Figure 12 shows that four design parameters can be used to characterized the geometry configuration. Specifically, the length R_1 and R_2 of two branches and the angles θ_1 and θ_2 are free to vary. The remaining length R_3 is chosen in order to keep the total area of the Y-shaped channel constant.

The fuel cell optimization is performed by considering two objective functions. The first objective function F_1 is the global entropy generation rate G_p, namely

$$\mathrm{F_1} = \int\left(\mathrm{g_\mu} + \mathrm{g_h} + \mathrm{g_m} + \mathrm{g_c} + \mathrm{g_{ohm}}\right)\mathrm{dV} \qquad (29)$$

The second objective function F_2 is the electric power produced by the fuel cell, that is

$$\mathrm{F_2} = \dot{\mathrm{W}}_\mathrm{el} \qquad (30)$$

Clearly is desirable to maximize the electrical power, i.e. F_2, and at the same time reduce as much as possible the sources of irreversibilities, that is minimize F_1. For this reason the optimization has been performed using the Non-dominated Sorting Genetic Algorithm version II (NSGA-II) [16]. This is an evolutionary algorithm suitable for simultaneously optimization of two or more conflicting objectives. NSGA-II uses some mechanisms inspired by biological evolution: reproduction, mutation, recombination, and

selection. Candidate solutions to the optimization problem play the role of individuals in a population, and the objective function determines the environment within which the solutions survive. Evolution of the population then takes place after the repeated application of the above operators.

8. Optimization results

Various geometries have been analyzed during optimization. Figure 13 shows the scatter plot of global entropy generation versus power density, the Pareto front of optimal designs are indicated with red squares.

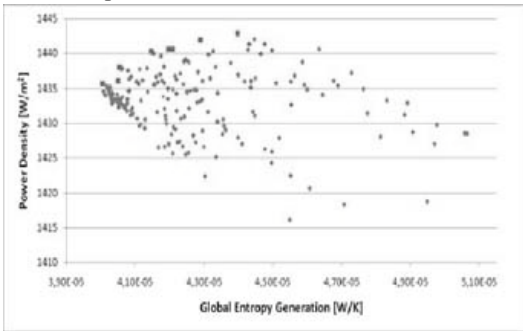

Figure 13. Parameterized MCFC geometry.

The figure confirms that the two objective functions are conflicting. According to the Pareto curve is possible to achieve an higher power density to the detriment of a larger value of entropy generation.

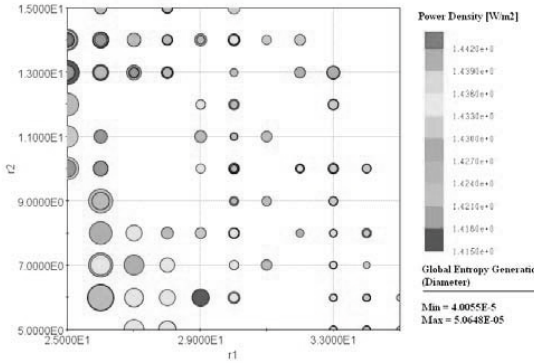

Figure 14. Bubble chart of R_1 and R_2.

A bubble chart can be used to understand the influence of each design parameter on the objective functions. This representation is used as the data have four dimensions that need to be shown on the same chart. In Figure 13 the design variables R_1 and R_2 are reported along abscissa and ordinate, the color maps shows the power density of the fuel cell, finally the diameter of the bubble indicates the global entropy generation.

Higher power density is achieved by geometrical configurations with small values of R_1 and large R_2. This means that an inlet channel with a short central branch and long secondary branch promotes an higher electrical power. When the opposite situation occurs, that is large R_1 and small R_2, the entropy generation is minimized.

This is similar to the result obtained with fluid flow analysis shown in Figure 10. Differences in the optimal lengths are also due to the different position of the inlet section: in the network model the central area is considered, while this is not considered in the three dimensional model.

It is also necessary to understand how the other two design parameters, i.e. the angles θ_1 and θ_2, affect the objective functions. This is shown in Figure 15.

When the angles θ_1 and θ_2 are as large as possible higher power density are achieved. Moreover from Figure 15 it is obvious that the two angles should be both large, this also means that a symmetrical anodic inlet channel is preferable when high electric power is required. Controversy, if the Y-shaped channel assumes a close configuration, i.e. small θ_1 and θ_2, the entropy generation is reduced.

The Pareto designs are the best compromise with respect to the two objective functions adopted here. One of these designs is illustrated in the next figures. In particular the case characterized by R_1 = 14 mm, R_2 = 27 mm, θ_1 = 60° and θ_2 = 60°. Accordingly to the two previous bubble chart, this configuration provides an high power density due to the ample angles. However, the relatively long central branch assures a relative low global entropy generation.

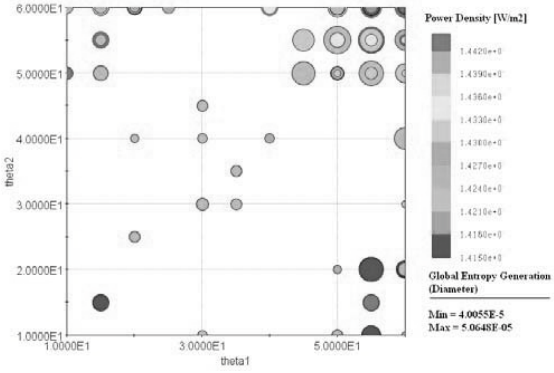

Figure 15. Bubble chart of θ_1 and θ_2.

The current density distribution corresponding with this design is illustrated in Figure 16; the inlet

channel outline is highlighted in blue. The presence of the two secondary branches allows one to obtain larger current density, especially for large radius. Moreover in the area spanned by the Y-channel the current density gradients are reduced if compared to the original configuration. This means that in the optimized design more homogeneous operating conditions take place. In the region far from the channel, the current density assumes lower values since this region is fed by partially depleted fuel, that is with a lower hydrogen concentration.

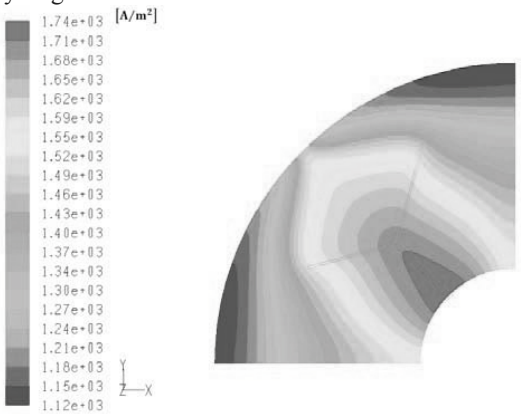

Figure 16. Current density distribution.

The velocity field is also affected by this configuration; the pathline patterns are illustrated in Figure 17. Now the fluid departs from the inlet channel, consequently higher velocities are achieved in the middle region on the fuel cell. Moreover, this channel allows one to reduce the size of the stagnation regions inside the cell, which permits to obtain more homogeneous conditions inside the system.

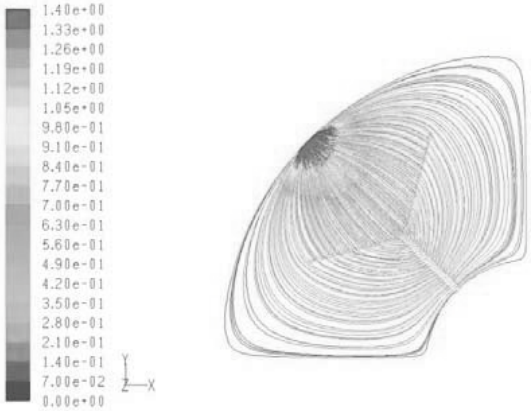

Figure 17. Pathlines colored by velocity magnitude (m/s).

9. Entropy generation analysis

The distribution inside the fuel cell of the various contributions to the entropy generation are analyzed in this section. Local rate of entropy generation due to viscous effects in the anodic compartment of the cell is depicted in Figure 18. The largest values of g_μ are located where there are strong velocity gradients. In particular, they take place in a confined region in the nearness of anodic compartment outlet. It is clear from Figure 17 that in this region the fluid velocity increases because of the relatively small outlet cross-section, therefore here are located the strongest velocity gradients.

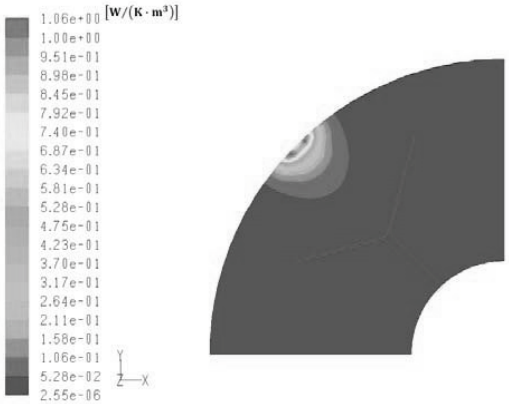

Figure 18. Viscous entropy generation in the anodic channel.

The contribution to entropy generation due to mass transfer is shown in Figure 19. The electrochemical reactions cause strong species mass fraction gradients. Moreover, because of the presence of porous matrix, the species motion in the fuel cell is mainly driven by diffusion, i.e. concentration gradient. These gradients are the sources of entropy generation. The species mass fractions are uniformly distributed in the area spanned by the Y-shaped inlet channel. For this reason the irreversibilities due to mass transfer are negligible in this zone of the fuel cell. In contrast, the outer region of the fuel cell is not reached by the inlet channel. It follows that in this part of the cell chemical species are distributed only by means of diffusion, consequently mass transfer entropy generation is large. This is particularly evident for the extremities of secondary inlet channel branches. Finally, in the outlet section region the convective transport becomes no more negligible. Therefore chemical species are strongly advected, together with the presence of outer wall

-dwT bMxT(T T-ql[v T](bwT vqMFw[-T -dxT IMqv(([-ql]J v([(qM4w[

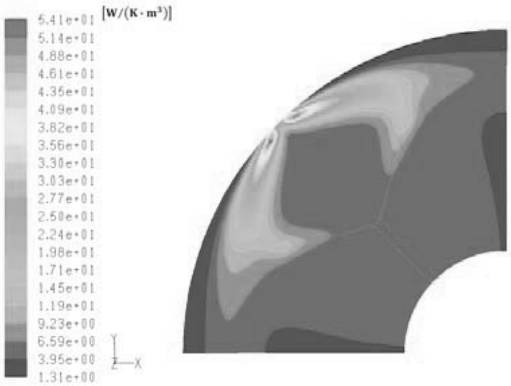

wxq(o MTT-qM[T)(q([-ql]J v([(qM4w[

ed(([-ql]J v([(qM4(F CJ b1x]Iwv C(-k(([d(M4 M[F j MTT-qM[T)(q wT F(]wb-(F vy wxq(edwT b1[-qvCx-w[wT x[wy1qj IJ FwT-qvCx-(F vy -d( )x(I b(II mMqv(T-zMkx(T Mq(I1bMw(F M[1[v -d(vy I(-bdM[[(I]ql)w((T C(bMxT(1) -d(b1[-(j]1qMqJ]q(T([b(1) -(j](qM4xq(vqMFw[-T M[F T](bwT b1[b([-qM4w[vqMFw[-T g[-d(1-d(qdM[F vy -d( ]qlEvjy wJ 1))x(I b(II Tx]]1q-vyv T-qxb-xq(wT /(ql TwYb(MFwMCM4wb b1[Fwww[T Mq(b1[TwF(q(F -d(q())1q(-(j](qM4xq(vqMFw[-wT/(ql

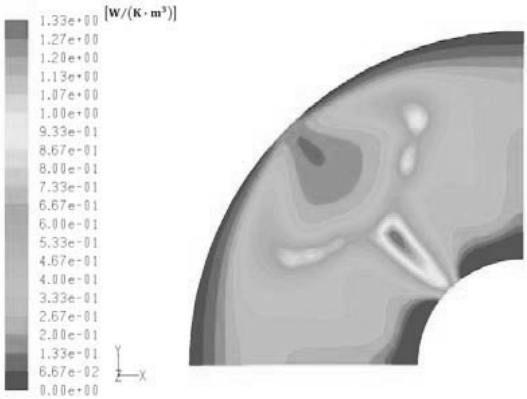

wxq([-ql]J v([(qM4w[Fx(-1 b1x]Iwyv C(-k(([d(M4M[F j MTT-qM[T)(q

ed(([-ql]J v([(qM4w[qM4(1z(q-d(([-wq(F1j M4y wT vyz(T-wM4(F Fxqvyv -d(1]-vjy w/M4w[ ]qlb(Fxq(Mbd b1j]1[([- 1) -d(vI1CMI([-ql]J v([(qM4w[bM[C((zMkxM4(F MT)1II1k

k d(q(M4(-d(b1[-qvCx-w[T -1 -d(([-ql]J v([(qM4w[[-d(D -d(vy-(vqMIwT(E-([F(F -1 -d(k d1I(F1j M4y 1) -d( )x(I b(II [wxq(M b1j]MqwI1[C(-k(([(Mbd 1) 1z(qMI ([-ql]J v([(qM4w[b1j]1[([-TwT Td1k[ed(wqq(z(qTwC(I1TT(T Fx(-1)IxwF)qvb-w[Mq(b1j]I(-(IJ [(vIwwC(I TwYb(-d(b1qq(T]1[FwYv T](bwvb-(qj wT q(I(zM[-1[IJ vy MTj MII q(vw[1) -d( )x(I b(II MT Td1k[vy wxq(ed(vI1CMI([-ql]J v([(qM4w[Fx(-1 b1x]IwYv C(-k(([d(M4M[F j MTT-qM[T)(q wT -d(T(b1[Fj 1T-q(I(zM[-b1[-qvCx-w[edwT bM[C(x[F(qT-11F CJ I11.vyv M4 -d(FwT-qvCx-w[q[]q(T([-(F vy wxq(edwT.vyF 1) I1TT wT]q(T([-vy -d(j M4[qwJ 1) -d( )x(I b(II d1k(z(q -d(j M4[wxF(1) wT Tj MII w)1II1k T-dM4-d(vI1CMI-(qj wT[1-]q[]1[F(qM[- TTd1k[vy wxq(-d(j M4y b1[-qvCx-w[-1 -d(-1-MI ([-ql]J v([(qM4w[wT Fx(-1 j MTT-qM[T)(q wqq(z(qTwC(IwwJ edwT wT Fx(-1 -d( )Mb- -dM4 MT]1vy-(F 1x-C())1q(-d(Fvy)xTw[wT[1-[(vIwvC(I vy -d(([-wq(F1j M4y 1) -d( )x(I b(II TvYb(b1[z(b-wz(-qM[T]1q-wT Iwjy w(F CJ -d( ]q(T([b(1)]1qlxTj M4qwE edwT bMxT(T -1 C(q(I(zM[-vy -d(([-wq(F1j M4y M[F vy]M4-vbxIM4qvy -d(1x-(q q(vw[1) -d( )x(I b(II T M q(TxI- -d(vI1CMI([-ql]J]qlFxb-w[Fx(-1 j MTT-qM[T)(q wT -d(j 1T-vjy]1q-M[- FFwww[M4q(Fxb-w[T1) -dwT-(qj j M4 C(Mbdw(z(F xTwYv FwT-qvCx-w[bdM[[(ITMII1 1[-d(bM4d1Fwb TwF(k dwbd j (M[T -dM4 -d( )x(I b(II](q)1qj M[b(bM[C( )xq-d(qvybq(MT(F

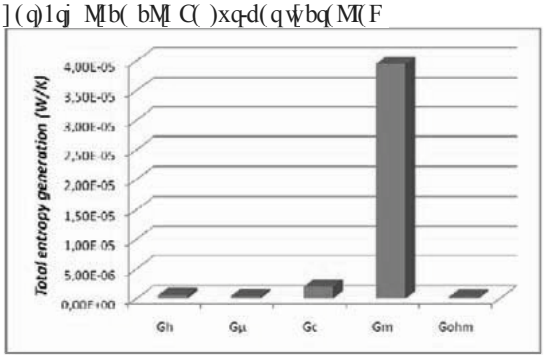

wxq(I1CMI([-ql]J v([(qM4w[

y dMat ya

[-dwT]M[(q([-ql]J v([(qM4w[M[MUTwTwT xT(F vy 1qF(q-1 1]-vjy w/(-d( )IxwF FwT-qvCx-w[vy Mj 1I-([bMqC1[M4( )x(I b(II wqT-d(Mqbdw(b-xq(1) -d(FwT-qvCx-w[bdM[[(IT wT T(I(b-(F xTwYv M[(-k 1q j 1F(I M[F-d([-d( )vyMIF(Tw[wT b1[Fxb-(F xTwYv M j 1F(I 1) -d(b(II qx[-dqlxvd M[1]-vjy w/M4w[Mlv1qwdj

i(TxI-TTd1k-dM4-d(([-ql]J v([(qM4w[M[MUTwT wT]M4-vbxIMqUxT()xI)1q Txbd M[]IwbM4w[a wd q(T](b- -1 -d(vywxMI F(Tw[-d(1]-vjy w/(F b1[)wxqM4w[MII1k T M[vybq(MT(vy -d(M4(qM4(bxqq[-F([TwJ 1) MC1x- ed(M[MUTwT wT

conducted considering distribution channels on the anodic side only. Entropy generation analysis shows that the largest contribution to the irreversibilities is due to mass transfer in the porous media. This means that additional improvements are expected using distribution channels on the cathodic side.

References

[1] NETL (2004) *Fuel Cell Handbook*, seventh ed. US Department of Energy, National Energy Technology Laboratory, Morgantown.

[2] Nield D.A., Bejan A. (1999). *Convection in porous media*. New York: Springer.

[3] R. Krishna, J. A. Wesselingh (1996). *The Maxwell-Stefan approach to mass transfer*. Chemical Engineering Science, Vol. 52, No. 6, pp. 861-911.

[4] Hwang JJ, Chen CK, Lai DY (2005). Computational analysis of species transport and electrochemical characteristics of a MOLB-type SOFC. Journal of Power Sources, Vol. 140, pp. 235-42.

[5] Joon-Ho Koh, Hai-Kung Seo, Young-Sung Yoo, Hee Chun Lim (2002). *Consideration of numerical simulation parameters and heat transfer models for a molten carbonate fuel cell stack*. Chemical Engineering Journal, Vol. 87, pp. 367-379.

[6] Patankar SV. (1980) *Numerical heat transfer and fluid flow*. Hemisphere Publishing Corporation.

[7] C. Massano, A. Sciacovelli, V. Verda (2009). Detailed Model of Molten Carbonate Fuel Cell Stacks. ECOS 2009. August 31 – September 3, 2009, Foz do Iguaçu, Paraná, Brazil

[8] C. Amelio, G. Diaz, E. Ferrari, E. Ghisolfi, L. Mannarino, C. Spadaro, E. Poskovic, S. Baccaro (2009). A New Approach to MCFC Ceramic Matrixes Manufacturing and Laboratory Small scale Stack Testing, Development of Innovative SOFC Cell Porous Components. European Fuel Cell Conference. Paper EFC09-17166.

[9] M. Calì, R. Borchiellini, (2002). *District Heating Network Calculation and Optimization. Encyclopedia of Life Support Systems*, UNESCO (paper 3.19.3.8).

[10] M. Chandrashekar, F. C. Wong (1982). *Thermodynamic System Analysis – A graph-theoretic Approach*. Energy, Vol.7 No.6, pp.539-566.

[11] A. Bejan, S. Lorente (2004). The constructal law and the thermodynamics of flow systems with configuration. International Journal of Heat and Mass Transfer 47: 3203–3214.

[12] V.D. Zimparov, A.K. da Silva, A. Bejan (2006). *Thermodynamic optimization of tree-shaped flow geometries*. International Journal of Heat and Mass Transfer 49: 1619–1630.

[13] Diego Copiello, Giampietro Fabbri (2009). *Multi-objective genetic optimization of the heat transfer from longitudinal wavy fins*. International Journal of Heat and Mass Transfer 52: 1167–1176.

[14] Xiu Qing Xing, KahWai Lum, Hee Joo Poh, Yan LingWu (2009). *Geometry optimization for proton-exchange membrane fuel cells with sequential quadratic programming method*. Journal of Power Sources 186, 10–21.

[15] Sciacovelli A., Verda V. (2009) Entropy generation analysis in a monolithic-type solid oxide fuel cell (SOFC). Energy 34. 850-865.

[16] Kalyanmoy Deb (2002). *A Fast and Elitist Multiobjective Genetic Algorithm*. IEEE TRANSACTIONS ON EVOLUTIONARY COMPUTATION, Vol. 6, No. 2, pp. 182-197.

Energy recovery from biogas: internal combustion engines coupled with Organic Rankine Cycle

Lidia Lombardi[a], Andrea Corti[b], Ennio Carnevale[a]

[a] *Dipartimento di Energetica "Sergio Stecco"- Università degli Studi di Firenze - Italy*
[b] *Dipartimento di Ingegneria dell'Informazione - Università degli Studi di Siena - Italy*

Abstract:
A specific thermodynamic analysis of organic Rankine cycle, in reference to different sizes of internal combustion engines conventionally used for biogas/landfill gas, was carried out, considering several working fluids, different cycle configurations (simple cycle or regenerated cycle) and conducting a parametric analysis in order to determine optimal evaporating pressures for each fluid. The analysis demonstrates that the overall efficiency can be increased by 1,7-4,7 percentage points and the power can be incremented by 5-13% with respect to the engine without any bottoming cycle, depending on the organic fluid and the type of engine.

Keywords: organic Rankine cycle; internal combustion engines; biogas; landfill gas.

1. Introduction

Landfill gas, which consists mainly of the powerful greenhouse gases methane and carbon dioxide, is produced when biodegradable wastes decay anaerobically in landfill sites. Gas recovery from landfills has become a standard technology in most of the industrialised countries for energy recovery and environmental and safety reasons. As a matter of fact, the EC strategy to reduce the greenhouse effect deriving from landfill gas emission consists of a progressive reduction of biodegradable municipal waste landfill disposal in order to reduce the production of landfill gas, as stated in the European Directive 1999/31/EC. Of course this reduction duty will contribute to increase the separate collection of biowaste boosting the use of industrial anaerobic digestion processes, in which biodegradable material is decomposed, in industrial reactors, in the absence of oxygen, by bacteria forming digestate and biogas, a mixture of carbon dioxide and methane, generally with a better quality with respect to landfill gas. In this view, a progressive reduction of landfill gas and a progressive increment of biogas from anaerobic digestion are expected.

Increasingly, the biogas (from landfills or anaerobic digestion plants), which is a renewable, is used in reciprocating Internal Combustion Engines (ICEs).

ICEs are often chosen for their reliability, low specific cost and high electrical efficiency, especially in the power range of hundreds of kW to few MW [1].

Biogas in ICEs is mainly used to produce electric power, while heat recovery is less common mainly due to the distance at which waste treatment plants generally are from potential heat users. Also, the existence of incentives for electric energy production (such as Green Certificates in Italy) for plants based on renewables – makes the operation of these units a viable solution even if no heat is usefully recovered [1].

However, due to the rather high temperature at which exhausts are discharged, disregarding the heat recovery option for the previously mentioned reasons, there is still a potential for increasing the overall efficiency of conversion into electric power. This can be accomplished by adding as a bottoming cycle an Organic Rankine Cycle (ORC) using engine exhaust gases as a thermal source.

2. Organic Rankine Cycles

ORCs can use different working fluids in order to exploit low grade heat sources to produce useful work. An interesting application of ORCs is to couple them with other prime movers and utilize their wasted heat, thus realizing a combined power unit with the effect of enhancing the overall system efficiency [2]-[6]. Since the ORC systems generate additional power without requiring extra fuel, the specific pollutant emissions of the combined plant are reduced.

Organic fluids are to be preferred to water when the required power is limited and the heat source temperature is low, as these fluids often have lower heat of vaporization and can better follow the heat source to be cooled, thus reducing temperature differences and therefore irreversibilities at the evaporator [1]. Furthermore, turbines for organic cycles can provide higher efficiencies at part loads as well and are usually less complex (1 or 2 stages, for an axial turbine) due to the lower enthalpy drop of the fluid [7]-[8]. Also ORC systems exhibit great flexibility, high safety and low maintenance requirements in recovering low-medium grade waste heat, from industrial processes or power plants [9].

Evaporators for ORCs are usually simple components with one level of evaporating pressure [1]-[2][5].

Few examples of ORCs coupled to ICEs exist and usually the ORC is conceived to efficiently exploit only the heat released at high temperatures such as the engine exhaust gases [1],[5].

3. Model

The preliminary analysis was carried out in reference to a commercial cogeneration engine as a topping system (engine A). The engine is a 20 cylinder 4 stroke supercharged fuelled with biogas characterised by 65% in volume of methane and 35% in volume of carbon dioxide. The main parameters of the engine are reported in Table 1.

Table 1. Engine A main characteristics

Engine parameter	Value	Units
Low Heating Value of biogas	6,40	kWh/Nm^3
Entering power (100% load)	5.513	kW
Biogas flow rate	861	Nm^3/h
Mechanical power output	2.183	kW
Electrical power output	2.118	kW el.
Electric efficiency	38,40	%
Exhaust gas temperature	444	°C
Exhaust mass flow	14.222	kg/h
Combustion air mass flow	13.236	kg/h

It has been calculated that the excess air coefficient is 0,9204 at nominal conditions, under the hypothesis of perfect combustion of the methane contained in the biogas. The composition of the exhaust gases on the basis of the mass was calculated at: CO_2=0,119; H_20=0,064; N_2=0,713; O_2=0,104. This composition was used to evaluate exhaust gases properties.

In the study, the engine is assumed to operate at rated load as the aim is to determine which organic fluid would perform better in reference to the overall heat available for these conditions.

3.1. Organic fluids

Organic fluids used for power applications may have different characteristics in the T-s diagram and the saturation lines may be bell shaped, nearly isentropic or overhanging (positive slope) depending on the fluid molecule complexity. Typically fluids with simpler molecules are characterised by bell shaped vapour line and lower critical temperatures and fluids with more complex molecules display an overhanging vapour line and higher critical temperatures [1],[10].

In this paper twelve organic fluids, characterised by overhanging vapour lines (also called dry fluids), were considered for a preliminary screening analysis. The saturated vapour phase of a dry fluid becomes superheated after the expansion, so there is no need for superheating the vapour before entering the turbine, which is conventionally used for avoiding liquid droplets at the end of the expansion. Also, dry fluids generally have much lower enthalpy drops during expansion than water-steam mixture [10], therefore, a single-stage turbine is usually used in an ORC.

Table 2. Properties of the considered organic fluids.

Organic fluid	Saturation pressure at 35°C [kPa]	Critical temperature [°C]	Critical pressure [kPa]
n-pentane [6]	98,35	196,50	3.364
n-butane [6]	329,00	152,00	3.796
n-Hexane [6]	30,59	234,70	3.058
R113 [6]	65,26	214,10	3.439
R114 [10]	290,90	145,70	3.289
R218 [12]	1.131,00	71,87	2.640
R227ea [5]	608,70	102,80	2.999
Isobutane [6]	464,50	134,70	3.640
Isopentane [6]	128,80	187,20	3.370
n-Heptane [11]	9,83	267,00	2.727
n-Nonane [11]	1,07	321,40	2.281
n-Octane [11]	3,19	296,20	2.497

The selected fluids are listed in Table 2, together with their critical pressure and critical temperature. Table 2 also shows the saturation pressure at 35°C, which was assumed as the set ORC condenser temperature. The considered fluids were commonly quoted in literature as possible fluids for ORC, according to the references reported in Table 2, as well.

It should be remarked that, in the proposed analysis, only thermodynamic aspects will be considered. However, it is worth underlying that fluids for ORC applications must not only be favourable from a thermodynamic point of view, but have to satisfy also requirements of chemical stability at the operating pressures and temperatures; environmental friendliness; non toxic, non corrosive and compatible with engine materials; low flammability and auto-ignition properties [1].

3.2. Model assumptions

In this work it was assumed to recover the heat only from exhaust gases (disregarding the potential heat from engine cooling water), in order to consider a simplified layout for the plant, assuming that exhaust gases are cooled down to 180 °C. The energy recovery from exhaust gases was assumed to take place by means of an intermediary fluid, such as diathermic oils, according to some ORC proposed commercially. The entering temperature for the cool diathermic oil stream was assumed at 120 °C, while the exiting temperature was assumed at 300 °C. The heat exchange between exhaust and Diathermic oil, takes place in the Gas-Oil Heat Exchanger (GOHE).
In the preliminary screening analysis two cycle configurations will be assumed:
-ORC simple cycle thermally powered by engine exhaust gases (Figure 1);
-ORC regenerated cycle thermally powered by engine exhaust gases (Figure 2).

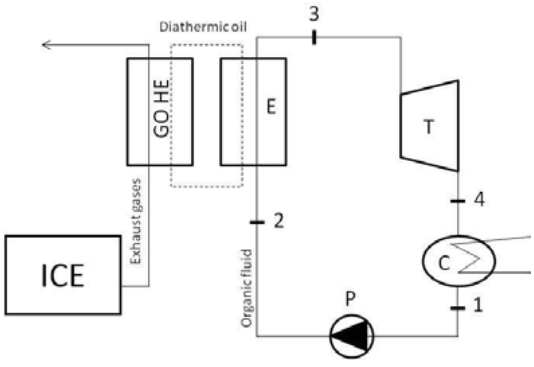

Fig.1. Layout of the ORC simple cycle.

For all considered cycles the following assumptions were deliberated:
- isentropic turbine efficiency: 0,8 (this value is conservatively below usual values that may range between 0,8 and 0,88 [8],[13];
- isentropic pump efficiency: 0,8;
- working fluid condensing temperature: 35 °C;
- vaporizing pressure varying between condensation pressure and critical pressure;
- negligible pressure losses in the heat exchangers and pipes;
- heat exchanger (gas-oil heat exchanger and evaporator) effectiveness: 0,9.
Then, for the simple ORC cycle two possibilities were considered:
- expansion for all fluids starts directly from dew line (no superheating);
- expansion for all fluids starts at superheated conditions (superheating).
The thermodynamic model of the proposed cycles were built by means of Engineering Equation Solver (E.E.S.), using the internal properties database available for the selected fluids [14].
The ORC efficiency was calculated according to:

$$\eta_{ORC} = \frac{W_{ORC}}{Q_{exhausts}} \qquad (1)$$

where:
η_{ORC} = efficiency of ORC;
$W_{ORC} = W_{turbine} - W_{pump}$ = net power of ORC;
$Q_{exhausts}$ = thermal power released by the exhaust cooling from 444°C to 180 °C.

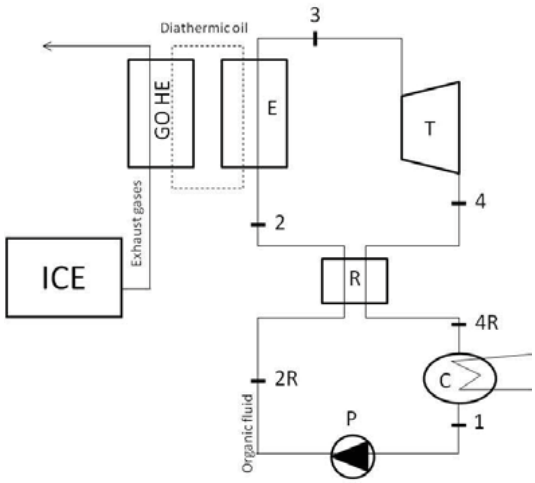

Fig.2. Layout of the ORC regenerated cycle.

4. Simple ORC results

In Figure 3 the simple ORC efficiency, in the case of no superheating, is plotted for the selected fluids, in the range of turbine inlet pressure

between condenser pressure (assumed as the value of saturation pressure at 35°C for each fluid) and critical pressure of each fluid, with the exception of n-Nonane and n-Octane. In fact, the critical point for n-Nonane and n-Octane are, respectively, at 2.281 kPa; 321,40 °C and 2.497 kPa; 296,20 °C. Since the maximum temperature at which diathermic oil is available is 300°C, it was assumed to vary the turbine inlet pressure for these two fluids up to the correspondent saturation pressure at 270 °C, allowing for a temperature difference of 30°C between the fluid maximum temperature and the diathermic oil temperature, in the devoted heat exchanger.

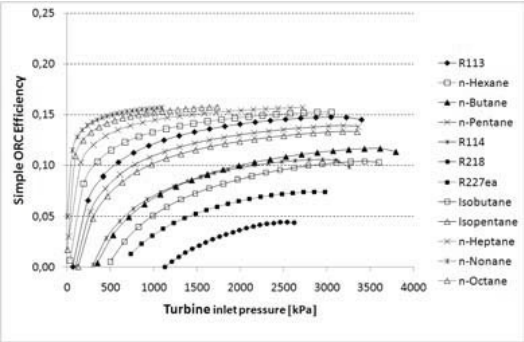

Fig. 3. Simple ORC efficiency for evaporation pressure between condenser pressure and critical pressure, for each fluid, in the case of no superheating.

The simple ORC efficiency curves show a maximum value for pressures not far from critical (except for n-Nonane and n-Octane, for which critical pressure was not reachable, according to the assumed constraints). The best efficiency values observed were 15,7%, belonging to n-Nonane; n-Octane and n-Heptane, while in the case of n-Hexane the value was about 15,2%.
In Figure 4 the simple ORC efficiency, in the case of superheating, is plotted for the selected fluids in the range of turbine inlet temperature between saturation temperature (at the selected pressure, reported for each fluid in the figure legend) and 270 °C, assumed as the maximum allowable superheating temperature, in order to keep 30 °C temperature difference between the fluid and the diathermic oil (300 °C). The values assumed for pressure, for each fluid, are correspondent to the cases of maximum efficiency values of the previous analysis of Figure 3, with the exception of n-Nonane and n-Octane. For these fluids, the maximum pressure was assumed as the correspondent value at 250 °C, in order to leave up-to 270° room for superheating.
The efficiency curves show how the efficiency is a weak function of turbine inlet temperature, once the evaporating pressure is chosen, and how it starts to decrease at increasing temperature.

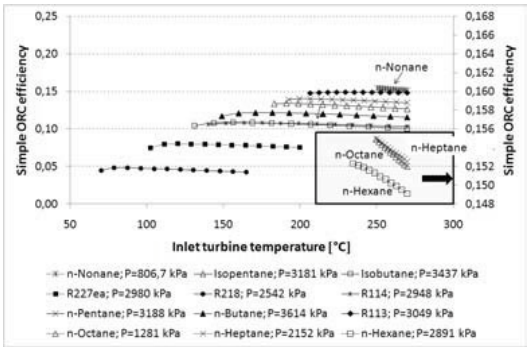

Fig. 4. Simple ORC efficiency for increasing turbine inlet temperature, in the case of superheating.

This results is in agreement with literature data [10], confirming that superheating is not convenient from a thermodynamic point of view [1]. In some cases, the highest cycle efficiencies are obtained when superheating is avoided and the fluid is expanded directly from dew line, as demonstrated in [10]. In [13] it has been also shown, through a comprehensive analysis based on irreversibility calculations, that superheating organic cycles (especially if based on overhanging fluids) increases cycle irreversibility and decreases the second law efficiency.
For these reasons, in the following, the regenerated ORC will be considered without superheating. For all the fluids, in the case of expansion of saturated vapour, it was checked that the fluid at the turbine exit was in the vapour phase (vapour quality equal to one).

5. Regenerated ORC results

The use of working fluids with overhanging vapour lines is generally a favourable condition, as it allows dry expansions without superheating and regenerate the cycle by sub-cooling the vapour at the end of expansion (direct regeneration) without vapour extraction.
Actually, not all the considered organic fluids offered the possibility of applying the internal regeneration of the cycle and not for the whole range of considered turbine inlet pressure. As a matter of fact the regeneration was applied only in the cases when the turbine outlet temperature was

20 °C higher than the condenser temperature.
Regeneration could not be applied at all, in any turbine inlet pressure condition, for: Isobutane; R227ea; R218; R114; n-Butane.

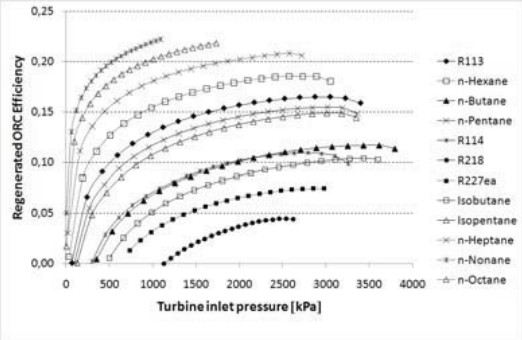

Fig. 5. Regenerated ORC efficiency for evaporation pressure between condenser pressure and critical pressure, for each fluid, without superheating.

In Figure 5 the regenerated ORC efficiency is plotted for the selected fluids in the range of turbine inlet pressure between condenser pressure (assumed as the value of saturation pressure at 35°C for each fluid) and critical pressure of each fluid, with the exception of n-Nonane and n-Octane. The curves for Isobutane, R227ea, R218, R114 and n-Butane are exactly the same of Figure 3, being correspondent to the non-regenerated cycles.
For all the other fluids the curves correspond to the regenerated cycles, showing a general increment in the efficiency. Also in the case of regenerated ORC, efficiency curves show a maximum value for pressures not far from critical point. In particular, maximum efficiency for n-Nonane increased up to 22,07%, for n-Octane up to 21,86%, for n-Heptane up to 20,61%, for n-Hexane up to 18,04.
Similar trends were found also for the ORC power curves plotted against the turbine inlet pressure. The turbine inlet pressure value which maximises the efficiency, for each fluid, also maximises the power output, as shown in Figure 6. Also, the fluid classification on the basis of the efficiency is the same of the classification on the basis of the power output. Table 3 shows the maximum values of efficiency, power output and specific work for the fluids which perform better.
In Figure 7 the efficiency of the ICE with ORC combined cycle is reported. The combined cycle efficiency was calculates as follows:

$$\eta_{CC} = \frac{W_{ICE} + W_{ORC}}{\dot{V}_{biogas} \cdot LHV_{biogas}} \qquad (2)$$

where:
η_{CC} = efficiency of ICE+ORC combined cycle
W_{ICE} = ICE power
$\dot{V}_{biogas}$ = biogas volumetric flow rate
LHV_{biogas} = biogas Low Heating Value

It can be noticed that the combined cycle efficiency increases, with respect to the simple ICE efficiency (38,40%), by only less than 1 percentage point, in the case of R218 non-regenerated ORC, up to 4,71 percentage points, in the case of n-Nonane regenerated ORC.

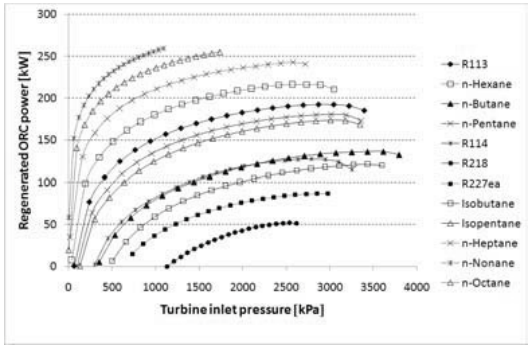

Fig. 6. Regenerated ORC power for evaporation pressure between condenser pressure and critical pressure, for each fluid, without superheating

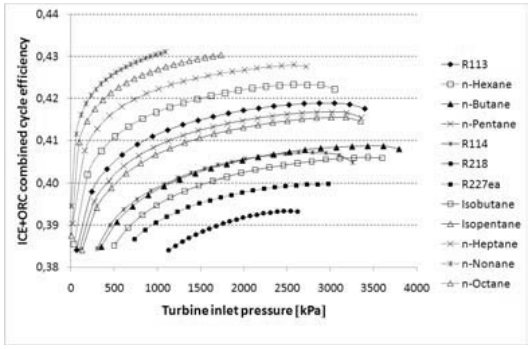

Fig. 7. ICE+ORC combined cycle efficiency, in the case of regeneration (when possible), without superheating.

5. Combined cycle performances for different ICEs

The analysis was then focused on those fluids which allowed the regeneration and showed the better performances: n-Nonane, n-Octane, n-Heptane and n-Hexane. For these fluids, it was assumed to set the evaporation pressure at the values reported in Table 3, which, according to the assumed constraints, generate the maximum regenerated, non superheated, ORC efficiencies, reported in Table 3, too.

Table 3. Assumed pressure values and corresponding ORC efficiency, power output and specific work

Fluid	Evaporation Pressure [kPa]	η_{ORC}	Power output [kW]	Specific work [kWh/kg]
n-Nonane	1.093	22,23	259,5	0,045
n-Octane	1.737	21,86	255,2	0,043
n-Heptane	2.578	20,8	242,8	0,040
n-Hexane	2.574	18,56	216,6	0,034

Also, three other different types of ICE were considered, representative of engine size smaller than the previously described in Table 1. The main characteristics for these three additional engines (B, C and D) are reported in Table 4-6. Also for these three cases, in reference to nominal conditions and under the hypothesis of perfect combustion of the methane contained in the biogas (65% CH_4 and 35% CO_2), the composition of the exhaust gases was calculated and used to evaluate exhaust gases properties.

Table 4. Engine B main characteristics

Engine parameter	Value	Units
Low Heating Value of biogas	6,40	kWh/Nm^3
Entering power (100% load)	2.693	kW
Biogas flow rate	421	Nm^3/h
Mechanical power output	1.077	kW
Electrical power output	1.048	kW el.
Electric efficiency	38,9	%
Exhausted gas temperature	510	°C
Exhausted mass flow	5.677	kg/h
Combustion air mass flow	5.195	kg/h

In Table 7 the main results, in terms of ICE+ORC combined cycle efficiency, ORC power output and organic fluid required mass flow rate, are reported for the four considered engines (A, B, C, and D) and for the four organic fluids (n-Nonane, n-Octane, n-Heptane and n-Hexane).

Table 5. Engine C main characteristics

Engine parameter	Value	Units
Low Heating Value of biogas	6,40	kWh/Nm^3
Entering power (100% load)	1.399	kW
Biogas flow rate	219	Nm^3/h
Mechanical power output	529	kW
Electrical power output	511	kW el.
Electric efficiency	36,5	%
Exhausted gas temperature	510	°C
Exhausted mass flow	2.941	kg/h
Combustion air mass flow	2.690	kg/h

Table 6. Engine D main characteristics

Engine parameter	Value	Units
Low Heating Value of biogas	6,40	kWh/Nm^3
Entering power (100% load)	3.375	kW
Biogas flow rate	527	Nm^3/h
Mechanical power output	1.451	kW
Electrical power output	1.413	kW el.
Electric efficiency	41,9	%
Exhausted gas temperature	448	°C
Exhausted mass flow	7.585	kg/h
Combustion air mass flow	6.982	kg/h

For each considered engine, the required mass flow rate of organic fluid is the lowest (smaller devices) corresponding to the organic fluid which performs better (n-Nonane).

Table 7. Main results of combined cycle simulation for different engines and different fluids.

		n-Nonane	n-Octane	n-Heptane	n-Hexane
		Engine A			
η_{CC}	[%]	43,11	43,03	42,8	42,33
W_{ORC}	[kW]	259,5	255,2	242,8	216,6
$\dot{m}_{fluid}$	[kg/h]	5.830	5.873	6.039	6.456
		Engine B			
η_{CC}	[%]	43,82	43,74	43,5	43,01
W_{ORC}	[kW]	132,5	130,3	124	110,6
$\dot{m}_{fluid}$	[kg/h]	2.978	3.000	3.084	3.297
		Engine C			
η_{CC}	[%]	41,4	41,32	41,09	40,59
W_{ORC}	[kW]	68,74	67,59	64,3	57,38
$\dot{m}_{fluid}$	[kg/h]	1.544	1.556	1.599	1.710
		Engine D			
η_{CC}	[%]	46,1	46,03	45,83	45,41
W_{ORC}	[kW]	141,8	139,4	132,6	118,4
$\dot{m}_{fluid}$	[kg/h]	3.186	3.209	3.299	3.527

The combined cycle efficiency increases by 3,9-4,7 percentage points with respect to the simple ICE efficiency of engine A (38,40%); by 4,1-4,9 percentage points with respect to the simple ICE efficiency of engine B (38,90%); by 1,7-2,5 percentage points with respect to the simple ICE efficiency of engine C (36,50%); by 3,5-4,2 percentage points with respect to the simple ICE efficiency of engine D (41,90%).

The combined cycle power output increases by 10-12% with respect to the simple ICE power of engine A (2.118 kW); by 11-13% with respect to the simple ICE power of engine B (1.048 kW); by 5-7% with respect to the simple ICE power of engine C (511 kW); by 8-10% with respect to the simple ICE power of engine D (1.413 kW).

Plotting the combined cycle efficiency vs. the ICE simple efficiency (Figure 8), for the different considered organic fluids, shows how the first one is directly correlated on the second one (Table 8). On the contrary, no correlation was found between combined cycle efficiency and exhaust gas temperature or engine size, with regard to the analysed engine cases.

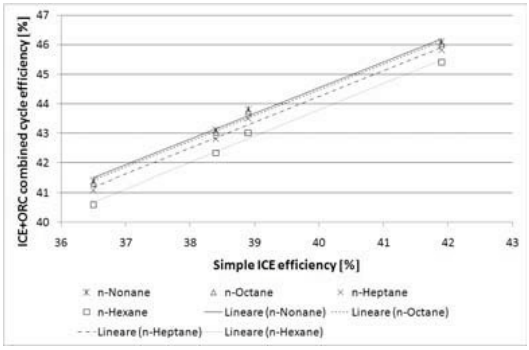

Fig. 8. Correlation between ICE+ORC combined cycle efficiency and ICE simple efficiency.

Table 8. Correlation coefficient between combined cycle efficiency and ICE simple efficiency, for the different fluids.

Organic fluid	R^2
n-Nonane	0,9934
n-Octane	0,9936
n-Heptane	0,9945
n-Hexane	0,9956

Conclusion

Organic Rankine cycles (ORC) were analyzed as possible bottoming cycles coupled with internal combustion engines (ICE), as topping cycle, fuelled by biogas from landfill or anaerobic digestion. At present time, the potential for cogeneration by internal combustion engines fed with biogas is scarcely diffused, while the electric energy production is promoted by economic benefits, in several European Countries. For these reasons, the possibility of increasing the electric power output seems to be attractive. This incremental production can be accomplished by adding as a bottoming cycle an ORC using, in the simplest case, engine exhaust gases as a thermal source.

In order to increase as much as possible the incremental power output obtainable from the ORC, twelve organic fluids were considered, all characterized by an overhanging vapour line and dry expansion.

In the case of simple ORC, without superheating, the efficiency curves, for the different fluids, show a maximum value for pressures not far from critical one. The best efficiency values observed were 15,7%, belonging to n-Nonane; n-Octane and n-Heptane, while in the case of n-Hexane the value was about 15,2%. In the case of simple ORC with superheating, the efficiency results a weak function of turbine inlet temperature, once the evaporating pressure is chosen, and it starts to decrease at increasing temperature. Therefore, superheating was disregarded.

The use of working fluids with overhanging vapour lines is a favourable condition also because it allows the internal regeneration by sub-cooling the vapour at the end of expansion (direct regeneration) without vapour extraction. Actually, not all the considered organic fluids offered the possibility of applying the internal regeneration of the cycle.

When regeneration is applicable, a general increment in the efficiency is observed. Also in the case of regenerated ORC, efficiency curves show a maximum value for pressures not far from critical point, for each fluid. In particular, maximum efficiency for n-Nonane increased up to 22,07%, for n-Octane up to 21,86%, for n-Heptane up to 20,61%, for n-Hexane up to 18,04.

The ICE+ORC combined cycle efficiency increases, with respect to the simple ICE efficiency (38,40%) up to 4,71 percentage points,

in the case of applying a regenerated ORC, using n-Nonane as working fluid.
Depending on the primary ICE type: the combined cycle power output increases by 5-13% with respect to the simple ICE power of engine; the combined cycle efficiency increases by 1,7-4,9 percentage points with respect to the simple ICE efficiency.

The actual advantage of adding an ORC as the bottoming cycle for an ICE, however, should be evaluated, in future works, from an economic point of view, in reference to the different combined cycle sizes.

Also, taking into account in the model the variation of the turbine isentropic efficiency in function of the pressure ratio will be done in the near future to improve the quality of the model and the accuracy of results.

Nomenclature

$\dot{m}$ mass flow rate, kg/h

$\dot{V}$ volumetric flow rate, Nm^3/s

W power, kW

Q thermal power, kW

LHV Low Heating Value, kJ/Nm^3

R Linear correlation coefficient

C condenser

T turbine

$GOHE$ Gas-Oil Heat Exchanger

P Pump

R Regenerator

Greek symbols

η efficiency

Subscripts and superscripts

CC Combined Cycle

ORC Organic Rankine Cycle

ICE Internal Combustion Engine

fluid organic fluid

References

[1] Vaja, I. and Gambarotta, A. Internal Combustion Engine (ICE) bottoming with Organic Rankine Cycles (ORCs), Energy (2009), doi:10.1016/j.energy.2009.06.001. In Press.

[2] Invernizzi, C., Iora, P., Silva, P. Bottoming micro-Rankine cycles for micro-gas turbines. Appl Ther Eng 2007;27:100–10.

[3] Liu, B.T., Chien, K.H., Wang, C.C. Effect of working fluids on organic Rankine cycle for waste heat recovery. Energy 29 (2004) 1207–1217

[4] Dai, Y., Wang, J., Gao, L.. Parametric optimization and comparative study of organic Rankine cycle (ORC) for low grade waste heat recovery. Energy Conversion and Management 50 (2009) 576–582

[5] Schuster, A. et al.. Energetic and economic investigation of Organic Rankine Cycle applications. Applied Thermal Engineering 29 (2009) 1809–1817

[6] Desai, N.B. and Bandyopadhyay, S. Process integration of organic Rankine cycle. Energy 34 (2009) 1674–1686

[7] Larjola J. Electricity from industrial waste heat using high speed organic Rankine cycle (ORC). Int J Prod Econ 1995;41:227–35.

[8] Drescher, U. and Bruggermann, D. Fluid selection for the organic Rankine cycle (ORC) in biomass power and heat plants. Appl Therm Eng 2007;27:223–8.

[9] Wei D, Lu X, Lu Z, Gu J. Performance analysis and optimization of organic Rankine cycle (ORC) for waste heat recovery. Energy Conversion and Management 2007;48:1113–9.

[10] Hung, T.C., Shai, T.Y., Wang, S.K. A review of organic Rankine cycles (ORCs) for the recovery of low-grade waste heat. Energy 1997;22:661–7.

[11] Vijayaraghavan, S. and Goswami, D. Y. Journal of Energy Resources Technology, 2005, ASME JUNE 2005, Vol. 127

[12] Saleh, B. et al.. Working fluids for low-temperature organic Rankine cycles. Energy 32 (2007) 1210–1221

[13] Mago, P.J. et al. An examination of regenerative organic Rankine cycles using dry fluids. Appl Therm Eng 2008;28:998–1007.

[14] http://www.fchart.com/ees/ees.shtml

EXHAUST HEAT RECUPERATION FROM DI DIESEL ENGINES USING MECHANICAL AND ELECTRICAL TURBOCOMPOUNDING

Hountalas D.T.[a], Knecht W.[b] and Zannis T.C.[c]

[a] *National Technical University of Athens, Greece*
[b] *Knecht Engine Consulting GmbH, Kesswil, Switzerland*
[c] *Hellenic Naval Academy, Piraeus, Greece*

Abstract: A considerable amount of fuel chemical energy supplied to diesel engines is rejected to the environment through exhaust gases. It is approximately 30-40% of the energy supplied by the fuel depending on engine load. Therefore if part of this energy is recovered, it could result to significant reduction of engine bsfc compared to other technological solutions. A promising solution for the utilization of exhaust heat is turbocompounding, which has various advantages compared to other techniques as far as packaging, cost and applicability of the system is concerned. The idea is not new because various attempts have been reported but with marginal fuel savings. However, there exists a potential for significant improvement of fuel saving especially when the system is applied on engines with reduced heat losses. For this reason, in the present work, a detailed investigation is conducted to investigate and compare the effect of mechanical and electrical turbocompounding technologies on engine performance and exhaust emissions. In case of mechanical turbocompounding, a power turbine is mounted downstream of the engine turbocharger (T/C) whereas in case of electrical turbocompounding, a high-speed electrical generator is coupled to the T/C shaft for recuperating the excess exhaust power produced from the T/C turbine. The investigation is conducted on a heavy-duty (HD) direct injection (DI) truck diesel engine at various operating conditions. The examination involves mainly the effect of T/C and power turbine efficiency for both turbocompounding arrangements on engine performance characteristics and pollutant emissions. Variation of power turbine pressure ratio has also been taken into account in the case of mechanical turbocompounding. From the analysis it is revealed a potential for considerable fuel saving in the range of 8-9% when electrical turbocompounding is accompanied with high efficiency T/C equipment.

Keywords: Diesel engine, Exhaust heat recovery, Turbocompounding

Nomenclature

a_{del}	ignition delay constant
a_f	combustion rate exponent
a_o	combustion rate exponent
C_f	mass fraction of fuel
C_o	mass fraction of oxygen
E	activation energy, J/kmol
K_b	combustion rate constant
m	mass, kg
N	engine rotational speed, rpm
P_e	power, W
p	pressure, Pa
R_m	gas constant, J/kmolK
S_{pr}	ignition delay integral
T	temperature, K

Greek symbols

η	efficiency
Φ_{eq}	equivalence ratio

Subscripts and superscripts

b	burnt
C	compressor
del	delay
e	brake
E	engine
el	electric
f	fuel
g	gas
m	mechanical
tot	total
T	turbine

Abbreviations

ATDC	after top dead centre
bsfc	brake specific fuel consumption
CA	crank angle

1. Introduction

Recovery of waste heat from the exhaust gas is considered as one of the key advances concerning mid-term developments of diesel engines used in heavy-duty (HD) truck applications focusing on the reduction of bsfc [1,2]. Depending on engine operating conditions the amount of fuel energy which is rejected to the ambience is in the order of 30-40%. It is inevitable that the partial utilization of this energy amount creates expectations for considerable reduction of diesel engine brake specific fuel consumption (bsfc). A promising waste heat recovery solution is turbocompounding. According to the literature [3-9], the dominant turbocompounding technologies, which have been used up to now in diesel engines are the following:

- *Mechanical turbocompounding*: A power turbine is placed after engine turbocharger (T/C) to extract additional mechanical power from exhaust gases. The power turbine is mechanically coupled to engine crankshaft through mechanical gear [3-7].
- *Electrical turbocompounding*: An electrical generator is coupled to the T/C shaft which converts the excess power of the turbine to electric power [7-9]

Previous studies [3-7] considering various mechanical turbocompounding configurations revealed that an improvement of overall bsfc up to 5-6% is feasible. Specifically, Caterpillar [4,5] has used an axial power turbine on a 14.6-liter diesel and reported an average bsfc reduction of about 4.7% for a 50,000 miles extra-urban driving test in the US. In addition, Cummins [3] used a radial flow power turbine and reported 6% maximum improvement of bsfc at full load and 3% at partial load. Finally, Scania [4] applied turbocompounding technology on an 11-liter displacement 6-cylinder turbocharged diesel engine and reported a bsfc improvement of 5% at full load.

Previous investigations have also shown that significant improvement of the overall efficiency of HD DI diesel engines may be attained by implementing various electrical turbocompounding configurations [7-9]. Caterpillar has considered electrical turbocompounding technology in a research program [8,9] and reported indications for 5% reduction of bsfc on a cycle basis. They also indicated [8,9] a maximum reduction of approximately 9-10% when using turbocharger components with high efficiency. Considering the previous, it appears that the potential for recovering the exhaust gases enthalpy using both turbocompounding approaches can be beneficial considering the trend for increasing oil prices.

For this reason, in the present work, a theoretical investigation is conducted to estimate the potential for exhaust energy recovery from a heavy-duty diesel engine using mechanical and electrical turbocompounding. The influence of both turbocompounding technologies on HD DI diesel engine performance and emissions is also examined in this study. For both cases the investigation focuses on the effect of T/C efficiency and pressure increase before the turbine on engine performance and emissions. For mechanical turbocompounding, a parametric study has been conducted considering for the effect of turbine expansion ratio on diesel engine performance and emissions. This is done since the effect of power turbine efficiency can be independently investigated because only exhaust manifold pressure affects engine operation. The parametric investigation has been conducted using a diesel engine simulation model, which has been appropriately modified to consider for both technologies. The theoretical results focus mainly on the overall bsfc benefit from the application of both exhaust heat recovery techniques. Predictions also demonstrate the impact of mechanical and electric turbocompounding on engine exhaust pressure and temperature (before the turbine), net power output and pollutant emissions.

As revealed from the analysis, the potential for recovering exhaust heat and converting it into useful mechanical or electrical energy is good. Considering the continuous increase of oil prices and the necessity for dramatic reduction of CO_2 emissions, it appears that the proposed exhaust heat recovery techniques may be potential solutions for further improvement of engine bsfc.

2. Engine simulation model

2.1 Brief outline of the simulation model

For the investigation an engine simulation code based on a multi-zone combustion model was properly modified and used [10,11]. The fuel jet is divided into discrete control volumes, called "zones", each having its own history, i.e. temperature, composition etc [10,11]. The pressure in the engine cylinder is considered to be uniform. The condition in each zone is calculated using the first law of thermodynamics and the conservation equations for mass and momentum.

2.2 Heat transfer

A turbulent kinetic energy viscous dissipation rate k-ε_t model [12] is used to determine the characteristic velocity for the heat transfer calculations. The heat transfer coefficient is evaluated from a widely tested correlation as described in [13]. The heat exchange rate obtained is then distributed among the jet zones according to their mass, temperature and specific heat capacity [10,11].

2.3 Air swirl

A hybrid scheme is considered consisting of a solid body core surrounded by a potential flow region for modeling the swirling motion of air inside the combustion chamber [10,11]. During induction, angular momentum is continuously added to the engine cylinder, part of which is destroyed because of friction while the remaining part forms the flow field. Details concerning the method of solution to determine the swirling velocity are provided in [10,11].

2.4 Spray model

After initiation of fuel injection, zones start to form and penetrate inside the combustion chamber. Zone velocity along the jet axis is obtained from correlations providing the penetration of the fuel jet inside the cylinder, as described in [10,11]. The velocity of zones on the jet periphery is estimated using the methodology described in detail in [10,11] by considering their radial distance from the jet axis. The effect of air swirl upon the jet is also considered for from the local components of the air velocity in the radial and axial directions and conservation of momentum in both axes.

2.5 Air entrainment into the zones

The air entrainment rate into the zones is obtained from momentum conservation. In addition the affect of wall impingement is also considered for.

2.6 Droplet breakup and evaporation

The injected fuel is distributed to the zones according to the instantaneous injection rate, while inside each zone the fuel is divided into packages (groups) where the droplets have the same Sauter Mean Diameter. For the evaporation process the model of Borman and Johnson [14] is adopted, as described in [15].

2.7 Combustion model

The time period of fuel chemical preparation ends and ignition commences when the following integral becomes equal to unity [10,11]:

$$S_{pr} = \int_0^t \frac{1}{a_{del} P_g^{-2.5} \Phi_{eq}^{-1.04} \exp\left(\frac{5000}{T_g}\right)} dt = 1 \quad (1)$$

where "Φ_{eq}" is the local fuel equivalence ratio, T_g is the local zone temperature and p_g is the in-cylinder pressure. The combustion rate of fuel is modeled using an Arrhenius type equation of the form,

$$\dot{m}_{fb} = K_b C_f^{af} C_o^{ao} \exp(-\frac{E_c}{R_m}) \frac{1}{6N} \quad (2)$$

where K_b is a constant, E_c the reduced activation energy and C_f, C_o are the mass concentrations of fuel and oxygen respectively

2.8 Nitric oxides and soot formation

The contents of each zone are initially assumed to consist only of air and perfect combustion products (O_2, N_2, CO_2 and H_2O). Using this as an initial estimate and applying a complete chemical equilibrium scheme [16], the equilibrium mixture composition is calculated considering 11 chemical species (O_2, N_2, CO_2, H_2O, H, H_2, N, NO, O, OH, CO). Therefore, the concentration of species inside each zone is known at any instant of time and can be used to estimate exhaust emissions.

The formation of nitric oxide is controlled by chemical kinetics. Herein, the extended Zeldovich chain reaction model is used [17] as described in [10,11].

The proven successful model of Hiroyasu et al. [18] is used to calculate soot emissions. According to this model, in-cylinder soot is the net difference of two competitive mechanisms: one delineating soot formation and the other describing the soot oxidation rate. Soot formation rate is governed by the local availability of vaporized fuel mass, cylinder pressure and local temperature, whereas soot oxidation rate is determined by the partial pressure of oxygen inside combustion zone.

2.9 Gas exchange

The filling-emptying method [10,11] is used to estimate the pressure and temperature histories inside the intake and exhaust manifolds. The exhaust mass flow rate through the turbine is calculated using isentropic flow relations and an equivalent effective flow area A_{eff}.

2.10 Modeling of T/C and power turbine

In the present study, T/C modeling was based on T/C maps which were used for both mechanical and electrical turbocompounding. In the case of electrical turbocompounding, the turbine effective flow area A_{eff} was calculated from an iterative

procedure to provide the required exhaust pressure value before the turbine [4]. Then turbine excess power was estimated from the following relation:

$$P_{el,p} = P_{eT}\eta_{mT} - \frac{P_{eC}}{\eta_{mC}} \quad (3)$$

where P_{eC} is the compressor power, P_{eT} the turbine and $P_{el,p}$ the excess power of the turbine, which is then converted, to electric power.

Modifications were conducted to the engine simulation model to consider for the existence of the power turbine in the case of mechanical turbocompounding since the last is mounted downstream of the engine T/C. Its inlet conditions have been calculated from the conditions of the gas at the T/C exit. Therefore a new calculation procedure has been adopted, which estimates the pressure at the T/C turbine inlet which is necessary to produce the required boost pressure in order to providing the necessary amount of air to the engine.

For the case of mechanical turbocompounding, constant power turbine efficiency (80%) has been considered due to the parametric nature of the investigation. However this assumption is not critical because results can be easily extrapolated to other power turbine efficiencies since this will have no effect on the T/C or the engine. For the present application, the mechanical efficiencies of turbine and compressor, n_{mT} and n_{mC} were taken equal to 0.95.

In both cases, the simulation estimates the total generated power which corresponds to the net engine power and the mechanical power produced from the power turbine or the electric generator in the case of electrical turbocompounding. The total generated power $P_{e,tot}$ has as follows:

$$P_{e,tot} = P_{eE} + P_{e,Tnet}\eta_{GT} \quad (4)$$

where $P_{eT,net}$ is the power turbine power or the net power produced from the electric generator for electrical turbocompounding and P_{eE} is the net engine power. Term n_{GT} represents the mechanical efficiency of the gear train for mechanical turbocompounding or the generator efficiency for electrical turbocompounding

3. Engine description

The engine considered herein is the downsized version of a six-cylinder heavy-duty turbocharged truck engine having a bore of 125 mm, a stroke of 140 mm and compression ratio of 16.5:1. The engine is equipped with a common-rail fuel injection system. The maximum brake mean effective pressure (bmep) of the engine is 33 bar (downsized version) and the engine peak power is 360kW at 1700 rpm engine speed.

4. Test cases examined

The engine operating conditions, which are considered in order to examine the effect of mechanical and electrical turbocompounding on engine performance and emissions, are given in Table 1. Simulations have been also conducted at four different engine loads (i.e., 25%, 50%, 75% and 100%) at 1300 and at 2100 rpm respectively. However, for the sake of the brevity of space, results are given herein only for 1700 rpm at 50% and 100% of engine load. To insure that the combustion mechanism is not affected from turbocompounding both the fuelling rate and the air-to-fuel ratio (AFR) have been maintained the same as for the non-turbocompound case (standard engine operation). Thus, boost air pressure and temperature are maintained the same as in the case of standard engine operation.

Table 1. Engine operating conditions considered for the investigation

Speed (rpm)	Load (%)	Fuel Consumption (kg/h/cyl)	Inlet Pressure (bara)	Injection Advance (deg ATDC)
1700	25	3.45	1.50	-6
	50	6.10	2.23	-7
	75	8.90	2.65	-8
	100	11.80	3.08	-8

5. Model calibration and validation

Before examining theoretically the effect of mechanical and electrical turbocompounding systems on engine performance and exhaust emissions, the simulation model has been calibrated at a single operating point for both performance and emissions. However no calibration was made for exhaust soot due to lack of experimental data and therefore, results for exhaust soot are valid only on a qualitative basis. The last should be taken into account when examining the relative variation of soot with turbocompounding because small absolute values can result to significant percentage variations.

After calibration, the predictive ability of the simulation model was tested against pertinent experimental data for engine performance characteristics and NO emissions for the entire engine operating range. The comparison of predicted and measured values revealed a good predictive ability which motivated the use of the simulation for the present investigation. Details for model validation have been provided in [6].

6. Comparative evaluation of mechanical and electrical turbocompounding

6.1 Overview of the evaluation

In the case of mechanical turbocompounding, the parametric investigation involved mainly the effect of power turbine pressure ratio [4,6] on total power output, overall engine bsfc improvement and pollutant emissions. On the other hand, power turbine efficiency has been kept constant since the results produced for generated power can be easily extrapolated to other efficiencies. This results from the fact that power turbine efficiency does not affect its boundary conditions and the ones of the engine. For this reason an isentropic efficiency of 80% was considered for the power turbine, which is feasible by present turbine technology. The parametric investigation has been conducted for all engine-operating points tabulated in Table 1. It was examined also the effect of T/C efficiency on overall engine performance parameters and pollutant emissions. Three different values of both compressor and turbine efficiency have been examined, i.e. the standard values |and two additional ones considering an increase of 5% and 10% on a percentage basis.

A similar analysis has been conducted using electrical turbocompounding for all test cases shown in Table 1. The parameters of this investigation were: turbocharger efficiency (standard and 5%, 10% increase) and exhaust pressure increase before the turbine.

The mechanical efficiency of the gear train n_{GT} was considered constant and equal to 90% and for electrical turbocompounding, generator efficiency was also assumed constant and equal to 95%.

Predictions for bsfc improvement, net engine power, generated power and overall power output as well as turbine exhaust temperature and soot and NOx emissions are presented as a function of exhaust back pressure. This guarantees the use of a common basis when comparing the effects of mechanical and electrical turbocompounding on engine performance and emissions.

6.2 Effect of the turbocompounding system on engine performance characteristics

Figure 1 illustrates the effect of power turbine pressure ratio and T/C efficiency on exhaust manifold pressure for the case of mechanical turbocompounding. As shown the increase of power turbine pressure ratio results to significant increase of exhaust manifold pressure that may have a negative impact on T/C operation. This may affect the isentropic efficiency of the T/C turbine. On the other hand, the situation is more severe for the case of electric turbocompounding because the pressure ratio across the T/C is higher since the downstream pressure is the ambient pressure. Figure 1 also depicts the influence of T/C efficiency on power turbine pressure ratio. As observed, the simultaneous increase of compressor and turbine efficiency results to lower exhaust pressures for the same pressure ratio. The maximum value of exhaust pressure is in the order of ~ 6bar at full engine load for a power turbine pressure ratio of 3÷1. However this is reduced drastically up to ~ 4bar when increasing the efficiency of the turbocharger.

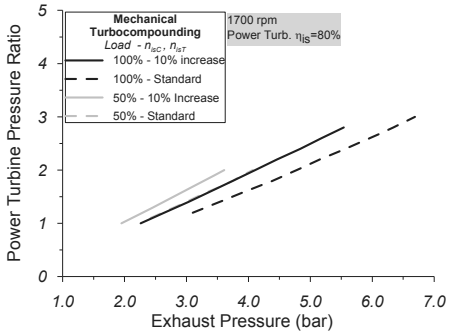

Fig. 1. Power turbine pressure ratio vs. exhaust pressure at 1700 rpm and at 50% and 100% engine load.

The variation of bsfc relative improvement vs. exhaust manifold pressure is presented in Fig.2 for various T/C efficiencies. Predictions are given for both mechanical and electrical turbocompounding at all operating conditions herein. Obviously both turbocompounding technologies result in reduction of bsfc compared to conventional diesel operation. In the case of mechanical turbocompounding and for standard T/C efficiency, the maximum bsfc improvement is ~ 2.1% at partial load and ~ 4.9% at full engine load. For electrical turbocompounding and for standard T/C efficiency, the maximum bsfc improvement is ~1.2% at partial load and ~ 3.5% at full engine load. Hence, for standard T/C efficiency, mechanical turbocompounding is obviously more influential regarding bsfc improvement compared to electrical turbocompounding the limiting factor being the increase of T/C pressure ratio.

For both turbocompounding technologies, the increase of compressor and turbine efficiency by 10% results in further bsfc improvement. This effect is more pronounced in the case of electrical

turbocompounding, where the maximum bsfc improvement is now ~ 6.5% at partial engine load and ~ 9.5% at full load. The corresponding values for mechanical turbocompounding are ~ 6.0% and ~ 8.3% respectively.

From Fig.2 it is obvious that after a certain exhaust manifold pressure the bsfc improvement is reduced revealing that an optimum has been reached. This comes from the negative impact of exhaust manifold pressure on engine performance. The optimum exhaust pressure value for bsfc improvement is shifted to higher values with the increase of engine load. However after a certain point the additional decrease of bsfc is rather limited while it has a negative effect on exhaust pressure.

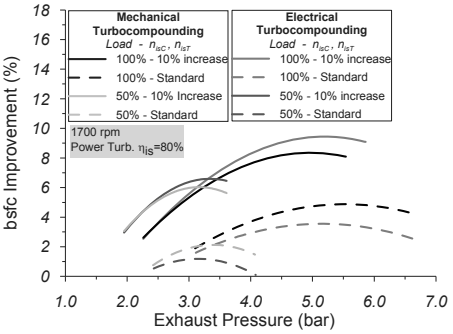

Fig. 2. Relative improvement of bsfc vs. exhaust pressure at 1700 rpm and at 50% and 100% engine load.

The variation of generated power with exhaust manifold pressure is given in Fig. 3. In the case of mechanical turbocompounding, this refers to the mechanical power generated by the power turbine and in the case of electrical turbocompounding to the electrical power produced by the electrical generator. An increase of generated power with increasing exhaust pressure is observed for both turbocompounding technologies at all operating cases considered. For the case of the standard T/C efficiency, the maximum generated power at part load is ~ 29 kW, which corresponds to ~ 18.5% of net engine power while the corresponding values for full load are ~ 79kW and ~ 24%.. For electrical turbocompounding the corresponding values are 27 kW and ~ 17.1% at part load and 71.4 kW and ~ 21.9% at full load.

In the case of 10% increased T/C component efficiency, the generated power increases with exhaust manifold pressure but the effect is more favourable in the case of electric turbocompounding. The increase of T/C component efficiency by 10% results in an additional increase of generated power by 7.5% in case of mechanical turbocompounding and by ~ 12.8% in the case of electric turbocompounding. Most important is the fact that the increase of T/C efficiency shifts generated power curve to lower exhaust pressure values. Hence, more mechanical or electrical power may be produced with less detrimental effects to diesel engine operation i.e. lower exhaust manifold pressures.

In Fig. 3, is also given the variation of net engine power with exhaust pressure for both turbocompounding technologies. As observed, the implementation of either mechanical or electrical turbocompounding results in reduction of primary engine output, which is linear with exhaust pressure variation. Reduction of net engine power with exhaust manifold pressure is directly attributed to the increase of gas exchange work. However, due to the power produced from the power turbine or the electric generator the overall power is increased as shown in Fig. 4.

As observed overall system power increases with the increase of exhaust manifold pressure obviously due to the interrelated increase of the pressure expansion ratio. For standard T/C efficiency, the mechanically turbocompounded engine generates in total more power compared to the pertinent electrically compounded engine at all loads considered. The opposite effect is witnessed for increased T/C efficiency at both engine loads examined. For an increased T/C efficiency in the case of mechanical turbocompounding, the overall power output is increased by ~ 5% at full load while the corresponding value for electric turbocompounding is ~ 3.5%. The increase of T/C component efficiency by 10% results in an increase of ~ 8.0% for mechanical turbocompounding and ~ 9.5% for electrical.

An important parameter for the turbocompounded engines and the especially the mechanically compounded ones is the level of gas temperature at the T/C turbine exit i.e. power turbine inlet temperature. This temperature is indicative of the thermodynamic state of exhaust gases.

The effect of turbocompounding technology and T/C efficiency on T/C turbine outlet temperature as a function of exhaust manifold pressure is shown in Fig. 5 for all operating cases considered. In the case of mechanical turbocompounding, the increase of power turbine pressure ratio and subsequently the increase of exhaust manifold pressure results to an increase of exhaust gas temperature at the T/C turbine exit.

On the other hand, for electrical turbocompounding, turbine exhaust temperature remains almost unaffected from exhaust pressure increase. For mechanical turbocompounding the exhaust temperature at the turbine outlet is increased up to 425°C (percentage variation of ~ 20.5% with respect to normal diesel operation) at part load and up to 611°C (~ 28% relative change with respect to diesel operation) at full load.

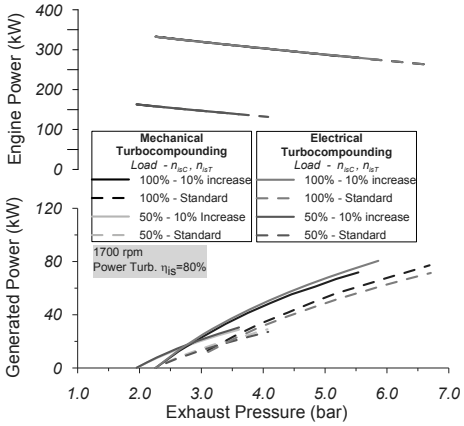

Fig. 3. Generated power and engine power output vs. exhaust pressure at 1700 rpm and at 50% and 100% engine load.

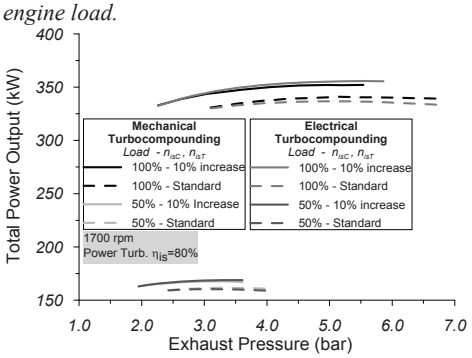

Fig. 4. Total power output vs. exhaust pressure at 1700 rpm and at 50% and 100% engine load

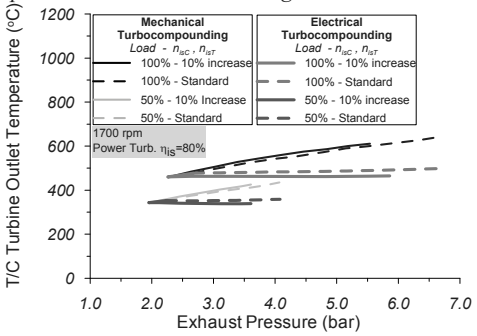

Fig. 5. T/C turbine outlet temperature vs. exhaust pressure at 1700 rpm and at 50% and 100% engine load.

6.3 Effect of turbocompounding system on pollutant emissions

Another important aspect for turbocompounding is its effect on engine out emissions. For this reason, the effect of turbocompounding technology and T/C efficiency on the variation of soot and NOx emissions with exhaust pressure is shown in Figs. 6 and 7.

Considering the fact that fuelling rate and AFR have been maintained constant, any variation of specific emissions should be attributed to the variation of either in-cylinder pollutant formation or power output since specific values have been used for both pollutants, i.e. g/kWh. The increase of exhaust pressure results to an increase of the residual gas fraction inside engine combustion chamber. Therefore, when a new compression stroke initiates the trapped exhaust gases reduces oxygen availability resulting to "internal" EGR.

Hence, the increase of back pressure caused by turbocompounding is expected to have a positive effect on NOx emissions (reduction) and a negative one on soot (increase). Also it is expected to have no significant differences between the two turbocompounding options when expressing the results as a function of exhaust manifold pressure. This is verified by the predictions given for overall soot and NOx emissions in Figs. 6 and 7 respectively. However, it is noteworthy to mention that results provided herein can only be treated as indicative ones. This is due to the fact that the relative impact on exhaust emissions depends not only the turbocompounding technology but also to other parameters such as the inlet and exhaust system configuration, the engine compression ratio etc.

According to Fig.6 the increase of soot is more pronounced at high engine load. The slope of specific soot increase with increasing back pressure is curtailed when T/C efficiency is increased. Nevertheless, it should be mentioned that the high percentage increase of soot experienced in the present work depends on the absolute engine out soot emissions.

On the other hand, NOx reduction with exhaust back pressure is mainly attributed to internal EGR and secondarily to the increase of overall engine power output, because specific NOx values i.e. in g/kWh have been used. The highest percentage increase of soot is observed for electrical turbocompounding in the case of increased T/C efficiency which is ~ 80% due to the extremely high exhaust manifold pressure This case presets

the highest percentage reduction of NOx which is ~ 20% compared to conventional diesel operation.

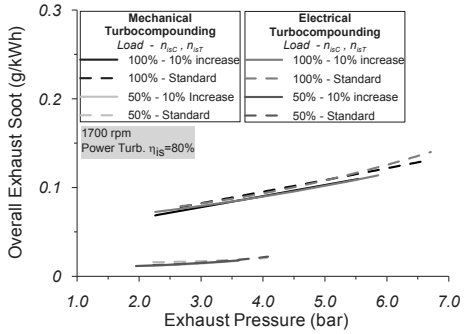

Fig. 6. Total emitted soot vs. exhaust pressure at 1700 rpm and at 50% and 100% engine load.

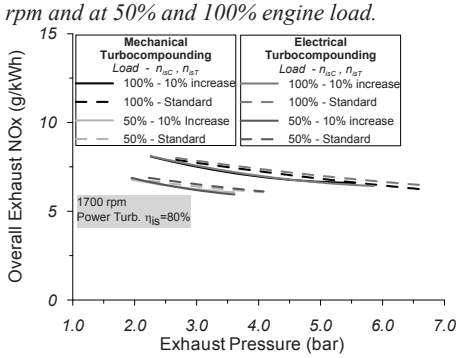

Fig. 7. Total emitted NOx vs. exhaust pressure at 1700 rpm and at 50% and 100% engine load

Conclusions

The analysis of the theoretical results generated for mechanical and electrical turbocompounding technologies at a constant fuelling rate and AFR has lead to the following conclusions:

- Both mechanical and electrical turbocompounding resulted in improvement of brake specific fuel consumption (bsfc). For standard T/C efficiency, the positive effects of turbocompounding on bsfc improvement are more pronounced in the case of mechanical turbocompounding at all operating points. The effect is reversed when increasing T/C efficiency. Overall the highest bsfc improvement is ~ 9.5% and is observed for electrical turbocompound using a T/C with 10% component efficiency. The corresponding value for mechanical turbocompounding is ~ 8.3 %.
- Both technologies resulted in reduction of primary engine power output. The effect on a percentage basis is higher at low engine load. However, both mechanical and electrical turbocompounding result in an improvement of overall power output due to the power generated from the exhaust gas energy. The percentage improvement is similar to the reduction of bsfc.
- In the case of mechanical turbocompounding, increase of T/C turbine outlet temperature with power turbine pressure ratio i.e. exhaust manifold pressure was observed. The maximum increase was ~ 28% on a Celsius basis. The increase of T/C efficiency in this case resulted in the increase of the slope of turbine outlet temperature with exhaust back pressure. On the other hand, in case of electrical turbocompounding, the variation of turbine outlet temperature with engine back pressure was rather imperceptible.
- The increase of exhaust manifold pressure especially in the case of mechanical turbocompounding resulted in the increase of exhaust gas mass trapped inside combustion chamber. This resulted to significant increase of soot emissions up to 80% and to a milder decrease of NOx emissions up to 20%. The effect of turbocompounding on NOx specific emissions is partially attributed to the increase of total power output.

Acknowledgments

The authors would like to express their appreciation to the European Union for supporting financially the project “GREEN” (TIP4-CT-2005-516195) under which the current investigation has been conducted.

References

[1] Knecht, W., 2008, “Diesel engine development in view of reduced emission standards”, Energy, 33(2), pp. 264-271.

[2] Miller, P., et al., 2009, “Reducing heavy-duty long haul combination truck fuel consumption and CO_2 emissions”, NESCCAF - Northeast States Center for a Clean Air Future, Southwest Research Institute and TIAX, LLC, DOE Final Report.

[3] Brands, M.C, Werner, J. and Hoehne, J.L., 1981, “Vehicle testing of Cummins turbocompound diesel engine”, SAE Paper No. 810073.

[4] Tennant, D.W.H. and Walsham, B.E., 1989, “The turbocompound diesel engine”, SAE Paper No. 89064.

[5] Wilson, D.E., 1986, “The design of a low specific fuel consumption turbocompound engine”, SAE Paper No.860072.

[6] Hountalas, D.T., et al., 2007, "Study of available exhaust gas heat recovery technologies for HD diesel engine applications", International Journal of Alternative Propulsion, 1(2/3), pp. 228 – 249.
[7] Sendyka, B. and Soczowka, J., 2001, "Recovery of exhaust gases energy by means of turbocompound", Politechnika Krakowska.
[8] Hopmann, U., 2004, "Diesel engine waste heat recovery utilizing electric turbocompound technology", Caterpillar, DEER Conference, San Diego, California, USA.
[9] Hopmann, U. and Algrain, M., 2003, "Diesel engine waste heat recovery utilizing electric turbocompound technology", Caterpillar Inc., Presentation in 2003 DEER Conference Newport Rhode Island.
[10] Hountalas, D.T., et al., 2005, "Possibilities to achieve future emission limits for HD DI diesel engines using internal measures", SAE Paper No 2005-01-0377.
[11] Rakopoulos, C.D. and Hountalas, D.T., 1998, "Development and validation of a 3-D multi-zone combustion model for the prediction of a DI diesel engines performance and pollutants emissions". SAE Transactions, Journal of Engines, 107, pp.1413-1429.
[12] Dent, J.C. and Derham, J.A., 1974, "Air motion in a four-stroke direct injection diesel engine", Proc. Inst. Mech. Engrs, 188, pp.269-280.
[13] Heywood, J.B., 1988, *Internal Combustion Engine Fundamentals*, McGraw-Hill, New York.
[14] Borman, G.L. and Johnson, J.H., 1962, "Unsteady vaporization histories and trajectories of fuel drops injected into swirling air", SAE Paper No. 598C, National Powerplant Meeting, Philadelphia, PA.
[15] Ramos, J.I., 1989, *Internal Combustion Engine Modeling*, Hemisphere, New York.
[16] Rakopoulos, C.D., et al., 1994, "A fast algorithm for calculating the composition of diesel combustion products using an eleven species chemical equilibrium scheme", Advances in Engineering Software, 19, pp.109-119.
[17] Lavoie, G.A., Heywood, J.B. and Keck, J.C., 1970, "Experimental and theoretical study of nitric oxide formation in internal combustion engines", Combustion Science and Technology, 1, pp. 313-326.
[18] Hiroyasu, H., Kadota, T., and Arai, M., 1983, "Development and use of a spray combustion modeling to predict diesel engine efficiency and pollutant emissions", Bulletin of the Japan Society of Mechanical Engineers 26, pp. 569-576

Comparative Study of Water-Steam- and Organic-Rankine-Cycles as bottoming Cycles for Heavy-Duty Diesel Engines by means of Exergetic and Economic Analysis

Daniela Gewald[a], Andreas Schuster[a], Hartmut Spliethoff[a] and Nikolaus König[b]

[a] *Institute for Energy Systems, TU München, Germany*
[b] *MAN Diesel SE, Augsburg, Germany*

Abstract: Heavy-duty Diesel engines are used for the production of electric energy in different applications, e.g. as IPPs in island networks or as net integrated power plants. Diesel engines are also able to run on different fuels such as heavy fuel oil, diesel oil, natural gas, biogas and biofuels. To increase the thermodynamic efficiency of Diesel engine power plants, different bottoming cycles can be applied to the engine cycle in a combined power plant.
This paper presents a comparative study of the water-steam and the Organic-Rankine-cycle (ORC) as bottoming processes. Water-steam cycles are commonly used for power production units from 2 MW and larger, while ORC modules are commercially available up to 2 MW. According to this fact, criteria are necessary for the decision between water-steam- and Organic-Rankine-cycles with respect to the boundary conditions for the operation of a combined-cycle engine power plant. For the variable cases of Diesel engine applications and variable fuels, optimal working parameters for the tradeoff between additional power generation and additional investment costs are calculated for the steam- and the ORC-process, respectively. Concerning the ORC, calculations with two different state of the art working fluids (R245fa, pentane) are conducted. All calculations are done by means of a software for thermodynamic cycle simulations (Ebsilon Professional) with a detailed modeling of the components.
The two bottoming cycles are compared by their energetic and exergetic efficiency and their specific costs for installation, operation and electricity production respectively, in order to derive decision criteria for the installation of water-steam- or Organic-Rankine-cycles.

Keywords: internal combustion engine, combined cycle, Clausius Rankine cycle, Organic Rankine Cycle.

1. Introduction

Heavy-duty Diesel engines can be employed as power producers in various applications. Their advantages are:

- high single cycle efficiencies
- fuel flexibility
- favorable costs for installation and operation
- short time periods for construction and commissioning

However, due to rising fuel prices and increasing environmental restrictions on pollutants and CO_2 emissions, internal combustion engines (ICE) are more often considered as prime movers in combined cycle applications to improve the system efficiency.

The waste heat of ICEs, which can be utilized for power generation in a bottoming cycle, usually arises at two different temperature levels. While the exhaust gases have a temperature level of 300 °C to 400 °C depending on the engine type, the high temperature (HT) cooling water has a level of about 90 °C. The exhaust gas heat accounts for about 30 % of the fuel energy, the HT cooling water contains another 15 % of fuel energy.

To use these amounts of waste heat for additional power generation in the most efficient way, two bottoming cycles can be considered: the Organic Rankine Cycle (ORC) and the Clausius Rankine Cycle (CRC). In current literature, ORCs are commonly considered as bottoming cycles for low and medium temperature heat sources and lower power outputs. Competing CRCs are more often considered for medium and high temperature heat sources. Due to disproportionally high efficiency losses in small steam turbines [1], reasonable performance of CRCs is only obtained for larger scales of power outputs, as compared with ORCs.

Optimal design parameters with respect to the working and ambient conditions of ICEs, have previously been presented in literature either for

the CRC [2-5] or the ORC [6-8] as the bottoming cycle. A comparative study on performance and costs between these two cycles does not exist. But since temperature levels of the engine waste heat sources are at medium level and the power output of the bottoming cycle depends on the output of the prime mover or prime movers (if more than one engine is installed in a combined cycle power plant), the question of installing an ORC or CRC is a decisive point for plant manufacturers and operators, which needs to be adressed.

This study presents decision criteria for the installation of an ORC or CRC with respect to cycle performance and costs of installation and operation.

2. Thermodynamic cycle modeling

This section presents the design criteria for the thermodynamic models of the CRC and ORC cycles respectively. Both are designed with the objective of using as much waste heat as possible but with reasonable effort in cycle construction. All calculations in this paper are presented assuming the following:

- the systems are simulated under steady state conditions,
- the pressure drops and radiation heat losses in all the heat exchangers and pipelines are neglected,
- isentropic efficiency for turbines and pumps.

2.1. Prime movers and boundary conditions

In the presented analysis commercially available four stroke Diesel engines manufactured by MAN Diesel SE, which are typical engines for stationary applications, are considered as prime movers in a combined cycle. Each engine is a supercharged medium speed engine, which is either fired with heavy fuel oil, biofuel or natural gas. The following engines are considered as prime movers:

- 18V48/60: HFO-fired 18 cylinder engine (bore 480 mm, stroke 600 mm)
- 18V48/60 bio: biofuel-fired 18 cylinder engine (bore 480 mm, stroke 600 mm)
- 18V32/40: HFO-fired 18 cylinder engine (bore 320 mm, stroke 400 mm)
- gas engine: with exhaust gas temperatures < 300 °C

The main engine parameters, which give the boundary conditions for the bottoming cycles, are reported for an ambient temperature of 30 °C in Table 1.

Table 1. Main engine characteristics (30 °C ambient)

	48/60 HFO	48/60 bio	32/40	gas engine
engine power el. (kW)	18430	17500	9080	
el. efficiency (%)	44.1	46.2	43.4	
exhaust gas temperature (°C)	364	364	333	< 300
exhaust gas flow (kg/s)	34.7	34.8	18.3	
heat content exhaust gas (% of fuel input)	29.6	32.3	28.6	
heat content HT cooling water (% of fuel input)	14.5	13.9	15.6	

2.2. Cycle modeling

2.2.1. Clausius Rankine Cycle

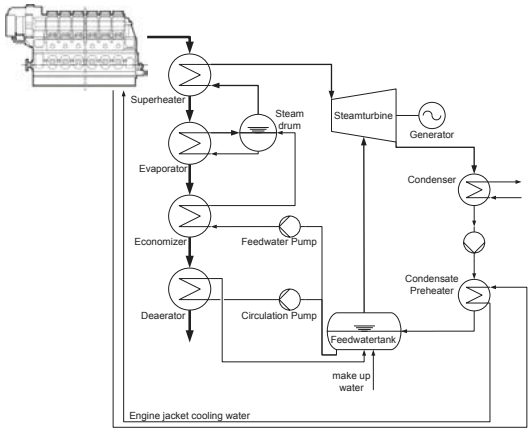

Fig. 1. Schematic drawing of Diesel Combined Cycle

In this study the combined cycle power plant working with a CRC is equipped with one heat recovery steam generator (HRSG) behind each engine and one steam turbine which expands the collected steam from each HRSG to the condensing pressure level. Depending on the availability of cooling water on-site, the steam is condensed by an air or water cooled condenser. In the following calculations a water cooled condenser is assumed which can achieve a pressure level of 0.1 bar. This Diesel Combined Cycle system (DCC) was developed by MAN Diesel SE by means of achieving the two objectives of high efficiency and simple construction. A schematic drawing of this system is shown in Figure 1. Figure 2 shows an exemplary

Q-T-diagram for an HRSG using the exhaust gas of a biofuel engine.

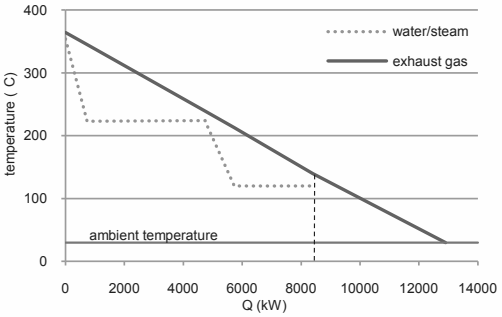

Fig. 2. Q-T-diagram of the bottoming cycle of a biofuel engine

The cycle components are modeled and simulated with the software package Ebsilon Professional. The cycle design parameters are given in Table 2. It must be noted that the temperature to which the exhaust gases can be cooled down, differs with the type of fuel used. For example, since HFO contains a significant percentage of sulphur, it is not possible to cool down the HFO exhaust gas as much as the others due to the sulphuric acid dew point. This fact also affects the pressure level of the feedwater tank.

Table 2. CRC design parameters

	48/60 HFO	48/60 bio	32/40	gas engine
live steam pressure	25 bar	25 bar	25 bar	18 bar
live steam temperature	T_{ex} – 10 K			
evaporator pinch point	15 K			
pump efficiency	80 %			
HP turbine efficiency	85 %	85 %	82 %	82 %
LP turbine efficiency	80 %	80 %	78 %	78 %
feedwater pressure	3,6 bar	2,0 bar	3,6 bar	1,4 bar
exhaust gas temperature after HRSG	160 °C	140 °C	160 °C	125 °C

2.2.2 Organic Rankine Cycle

Using an ORC instead of a CRC as bottoming cycle in an engine combined cycle power plant can provide several advantages:

- high turbine efficiencies even in small power ranges due to dry expansion and low rotational speed
- simple and automated plant operation
- direct drive of the electric generator without reduction gear

For the ORC system, a cycle configuration which works with subcritical saturated steam is considered. The engine exhaust heat is used as heat source for a thermal oil intermediate cycle from which the heat is transferred to the ORC working fluid, while the heat of the HT cooling water is directly transferred to the ORC. The intermediate cycle is required firstly for safety reasons in order to avoid superheating and cracking of the organic fluid by the hot exhaust gases (this is not valid for all ORC working fluids, but in the case of the examined working fluids). Secondly it is required if the exhaust heat of several engines in a power plant is collected for one ORC module. A schematic drawing of the ORC configuration used in the calculations is given in Figure 3.

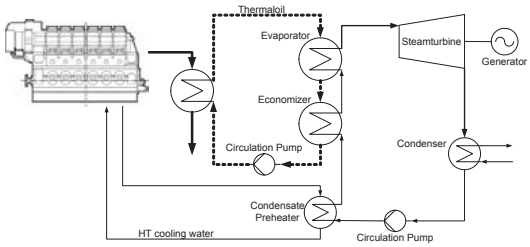

Fig. 3. Schematic drawing of the ORC-engine-configuration

Figure 4 shows the Q-T-diagram of an ORC bottoming a gas engine. The figure shows the cooling curves for the exhaust gas and the thermal oil and the heating curve of the working fluid.

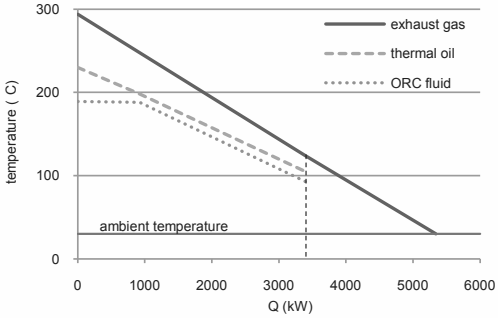

Fig. 4. Q-T-diagram for a pentane-ORC process bottoming a gas fired engine

Two different organic fluids, which are state-of-the-art working fluids, are examined with the

above mentioned configuration. The important properties of these fluids are compared to water in Table 3 [9].

Table 3. Fluid properties

	critical temperature	critical pressure
R245fa	154.01 °C	36.51 bar
Pentane	196.55 °C	33.7 bar
H2O	374 °C	221 bar

Even though regenerative preheating is considered as state-of-the-art in many ORC applications, it is not necessary for R245fa and pentane, due to the fact that the HT cooling water provides much low temperature heat. For working fluids which have strongly overhanging vaporization lines in the T-s-diagram (e.g. OMTS [10]), implementing regenerative preheating additionally to the preheating by HT cooling water, is advantageous to increase the cycle efficiency.

All examined engines have exhaust gas temperatures which are significantly higher than the critical temperatures of the working fluid. It is therefore possible to work with a vapour pressure near the critical pressure for which the highest power outputs at the turbine can be reached. The vapour pressures and some other working parameters for both of the fluids are given in Table 4. The condensation pressures correspond to a condensation temperature of 45 °C and a cooling water temperature of 30 °C (=ambient temperature), respectively.

Table 4. ORC design parameters

	R245fa	pentane
vapour pressure	35 bar	30 bar
vapour temperature	151.7 °C	189.0 °C
evaporator pinch point	10 K	
turbine efficiency	85 %	
pump efficiency	80 %	
condensation pressure	2.95 bar	1.36 bar
temperature after turbine	53.3 °C	93.6 °C

The exhaust gas outlet temperatures are dependent on the type of engine and fuel, respectively, and are the same for the ORC and CRC processes.

3. Thermodynamic calculations

For each engine the thermodynamic properties and power outputs of the three possible bottoming cycles were calculated with the software package Ebsilon [11].

The energetic efficiency is then calculated according to:

$$\eta_{en} = \frac{P_{Turbine} - P_{Pump}}{\dot{Q}_{ex} + \dot{Q}_{preheater}} = \frac{P_{net}}{\dot{Q}_{in}} \quad (1)$$

To calculate the exergetic efficiencies and the rates of exergy loss and destruction for each component a second law analyses is performed by applying exergy balances on each component [12]. The exergy destruction is calculated by using the following equations:

$$e_{h,in} = h_{h.in} - h_{h,0} - T_0(s_{h,in} - s_{h,0}) \quad (2)$$

$$e_{h,out} = h_{h,out} - h_{h,0} - T_0(s_{h,out} - s_{h,0}) \quad (3)$$

$$\begin{aligned} \Delta e_{\mathrm{h}} &= e_{h,in} - e_{h,out} \\ &= h_{h,in} - h_{h,out} - T_0\left(s_{h,in} - s_{h,out}\right) \end{aligned} \quad (4)$$

$$\Delta e_c = h_{c,in} - h_{c,out} - T_0\left(s_{c,in} - s_{c,out}\right) \quad (5)$$

$$\dot{E}_{destruction} = \dot{m}_h \Delta e_h - \dot{m}_c \Delta e_c \quad (6)$$

The exergy loss of a component is defined as the exergy of that mass flow, which leaves a component without being further used in the cycle. Exergy losses occur e.g. in the heat exchanger system due to the fact that the engine exhaust gases cannot be cooled down to ambient temperature. In the condenser and preheater there are also the following exergy losses.

$$\dot{E}_{loss} = \dot{m}_{out} \cdot [h_{out} - h_0 - T_0(s_{out} - s_0)] \quad (7)$$

The values for the enthalpy h_0 and entropy s_0 of the fluid at ambient conditions are calculated by the Ebsilon software package. The exergetic efficiency is evaluated by:

$$\eta_{ex} = 1 - \frac{\dot{E}_{destruction} + \dot{E}_{loss}}{\dot{E}_{in}} \quad (8)$$

The results of calculations are presented below.

All bottoming cycles significantly increase the system efficiency of a combined cycle power plant (up to 5.6 percentage points in the case of the biofuel engine). The efficiency increasing potential is shown in Figure 5. It has to be noted that mechanical losses and efficiency losses, due to the own consumption of the power plant apart from the working fluid circulation pumps, were not considered in the calculations.

The results also show that the ORC cycle does not have a higher turbine power output than the CRC, until the temperature level of the heat input is very low (below 300 °C in the case of the gas engine). See Figure 6.

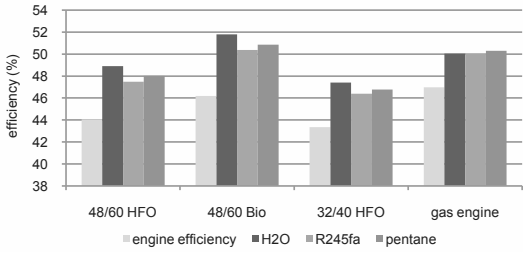

Fig. 5. Combined cycle efficiency compared to single cycle efficiency

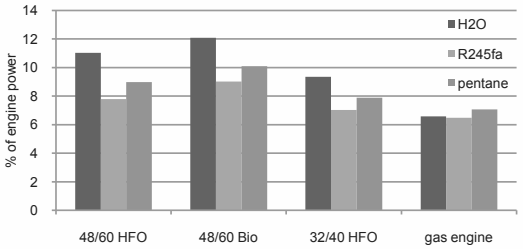

Fig. 6. Turbine power output of bottoming cycles

This fact is also reflected by the energetic and exergetic cycle efficiencies which are given in Figure 7 a) and b).

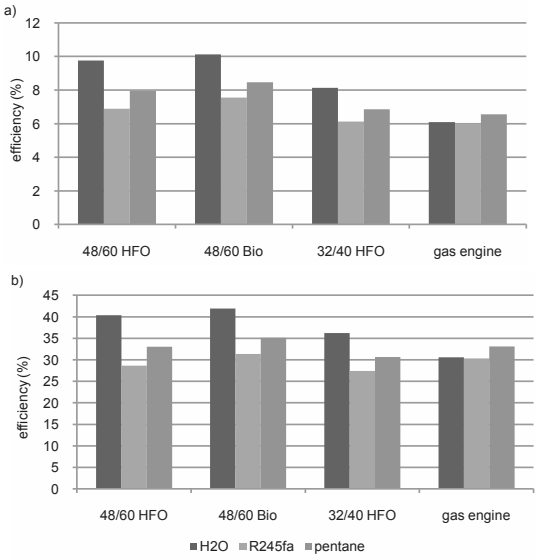

Fig. 7. a) Energetic efficiency
b) Exergetic efficiency

In all cases the working fluid pentane achieves better results than R245fa, due to its higher critical temperature. The higher temperature of the working fluid leads to a higher temperature level in the intermediate thermal oil cycle and therefore to lower temperature differences between the thermal oil cycle and the exhaust gas. Due to (9), the exergy losses in the heat exchangers decreases with lower temperature differences and thus efficiency increases.

$$d\dot{E}_{destruction} = T_0 \cdot d\dot{Q} \frac{T_h - T_c}{T_h T_c} \qquad (9)$$

In Figure 8 a) and b), the losses of the cycle components in % of the overall system losses are shown for the biofuel engine and the gas engine, respectively. The heat exchanger losses are about 11.6 % smaller with pentane than with R245fa for the 18V48/60 bio. For the gas engine, pentane has about 24 % smaller losses than R245fa.

It is also clear from the results that in the case of the gas engine, the losses of the ORC heat exchanging system are nearly the same as the losses of the CRC HRSG, while the losses of the preheater are smaller with an ORC than with a CRC. This explains the higher turbine output, the higher energetic and exergetic efficiencies, compared to the CRC cycle when either one of both ORC cycles is applied to the gas engine.

Since pentane has more overhanging vaporization lines in the T-s-diagram than R245fa, the outlet steam of the turbine is more superheated in the case of pentane. Thus the exergy losses in the condenser are higher for pentane than for R245fa in all calculated cases.

Considering the gas engine, the losses of the preheater exceed even the losses of the heat exchangers, because of the differences in the HT cooling water temperature. The HT cooling water temperature is higher for the gas engine than for the other engines. This leads to a higher inlet temperature of the working fluid in the steam generator and thus to lower exergy losses due to smaller temperature differences and a higher temperature level in the heat exchangers (see (9)). However, it also leads to higher exergy losses in the preheater, due to higher outlet temperature of the HT cooling water.

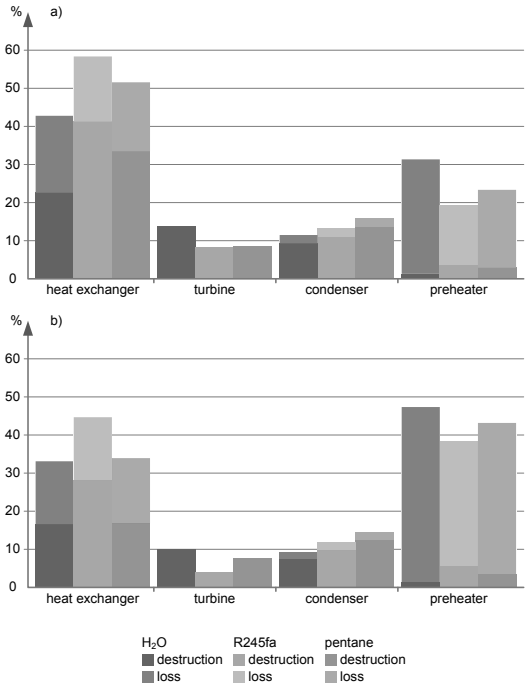

Fig. 8. a) losses of cycle components, 18V48/60 bio b) losses of cycle components, gas engine

From the thermodynamic point of view some design criteria for bottoming cycles can be derived from the above calculations:

A bottoming cycle always increases the system efficiency and should in all cases be applied.

For engines with exhaust gas temperatures above about 300 °C, a CRC bottoming cycle is recommended, because of the higher power outputs of the CRC.

When exhaust gas and engine cooling water gives the heat input to an ORC system, a working fluid should be selected, which has a high critical temperature and vaporization lines which are just slightly overhanging in the T-s-diagram.

But engine manufacturers, system manufacturers and operators have to derive their decisions about applying a bottoming cycle and which bottoming cycle not only due to thermodynamic considerations but also from an economic point of view. Thus the next section presents some calculations of installation and operation costs for the different cycles.

4. Economic calculations

The economic comparison between the different systems is based on the specific costs of electricity production of each system. Only the bottoming systems are considered for economic calculations. The electricity production costs of the engine cycle are not calculated. Since the combined cycles of an 18V48/60 engine and an 18V48/60 bio engine, are very similar, only the biofuel engine will be examined. For the calculation of investment costs no distinction is made between the two ORC working fluids, R245fa and pentane, since the choice of the working fluid does not crucially influence the design of the ORC system in this case. Specific costs are calculated with the power output of a pentane driven ORC.

Table 5 shows the specific investment costs for the different bottoming systems of the three engines.

Table 5. Specific investment costs of bottoming systems

		18V48/60 bio	18V32/40	gas engine
CRC	spec. invest	5 ,	5 ,	5 ,
	power	2115 kW	848 kW	696 kW
ORC	spec. invest	5 ,	5 ,	5 ,
	power	1767 kW	715 kW	748 kW

The calculation of the specific costs of electricity production is based on the static annuity method provided by VDI 2067 [13]. Therefore costs are subdivided into three categories:

capital-related

consumption- and requirement related

operation related

To simplify calculations only the main costs are considered, which include the following:

investment costs as capital-related costs,

costs for operation (salaries of operators), maintenance and repair as operation related costs.

Since CRC as well as ORC run on the exhaust gas heat of an engine, there are no consumption related costs since no additional fuel is needed (costs for lubrication oil, chemicals for water treatment, losses of working fluid etc. are neglected).

A price change factor will not be considered, since a static method of calculation is used. The interest factor, which is assumed for investments in energy production facilities, is 5 %.

The annuities of capital-related and operation-related costs are calculated with the equations given by VDI 2067, as follows:

Annuity factor a: required to allocate singular payments (e.g. the investment costs A_0) to yearly amounts that are all equal throughout the period of observation T.

$$a = \frac{(q+1)^T \cdot q}{(q+1)^T - 1} \tag{10}$$

Annuity of capital related costs A_c: the equalized yearly payment, that is calculated with the annuity factor a, the investment costs A_0, the costs for replacement purchases of components $A_1 \dots A_n$ and the residual value R of these components. The annuity is calculated separately for the main cycle components, with the following equations:

$$A_c = (A_0 + A_1 + A_2 + \cdots + A_n - R) \cdot a \tag{11}$$

$$A_i = \frac{A_0}{(q+1)^{i \cdot T_l}}; i = 1 \dots n \tag{12}$$

$$R = A_0 \cdot \frac{T_l - T}{T_l \cdot (1+q)^T} \tag{13}$$

Annuity of operation related costs A_{op}: the yearly payment that is necessary for operation and maintenance of a CRC or ORC cycle:

$$A_{op} = f_r \cdot A_0 + f_m \cdot A_0 + T_{op} \cdot S \tag{14}$$

The expenses for repair and maintenance f_r and f_m in percentage of investment total per year are given by VDI 2067 for each component. The hours of operation per year T_{op} and typical life times of components T_l are also given by VDI 2067. The assumed observation period T is 12 years.

The specific costs of electricity production are then calculated by:

$$c_{EP} = \frac{A_c + A_{op}}{P_{net} \cdot T_{full\ load}} \tag{15}$$

As engine combined cycle power plants are mostly working in base load operation, the hours of the full load $T_{full\ load}$ will be assumed with 8000 h.

Results of the calculations are presented in Figure 9.

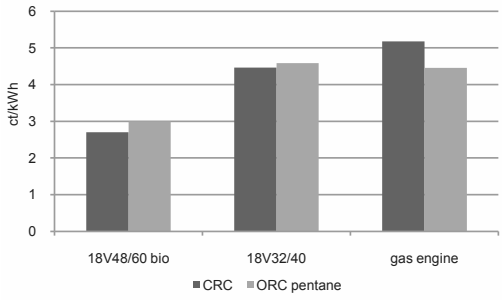

Fig. 9. Specific costs of electricity production

5. Conclusion

Thermodynamic and economic calculations of CRC and ORC bottoming cycles for different types of Diesel engines are presented in this paper.

The thermodynamic results show that the considered CRC cycle always has better efficiencies and higher power outputs for engine exhaust gas temperatures above 300 °C. On the contrary, economic calculations show that the specific costs of electricity production of the CRC systems significantly increase with decreasing exhaust gas temperature and therefore decreasing power outputs. Figure 9 shows that for the 18V32/40 engine, which has an exhaust gas temperature of 333 °C, the specific costs of electricity production are nearly the same for a CRC and the ORC bottoming system.

With further decreasing exhaust gas temperatures, the ORC system has better efficiencies and higher power outputs than the CRC cycle and also has decreasing specific costs of installation. Thus the specific costs of electricity production are significantly less for an ORC than for a CRC (see Figure 9, gas engine) in the examined cases.

These results provide some first decision criteria for the installation of a CRC or ORC cycle. Of course for actual projects, cycle parameters have to be optimized and economic calculations should be more precise. But as shown in this paper, it is not sufficient to decide between the two possible cycles simply on the basis of thermodynamic considerations. Economic calculations should always be an important part in the planning process of a combined cycle system.

Nomenclature

A	annuity, €
A_0	initial installation costs, €
a	annuity factor
c	specific costs, $\frac{€}{kW}$
$\dot{E}$	exergy flow rate, kW
e	specific exergy, $\frac{kJ}{kg}$
f	effort factor, $\frac{\%}{a}$
h	specific enthalpy, $\frac{kJ}{kg}$
i, n	counters
$\dot{m}$	mass flow rate, $\frac{kg}{s}$
P	power, kW
$\dot{Q}$	heat flow rate, kW
q	interest factor, %
R	residual value, €
S	salary, $\frac{€}{h}$
s	specific entropy, $\frac{kJ}{kgK}$
T	time, h
T	Temperature, K

Greek symbols

η	efficiency

Abbreviations

CRC	Clausius Rankine Cycle
DCC	Diesel Combined Cycle
HFO	heavy fuel oil
HRSG	heat recovery steam generator
HT	high temperature
ICE	internal combustion engine
OMTS	octamethyltrisiloxane
ORC	Organic Rankine Cycle

Subscripts and superscripts

c	cold
c	capital-related
EP	electricity production
en	energetic
ex	exergetic
h	hot
in	inlet
l	life time
m	maintenance
op	operation related
out	outlet
R	repair
0	at ambient conditions

References

[1] Thomas, H.-J., 1985, Thermische Kraftanlagen: Grundlagen, Technik, Probleme, 2nd ed., Springer-Verlag, New York, Chap. 6.

[2] Ahnger, A., 2007, ECC with internal combustion engines, *Wärtsilä Technical Journal* [online journal], 2, URL: http://total.com.sg/Wartsila/global/docs/en/about_us/in_detail/2_2007/engine-combined-cycle-with-internal-combustion-engines.pdf.

[3] Cymbron, L. and Azevedo, J. T., 2008, Heat Recovery from Diesel enigne exhaust gases for the implementation of a combined cycle, *Proc. European Conference on Industrial Furnaces and Boilers*, pp. 1–9.

[4] Danov, S.N., and Gupta A.K., 2004, Modeling the performance characteristics of diesel engine based combined-cycle power plants - Part II: Results and applications, Journal of Engineering for Gas Turbines and Power, 126(35), pp. 35-39

[5] Hountalas, D.T., et al., 2007, Study of available exhaust gas heat recovery technologies for HD diesel engine applications, International Journal of Alternative Propulsion, 1(2-3), pp. 228-249

[6] Gambarotta A. and Vaja I., 2008, Internal Combustion Engines bottoming with Organic Rankine Cycles. A thermodynamic analysis, *Proc. of ECOS 2008*, Ziebik A., Kolenda Z., Stanek W., eds., pp. 715-722.

[7] Mago P.J. and Charma L.M., 2008, Exergy Analysis of a combined engine-organic Rankine cycle configuration, *Proc. IMechE*, Vol. 222 Part A, pp. 761-770.

[8] Bombarda P., Invernizzi C., Pietra C., 2009, Heat recovery from Diesel engines: A thermodynamic comparison between Kalina and ORC cycles, Applied Thermal Engineering, In press.

[9] REFPROP, 2007, Reference Fluid Thermodynamic and Transport Properties, NIST Standard reference database 23 Version

8.0, Lemmon E.W., Huber M.L., McLinden M.O..

[10] Colonna, P., et al., 2008, Multiparameter phase equations of state for siloxanes: $[(CH_3)_3\text{-Si-}O_{1/2}]_2\text{-}[O\text{-Si-}(CH_3)_2]_{i=1...3}$, and $[O\text{-Si-}(CH_3)_2]_6$, Fluid Phase Equilibria, 263, pp. 115-130.

[11] Ebsilon Professional, 2009, Release 8.00, Evonik Energy Services, Germany.

[12] Nikulshin, V., et al., 2002, Exergy efficiency calculation of energy intensive systems, Exergy, an International Journal, 2, pp. 78–86.

[13] VDI 2067, Part 1, 2000, Economic efficiency of building installations: Fundamentals and economic calculation, Verein deutscher Ingenieure eds., Beuth-Verlag, Berlin.

Performance Improving of an Internal Combustion Engine for Ship Propulsion with a Bottom ORC

J. Bonafin[a], P. Pinamonti[a], M. Reini[b], P. Tremuli[c]

[a] *Dipartimento di Energetica e Macchine, University of Udine, Udine, Italy*
[b] *Dipartimento di Ingegneria Meccanica, University of Trieste,"Polo di Pordenone" Italy*
[c] *Ricardo Large Engines Group, UK*

Abstract: This work is part of a study aiming to achieve high efficiency and low emissions in a marine propulsion system. In order to significantly enhance the efficiency of a propulsion plant, it is possible to recover the exhaust gas heat normally rejected to the atmosphere and the heat of the cooling water usually rejected to the sea. The study examines the possibility of energy recovery applying ORC (Organic Rankine Cycle) technology; this technology is very effective for recovering waste heat from low temperature sources, both from the thermodynamic and the economic standpoint. When a "combined cycle" ORC-diesel engines set up is considered for this size of engines, an increase in power output of about 10% can be expect. In addition, a significant amount of heat is released at low temperature and could be used by other ship services, or by other thermal users, in case of land based applications. In the present study several possible thermodynamic cycles are simulated using the Aspen® code, considering also different working fluids. The results are evaluated in both thermodynamics and economics terms.

Keywords: Organic Rankine Cycle, dual fuel engines, bottoming cycle.

1 Introduction

The today's cost survey of fossil fuels is constantly evolving. The present economic crisis, combined with political pressures, influences from day to day the price of each barrel of oil. In this changing scenario the need arises to explore the possibility of using alternative fuels instead of the traditional oil from crude. The research points towards fuels with economically sound potentials and with limited impact on the environment.

The technology development occurred in large gas engines during the recent last years has achieved high thermal efficiency and low emissions utilising natural gas, suggesting this fuel as a potential substitute of heavy fuel oil.

Modern gas engines abate CO_2 by 30%, NO_x by 85% (without after treatments), ensuring the complete absence of SO_x compared to the correspondent engine burning liquid fuel oil. In order to benefit from these advantages, the major engine manufacturers have designed several set of gas engine for both ship propulsion and land based power generation.

Corresponding Author: Mauro Reini, Email: reini@units.it

1.1 The reference ship engine

In this study a dual fuel engine (Wärtsilä 6L50 DF) has been considered as propulsion engine. This engine model is a six cylinder in-line, it produces it 5,7 MW with efficiency of about 49%, operating at 514 rpm. It is very flexible from the fuel point of view: it can switch almost instantaneously from gas (LNG) to liquid diesel (LFO-HFO), and vice versa, allowing the choose of the cheaper fuel. Because of its complexity, a dual-fuel engine costs up to 30% more than a traditional diesel engine, but it allows an annual saving in term of fuel equal to 5-8% [1].

1.2 Possibility of recovery of waste heat engine

The benefits mentioned above can still be enhanced by recovering the thermal energy mainly available in the exhaust gases and in other engine's fluids, which is discharged to the environment in the traditional propulsion plants.

The heat balance of a Wärtsilä 6L50DF engine at maximum load shows about 11,5 MW as fuel input and a power output of 5,7 MW (Figure 1.1). The remaining energy is rejected to the environment by the exhaust gas (about 3,1 MW

available at 400°C) and the cooling circuit (2,6 MW at temperatures between 50 and 90°C).

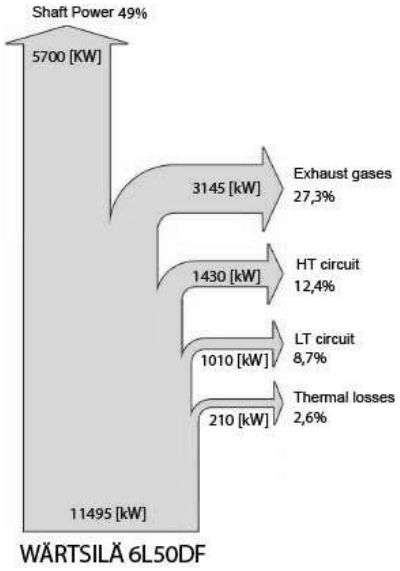

Fig. 1.1. Energy balance of the engine W6L50DF [1].

In this type of engines, the cooling circuit is split in two parts, according to the temperature level: a high temperature circuit (HT, at about 90°C) and a low temperature circuit (LT, at 50°C). A first selection of possible energy recovery can be based primarily on the availability of high temperature heat sources, like the exhaust gas and HT water.

The energy and exergy contents of the two streams are illustrated in Figure 1.2. On the basis of Second Law, it can be inferred that the amount of work ideally obtained from the flue gas is three times higher than that from the circuit HT, even if the amount of energy rejected by the engine is equally split between the two heat sources.

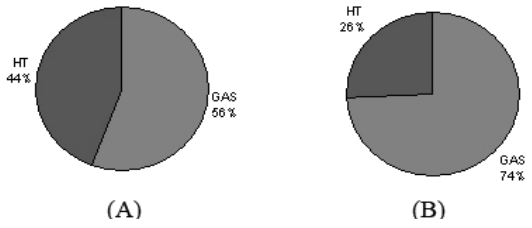

Fig. 1.2. Energy (A) and exergy (B) contents at the maximum engine load.

It comes straight that the optimisation of heat recovery should focus more on the exhaust gas stream.

To introduce the feasibility of the heat recovery, a brief description of the cooling circuits and of exhaust gas circuit is necessary (Fig. 1.3).

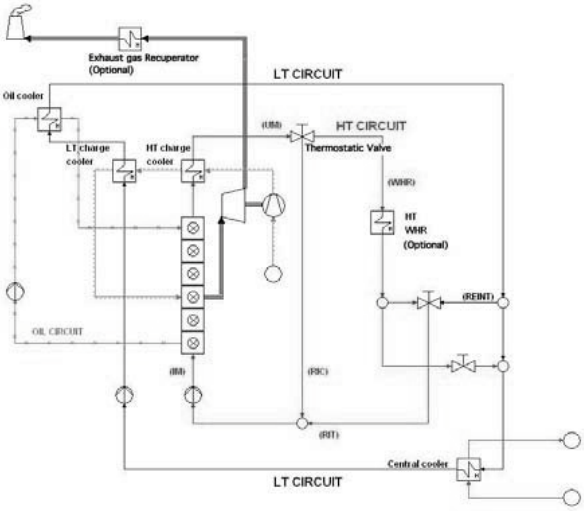

Fig. 1.3. Simplified schematic of the cooling circuits and exhaust of the engine.

HT circuit water goes through the cylinder jackets, the cylinder heads and the first stage of the air-cooler; the water in the LT circuit cools the second stage of the air-cooler and then the lubricant oil. The control of the HT circuit is based on the temperature of the water leaving the engine. A three-way thermostatic valve set at 91° C re-circulates part of the flow (RIC) to keep the water inlet temperature at the right level. Fresh water is then cooled in a central cooler, with sea water. A heat exchanger (HT WHR) allows the recovery of thermal energy from the HT cooling circuit. The object of this recovery is to allow the maximum power production from the bottom cycle, without preventing the proper operation of the temperature control loop.

To maximize heat recovery from the cooling circuit HT, the extracted thermal power shall be equal to the engine thermal production, at each different load.

1.3 Feasibility of the energy recovery with ORC technology.

In installations as described above, the use of organic fluids in Rankine cycles appears an

attractive technology. Many applications of this technology are made in land based installations, such as biomass, solar and geothermal energy plant [2-6]. Recently, some studies have been conducted on the possible application of ORC groups coupled to diesel engines [7], although there are currently no applications of ORC on ships.

The goal of this study is the definition of an ORC system dedicated to the heat recovery from an engine Wärtsilä 6L50DF. The study is performed in three steps: first step is the choice of the organic working fluid for the cycle, then it comes the cycle analysis to optimise the cycle and finally the components design.

For this purpose it is useful the support of a computer software containing an extensive library of fluids, including all their chemical and thermodynamic properties.

The different plant solutions have been analysed with the Aspen Plus® code, utilizing the standard components of its library.

2 First plant modelling and choice of the working fluid

2.1 The working fluid

The convenience of using systems based on ORC cycles lies primarily on favourable characteristics of some organic liquids in comparison with water, i.e. larger molecular mass, lower critical temperature, lower critical pressure, lower condensation entropy and lower solidification temperature [8-10]. To explain this difference, it is useful to refer to the T-s diagram (Figure 2.1). It is possible to notice that the water cycle has certainly a specific work per unit mass greater than that of the toluene (the area of the water cycle is 4,5 times grater than that of the toluene cycle). The feature that makes water unsuitable to use in applications of small size and low maximum temperature of the cycle, is its large entropy of evaporation, compared with that of organic fluids.

It is possible to conclude that with an organic fluid cycle it is possible to operate with flow rates higher and lower pressures of expansions, achieving a power output higher than the steam cycle working with the same conditions.

In the present study were compared to five different pure substances which have already found industrial application in ORC cycles [10 - 12]: benzene, cyclohexane, isobutene, octamethylsiloxane (MDM) and toluene. Their behaviours have been simulated for a simple Rankine cycle, according to the scheme shown in Figure 2.2. In order to assure safe operation on board of ships, thermal oil is used as intermediate media between the exhaust gasses and the organic fluid.

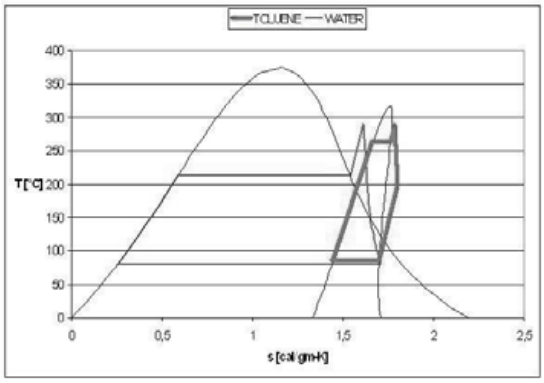

Fig. 2.1. Diagram T-s for Rankine cycles with water and toluene.

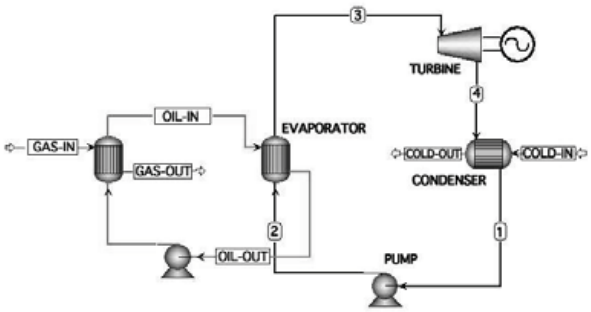

Fig. 2.2. Flowchart of simple ORC circuit.

The following operating conditions are set for all the working fluids, consistently with the hypothesis of recovering energy from the engine exhaust gas only [1].

- temperature of hot source: 350° C;
- mass flow rate of hot source (thermal oil Dowtherm-G® [13]): 5 kg/s;
- evaporating temperature: 250° C;
- maximum pressure: 15 bar;
- condensing pressure: 0,3 bar;

• cold flow temperature to the condenser: 38°C;

• working fluid flow rate: 3 kg/s.

The main components of the plant have been modelled on the basis of the hypothesis below.

• Turbine: discharge pressure (minimum of the cycle) and isentropic efficiency are set constant.

• Condenser: it allows the condensation of the full amount of the working fluid, with no limits on the maximum temperature reached by the cold fluid.

• Circulation pump: output pressure is set constant (maximum of the cycle).

• Evaporator: the outlet temperature of the working fluid has been fixed (maximum temperature of the cycle); taking the maximum pressure into account, the full amount of the organic fluid may reach the state of dry saturated or superheated vapour.

A comparison of the results obtained for the different working fluids is shown in table 2.1. The isobutene was not included in the comparison because its thermo-physical characteristics do not allow operating at the considered temperatures. It is better suited for lower temperatures (T_{cr}= 135° C).

Table 2.1. Performance comparison of simple cycles with different fluids.

	Power output kW	Oil out temp. °C	Efficiency %
Benzene	420	155	20,2
Cyclohexane	411	147	18,7
MDM	97	276	12,5
Toluene	364	174	20,6

This first comparison shows that the most promising fluids appear to be benzene and toluene. It was therefore decided to further analyse the performance achievable by these fluids, as it was possible to raise the evaporation temperature of the cycle at 290°C and the maximum cycle pressure to 28 bar. For toluene in particular, it has been possible to further reduce the condensing pressure to 0,1 bar, thanks to the temperature of cold fluid source.

The results obtained in these new conditions are presented in Table 2.2; they confirm that toluene is the fluid with higher performance among those examined. For the toluene is also experimentally demonstrated a good resistance to degradation using high temperature (above 300° C [13]); this fluid is also less toxic than benzene.

Table 2.2. Comparison of performance obtained with toluene and benzene, for T_{vap}=290°C, p_{vap}=28 bar and minimumcondensation pressure.

	Power output kW	Oil out temp. °C	Efficiency %
Benzene	514	138	22,4
Toluene	523	145	25,8

Then, it has been decided to utilise the toluene as working fluid, increasing the mass flow rate up to 3.5 kg/s and achieving an additional power of 611 kW from the bottoming cycle.

As previously described, the engine also releases a flow of hot water (the HT cooling circuit) that is an additional opportunity of energy recovery. But this heat source is at low temperature (91° C), so that the fluids considered in Table 2.1 are not suitable for energy recovery in a Rankine cycle, because they are characterized by high boiling temperatures. In this case it would be appropriate using a low temperature boiling fluid, like isobutene (evaporation temperature equal to -12°C at 1 bar).

It has been therefore simulated a simple Rankine cycle coupled to the HT water circuit, with isobutene as the working fluid and consistent with the operating parameters of the engine at maximum load.

• temperature of hot source: 91° C;

• mass flow rate of HT water circuit: 37,5 kg/s;

• evaporating temperature: 81° C;

• maximum pressure: 13 bar;

• condensing pressure: 6,5 bar;

• temperature of condenser cooling flow: 38°C;

• working fluid flow rate: 7 kg/s.

Under these conditions the additional power of 155 kW has been obtained from the low temperature ORC cycle, with an efficiency of 6.1%.

2.2 Functional parameters of the ORC

A sensitivity analysis has been performed on the main parameters of the cycle at five engine operation points (100%, 85%, 75%, 50%, 25% of nominal load), obtaining information on the behaviour of the cycle related with a change of

available energy for the bottom cycle. In details, the upper and lower extremes of the cycle (both temperature and pressure) have been varied, according to the power recovered from the engine exhaust gases.

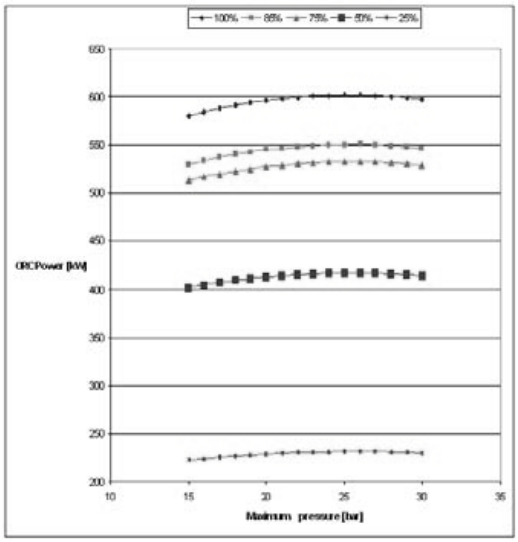

Fig. 2.3. ORC output power vs. maximum cycle pressure, for different engine loads (cooling water temperature equal to 38°C).

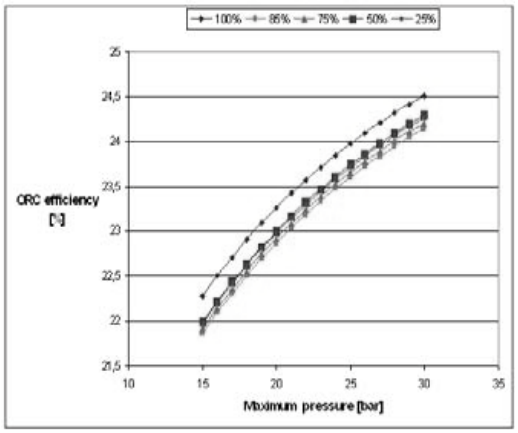

Fig. 2.4. ORC efficiency vs. maximum cycle pressure, for different engine loads (cooling water temperature equal to 38°C).

The cycle's powers and efficiencies achieved changing the maximum pressure are shown in Figures 2.3 and 2.4.

Increasing maximum pressure, the efficiency has a monotonous increasing trend, but the power is about constant in the range 20-30 bar, showing that the cycle efficiency increase is compensated by a reduction in the energy recovery from exhaust gas, if the maximum pressure rises over 20 bar. Therefore this last value has been assumed in the further evaluations.

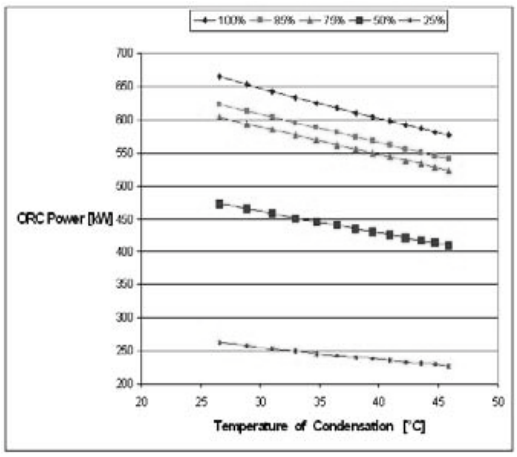

Fig. 2.5. ORC power vs. condensation temperature, for different engine loads and maximum pressure equal to 20 bar.

Figure 2.5 shows that a significant increase in power output can be obtained by considering the engine operating in a cold sea. The condensation pressure, for the considered temperatures range, is from 0,04 to 0,1 bar. The power is increasing with decreasing condensation temperature, as the area of the Rankine cycle can only increase as a result of the lower limit. When condensation temperature can be kept at about 27°C (as it is possible only if see water temperature is below 20°C) the power output shows a surplus of about 100 kW, with respect to full load operation with a condensation temperature of 46°C. The efficiency also increases with decreasing the condensation temperature, varying between 23% and 25,3%, with very limited influence, however, by the engine load .

3 Choice of cycle configuration

In the next step of the study, an assessment of different configurations of the bottoming thermodynamic cycle has been made. The criteria used for each configuration (pressures and temperatures) are those that allow to maximize the power produced by the cycle for

each level of output of the engine. At this stage, the constraints related to the real geometrical dimensions of the heat exchangers are not explicitly taken into account; they will be introduced in the next step, in view of the economic evaluation of the installed components.

The following parameters have been kept constant for all engine load:

• cycle maximum pressure 20 bar (in order to avoid to stress of pipes and components);

• cycle maximum temperature 290°C (in order to obtain a slight overheating above the toluene saturation temperature at 20 bar (260°C), and below the degradation limit for the same fluid);

• condensing mass flow rate 80 kg/s;

• maximum oil temperature 350° C;

• maximum gas temperature 468°C;

• overall heat transfer coefficient constant for all exchangers, equal to 850 W/m^{2}K (average value recommended by Aspen for the used fluid);

• no pressure drops in the bottoming cycle components (as it is consistent with a simplified initial analysis).

The performance of the simple cycle, as described in Section 2, will be compared below with those of three other more complex configurations of the energy recovery cycle, obtained by considering the preheating with the water of the HT engine cooling circuit, thermal regeneration and two combined ORC cycles.

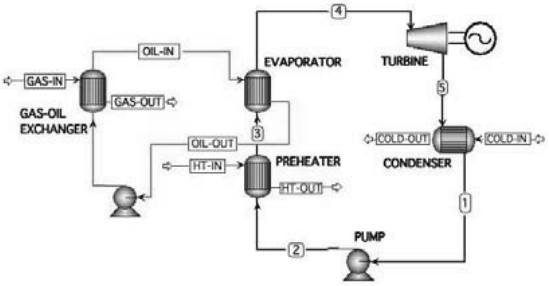

Fig. 3.1. Simple ORC cycle with preheating from the engine HT cooling circuit.

3.1 Cycle with preheating

A first evolution of the simple cycle is obtained by adding a heat exchanger before the evaporator, which preheats the toluene with the stream of hot water of the engine HT cooling circuit (Figure 3.1). This water is produced at 91°C, so that its preheating can be useful only if the working fluid leaves the pump at a lower temperature.

The additional supply energy at low temperature allows operating with a greater mass flow rate of working fluid, increasing the power developed by the turbine. This can be inferred from Table 3.1, where the results obtained are compared with those of the simple cycle.

3.2 Regenerative cycle

The Rankine cycles with dry organic fluids show superheated steam conditions and quite high temperature at the end of expansion, with a limited enthalpy difference across the turbine, so that the enthalpy of the expanding flow is not fully utilized.

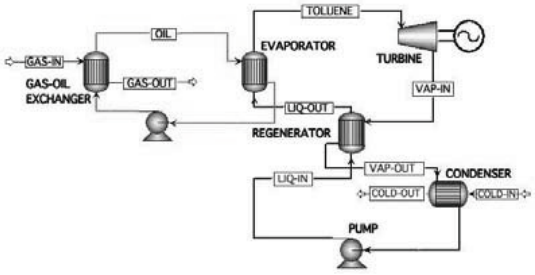

Figure 3.2. Regenerated ORC cycle.

The most natural solution, from the thermodynamic point of view, is therefore to realize the internal regeneration of the cycle, by adding a heat exchanger for preheating the organic fluid at the pump outlet (Figure 3.2).

As in the previous case, the internal regeneration makes possible to operate with a higher mass flow rates than that of the simple cycle, getting more power from the turbine (Table 3.1).

3.3 Two combined ORC with different temperature levels

Let's finally consider two combined cycles, operating with different organic fluids at two different thermal levels (Figure 3.3). The cycle at higher temperature (toluene) is coupled to the exhaust gas through the thermal oil circuit; the cycle at the lower temperature (isobutene) receives energy directly from the cooling water.

As mentioned before, the flow in the HT cooling circuit is adjusted to maintain a constant return temperature to the engine. In case water in the

HT cooling circuit is used for the evaporation of the isobutene, the return temperature of the HT water circuit must not drop below the value set in the engine-control system. To avoid this eventuality and to enable the combined cycles to operate with the highest possible flow in the evaporator, an exhaust gas/water recuperator has been introduced to rise the temperature of the water leaving the engine (Fig.3.3), assuming that the gas at the chimney has not to be cooled below 140°C.

The two cycles exchange energy also each other. To take advantage from the high temperature of toluene vapour exiting the turbine an additional heat exchanger is introduced for superheating the isobutene, allowing the lower temperature cycle to increase its power output (Table 3.1).

3.4 Performance comparison of different configurations

Figure 3.4 shows the total power obtainable by combining the engine and the ORC system, at different engine loads, for the considered configurations of the bottom cycle.

A significant power gain (about 10%) is already achieved with the simple cycle. For the other configurations the increase is slightly higher, at least with reference to the full load of the engine. The corresponding efficiencies are reported in Figure 3.5, showing that they grow (up to 8 points) with decreasing engine load. In fact, if the engine efficiency reduces, a bigger fraction of the energy of the fuel input is available as waste heat for the bottom cycle.

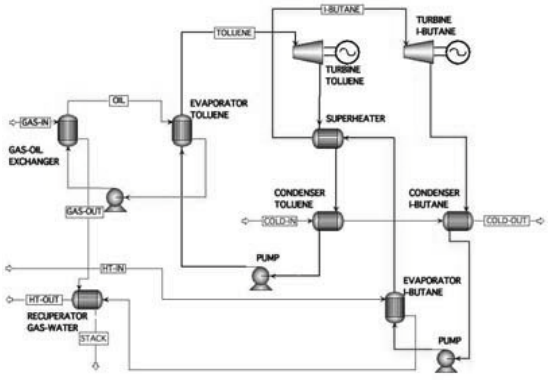

Fig. 3.3. Combined ORC cycles with two temperature levels.

The regenerated and the two combined cycles show the bigger efficiency increase, but the latter is affected by the temperature decrease in the HT cooling circuit at low engine loads. Therefore, it can be inferred that the regenerated cycle gives the best performance, without excessive plant complexity. Than, the following design analysis has been carried out on this plant configuration and the sizing and the realistic off-design performance of the required heat exchangers have been obtained.

Table 3.1. Performance Comparison of different configurations of the bottom cycle.

	Engine load [%]				
	100	85	75	50	25
Simple cycle					
Power [kW]	592	541	523	410	227
η [%]	23,2	22,8	22,9	23	22,9
Pre-hated cycle					
Power [kW]	671	637	620	484	280
η [%]	23,7	23,7	23,9	23,9	21,9
Regenerating cycle					
Power [kW]	684	639	622	488	288
η [%]	26,7	26,7	26,8	26,8	26,7
Cascade cycle					
Power [kW]	706	652	608	459	275
η (toluene) [%]	20,8	20,4	19,6	19,2	19
η (isobutene) [%]	10	10,2	10	10,2	10

4 Design of the regenerated cycle

4.1 Heat exchanger's simulation tools

The specific design of shell and tube heat exchangers has been performed by using the software Aspen Tasc, to address in detail the performance of the regenerative cycle and to perform the economic analysis of the investment. The used software incorporates an extensive library of organic fluids and therefore it has been possible to define in detail the geometry of heat exchangers, according to the prescriptions of the Tubular Exchanger Manufacturers Association (TEMA) [15], and to calculate accurately the phase transition and the pressure drop in the shell and in the tubes.

4.2 Main exchangers

The heat exchangers in the regenerated cycle are the exhaust gas/thermal oil heat exchanger, the evaporator, the regenerator and the condenser (Figure 3.2). During sizing and geometry selection, it has been paid attention to limit the size, in view of a possible installation in a room next to the engine room. The main data obtained for the different heat exchangers are summarized in Table 4.1.

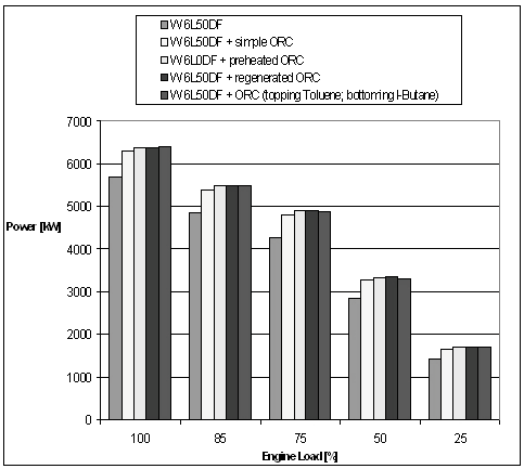

Fig. 3.4. Power of the plant, according to the load, for the cycle configurations studied.

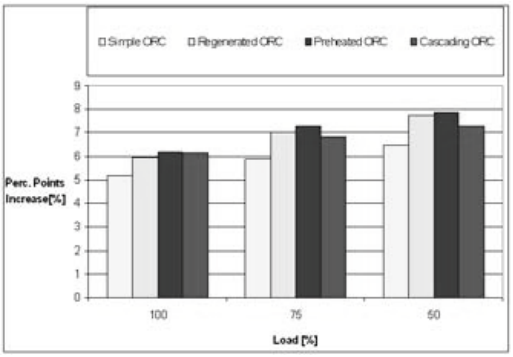

Fig. 3.5. Increase in percentage points of plant efficiency, according to the load, for the cycle configurations studied.

To ensure the proper operation of the engine, the pressure drop of the gas stream through the exhaust gas circuit must be below 3 kPa [1], therefore the maximum loss through the exhaust gas/thermal oil heat exchanger has been set to 1.2 kPa. In this way, an acceptable backpressure is guaranteed for the engine turbocharger, which is just upstream this heat exchanger.

The exhaust gas/thermal oil heat exchanger is a vertical tube bundle (containing the thermal oil), with the direct flow of gases in the shell without support baffles, for reducing losses.

Table 4.1. Main exchangers sized

	Regenerated cycle heat exchangers			
	Gas/oil	**Evaporator**	**Regenerator**	**Condenser**
Shell kg/s	9,1 (Gas)	5,5 (Oil)	3,36 (Tol)	3,36 (Tol.)
Tubes kg/s	5,5 (Oil)	3,36 (Tol.)	3,36 (Tol.)	80 (Water)
T_{HOT-IN} °C	400	340	145	68
$T_{HOT-OUT}$ °C	209	164	68	41
$T_{COLD-IN}$ °C	163	101	42	38
$T_{COLD-OUT}$ °C	340	262	101	42
Configuration	/	CFU (parallel)	DFU	BIM
Δp_{shell} bar	0,008	0,027	0,019	0,013
Δp_{tubes} bar	0,28	0,017	0,025	0,04
Q exchanged kW	2064	2097	367	1472
U_0 W/m^2-K	263	174	39	751
Tot cost €	34.740	124.800	60.720	47.740
Exchangers area m^2	152	791	266	395
Tube length mm	2700	6000	3000	3500
Ext. diameter mm	1300	800	1400	1200

For the evaporator it was used a shell and tube heat exchanger, with geometry type CFU [15] and two shells in parallel. Taking the toluene pressure (20 bar), it is better to locate it inside the tubes [16], while the flow of hot thermal oil circulates outside. The losses are not a limit for this heat exchanger, as a sensitivity analysis has shown that fluctuations in the maximum cycle pressure of about few bars lead to negligible power losses. The pinch-point obtained in the oil/toluene exchanger is equal to 5,3°C, a value that demonstrates a high heat transfer efficiency.

The chosen geometry for the regenerator is a shell-type DFU [15], with a finned tube bundle in order obtain more compactness.

One possible concern is the pressure drop affecting the vapour of toluene coming from the turbine. This loss not only increases the size of the exchanger, but also penalizes the turbine, reducing the available enthalpy drop. By limiting this loss in 0,025 bar, a power penalty

of approximately 30 kW only has been obtained for the turbine.

The condenser is cooled by the demineralised water of an intermediate ring, cooled by the sea. The same ring can cool in series the central cooler of the engine HT cooling circuit (see Figure 1.3).

It has been verified that a shell of type "I" is the most suitable, allowing better performance while limiting the size and the final cost. In the shell the stream inputs are two and the output is single. In this case also it is required that the pressure drop in the vapour side is the lowest as possible. In fact, each loss means a pressure increase at the end of the expansion, limiting the power of the turbine. Comprising such loss in 0,013 bar only, it has limited the penalty for the turbine power in about 20 kW.

4.3 Off design analysis of the ORC regenerated cycle

Once the geometry of the heat exchangers has been defined, it was possible to switch to the off-design analysis of the bottoming cycle. The simulations has been done at different engine loads, taking into account the actual size of the heat exchangers obtained by the detailed design.

A simplified turbine model has been considered, taking into account the isentropic efficiency reduction vs. mass flow rate [2].

It should be emphasized that, by using exchangers with fixed characteristics, the performance of the cycle are usually lower compared to those derived from the preliminary analysis of the different possible configurations, presented in section 3. The main differences lie in a reduction in the mass flow rate of toluene (3,3 instead of 3,8 kg/s) because of the limited effectiveness of the heat exchangers; in addition superheated conditions have not been reached at turbine inlet.

Furthermore, the pressure losses in the heat exchangers reduce the turbine enthalpy drop, with a consequent lower power of about 50 kW at maximum load. Finally, the heat transfer coefficients calculated through the libraries of Aspen Tasc have been almost always lower than the default value used in Aspen Plus, increasing the area of heat exchangers. This last aspect significantly affects their costs and overall dimensions.

The actual performance obtained by the bottom regenerative Rankine cycle is presented in Table 4.2. The gross power gain reaches 520 kW and it is constant for medium and high engine loads, until the organic fluid flow rate can be kept constant.

Knowing the real off-design performances of the energy recovery system, it is possible to calculate the real power of the combined engine and ORC system at each load, in order to evaluate the annual achievable fuel saving.

Table 4.2. Main characteristics for the regenerated ORC cycle in off-design analysis.

Load	%	100	85	75	50	25
$P_{ORC\ gross}$	kW	520	520	520	374	174
$P_{ORC\ net}$	kW	480	480	480	340	150
η_{ORC}	%	25,7	25,7	25,7	22,5	19,2
T_{gas}	°C	400	420	438	468	443
T_{oil}		340	340	340	340	340
T_{vap}		262	262	262	262	262
p_{max}	bar	20	20	20	20	20
p_{cond}		0,12	0,12	0,12	0,12	0,12
$\Delta p_{regen.}$		0,025	0,025	0,025	0,008	0,003
$\Delta p_{cond.}$		0,013	0,013	0,013	0,011	0,006
M_{oil}	kg/s	5,5	5,5	5,5	4,5	2,5
$M_{tol.}$		3,36	3,36	3,36	2,76	1,5
$\eta_{is\text{-}turb}$	%	80	80	80	70	60

By considering the engine average operation duty equal to 6.960 hours per year, the fuel saved can be calculated taking the engine load distribution into account:

- 100% load is typically used 1.5% of the time for maximum operating speed;
- 85% load is used to obtain the cruising speed, with the minimum specific consumption of the engine, and is usually kept for 85% of the time;
- 75% load is used for 5% of the time;
- 50% load is used in ancillary services, when the ship stops in port, for 7% of the time;
- 25% load is used for 1.5% of the time in port operation.

Table 4.3 lists the data obtained for both conventional and combined engine, assuming the LHV of LNG fuel, equivalent to 36 MJ/Nm^3 and the price of natural gas at 0,32 €/ Nm^3 [17]. It can be appreciated how the ORC gives a significant contribution to fuel savings at the most frequent load used during a year, (85% of maximum load).

Table 4.3 Annual savings with the bottom ORC.

Load	Engine + ORC Power	CONSUMPTIONS			Fuel saved	Saving per year
		Specific	Engine	Engine + ORC		
%	kW	kJ/kWh	Nm^3/h	Nm^3/h	Nm^3/h	€
100	6.180	7.220	1.143	1.047	96	3.216
85	5.325	7.400	996	897	99	186.788
75	4.755	7.420	881	782	99	11.017
50	3.190	7.890	625	550	75	11.613
25	1.575	7.900	313	280	33	1.100
					TOT	213.733

5 Economic and Environmental Remarks

5.1 Economic Analysis

A first approximation of the installation cost of a ORC group can be evaluated as the sum of turbine, pumps, exchangers and fluids costs. The costs of the heat transfer components have been obtained by means of Aspen Tasc:

- Gas/oil heat exchanger 130.000 €;
- evaporator 190.000 €;
- regenerator 95.000 €;
- condenser 100.000 €.

For the other components, the following economic estimates have been considered on the basis of information from manufacturers:

- turbine 150.000 €;
- generator 30.000 €
- toluene pump 20.000 €;
- thermal oil pump 10.000 €;
- toluene 30.000 €;
- diathermic oil 15.000 €;
- balance of the plant (piping, filters, valves, etc.) 115.500 €.

The expected total cost for the bottom regenerated cycle could be obtained adding to the sum of all these terms (€885.000) a mark-up of 20%, resulting in a total price of 1.062.600 €.

Taking into account the estimation of actual fuel saving for each engine load, a simple payback time of the investment equal to 5,9 years has been obtained.

The recovery of waste heat downstream of the propulsion engine by means of a bottom ORC has also a good cost/performance ratio, equal to 2.214 €/kW.

5.2 Environmental Remarks

The adoption of an ORC group as a supplement of the propulsion system, allows saving large amounts of LNG fuel, implying a reduction in atmospheric emissions of pollutant agents, such as carbon dioxide and nitrogen oxides.

To evaluate the quantity of CO_2 avoided, the specific average amount of CO_2 emitted by the Wärtsilä 6L50DF engine, equal to 430 g/kWh, can be considered. By applying this value to the average power produced by the ORC, and on the basis of the hours of use per year of the propulsion system, 1.380 ton/year of CO_2 non emitted into the atmosphere can be obtained.

Not emitted into the atmosphere NO_x tons can be derived in the same way. Starting from the engine average emission of 2.5 g/kWh, a total amount equal to 8,4 ton/year of avoided NO_x emission has been obtained.

6 Conclusions

The main results of the performance improving obtainable adding to a marine Internal Combustion Engine a bottoming ORC, can be summarized as follows:

• the main heat recovery is carried out by the exhaust gas, considering HT cooling circuits as a subsidiary recovery;

• the engine LNG feeding is advantageous compared to fuel oil, due to the higher exhaust gas exergy (lower flow rates but higher temperatures);

• a bottom Rankine cycle, to be combine with a marine engine, must operate with an organic fluid, to reach the best performance;

• Toluene well-matches with the exhaust gases, working with a maximum temperature of 262° C at 20 bar (saturated steam) and condensing to 0,09 bar, by adding a middle ring of thermal oil between exhaust gas and toluene, because of its high flammability;

• Isobutene is better suited to be coupled with the HT circuit (91° C), evaporating at 14 bar and at a temperature of 81° C, with a condensing pressure of 6 bar;

• the best performance can be obtained when the bottom cycle is a regenerated cycle, with an additional power of 520 kW (equal to about +10%);

• the economic analysis shows that the addition of the bottom ORC to the propulsion system has a payback time equal to about 6 years, thanks to the fuel savings obtained as a result of greater efficiency.

• finally the ORC brings benefits in terms of reducing atmospheric pollutant emissions of both carbon dioxide and nitrogen oxide.

References

[1] Wärtsilä Italy, personal communication, 2009.

[2] Micheli D., Pinamonti P., Reini M., Taccani R., *Application of Biomass Power Systems Fed ORC in the Furniture Manufacturing Industrial District of Pordenone: Part II: Development of Thermodynamic Cycle Simulation Model*, 3rd Intern . Symp. Energy and Environment 2004, Sorrento, Italy, June 2004.

[3] Desideri U., Bidini G., *Study of Possible Criteria for Optimization Geothermal Power Plants*, Energy Conversion and Management, Vol. 38, Issue 15-17, Oct. 1997, pp. 1681-1691.

[4] Hung T.C., Shai T.Y., Wang S.K., *A Review of Organic Rankine Cycles (ORCs) for the Recovery of Low-Grade Waste Heat*, Energy, vol. 22, Issue 7, July 1997, pp. 661-667.

[5] Obernberger, I., *Biomass CHP based on the ORC process-EU-Thermie Project Admont*, Tagungsband zur VDI-Tagung "Thermische Nutzung von fester Biomasse", Salzburg, A, VDI Bericht 1588, 2001, pp. 283-302.

[6] Duvia A., Gaia M., *ORC Plants for Power Production from Biomass from 0.4 MWe to 5 MWe*: Technology, Efficiency, Practical Experiences and Economy, Proceedings of the 7th Holzenergie-Symposium, Zurich, CH. 1998.

[7] Gambarotta A., Vaja I., *Internal combustion engine with Organic Rankine bottoming cycles. A thermodynamic analysis*. Proceedings of ECOS 2008, Krakow, Poland, June 24-27, 2008.

[8] Angelino G., Colonna di Paliano P., *Multicomponent Working Fluids for Organic Rankine Cycles (ORCs),* Energy, Vol. 23, Issue 6, June 1998, pp. 449-463.

[9] Saleh B., Koglbauer G., Wendland M., Fischer J., *Working fluids for low-temperature organic Rankine cycles*. Energy, Vol. 32, Issue 7, July 2007, pp. 1210-1221.

[10] G. Angelino, C. Invernizzi, *Cyclic Methyl-siloxanes as Working Fluids for Space Power Cycles*, Trans. ASME, Journal of Solar Energy Engineering, Vol. 115, 1993,pp. 130-137.

[11] Bruno J.C., López-Villada J., Letelier E., Romera S. et al., *Modeling and optimization of solar organic Rankine cycle engines for reverse osmosis desalination*. Applied Thermal Engineering, Vol. 28, Issue 17-18, Dec., 2008, pp. 2212-2226.

[12] Dow technical report,:
http://www.dow.com/heattrans/tech/data.htm.

[13] Prabhu E., *Solar Trough Organic Rankine Electricity System (STORES)-Stage 1 Power Plant Optimization and Economics*. National Renewable Energy Laboratory, Report NREL/SR-550-39433, March 2006.

[14] TEMA Tubular Exchanger Manufacturers Association, Available on line from: http://www.tema.org/.

[15] Serth R.W., *Process Heat Transfer Principles and Applications*, Elsevier Science & Technology Books, 2007.

[16] Purvin & Gertz, Oil and Gas Journal, December 2008.

NUMERICAL MEANLINE SIMULATION AND OVERALL PERFORMANCE PREDICTION OF RADIAL INFLOW TURBINE FOR A 600 kW CYCLE GAS ENGINE

Rubén A. Miranda Carrillo[a], Marco A.R. Nascimento[a] and Elkin I. Gutiérrez Velásquez[a]

[a]*Universidade Federal de Itajubá – UNIFEI, Itajubá - Minas Gerais, Brasil*

Abstract: This paper presents the numerical meanline investigations on the aerothermodynamic design and overall performance prediction for a 600 kW simple cycle gas turbine engine using a one-dimensional computer FORTRAN code (OFC), on the grounds of non-dimensional parameters aimed at computational and work time reduction. In order to find the most promising design option, a computational fluid dynamics (CFD) simulation has been used to study the performance, the aerothermodynamic design and off-design point of the turbine components. The OFC results were compared with the CFD simulation, a computer program for the design and off-design analysis of radial inflow turbines, analytical and experimental results taken from specialized literature showed the results were in agreement.

Keywords: Numerical meanline investigations, radial inflow rotor, performance prediction.

1. Introduction

Microturbines as have been used as primary drivers in the industrial and aircraft sectors for electric power generation [1], nevertheless, the technical evolution of their components and the drop in prices has substantially increased the share of industrial gas turbines worldwide [2]. For this reason, the Federal University of Itajubá and its Energy Conversion Technology Research Group (GETEC), has worked on the development of projects focusing on the design of power units with varied fuel types.

This paper presents the numerical meanline investigations on the aerothermodynamic design and overall performance prediction of the nozzle and the radial inflow rotor for a 600 kW simple cycle gas turbine engine using a one-dimensional computer FORTRAN code (OFC), based mainly on non-dimensional parameters aimed at computational and work time reduction. The microturbine design and off-design model presented in this paper aims both at computational simplicity and at the ability to deal with plants having large variations in the operating parameters. The OFC results were compared with the CFD simulation, a computer program for the design and off-design analysis of radial inflow turbines, analytical and experimental results taken from specialized literature. The comparisons showed the results were in agreement.

2. Gas turbine engine simulation

The thermal performance simulation for the 600 kW simple cycle gas turbine engine at the design point and steady state condition was carried out through the use of the GE Gate Cycle Enter software 5.51 and the model created for a simple cycle is show in Fig. 1.

The designs input parameters used in the Gate Cycle simulation are shown in Table 1 [3] and were based on current technologies for radial turbo machineries. The pressure ratio was 4 and T_{00} of 1123 K was selected as it is the highest temperature put up by the material of the radial turbine, while maintaining the mechanical resistance and the useful life without any blade cooling [4].

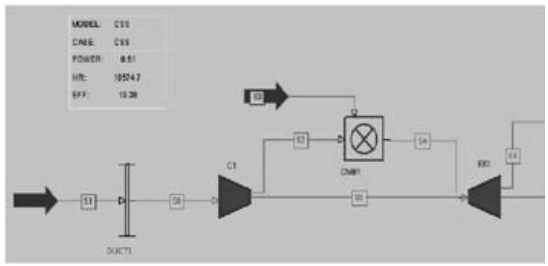

Fig. 1. The Gate Cycle software simulation scheme: simple cycle.

Corresponding Author: Rubén Miranda, Email: ruben.miranda@unifei.edu.br

Table 1. Design parameters for the Gate Cycle software simulation.

Description	Values	Units
Ambient temperature	288	K
Ambient pressure	101.32	kPa
Turbine inlet temperature	1123	K
Pressure ratio	4	--
Compressor adiabatic efficiency	80	%
Combustion adiabatic efficiency	99	%
Turbine efficiency	85	%
Mechanical efficiency	98	%
Combustion chamber pressure loss	2	%
Gas turbine power output	600	kW

3. A meanline preliminary design

The meanline analysis is based on the assumption that there is a mean streamline running through the machine and the conditions on this streamline are representative of the stations being considered [5]. The objective of a meanline analysis is to determine the machine's overall performance or the combination of overall geometric parameters achieving maximum efficiency [6]. Figure 2 shows the meanline method.

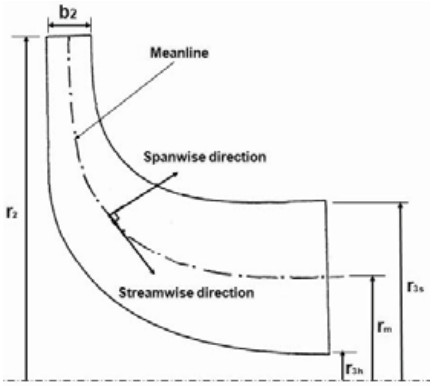

Fig. 2. The meanline method.

The Figure 3 shows the blockage factor (B) and the equation (1) calculates its effect in the turbomachine geometry in percentage, (%). The blockage refers to the difference between the effective area (A_{eff}) that circulates the fluid and the geometric area (A_{geo}) of the component, in m^2

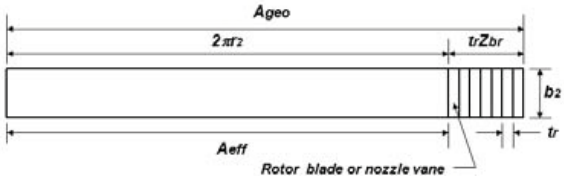

Fig. 3. The blockage factor.

$$B=1-\frac{A_{eff}}{A_{geo}} \quad (1)$$

The Figure 4 shows the geometrical size of the nozzle and the radial inflow rotor turbine calculated by OFC. The axial, tip and radial clearance effect on the aerodynamic performance is taken into account and is assumed to act as an orifice.

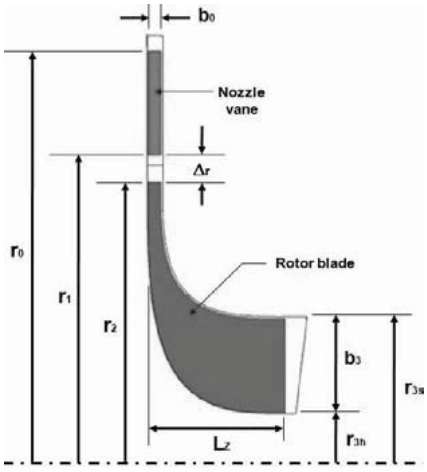

Fig. 4. Radial turbine geometry.

3.1 Velocity Triangles

This computer program initially calculates the velocity triangle and the Mach number at the rotor inlet, simultaneously with the thermodynamic relation between the temperatures and pressures at this point. The next step is the calculation of the velocity triangle at the discharge, aimed at finding the discharge end speed and the relative Mach number. Once the velocity triangles are established, the OFC initiates the calculation of the non-dimensional performance parameters. Figs 5 to 6 illustrate both the velocity triangles at the nozzle and radial rotor inlet and exit of a radial turbine, and the nomenclature used in the paper for the velocity vectors.

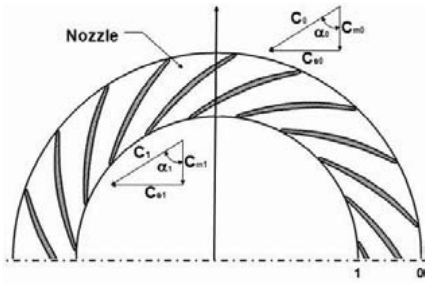

Fig. 5. Nozzle velocity triangles.

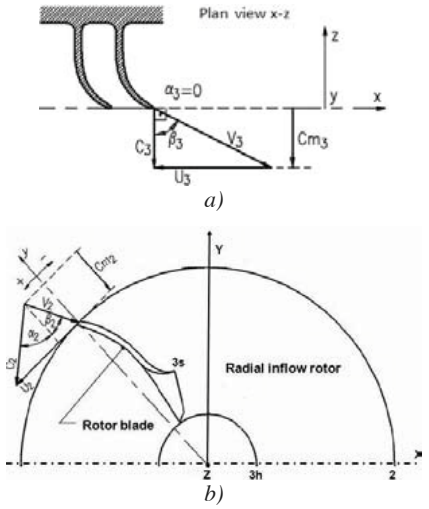

Fig. 6.Rotor velocity triangles; a) exit, b) inlet.

In the OFC method the flow in the radial inflow turbine passage is divided into several regions and modelled in each part separately. Figure 7 show the imaginary inlet duct (a-0), nozzle (0-1), interspaces (1-2), rotor (2-3) and the imaginary outlet duct (3-b).

The general requirement for the analytical procedure is to predict the component discharge conditions from the known inlet conditions and component geometry. The computed discharge conditions then become known inlet conditions for the next component. The principal flow equation model is the non-dimensionless power ratio, equation (16) which combines the total to static turbine efficiency and the total to static turbine pressure ratio. The power ratio determines the blade speed necessary to achieve it. The equations (17), (18), (19), (20) and (21) describe the rotor inlet velocity triangle. The equations (24), (25) and (26) describe the rotor outlet velocity triangle whereas the other equations calculate the rotor non-dimensional parameters. The nozzle most important equations are (2) and (3). The equation (2) calculates the nozzle inlet radius through the nozzle radius ratio and the equation (3) calculates the nozzle inlet absolute velocity while the other equations calculate the nozzle non-dimensional parameters.

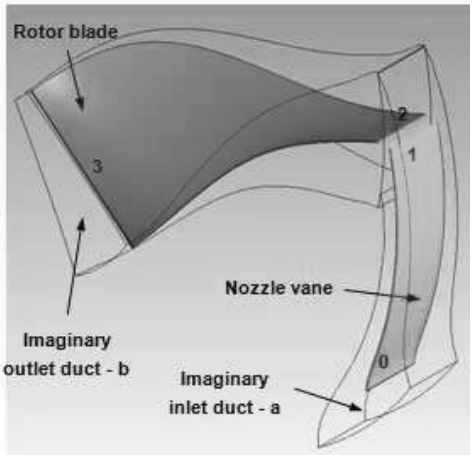

Fig. 7. Simulation regions

Table 2 describes the basic design input values of the thermodynamic parameters for a 600 kW simple gas turbine engine.

Table 2. Design parameters of the nozzle and radial inflow rotor.

Description	Values	Units
Mass flow rate	4.5	kg/s
Inlet turbine total temperature	1123	K
Inlet turbine total pressure	396	kPa
Total to static turbine pressure ratio	3.96	--
Total to static rotor efficiency	85	%
Total nozzle efficiency	90	%
Inlet relative flow angle	-25	°
Outlet relative flow angle	-60	°
Rotor exit hub to shroud radius ratio	0.23	--
Specific heat ratio	287	J/kgK
Tip clearance	1	mm
Relative velocity ratio	3.06	--
Rotor blade thickness	1	mm
Nozzle vane thickness	1	mm

3.2. Nozzle design

The radius of the nozzle vane inlet and outlet at the design point were determined according to the turbine rotor diameter and the geometric constraint conditions. Both the trailing-edge and the leading-edge thickness are constant and the blockage factor is 0.98. Figure 8 shows the nozzle geometry calculates by OFC computer program.

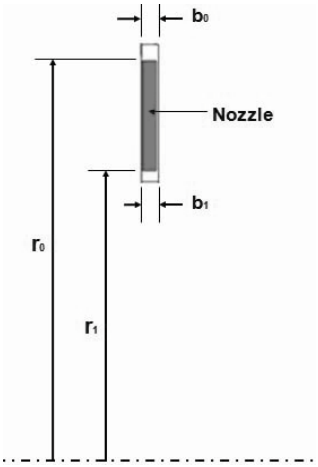

Fig. 8. Nozzle geometry.

Table 3 shows the nozzle inlet and the outlet aerothermodynamic model [7].

Table 3. Nozzle aerothermodynamic model.

Nozzle condition			
Inlet		Outlet	
$r_0 = r_1(r_0/r_1)$	(2)	$r_1 = r_2 + \Delta r$	(9)
$C_0 = \frac{\dot{m}}{\pi D_0 b_0 \rho_0 \cos\alpha_0}$	(3)	$C_{\theta 1} = \left(\frac{r_2}{r_1}\right) C_{\theta 2}$	(10)
$C_{\theta 0} = C_0 \sin\alpha_0$	(4)	$C_1 = C_{\theta 1}/\sin\alpha_1$	(11)
$C_{m0} = C_0 \cos\alpha_0$	(5)	$C_{m1} = C_{\theta 1}/\tan\alpha_1$	(12)
$\frac{T_0}{T_{00}} = 1 - \frac{C_0^2}{2T_{00}C_P}$	(6)	$\frac{T_1}{T_{01}} = 1 - \frac{C_1^2}{2T_{01}C_P}$	(13)
$\frac{P_0}{P_{00}} = \left(\frac{T_0}{T_{00}}\right)^{\frac{k}{k-1}}$	(7)	$\frac{P_{00}}{P_1} = \left(1 + \frac{C_{1s}^2}{2C_P T_{01}}\right)^{\frac{k}{k-1}}$	(14)
$\rho_0 = P_0/(RT_0)$	(8)	$\rho_1 = P_1/(RT_1)$	15)

Table 4 describes the nozzle geometric and thermodynamic output parameters at the design point calculate by OFC.

Table 4. Nozzle aerothermodynamics outputs.

Description	Inlet ($_0$) Values	Outlet ($_1$) Values	Units
Vane height	33.51		mm
Nozzle radius	278.48	227.67	mm
Thickness	1		mm
Number of vanes	17		--
Absolute flow angle	54.59	77.97	°
nozzle radius ratio	1.19		--
Total temperature	1123	1123	K
Static temperature	1117.05	981.95	K
Total pressure	396	374.31	kPa
Static pressure	388.70	234.00	kPa
Absolute velocity	109.30	532.30	m/s

3.3. Radial-inflow rotor design

The rotor consists of 15 full blades with radial-flow inlet and axial-flow outlet. The trailing-edge, the leading-edge thickness and the rotor axial, tip and radial clearance are constant whereas the blockage factor is 0.98. Figure 9 shows the radial inflow rotor geometry calculates by OFC computer program.

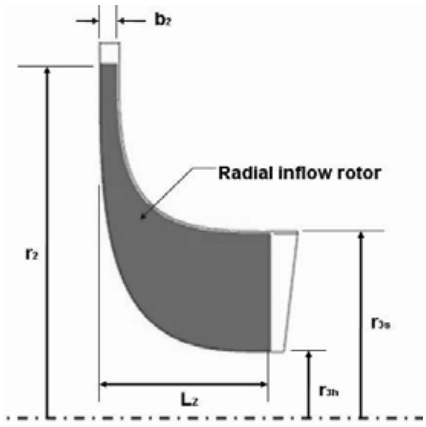

Fig. 9. Radial rotor geometry.

Table 5 shows the rotor inlet and the outlet aerothermodynamic model [7].

Table 6 describes the rotor geometric and thermodynamic output parameters at the design point calculate by OFC.

Table 5. Rotor aerothermodynamic model.

Rotor condition	
Inlet	Outlet
$S_w = \eta_{ts}\left[1-\left(1/RP_{ts}\right)^{\frac{k-1}{k}}\right]$ (16)	$\frac{P_{02}}{P_2}=\left(\frac{T_{02}}{T_2}\right)^{\frac{k}{k-1}}$ (23)
$\frac{C_2}{a_{00}}=\sqrt{\left(\frac{S_w}{k-1}\right)\left(\frac{2\cos\beta_2}{1+\cos\beta_2}\right)}$ (17)	$\frac{V_3}{a_{03}}=\frac{W_R\left(V_2/a_{00}\right)}{\sqrt{T_{03}/T_{00}}}$ (24)
$\frac{C_{\theta 2}}{a_{00}}=\left(\frac{C_2}{a_{00}}\right)\sin\alpha_2$ (18)	$\frac{C_3}{a_{03}}=\left(\frac{V_3}{a_{03}}\right)\cos\beta_3$ (25)
$\frac{U_2}{a_{00}}=\left(\frac{S_w}{k-1}\right)\left(\frac{a_{00}}{C_{02}}\right)$ (19)	$\frac{U_3}{a_{03}}=-\left(\frac{C_3}{a_{03}}\right)\tan\beta_3$ (26)
$\frac{C_{m2}}{a_{00}}=\left(\frac{C_2}{a_{00}}\right)\cos\alpha_2$ (20)	$\frac{T_{03}}{T_3}=1+\left[\left(\frac{k-1}{2}\right)\left(\frac{C_3}{a_{03}}\right)^2\right]$ (27)
$\frac{V_2}{a_{00}}=\frac{\left(C_{m2}/a_{00}\right)}{\cos\beta_2}$ (21)	$\frac{P_{03}}{P_3}=\left(\frac{1}{T_3/T_{03}}\right)^{\frac{k}{k-1}}$ (28)
$\frac{T_{02}}{T_2}=1+\left[\left(\frac{(k-1)}{2}\right)M_2^2\right]$ (22)	$\frac{\rho_3}{\rho_{03}}=\left(\frac{T_3}{T_{03}}\right)^{\frac{1}{k-1}}$ (29)

Table 6. Rotor aerothermodynamic outputs.

Description	Inlet (2) Values	Outlet (3) Values	Units
Blade height	33.51	99.67	mm
Radius	227.94	(3s) 131.0 (3h) 31.39	mm
Axial length	125.15	--	mm
Thickness	1	1	mm
Number of blades	15		--
Relative flow angle	-25	(3s) -22.52 (3h) -60	°
Abs. flow angle	77.50	0	°
Tip clearance	1		mm
Total temp.	1123	812.66	K
Static temp.	975.45	793.09	K
Total pressure	373.19	108.90	kPa
Static press.	227.94	100	kPa
Abs. velocity	544.42	200.68	m/s
Blade speed	586.468	(3s) 83.24 (3h) 347.5	m/s
Relative velocity	130.01	(3s) 217.2 (3h) 401.3	m/s

4. CFD simulations models

Once of the geometric components of the turbine stages have been defined, as a result of the preliminary design, using an OFC, such parameters are transferred to the blade generator using ANSYS BladeGen so that the full three-dimensional geometry of the blades, for both nozzle and rotor, can be developed. The mesh of the nozzle vanes and rotor blades are internally defined using the ANSYS TurboGrid 12.0.; the simulations models were produced using the commercial package ANSYS CFX 12.0® codes [8]. The computational domain of the whole stage was dissected by the hexahedron structural multi-block grid topology. In this case an H grid was used, reaching good resolution at the leading-edge and trailing-edge. The meshes used around the nozzle vanes and the rotor blades are show in Figs 10 to 11, respectively.

Fig. 10. Computational nozzle vane mesh

Fig. 11. Computational rotor blade mesh.

The grids are refined at the near-wall, end wall, leading-edge and trailing-edge of the rotor blade and nozzle guide vane. Table 7 shows the mesh information uses in the CFD simulation.

Table 7. Nozzle and rotor mesh information.

Domain		Nodes	Elements
Domain I	Nozzle	262238	241704
Domain II	Rotor	248861	228316

4.1. Boundary conditions

The boundary conditions were as follows:

- Total pressure and total temperature were imposed at the inlet area.
- Static pressure was imposed at the outlet area.
- Heat transfer model = Total energy.
- Turbulence model = SST.
- Rotor domain motion = Rotating.
- Nozzle domain = Stationary.

The CFD simulations were made with SST (Shear Stress Transport) and k-ε turbulence model. Figure 12 shows the streamline entropy distribution for plane radial turbine flow for both models. The SST model predicts the separation zone, whereas the k-ε model fails to capture the physics of this flow entirely.

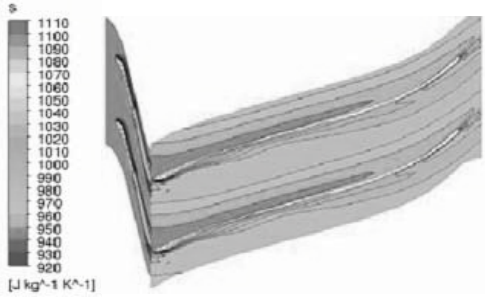

a)

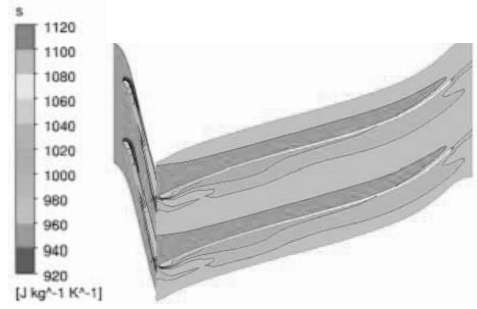

b)

Fig. 12.Radial turbine entropy distribution: a) *SST model*, b) *k-ε model*

5. Validation of numerical models

The differences between the NASA and the OFC computer program consist of the quantity of the program input parameters utilized in the components preliminary design and the calculus methodology. The OFC program utilizes 57% of input parameters while the NASA TN D-8164 utilizes 70%; also, knowledge of the turbine geometry is required for the preliminary design.

The results obtained using the OFC method, were compared with theoretical results provided by NASA TN D-8164 report. This report provides sufficient information and comprehensive geometric design data for the comparison test case. The discrepancies observed for each computer program are because Glassman [9] considered the nozzle and rotor loss coefficient calculated by Reynolds number equal to 1.

Table 8 describes the rotor comparisons between the NASA TN D-8164 and the OFC.

Table 8. Rotor numerical model.

Description	Units	OFC	NASA[9]	Variat.
Rotor inlet				
Diameter	mm	158.83	155.39	3.44
Total temp.	K	1083.3	1083.3	0
Total pressure	kPa	87.16	89.95	-2.79
Static temp.	K	1005.98	1010.85	-4.87
Static pressure	kPa	72.43	75.65	-3.22
Abs. flow angle	°	74.25	71.92	2.33
Abs. velocity	m/s	283.64	274.59	9.05
Blade speed	m/s	320.18	313.24	6.94
Rel. flow angle	°	-31.50	-31.50	0
Rel. velocity	m/s	90.30	99.93	-9.63
Shaft power	kW	24.22	22.37	1.85
Num. of blades	--	13	12	1
Rotor outlet				
Shroud diameter	mm	34.98	38.72	-3.74
Hub diameter	mm	100.16	110.84	-10.68
Total temp.	K	915.27	926.12	-10.85
Total pressure	kPa	57.18	57.35	-0.17
Static temp.	K	910.46	920.20	-9.74
Static pressure	kPa	56.44	56.44	0
Abs. velocity	m/s	70.90	78.48	-7.58
Blade speed	m/s	201.91	223.44	-21.53
Rel. flow angle	°	-70.65	-70.65	0
Rel. velocity	m/s	213.99	236.82	-22.83

Table 9 describes the nozzle comparisons between the NASA TN D-8164 and the OFC.

Table 9. Nozzle numerical model.

Description	Units	OFC	NASA[9]	Variat.
Nozzle inlet				
Diameter	mm	199.24	195.55	3.69
Total temp.	K	1083.3	1083.3	0
Total pressure	kPa	91.01	91.01	0
Static temp.	K	1076.3	1072.02	4.32
Static pressure	kPa	89.55	88.65	0.9
Abs. flow angle	°	51.45	55.60	-4.15
Abs. velocity	m/s	105.73	108.49	-2.76
Num. of vanes	--	17	16	1
Nozzle outlet				
Diameter	mm	161.04	158.75	2.29
Total temp.	K	1083.3	1083.3	0
Total pressure	kPa	87.27	89.95	-2.68
Static temp.	K	1008.2	1013.94	-5.75
Static pressure	kPa	72.92	76.23	-3.31
Abs. flow angle	°	74.38	72.00	2.38
Abs. velocity	m/s	279.56	268.60	10.96

6. Comparison of simulations

Table 10 describes the comparison between the CFD simulation and the OFC for a nozzle turbine

Table 10. Nozzle numerical simulation.

Description	Units	CFX 12.0	OFC	Variat.
Mass flow rate	kg/s	4.55	4.50	0.05
Nozzle inlet				
Static pressure	kPa	393.02	395.78	-2.76
Total pressure	kPa	396.00	396.00	0
Static temperature	K	1119.48	1122.82	-3.34
Total temperature	K	1123.00	1123.00	0
Abs. flow angle	°	-0.11	54.51	-54.62
Nozzle Outlet				
Static pressure	kPa	212.35	233.83	-21.48
Total pressure	kPa	369.29	374.28	-4.99
Static temperature	K	959.85	981.77	-21.92
Total temperature	K	1122.48	1123.00	-0.52
Absolute velocity	m/s	565.68	532.39	33.29
Abs. flow angle	°	77.17	77.72	-0.55

Table 11 describes the comparison between the CFD simulation and the OFC [10] for the radial inflow rotor turbine

Table 11. Rotor numerical simulation.

Description	Units	CFX 12.0	OFC	Variat.
Rotor inlet				
Static pressure	kPa	212.38	227.94	-15.56
Total pressure	kPa	361.83	373.19	-11.36
Static temperature	K	961.57	975.45	-13.88
Total temperature	K	1123.47	1123.00	0.47
Abs. Mach numb.	--	0.93	0.87	0.06
Blade speed	m/s	589.91	586.48	3.43
Absolute velocity	m/s	569.11	544.43	24.68
Abs. flow angle	°	77.28	77.50	-0.22
Relative velocity	m/s	132.07	130.02	2.05
Rotor outlet				
Static pressure	kPa	99.97	100.00	-0.03
Total pressure	kPa	111.35	108.90	2.45
Static temperature	K	788.76	793.09	-4.33
Total temperature	K	813.34	812.66	0.68
Abs. Mach numb.	--	0.39	0.35	0.04
Blade speed	m/s	242.64	215.42	27.22
Absolute velocity	m/s	218.53	200.68	17.85
Abs. flow angle	°	15.02	0.00	15.02
Relative velocity	m/s	281.87	294.41	-12.54

7. Off-Design characteristics

The overall performance of the turbine was evaluated in terms of efficiencies, turbine pressure ratio and the velocity ratio. Table 12 describes the non-dimensional performance parameters at the off-design point calculate by OFC.

Table 12. Non-dimensional performance parameters.

$\phi = U_2 / C_s$	(32)	Velocity ratio
$\dot{m}\sqrt{T_{02}} \,/\, P_{02}$	33)	Mass flow parameters
$n_{ss} = \omega\sqrt{\dot{Q}_3} \,/\, W_{espos}^{0,75}$	(35)	Specific speed

Table 13 describes the design input parameters used in the experimental test of the radial inflow turbine for a 100 kW microturbine [11].

Table 13. Basic design parameters of the radial inflow turbine for a 100 kW microturbine.

Design parameters	Values	Units
P_{00}	360.0	kPa
T_{00}	1173.15	K
$\dot{m}$	1.006	Kg/s
N_{rpm}	61000	rpm
P_3	106.77	kPa

Figure 13 presents the mass flow parameter plotted against total to static pressure ratio for a series of speeds. The design point was 3.80 and at each speed the mass flow increases with pressure ratio until it reaches a maximum when the turbine is to be in choked.

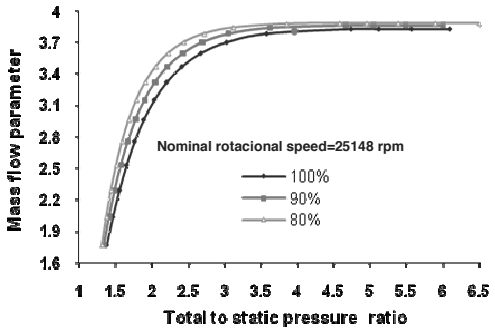

Fig. 13. Mass flow parameter vs total to static pressure ratio.

Figure 14 shows the total to static efficiency plotted against total to static pressure ratio. The maximum efficiency occurs in quite narrow band of pressure ratio 2.5 to 3.5, particularly at speeds below the design point (rotational speed = 90%).

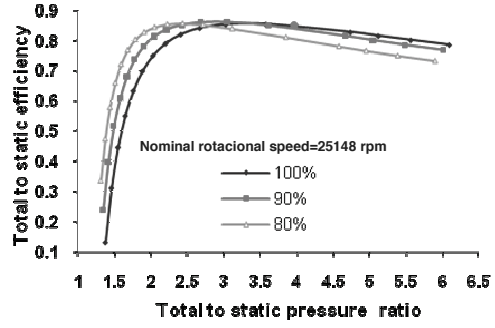

Fig. 14. Total to static efficiency vs total to static pressure ratio.

Figure 15 shows the total to static efficiency plotted against total to static pressure ratio for a 100 kW microturbine [11]. There is always a maximum point of the total to static efficiency on each line of rotor rotational speed and each peak of efficiency corresponds to different total to static expansion ratio, which in agreement with the Fig 14.

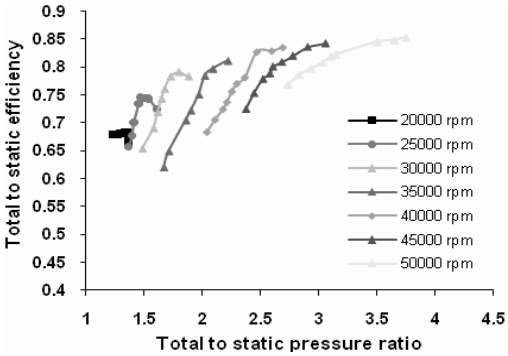

Fig. 15. Total to static efficiency vs total to static pressure ratio.

Figure 16 presents the total to static efficiency over the range of turbine velocity ratio investigated for lines of constant blade speed. The figure shows that a static efficiency of 85% and the velocity ratio $\phi = 0.66$ were obtained at equivalent design point operation. This value is lower than of the ideal value ($\phi = 0.7$) of 4.9%.

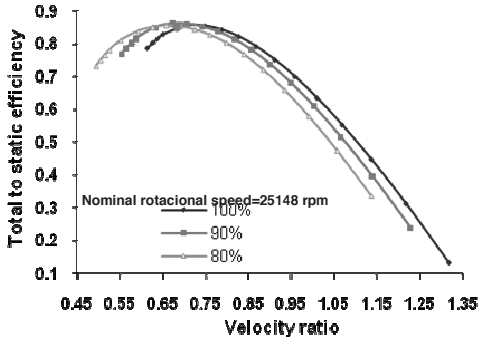

Fig. 16. Total to static efficiency vs velocity ratio.

Figure 17 shows the total-static efficiency of the radial inflow turbine as function of velocity ratio [14]. When the velocity ratio is about 0.7, total to static efficiency arrives at the maximum whatever the rotor rotational speed of the radial inflow turbine will be, which in agreement with the Fig. 16.

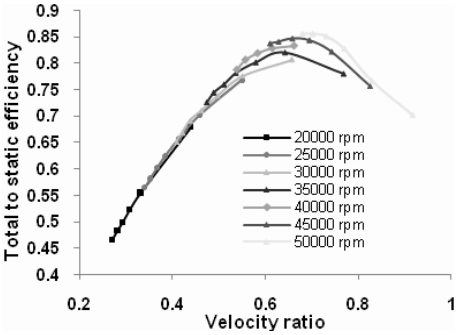

Fig. 17. Total to static efficiency vs velocity ratio.

Figure 18 presents the mass flow parameters as a function of turbine expansion ratio for a nominal rotational speed, generated by CFD and OFC for the design point. The both programs have the same behavior in quite narrow band of pressure ratio 2.3 to 4.7 and the mass flow parameter obtained by OFC was 3.8080. This value is 1.1473% lower than of the value obtained by CFD.

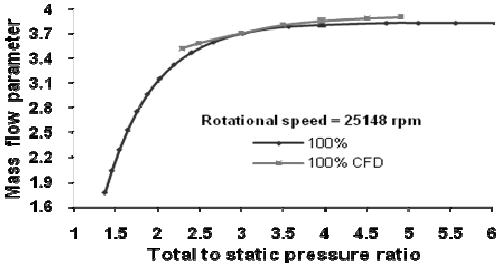

Fig. 18. Mass flow parameter by CFD and comparison with OFC.

Figure 19 presents the total to static efficiency as function of total to static pressure ratio at the nominal rotational speed, generated by CFD and OFC for the design point. The both programs have the same behavior in quite narrow band of pressure ratio 3.0 to 4.8.

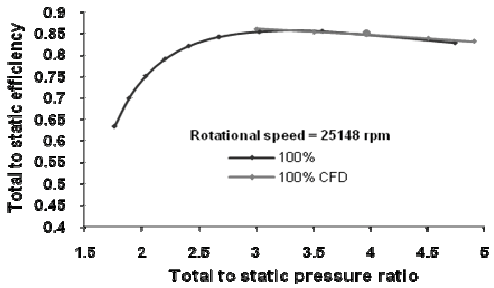

Fig. 19. Total to static efficiency by CFD and comparison with OFC.

Finally, Figure 20 presents the total to static efficiency as function of total to static pressure ratio by CFD and comparison with test point in detail [11]. The figure shows the same behavior and agreement with the Fig. 19 for the nominal rotational speed.

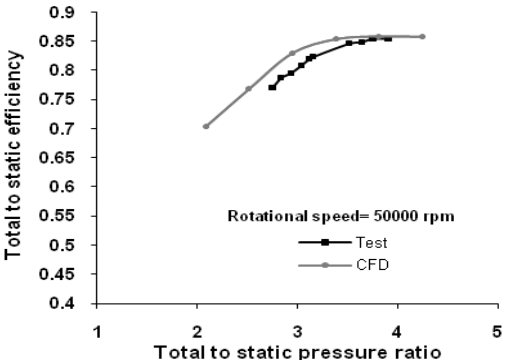

Fig. 20. Total to static efficiency by CFD and comparison with test point.

8. Conclusions

The main conclusions are:

- The OFC used in the design of radial turbine components is an effective route to preliminary design and optimization. No knowledge of the turbine geometry beyond basic overall dimensions is only required. The meanline model was tested and proved capable of providing the designer with reliable performance estimates.
- The overall computed results from the program of this paper show a marked improvement over those from the previously used program and good agreement with experimental data.
- Minor discrepancies were observed between the values calculated by each simulation program, as the incidence angle was not considered and it was assumed equal to the blade angle and its value zero [12]. Future version of this program will calculate, simulate and compare the incidence angle.
- The main contribution of this work is that it provides a one-dimensional computer FORTRAN code (OFC) method that helps designers to quantify the performance of the nozzle and the radial inflow rotor turbine at a preliminary design stage.

Nomenclature

b	Blade or vane height, mm
C	Absolute velocity, m/s
$\dot{m}$	Mass flow rate, kg/s
P	Static pressure, kPa
P_{oo}	Inlet turbine total pressure, kPa
R	Gas constant, J/kgK
r	Radius, mm
S_w	Power ratio
T	Static temperature, K
T_{oo}	Inlet turbine total temperature, K
t	Thickness, mm
U	Blade speed [m/s]
V	Relative velocity [m/s]
W_R	Relative velocity ratio

Greek symbols

α	Absolute flow angle
β	Relative flow angle
η	Efficiency
ρ	Density, kg/m^3
k	Specific heat ratio
Δ	Radius variation, mm
ω	Angular speed, rad/s

Subscripts

ts	Total to static
θ	Tangential direction

References

[1] Feng, Z., et al., 2005, Aerothermodynamic Design and Numerical Simulation of Radial Inflow Turbine Impeller for a 100 kW Microturbine", *ASME TURBOEXPO 2005*, Montreal, ASME GT2005-68276, 8, pp.

[2] Cohen, h., Rogers, G. F. C. and Saravanamutto, H., I., H., 1996, *Gas Turbine Theory*, 4th edition, Longman Scientific & Technical, Essex CM20 2JE, England, Chap 8, 442 p.

[3] Oliveira, L., et al., 2009, The Thermal Impact of Using Syngas as Fuel in the Regenerator of Regenerative Gas Turbine Engine", *ASME TURBOEXPO 2009*, Florida, ASME GT2009-59846, 9, pp.

[4] Nascimento, M.A., et al., 2008, Cycle Selection and Compressor Design of 600 kW Simple Cycle Gas Turbine Engine, *ASME TURBOEXPO 2008*, Berlin, ASME GT2008-51523, 7, pp.

[5] Qiu, X., and Baines, N., 2007, Performance Prediction for High Pressure-Ratio Radial Inflow Turbines, *ASME TURBOEXPO 2007*, Montreal, ASME GT2007-27057, 12, pp.

[6] Moustapha, H., Zelesky, M., Baines, N. C. and Japikse, D., 2003, *Axial and Radial Turbines*, Concepts NREC, Vermont, USA, Chaps 7, 8, 358 p.

[7] Zhang, J., Zhuge, W., Hu, L. and Li, S., 2007, Design of turbocharger variable nozzle, *ASME TURBOEXPO 2007*, Montreal, ASME GT2007-27562, 7 p.

[8] Ansys, Inc. ANSYS CFX 12.0. 2009.

[9] Glassman, A.J., 1976, Computer Program for Design Analysis of Radial-Inflow Turbines, Technical Note, NASA TN D-8164, Report N° E-8394, Lewis Research Center, National Aeronautics and Space Administration, Cleveland, Ohio, USA, 64 p.

[10] Compaq Computer Corporation. Compaq Visual Fortran. 2000.

[11] Deng, Q., et al., 2007, Experimental and Numerical Investigation on Overall Performance of a Radial Inflow Turbine for 100 kW Microturbine, *ASME TURBOEXPO 2007*, Montreal, ASME GT2007-27707, 8, pp.

[12] Futral, S.M. and Wasserbauer, C.A., 1965, Off-design Performance Prediction with Experimental Verification for a Radial-Inflow Turbine", Technical Note, NASA TN D-2621, Lewis Research Center, National Aeronautics and Space Administration, Cleveland, Ohio, USA, 26 p.

Acknowledgments: The authors wish to thank the Petrobras Research and Development Center (CENPES), the Coordination of Improvement of Higher Education (CAPES), the National Council of Technological and Scientific Development (CNPq), and the Foundation for Research Support of Minas Gerais (FAPEMIG) for their collaboration and support in the development of this work.

A Multi-Criteria Decision Analysis on Personal Transportation Technology Using Heuristic Design

Erik Wilhelm, Warren Schenler

Paul Scherrer Institut, Villigen, Switzerland

Abstract: The evaluation of technology to reduce the environmental impacts of light duty vehicles while meeting consumer requirements is complicated by the large number of options that must be considered. For example, hydrogen competes not only with fossil fuels, but also with bio-fuels, synthetic fuels, and electricity. Heuristic design rules based on first principles and engineering practice are used to combine exogenous options like hybridization architecture and primary energy converter (engine or fuel cell) with endogenous options like electric motor power and component sizing to generate a large set of self-consistent vehicle designs. The resulting virtual fleet of vehicles is modeled using drivetrain simulation with optimized control for hybrid designs. Life-cycle technology performance is based on data from the ecoinvent and GREET databases. Cost, performance, environment, and utility indicator results are used for multi-criteria decision analysis (MCDA). Stakeholders valuing emissions reductions prefer either fuel cells using hydrogen made with renewable energy or all-electric vehicles depending on total cost of ownership preferences. The conclusions provide insight into future vehicle technologies (with emphasis on comparing hydrogen to alternatives) and how underlying stakeholder preferences may be reconciled to promote sustainable transportation.

Keywords: all-electric, fuel cell, heuristics, hybrid, multi-criteria decision analysis, transportation

1. Introduction

Consider a family looking for a new car. They are likely to weigh the car's purchase price, whether it is safe, the number of people and grocery bags it can carry, how fast it goes, whether it can play mp3's, and, last but not least, what colour it is. Now consider a policy maker serving his constituents. For him, light-duty vehicles must be evaluated on the fuel they use, how much pollution they emit, and their collision safety (stakeholder preferences are rarely mutually exclusive), among others. The task of choosing between personal transportation technologies is complicated by the number of options available, as well as the scarcity of (reliable) criteria data. While stakeholders may consider the same criteria, the value that they place on each vehicle attribute reflects their often conflicting objectives. The environmental regulator attempts to mitigate the global commons dilemma [1], while the consumer is primarily interested in personal mobility. The goal of performing multi-criteria assessment in the transportation field is to help stakeholders to understand the trade-offs between various vehicle technologies, and, more importantly, understanding which technology best matches their real or preconceived preferences.

2. Methods

The difficulty in assessing transportation technology arises first from the radically different technologies (hybrids, all-electric, fuel cell, etc) that engineers are developing for tomorrows' vehicles and second from the uncertainty associated with technology improvement for each of these approaches (i.e. will economies of scale reduce costs sufficiently?). While there have been various notable studies preceding this one [2],[3],[4], the heuristic design approach is unique in its ability to generate and compare a large range of present and future transportation options.

2.1. Technology options

The technologies listed in Table 1 were selected from a larger set to generate the simulation results presented here. This subset still represents close to two million distinct vehicle designs, illustrating the importance of using design heuristics to eliminate nonsensical combinations. Each technology has both present (2010) and future (2030) performance values based on the assumed technology development detailed in Appendix A. Power-split hybrids (i.e. Toyota Prius) are not included in this paper due to complexity of control, but will be treated in future publications.

Corresponding Author: Erik Wilhelm, Email: erik.wilhelm@psi.ch

Table 1: Available technology options

Option Category	# options										
Classes	3	compact	midsize	midsize truck							
Markets	2	passenger	sport								
Engines	3	otto	diesel	fuel cell							
Hybridization	5	none	mild	series	parallel	EV					
Fuels	4	gasoline	diesel	hydrogen	electricity						
Displacements (L)	12	1.0	1.1	1.7	1.9	2.0	2.1	2.7	2.9	3.0	3.1	3.7	3.9
Fuel Cell Power (kW)	3	30	40	50									
Electric Power (kW)	10	3	30	40	50	60	70	80	90	100	110		
Battery Chemistry	2	NiMH	LiON										
Battery Energy (Ah)	7	4.5	30	40	50	60	70	80					
Total:	**1.81E+06**												

2.2. Heuristic vehicle design

Heuristic design refers to the application of rules taken from first principles as well as from engineering practice to create a set of self-consistent vehicle designs as shown in Fig. 1. The advantages of heuristic design approach are the ability to easily test the plausibility of a design set by comparing it to the real world fleet, the broad scope of analysis that it enables, as well as the flexibility to hypothesize about future vehicle designs without changing the modeling structure.

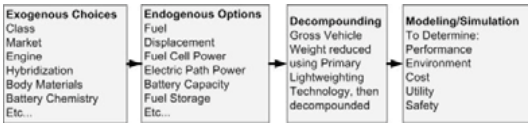

Fig. 1: Generalized heuristic design procedure

The rules used in generating the heuristic designs are detailed in [5,6].

2.3. Optimal hybrid control

To ensure a fair comparison of hybrid powertrain technology the simulation should be carried out under optimal control conditions. For this work, dynamic programming techniques were used to guarantee that each vehicle design was simulated with optimal power split (U), and hence the lowest possible energy consumption. Fig. 2 shows an optimal control policy for a parallel hybrid over the UDDS drive cycle. Further detail on the methods used in this work can be found in [7-9].

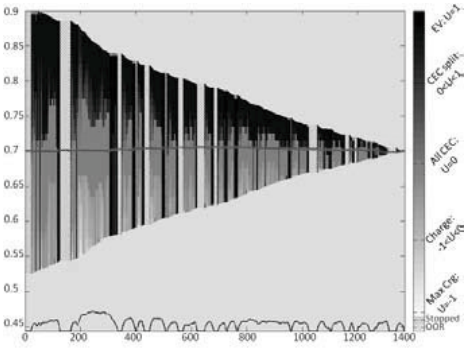

Fig. 2: UDDS optimal control policy

2.4. Multi-criteria Decision Analysis

The goal of multi-criteria decision analysis (MCDA) is to use stakeholder preferences to rank the best alternative technologies balancing conflicting stakeholder objectives and, in the best case, to identify technologies that are robust over different criteria weightings. The full set of stakeholder criteria studied is listed in Table 2, but for simplicity only 8 were selected for the MCDA.

Table 2: Stakeholder criteria and data sources [10-14]

Category	Criteria	Units	Primary Source
Cost	Purchase	CHF	NREL, UC Davis, Kromer
	Operating/Maintenance	CHF/km	ADAC
	Total cost of ownership	CHF/year	Vias, et al (Argonne/MIT)
Performance	Acceleration (0-100)	s	power/weight ratio
	Acceleration (80-110)	s	aero/power/weight
	Top Speed	kph	aero/power relationship
Utility	Range	km	simulation
	All-electric range	km	simulation
	Passenger volume	m^3	US EPA
	Cargo volume	m^3	fueleconomy.gov
	Towing capacity	kg	max traction power
Environment	Direct emissions	g/km	ecoinvent/GREET
	Well-to-pump emissions	g/km	ecoinvent/GREET
	Vehicle cycle emissions	g/km	ecoinvent/GREET

For this work the 'pairwise-outperformance approach' (POA) to multi-criteria decision analysis was adapted from the EU NEEDS project [15], and was used to rank technologies according to stakeholder preferences. The POA is characterized by equations 1-4, where technologies *i* and *j* are described by the indicator vector *r*, and ranked according to the weight vector *w*, and scaled by β, the absolute performance weighting factor,

$$dc_{ijk} = w_k \cdot (r_{ik} - r_{jk}) \cdot \beta(r_{ik}), \quad (1)$$

$$dc_{jik} = w_k \cdot (r_{jk} - r_{ik}) \cdot \beta(r_{jk}), \quad (2)$$

$$\beta(x) = \alpha^{-x} \ (\alpha = 10;\ 0 \le x \le 1), \quad (3)$$

$$d_{ij} = \sum_{k=1}^{n} (dc_{ijk} - dc_{jik}). \quad (4)$$

If $d_{ij} > 0$ then vehicle design *i* is preferred to alternative *j*. The heuristic design algorithm, drivetrain simulation, and the multi-criteria analysis were all performed in the MATLAB environment. By vectorizing the MATLAB code as much as possible, the execution time was reduced by a factor of 5 for an average sized set (and more for larger sets) [16].

3. Results

The results presented here are divided into two sections. The first examines stakeholder preferences derived from an anonymous online survey distributed through the social networking platform Facebook and through personal email,

and the second investigates the sensitivity of the MCDA results. Drivetrain simulations were all carried out using the New European Driving Cycle (NEDC), and selected design-average model outputs are shown in Appendix B to provide insight into the vehicle performance assumptions. Please note that due to an error in the model input, the annual vehicle km travelled was overestimated by a factor of 10, resulting in over-emphasis on fuel cost in total cost calculations and a favouring of fuel efficient options for this criterion. Future tests are expected to show that this does not have a dramatic impact on MCDA results. Validation of model results for various criteria (fuel consumption, acceleration, greenhouse gas emissions etc) is detailed in work previously published by this group [17]. Life cycle modeling performed here includes vehicle production, use, and disposal, as well as fuel extraction, refining, and transportation according to data from the ecoinvent and GREET databases.

3.1. Stakeholder preferences

The online survey generated 70 complete responses and roughly 50 more partially complete responses. A cluster analysis was performed on the set of complete survey responses in order to cluster the respondents into three stakeholder groups with adequate (but not perfect) partitioning using the k-means method. With more than three clusters, the 'goodness' of clustering (quantified using a silhouette analysis) was poor. The response set was distributed between the European Union/Switzerland (29), and North America (41), with respondents primarily colleagues from industry and academia as well as family and friends. Survey participants were supplied with no additional information regarding technology options because they were not asked to choose between vehicle designs. An aggregation of the survey results can be found in Appendix C.

The best metrics for distinguishing between groups turned out to be vehicle ownership and daily kilometers travelled, with North Americans travelling an average of 13 km more per day. Fig. 3 shows how individual responses regarding daily travel, tendency to plan finances, and desire for good acceleration performance are grouped around three centroids. The 'Frequent' driving group tended to own their own vehicles, commute an average of 100 km daily, and valued speed and financial planning more than the 'Seldom' driving group, who tended not to own their own vehicles, travelled by car less than 7 km per day on average, and neither planned their finances nor needed fast vehicles. Members of the 'Occasional' driving group travel an average of 41 km by car per day, also tend to own vehicles, and represent a slightly younger age demographic.

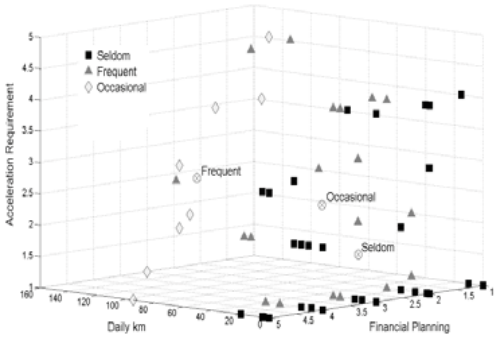

Fig. 3: Stakeholder group clustering according to daily travel, tendency to plan finances, and desire for acceleration performance

The eight vehicle characteristics shown in Table 4 were chosen as being representative of the most important consumer criteria in the questionnaire, and served as inputs to the MCDA algorithm: two from each of the performance, utility, environment, and cost categories. It should be noted that while the survey did not explicitly ask respondents about their preference for low 'total cost of ownership', the responses for 'operating cost' were deemed an appropriate surrogate for this criteria. Additionally, greenhouse gas emissions criteria preferences (GHG emis.) were equated to CO_2 emissions performance indicators and 'health related emissions' were equated to NO_x vehicle performance indicators throughout the MCDA.

Table 4: Representative stakeholder criteria weightings derived from survey responses

	Accel	Top speed	Range	GHG emis.	Health related emis.	Pass. Cap.	Purch. cost	Op. cost
Seldom	0.50	0.42	0.74	0.79	0.83	0.72	0.77	0.77
Frequent	0.58	0.40	0.65	0.70	0.68	0.58	0.85	0.80
Occasional	0.53	0.42	0.68	0.78	0.79	0.67	0.80	0.77

The result of performing MCDA using criteria weights from the three stakeholder groups for both present and future vehicle technologies are shown in Table 5. The top 5 vehicles chosen by all three groups were identical, mostly due to how small the differences in clustered criteria preferences were

between stakeholders. It is interesting that diesel hybrids were selected most often, and that, in the near term, parallel hybrids were preferred to mild hybrids, which in turn were preferred to no hybridization. This reflects the trend (at least in Europe) towards diesel vehicles, as well as the current tendency towards parallel hybrid architectures before plug-in series architectures. It is slightly confusing that compact vehicles were preferred in all cases over mid-sized sedans, but this can perhaps be explained by the absence of a luggage volume criterion in the MCDA (and the general difficulty with distilling vehicle choices down to eight stakeholder criteria).

Table 5: MCA results for stakeholder responses

	With Current Technology Options				
	Class	**Market**	**Powertrain**	**Fuel**	**Battery**
Group 1	Compact	Passenger	Parallel>Mild>None	Diesel	LiON>None
Group 2	Compact	Passenger	Parallel>Mild>None	Diesel	LiON>None
Group 3	Compact	Passenger	Parallel>Mild>None	Diesel	LiON>None
	With Future Technology Options				
	Class	**Market**	**Powertrain**	**Fuel**	**Battery**
Group 1	Compact	Passenger	Series	Diesel	LiON
Group 2	Compact	Passenger	Series	Diesel	LiON
Group 3	Compact	Passenger	Series	Diesel	LiON

3.2. Sensitivity analysis

A sensitivity analysis was performed in order to better understand the results of the stakeholder survey MCDA. The first series of tests were performed to determine the influence that each individual stakeholder criterion has on the top design choice. Table 6 shows the results of performing 8 'polarized' runs where each criterion weight was sequentially set to 1 and while all other criterion weights were set to 0 for current and future technologies. The fact that hybrid vehicles were selected when acceleration and top speed criteria were maximized is consistent with the performance advantages offered by electric drivetrains. The results for autonomy are not surprising: diesel series hybrids have the highest on-board energy content, and are among the most efficient vehicles. That the lowest CO_2 emissions and total cost of ownership are achieved by all-electric vehicles also comes as no surprise, given the Swiss consumption mix assumption of 104g CO_2/kWh and relatively cheap electricity. A conventional gasoline vehicle was selected when the maximum weight was placed on both the purchase cost and passenger volume criteria. This makes sense because of this technology's status as the incumbent (and hence cheaper) technology and the lack of bulky powertrain elements impinging on passenger space. The choice of fuel cell as the top performing design on the basis of its NO_x emissions is also logical, because it was assumed that the hydrogen would be produced from solar PV electricity with low associated life-cycle NO_x emissions.

Table 6: Polarized design choices

	With Current Technology Top Design Choice							
Acceleration	compact	sport	mild	3.9 L	gasoline	NiMH	3 kW	0.5 Ah
Top speed	compact	sport	parallel	3.1 L	gasoline	LiON	50 kW	50 Ah
Autonomy	compact	passenger	series	1.1 L	diesel	LiON	90 kW	80 Ah
CO2 emissions	compact	sport	EV	-	-	LiON	60 kW	40 Ah
NOx emissions	compact	sport	EV	-	-	LiON	60 kW	40 Ah
Passenger volume	midsize	passenger	none	1.9 L	gasoline	-	-	-
Purchase cost	compact	passenger	none	1.9 L	gasoline	-	-	-
Total cost	compact	passenger	EV	-	-	LiON	60 kW	40 Ah
	With Future Technology Top Design Choice							
Acceleration	compact	sport	mild	3.9 L	gasoline	NiMH	3 kW	0.5 Ah
Top speed	compact	sport	parallel	3.1 L	gasoline	NiMH	50 kW	50 Ah
Autonomy	compact	sport	series	1.1 L	diesel	LiON	90 kW	80 Ah
CO2 emissions	compact	sport	EV	-	-	LiON	60 kW	40 Ah
NOx emissions	compact	sport	fuel cell	30 kW	hydrogen	LiON	90 kW	60 Ah
Passenger volume	midsize	passenger	none	1.9 L	gasoline	-	-	-
Purchase cost	compact	passenger	none	1.9 L	gasoline	-	-	-
Total cost	compact	passenger	EV	-	-	LiON	60 kW	40 Ah

To further examine the sensitivity of the optimal design to changes in criteria preferences, two criteria weightings were increased as two criteria weightings were decreased while the remaining four are held constant. The future technology vehicle design set was used for all of the following analysis. Fig. 4 shows how the vehicle purchase cost is much more sensitive to performance preference than to environment criteria preference due to the selection of a much larger series hybrid motor and battery above a 0.4 performance preference weighting level. Note that fuel cell series and diesel series hybrids are the optimal vehicles selected using the future design set.

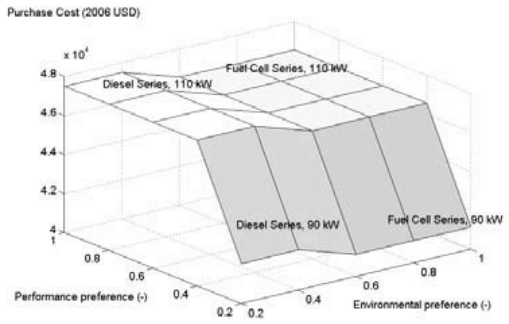

Fig. 4: Purchase cost is primarily sensitive to performance preference: future fuel cell hybrid purchase price is 2% lower than that of future diesel series hybrids

Still considering environment and performance criteria, Fig. 5 shows how life cycle CO_2 emissions

are much more sensitive to environmental criteria weighting than they are to performance criteria weighting. Past a 0.5 environment criteria weighting, fuel cell vehicles are selected over diesel series hybrids leading to the large discontinuity in the figure.

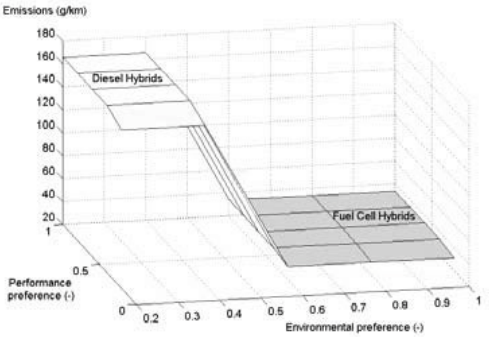

Fig. 5: CO_2 emissions are largely insensitive to performance preferences

Considering these two results together, it can be concluded that a larger purchase cost penalty is paid for performance than for CO_2 reduction.

Looking at two different criteria, Fig. 6 shows how range is affected by utility and cost preferences. The selected vehicle designs are mostly diesel series hybrids with lithium ion batteries when the , 3 , and switches to metal hydride batteries when the preference for low cost increases. The outlier at maximum (low) cost preference and minimum utility (range) preference is a diesel non-hybrid.

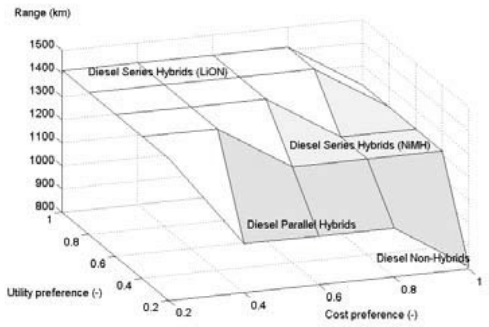

Fig. 6: As sensitivity to cost increases, range decreases towards smaller battery diesel hybrids until a non-hybrid is selected

Returning to environmental preferences, Fig. 7 shows that as the preference for low cost and environmental criteria increases, the total cost of ownership reaches a maximum with all fuel cell hybrid designs, until an EV is selected causing the cost to fall dramatically. For low environmental criteria weights and almost all cost preferences, diesel hybrids are selected over fuel cell hybrids.

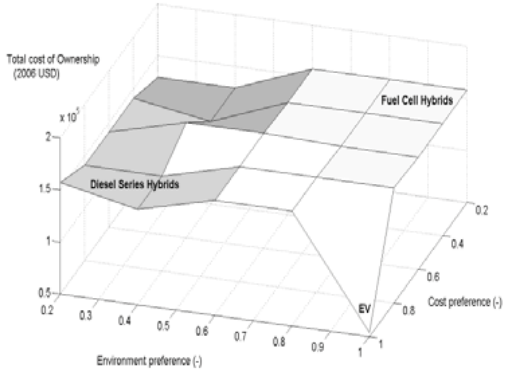

Fig. 7: Total cost of ownership falls dramatically as an EV design is selected

The results shown in Fig. 8 reiterate more explicitly those of Fig. 7, with fuel cell and electric options dominating when environmental preferences are high, and diesel series otherwise.

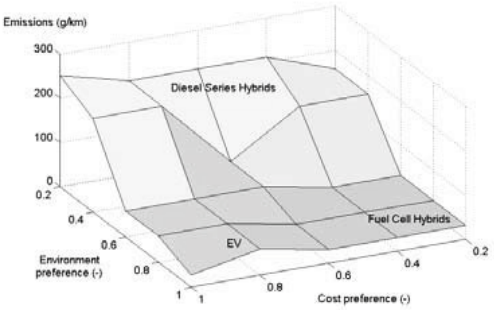

Fig. 8: Fuel cell and EV options dominate on CO_2 emissions for high environmental preference weightings

3. Conclusions

The conclusions of this multi-criteria assessment of personal transportation technology options are:

- Although survey respondents could be clustered (primarily according to vehicle ownership and daily driving distances) the criteria preferences between groups were not drastically different, leading them to select similar optimal designs,
- Survey results suggest that, in the near term, most consumers are willing to pay a

premium for the improved performance and reduced emissions of parallel/mild diesel hybrids, and in the future prefer series hybrids as batteries become cheaper,
- Future all-electric options are interesting only when range (utility, passenger volume, etc) is weighted low,
- Conventional parallel hybrid and Otto drivetrains dominate the current design sets while diesel and fuel cell options dominate the future design sets for many of the sensitivity analysis criteria preference weightings.

While it is clear that there are significant hurdles to cross for cars based on hydrogen fuel cells, the barriers may not be as high as commonly assumed. This is demonstrated through the selection of fuel cell powertrains when the preferences for environmental, total cost, and range criteria are high, even under conservative future cost and performance assumptions.

References

[1] Ostrom, E. et al, 1999, Revisiting the Commons: Local Lessons, Global Challenges. *Science* 284, 279-282.

[2] MacLean HL, Lave LB, 2003, Evaluating automobile fuel/propulsion system technologies. *Progress in Energy and Combustion Science* 29, 1-69.

[3] Weiss MA, et al, 2000, *On the Road in 2020: A life-cycle analysis of new automobile technologies*.

[4] Mierlo JV, Maggetto G, Lataire P, 2006, Which energy source for road transport in the future? A comparison of battery, hybrid and fuel cell vehicles. *Energy Conversion and Management* 47, 2748 2760.

[5] Wilhelm EJ, Schenler WW ,2009, Heuristics for the Design of Advanced Powertrains: Strategies for Vehicle Manufacturers. In *Proceedings of the IAMF 2009* , Geneva, Switzerland.

[6] Wilhelm EJ, Schenler WW, 2009, Heuristic Design of Advanced Drives: Analysis of Trade-offs in Powertrain Electrification. *World Electric Vehicle Journal* 3,

[7] Guzzella L, Sciarretta A, 2007, *Vehicle Propulsion Systems: Introduction to Modeling and Optimization*, Springer Verlag, Berlin, Germany.

[8] Sundström O, Guzzella L, Soltic P , 2008, Optimal Hybridization in Two Parallel Hybrid Electric Vehicles using Dynamic Programming. In *Proceedings of the 17th World Congress* , Seoul, Korea, pp. 4642-4647.

[9] Sundström O, Ambühl D, Guzzella L, 2008, On Implementation of Dynamic Programming for Optimal Control Problems with Final State Constraints. In *Les Advances in Hybrid Powertrains*, IFP, Rueil-Malmaison, France.

[10] Kromer, MA, Heywood, JB, 2008, A Comparative Assessment of Electric Propulsion Systems in the 2030 US Light-Duty Vehicle Fleet. In *SAE Technical Paper Series*, Detroit, Michigan.

[11] Delucchi, MA, Lipman, TE, 2001, An analysis of the retail and lifecycle cost of battery-powered electric vehicles. *Transportation Research Part D,* 6, 371-404.

[12] Eaves, S, Eaves, J, 2004, A cost comparison of fuel-cell and battery electric vehicles *Journal of Power Sources* 130, 208-212.

[13] ecoinvent.ch, Ecoinvent Database, Last updated September 2009, Accessed on September 2009.

[14] Argonne GREET Model 1.8c.0 & 2.7, Last updated 2009, Accessed on 2009.

[15] Makowski M, Granat J, Ogryczak W ,2009, *Multiple Criteria Analysis of Discrete Alternatives with a Simple Preference Specification: Pairwise-outperformance based Approaches*, International Institute for Applied Systems Analysis.

[16] Mathworks Vectorization Documentation, http://www.mathworks.com/support/tech-notes/1100/1109.html, Last updated February 1, 2010, Accessed on February 1, 2010.

[17] Wilhelm EJ, Schenler WW ,2008, The Co-Evolution of Plug-in and Fuel Cell Hybrid Vehicles. In *Proc. EET 2008 European EleDrive Conference* , Geneva, Switzerland.

Acknowledgments: This work was supported by the Swiss Competence Center for Energy and Mobility (CCEM-CH), in collaboration with MIT and the industrial partners Ford and ENI.

Appendix

A. Selected Input Assumptions

Selected Powertrain Cost	Present	Future	
ICE engine ($/L)	$ 755.00	$ 755.00	
LiON battery ($/kWh)	$ 2'000.00	$ 1'050.00	Battery costs are scaled by W/Wh. These values are for high-power packs
NiMH battery ($/kWh)	$ 1'384.00	$ 400.00	
Fuel cell cost ($/kW)	$ 108.00	$ 52.00	Based on assumptions from Kromer [10]
Hydrogen Emissions	**Present**	**Future**	
VOC (g/kg)	1.40	0.18	
CO (g/kg)	3.33	0.51	
NOx (g/kg)	8.16	2.11	H2 produced from natural gas at Present, photovoltaic electrolysis in the Future
PM10 (g/kg)	4.32	2.70	
PM2.5 (g/kg)	2.20	0.71	
CH4 (g/kg)	40.95	2.70	
N2O (g/kg)	0.06	0.03	
CO2 (g/kg)	12456.55	1999.86	Grid emissions are from the Swiss mix (104 gCO2/kWh)
Fuel Cost Assumptions	**Present**	**Future**	
Gasoline (E-10) ($/L)	$ 0.77	$ 0.77	Fuel costs, where taken as approximate untaxed Swiss costs, and what is
Diesel ($/L)	$ 0.88	$ 0.88	important is the relative cost rather than the absolute cost for this analysis
Hydrogen ($/kg)	$ 6.49	$ 6.49	
Electricity ($/kWh)	$ 0.055	$ 0.055	

B. Characteristics of the Present and Future Vehicle Designs Simulated

CURRENT Midsize Passenger vehicles

Characteristics	Hybrid: All Vehicles	None Otto	None Diesel	Mild Otto	Mild Diesel	Series Otto	Series Diesel	Series Fuel Cell	Parallel Otto	Parallel Diesel	EV EV
Weight (kg)	1366	1208	1227	1213	1232	1456	1309	1543	1456	1357	1327
Total power (kW)	94	151	141	154	144	96	92	91	145	142	66
Cost											
Purchase (2006 USD)	60764	29086	31255	31661	33830	73954	73028	75461	50433	52359	62651
Operating/Maintenance (2006 USD)	12421	35730	22895	35419	22733	16398	10554	14927	31378	20743	2268
Total cost of ownership (2006 USD)	172090	328704	219972	328141	220727	223205	171150	212835	316367	225171	90410
Performance											
0-100 Acceleration time (s)	12.4	6.4	7.1	6.3	6.9	12.3	12.6	12.8	7.6	7.9	15.2
Top Speed (kph)	207	244	238	246	240	212	209	208	241	239	187
Utility											
Range (km)	392	330	613	334	621	734	1299	534	400	707	155
Passenger volume (m^3)	2.8	2.8	2.8	2.8	2.8	2.8	2.8	2.8	2.8	2.8	2.8
Towing capacity (kg)	1174	2855	2559	2930	2633	1031	945	918	2562	2456	472
Environment											
Gasoline Equivalent cons. (L/100km)	5.0	12.2	11.8	12.0	11.7	5.7	5.6	3.8	10.7	10.6	1.6
Life cycle CO2 (g/km)	170	401	352	396	347	218	190	163	366	329	51
Life cycle NOx (g/km)	0.20	0.37	0.29	0.36	0.28	0.21	0.16	0.17	0.34	0.27	0.14
Life cycle PM10 (g/km)	0.09	0.14	0.08	0.14	0.08	0.12	0.08	0.10	0.14	0.09	0.07

FUTURE Midsize Passenger vehicles

Characteristics	Hybrid: All Vehicles	None Otto	None Diesel	Mild Otto	Mild Diesel	Series Otto	Series Diesel	Series Fuel Cell	Parallel Otto	Parallel Diesel	EV EV
Weight (kg)	1378	1208	1227	1213	1232	1456	1366	1601	1456	1357	1327
Total power (kW)	95	151	141	154	144	96	96	96	145	142	66
Cost											
Purchase (2006 USD)	40724	29086	31255	30288	32456	45457	47837	47626	36015	38385	40335
Operating/Maintenance (2006 USD)	12520	35730	22895	35419	22733	16398	11027	15546	31378	20743	2268
Total cost of ownership (2006 USD)	150824	328704	219972	326621	219207	191652	146971	186819	300403	209699	65701
Performance											
0-100 Acceleration time (s)	12.4	6.4	7.1	6.3	6.9	12.3	12.6	12.6	7.6	7.9	15.2
Top Speed (kph)	208	244	238	246	240	212	212	212	241	239	187
Utility											
Range (km)	416	330	613	334	621	734	1248	516	400	707	155
Passenger volume (m^3)	2.79	2.79	2.79	2.79	2.79	2.79	2.79	2.79	2.79	2.79	2.79
Towing capacity (kg)	1169	2855	2559	2930	2633	1031	999	996	2562	2456	472
Environment											
Gasoline Equivalent cons. (L/100km)	5.0	12.2	11.8	12.0	11.7	5.7	5.8	4.0	10.7	10.6	1.6
Life cycle CO2 (g/km)	127	231	352	227	347	138	203	61	216	329	51
Life cycle NOx (g/km)	0.17	0.27	0.29	0.26	0.28	0.16	0.18	0.11	0.25	0.27	0.14
Life cycle PM10 (g/km)	0.09	0.11	0.08	0.11	0.08	0.10	0.09	0.09	0.12	0.09	0.07

C. Survey Questionnaire and Aggregated Responses

1 **How old are you?**	16-21	21-28	28-35	35-50	50+	
	0	32	29	20	7	
2 **What is your gender?**	male	female				
	60	28				
3 **Do you own a car?**	yes	no				
	62	21				
4 **Daily travel by car (as driver or passenger, please answer in km):**	Various (not listed)	Average =	26.25			
5 **How much do you agree with each of the following statements?**	not at all	a little	yes and no	pretty close	completely right	
a I like to be the first to pull away from a stop light	36	18	14	12	3	
b I am very concerned about the future	0	9	23	30	21	
c I take my career very seriously	4	8	18	29	24	
e I commute using a car daily	30	7	8	10	28	
f I care very much about costs	1	8	28	28	18	
g I have a high level of education	0	3	8	21	51	
h I have a strong feeling of social responsibility	1	2	22	37	21	
i I am very aware of environmental issues	0	1	18	35	29	
j I welcome change	0	2	32	32	17	
k I always make rational choices	0	12	32	30	9	
l I often do detailed financial analysis and planning	8	20	24	23	8	
6 **How important are these COST criteria to you?**	not at all	very little	moderately	quite a bit	extremely	
a Purchase cost	1	3	19	37	21	
b Operating cost (fuel, oil etc)	1	1	26	35	18	
c Maintenance cost (service and repairs)	1	3	25	35	17	
7 **How important are these PERFORMANCE criteria to you?**	not at all	very little	moderately	quite a bit	extremely	
a Off-the-line acceleration (0-100 kph)	14	20	32	13	2	
b Passing acceleration (80-110 kph)	4	18	31	25	3	
c Top speed	19	36	20	6	0	
d Braking	2	4	14	38	23	
e Handling	3	3	10	40	25	
f Reliability	0	2	3	21	41	
g Refuelling time	11	14	18	14	10	
8 **How important are these ENVIRONMENTAL criteria to you?**	not at all	very little	moderately	quite a bit	extremely	
a Global-warming causing emissions (CO_2, methane, etc)	1	3	17	41	18	
b Health related emissions (NOx, Ozone, etc)	0	3	14	39	24	
c Noise	0	9	33	25	13	
9 **How important are these UTILITY criteria to you?**	not at all	very little	moderately	quite a bit	extremely	
a Range (autonomy)	3	10	17	38	12	
b Passenger capacity	2	7	22	45	4	
c Cargo capacity	3	9	30	33	5	
d Towing capacity	38	21	13	6	2	
e Multimedia features (on-board video, stereo, etc)	12	25	18	8	3	
f Sufficient drink holders	20	13	20	7	6	
10 **How important are these SAFETY criteria to you?**	not at all	very little	moderately	quite a bit	extremely	
a Fatality risk to drivers/passengers	0	3	9	19	49	
b Fatality risk to pedestrians	1	9	19	21	30	
c Presence of active safety technology (anti-lock brakes, traction control etc)	0	0	20	26	34	
d Presence of passive safety technology (seat belts, air bags, crumple zones)	0	0	8	21	51	

Feasibility Study of a Gas Turbine-Based, Series-Hybrid Minibus

Paolo Capobianchi, Simone Pacelli, Michele Santoro

Department of Mechanical &Aeronautical Engineering, University of Roma La Sapienza - Italy

Abstract: This work describes the preliminary sizing of a series hybrid vehicle with a small Turbogas (GT) as the thermal engine, equipped with a regenerative braking. The reference vehicle is a minibus to be used for urban transportation. The analysis is based on a physical model of the instantaneous power required by the mission, which leads to a non-linear system of equations that are numerically integrated in time. Several sets of standard, real cycles are defined as missions the vehicle under study must fulfil: these cycles are characterized by repeated stop-and-go patterns that make a high level of energy recovery possible. The minibus behaviour is simulated under each one of the examined conditions, in this way one derives an installed power of 170 kW with a proper GT power of 21,5 kW and the corresponding degree of hybridization of about 90%. On this basis, the GT is designed anew, using standard performance charts and state-of-the art technology. The battery pack and the electric engine are both designed using commercially available software. The CO_2 emission analysis is also performed. The technical feasibility of the vehicle is briefly discussed in the conclusions.

Keywords: Series Hybrid Vehicle, Urban driving cycles, Lithium cells, Micro Gas Turbine

1. Introduction

This paper presents an assessment of the technical feasibility of a series hybrid electric vehicle in which the thermal engine is a small GT unit. This study follows along the lines of a previous research on "turbo-hybrid" vehicles [3-8] conducted at the University of Roma 1

The work discussed here is characterized by three innovative aspects:

- The vehicle under analysis is a minibus for public transportation with a weight and a aerodynamic drag coefficient (C_x) values quite different from those of a common city car;
- Real urban driving cycles are assumed from the ADVISOR library [9] as vehicle mission instead of standard European emission cycles. The seven cycles selected for the present analysis are very different from each other as for instantaneous power requirements;
- The storage energy system consists of a Lithium-Polymer (LiPo) battery pack.

1.1. The Hybrid Electric Vehicle (HEV)

HEV combine the benefits of high fuel economy and low emissions with the power and range of conventional Internal Combustion Engine (ICE). These performances are obtained by using a process called Kinetic Energy Recovery System (KERS), in which the excess kinetic energy usually dissipated when braking is instead recovered by charging a suitable storage system. There are two types of hybrid vehicle, called respectively "parallel" and "series". In the parallel configuration, the ICE and the electric motor operate in such a way that the vehicle is constantly powered by a proper combination of "thermal" and electric power. In the series hybrid concept, the electrical and thermal systems are mechanically separated but electrically coupled. When the purely electric traction mode is enforced, energy is extracted from the batteries that are then recharged when travelling in "thermal mode" and by recovering braking energy. This type of configuration is a very convenient vehicle range extender for electric vehicles. Parallel hybrids have greater fuel efficiency than series ones at constant high speed (highway driving) while series hybrids are better in stop-and-go urban driving.

A fundamental parameter for HEV is the degree of hybridization (H_r). This factor is defined as the ratio between the battery electric power (P_{el}) and the total installed power (P_{tot}):

$$H_r = \frac{P_{el}}{P_{tot}} = \frac{P_{el}}{P_{el} + P_{GT}} = 1 - \frac{P_{GT}}{P_{tot}}, \qquad (1)$$

where H_r=0 denotes a traditional vehicle equipped only with thermal engine and H_r=1 denotes a pure electric vehicle.

Corresponding Author: Michele Santoro, Email: minibusturboibrido@gmail.com

The present work is a preliminary assessment of a hybrid system for a minibus to be used in historical city centres for public transportation. For completeness, several driving cycles ("missions") characterized by stop-and-go patterns compatible with a real utilization of the minibus were considered. Methane (CH_4) was adopted as the GT fuel, both to reduce the CO_2 emissions, as demonstrated by the results shown below, and to simplify the GT ignition system. Compared with conventional ICE-hybrid vehicles, the Gas Turbine Hybrid Vehicle (GTHV) has a small number of moving parts, a more compact size, a higher energy density, lower energy costs, lower emissions and fuel flexibility [5-7].

2. Vehicle and mission analysis

The minibus considered in this study carries between 19 and 40 passengers and has a total mass ranging from 5 to 10 tons. Assuming an average passenger weight of 75 kg and a minimal ground clearance of 350 mm the vehicle data are defined in Table 1.

Table 1. Vehicle data.

DIMENSIONS	length [mm]	7164
	width [mm]	2162
	height [mm]	2879
S	[m^2]	5.49
CARGO ABILITY	[n° persons]	27
TOTAL MASS	empty [kg]	6258
	fully loaded [kg]	8247

To correctly size the power plant, all of the operational aspects of the vehicle must be considered, including the comfort requirements for public transportation buses. The total power absorbed by auxiliaries has been obtained by composite weighted total of the individual contributions multiplied by their respective Coefficient of Use. The resulting load is considered as an equivalent, constant power absorption: in this study the value of 6 kW has been estimated.

To select the GT nameplate power a complete mission analysis is necessary. In this work seven real urban cycles have been considered. The respective velocity patterns of two different cycles are shown in Figure 1.

For each of these missions four different cases were simulated by varying two main system parameters:

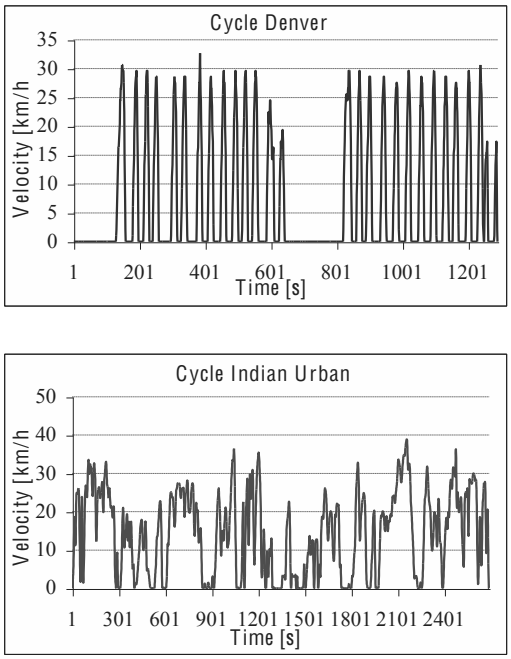

Fig. 1. Driving cycles examples.

the vehicle mass and the rate of braking recovery that is the fraction of the instantaneous kinetic energy the KERS must recover. The mass varies between 6 and 8 tons (empty and full load), the coefficient of braking recovery (ε_{KERS}) was varied in the range 0.6-0.8.

2.1. Mission power analysis

The analysis of the power flows of each mission has been carried out starting from the equation of dynamic equilibrium in the direction of motion:

$$M_{eq}\frac{dv}{dt} = T - R_a - R, \tag{2}$$

where the first term represents the inertia force (F_{in}), M_{eq} is an equivalent vehicle mass taking into account the rotating parts inertia [1], T is the traction force, the aerodynamic resistance (R_a) is given by:

$$R_a = \frac{1}{2}\left(\rho \cdot S \cdot C_x \cdot v^2\right), \tag{3}$$

the Rolling Resistance (R) by:

$$R = f \cdot m_s \cdot g. \tag{4}$$

On this basis, the different flows through the system were computed, as the Useful Power (P_u):

$$P_u = T\frac{v}{\eta_{tr}} = \left[R_a + R + M_{eq}\frac{dv}{dt}\right]\frac{v}{\eta_{tr}}, \quad (5)$$

and the Braking Power (P_b):

$$P_b = \left[\left(F_{in} - R_a - R\right)\cdot\eta_{tr}\right]\cdot v, \quad (6)$$

Table 2 reports a summary of the parameters used in the calculation of equations 2-6:

Table 2. Design data

Δt [s]	1	S [m^2]	5,49
m_s [kg]	6000-8000	ρ [kg/m^3]	1,225
f	0,018	η_{tr}	0,98
Cx	0,5	Meq [kg]	1,03 m_s
g [m/s^2]	9,8	ε_{KERS}	0,6-0,8

Figure 2 displays the instantaneous power flows for one of the considered cycles.

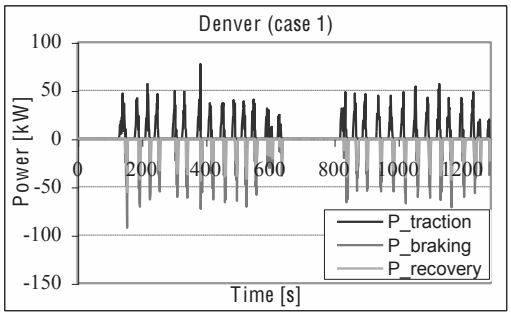

Fig. 2. Example of Mission power analysis

2.2. Mission energy balance

All analyses carried out in this study assume an on/off control logic of the GT set. The settings are such that whenever the vehicle power is positive (that is in phase of traction) and exceeds 70% of the nominal installed GT power, the GT is ignited and supplies the additional power requested by the instantaneous power balance. The following procedure of calculation was adopted: first, for each configuration, the values of the design parameters listed in Table 2 are used to calculate the instantaneous values of the power required at the wheels: at this step, no account is made of the presence of the GT. By considering a discrete set of GT with installed power ranging between 1 and 100 kW, the following step consists of the compilation of a mission budget, obtained by adding the instantaneous values of all power flows (here, the GT is accounted for). These calculations are repeated for every P_{GT} within the range defined at the onset. Consider that given the timestep adopted equal to 1s, these "powers" are in fact instantaneous energies. The curves obtained with this procedure may display a negative, zero or positive "integral" budget, indicating respectively a defect, a balance or an excess of the total energy used for the mission. A "defect" balance indicates an undersized GT, an "excess" one an oversized GT. Obviously, the P_{GT} that result in curves with a zero balance are those that are most convenient for use in that type of mission.

Figure 3 reports such diagrams for one of the cases studied here, denoted as "Case 4".

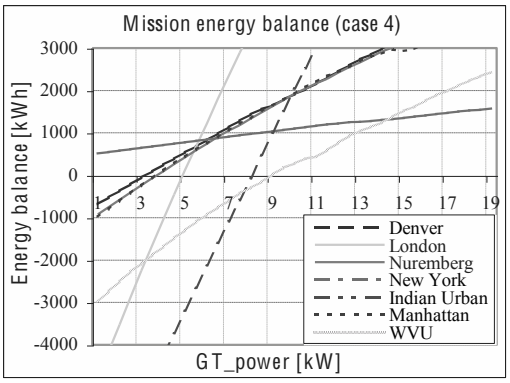

Fig. 3. Mission energy balance: Case 4

Different mission types lead to different "optimal" P_{GT} (and therefore to optimal H_r values), a 3-kW GT would be convenient for the Denver and Nuremberg cycles, a 5-kW GT for the London cycle, a 9-kW GT for both the Indian Urban & WVU cycles (that so represent the heaviest). For real operations, it is more convenient to install an oversized GT and operate it at part load for some of the time, or to adopt a more efficient but costlier system with two smaller GT's [7].

From a critical analysis of the results (for a complete report, see [3]) it was concluded that:

- The global energy balance displays little sensitivity to the variation of the total mass of the vehicle.
- The balance is, on the contrary, very sensitive to a variation of the braking recovery coefficient, which therefore is a fundamental design parameter.

The Case 4 examined here refers to the mass upper limit reported in Table 1 and the braking recovery

factor ε_{KERS} is equal to 0.8 (a very high value). By considering the heaviest cycle power request, of 9 kW, and taking into account also the auxiliaries absorption, the optimal GT power results:

$$P_{GT}=15kW$$

The total power to install on the vehicle, in order to satisfy the maximum peak on all the examined missions, is equal to 169 kW. The degree of hybridization is then:

$$H_r = 1 - \frac{P_{GT}}{P_{tot}} \approx 0{,}9$$

3. Functional scheme of the vehicle

3.1. The Vehicle management unit

In a GTHV the traction is purely electric. The presence of the KERS requires both a rather complex electric connectivity and the presence of a suitable, electronically managed, control protocol. Fig. 4 shows the scheme of the propulsive system considered in this work: it consists of the energy production unit (GT), the energy storage system (battery pack), the electric machines (two motors, one per axle, only one displayed in Fig. 4), the current and frequency converters, and the related electronic control circuits with the Power Distribution Unit (PDU) and the Vehicle Control Unit (VCU). The last two components form the Vehicle Management Unit (VMU). In this scheme the thermal unit generates mechanical power which is converted into electrical power by a high speed generator (that acts as a starter for the GT as well). The electricity produced by this generator can charge the batteries or directly power the motors when the traction power has a peak. These motors are reversible machines so that when the vehicle is braking they work as generators producing electric power that is channeled to the battery pack. At each instant of time the power flows are regulated by the VMU.

Because of the complexity of the real system, the detailed design of the individual units has not been included in this work, and the system is designed on the basis of the accepted performance characteristics of commercially available components. At this study level, a simple on-off control logic for the GT operation has been adopted. Actually, for a scheme like the one under discussion, the electronic VMU carries out many tasks [4-6]: it controls the thermal engine operation under a suitable logic, determines

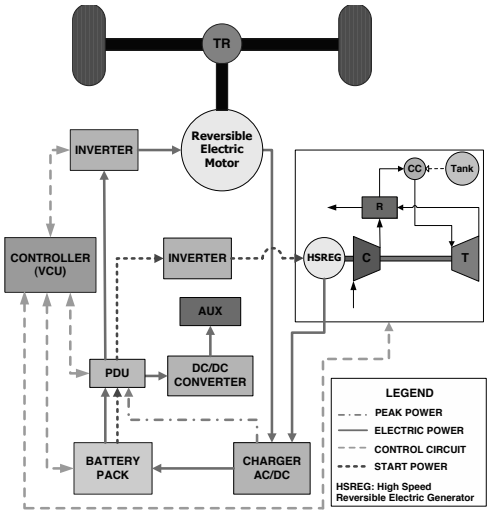

Fig. 4. Vehicle functional scheme

at each time how much of the energy produced by the GT reaches the battery package or the electric engine directly, monitors the electrical parameters of the battery package and also records historical data; in other words it performs its energy-management task on the basis of a quite large number of instantaneous mission parameters [4].

3.2. Li-Po cells technology

A GTHV is an electric vehicle with a "thermal range extender" and provided with a regenerative braking system to improve its energy performance. Thus the storage system is a fundamental component: at each instant of time, it must either provide the electric power required for traction by the wheels or receive the excess energy recovered by the KERS. Storage systems can be electro-chemical (batteries), mechanical (flywheels) and electrical (supercapacitors). In the configurations analyzed in previous works [3-6], it was clearly established that one of the weak links in the system -from the point of view of performance, weight-to-power ratio- is the lead-acid battery. In this study the LiPo cells technology has been adopted instead. The performance of a battery is identified by several factors, Table 3 reports a comparison of three battery types of current technology. LiPo cells show the highest specific power and energy but they also represent the most expensive solution, because this technology has not reached maturity yet.

Table 3. Batteries performances comparison

	Pb-acid	Ni-MH	Li-Po
Specific power [W/kg]	150	220	315
Specific energy [Wh/kg]	35	80	155
Energy density [Wh/l]	71	200	220
Life cycle	500-1000	1000	1000
Cost [€/kWh]	0,3	1,2	3

This technology differs from the Li-ion batteries because here there aren't liquid solutions (replaced with a solid polymer) so they don't need any metallic wrapper, and thus they are lighter and smaller than their competition. Important characteristics are also: the nominal voltage of the single cell equal to 3,7 V (versus 2,1 V of the Pb-acid); the safe operative range ranging from 2,7 V (cut-off voltage under which the cell is totally discharged) and 4,25 V (overvoltage limit above which the cell can be damaged) and the acceptable State of Charge (SOC) contained between 30% and 80%. Also important are the maximal charging/discharging current and power values set by the cell manufacturers. The battery pack is assembled with a number of cells connected in a proper series-parallel configuration (denoted by the number of cells connected in series followed by s and that of cells in parallel followed by p).

3.3. Battery pack sizing

The following data are assumed for the battery pack: nominal voltage $E_{nom}= 400\,V$ and nominal capacity $C = 100\,Ah$. By analyzing several commercially available LiPo cells, these data led to the configuration described in the Table 4:

Table 4. Preliminary battery pack sizing.

Commercial model	Kokam SLPB 68216216
Type of connections	108s3p
Nominal voltage, E [V]	399,6
Nominal capacity, C [Ah]	90
Weight [kg]	227
Volume [dm^3]	104
Price [$]	50350

After this preliminary sizing the described configuration was analyzed in order to verify whether -and how- it satisfies the mission requirements.

The sizing of the battery pack is performed on the basis of the maximum power demand and maximum absorbable battery power: this means that the following parameters must be minimized at each instant of time:

- instantaneous power deficit
$$P_{deficit} = P_{required} - P_{\max\_discharge}, \quad (7)$$
- instantaneous power dissipated in braking:
$$P_{diss} = P_{brake} - P_{\max\_charge}. \quad (8)$$

The design process begins with the calculation of the electric power and current flows through the batteries at each instant of time. In this phase the battery is modeled as a Multiple Input Multiple Output (MIMO) system with two inputs:

1. Power generated by the GT unit;
2. Power available during the braking;

and two outputs:

3. Power required by transmission;
4. Power required by auxiliary units.

The battery pack is modeled as a part of an electric circuit. It is assumed a Constant Voltage charge process in which the voltage, applied by the chargers, has a fixed value near overvoltage to enforce the current to enter into the battery. During the discharge time a different model is assumed: the battery is considered as a generator, so it carries out the required power applying to the circuit the voltage E(t), corresponding to the contemporary SOC. In order to calculate the instantaneous SOC an algorithm is developed basing on a "Coulomb counting" method. The adopted procedure of calculation is described below. First, the quantity of electric charge $Q(t)$ flowing trough the battery pack at each instant is evaluated by the time integration of the Instantaneous Current $I(t)$:

$$Q(t) = \int_0^T I(t)\,dt. \quad (9)$$

Assuming $T=\Delta t=1$s, the previous equation can be written in a numerical form:

$$Q_t = Q_{t-1} + \Delta Q_t = Q_{t-1} + I_t \cdot \Delta t, \quad (10)$$

where:

$\Delta Q_t = I_t \cdot \Delta t$: electric charge flowing trough the battery in a single t instant.

The expression for the SOC variation at the same second results:

$$SoC_t(\%) \quad \frac{Q_t}{3,6\ C}, \tag{11}$$

while the instantaneous SOC is:

$$SoC_t(\%) \quad SoC_{t\ 1} \quad SoC_t \tag{12}$$

Figure 5 shows the charge/discharge curves related to the 108s3p pack based on Kokam SLPB216216 as regard to the SOC range 30%-80%.

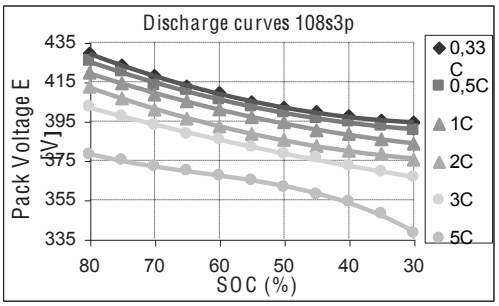

Fig. 5. Discharge curves.

Each curve is obtained discharging the battery with a constant current value but basing on the calculated electric power flows one has that the current is not constant in time, so at each instant, a different curve must be considered. By the knowledge of the instantaneous current the relation SOC-E is determined. For every SOC value, the battery voltage is given by the equation of the considered curve. One has at each instant :

$$E_t \quad E_{t\ 1} \quad E_t|_{curve}, \tag{13}$$

where the last term represents the voltage variation calculated by the curve equation. By the iteration of the described algorithm a numerical simulation of the batteries behavior during a complete mission is carried out.

1. Analyzing the results one has that: $P_{deficit}$ is equal to zero for all instants of each mission. Braking power, and so braking energy, is absorbed almost in a total way: only in a few seconds of three missions P_{diss} is different from zero. These results are shown in Fig. 6.
2. The SOC is always contained between 60% and 80%. Basing on the assumed equivalent constant auxiliaries absorption, the SOC is always decreasing as presented in Fig.7.

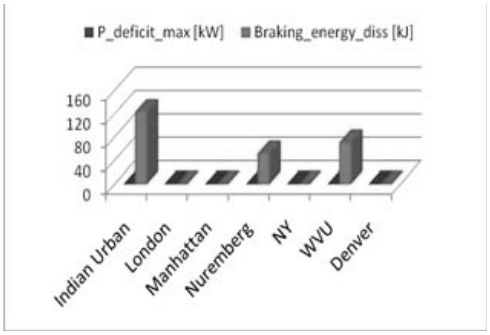

Fig. 6. Power deficit and Energy dissipation

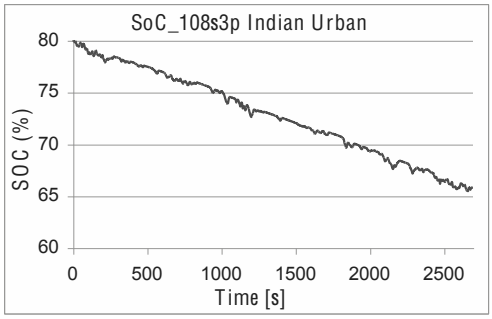

Fig. 7. SOC trend example

In all calculations the additional constraint is imposed of the initial battery SOC being recovered at the end of each mission. Because of this, at the end of every driving cycle, a period of recharge made by the GT operation is necessary.

The configuration 108s2p was also analyzed but it results unsuitable for this application because it H G C R = C CHG H C IHP demand.

4. The Micro Gas turbine unit (MGT)

The optimal H_r was previously determined by considering a net power of 15 kW reaching the batteries. Actually this power value is smaller than the one provided by the GT because of the losses in several devices such as the power splitter, the high speed generator and the chargers. Referring to the assumed components efficiencies the GT power is imposed to be:

$$P_{GT}=21.5kW.$$

In the last years several tests have indicated that although a commercially available GT set may be used with satisfactory results, it is advisable to design a dedicated GT for use in this particular

application [4]. Basing on the existing MGT with a similar power output, it was selected to design a MGT with a *compact cross-flow heat regenerator*. The degree of regeneration (R) was hypothesized as highest as possible for the type of adopted solution. In this way good efficiency, low emissions and high compactness are ensured.

4.1.Thermodynamic cycle parameters

In order to define the real thermodynamic cycle it was necessary to establish several parameters.
The inlet compressor temperature (T_1) was selected as the standard ambient value while the inlet turbine temperature (T_3) was selected basing on the previous study [7].
The pressure ratio (β) was selected reaching a suitable compromise between two set against necessities: on one hand the work and cycle efficiency maximization and, on the other side the number of compressor and gas turbine stages reduction. By choosing β=4,5 one has as a proper solution a two stages configuration both for compressor and turbine. The respective isentropic efficiencies (η_{SC} , η_{ST}) were selected on the basis of similar commercial microturbines. All the parameters are resumed in the Table 5:

Table 5. Design thermodynamic parameters

$T_1 = 298\ K$	$\eta_{S,C} = 0,7$
$T_3 = 1300\ K$	$\eta_{S,T} = 0,8$
$\beta = 4,5$	$R = 0,8$

4.2. Thermodynamic process simulation

The thermodynamic process simulation was conducted through the software CAMEL-PRO™ [2] developed by the Department of Mechanics and Aeronautics in the University of Roma 1

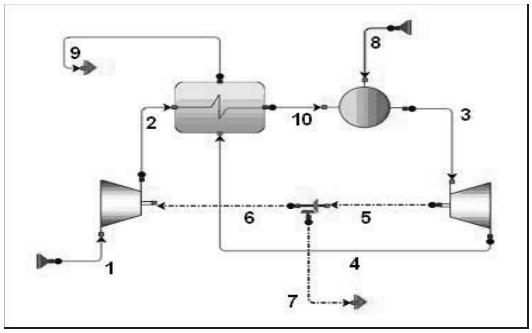

Fig. 8. Gas Turbine layout

The power plant gas turbine layout, which the simulation refers to, is shown in Fig. 8.

Referring to the "identification numbers" (*id*) displayed on the figure 8, the simulation process results are resumed in the Tables 6-7:

Table 6. Thermodynamic cycle simulation results.

id	m [kg/s]	p [kPa]	T [K]	h [kJ/kg]
1	0,172	101,3	298,0	0
2	0,172	455,9	524,5	233,6
3	0,173	428,9	1300	1145,1
4	0,173	104,6	999,0	777,8
9	0,173	101,5	625,7	348,6
10	0,172	442,2	918,8	667,2

Table 7. Outlet turbine gas composition.

id	xO_2 [kg/kg]	xN_2 [kg/kg]	xCO_2 [kg/kg]	xH_2O [kg/kg]
4	0,187	0,750	0,0290	0,0348

4.3. MGT design

A feasible design has been produced using the optimal n_s criterion so that the gas turbine unit is designed anew, using standard performance charts and state-of-the art technology. The resulting GT unit consists of a two stages radial compressor and two stages axial turbine. Table 8 reports the main results:

Table 8. Design specifications for the GT engine.

Rotational speed, n	110000 rpm
Nameplate power, P	21,5 kW
Max. allowable peripheral velocity, U_{max}	400 m/s
Fuel Lower Heating Value, LHV	48000 kJ/kg
Max allowable shaft torsion stress, τ	50 MPa
Compressor polytropic efficiency, η_{PC}	0,78
Turbine polytropic efficiency, η_{PT}	0,80
Real cycle efficiency η_r	0,23

5. Emission analysis

The present study led to some interesting results about greenhouse gas emissions. A series of numerical simulations made it possible to estimate the CO_2 emissions for each mission. Emissions are evaluated in two different cases: in the first, only the driving cycle is performed, while in the second also a final recharge is performed by GT to bring the SOC back to its original value. Table 9 shows the values of the emissions per passenger per km.

Table 9. Average CO_2 emission levels [kg/km psg]

Traditional minibus	0,055
Hybrid minibus (without recharge)	0,015
Hybrid minibus (with final recharge)	0,044

By comparing the calculated results (average value for the seven missions) with available data for traditional vehicles, a decrease of greenhouse gas emissions of about 15-20% is attained, even including the final recharge. In real operation the emission values depend on the type of mission and ought to be evaluated on a case-by-case basis.

6. Conclusions

The present study consists of a preliminary evaluation of the technical feasibility of a GTHV equipped with a Li-Po battery pack. A tentative design of each component was performed on the basis of current technological standards. The configuration discussed here (referred to as "Case 4") is in no way the "optimal" one, because:

A) The system performance strongly depends on the type of driving mission the vehicle is called to perform. In this study, seven different missions are analyzed to obtain general results.

B) The size of the battery pack and the CO_2 emission level are based on a simple on/off control logic for the GT operation, whereas previous work confirms [4,6] that the best performance is reached by using a "load following" model.

It is interesting to investigate the possibility of performing extended highway driving cycles. In these cases (results not reported here) the SOC trend for the batteries is similar to the one obtained in urban missions, but this requires a cumulatively longer "on" time of the GT and inevitably leads to a substantial increase in the fuel consumption.

Nomenclature

f coefficient of rolling friction road tire

g acceleration of gravity, m/s^2

h specific enthalpy, kJ/kg

m mass flow rate, kg/s

m_s vehicle static mass, kg

n_s specific number

p pressure, Pa

S Vehicle frontal surface, m^2

P power, kW

v vehicle velocity, m/s

Greek symbols

η efficiency

ρ air density, kg/m^3

Subscripts and superscripts

tr transmission

References

[1] Benzing E., 2004, *Dall'aerodinamica alla potenza in Formula 1,* Nada ed.,Milano.

[2] CAMEL-PRO™, 2008, *User's guide*, http://www.turbomachinery.it.

[3] Capata R., Coccia A., 2010: *Procedure for the design of a Hybrid-Series vehicle and the Hybridization Degree choice.* Int. J. of Energies, Apr. 2010.

[4] Capata R., Lora M., 2007: *The LETHE™ Gas Turbine Hybrid Prototype Vehicle of the University of Roma 1:Drive Cycle Analysis of Model Vehicle Management Unit*, J. of Energy Resources Technology, V. 129, pp 107-116.

[5] Capata R., Lora M., Sciubba E., 2008: *Comparative assessment and selection of an "optimal" configuration for a Gas Turbine-Based Hybrid city car*. J. of Eng. for GT & Power, 2008, vol 129, n.2, pagg 107-117.

[6] Capata R., Sciubba E., 2005: *An innovative solution for suburban railroad transportation: the gas turbine hybrid train*, Int. J. of Thermodynamics, V. 8 n. 1, pp. 55-66

[7] Capata R., Sciubba E., 2006: *The concept of the turbine-based hybrid vehicle: System, design and configuration issues*, Int. J. of Energy Res., 30, pp 671-684.

[8] Cioffarelli E., Sciubba E., 2000: *A new type of gas turbine based-hybrid propulsion system-Part I: concept development, definition of mission parameters and preliminary sizing,* Proc. AES/ASME Winter Meeting, Orlando.

[9] Wipke K. B., Cuddy M. R., Burch S. D., 1999, *ADVISOR 2.1: A User-Friendly Advanced Powertrain Simulation Using a Combined Backward/Forward Approach,* Special Issues on Hybrid and Electric Vehicles National Renewable Energy Laboratory NREL /JA-540-26839

Energy Performance of Dump Trucks in Opencast Mine

Lalit Kumar Sahoo, Santanu Bandyopadhyay and Rangan Banerjee

Department of Energy science and Engineering, Indian Institute of Technology Bombay,India

Abstract: Dump trucks are used worldwide for handling ore and waste in most of the opencast mines. The energy consumption in dump trucks accounts for about 32 % of the total energy requirement in opencast mines. In this paper a modeling framework is developed to analyse a generic mine transportation problem with multiple dump trucks operating between multiple crushers and excavators. The minimum specific fuel consumption (SFC) of dump trucks for a specified pay load and material handling rate is optimized. The model investigates the variations of SFC with operating parameters like pay load, speed, wind speed etc. A case study of down gradient opencast limestone mine of capacity 2600 t/h shows a fuel savings of 15%. An achievable minimum SFC of 86 g/ton of ore handled is estimated using proposed model.

Keywords: Dump truck, opencast mine, energy performance, specific fuel consumption, optimization

.

1. Introduction

Mining processes are basically exploration, excavation, transportation and finishing of ore. Coal, metal and other minerals are excavated from the earth by opencast mining or underground mining. Mining industry consumes both electrical energy and diesel for processes like excavation, transportation and pumping. Dump trucks are used in excavator-truck based opencast mines for transferring ore or waste from the production site to either crushers or waste dump stations. The transportation network of the mine includes a fleet of dump trucks moving between crushers and excavators. The fleet size of dump trucks depends on the payload, material handling capacity of both excavators and crushers. Excavators are used to load the ore into the dump trucks and are movable depending upon the availability of ore. Crushers are stationary mechanical equipment used for sizing and finishing of ore.

Most opencast mines follow the same basic steps to produce the finished minerals. The schematic of opencast mining process is presented in Figure 1:

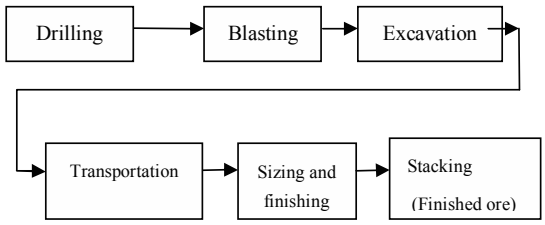

Fig. 1. Schematic of opencast mining process

Energy consumption in dump trucks accounts for 32% of total energy consumption in a typical Indian opencast coal mine [1]. The factors affecting specific fuel consumption of dump trucks are distance between crusher and excavator, payload, speed of vehicle and mine topography. The objective of this paper is to develop a mathematical model for calculating minimum energy consumption in dump trucks.

Statistical benchmarking has been used for industrial sectors to calculate minimum energy consumption. The evolution of energy star as an energy performance indicator (EPI) for benchmarking the industrial plant energy usage is discussed [2]. An energy benchmarking model [3] is developed for calculating minimum energy consumption for glass industries.

Corresponding Author: Lalit Kumar Sahoo, Email: lalitsahoo@yahoo.co.in

Studies for optimization of transportation have been based on linear programming approach. The optimization of loading and transport system in open cast mine has been done based on mathematical model [4] to optimize number of trucks required serving at loading point, number of trips per hour and theoretical output of dump trucks. Optimization of journey schedule of high capacity dump truck has been done to reduce the travel time of dump truck based on random variables with given expectation [5]. Constant speed profile minimizes the fuel consumption [6] in land transport vehicles. Fuel consumption increases as mass increases and is different for different combination of fuel and transmission type [7].

The literature reveals that there is no model that can be used to assess energy performance of dump truck operating in mines with variation of mine gradient, topography and payload. The objective of this paper is to develop a generic model for dump trucks operating in an opencast mine.

2.0. Problem statement

The objective is to develop a generic model for calculating minimum specific fuel consumption of dump trucks operating in opencast mine for different payload, gradient and varying mine topography.

2.1. Model development

The present model is developed for multiple dump trucks operating between multiple crushers and excavators for an opencast mine. When a vehicle moves, the engine has to deliver power against air, friction, rolling and gradient resistances. Theoretical power requirement for movement of both empty and loaded dump truck is calculated using mass balance and theory of vehicle dynamics. Fuel consumption per trip is calculated considering loading, unloading and travel time. Theoretical material handled is estimated from number of trips based on cycle time. Specific fuel consumption is calculated as the ratio of fuel consumption to the theoretical output

2.2. Governing equations of model

2.2.1. Mass balance of dump truck

The gross mass of dump truck (W_G) is the sum of the weight of empty dump truck (W_E) and the payload (W_L). The payload is defined as the material transferred by a dump truck in a single trip.

The mass balance of dump truck is given as

$$W_G = W_L + W_E , \quad (1)$$

Pay load depends on volumetric capacity of dump truck (S_L) and the density of ore (ρ_{ore}) to be transferred and is given as

$$W_L = S_L \rho_{\text{ore}} , \quad (2)$$

The pay load is restricted by the maximum capacity of truck as given in (3).

$$W_L \le W_{L,\max} \quad (3)$$

2.2.2. Power requirement of dump truck

The equations for power requirement for empty truck moving from crusher to excavator (P_{ce}) and loaded dump truck moving from excavator to crusher (P_{ec}) are given in (4) and (5).

$$P_{ce} = V_{ce}(aV_{ce}^2 + bW_E) , \quad (4)$$

$$P_{ec} = V_{ec}(aV_{ec}^2 + cW_G) , \quad (5)$$

Where a, b and c are constants for drag resistance; rolling, friction and gradient resistances for down gradient mine and are given as (6) to (8)

$$a = \frac{1}{2} C_d \rho_{air} A_F , \quad (6)$$

$$b = g\cos\theta(f + C_{rr}) + g\sin\theta , \quad (7)$$

$$c = g\cos\theta(f + C_{rr}) - g\sin\theta , \quad (8)$$

$$V_{ce,ec} \le V_{\max} , \quad (9)$$

$$P_{ce,ec} \le P_{\max} , \quad (10)$$

The gradient resistance increases with an increase in gradient in case of up gradient mine and decreases in case of down gradient mine. ($\pm$) sign is considered depending on mine topography. (+) sign is taken for all up gradient mines and (-) sign is considered for

all down gradient mine or hill mines for loaded dump trucks and vice versa for empty trucks.

2.2.3. Engine Characteristics

The engine power of internal combustion engine is the function of angular velocity as

$$P = \sum_{i=1}^{3} P_i \, w_{e,}^{\,i} \quad , \tag{11}$$

Where, P_1, P_2, P_3 for direct injection diesel engine are $P_1 = 0.87\ P_m/w_m$, $P_2 = 1.13\ P_m/w_m^2$ and $P_3 = -\ P_m/w_m^3$

Power supplied by engine are presented as (12) and (13) by converting angular velocity to linear velocity using equation (14).

$$P_{ce} = a_1 V_{ce} + a_2 V_{ce}^{\,2} - a_3 V_{ce}^{\,3}, \tag{12}$$

$$P_{ec} = a_1 V_{ec} + a_2 V_{ec}^{\,2} - a_3 V_{ec}^{\,3}, \tag{13}$$

Where,

$$V_{ce,\,ec} = \frac{R_w w_e}{G_R} \tag{14}$$

And, a_1 , a_2 , a_3 are constants .

Limiting speed for empty and loaded dump trucks V_{ce} and V_{ec} are obtained by equating (4, 5) and (12, 13) at the condition of maximum power that engine can deliver.

Brake specific fuel consumption

The brake specific fuel consumption (B_F) is a function of speed of vehicle for empty and loaded truck and are presented as (15) and (16)

$$B_{F,\,ce} = b_1 V^2{}_{ce} - b_2 V_{ce} + b_3, \tag{15}$$

$$B_{F,\,ec} = b_1 V^2{}_{ec} - b_2 V_{ec} + b_3, \tag{16}$$

Where b_1 , b_2 , b_3 are constants and are obtained from engine characteristic curve.

2.2.4. Fuel consumption per trip

Fuel consumption in dump truck moving between crusher and excavator s is given in (17), (18).

$$m_{f,\,ce} = P_{ce} B_{F,\,ce} \tag{17}$$

$$m_{f,\,ec} = P_{ec} B_{F,\,ec} \tag{18}$$

Now travel times from ith crusher to jth excavator and return journey are calculated using (19), (20).

$$t_{ij} = \frac{L_{ij}}{V_{ce}} \quad \text{(i = 1, 2….M; j = 1,2,3……N),} \tag{19}$$

$$t_{ji} = \frac{L_{ji}}{V_{ec}} \quad \text{(i = 1, 2….M; j = 1,2,3……N),} \tag{20}$$

The generalized equation for fuel consumption per trip of dump truck moving between ith crusher and jth excavator considering travel time , load and un load time , waiting or delay time is written as (21).

$$M_{f,\,ij} = m_{f,\,ce} t_{ij} + m_{f,\,ec} t_{ji} + m_{f,\,idle}(t_{load,\,UL} + t_{wait}), \tag{21}$$

For optimization, $t_{wait} = 0$ (22)

2.2.5. Theoretical material handling output

Theoretical material handling output per hour of mine is calculated from cycle time and maximum pay load of dump truck.

Cycle time

Cycle time of dump truck is defined as the time required for complete cycle of dump truck movement from one excavator to one crusher or waste dumping station. Mathematically, the travel time and cycle time are given in (23), (24)

$$t_{travel} = t_{ce} + t_{ec}, \tag{23}$$

$$t_{d,\,cycle} = t_{load,\,UL} + t_{travel} + t_{wait}, \tag{24}$$

Trip Frequency

The trip frequency of dump truck directly affect the production output of opencast mine. The trip frequency should be maximized to achieve minimum fuel consumption per ton of ore handling. The trip frequency is calculated using (25)

$$x_{ce} = \frac{1}{t_{d,\,cycle}}, \tag{25}$$

Theoretical handling output dump truck

Now theoretical output per hour of single dump truck is calculated using (26)

$$q_d = W_L x_{ce}, \tag{26}$$

2.2.6. Specific fuel consumption

Specific fuel consumption of dump truck on hourly basis is calculated using (27)

$$SFC_{dump\,truck} = \frac{M_{f,\,ij} x_{ce}}{q_d} \tag{27}$$

3. Optimization of specific fuel consumption

The objective is to minimize fuel consumption of dump trucks moving between multiple crushers and excavators. In solving optimisation problem speed of empty and loaded truck are taken as decision variables. The optimization problem is formulated to calculate minimum specific fuel consumption for specific material handling demand and payload as (28) to (34) including equation (1) to (27).

Minimize

$$SFC_{dump\ \text{truck}} = \frac{\sum_{i=1}^{M}\sum_{j=1}^{N} HX_{ij}M_{f,ij}}{\sum_{i=1}^{M} D_i} \quad (28)$$

Subject to

$$\sum_{j=1}^{N} X_{ij}W_L H \geq D_i (i = 1,2,3...M)\ , \quad (29)$$

$$\sum_{j=1}^{N} X_{ij}W_L \leq Q_{c,i} (i = 1,2,3...M)\ , \quad (30)$$

$$\sum_{j=1}^{M} X_{ij}W_L \leq Q_{e,j} (j = 1,2,3...N)\ , \quad (31)$$

$$\sum_{j=1}^{N} n_{dj} = \sum_{i=1}^{M} n_{di}\ , \quad (32)$$

Where,

$$n_{dj} = \frac{t_{d,cycle,ij}}{t_{load}}$$

(j = 1,2,3……N) (i = 1,2,3…M) , (33)

$$X_{ij} = n_{dj}x_{ij} \quad (34)$$

All variables are positive

4. Case study of downgrade opencast mine

A case study of downgrade opencast limestone mine of M/s Shree cement Ltd, Rajasthan, India is considered for optimization and simulation of model.

4.1. Input Parameters of Model

Design data and operating parameters of dump trucks, crushers and excavators are taken as input data of model and shown as Table No. 1- 3[9].

Table 1: Design specification of engine of dump truck

Parameter	Specifications
Type	Water cooled, Turbocharged , 4 stroke
No. of cylinder	6
Bore x Stroke	159 x 159 mm
Cylinder displacement	19 Litres
Rated power	522 kW @2100 RPM
Idle speed	750 RPM
T max	2731 Nm @1500 RPM

Table 2: Rated Physical parameters of dump truck

Parameters	Designed	Actual
Net vehicle mass	41t	
Rated Pay load	45.5t	52t,65t
Gross Vehicle mass	86.5t	93t,106t
Wheel radius	0.812m	
Frontal area	15.408 m^2	

Table 3: Mine Topography and Resources

Parameters	Mine operating condition
Mine topography	Downgrade mine
Distance between crusher and excavator	
Minimum distance	1km
Maximum distance	2 km
Gradient	1:14 (4°)
Material	Limestone
Ore density (Limestone)	1550 kg/m^3
Total no. of dump trucks	21
Capacity of dump trucks	52t,65t
Total no. of excavators	5
Capacity of excavators	1200 ton/h
Total no. of crushers	2
Capacity of crushers	1400 ton/h

4.2. Solution Procedure and simulation

Fig.A.1 shows the information flow diagram for energy performance model of dump truck. The model is solved using excel solver with minimising SFC as objective function by changing V_{ce} and V_{ec}. The optimum speed is found to be 7.62 m/s (28 km/h) and 7.04 m/s (25 km/h) for empty and loaded dump truck respectively.

4.2.1. Parametric analysis

The model capability is investigated for down gradient mine by parametric analysis and shown in Table 4.Varaitions of SFC with input parameters are presented in Fig no. 2-5 .The effect of mine gradient and wind speed on SFC is not significant.

Table 4: Parametric analysis of input parameters

Parameters	Designed	Actual
Pay load	65t	30-65 t
Material handling	360 t/h	150-400 t/h
Distance	1.5 km	1.45 -1.7km
Mine gradient	4°	1-15 °
Wind speed	0 m/s	0-8 m/s

4.2.2. Single Dump truck application

The optimal SFC of dump truck is 81.5 g/ton as shown in Fig.2 for a payload of 65t and handling of 360 ton/h in a distance of 1.5km. The corresponding fuel consumption is 29.3 kg/hr. The minimum cycle time estimated is 10.8 minute. Increasing the material handling rate will result in further increase of SFC as shown in Fig.3 and material handling per truck is limited up to 400 ton/h. The minimum SFC for 52t and 65t payload dump trucks is 93.7 g /ton and 81.5 g /ton respectively.

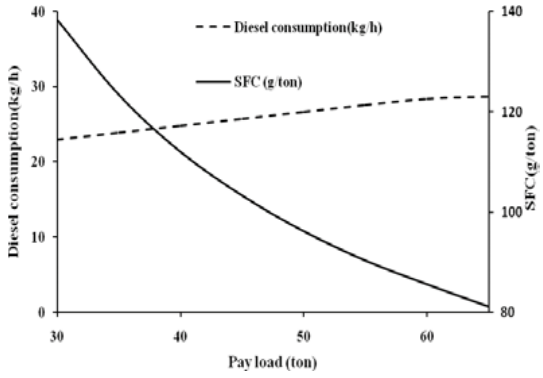

Fig. 2. Variation of diesel consumption and SFC for 65t payload

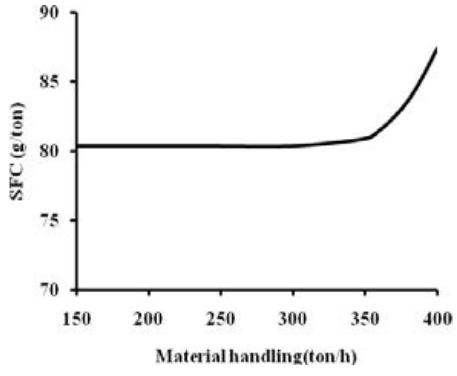

Fig. 3. Variation of SFC with handling due to increase in speed

4.2.3. Multiple dump trucks

The optimal SFC variations with different material handling rate is shown in Fig.4 for single and multiple dump trucks. The maximum number of trucks allocation per excavator is 3 for a distance of 1.5km. The variation of SFC with distance shown in Fig.5 confirmed that the trend is linear for multiple excavator models located at different locations. The material handling of 1114 ton/h remains constant as an increase in distance decreases trip frequency and increases number of truck required to serve at loading point. The optimization problem as shown in (28) to (34) is solved by linear programming method. The solution of optimization problem yields SFC of 86 g/ton for ore handling of 2600 ton/h and pay load of 65t.The locations of excavators from crushers are 1.45km,1.5km , 1.6 km,1.65km and 1.7km.

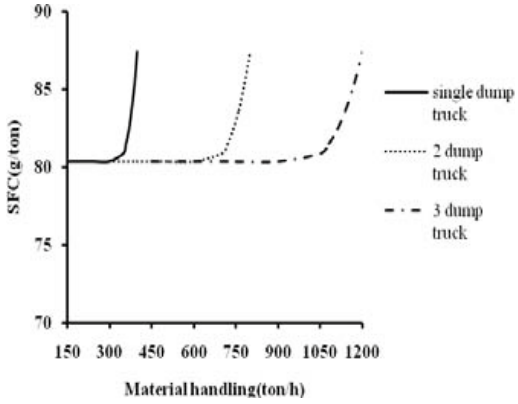

Fig. 4. Effect of multiple dump trucks on overall SFC

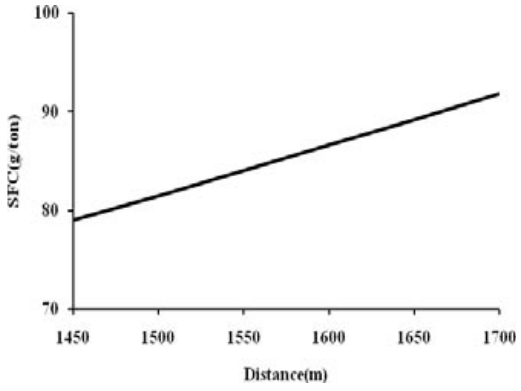

Fig. 5. Variation of SFC with distance for 65t dump truck

4.3. Experimentation and comparison of model result

Field studies have been conducted for experimentation for 1 hour at Nimbeti opencast mines of M/s Shree cements Ltd, Rajasthan, India and model results are compared with experimental results obtained from sample of 10 dump trucks. The full load diesel consumption was measured with calibrated dip-stick along with the corresponding number of trips to calculate the specific fuel consumption. There are two different capacities of dump trucks operating in the mine with same engine of 522 kW. The standard BH50M dump trucks of with Cummins engine has been converted to 52t and 65t capacity dump trucks by extending the body. The trend of diesel consumption shows that average hourly fuel consumption is 26.35 kg/h for material handling of 260 ton/h. The average SFC is 105 g/ton whereas minimum SFC using model is calculated to be 86 g/ton for pay load of 65t .The fuel saving potential estimated is 15 %.

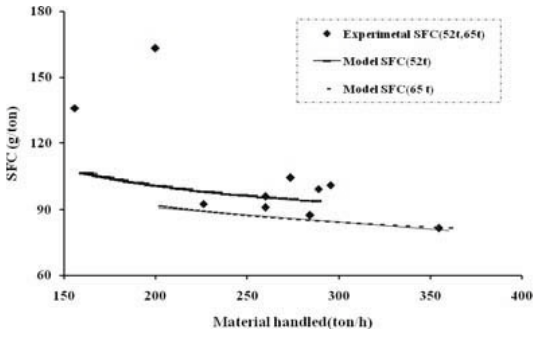

Fig. 6. Variation of SFC for 52t and 65t dump truck model and comparison with experimental data

4.4. Assumptions and limitations

4.4.1. Assumptions taken in model

Model is based on steady flow of dump truck which moves at constant speed. Initial acceleration and final deceleration may change the fuel requirement. However as reported by Chang et al. [6] such changes are negligible and hence this aspect is neglected in this paper. Loading time is presently assumed as constant. Model is developed considering fixed locations of crushers and excavators. The distance between crusher and excavator is taken as mean of maximum and minimum distances for assessing energy performance of dump trucks based on the mine layout.

4.4.2. Limitations of Model

Uncertainty of loading time that depends on ore hardness, density and digging geometry is not considered. Therefore it is difficult to assess the exact fuel consumption. Hence model can assess average energy performance of dump truck.

5. Results and discussions

The minimum specific fuel consumption calculated for a simple mine transportation system of 2 crushers and 3 excavators for Nimbeti opencast mine of Shree cement is 86 g/ton. The annual material handling demand is 10.4 million ton and the dump truck operating hour is 4000h. Experimental results of 52t and 65t dump truck operating in an opencast mine result in average SFC of 105 g/ton. The optimum path and number of trips/h are E1-C2 (18), E2-C1 (18), E3-C1 (2) and E3-C2 (2). E1, E2, E3 and C1, C2, C3 are specified excavators and crushers in the mine site respectively. The sensitivity analysis is done for the model and given in Table A.1.

6. Conclusion

An energy performance model for dump trucks in opencast mine has been developed. The model is used for predicting the minimum fuel consumption of mine transport with multiple dump trucks. The model is used for recommending speed required for empty and loaded truck, optimal allocation of number of trucks and optimum trip frequency. The optimal speed is 28 km/h for empty dump truck and 25 km/h for loaded dump truck.

The minimum SFC is 86g/ton for present case of down gradient mine and the fuel saving potential is 15%. The model can be extended for evaluating minimum SFC for different mine gradient and topology. The model can be applied for other end use opencast mines like coal, lignite, manganese, iron etc. The model can be used to assess energy performance of other truck transport system. The model is useful to predict the optimum number of dump truck required and expected fuel consumption of new opencast mine during mine planning.

Nomenclature

A_F Frontal cross sectional area of dump truck, m^2

B_F Brake specific fuel consumption, gm/kWh

C_d Drag coefficient
C_{rr} Coefficient of rolling resistance
D Annual demand of material handling/crusher, tons
f Coefficient of friction between tyre and soil
g Acceleration due to gravity, m/s^2
G_R Gear ratio of dump truck
H Annual operating hours of dump truck
L Distance between crusher and excavator, m
m_f Mass of fuel consumption during dump truck movement, kg/h
$m_{f,idle}$ Mass of fuel consumption during engine idling of dump truck , kg/h
M_f Mass of fuel consumption in one trip , kg
n Number of dump trucks
P Power required by dump truck, kW
q_d Theoretical material output , ton/h
Q Maximum Capacity of crusher or excavator
R_w Wheel radius of dump truck, m
SFC Specific fuel consumption, kg/ton
S_L Volume of dump truck , m^3
t Time taken, h
$t_{load,UL}$ Loading and unloading time , h
t_{wait} Waiting time , h
t_{load} Loading time of dump truck, h
t_{travel} Travel time during empty and loaded cycle, h
$t_{d,cycle}$ Cycle time of dump truck, h
V Average speed of dump truck, m/s
W_E Weight of empty dump truck, ton
W_L Rated Pay load, ton
W_G Gross vehicle mass, ton
w_e Angular velocity of engine, rad/s
w_m Rated angular velocity of engine, rad/s
x Trip frequency of dump truck , h^{-1}
X Total number of trips per hour, h^{-1}

Greek symbols

ρ_{air} Density of air, kg/m^3
ρ_{ore} Density of ore, kg/m^3
θ Mine gradient , radian

Subscript and superscript

c,e,m
crusher, excavator, maximum
i,j demand, supply

References

[1] Central Institute of Mining & Fuel Research (CIMFR), 1998, Energy Audit report of Umrer open cast mine,WCL ,Nagpur,201207

[2] Boyd G., Dutrow E. and Tunnesssen W., 2008, ' The evolution of energy star energy performance Indicator for benchmarking industrial plant energy use', Journal of cleaner production,16, 709-715

[3] Sardeshpande V., ,Gaitonde U.N. and Banerjee R,2008,Model based energy benchmarking for glass furnace,Energy conver.Mgmt.,48,2718-2378

[4] Vemba M.M.D.S , 2004,The loading and transport system at SMC-Optimization, The Journal of South African Institute of Mining and Metallurgy , 139-147

[5] Vasil'ev M. V , Smirnov V. P. , 1974, Optimization of the journey schedules of high capacity Quarry dump trucks , The Institute of mining , Ministry of Ferrous metallurgy of USSR, Sverdlovsk., translated from Fiziko-Tekhni-cheski Problemy Razrabotki Poleznykh Isokopaemykh, No.1, 63-69

[6] Chang D.J ,Morlok E.K., 2005, Vehicle speed profiles to minimize work and fuel consumption , The Journal transportation engineering , 173-182

[7] Tolouei.R.,Titcheridge H., 2009, Vehicle mass as a determinant of fuel consumption and secondary safety performance, Transport research Part D

[8] Jajar R.N., 2009,Vehicle Dynamics: Theory and application,Springer,USA

[9] M/s Shree cement Ltd, 2009, Data received by correspondence based on CIMFR study on energy efficiency in opencast mine.

Acknowledgements:

The first author is grateful to Mr. S.C.Suthar of Shree cement Ltd, Dr A.Sinha, Mr A.K.Chowdhuy, Mrs Seema Topno of CIMFR and Cummins (India) Ltd for their help.

Appendix

Table A.1: Sensitivity Analysis of Model

Input parameter	Base value (ton)	% change	Change over base value(ton) (Upper)	Change over base value(ton) (lower)	SFC ,base (g/ton)	SFC,change over(g/ton) base value (upper)	SFC,change over base (g/ton) value(lower)	Sensitivity Index (upper)	Sensitivity Index (lower)
Pay load	65	5%	68.25	61.75	81.5	79.2	84.1	-0.572	-0.630
V_{ce}	7.62	5%	8.001	7.239	81.5	83.2	80.0	0.410	0.375
V_{ec}	7.04	5%	7.39	6.68	81.5	82.1	81.2	0.141	0.079
Mine gradient	4	25%	5	3	81.5	81.3	81.7	-0.011	-0.008

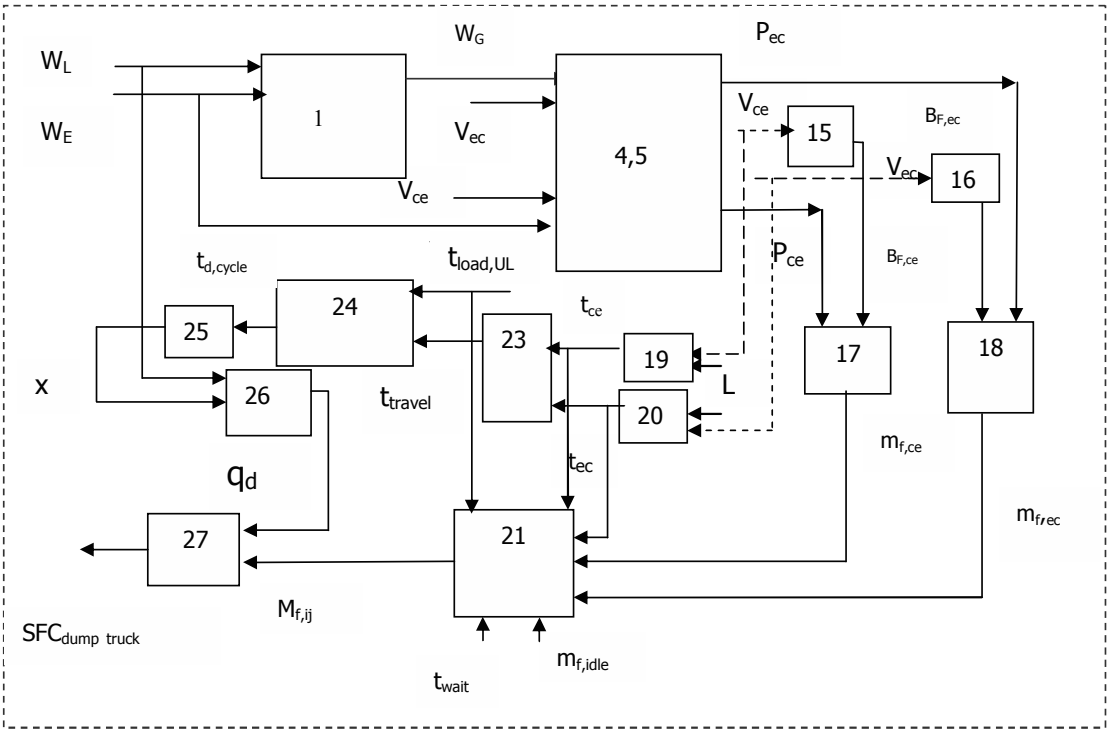

Note : Block numbers in Information flow diagram refers to equations in paragraph 2.2

Fig A.1. Information flow diagram for energy performance assessment model of dump truck

Electric Vehicles Must be Light

Walter E. Janach

Lucerne University of Applied Sciences, Horw, Switzerland

Abstract: Oil depletion and climate change will force individual urban transportation to become more energy efficient, especially for high traffic density and including the life cycle of vehicles. Internal combustion engines are best suited for normal cars on highways, whereas electric motors and batteries are ideal for light vehicles with moderate speed, typical for dense urban traffic. Normal size cars with electric motors and batteries do not allow to reduce primary energy input when the entire life cycle is taken into account.

Keywords: Internal combustion engines, Electric motors, Batteries, Electricity generation

1. Introduction

The global energy system is confronted with three "hard truths": a rising demand, a declining supply and climate change. The total energy used for individual transportation by automobiles and motorcycles with internal combustion engines (IC-engines) is large and must be strongly reduced in the future. The main pathways are a reduction of vehicle weight and engine power, hybridisation and fully electric drive (E-motors). While the electricity at present comes from the grid, fuel cells with hydrogen could provide it sometimes in the future.

In densely populated cities of developing countries road and parking space represent an additional limit. Here cars are more a problem than a solution. The result is a dramatic slow-down of traffic, causing an enormous waste of energy. The challenge is to find and introduce new vehicle concepts optimized for individual urban transportation that require much less energy under these conditions and also less road space. This must include all energies over the entire life cycle of the vehicles, which means their fabrication, the supply chain for propulsion energy and vehicle disposal. The environmental advantage of electric vehicles using electricity from the grid is reduced with such a life cycle approach.

There is no simple and clear answer to which drive system requires the lowest life cycle energy because this depends strongly on the power required by the vehicle, which in turn depends on its weight and maximum speed. The problem is that in urban traffic the speed is so low that cars are used far below their optimum operating conditions.

2. Electric (E) motor versus internal combustion (IC) engine

Apart from different characteristics, the energy efficiency of alternative vehicle propulsion concepts is the main criterion for their future use in road vehicles. A great difference lies in part load operation. Electric motors (E-motors) reduce their torque and thereby power by means of lowering the current, whereby electric losses are also reduced. In contrast, the losses of internal combustion engines (IC-engines) do not decrease much at part load (friction and heat loss to cylinder walls); or they can even increase (throttling losses). As a consequence, the efficiency of IC-engines decreases progressively at part load. This causes unnecessary high fuel consumption in urban traffic and is the main reason for the introduction of hybrid vehicles.

It is not reasonable to compare the efficiencies of E-motor and IC-engine directly with each other because electricity and fuel are different forms of input energy. When electricity is generated from chemical fuel, large losses occur in the power plant, which reduces the overall efficiency of electric propulsion.

3. Limits from size effects

Physical limits are present both in nature and in technology. We know for example that trees cannot become taller than about 50 m and that ants can walk on a ceiling. Gas turbines, the primary

mover for air transportation, cannot be downsized to a power level of only a few kilowatts.

Frictional and heat losses of IC-engines are proportional to cylinder surface while the power is proportional to cylinder volume. As a consequence these losses vary with the square of linear dimension whereas the power with the cube. When IC-engines are downsized to reduce power for lighter and slower vehicles, the losses do not decrease as much as the engine power, resulting in a size dependent decrease of efficiency. For non-turbocharged IC-engines, a cylinder volume of about 0.3 litres is the lower limit to avoid this effect. This is the main reason why small engines have 3 cylinders or only two like the Tata Nano. Turbocharging a small engine increases both the power and the efficiency but does not eliminate the above size effect. This becomes more and more severe in the power range below about 10 kW per cylinder.

E-motors with permanent magnets need no electricity for generating the magnetic field. They are ideal for power levels of a few kilowatts [1]. Here the efficiency of asynchronous motors decreases as they become smaller, especially at part load [1]. At higher power levels, asynchronous motors have also high efficiency, whereas the cost of the large permanent magnets becomes too high.

These size effects explain why IC-engines are best suited for conventional automobiles while electric motors with permanent magnets are ideal for vehicles with much lower power requirement. This is demonstrated by the 120 million electric two-wheel vehicles on Chinas roads.

4. Batteries

Batteries are expensive, need much energy for their fabrication and have a size effect also. One cannot compare a battery to a fuel tank because the electric energy is stored in electrochemical form on the surface of electrodes, separated by an electrolyte. The fabrication of batteries is a delicate process requiring high quality. The reason is that in order to attain high energy density, the electrodes and electrolyte layer must be as thin as possible. At the same time the current density must be distributed regularly over the electrode surface, which requires a precise thickness of the electrolyte layer. These two requirements are conflicting and explain partly the high cost of batteries.

The energy needed for fabrication of batteries is known to be high. For lead acid batteries it is of the same order of magnitude as the total electric energy stored over the entire life of the battery. A new US National Science study [2] on the life cycle of energy systems finds that the energy used for manufacturing and disposal of gasoline electric hybrid vehicles is 45 % higher than for normal cars. When included, this reduces the 40 % energy saved on the road by a Toyota Prius, relative to a normal car, to 25 % saved over the entire life cycle (150’000 km distance). The study gives no figures for battery electric cars, which means that fabrication energy of modern batteries is not available, an indication that it could also be high.

High capacity batteries have also a size effect, resulting in a size dependent quality challenge. For high energy density, the electrode foils and the electrolyte layer between them must be as thin as possible. When the electrode surface of a battery cell is enlarged to increase its capacity, the thickness of electrodes and electrolyte must remain constant to keep the ratio of energy per volume constant. This means that larger electrodes must remain as thin as in small cells, which is a challenge for fabrication and quality assurance. And a precise thickness of the thin electrolyte layer is important in order to avoid hot spots during operation, caused by irregularities of internal resistance over the surface.

In small cells hot spots remain small and thermal smoothing is fast. In large cells, hot spots can become persistent and must be avoided by even higher quality of electrolyte layer thickness. For large batteries in kWh, one needs also higher voltage and therefore a larger number of cells in series. This poses another quality problem because the internal resistance of individual cells is not exactly equal, so that electronic battery management is needed to protect each one of them from too high voltage when its resistance is higher than the average. This quality challenge increases with the number of cells in series. Therefore the batteries for road vehicles, which consist of many large cells, cannot be compared with the small high density one cell batteries of mobile phones. In conclusion, the fabrication of high density batteries for electric vehicles becomes more difficult as their capacity in kWh increases.

5. Electricity generation

The critical issue with electric vehicles is not the motor but the storage of electricity in batteries and the energy supply chain with generation in power plants or in alternative ways. Most of the electricity generated worldwide comes from fossil energy, in the United States and China about 70 % from coal. Because these thermal power plants are costly and have a life of many decades, the fossil source for electricity can only decrease gradually in the future. The efficiency of thermal power plants is about 40 % with coal, 60 % with natural gas and 30 % with nuclear power. Hydropower generation has high efficiency and no greenhouse gas emissions but the potential for future expansion is limited in industrialized countries. The main alternative sources for electricity are wind, solar and biomass. Common for all three is the higher cost. Biomass energy has limited potential, competes with agriculture and can increase deforestation.

In conclusion, electricity generation will bias the environmental friendliness of electric vehicles when their market grows beyond the present niche.

6. The Unique City Vehicle UCV

Constraints from oil depletion and global warming require that the energy efficiency of individual transportation must become much higher, and this including the influence of slow urban traffic and the life cycle of vehicles. Ideally such vehicles should be as compact, as light and as safe as possible, but most important not faster than necessary. The electric bicycle with a motor power of 0.25 kW is at the low end of the range, while the automobile with about 15 kW per seat is at the high end. Busses lie between with about 5 kW per seat. For comparison airliners reach 100 kW per seat. The physical reason for this large spread of specific power is the large difference of speeds. In dense urban traffic the average speed is typically about 25 km/h or even lower during rush hour. As a result, the energy used by cars in cities is much higher than necessary under such conditions, which represents not only a waste of energy but also of materials for fabrication of the vehicles that are too large and much too heavy.

Fig.1 Unique City Vehicle UCV with weight of two electric bicycles.

Fig.2 Unique structure of UCV, with sandwich plate for rolling platform and foam cabin in form of a large safety helmet.

The Unique City Vehicle UCV [3] shown in Fig.1 is an example of a very compact, light and at the same time safe electric vehicle with 4 wheels and two seats and represents a benchmark. It needs no more road space than two bicycles and weighs less than 50 % of the two persons on board.

Specifically designed for urban traffic in densely populated cities, the UCV has a closed cabin, is 1.7 m long and 1.2 m wide and will weigh 65 kg

Fig.3 For access, the helmet type cabin is lifted up and swings back.

with batteries in the final road version. The innovation consists of a light and strong sandwich plate with a foam core, to which the 4 wheels and two seats are attached (Figs. 2 and 3). The cabin is made of elastic foam with exterior fabric

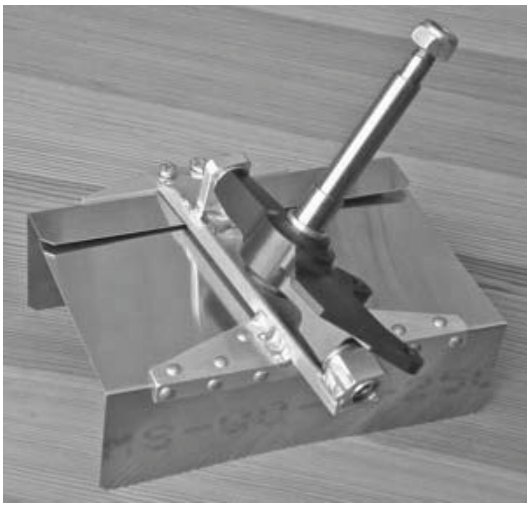

Fig.4 Riveted lightweight structure for attaching front wheel to platform, with thin aluminium sheet for adhesive bonding to thick sandwich plate.

reinforcing and has the shape of a large safety helmet. Instead of doors, the entire cabin is lifted up from the platform and swings back (Fig. 3). The foam cabin can be mass-produced at low cost and provides more safety than an electric bicycle, also in a collision with pedestrians.

Steering is with a mechanical "joystick", provided with a sliding sleeve for controlling the motor power and a lever for braking. Using the hand for braking is faster than the foot, which also increases safety. The brushless DC motor with permanent magnets provides 1.25 kW of mechanical power at 4000 rpm. On a flat road with only one person on board, only 0.35 kW of electricity is needed from the battery. The electricity used by the motor over 100 km is 1.6 kWh. When the efficiency of the thermal power plant and the energy used for fabrication of the battery are included, this corresponds in total to 0.6 litres of gasoline per 100 km [3].

7. Summary and conclusions

Electric (E) motors cannot directly replace internal combustion (IC) engines in automobiles because their energy systems are radically different. IC-engines provide high power and use liquid fuel with a high energy density. They have been the primary mover of automobiles during one century. E-motors are clean and have an unsurpassed high efficiency, especially at part load, which is important in dense and slow urban traffic. But the electricity for E-motors must be stored in expensive on board batteries with much lower energy density and therefore capacity.

Physical size effects let thermal and frictional losses increase when IC-engines become too small, reducing their efficiency. But light vehicles with reduced speed in urban traffic need much less power. On the other hand the two main drawbacks of batteries, their low energy density and high cost, become less critical for the smaller batteries used in light vehicles.

The electricity supply chain is affected by high losses in thermal power plants, which provide most of the electricity worldwide today and in coming decades. Thermal power plants have efficiencies between 30 and 60 %. Generation with hydro and wind power has high efficiency, but hydropower has limited grows potential and wind power is expensive.

In addition the energy for the fabrication of batteries can be of the same order of magnitude as the total electricity stored during their entire life. The result is, taking all this into account, that when the IC-engine of a normal automobile is replaced by an E-motor with the same power, only the vehicle efficiency is better. But when the electricity supply chain is included, the electric automobile needs more energy in total than with an IC-engine [2].

From a life cycle energy point of view, electric vehicles can only be better in the low power range, where size effects lead to an efficiency decrease of IC-engines. Since the power needed by a vehicle is strongly dependent on its weight and maximum speed, electric propulsion is best suited for light vehicles in densely populated cities over short distances. This allows also frequent recharging, which helps to keep battery size small.

References

[1] Lindegger, M., et al., 2009, Economic Viability, Applications and Limits of Efficient Permanent Magnet Motors, Final Report, Swiss Federal Office of Energy, Bern.

[2] National Research Council of the National Academies, 2009, Hidden Costs of Energy: *Unpriced Consequences of Energy Production and Use,* The National Academy Press, Washington, pp. 143-146.

[3] Janach, W., 2008, Ultralight Electric Vehicle for Urban Mass Transportation, *IEEE Vehicle Power and Propulsion Conference (VPPC)* [CD-ROM], Harbin, China.

Numerical Analysis of Thermoelectric Power Generation: Aircraft Systems Application

Tarik Kousksou[a], Jean-Pierre Bédécarrats[a], Daniel Champier[b], Pascal Pignolet[b], Sebastien Koch[a], Christophe Brillet[c]

[a] *Laboratoire de Thermique, Énergétique et Procédés, Université de Pau et des Pays de l'Adour, Rue Jules Ferry, BP 7511, 64075 Pau Cedex, France.*
[b] *Laboratoire de Génie Electrique, Université de Pau et des Pays de l'Adour, Pau, France.*
[c] *Turbomeca – Groupe SAFRAN, BP 41-64511 Bordes Cedex, France*

Abstract: This paper investigates the electric power extractable from thermoelectric modules placed in a conical nozzle which is heated by a hot fluid (the final exhaust gas from aircraft systems) and cooled by another cold fluid. A computer model has been developed to simulate the performance of the thermoelectric system. The results were obtained for various operating conditions. The numerical model is also used to optimize the electric power.

Keywords: Thermoelectric generator, Power generation, Numerical simulation, Low Mach number, Conical nozzle

1. Introduction

The increase in the price of crude oil, accompanied by a better knowledge of environmental problems associated with global warming, resulted in an upsurge of scientific activity to identify and develop environmentally friendly sources of electrical power.

In the scope of energy harvesting, thermoelectric generators (TEG) are among technologies that can recover and convert engine waste heat to electrical energy to improve the overall thermal efficiency of thermal energy systems. Even for currently used TEG devices with a low energy conversion efficiency of around 5-10%, they are still strongly advantageous as compared to conventional energy technologies, not only for their well-known merits such as high reliability, silence and low environmental impact but also because of their capability of utilizing huge amounts of industrial waste heat as an energy source in a simple and easy manner. The total reliability of thermoelectric generators has been demonstrated in many applications [1]. Matsuura [2] analyzed a heat pump/TEG system to identify the best use of the cogeneration rather than only to produce electricity, and proposed to apply TEG to the stream turbine of the power station for superconducting synchronous power resource, in which part of the steam heat from the turbine is transformed into power by TEG for field excitation. Yodovard et al. [3] assessed the potential of waste heat recovery from the stack exhaust of around 200°C for diesel engines and gas turbine cogeneration in the manufacturing industrial sector in Thailand. Kametani et al. [4] assumed that TEG modules were mounted between the high temperature exhaust gas heat exchanger (around 600°C) and the cooling water (around 90°C) of gas engines and gas turbines, respectively, and then investigated the effects. Chen et al. [5] presented an analysis of system efficiency related to the integration of TEG into thermal energy systems, especially Combined of Heat and Power production (CHP). They also estimated the overall conversion efficiency improvements and economic benefits of this integration.

Although the commercial/practical applications of thermoelectric generators still remain marginal in electric generation, significant advances have been made in synthesizing new materials and fabricating material structures with improved thermoelectric performance. Efforts have focused primarily on improving the material's figure-of-merit, and hence the conversion efficiency, by reducing the lattice thermal conductivity [6]. Recent advances in materials and materials processing, as summarized in reviews [7-10], have led to higher non-dimensional figure of merit values and, thus, higher theoretical conversion efficiency of TE modules. In addition to the improvement of the thermoelectric material and module, the analysis of thermoelectric systems is equally important in designing a high-performance of these ones. Wu [11] performed a theoretical analysis on waste-heat thermoelectric power

Corresponding Author: Tarik Kousksou, Email: tarik.kousksou@univ-pau.fr

generators. In this study, a real waste-heat thermoelectric generator model was presented accounting for both internal and external irreversibilities to predict realistic specific power and efficiency. The internal irreversibility is caused by the Joulean loss and conduction heat transfer, and the external irreversibility is caused by the temperature differences between the hot and cold junctions and the heat source and sink in the real waste-heat thermoelectric generator. Esarte et al. [12] applied NTU-ε methodology to study the effect of the fluid flow rate, heat exchanger geometry, fluid properties and inlet temperatures on the power supplied by the TEG. Stevens [13] proposed an approximate procedure for the optimal coupled design of a thermoelectric generator with a small temperature difference. Crane and Jackson [14] investigated thermoelectric materials with advanced heat exchangers. In this study, numerical heat exchanger models integrated with thermoelectric modules are validated by experimental data from previous cross flow heat exchanger studies as well as experiments using thermoelectric between counterflow hot water and cooling air flow channels. Suzuki and Tanaka [15] studied thermoelectric power generation with multi-panels. Electric power was estimated in the case of the large scale flat thermoelectric panels exposed to two fluids. The output powers of the proposed system were analytically deduced from heat transfer theory, and written by non-dimensional functions to reflect the characteristics of system design. Another study on the thermoelectric power generation with cylindrical multi-tubes was also carried out by the same authors [16]. Yu and Zhao [17] presented a numerical model to predict the performance of a thermoelectric generator with a parallel-plate heat exchanger.

In a large-scale power plant, thermal energy is carried to the power generator. When it is extracted by a fluid and passed to the TEG, a hot fluid offers the heat to the junctions in the thermoelectric modules. The Seebeck effect can generate the thermoelectric power depending on a temperature difference between the hot and cold junctions. The Seebeck electromotive force is the sum of multiplication of the relative Seebeck coefficient and the temperature difference ΔT over all the serial connections. The problem to obtain the larger power is, therefore, how to give the larger ΔT to all the thermoelectric modules existing between two hot and cold fluids [18-19]. The heat applied at the hot junction is scattered and lost at the cold junction, corresponding to the temperature gradient inside the thermoelectric module. The heat from the hot fluid is transferred to the panel surface by convection, the cold surface by heat conduction through the solid and finally to the cold fluid again by convection. The fluids are heated or cooled along the flow path, and their temperature profiles through the path, $T(x)$, change as a function of position x.

The purpose of this work is to evaluate the electric power extractable from thermoelectric modules placed in the conical nozzles of aircraft turbines. These conical nozzles are heated by a hot fluid and cooled by another cold fluid. The heat transfer through the conical nozzle and the temperature variation along the fluid path are analyzed mathematically. Applying a heat transfer analysis, their temperature profiles and power output P_o can be determined numerically using the finite volume method. The physical model enables us to select the best system, independently of the thermophysical properties of the thermoelectric materials and working fluids. The originality of our work is to study the feasibility of using thermoelectrical modules in an aircraft turbine to generate electricity.

2. Physical model

2.1. Heat transfer analysis

The physical model is illustrated schematically in Fig. 1. The thermoelectric modules are sandwiched between the hot exhaust fluid and the cold fluid and they are electrically insulated by ceramic plates (see Fig. 2).

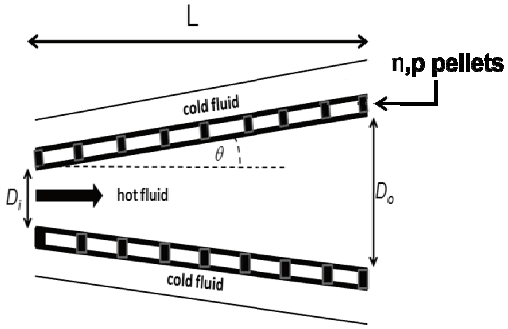

Fig. 1: Schematic layout of the model

It is interesting to note that the conical nozzles geometries are often used in gas turbine engines.

In the case of divergent conical nozzles and for subsonic flows, it consisted in slightly decreasing the velocity and minimizing the total pressure losses. The conical nozzle performance, flow and heat transfer characteristics are strongly coupled so that the knowledge of flow conditions is absolutely necessary in the interpretation of performance parameters.

In order to simplify the physical model of the thermoelectric conical nozzle, the following assumptions were made:

- The hot and cold fluids are separated by a panel, and flow along both conical surfaces.
- The fluid flow is considered unidirectional.
- The hot fluid flow is compressible and Newtonian.
- The cold fluid flow is incompressible and Newtonian.
- The axial conduction in the hot fluid is negligible.
- All the thermoelectric modules are supposed to be conical and are composed of a single layer of p-n junctions as illustrated in Fig. 2.
- The thermoelectric pellets are homogeneously aligned perpendicular to the heat flow, combined slightly without an open space, and connected electrically in series.
- The electrical contact resistance between the p and n couples is assumed to be negligible.
- The material properties for the TE pellets vary along the length of the conical nozzle with changes in temperature **[20].**

Based on these assumptions the energy balance equations for the hot fluid and the cold fluid are:

Hot fluid

A one dimensional non-viscous flow in a conical nozzle with variable section *S(x)* is considered. The equations governing this type of flow are continuity, momentum and energy equations:

$$\frac{\partial(\rho_H S)}{\partial t} + \frac{\partial(\rho_H u_H S)}{\partial x} = 0 \quad (1)$$

$$\frac{\partial(\rho_H u_H S)}{\partial t} + \frac{\partial(\rho_H u_H u_H S)}{\partial x} = -S\frac{\partial p_H}{\partial x} \quad (2)$$

$$\frac{\partial(\rho_H E_H S)}{\partial t} + \frac{\partial(\rho_H u_H H_H S)}{\partial x} = \frac{(T_C - T_H)}{R_{th} V_H} \quad (3)$$

Where ρ_H, u_H, p_H and E_H respectively represent the density, velocity, pressure and total energy of the hot fluid. V_H is the volume occupied by the hot fluid. R_{th} is the total thermal resistance between the hot fluid and the cold fluid. T_C and T_H are respectively the temperature of the cold and hot fluid. x is the special coordinate, and t is the time. Furthermore, the following thermodynamic relations hold:

$$H_H = h_H + \frac{1}{2}u_H^2 \quad (4)$$

$$E_H = e_H + \frac{1}{2}u_H^2 \quad (5)$$

$$\rho_H H_H = \rho_H E_H + p_H \quad (6)$$

where H_H is the total enthalpy, h_H the specific enthalpy and e_H the internal energy. The system of equations (1)-(3) is closed by the equation of state for a perfect gas:

$$p_H = \rho_H r T_H \quad (7)$$

where r is the gas constant.

Cold fluid

Energy equation :

$$\rho_C c_{p,C}\left(\frac{\partial T_C}{\partial t} + u_C\frac{\partial T_C}{\partial x}\right) = \lambda_C\frac{\partial^2 T_C}{\partial x^2} + \frac{(T_H - T_C)}{R_{th} V_C} \quad (8)$$

Where ρ_C, $c_{p,C}$, u_C and T_C respectively represent the density, specific heat capacity, velocity, and temperature of the cold fluid. λ_C is the thermal conductivity of the fluid, V_C the volume occupied by the cold fluid.

The initial and boundary conditions were chosen as follows:

Hot fluid:

Since the flow regime is subsonic (0<Mach<1), we define the values for the density and velocity at the inlet face. At the outlet face we impose the pressure.

Cold fluid

$$T_C(x,0) = T_{C\,in};\ T_C(0,t) = T_{C\,in};\ \frac{\partial T_C(L,t)}{\partial x} = 0 \quad (9)$$

2.2. Numerical strategy

The flow domain is subdivided into a finite number of control volumes with length Δx_i for the hot fluid and $\Delta x_j = \left(cos(\theta)\right)^{-1}\Delta x_i$ for the cold fluid (Fig. 2). All the variables are stored in the control volume center (collocated arrangement).

It is well known that the efficiency and the accuracy of methods designed to compute the compressible flows (Mach number, M>0.2) deteriorate drastically when M decreases below

0.2. On the other hand, when the Mach number remains uniformly small (below 0.2), an accurate and useful approximation is to consider the flow incompressible. This observation has led to the development of computing methods exclusively suited to incompressible flows. No class of methods is suitable for computing flows in domains in which incompressible subregions as well as compressible subregions occur simultaneously, or for computing weakly compressible flows. For this, methods are required with uniform accuracy and efficiency whatever the Mach number is. We refer to such unified methods for incompressible and compressible flow computation as Mach-uniform methods. In our work, to resolve the equations (1)-(3), we have used a coupled pressure and temperature correction algorithm. The description of this algorithm is largely detailed and presented in references [21-22] and it is not deemed to repeat it in the present work.

The energy equation (8) is solved using a finite volume solution method. Upwind scheme is used for the convection term and a fully implicit scheme for the time integration [23].

Because the Eqs. (1)-(3) and (8) are coupled, the resulting algebraic equations have been solved using an iteration procedure, at each time step, until the convergence has been achieved.

2.3. Total thermal resistance

The overall thermal resistance through the control volume (i, j) is giving by the following expression:

$$R_{th} = R_{metal} + R_{ceramic} + R_H + R_C + R_{cont} + R_{TE} \qquad (10)$$

where R_H and R_C are the thermal convection resistances of the hot and the cold fluid, respectively. R_{metal} and $R_{ceramic}$ are the thermal conduction resistance of the metal and ceramic materials, respectively. R_{cont} is the thermal contact resistance and R_{TE} is the thermal conduction resistance of the TEG. The overall thermal resistance is obtained by determining each individual resistance through a control volume.

$$R_H = \frac{1}{A_{H,j} S_i} \quad ; \quad R_C = \frac{1}{A_{C,j} S_j} \quad ; \quad R_{TE} = \frac{ln\left(\frac{r_4}{r_3}\right)}{2\pi\lambda_{TE}\Delta x_j}$$

$$R_{metal} = \frac{ln(\frac{r_2}{r_1}) + ln\left(\frac{r_6}{r_5}\right)}{2\pi\lambda_{metal}\Delta x_j}; \; R_{ceramic} = \frac{ln(\frac{r_3}{r_2}) + ln\left(\frac{r_5}{r_4}\right)}{2\pi\lambda_{ceramic}\Delta x_j}$$

where r, $A_{H,i}$ and $A_{C,j}$ are the radius of the conical tube and the heat transfer coefficient between the fluid and the conical tube, respectively (see Fig. 2). S_i and S_j are the wetted areas for hot and cold fluid, respectively. λ_{TE} is the average heat conductivity of the module, defined by :

$$\lambda_{TE} = \frac{\lambda_p s_p + \lambda_n s_n}{s_p + s_n} \qquad (11)$$

where λ_p, λ_n, S_p and S_n are the heat conductivity and the cross-sectional area of p- and n-type elements, respectively.

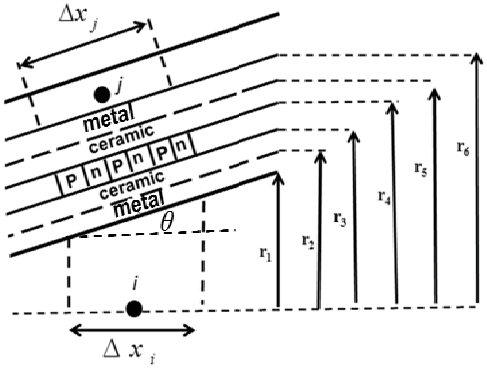

Fig. 2: Control volume of TEG

In order to facilitate the parametric design optimization, the conical nozzle model implements empirical correlations for hot side $A_{H,i}$ and cold side $A_{C,j}$ convective heat transfers.

For the cold fluid flows through an annular section, the heat transfer coefficient is determined using the hydraulic diameter D_h which is defined as :

$$D_h = \frac{4 A_c}{P} \qquad (12)$$

where A_c and P are respectively the flow cross sectional area and the wetted perimeter. It is this diameter that will be used in calculating parameters such as *Re* and *Nu*:

- For turbulent flow regime, which still occurs if $Re \geq 2300$ the following correlation is adopted [24]:

$$Nu = 0.023 Re^{4/5} Pr^{1/3} \qquad (13)$$

- For laminar flow regime, the Nusselt number varies from 3 to 5 with variations in hydraulic diameter and the fluid temperature.

For the hot fluid flows through the inner section of the conical nozzle, the above correlations are used but the hydraulic diameter is substituted by the inner diameter of the conical nozzle.

2.4. Thermoelectric modeling

Since a thermoelectric converter is a heat engine and like all heat engines it obeys the laws of thermodynamics. When the heat conduction, the Joulean heat loss and the energy supply or removal to overcome the Peltier effects are combined for the whole generator arrangement, the rate of heat supply Q_H and heat removal Q_C in the control volume (i,j) are given by Angrist **[25]:**

$$Q_{H\,i,j} = n_x n_\varphi n_{TE}\left[\alpha I T_{H\,i,s} - \frac{R_{elec} I^2}{2} + K\left(T_{H\,i,s} - T_{C,j,s}\right)\right] \quad (14)$$

$$Q_{C\,i,j} = n_x n_\varphi n_{TE}\left[\alpha I T_{C,j,s} + \frac{R_{elec} I^2}{2} + K\left(T_{H\,i,s} - T_{C,j,s}\right)\right] \quad (15)$$

where I is the current flow through a single thermocouples, α, K and R_{elec} are respectively, the Seebeck coefficient, thermal conductance and electrical resistance of a single thermocouple. n_{TE} is the number of thermocouples in the TE module. n_φ and n_x the number of TE modules in a circumferential circulation, and the number of TE modules in the x direction, respectively. $T_{C,j,s}$ and $T_{H,i,s}$ are respectively, the temperatures of the cold and hot junctions. In practice, it is impossible to measure the temperature of both the hot and the cold junction ($T_{C,j,s}$, $T_{H,i,s}$) as the p- and n-legs are interconnected by metal and are thermally in parallel between two ceramic plates. However, it is feasible to calculate them using the fluid temperatures ($T_{C,j}$, $T_{H,i}$):

$$T_{H\,i,s} = T_{H\,i} - Q_{H\,i,j}\left(R_H + R_{metal} + R_{ceramic} + R_{cont}\right)$$

$$T_{C,j,s} = T_{C,j} + Q_{C\,i,j}\left(R_C + R_{metal} + R_{ceramic} + R_{cont}\right)$$

The current flow through the thermocouples aligned in series for a given thermoelectric generator is determined by the number of thermocouples aligned in series and the electrical resistance of circuit load. The total voltage is the sum of the voltages generated in each control volume, which are wired in series along x-coordinate direction. Therefore, the current can be written as:

$$I = \frac{\sum_{i,j=1}^{n} \alpha\left(T_{H\,i,s} - T_{C,j,s}\right) n_{TE} n_x n_\varphi}{R_{load} n_{TE} + \sum_{i,j}^{n}\left(R_e n_{TE} n_x n_\varphi\right)} \quad (16)$$

where n is the total number of the control volume and R_{load} is the load electrical resistance. In this work, the load resistance is selected to equal the effective internal resistance of the thermoelectric modules so that the maximum power output of a thermoelectric module could be achieved.

The output power of the thermoelectric generator is :

$$P_o = \sum_{i,j=1}^{n}\left(Q_{H\,i} - Q_{C,j}\right) \quad (17)$$

3. Results and discussion

In the following numerical simulation, the thermophysical values of Bi_2Te_3 semiconductors will be used for the thermocouples. The thermophysical properties of the metal and ceramic are determined using the temperature of the cold and hot fluids. Table 1 shows the fluid properties and the parameters for the thermoelectric conical nozzle. The simulation was carried out only for the counter flow type of conical nozzle.

Table 1: Parameters for thermoelectric power generation system

Variables	Values used in this work
Conical nozzle	
Length	0.32 m
Thickness	0.002m
Inlet diameter	0.236m
Outlet diameter	0.306m
Thermal sources	
Hot fluid	**Air**(T_H^{in} = 900K , $u_{H,in}$=130 m/s)
Cold fluid	**Oil**(T_C^{in} = 358K , $\dot{m}_C$ = 0.21 kg / s)

Figs. 3, 4 and 5 show the pressure, the temperature and the velocity variation of the hot fluid through the conical nozzle. For subsonic flows, increasing the cross-sectional area causes the flow to decrease the velocity and increase the pressure and temperature.

The increase in the hot fluid temperature is a direct result of the energy conservation. From a

knowledge of the conservation of mass for subsonic flows, we can design the test section to produce a desired velocity or Mach number since the velocity is a function of the cross-sectional area.

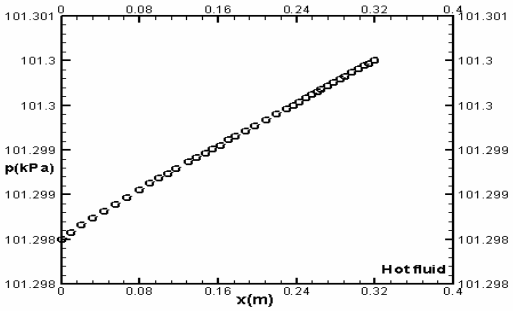

Fig. 3: Pressure profile of the hot fluid along the conical nozzle

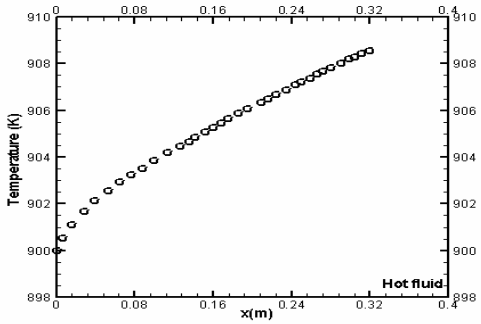

Fig. 4: Temperature profile of the hot fluid along the conical nozzle

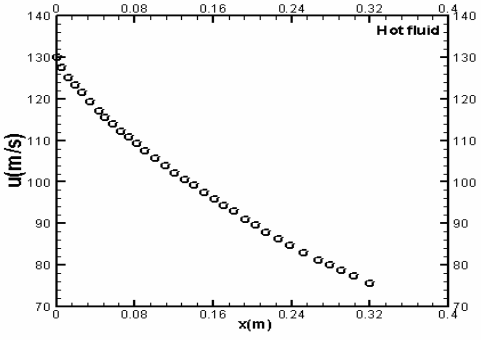

Fig. 5: Velocity profile of the hot fluid along the conical nozzle

Fig. 6 presents the evolution of the cold temperature through the conical nozzle. As can be seen in Fig. 6, the temperature variation tendency of the cold fluid flow along the axis of a thermoelectric generator is similar to that in an ordinary heat exchanger. Nevertheless, the variations in temperature are almost linear. This special feature in the conical nozzle of thermoelectric power generation is due to the Seebeck effect which is making a certain amount of energy from high-temperature fluid be taken away as electricity, and thus the heat flow from the high temperature fluid is not equal to the heat flow to the low temperature.

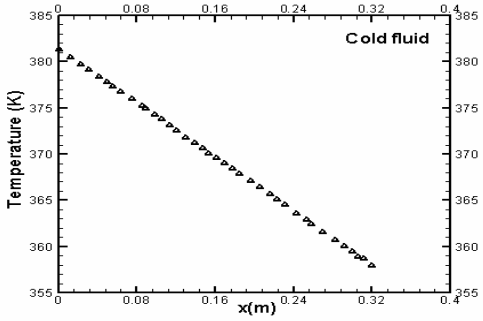

Fig. 6: Temperature profile of the cold fluid along the conical nozzle

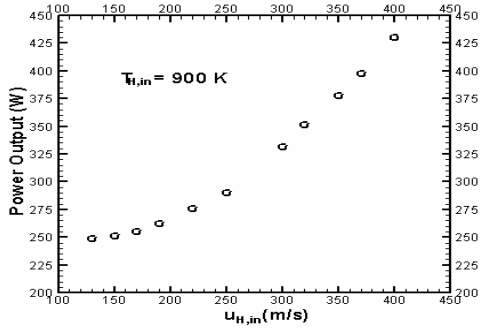

Fig. 7: The variation of power output with the hot fluid inlet velocity

We note that the power output increases with the increase in the inlet velocity for a fixed inlet temperature. This result can also be explained by the fact that the convective heat transfer coefficient is changed when varying the profile velocity through the conical nozzle. This change

also brings a change in the thermal resistances of the conical nozzle, results in an increase in the average temperature through the modules and therefore, an increase in the power output. Obviously, the hot fluid differential pressure through the conical nozzle also increases when the inlet velocity is increased. Therefore the appropriate inlet velocity should be determined to meet the optimal operating conditions for real thermoelectric generators. We can also note that the choice of the inlet parameters affects the design of the conical nozzle, due to the compressibility effects. Due to the energy conservation through the conical nozzle the increases in the inlet velocity lead to the increase in the hot fluid temperature through the conical nozzle (see Fig. 8).

4. Conclusion

A numerical model for a thermoelectric generator with a conical nozzle was proposed. This model is based on one-dimensional differential equations representing conservation equations for the compressible hot fluid and the incompressible cold fluid. These equations are restructured and linked to the formulations of thermoelectric modules. The proposed model gives much more detailed predictions for the fluid temperature variations through the thermoelectric modules along the conical nozzle.

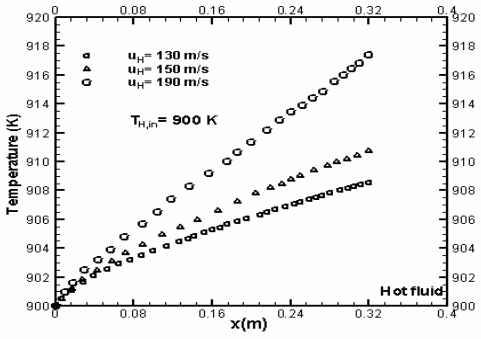

Fig. 8: The variation of the hot fluid temperature profile with the hot fluid inlet velocity

It is found that the power output is sensitive to the physical properties of the hot fluid at the inlet face of the conical nozzle.

Nomenclature

A Heat transfer coefficient, W/(m^{2}K)
c specific heat capacity, J/(kg.K)
D Diameter, m
E Total energy, J
I courant, A
K thermocouples thermal conductance, (W/K)
L Length of the conical nozzle, m
H enthalpy, J
h specific enthalpy, J/kg
M Mach number
$\dot{m}$ mass flow rate, kg/s
n_{TE} number of thermocouples
Nu Nusselt number
p pressure, Pa
Pr Prandtl number
P_o power output, W
Q the rate of the heat flow, W
R_{elec} electrical resistance, Ω
Re Reynolds number
R_{load} load electrical resistance, Ω
R_{th} total thermal resistance, K/W
S Area, m^2
T Temperature, K
u velocity, m/s
V volume, m^3

Greek symbols

α Seebeck coefficient, V/K
λ thermal conductivity, W/(mK)
ρ density, kg/m^3

Subscripts

C cold fluid
H hot fluid
in inlet

References

[1] Saqr, K.M., Mansour, M.K., Musa, M.N., 2008, Thermal design of automobile exhaust based thermoelectric generators: objectives and challenges, International Journal of Automotive Technology, 9, pp. 155-160

[2] Matsuura, K., 1993, Large scale thermoelectric generation of low-grade heat, the future. In Proceedings of 12th international conference on thermoelectrics, pp. 439-46.

[3] Yodovard, P., Khedari, J., Hirunlabh, J., 2001, The potential of waste heat thermoelectric

power generation from diesel cycle and gas turbine cogeneration plants, Energy Sources, 23, pp.213-24.

[4] Kametani, S., Fujita, T., Kajikawa, T., Yamaguchi, K., 2006, Application of thermoelectric conversion modules to cogeneration systems, In: 25nd International Conference on Thermoelectric.

[5] Chen, M., Lund, H., Rosendahl, L.A., Condra, T.J., 2009, Energy efficiency analysis and impact evaluation of the application of thermoelectric power cycle to today's CHP systems, Applied Energy, 78, pp. 1231-1238.

[6] Bhandari, C.M., Rowe, D.M., 1988 Thermal conduction in semiconductors, Wiley Eastern Ltd.

[7] DiSalvo, F.J., 1999, Thermoelectric cooling and power generation, Science, 285, pp.703-6

[8] Bell, L.E., 2008, Cooling, heating, generating power and recovering waste heat with thermoelectric systems, Science, 231, pp.1457-61

[9] Chen, G., 2003, Recent developments in thermoelectric materials, Int. Mater. Rev. 48, pp.45-66.

[10] Vining, C., 2008, Desperately seeking silicon, Nature, 451, pp.132-3.

[11] Wu, C., 1996, Analysis of waste-heat thermoelectric power generators, Appl. Therm. Eng. 16, pp. 63-69.

[12] Esarte, J., Gao, M., Rowe, D.M., 2001, Modeling heat exchangers for thermoelectric generators, J. Power Sources 93, pp.72-76.

[13] Stevens, J.W., 2001, Optimal design of small ΔT thermoelectric generation systems, Energ. Conv. Manage. 42, pp.709-720.

[14] Crane, D.G., Jackson, G.S., 2004, Optimization of cross flow heat exchangers for thermoelectric waste heat recovery, Energy Conversion and Management 45, pp.1565-1582.

[15] Suzuki, R.O., Tanaka, D., 2003, Mathematical simulation of thermoelectric power generation with the multi-panels, Journal of Power Sources, 122, pp.201-209.

[16] Suzuki, R.O., Tanaka, D., 2003, Mathematical simulation of thermoelectric power generation with cylindrical multi-tubes, Journal of Power Sources, 124, pp. 293-298.

[17] Yu, J., Zhao, H, 2007, A numerical model for thermoelectric generator with the parallel-plate heat exchanger, Journal of Power Sources 172, pp.428-434.

[18] Rowe, D.M., 2006, Thermoelectric waste heat recovery as renewable energy source, International Journal of Innovations in Energy Systems and Power, 1, pp. 13-23.

[19] Esarte, J., Min, G., Rowe, D.M., 2001, Modelling heat exchangers for thermoelectric generators, Journal of Power Sources 23, pp. 72-76.

[20] Melcor, 2007, available from: http://www.melcor.com/pdf/thermoelectric%20Handbook.pdf.

[21] Kousksou, T., Dick, E., Bruel, P., 2010, On the role played by numerical dissipation in some unsteady low Mach number flows computations, Fifth European Conference on Computational Fluid Dynamics (ECOMAS CFD), Lisbon, Portugal.

[22] Nerinckx, K., Vierendeels, J., Dick, E., 2005, Mach-uniformity through the coupled pressure and temperature correction algorithm, Journal of Computational Physics, 2006, pp.597-623.

[23] Kousksou, T., Majid, J., Bruel, P., 2010, Asymptotic Behavior of a Storage Unit Undergoing Cyclic Melting and Solidification Processes, AIAA Journal of Thermophysics and Heat Transfer, 43, pp.31-41.

[24] Shah, R.K., Bhatti, M.S., 1987, Handbook of Single Phase Convective Heat Transfer, Chap.3, Wiley-Inter-Science.

[25] Angrist, S.W., 1982, Direct Energy Conversion, 4th Edn. Allyn and Bacon, Boston.

Preliminary design of a torque converter for a GT-sport car

Marco De Petris[a], Francesco Toti[a], Christian Kupper[b]

[a] *"Sapienza" University of Rome, Department of Mechanical and Aeronautical Engineering, Rome, Italy*
[b] *Technische Universität Berlin, Faklutät III – Prozesswissenschaften, Berlin, Germany*

Abstract: Based on the engine performance maps of a super sports car of the GT class, with a maximum shaft power of 320 kW at 7000 rpm and a maximum torque of 490 Nm at 4800 rpm, a preliminary design of the torque converter has been developed and analyzed. The design is calibrated for a characteristic regime of the engine that ensures the maximum efficiency of the torque converter.

The configuration follows a quite conventional layout, with a centrifugal pump with a smaller diameter than that of the centripetal turbine. A smooth connection between the two rotors is attained by the interposition of a properly designed statoric channel. The general objective of the design is to maximize the efficiency of the fluid dynamic coupling between the working fluid (transmission oil) and the statoric and rotoric passages. The preliminary design of the blading is performed on the basis of available operational maps for radial pumps and centripetal turbines operating on incompressible fluids.

Keywords: Torque converter, hydraulic turbomachinery.

1. Introduction

The hydraulic torque converter (HTC in the following) is a complex turbomachinery used to transfer power from an engine to a transmission. It consists of three main elements: a pump connected to the engine shaft, a turbine that supplies the output torque and a stator. The HTC has two main functions: first, it provides a torque multiplication when turbine is blocked, this situation is called the stall condition and supplies the required high acceleration at start-up or at very low speeds. Secondly, it improves driveability by dampening the effects of road-induced disturbances from the vehicle body onto the engine and vice versa. It offers several additional advantages, such as protecting the engine in case of overload, cutting or absorbing the torsional vibration or impact of shaft system to extend the service life of components, and enabling automatic speed shifting. On the other hand, its maximum efficiency is low, i.e. 80% to 90% (compared with 95% attainable with a good gear transmission). This leads to an increased fuel consumption especially when operating at low speed, which is often encountered in real missions. Thus, a good design procedure is mandatory to obtain a high-efficiency HTC: this implies a good understanding of the complex fluiddynamics in the passages. However, it is not easy to identify the most convenient blade shape that can effectively control the flux in the complicated machinery channels, where fluid circulates along the blades of pump, turbine and stator, and the curvature of the passages is changing in the streamwise direction.

The peculiarity of the study presented in this paper consists in the HTC design method itself. No component-specific models and no semi-empirical torque converters similarity relations have been employed. In fact, the method adopted is consistent (with proper adjustments) with the design of any kind of turbomachinery. This is based on a set of fluid dynamic equations, constraint equations and similarity equations, which leads to a N-undetermined system of equations, where N -the number of design variables to be arbitrarily chosen by the designer- is called the degree of freedom, and depends on the type of machine.

Such an approach can be optimally matched with a properly programmed series of CFD calculations, to obtain both a more accurate performance

Corresponding Authors: Marco De Petris, Email: mr.depetris@gmail.com ; Francesco Toti, Email: francesco_toti@msn.com

assessment and a deeper insight into the real phenomenology.

2. Design method setting

The aim of this paper is the development of a general design method setting of a torque converter for automotive transmissions.

The design starts from the specifications defined by choosing the operative point, than proceeds by the classical approach of turbomachinery design resumed in the following point:

1. Choice of n_S and d_S for the impeller pump, which correspond to a given efficiency from Baljie charts.
2. Select a tentative value for inlet absolute velocity of the impeller.
3. Completion of the impeller's design by assignation of starting values for b_2/D_2, D_2/D_{1e}, D_1/D_2.
4. Choice of d_S for the turbine (based on the n_S imposed by the impeller) and its relative efficiency.
5. Assignation of a tentative value for the Euler work of the stator.
6. Choice of a tentative value for outlet absolute velocity of the turbine.
7. Complete of the turbine design by imposing its constraints and assuming a tentative value for the parameter b_1/D_1.
8. Adjustment of starting values of the impeller pump to satisfy the constraint on the Euler work (the Euler work gained by the fluid has to be the same of the work lost).
9. The stator has inlet and outlet kinetic conditions imposed by pump and turbine, so it's necessary to fix only its angular velocity.
10. Adjustment of geometrical entities of the three rotors to ensure the pressure's balance.

2.1. Choice of the pump, turbine and stator impellers type

Typically, the rotors configuration is derived by geometrical and functional constraints. Generally, radial rotors are utilized for pump and turbine, while axial stage is employed for stator. However, the shape of the actual torque converters impellers is quite different from the existing ones, which correspond to many tables, plots and operating maps in literature. Moreover, no one of the rotors is coupled with statoric blades.

In this work we adopt blade shapes similar to common impellers, such as radial hydraulic pumps and Kaplan impellers. In this way it was possible to operate through similitude's criteria.

Torque converter is subjected to considerable and rapid rotating speed variations. The preliminary design is referred to the operating point that corresponds to the maximum efficiency operating condition .

In Figure 1 is shown a tentative outline of a classic automotive torque converter.

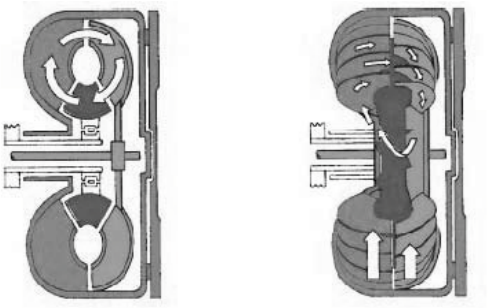

Figure 1. Scheme of an automotive torque converter

2.2. Design method description

In the design procedure some simplification were adopted: flow is stationary and inviscid, the fluid path is helical[1]. Moreover, there are no pressures and velocity gradients on the circumferential direction of the toroid.

The following equations are referred to the center of the flow area.

FLUID DYNAMIC EQUATION:

- $P = Q\rho L_E$ (1)
  for pump impeller;
- $Q = \frac{\pi}{4}\left(D_e^2 - D_i^2\right)\cdot U \cdot \varphi \cdot \delta_b$ (2)
  for planar annular sections;
- $Q = \pi \cdot D \cdot b \cdot U \cdot \varphi \cdot \delta_b$ (3)
  for cylindrical annular sections;
- $L_E = U_2V_2 - U_1 V_1$ (4)
  for pump impeller;
- $L_E = U_1V_1 - U_2 V_2$ (5)

[1] The flow path line is helical-centripetal for the turbine, helical-centrifugal for the impeller and helical for the stator.

for turbine runner and stator;

- $U = \omega \cdot D/2$ (6)
- $D = \frac{D_e + D_i}{2}$ (7)

CONSTRAINTS:

- The mass density is constant;
- V_{1t} imposed for impeller;
- V_{2t} imposed for turbine.

Other constraints are imposed by the shape of the stator: diameters at the inlet section are equal to the diameters at the outlet section. Thus:

- $D_{1S} = D_{2T}$
- $D_{2S} = D_{1P}$

Generally, imposing the proper equations for impeller and turbine results:

16 unknown variables – 8 equations – 3 design specifications = 5 degree of freedom.

Similarly we have, for axial stator, 2 d.o.f.

The procedure starts from the design of the impeller, so - for turbine and stator - the number of d.o.f. was reduced due to the following additional constraints:

- $Q_P = Q_T = Q_S$
- $D_{2T} = D_{1P}$
- $L_{E,T} = \eta_T \eta_S L_{E,P}$
- $L_{E,S} = \eta_P L_{E,P} - L_{E,T}$

This it is necessary to choose 2 d.o.f. for turbine and 1 d.o.f. for stator.

To close the procedure, it is necessary to consult Baljie charts referred to hydraulic stages[2].

For the pump impeller the study of Baljie charts allows to reduce the number of d.o.f from five to three, by imposing two additional constraints (n_S and d_S).

[2] Baljie charts are relative to the performances of single stages operating with: $Re \cong 10^8$, while the fluid used for torque converter is a low dynamic viscosity oil. This led to a lower Reynolds number, about: $Re \cong 10^6$, that implies a defect in the rotors efficiency. This correction was computed by:

$$\frac{1-\eta}{1-\eta_{ref}} = 0.50 + 0.50 \cdot \left[\frac{Re_{ref}}{Re}\right]^{0.084 \cdot \left(\frac{Re_{ref}}{Re}\right)^{0.25}} \quad [3]$$

The remaining three d.o.f. for impeller are provided by similitude criterion: imposing attempt value for geometrical entities, starting from existing values present in literature and proceeding with iterations until the exact ones, such as:

$$\frac{b_2}{D_2} \qquad \varepsilon = \frac{D_2}{D_{1e}} \qquad \frac{D_1}{D_2}$$

For turbine we need two choices:

- d_s specific diameter selected by Baljie charts (n_S is given for the turbine)
- b_1/D_1 selected by tables for hydraulic turbine

The stator has only one degree of freedom, solved by deciding the spin and modulus of the rotational speed, to avoid the exceeding maximum deviation for axial stages.

2.3. Blade shaping

Blade shaping is the remaining task to complete the preliminary design of the torque converter.

This step concerns some choice like the blade twist law, the choice of the blades' number, the design of the sectional areas along the design path.

For the blade twist it was chosen a free-vortex variation of absolute tangential velocity, that causes the blade relative angle's distribution. This assumption implies that Euler work remains constant along the radial edges of blading. Secondly, the blades number was computed using Stepanof law:

- $Z_b = \beta_2/3$, for impeller (8)
- $Z_b = K/\sqrt{\psi_1}$ $K = 14 \div 16$, for turbine (9)
- Z_b selected for stator by Howell charts. Howell charts for axial blading solidity were utilized with β_1 and $\Delta\beta = \beta_1 - \beta_2$ known, than having: $\sigma = l/t$. Thus, by the blade aspect ratio, the chord length was chosen and then the blade angular pitch resulted.

Those experimental laws determine a number of blades that was smoothly modified in order to have the required sectional area aspect ratios and to make sure that the impeller, turbine and stator's blade numbers were prime between themselves, avoiding striking phenomenon. Being the inlet diameter of the turbine such different from the outlet, vanes sectional area aspect ratios would be different along the vane itself. It has been necessary to introduce a splitter coefficient in the turbine from its inlet section to half vanes length.

Moreover, this choice allows to redistribute forces on a major number of elements.

The area variation laws has been obtained with the aim to avoid geometrical discontinuities and pressure gradients at the inlet/outlet sections.

Finally, blade angles computed by velocity triangles were modified by the real flow behavior. The corrected relative blade angles are obtained from the ideal ones by considering the sleep coefficient: $\sigma_{Stodola} = V_{2t,real} / V_{2t,ideal}$, that allows also to calculate the number of blades.

3. Preliminary design results

Design point has been fixed by the choice of a mid-range engine speed. Table 1 presents torque, power and regime values adopted for pump impeller.

Table 1. Design input specifications.

DESIGN SPECIFICATIONS	
T (Nm)	450
n (rpm)	3000
P (kW)	141
ρ_{oil} (kg/m^3)	850

The following tables present some design results obtained after a several number of iterations, due to the interfacing of the torque converter's parts.

In the passage through rotors the oil flow is subjected to stagnation enthalpy variation, so that it's necessary to adjust sectional areas parameters till the fluid flow is guided through a closed loop of adiabatic transformations.

Relative blade angles in Table 2 and 3 are referred to the "corrected angle".

Table 2. Pump impeller specifications.

PUMP IMPELLER	
Specifications	
ω_P (rad/s)	314
n_s	0.55
d_s	4.5
Q (m^3/s)	0.134
L_E (m^2/s^2)	1241
D_2 (m)	0.278
Design parameters	
D_1/D_2	0.61
b_2/D_2	0.09
$\varepsilon = D_2/D_{1a}$	1.5
Inlet section	
b_1 (m)	0.013
D_1 (m)	0.169
U_1 (m/s)	26.6
φ_1	0.89
ψ_1	0.65
$\beta_{1,tip}$ (deg)	67
$\beta_{1,mid}$ (deg)	69
$\beta_{1,hub}$ (deg)	70
Outlet section	
b_2(m)	0.022
D_2 (m)	0.278
U_2 (m/s)	43.6
φ_2	0.20
ψ_2	0.89
$\beta_{2,tip}$ (deg)	52
$\beta_{2,mid}$ (deg)	46
$\beta_{2,hub}$ (deg)	41
Z_b	23

Table 3. Turbine specifications.

TURBINE RUNNER	
Specifications	
$\nu = \omega_T/\omega_P$	0.5
ω_T (rad/s)	157
n_s	0.4
d_s	5
Q (m^3/s)	0.134
L_E (m^2/s^2)	980
D_1 (m)	0.348
Design parameter	
b1/D1	0.05
Inlet section	
b_1 (m)	0.017
D_1 (m)	0.348
U_1 (m/s)	27.4
φ_1	0.32
ψ_1	1.14
$\beta_{1,tip}$ (deg)	51
$\beta_{1,mid}$ (deg)	71
$\beta_{1,hub}$ (deg)	92
Outlet section	
b_2(m)	0.013
D_2 (m)	0.169
U_2 (m/s)	13.3
φ_2	1.8
ψ_2	0.5
$\beta_{2,tip}$ (deg)	80
$\beta_{2,mid}$ (deg)	77
$\beta_{2,hub}$ (deg)	75
Z_b	25+25 s.b.

Stator was designed to be an axial reaction turbine. Its role is redirecting flow coming from turbine towards the impeller and giving the torque multiplication. As shown in Figure 2 stator is mounted between the turbine and the pump and

redirects the flow from the turbine to the pump impeller vanes. The interposition of this element permits to overcome the counterproductive force of fluid coming from the turbine opposing engine rotation.

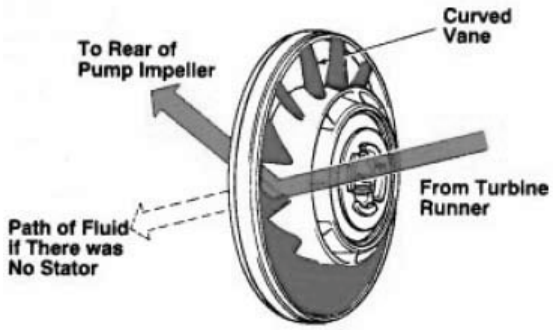

Figure 2. Stator flowpath.

Table 4. Stator specifications.

STATOR	
Specifications	
Q (m^3/s)	0.134
L_E (m^2/s^2)	71
$D_1 = D_2$ (m)	0.169
Design parameter	
ω_s (rad/s)	79
Inlet section	
$U_1 = U_2$ (m/s)	6.6
$\beta_{1,tip}$ (deg)	56
$\beta_{1,mid}$ (deg)	61
$\beta_{1,hub}$ (deg)	66
Outlet section	
$\beta_{2,tip}$ (deg)	43
$\beta_{2,mid}$ (deg)	45
$\beta_{2,hub}$ (deg)	47
Z_b	21

Torque ratio, for given engine regime and speed ratio, is: $\mu = 1.36$.

4. CAD renderings

Below are represented some results of CAD renderings. This activity has been carried out using general-purpose CAD/CAE software ANSYS and SOLIDWORKS. Figure 3 and Figure 4 show the sectional area variation of vanes for impeller and turbine along the design path.

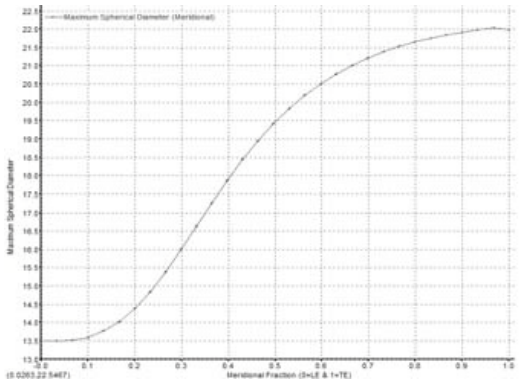

Figure 3. Pump vane's sectional area variation. Ordinate is the maximum spherical diameter varying with meridional fraction.

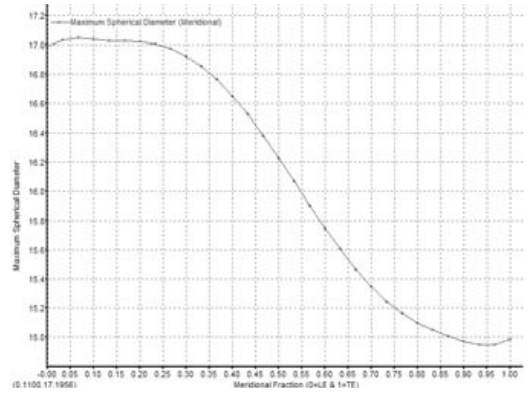

Figure 4. Turbine vane's sectional area variation. Ordinate is the maximum spherical diameter varying with meridional fraction.

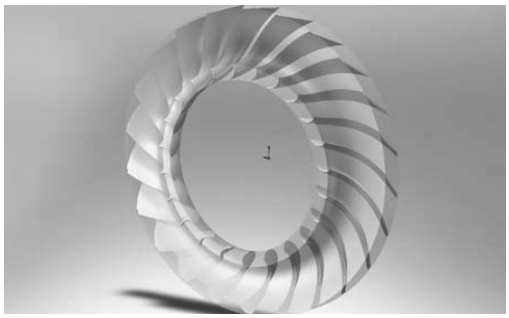

Figure 5. CAD renderins of the impeller

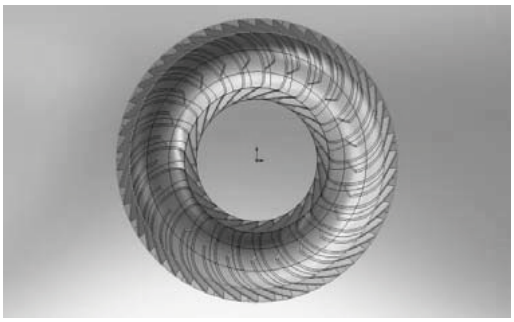

Figure 6. CAD rendering of the turbine.

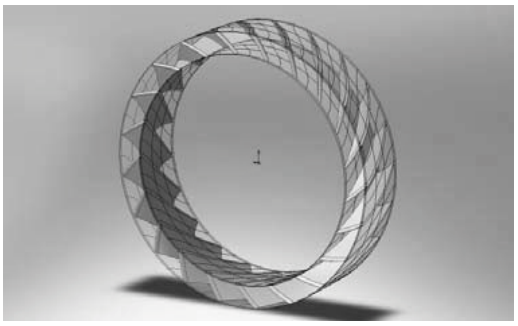

Figure 7. CAD rendering of the stator.

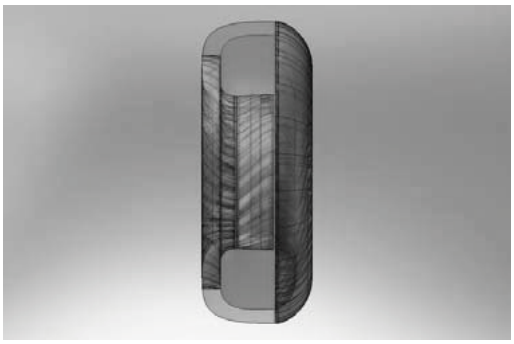

Figure 8. CAD rendering of the torque converter assembly.

5.Conclusions

This work is finalized to improve a simple preliminary design method setting for automotive torque converter design. The only input data is the engine torque-rpm relation, which allows to select the specific regime to which referring the entire machine sizing. The three elements composing the torque converter were design separately (considering the constraints that were imposed by the interfacing of the rotors), throughout similitude criteria relating to always built hydraulic machines. Every choice involves proper consequences about interfacing with other elements of the assembly.

The results obtained are supported by general performance curves about efficiency and torque ratios found in literature.

Finally, the aim of this work is giving evidence to a simple and alternative method for the torque converter's preliminary design.

Nomenclature

b blade height, m
D average diameter, m
D_e external diameter, m
D_i internal diameter, m
d_s specific diameter
l chord length
L_E Euler work, J/kg [m^2/s^2]
n rev per minute, rpm
n_s specific speed
P mechanical power, W [m^2/s^3]
Q volumetric flow rate, m^3/s
Re Reynolds number
T input torque, Nm
t blade angular pitch
U peripheral velocity, m/s
V absolute velocity, m/s
V_t tangential absolute velocity, m/s
Z_b number of blades

Greek symbols

β relative blade angle, deg
δ_b blade size coefficient
φ flow coefficient
η hydraulic efficiency
μ torque ratio
ν speed ratio
ω angular velocity, rad/s
ψ head coefficient
ρ mass density, kg/m^3
σ cascade solidity

Subscripts and superscripts

1 Inlet
2 Outlet
P Impeller pump
T Turbine runner

S Stator

B Blade

mid Midspan designpath

References

[1] Sciubba, E., 2001, *Lectures on Turbomachinery* , ed., Euroma, Roma.

[2] Capata, R., and Sciubba, E., 2004, *Selected Design Problems in Turbomachinery*, ed., Euroma, Roma.

[3] Capata, R., and Sciubba, E., 2007: *Effects of the Reynolds Number on the Performance of a Nano Compressor*, *ECOS 2007,* Padova, Italy.

[4] Kano, S., and Terasaka, Y., and Yano, K., 2004, *Prediction of Torque Converter Characteristics by Fluid Flow Simulation,* Komatsu Technical Report, Vol. 50 No. 154, URL: http://www.komatsu.com/Company Info/ profile/report/pdf/154-02_E.pdf.

[5] Kim, B. S., et al, 2008, *Performance Estimation Model of a Torque Converter. Part I: Correlation between the Internal Flow Field and Energy Loss Coefficient,* International Journal of Automotive Technology, Vol. 9, No. 2, pp. 141-148.

[6] Lechner, G., and Naunheimer, H., 1999, *Automotive Transmissions*, ed., Springer, Berlin.

Acknowledgments: The authors would like to acknowledge the help of Proff. E. Sciubba and R. Capata in the development of the Senior Project from which this paper has been originated, and the ECOS Scientific Committee for this precious opportunity to participate to ECOS'2010.

Experimental Real-Time Optimization of a Solid Oxide Fuel Cell Stack via Constraint Adaptation

Gene A. Bunin [a], *Zacharie Wuillemin* [b], *Grégory François* [a], *Arata Nakajo* [b], *Leonidas Tsikonis* [b], *and Dominique Bonvin* [a]

[a] *Ecole Polytechnique Fédérale de Lausanne (Laboratoire d'Automatique), Lausanne, Switzerland*
[b] *Ecole Polytechnique Fédérale de Lausanne (Laboratoire d'Energétique Industrielle), Lausanne, Switzerland*

Abstract: The experimental validation of a real-time optimization (RTO) strategy for the optimal operation of a solid oxide fuel cell (SOFC) stack is reported in this paper. Unlike many existing studies, the RTO approach presented here utilizes the constraint-adaptation methodology, which assumes that the optimal operating point lies on a set of constraints and then seeks to satisfy those constraints in practice via bias update terms. These biases correspond to the difference between predicted and measured outputs and are updated at each steady-state iteration, allowing the RTO to successfully meet the optimal operating conditions of a 6-cell SOFC stack, despite significant plant-model mismatch. The effects of the bias update filter values and of the RTO frequency on the power tracking and constraint handling are also investigated.

Keywords: Applied Fuel Cell Modeling, Constraint Adaptation, Optimal Fuel Cell Performance, Real-Time Optimization, SOFC Load Tracking, SOFC Operation.

1. Introduction

In the recent decade, fuel cells have received growing attention as viable energy alternatives, advocated as a cleaner and more efficient energy source. There remains, however, a number of open problems with fuel cell technology that must be resolved before it can be put into widespread use and become a practical, capable substitute for current methods. One of these issues lies in the life of a cell, which can be shortened significantly if the system does not successfully adhere to certain safe operating regions, qualified by constraints on certain input and output variables. In addition to simply being safe, the cell must also perform optimally and be able to operate at the highest efficiency for any immediate power demand. For these reasons, the domains of control and optimization have been increasingly called upon for improved fuel cell performance. Unfortunately, despite a large number of theoretical contributions - the majority of which have focused on control (see, for example, [5] or [13]) and few on optimization ([6] and [14]) - there still remains a large gap between simulation studies and reported experimental results. To the best of the authors' knowledge, all experimental studies so far have been limited to proton exchange membrane (PEM) cells ([1, 12, 9]), and many have sought efficiency based on specific criteria that were already known in advance, rather than formally treating the cell as a multiple-input, constrained optimization problem with changing optimal conditions.

In this paper, a previously developed and simulated constraint-adaptation methodology ([7]) is validated experimentally for a 6-cell SOFC stack. Unlike the method in [6], which seeks to track an optimality criterion via model-predictive control, or the approach in [14], which aims to achieve optimality by tracking the flow-dependent maximum power, the constraint-adaptation methodology discussed here works on the very simple - yet often true - premise that the optimum of the problem lies somewhere on the constraints. Therefore, if the proper set of constraints can be met in practice, then the optimality of the process is guaranteed as well. Because of uncertainty, the values of the constrained quantities given by the model will rarely match those provided by the real system, and so an adaptation - carried out by adding a bias term to the modeled constraints - is used to ensure that the constraints used by the optimization match those of the real system. In doing so, the RTO iteratively drives the system to the true constraints, with the speed of convergence dictated

Corresponding author: Dominique Bonvin, Email: dominique.bonvin@epfl.ch

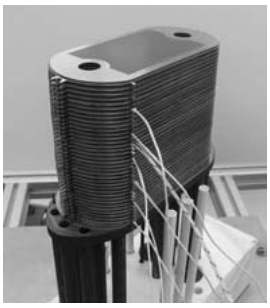

Figure 1: The setup of a typical stack.

by the way the bias update is filtered. As a demonstration of its robustness to uncertainty, the ability of this method to reject long-term system degradation has been shown via simulation in [2].

This paper will be structured as follows. In Section 2, the description of the experimental apparatus and a summary of the model used for the SOFC stack will be given. In Section 3, the constraint-adaptation methodology will be discussed in detail. Its application to the real system will then be outlined and the tested scenarios explained. Section 4 will focus on the results - looking not only at the general performance of the experimental stack, but also at the effects of altering the bias filters and optimization frequency, and Section 5 will conclude the paper.

2. System Description

2.1. Experimental Setup

2.1.1. Design and Interface

The study presented in this article concerns an SOFC short-stack developed at EPFL for HTceramix-SOFCpower ([11, 4]). This stack consists of planar anode-supported cells with an active area of 50 cm^2, pressed between gas-diffusion layers (SOFConnex^{TM}) and metallic interconnector plates. The anodes are made of standard nickel/yttrium-stabilized-zirconia (Ni-YSZ) cermet, while the thin electrolyte consists of dense YSZ. The cathodes are made of screen-printed $(La, Sr)(Co, Fe)O_3$, allowing standard operation temperatures between 650°C and 850°C. A detailed description of its construction can be found in [11], and a photo of a typical assembly is given in Fig. 1. A stack of 6 cells was used for this study.

The stack was placed in a high-temperature furnace at 775°C and connected to a testing station providing controlled flow rates of air and preheated fuel (~770°C). Additionally, an active load was used to control the delivered current. The control of the testing station was ensured by a LabVIEW interface in which the RTO algorithm was implemented via a MATLAB Script function.

2.1.2. System Constraints

Two key constraints limit the efficiency in an SOFC. While the cell may deliver a given electrical power at several different operating conditions (different fuel flows and currents), the maximum electrical efficiency is usually found close to the highest achievable fuel utilization (70-90%) - defined as the percentage of the fed fuel that reacts. However, to prevent damages to the stack by local fuel starvation and reoxidation of the anode [11], a conservative maximum fuel utilization of 75% is set. In addition, it is known that significant internal losses are detrimental to SOFC stacks. These losses appear as differences between the ideal and measured cell potential (overpotentials). Therefore, a minimum cell voltage of 0.75V is set to protect the stack from accelerated degradation, resulting in the second major constraint for the system.

In addition, the air excess ratio (or just the "air ratio"), defined as the stoichiometric ratio between the oxygen fed to the system and the oxygen needed to react with the fuel, must be kept within certain bounds so as to avoid steep thermal gradients. For this setup, the ratio is kept between 4 and 7. A lower bound of 3.14 ml/(min · cm^2)[1] is also placed on the fuel feed rate so as to avoid local (or widespread) fuel starvation, and an upper bound of 30A is placed on the current to avoid excessive heating ([7]).

To avoid damaging the stack, limits on the rate of input changes were defined as 0.54 ml/(min^2 · cm^2), 1.37 ml/(min^2 · cm^2), 2.0 A/min for the hydrogen flow, oxygen flow, and current, respectively. Conditional laws were written into the LabVIEW code so that any of these rates could be set to 0 in the case of a fuel utilization or air ratio violation.

2.2. Steady-State SOFC Model

The steady-state model used to optimize the stack is largely similar to that which has been previously reported in [7]. As such, only the most fundamental elements of the model, or any deviations from prior reported work, are given here. For a full and detailed treatment, the interested reader is referred to [7].

[1] All flux values, given in ml/(min · cm^2), are calculated under normal conditions.

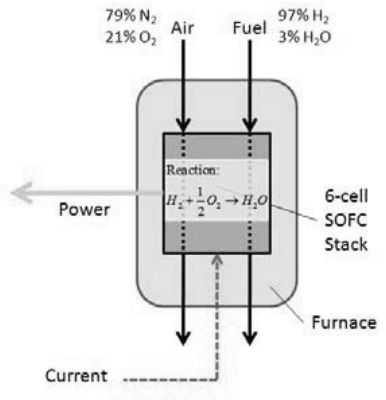

Figure 2: The diagram of the SOFC system. A fuel feed that is 97% hydrogen, 3% water is sent through the anode, while air is fed through the cathode. The stack is polarized with an exogenous current.

As mentioned in the previous section, the SOFC is a system fed with O_2 (air stream) and H_2 (fuel stream), which react electrochemically to produce electrical power and heat. The fuel cells are usually assembled in stacks in order to reach the desired voltage, and require an outside current source to operate (Fig. 2).

Three inputs are used to control the operation of the stack: the hydrogen flux $\dot{n}_{H_2}$ (in ml/(min · cm^2)), the oxygen flux $\dot{n}_{O_2}$ (in ml/(min · cm^2)), and the current I (in A):

$$\mathbf{u} = \begin{bmatrix} \dot{n}_{H_2} \\ \dot{n}_{O_2} \\ I \end{bmatrix}. \tag{1}$$

As will be shown in the following section, the three outputs of interest are the power density p_{el} (in W/cm^2), the cell potential U_{cell} (in V), and the electrical efficiency η. The potential is modeled based on the equivalent circuit approach ([8]) :

$$\begin{aligned} U_{cell} = U_N - U_{act,c} - U_{i,e} - U_{dis,c} \\ - U_{dif,a} - U_{dif,c} - U_{MIC}. \end{aligned} \tag{2}$$

Here, U_N denotes the reversible cell voltage, while $U_{act,c}$, $U_{dis,c}$, $U_{dif,a}$ denote the non-Ohmic overpotential losses (cathode activation, cathode oxygen dissociation, and diffusion at the anode, respectively). $U_{i,e}$, $U_{dif,c}$, and U_{MIC} denote the Ohmic losses (ionic conductivity, diffusion through the cathode, and metallic interconnect, respectively). The latter, not mentioned in [7], is defined as:

$$U_{MIC} = (R_{MIC,1} + R_{MIC,2})\, I, \tag{3}$$

with $R_{MIC,1}$ and $R_{MIC,2}$ denoting the resistances of the two interconnects.

The values of p_{el} and η follow as functions of U_{cell}:

$$\begin{aligned} p_{el} &= \frac{U_{cell} N_{cells} I}{A_c} \\ \eta &= \frac{p_{el} A_c}{\dot{n}_{H_2} Q_L}, \end{aligned} \tag{4}$$

where N_{cells} is the number of cells in the stack, A_c is the active area of the cell, and Q_L is the lower heating value of the fuel. Unlike in the work in [7], the parasitic power demand of the air blower is not included in the definition of η.

Because U_{cell}, and thus also p_{el} and η, depend substantially on the temperature of the stack ([7]), an energy balance is also required, and may be expressed as:

$$mc_P \frac{dT}{dt} = -\Delta \dot{H}_{gas} - p_{el} A_c - \dot{Q}_{loss}, \tag{5}$$

with m, c_P, and T used to express the mass, specific heat capacity, and temperature of the stack, respectively. $\Delta \dot{H}_{gas}$ denotes the enthalpy change for the gases, while $\dot{Q}_{loss}$ denotes the radiative heat loss calculated as:

$$\dot{Q}_{loss} = A\alpha\sigma_{SB}(T^4 - T_{furn}^4), \tag{6}$$

where A is the area of the stack, α is a transfer factor, σ_{SB} is the Stefan-Boltzmann factor, and T_{furn} is the temperature of the furnace.

To calculate the steady-state values of U_{cell}, p_{el}, and η, it is first necessary to integrate Eq. 5, and to use the resulting steady-state temperature to obtain the values of the potential, power, and efficiency. As a result, while the response of these quantities to changes in the inputs is practically instantaneous, the true steady state of the system is governed by the temperature as it gradually reaches its new value. While some SOFC systems may have additional dynamics depending on their setup ([10]), it is assumed that, for the system at hand, these two time scales - one instantaneous and one on the magnitude of approximately 30 minutes - are the only significant ones.

In testing this model against the real SOFC stack, one can see a divergence between the predicted potential and the actual value when the current is increased (Fig. 3). This is particularly crucial for the current range 18 to 25A, which is used throughout many of the experiments (Section 4.). However,

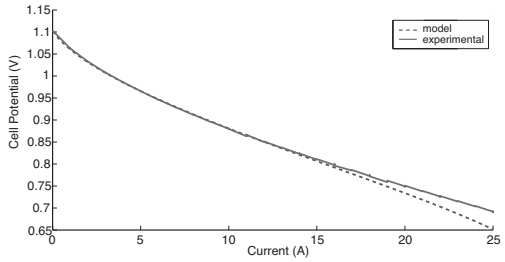

Figure 3: Current-potential (IV) curve for $\dot{n}_{H_2} = 5$ ml/(min · cm^2), $\lambda_{air} = 4$.

the constraint-adaptation methodology, introduced next, is an excellent tool for dealing with this deviation.

3. RTO via Constraint Adaptation

3.1. Methodological Overview

Process optimization typically involves the minimization of a cost (or the maximization of a profit) that is subject to certain equality and inequality constraints. This results in a nonlinear programming (NLP) problem which, for the system described in Section 2., may be written as:

$$\begin{aligned} \max_{\mathbf{u}} \quad & \eta(\mathbf{u}, \boldsymbol{\theta}) \\ \text{s.t.}: \quad & p_{el}(\mathbf{u}, \boldsymbol{\theta}) = p_{el}^S \\ & U_{cell}(\mathbf{u}, \boldsymbol{\theta}) \geq 0.75 \text{ V} \\ & \nu(\mathbf{u}) \leq 0.75 \\ & 4 \leq \lambda_{air}(\mathbf{u}) \leq 7 \\ & u_1 \geq 3.14 \text{ ml/(min cm}^2) \\ & u_3 \leq 30 \text{ A}, \end{aligned} \tag{7}$$

with the electrical efficiency η acting as the profit function to be maximized. Here, the superscript S denotes the setpoint for the power demand, effectively giving the optimization a second role as a load-following controller. The fuel utilization, ν, and the air ratio, λ_{air}, may be expressed in terms of the inputs as:

$$\nu = \frac{N_{cells} I}{2 \dot{n}_{H_2} F} = \frac{N_{cells}}{2F} \frac{u_3}{u_1} \tag{8}$$

$$\lambda_{air} = 2 \frac{\dot{n}_{O_2}}{\dot{n}_{H_2}} = 2 \frac{u_2}{u_1}, \tag{9}$$

where F is the Faraday constant.

The vector of uncertain parameters $\boldsymbol{\theta}$ in (7) is used to represent the model parameters that do not match those of the real system.

With the steady-state model described in Subsection 2.2., the NLP problem (7) may be solved to obtain an optimal set of inputs that theoretically maximizes the cell efficiency while satisfying all the constraints. However, due to plant-model mismatch and process disturbances, this nominal solution is unlikely to be optimal for the actual SOFC system. For the system presented in this article, the optimization is very intuitive and follows the following general rules:

- At lower power demands, maximize ν to maximize efficiency, i.e. ν is the active constraint.
- For higher power demands, U_{cell} becomes the active constraint, and pushing ν to its boundary is no longer optimal.

Because the fuel utilization ν is independent of $\boldsymbol{\theta}$, it is known with certitude and thus can be satisfied exactly in (7). This is not true for the cell potential, however, which cannot be modeled perfectly and is often susceptible to uncertainty (as demonstrated in Fig. 3). Therefore, it is possible for the nominal problem to either underestimate or overestimate this value, resulting in "optimal" input values that will, in practice, either violate the constraint or reach an early limit by assuming it is active when it is not. This problem has been resolved in simulation in [7] with the use of "modifiers", or bias terms which are added to the uncertain constraint quantities to correct the model estimation. Using the modifiers, ε, for the power demand and the cell potential (but not for the efficiency, as adding a constant term would not affect the solution) results in a modified NLP problem that reads:

$$\begin{aligned} \max_{\mathbf{u}} \quad & \eta(\mathbf{u}, \boldsymbol{\theta}) \\ \text{s.t.}: \quad & p_{el}(\mathbf{u}, \boldsymbol{\theta}) + \varepsilon^{p_{el}} = p_{el}^S \\ & U_{cell}(\mathbf{u}, \boldsymbol{\theta}) + \varepsilon^{U_{cell}} \geq 0.75 \text{ V} \\ & \nu(\mathbf{u}) \leq 0.75 \\ & 4 \leq \lambda_{air}(\mathbf{u}) \leq 7 \\ & u_1 \geq 3.14 \text{ ml/(min cm}^2) \\ & u_3 \leq 30 \text{ A}. \end{aligned} \tag{10}$$

As the modifiers are generally unable to converge to the optimal values in a single iteration, convergence is sought over a few iterations, using a low-pass filter with the filter constants $\mathbf{K}$ as suggested in [3]. At the k^{th} iteration, the optimization problem (10) is solved for $\mathbf{u}_k$ using the modifiers $\varepsilon_{k-1}^{p_{el}}$ and $\varepsilon_{k-1}^{U_{cell}}$ from the previous iteration. Then, the modifiers are

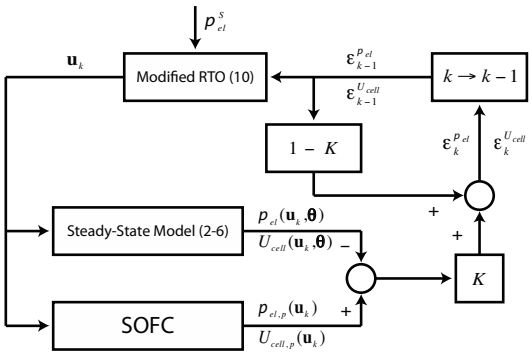

Figure 4: Constraint-adaptation RTO scheme.

updated as follows:

$$\begin{aligned}\varepsilon_k^{p_{el}} &= (1-K_{p_{el}})\varepsilon_{k-1}^{p_{el}} + \\ &\quad K_{p_{el}}[p_{el,p,k} - p_{el}(\mathbf{u}_k,\boldsymbol{\theta})] \\ \varepsilon_k^{U_{cell}} &= (1-K_{U_{cell}})\varepsilon_{k-1}^{U_{cell}} + \\ &\quad K_{U_{cell}}[U_{cell,p,k} - U_{cell}(\mathbf{u}_k,\boldsymbol{\theta})],\end{aligned} \tag{11}$$

with the subscript k indicating the iteration number and the subscript p used to denote a plant value. At the optimum (for $k \rightarrow \infty$), the modifiers will have converged and will simply be the difference (or bias[2]) between the actual and estimated values:

$$\begin{aligned}\varepsilon_\infty^{p_{el}} &= p_{el,p}(\mathbf{u}_\infty) - p_{el}(\mathbf{u}_\infty,\boldsymbol{\theta}) \\ \varepsilon_\infty^{U_{cell}} &= U_{cell,p}(\mathbf{u}_\infty) - U_{cell}(\mathbf{u}_\infty,\boldsymbol{\theta})\end{aligned} \tag{12}$$

With the addition of the modifiers, the solution given by the optimization is guaranteed, upon convergence, to satisfy the constraints of the plant. The general algorithm proceeds as follows:

1. Set $k = 1$ and choose initial values for the modifiers $\varepsilon_0^{p_{el}}$ and $\varepsilon_0^{U_{cell}}$.
2. Solve the modified optimization problem (10) to obtain new input values $\mathbf{u}_k$.
3. Apply these input values and let the system converge to a new steady state.
4. Update the modifiers according to (11). If $\|\mathbf{u}_k - \mathbf{u}_{k-1}\| \leq \delta$ (where δ is a user-specified criterion), assume convergence. If not, set $k := k+1$ and return to Step 2.

The algorithm is presented schematically in Fig. 4.

[2]To clarify, the complete differences between the model and plant values are referred to as "bias", while the partial, filtered differences used in the optimization are called "modifiers".

3.2. Application to the Real Stack

To test the effectiveness of the methodology presented above, a preset power demand profile,

$$p_{el}^{S}(t) = \begin{cases} 0.30\frac{\mathrm{W}}{\mathrm{cm}^2} & t \leq 90\,\mathrm{min} \\ 0.38\frac{\mathrm{W}}{\mathrm{cm}^2} & 90\,\mathrm{min} < t \leq 180\,\mathrm{min} \\ 0.30\frac{\mathrm{W}}{\mathrm{cm}^2} & t > 180\,\mathrm{min} \end{cases} \tag{13}$$

was taken to demonstrate how the change in active constraints (from ν to U_{cell}) may occur. Note that the power demand profile of Eq. 13 acts as a disturbance at the RTO layer: in other words, it is not known *a priori* when and how the power demand may change. An RTO iteration frequency of 30 minutes was used, as this was generally the time it took for the actual system to reach steady state. The initial (sub-optimal) steady-state inputs were 5 ml/(min · cm^2), 12.77 ml/(min · cm^2), and 20 A for the fuel flux, oxygen flux, and current, respectively.

4. Results and Discussion

4.1. Optimal Power Tracking with Different Filters

The scenario described in Subsection 3.2. was tested in the SOFC system for different values of the filter constants $\mathbf{K}$. For this set of scenarios, $K_{U_{cell}}$ was set equal to $K_{p_{el}}$, and the two were varied together. Three different filter values of 0.4, 0.7, and 1.0 (the latter corresponding to full adaptation) were investigated. Complete results, including the input and efficiency graphs, are presented in Fig. 5 for a filter value of 0.4. The subsequent sets (Fig. 6-7) are given in their cut versions, and focus only on the power tracking and constraints (the inputs and efficiencies in these latter cases follow trends that are very similar to those in the former).

It can be observed that the optimizer immediately seeks to maximize the air ratio for all cases. This is because, without any parasitic losses to the air blower in the objective function, there is no reason for the optimizer to keep it at low levels. The fuel utilization also seems extremely sensitive to small disturbances in the hydrogen flux, which leads to occasional fluctuations and violations in this constraint. Finally, there is a "dip" in the fuel utilization during power changes, which is due to the fact that the system must keep the air ratio below its upper limit during the transient and, for this reason, does not decrease the hydrogen flux quickly enough to

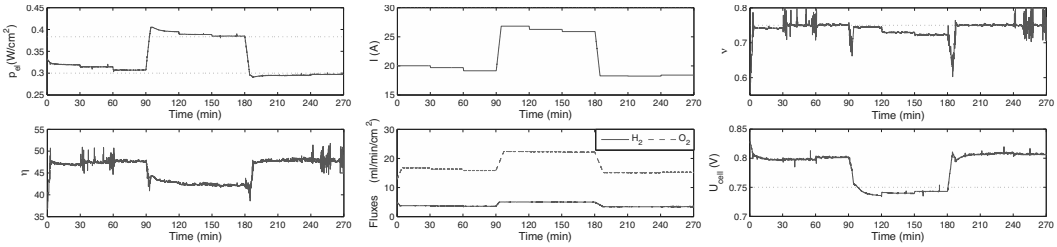

Figure 5: RTO performance with $K_{p_{el}} = K_{U_{cell}} = 0.4$.

match a decrease in current. What results is a temporarily low fuel utilization.

Otherwise, as expected, the filter constants affect the speed of convergence to the optimum. With a low filter, as in Fig. 5, convergence is very slow and damped. For the medium-sized filter in Fig. 6, it is quicker but still damped. For the full adaptation case in Fig. 7, convergence is fast but oscillatory.

Of additional interest is the way the algorithm handles the constraints. For fuel utilization, there are practically no issues (except for the noisy performance of the PI fuel flux controller), as there is no uncertainty. More interesting is the electric potential, whose constraint is initially violated when the algorithm tries to use the modifiers obtained for a low power demand to compute the optimum for a higher one. With steady-state RTO alone, there seems to be no means to solve this problem, as the converged modifiers from the first power demand always lead to this sort of violation in the second.

4.2. Optimal Filter Design

To improve power tracking and constraint satisfaction, it is possible to assign different values to the modifiers. From the bias values in Table 1 (taken from the experiment depicted in Fig. 7), it is clear that the bias for the electric potential constraint changes little during operation at the given conditions. Therefore, it is of interest to get to this value as quickly as possible so as to obtain and maintain an accurate prediction. One way is to use the highest possible value (i.e. 1) for $K_{U_{cell}}$ (it is readily seen that using lower values, as in Fig. 5, only leads to greater violations and slower convergence).

For the power demand, it is more difficult to estimate an optimal filter value. A value of 0.7 results in a second-iteration step that is too small, while a value of 1.0 leads to a step that is too big (compare the instances at $t = 120, 210$ between Fig. 6 and 7). Assuming that the optimal value lies somewhere in between, one may choose $K_{p_{el}} = 0.85$. Implementing this value does indeed result in much better power tracking, as shown in Fig. 8. The potential constraint is violated, but returns back to its bound quickly due to the large filter value.

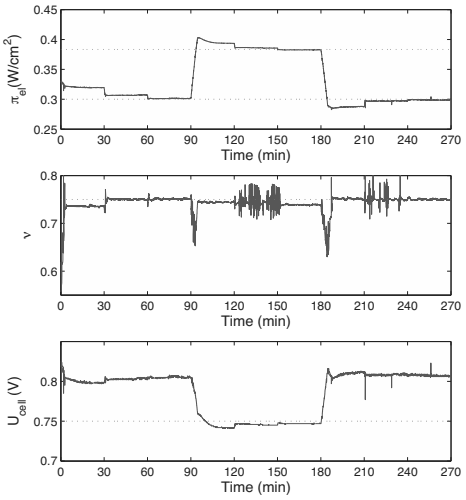

Figure 6: RTO performance with $K_{p_{el}} = K_{U_{cell}} = 0.7$.

4.3. Fast RTO

Although SOFCs with the capability to track constant power demand profiles may be of use industrially, many applications involve power demand changes that occur much more frequently than on the scale proposed in the preceding experiments. For this reason, the use of "fast" RTO was investigated. Instead of waiting for the system to reach true steady state with constant temperature (~30 min) before implementing the RTO, it was assumed that

Table 1: Values of the bias/modifiers for the experiment in Fig. 7.

t (min)	0	30	60	90	120	150	180	210	240	270
$\varepsilon^{P_{el}}$ (W/cm^2)	11.9	19.9	17.8	18.2	26.7	24.8	24.7	17.3	18.5	18.3
$\varepsilon^{U_{cell}}$ (V)	0.101	0.164	0.163	0.162	0.166	0.163	0.161	0.161	0.163	0.165

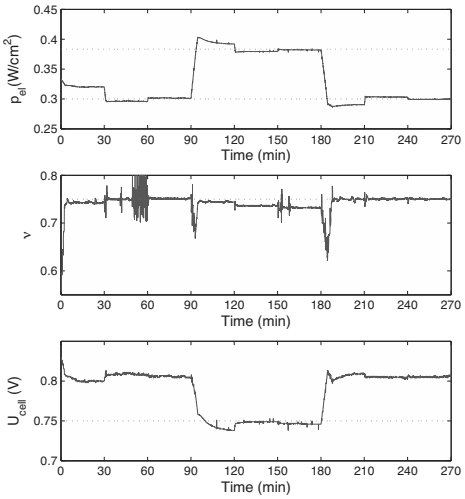

Figure 7: RTO performance with $K_{P_{el}} = K_{U_{cell}} = 1.0$.

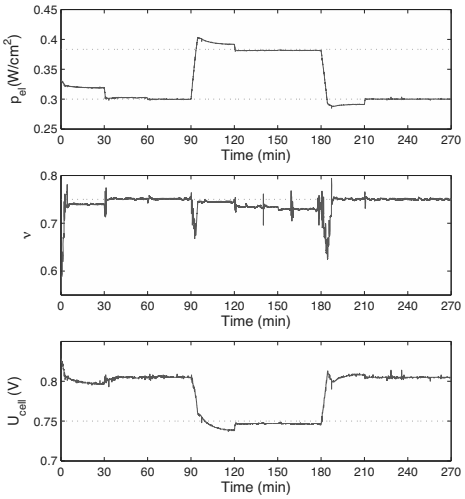

Figure 8: RTO performance with $K_{P_{el}} = 0.85$ and $K_{U_{cell}} = 1.0$.

the majority of the output response had already occurred at the electrochemical scale (< 1 sec). With this assumption, the temperature dynamics were ignored and treated like a slow-scale parametric drift, and the RTO frequency was increased to an action every 10 seconds. The optimal filter constants found in the previous section were retained. A power-demand profile spanning one hour of operation was generated, with a new random power demand between 0.30 and 0.38 W/cm^2 being given every 5 minutes. Towards the end of the experiment, a 15 minute stretch was used to manually test the ability of this algorithm to meet the maximum power without violating the constraint. A converged plant at $p_{el}^S = 0.30$ W/cm^2 was used as a starting point. The results are presented in Fig. 9.

The outcome is very promising. Owing to the fact that there is a very large difference between the two time scales, the optimizer does not suffer from the lack of true steady-state bias, and is able to also act as a very effective *controller* - quickly tracking the appropriate power demand without needing any extensive tuning. Via its role as an optimizer, it maintains the efficiency at near-optimal levels throughout the course of operation. Finally, unlike in the previous cases where the slow updates allowed violations, the potential constraint is approached and met, rather than violated, with this method. One does notice, however, that new power demands cannot be met if the change in the demand is too large (the last iteration in Fig. 9), but this is a limitation of the physical system, rather than of the algorithm.

5. Conclusions

An RTO with constraint adaptation was investigated for an experimental SOFC stack. It was shown that, despite uncertainty and plant-model mismatch, the adaptive optimization algorithm was able to successfully drive the system to its true optimum, converging to the specified power demand and to the proper active constraint. With additional studies, it was shown that tuning the filter values could result in even better performance and faster convergence. A high-frequency RTO was also attempted, and it was demonstrated that ignoring the transient effects of the temperature did not harm the performance of

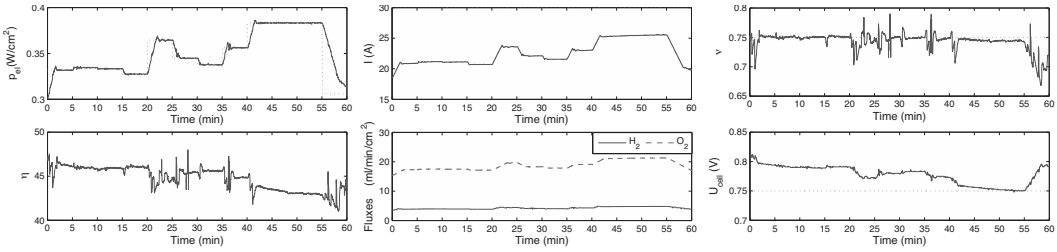

Figure 9: Performance of the fast RTO.

the algorithm. As a result, the RTO acted as both an optimizer and a controller in this case.

Though not addressed in this paper, this mechanism still has open issues that must be looked at. A more rigorous theoretical treatment of the filter tuning is still needed. The efficacy of the proposed method for more complicated SOFC problems, such as those involving steam reformers, cost criteria with parasitic losses, or heat demand-following with co-generation, is yet to be studied.

References

[1] A. Arce, A.J. del Real, C. Bordons, and D.R. Ramírez. Real-time implementation of a constrained MPC for efficient airflow control in a PEM fuel cell. *Accepted for publication in: IEEE Trans. on Industrial Electronics*, 57, 2010.

[2] G.A. Bunin, G. François, and D. Bonvin. Two-layered real-time optimization of a solid oxide fuel cell stack. In *DYCOPS, Leuven (accepted)*, 2010.

[3] B. Chachuat, A. Marchetti, and D. Bonvin. Process optimization via constraints adaptation. *J. Process Contr.*, 18:244–257, 2008.

[4] S. Diethelm, J. Van Herle, Z. Wuillemin, A. Nakajo, N. Autissier, and M. Molinelli. Impact of materials and design on solid oxide fuel cell stack operation. *J. Fuel Cell Sci. and Tech.*, 5(3):–, 2008.

[5] R. Gaynor, F. Mueller, F. Jabbari, and J. Brouwer. On control concepts to prevent fuel starvation in solid oxide fuel cells. *J. Power Sources*, 180:330–342, 2008.

[6] J. Golbert and D.R. Lewin. Model-based control of fuel cells: (2) optimal efficiency. *J. Power Sources*, 173:298–309, 2007.

[7] A. Marchetti. *Modifier-adaptation methodology for real-time optimization (No. 4449)*. PhD thesis, EPFL, 2009.

[8] A. Nakajo, Z. Wuillemin, J. Van Herle, and D. Favrat. Simulation of thermal stresses in anode-supported solid oxide fuel cell stacks. Part I: Probability of failure of the cells. *J. of Power Sources*, 193(1):203–215, 2009.

[9] P. Rodatz, G. Paganelli, A. Sciarretta, and L. Guzzella. Optimal power management of an experimental fuel cell/supercapacitor-powered hybrid vehicle. *Control Eng. Practice*, 13:41–53, 2005.

[10] C. Stiller, B. Thorud, O. Bolland, R. Kandepu, and L. Imsland. Control strategy for a solid oxide fuel cell and gas turbine hybrid system. *J. Power Sources*, 158:303–315, 2006.

[11] Z. Wuillemin. *Experimental and Modeling Investigations on Local Performance and Local Degradation in SOFC (No. 4525)*. PhD thesis, EPFL, 2009.

[12] Y.P. Yang, F.C. Wang, H.P. Chang, Y.W. Ma, and B.J. Weng. Low power proton exchange membrane fuel cell system identification and adaptive control. *J. Power Sources*, 164:761–771, 2007.

[13] X.W. Zhang, S.H. Chan, H.K. Ho, J. Li, G. Li, and Z. Feng. Nonlinear MPC based on the moving horizon state estimation for the solid oxide fuel cell. *Int. J. Hydrogen Energy*, 33:2355–2366, 2008.

[14] Z. D. Zhong, H. B. Huo, X. J. Zhu, G. Y. Cao, and Y. Ren. Adaptive maximum power point tracking control of fuel cell power plants. *J. Power Sources*, 176:259–269, 2008.

Acknowledgments: The authors would like to thank Stefan Diethelm and Luis Quina, from the Laboratoire d'Energétique Industrielle of EPFL, for their assembly of the stack, and for all subsequent laboratory assistance thereafter.

Transient Simulation of Polygeneration Systems Based on Fuel Cells and Solar Cooling Technologies

Francesco Calise[*,a], *Gabriele Ferruzzi*[a], *Laura Vanoli*[b]

[a] *DETEC – University of Naples Federico II, P.le Tecchio 80, 80125 Naples, Italy*
[b] *DIT – University of Naples "Parthenope" Centro Direzionale IS.5, 80143 Naples, Italy*

Abstract:

This paper presents a dynamic simulation of an innovative polygeneration system based on solar heating and cooling and PEM fuel cells technologies. The polygeneration system is based on the following components: evacuated solar collectors, single-stage LiBr-H2O absorption chiller and PEM fuel cell. The fuel cell operates at full load producing electrical energy which is in part consumed by the building. The fuel cell is grid connected in order to perform a convenient net metering. The cooling capacity of the absorption chiller and the solar collector area are designed on a fixed fraction of the maximum cooling load. Finally, the system also includes heat exchangers producing domestic hot water in case of scarce space heating/cooling demand. The analysis was carried out by means of a zero-dimensional transient simulation, developed using the TRNSYS software and includes the investigation of the dynamic behavior of the building, developed in TRNBUILD. An economic model was also developed, in order to assess the operating and capital costs of the systems under analysis. The results of the case study were analyzed on monthly and yearly basis, paying special attention to the energy and monetary flows. The results are excellent from the energy saving point of view. On the other hand, the pay back periods can be profitable for the final user particularly in case of significant public funding.

Keywords: solar energy, fuel cell, polygeneration

1. Introduction

The well known growth in world energy demand and population is forcing research toward more efficient energy conversion devices. A strong impulse to this scope has been given by new emerging energy-efficient technologies and by regulatory incentives related to energy production from renewable sources and environmental friendly systems [1]. In this framework, polygeneration technologies show a significant potential in term of energy savings and reduction of CO_2 emissions, due to their implicit peculiarities, such as: maximum utilization of energy and natural resources, reduction of unit cost of products and reduction of environmental burden [2]. Polygeneration, or multi-generation, is usually defined as the combined production of multiple energy vectors (e.g. electricity, cool, heat, etc) and/or products (e.g. hydrogen, methanol, etc) using natural resources (fossil fuels, wood, etc) and/or renewable energy sources (solar, wind, biomass, etc). Hence, the simplest example of polygeneration is the combined heat and power generation, CHP, also called cogeneration. In case of combined heat, cool and electricity production, polygeneration devices are defined as trigeneration systems. Cogeneration and trigeneration technologies are well known and widely adopted for industrial, residential and commercial applications [1-2]. An additional impulse regarding the analysis of polygeneration systems is also given by the studies concerning distributed generation. In fact, several papers available in literature [1] assess that small scale (below 1 MWe) distributed polygeneration systems are useful since they: i) promote energy efficiency and renewable sources; ii) can defer investments on large power plants; iii) promote the use of local energy resources, reducing energy dependency and increasing the reliability of the electrical systems; iv) contribute to reduce the impact of fuel supply infrastructures also reducing transmission losses; v) bring into play the local emission problem. Usually, polygeneration systems – adopted in distributed generation - are classified on the basis of: i) engine technology (reciprocating engines, micro gas turbines, fuel cells); ii) bottoming devices (absorption or electrical chillers); iii) auxiliary devices (heaters, gas-fired absorption chillers or heat pumps, engine-driven chiller); iv)

* Corresponding author: email: frcalise@unina.it, tel: +390817682301, fax: +390812390364

eventual renewable energy source (solar, biomass, wind, hydro); v) eventual products (ethanol, hydrogen, etc). Thus, it is clear that a large number of possible system layouts of polygenerations systems can be identified. Among them, this paper is focused on fuel cells technology combined with the use of solar energy. This kind of combination is diffusely investigated in literature. These papers mainly analyze the production of hydrogen using solar energy and its consequent use in fuel cells and/or storage [3]. Shapiro et al. designed and built a prototype of a photovoltaic solar-powered regenerative PEM-electrolyzer, demonstrating the system feasibility and characterizing system performance [4]. A similar study was performed by Hedstrom, showing the experimental and numerical performance of a PEM fuel cell fed by hydrogen produced both by photovoltaic cells/electrolyzer and by reformer, fed by biogas [5]. Hence, all the above mentioned papers are focused on the combination of PEM fuel cells and photovoltaic collectors. Literature review did not show any significant paper analyzing the possibility of integrating fuel cells and solar thermal collectors. Thus, this paper aims at covering this lack, developing a transient simulation model of a polygeneration system capable to produce electricity, cool and heat, powered by solar energy and natural gas fuelling a PEM fuel cells. The concept idea of the system under investigation comes from the combination of solar heating and cooling (SHC) systems – including evacuated tube solar collectors and single stage absorption chillers – and cogenerative PEM fuel cell as auxiliary system.

The basic concept of the solar heating and cooling systems (SHC) lies in the possibility of using the solar radiation to provide space heating during the winter and space cooling in the summer, using an heat-driven chiller. The SHC is a very promising technology, especially in summer operation mode, when the maximum demand for cooling coincides with the maximum availability of solar radiation. SHC may significantly contribute to achieve the goals in terms of energy savings, emissions reductions and increase of use of renewable energy sources, including those stated by UE in the Directive 2009/28/EC. Usually, the auxiliary energy, required in case of scarce solar irradiation, is supplied by a gas-fired heater. In this work, the auxiliary heat is provided by a cogenerative PEM fuel cell, also producing electrical energy for user and electrical grid. The majority of the papers available in literature about this topic, consider traditional auxiliary devices (electric chillers, gas-fired heater, biomass heaters etc) [6-10], and none of them analyzes the possible combination between solar cooling technology and fuel cells, under investigation in this paper. The simulation model was developed in TRNSYS on the basis of previous models developed by some of the authors [11-12], and it allows to calculate the time-dependent energy flows and key-points temperatures. It also includes a module which allows one to evaluate the energetic performance and to calculate system economic performance parameters.

2. System Layout

The system layout considered in this work is based on the combination of well-known SHC and fuel cells technologies. It is capable to produce electricity, space heating or cooling, domestic hot water all over the year, according with users' demand. Regarding to SHC technology, several studies showed that the most promising configuration is based on the coupling of evacuated tube solar collectors with single-stage LiBr-H_2O absorption chillers [2].

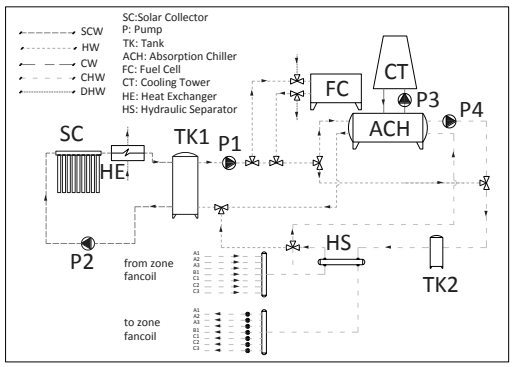

Figure 1 – System Layout

Usually, the auxiliary energy to be used in case of scarce solar irradiation is supplied by a gas-fired auxiliary heater. However, in this work the auxiliary heat is provided by a cogenerative fuel cell. In particular a PEM fuel cell was selected since: i) the operating temperature is suitable for the typical operating temperatures of solar collector and absorption chiller; ii) it can be considered as the more mature fuel cell technology commercially available.

In order to maximize the thermal utilization of the fuel cell, the solar collectors field was designed in order to satisfy only a part of the maximum cooling load of the building.

The system, schematically shown in Figure 1, consists of: 5 different system loops, solar collector water (SCW), hot water (HW), cooling water (CW), domestic hot water (DHW) and chilled/hot water (CHW), respectively. The SHC system consists of the following main components: a solar field with evacuated-tube collectors (SC); a hot water inertial storage tank (TK1); a LiBr-H_2O single stage absorption chiller (ACH); a PEM fuel cell (FC), providing auxiliary heating energy for both cooling and heating needs and simultaneously generating electrical energy for user demands and/or for the electrical grid; a closed circuit cooling tower (CT), providing cooled water to the condenser of ACH; a fixed-volume pump (P1) for the HW loop, pumping water from TK1 to FC or to the ACH or to the building; a variable speed pump (P2) for the SCW loop; a fixed-volume pump (P3) for the CW loop; a fixed-volume pump (P4) for the CHW loop; an inertial chilled/hot water storage tank (TK2); an hydraulic separator (HS), balancing fluid flows between the primary and secondary hydraulic circuits; a plate-fin heat exchanger producing Domestic Hot Water (HE); pipes connecting the HS with the fan-coils of the zones of the building.
The TRNSYS scheme used to simulate the system also includes several additional components (not displayed in Figure 1), such as: controllers, schedulers, weather database, etc. The basic operating principle of the SHC system is relatively simple: the solar irradiation incident on the SC field increases the SC outlet temperature up to the fixed set-point, determining the consequent growth of the water temperature in the storage tank TK1. In case of scarce request of building cooling or heating energy, the SC useful energy is used by the HE to produce DHW to be used by the showers installed in the building. During the summer operation, the hot fluid drawn by P1, from the top of TK1, supplies the ACH, which produces the chilled water (CHW) required for cooling the building. The cooling tower CT provides the cold water required to cool the absorption chiller, ACH. The cogenerative PEM fuel cell is located upstream the ACH and provides additional heat in case of scarce solar irradiation. Conversely, when TK1 outlet temperature is higher than the fixed set-points (different values in summer and winter operations), the FC cogenerative heat exchanger is used to produce additional domestic hot water. During the heating season, the water exiting the TK1 – and eventually passing trough FC - is sent directly to the HS.

TRNSYS model also includes a number of components required in order to simulate the control strategies of the components and of the whole system. In particular, some innovative control strategies were implemented in order to maximize system efficiency [11]. In addition, appropriate on/off controllers were also used in order to manage mixers and diverters on FC loop required in order to activate DHW or HW heating by the cogenerative heat exchanger of the fuel cell.
The building considered in the study is a small university hall, consisting of 7 classrooms (A1, A2, A3, C1, C2 and C3) and a common area (B1). This building is compliant with the requirements of Italian Law (D. Lgs. 311/06) in terms of walls and windows transmittances, system efficiency and primary energy consumption and is located in Naples, South Italy. The building was simulated in TRNSYS environment, using the TRNBUILD application, included in TRNSYS package. The transmittances of walls and windows are largely compliant with the limits of the Italian Law (U_{lim}). All the windows are also provided with shadings. The occupancy, light and the equipment load, the mechanical air change, the radiative and convective people load of the building is suggested by the Italian Standard (UNI 10339). Finally, the university hall was also assumed to be placed close to the university fitness centre. Thus, the DHW produced by the system can be supplied to those showers all the days of the year. The building electrical demand was simulated on the basis of the experimental load duration curve, measured for a similar existing building and shown in Figure 2.

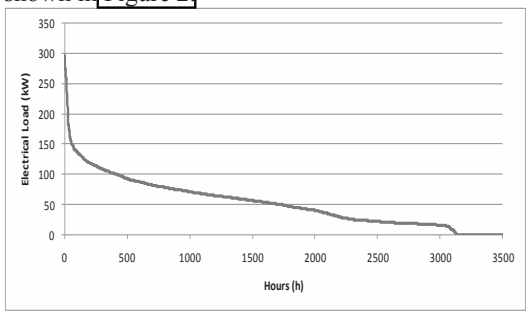

Figure 2 - Electrical load duration curve

The winter set point temperature is established by the Italian Law at 20 °C, whereas the summer set-point temperature is not ruled by Law and was arbitrarily set at 26 °C. According to the Italian Law, the heating system operates from November 15th to March 31st. As for the summer, the operating period is not fixed by Law, and the

interval from May 1st to October 21st was considered. The building was supposed to be occupied all year long, from Monday to Saturday, from 8.00 am to 6.00 pm.

3. Simulation model

The components of the solar assisted refrigeration systems previously described were simulated using both the TRNSYS built-in library [13] and user-developed models. In the following, the simulation models are briefly described, paying special attention to the variables used as synthesis/design parameters in the subsequent optimization.

Evacuated Tube Solar Collectors (SC). The model of the SC is based on Type 71, included in TRNSYS package. Here, the thermal efficiency of the collectors is calculated using the Hottel-Whillier-Bliss equation [14]. The values of a_0, a_1 and a_2 given in reference [11]. Correction factors are introduced in the model, in order to account for: series connection, clouds, biaxial Incidence Angle Modifiers (IAM), etc [13].

Pumps (P). The variable flow-rate pump, P2, is modeled on the basis Type 110. The 10 fixed-speed pumps (P1, P3, P4 and 7 zone pumps) are simulated using Type 3. Their simulation models are based on the energy and the mass balances [13]. The mass flow rate for P4 is related to the heating and cooling loads of the building, assuming a nominal temperature difference of 5 °C, the nominal mass flow rate for P2 is related to the value selected for the SC surface area, the mass flow rate of P1 depends on the nominal coefficient of performance of the absorption chiller, ACH [11]. The same procedure was implemented to set the water flow rate in the cooling tower CT (pump P3), that has to dissipate the heat produced by the condensing and absorption processes in the ACH [11].

Storage tanks (TK). The system layouts under evaluation included two storage tanks, both subject to thermal stratification. The first tank (TK1, simulated using Type 4) is used in the solar loop; the second one (TK2, modeled by Type 60) is used in the CHW loop to store chilled or hot water, respectively in summer and in winter. Their models are based on the assumption that the tanks can be divided into N fully-mixed equal sub-volumes. The tanks are also equipped with a pressure relief valve, in order to account for boiling effects [13, 15]. The TK1 volume is fixed on the basis of the value selected for A_{SC}:

$$V_{TK1} = \frac{v_{TK1} A_{SC}}{1000} \quad (1)$$

The TK2 volume is selected on the basis of the value of the building peak cooling load.

Absorption Chiller (ACH). A single-effect hot water LiBr-H_2O absorption chiller (ACH) was considered. The component is simulated by the TRNSYS Type 107 which uses a normalized catalogue data lookup approach [14]. Here, the performance data were modified in order to comply with the data sheet of a 300 kW single stage H_2O-LiBr hot water fired absorption chiller. The performance data are numerically expressed as a function of CHW, HW, CW inlet water temperatures, CHW outlet set-point temperature and of the cooling ratio factor and the input heat ratio factor, as shown in [14].

Cooling Tower (CT). In this paper the TRNSYS Type 510 (closed-circuit cooling tower) was considered. The working fluid (CW) flows in a circuit which is physically separated from the ambient air and process water. The TRNSYS simulation code is based on the model proposed by Zweifel [16] that matches the manufacturers' catalogue data over a wide range of operating conditions. Cooling tower air mass flow rate, cooling capacity and CW mass flow rate are calculated using the equations reported in [11].

Heat Exchanger. As above mentioned, the DHW is partly produced by a plate-fin compact heat exchanger, equipped with a control which enables DHW production only when SC outlet temperature overcomes the fixed set point. The HE is equipped with a diverter placed upstream the DHW inlet, a by-pass duct and a mixer downstream the DHW outlet. The diverter and the mixer are managed by the HE control system. The model of this heat exchanger was developed by the authors using a modified version of the ε-NTU method [17].

Hydraulic Separator. This device is required in order to balance the flow rates between the primary (pr) and secondary (se) loops of the system. In fact, the secondary loop flow rate may significantly vary during the day, depending on the heating/cooling loads of the different thermal zones. For such device, a new TRNSYS model was introduced, using the following criterion, based on simple energy and mass balances. In case the primary mass flow rate is higher than the secondary one, the primary and secondary outlet temperatures are calculated as follows:

$$t_{pr,out} = \frac{\dot{m}_{se} t_{se,in} + \left(\dot{m}_{pr} - \dot{m}_{se}\right) t_{pr,in}}{\dot{m}_{pr}} \quad (2)$$

$$t_{se,out} = t_{pr,in} \quad (3)$$

When the primary mass flow rate is lower than the secondary one, the primary and secondary outlet temperatures are:

$$t_{pr,out} = t_{se,in} \quad (4)$$

$$t_{se,out} = \frac{\dot{m}_{pr} t_{pr,in} + \left(\dot{m}_{se} - \dot{m}_{pr}\right) t_{se,in}}{\dot{m}_{se}} \quad (5)$$

Fan-coil (winter and summer operation). Each zone is equipped with a 2-pipes loop, supplying hot/chilled water to the respective fan-coils. In this work, the fan-coil, for both cooling and heating modes is simulated, developing a new TRNSYS type, based on a data lookup approach. In fact, TRNSYS library lacks in a fan-coil model, based on manufacturers' data, which can operate both in cooling and heating modes. In particular, the data file includes four correction factors, function of: fluid mass flow rate, inlet fluid temperature, air dry and wet bulb temperature, and air flow rate.

Pipe. Each zone is hydraulically connected to the system by a supply and return ductwork. This component is simulated on the basis of a non-steady model based on the mass and energy balances (Type 31) [13].

Building. The building considered in this work was simulated using the TRNBUILD software included in TRNSYS package which provides a very detailed and reliable simulation of the thermo-hygrometric behavior of the building. Here, the building is simulated by means of a non-geometrical balance model with one air node per zone, representing the thermal capacity of the zone air volume and capacities which are closely connected with the air node. The walls are modeled according to the transfer function of Mitialas and Arsenault [13]. The windows are considered as an external wall with no thermal mass, partially transparent to solar, but opaque to the long wave internal gains. Long-wave absorption occurs at the surfaces. The window model also includes a detailed optical and thermal model based on WINDOW 4.1 developed by Lawrence Berkeley Laboratory USA. Finally, the building model also includes detailed effective capacitance humidity, infiltration, ventilation, convective coupling and gain models [13].

PEM fuel cell. The electrochemical and thermodynamic model of the PEM included in this work is based on the model developed by Mann et al. [18] adopting both deterministic and empirical equations for the calculation of cell Nerst voltage and activation, ohmic and concentration overvoltages (both anodic and cathodic). The model is flexible since can be easily adopted for different PEM configuration. It was successfully validated using experimental data of several PEM fuel cells [18] and included in TRNSYS package (type 170). However, the model included in TRNSYS does not implement the cogenerative heat exchanger of the fuel cell. Thus, in this paper this device was simulated using a modified version of the ε-NTU method [17]. The considered PEM is equipped with an external reformer, including SMR and shift reactors, converting methane into hydrogen. In this work, a 360 kWe PEM fuel cell was considered, based on the performance data of Ballard PB2 system (Table 1).

PARAMETER		UNIT
Electrical Power	360	kW
Thermal Power	305	kW
Electrical Efficiency	34	%
Thermal Efficiency	42	%
Stack temperature	80	°C
Number of cells	100	
Number of stacks	1	
PEM Area	10000	cm^2
PEM thickness	0.250	cm

Table 1 - PEM parameters

Overall energy consumption. The energy analysis of the systems under evaluation requires the calculation of the non-renewable primary energy required to operate it; in this way, the primary energy savings of the polygeneration system with respect to a traditional HVAC system assumed as a reference (RS) can be evaluated, too. To this scope, a reference system was also implemented and simulated in TRNSYS, using the same building. In the case study presented in the paper, an air-to-water electric driven heat pump (EHP_{RS}) was considered as the reference system, producing hot water during the winter and refrigerated water during the summer. The RS also includes a gas fired heater, for DHW production. This system is commonly considered the reference HVAC system for Mediterranean climates, since it is largely more efficient than the combination of gas fired heater and electric water chiller used for continental climates. Thus, the primary energy consumed by the EHP_{RS} and its annual operating costs, calculated by the TRNSYS simulation, were used in polygeneration simulation in order to evaluate primary energy savings and operating cost savings. The primary energy consumed by the reference system is mainly due to the electrical energy consumed by the building and the one used for the

EHP and for the pumps of the primary and secondary water loops. Furthermore, the RS also uses an additional amount of a primary energy to produce: i) the same amount of DHW produced by the polygeneration system; ii) the electrical energy produced by the PEM and sold to the grid ($E_{el,+,i}$). The primary energy required by the polygeneration system, in terms of non-renewable sources, is only due to the yearly natural gas volume (V_{NG}) consumed by the fuel cell and to the fossil fuel consumed by the thermoelectric power plant (average efficiency, $\eta_{el,t} = 0.461$) in order to supply the auxiliary electrical energy ($E_{el,-,i}$) required by the building and not supplied by the PEM. Therefore the polygeneration primary energy is:

$$PE_{poly} = V_{NG} LHV + \frac{E_{el,-,i}}{\eta_{el,t}} \quad (6)$$

Economic model. A detailed cost model was also implemented in the simulation tool, relating the cost of each component to the main design parameters. In addition, the operating costs due to natural gas and electrical energy consumption were evaluated, whereas maintenance costs were neglected. The components capital costs (J_i) were reported on a yearly base by means of an annuity factor (AF), depending on the expected life of the system and the discount rate. So, the total cost (owning and operating) of the polygeneration was expressed as:

$$C_{tot} = \frac{\sum_i J_i}{AF} + C_{op} \quad (7)$$

The operating cost, C_{op}, is mainly due only to the natural gas consumption required to supply the PEM fuel cell. For each time-step, the simulation code compares the electrical power produced by the fuel cell with the electrical demand of the buildings plus the passive loads of the SHC. Thus, it considers the eventual purchase/selling from/to the grid at the actual (for the considered hour of the year) price (p_{EE}) or cost (c_{EE}) :

$$C_{op} = \sum_i \left(V_{NG,i} c_{NG} - E_{el,+,i} p_{EE,i} + E_{el,-,i} c_{EE,i} \right) \quad (8)$$

Capital costs were estimated by introducing a cost function for each component, obtained by regression of manufacturers data, as described in [11]. PEM cost was estimated in 1500 €/kW, which is the goal to be achieved by manufacturers in the next years[19]. RS operating costs are due to electricity and Natural gas, required to drive the DHW heater. In case of RS, the total electrical energy considered in the economic and energetic calculations, include: i) the exceeding electricity produced by the PEM and sold to the grid; ii) the electricity required to the building and to supply the HVAC system. Finally, the economic performance of the SHC system can be calculated using the Simple Pay Back Period (SPB) both with and without public contributions.

4. Results and Discussion

The polygeneration under investigation was simulated using the set of design parameters shown in Table 2. The yearly energetic and economic results are summarized in Table 3. Here, it is clearly shown that the building under investigation is dominated by internal loads, determining a winter heating demand dramatically lower than the cooling one. The system capital cost is one order of magnitude higher than RS corresponding cost. However, the payback periods are acceptable, especially in the framework of renewable energy sources. Considering the present Italian public funding of 55% of capital costs of SC and ACH, the pay back period is slightly higher than 10 years (SPB2 in Table 3). The electricity produced by the fuel cell is mainly sold to the grid since PEM size (designed on thermal demand) is overestimated for building electrical energy demand.

PARAMETER	UNIT	
A_{SC}, Collector area	°C	200
Collector slope	°	30°
TK1 Volume per Collector Area	m^2	54 l
TK1 Volume	m^3	10.8
TK2 Volume	m^3	2.0
P4 Flow rate	kg/h	43.0 10^3
P2 Flow rate	kg/h	92.1 10^3
SC outlet winter set point temp.	°C	50.0
SC outlet summer set point temp.	°C	90.0
DHW Set point temp. PEM wint.	°C	45.0
DHW Set point temp. PEM sum.	°C	71.5

Table 2 - SHC main design parameters

In addition, although PEM size is designed for the maximum heating demand, most of its thermal energy is used for DHW rather than for the fancoil winter operation or for driving the absorption

chiller. Finally, DHW is crucial for achieving acceptable primary energy savings and simple pay back periods. Finally, the overall energetic performance parameters are shown in Table 4. These results are more clearly shown in Figure 3 and Figure 4, were energetic and economic flows are reported on a monthly basis.

PARAMETER	UNIT	
Fancoil cooling energy	kJ	$7.33 \cdot 10^7$
Fancoil heating energy	kJ	$6.42 \cdot 10^8$
$E_{el,+,i}$	kJ	$2.76 \cdot 10^9$
PEM Electrical Energy	kJ	$3.44 \cdot 10^9$
DWH Energy (SC)	kJ	$2.51 \cdot 10^8$
DWH Energy (PEM)	kJ	$3.54 \cdot 10^9$
PEM thermal Energy	kJ	$4.24 \cdot 10^9$
Passive electr.energy	kJ	$5.91 \cdot 10^7$
SC useful energy	kJ	$5.92 \cdot 10^8$
V_{NG}	Sm^3	$2.97 \cdot 10^5$
PE	kJ	$1.03 \cdot 10^{10}$
PE_{RS}	kJ	$1.27 \cdot 10^{10}$
SPB	years	12.9
SPB2	years	10.3
Electrical Energy selling	€	71213
Capital Cost	€	1073352
$C_{op,RS}$	€	110929
C_{op}	€	34210

Table 3 – simulation yearly results

PARAMETER	
Fsol	0.30
η_t SC	0.47
η_e PEMFC	0.33
η_t PEMFC	0.41
COP ACH	0.71

Table 4 – Energetic performance parameters

In particular, Figure 3 shows building cooling (Q_{cool}) and heating (Q_{heat}) energies, solar field useful energy (Q_{SC}), absorption chiller cooling energy ($Q_{c,ACH}$), PEM cogenerative energy ($Q_{h,PEM}$) and DHW energy. Here, it is clearly shown that building heating energy demand is negligible if compared with the cooling one (e.g., February vs. June). Thus, during the winter the thermal energy produced by the solar field is often higher than building space heating demand. As, a consequence, in the winter and in the middle seasons, most of the PEM cogenerative heat and SC useful gain is converted in DHW. In addition, the electricity required by SHC equipments (not shown in Figure) is negligible for all the months, showing some peaks during the summer, due to the fans of the cooling towers.

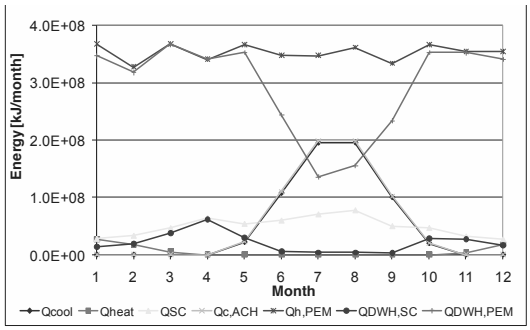

Figure 3 - Monthly thermal energy

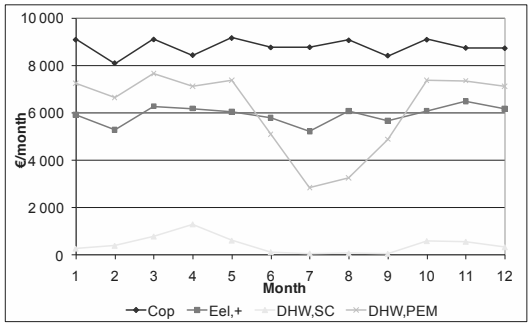

Figure 4 – Monthly costs

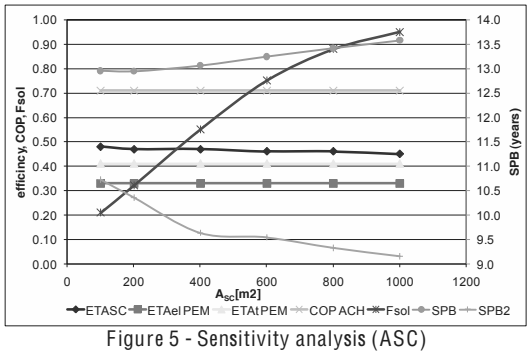

Figure 5 - Sensitivity analysis (ASC)

Furthermore, the electricity produced by the cell is mostly sold to the grid. The operating costs of the SHC are always lower than reference system ones, only in winter and in middle seasons. During the summer, the incomes due to DHW production are lower, due to the larger amount of cogenerative heat used to drive the absorption chiller. This circumstance also shows that the production of cooling energy, using an electric driven heat pump (reference system), is economically more favorable than the combination of PEMFC and absorption chiller. This circumstance is also emphasized by the sensitivity analysis shown in Figure 5, where the minimum SPB is achieved at the lowest SC area. On the other hand, according to SPB2 criteria, a larger SC solar field would

determine a better economic performance. Such figure also shows that solar fraction increases less than proportionally with solar collector area.

5. Conclusions

The paper presents a dynamic simulation of a novel polygeneration system based on the coupling of a PEM fuel cell and a solar cooling system. The polygeneration system is capable to supply space heating and cooling and domestic hot water all year long. The system is powered by natural gas and solar energy. The dynamic model showed the technical feasibility of such system also providing acceptable economic performance both with and without public funding. Future developments of this work will include the use of high temperature fuel cells (SOFC) combined with parabolic through collectors and double stage absorption chillers.

6. References

[1] G. Chicco, P.M., *Distributed multi-generation: A Comprehensive view* Renewable and Sustainable Energy Reviews, 2009. 13: p. 535-551.

[2] L.M. Serra, M.A.L., J. Ramos, A.V. Ensinas, S.A. Nebra, *Polygeneration and efficient use of natural resources.* Energy, 2009. 34: p. 575-586.

[3] A. Yilanci, I.D., H.K. Ozturk, *A review on solar-hydrogen/fuel cell hybrid energy systems for stationary applications.* Progress in Energy and Combustion Science, 2009. 35: p. 231-244.

[4] D. Shapiro, J.D., M. Kimble, M. Pien, *Solar-powered regenerative PEM electrolyzer/fuel cell system.* Solar Energy, 2005. 79: p. 544-550.

[5] L. Hedstrom, C.W., P. Alvfors, M. Rissanen, B. Stridh, J. Eckman, *Description and modelling of the solar-hydrogen-biogas-fuel cell system in GlashusEtt.* Journal of Power Sources, 2004. 131: p. 340-350.

[6] Mateus, T., Oliveira, A.C., *Energy and economic analysis of an integrated solar absorption cooling and heating system in different building types and climates.* Applied Energy, 2009. 86: p. 949-957.

[7] Folrides, G.A., Kalogirou, S.A., Tassou, S.A., Wrobel, L.C., *Modelling, simulation and warming impact assessment of a domestic-size absorption solar cooling system.* Applied Thermal Engineering, 2002. 22: p. 1313-1325.

[8] Folrides, G.A., Kalogirou, S.A., Tassou, S.A., Wrobel, L.C., *Modelling and simulation of an absorption solar cooling system for Cyprus.* Solar Energy, 2001. 72(1): p. 43-51.

[9] Assilzadeh, F., Kaligirou, S.A., Ali, Y., Sopian, K., *Simulation and optimization of a LiBr solar absorption cooling system with evacuated tube collectors.* Renewable Energy, 2005. 30: p. 1143-1159.

[10] Ardehali, M.M., Shaharestani, M., Adams C.C., *Energy simulation of solar assisted absorption system and examination of clearness index effects on auxiliary heating.* Energy Conversion and Management, 2007. 48: p. 864-870.

[11] Calise, F., Palombo, A., Vanoli, L., *Maximization of primary energy savings of solar heating and cooling systems by transient simulations and computer design of experiments.* Applied Energy, 2009. In press.

[12] Calise, F., Dentice d' Accadia, M., Palombo, A., Vanoli, L. *Simulation model and analysis of a small solar-assisted refrigeration system: dynamic simulation and optimization*. in *Proceedings of the ASME International Mechanical Engineering Congress & Exposition 2008 IMECE08*. 2008. Boston, USA.

[13] Klein, S.A., et al., Solar Energy Laboratory, , *TRNSYS. A transient system simulation program*. 2006: University of Wisconsin, Madison.

[14] ASHRAE, *Handbook of Fundamentals*. 2001, Atlanta: American Society of Heating, Refrigerating and Air-Conditioning Engineers.

[15] Klein, S.A., *A design procedure for solar heating systems.* Solar Energy, 1976. 18: p. 113-127.

[16] Zweifel, G., Dorer, V., Koshenz, M., Weber, A. *Building energy and system simulation programs: model development, coupling and integration*. in *Building Simulation 1995*. 1995. Madison, USA.

[17] Kakac, S., Liu, H., *Heat Exchanger Selection, Rating, And Thermal Design.*, ed. CRC Press. 1998.

[18] R.F. Mann, J.C.A., M. A.I. Hooper, H.M. Jensen, B.A. Peppeley, P.R. Roberge, *Development and application of a generalised steady-state electrochemical model for a PEM fuel cell.* Journal of Power Sources, 2000. 86: p. 173-180.

[19] Larminie, J., Dicks, A., *Fuel cell system explained*, ed. John Wiley & sons LTD. 2004.

Numerical analysis of a Small Scale Polygeneration Plant with a Desiccant-Based Air Handling Unit

Giovanni Angrisani[a], Carlo Roselli[a], Maurizio Sasso[a]

[a]*Faculty of Engineering, University of Sannio, Piazza Roma 21, 82100 Benevento, Italy*

Abstract: Domestic and light commercial sectors, especially in the Mediterranean area, are involved in an increasing space cooling demand, generally satisfied by electrically-driven units; this has determined summer electric peak loads and black-outs. Thus, an increasing interest occurs in systems, fuelled by natural gas, able to satisfy space cooling requirements, such as polygeneration one. These are based on a prime mover that drives in different ways (mechanically, electrically, thermally) electric generators and/or electric heat pumps, absorption heat pumps, desiccant wheels, … in order to satisfy thermal (heating and cooling) and electric energy requirements. In this paper, attention is paid to a small scale polygeneration system based on a natural gas-fired Micro-CHP and a desiccant-based hybrid HVAC system. The MCHP provides thermal power to regenerate the desiccant wheel, domestic hot water and space heating purposes. It also supplies electric power for air handling unit, chiller and external appliances. A numerical analysis, based on design operating conditions and nominal characteristics of the devices, is carried out in order to compare primary energy consumptions, annual operating costs and greenhouse gas emissions of the system with respect to a conventional cooling dehumidification HVAC system powered by separate electric and thermal "production".

Keywords: Combined Heat and Power, Desiccant wheel, Hybrid HVAC, Micro-CHP, Polygeneration.

1. Introduction

During last years great attention, both in the research and application fields, was focused on the transition from centralized to decentralized energy "production" systems, Distributed Generation, DG [1]. Furthermore the actual industrial trend to the miniaturization of the energy conversion equipments, mainly due to reduced manufacturing costs, drives to the market availability of a wide variety of small scale power, refrigeration and heat pump systems.

Usually, energy flow starting from a primary source is converted in a large plant and then transmitted to the end user to satisfy its desired energy demands. In many cases the energy flow is converted in further equipments close to the end-user, decentralized energy conversion plant, and distributed to the final appliances. In its path and in each energy conversion system, losses occur and consequently the desired energy flow is always different than the required one. The miniaturization process of the energy conversion devices, that is in progress in last years, leads to a reduction of the ducting losses due to distribution and/or transmission of working fluids and energy cycling losses.

In [2], the comparison between the centralized power system, based on an average over 20 years old plants, and the distributed one is analyzed: small, modern generators can be more efficient and less costly to operate than large and old generators. Since the "size" effect does not always lead to energy savings and pollutant emissions reduction, there is the need to support the diffusion of on-site small complex energy conversion devices, Decentralized Polygeneration, DP, able to supply, with high performance, two or more energy requirements (electric, cooling and heating) of the end-user rather than the simple single-output requirement. In many cases, mainly in tertiary sector (hotels, offices, commercial buildings …), a widespread use of DP systems has allowed energy, economic and environmental benefits.

Furthermore, in last years in the Mediterranean area, during warm season, there was an increasing demand of cooling energy in domestic sector, generally satisfied by electrically-driven units; this trend has involved an increase in power generation capacity of electric utilities and a summer peak load of electric energy consumption with the related problem of electric black-out. This problem has been the driving force to an increasing interest to small scale polygeneration systems fuelled by

Corresponding Author: Giovanni Angrisani, Email: giovanni.angrisani@unisannio.it

natural gas, especially in Southern Europe. The main benefits of gas fuelled CCHP (Combined Cooling Heat and Power) with respect to the reference separate energy "production" system are primary energy saving, low pollutant emissions, reduction of operating costs, the shift from electricity to gas of the high summer cooling energy demands and energy dependence reduction. Moreover, a strong interest in the research field has been focused on polygeneration plants based on desiccant HVAC systems.

In [3], an innovative CCHP system, based on a cogenerator driven by an automotive derived natural gas-fired internal combustion engine, coupled to a LiCl-water desiccant cooling system regenerated by thermal energy recovered from exhaust gases and from the engine coolant is numerically analyzed. The paper deals with the energy and economic analyses of the plant; in particular attention is paid on the effects of fuel and electricity prices and of the subsidies and plant costs on the economic indices of the system.

In [4], the performance of a desiccant cooling system coupled to a CHP (Combined Heat and Power) system has been evaluated. The desiccant unit is regenerated through heat recovery from a gas-fired reciprocating internal combustion engine. The system satisfies both sensible and latent cooling loads for a wide range of climatic conditions. Energy efficiencies of the desiccant cooling system were also evaluated and compared with those of a conventional system.

Nevertheless, few investigations have been carried out on desiccant hybrid systems coupled to small scale CHP systems, without a deep analysis on both energy and environmental performances [5-7]. So in this paper attention is paid to a small scale polygeneration system that consists of a natural gas-fired MCHP (Micro-CHP) and a desiccant-based hybrid HVAC (Heating Ventilation and Air Conditioning) system (the term hybrid refers to the contemporary presence of a desiccant wheel and a cooling coil interacting with an electric chiller). The MCHP can provide thermal power, recovered by engine cooling and exhaust gas, in summer for the regeneration of the desiccant wheel and for the domestic hot water purposes, while in winter for domestic hot water and space heating purposes. It also supplies electric power for air handling unit (fans, pumps…), chiller and external appliances (computers, lights, etc.). The hybrid HVAC system can also operate in traditional way, interacting with separate "production" systems (electric grid and gas-fired boiler). A numerical analysis, based on design operating conditions and on nominal characteristics of the devices, is carried out in order to compare the performance, in terms of primary energy consumptions, annual operating costs and greenhouse gas emissions, of such systems with respect to conventional cooling dehumidification HVAC systems powered by separate electric and thermal "production".

2. Description of the trigeneration system

At Sannio University, in Benevento (South Italy), a Micro-CCHP system is located, that consists of:

- a natural gas-fired cogenerator based on a reciprocating internal combustion engine with the following nominal characteristics: electric power P_{el}=6.0 kW (0.22 kW is used for the cogenerator self-consumptions, so the effective electric power "production" is $P_{el}^{*} = 5.78$ kW), thermal power P_{th}=11.7 kW, nominal power input P_p=20.8 kW, electric efficiency η_{el}=28.8% (considering MCHP self-consumptions, the effective electric efficiency is $\eta_{el}^{*} = 27.8\%$), thermal efficiency η_{th}=56.2%;
- a desiccant based AHU (Air Handling Unit) with a desiccant wheel, which material is silica gel. It allows, during summer operation, to process 800 m^3/h of air that achieves the supply conditions for the room (supply air: temperature T=13-20 °C, humidity ratio ω=7-11 g/kg);
- an electric chiller with a cooling capacity of 8.50 kW and a COP of 3.00 at nominal operating conditions;
- a natural gas boiler with a thermal capacity of 24.2 kW and a thermal efficiency of 90.2%.

Three air streams flow in the hybrid AHU (Fig. 1):

- process air, which, after being dehumidified in the desiccant wheel (1-2), is pre-cooled interacting with the cooling air stream in an air-to-air cross flow heat exchanger (2-3), and finally cooled to the desired temperature by an electric chiller (3-4);

- regeneration air, which, after being heated by the MCHP (1-5) and/or by the boiler (5-6), is used to regenerate the desiccant wheel (6-7);
- cooling air, that, after being cooled by a direct evaporative cooler (1-8), is used to pre-cool process air exiting the desiccant wheel (8-9).

All these air streams are entirely drawn from the outdoor, therefore no recirculation is considered.

In [7], a wider description of the polygeneration system can be found.

3. Energy analysis

A simplified numerical analysis of the MCCHP plant has been conducted, considering nominal outdoor and indoor air thermohygrometric conditions, nominal devices characteristics and assuming that the MCHP always works at full load [1]. Obviously this is a simplified approach and a more detailed analysis, considering part load performance and the influence of thermohygrometric conditions, has been carried out in [8].

The energy, environmental and economic comparison is carried out on equal useful energy delivered to final user. In particular it is supposed that thermal, cooling and electric energy are fully supplied to an office building, for space heating and cooling, for domestic hot water purposes and to power electric appliances (lights, computers, AHU auxiliaries,…).

3.1. Winter season

3.1.1 The MCCHP system

During the winter season the polygeneration system works in cogeneration mode: in fact, the desiccant-based AHU does not work and only electrical and thermal energy are available, respectively for direct electric use (computer, lights…) and for space heating and hot sanitary water production. MCHP primary power input is P_p=20.8 kW.

3.1.2 The reference system

The reference system, based on separate energy "production" systems (natural gas-fired boiler and electricity grid), has to supply the same electric and thermal power of the MCHP; so its primary power input is (1):

$$P_{p,r,w} = P_{el}^{*} / \eta_{el,r} + P_{th} / \eta_{th,r} = 25.8 \text{ kW} . \quad (1)$$

The energy efficiency of both electric grid ($\eta_{el,r}$) and boiler ($\eta_{th,r}$) have been evaluated, with respect to Italy, according to the European Directive 2004/8/EC and its associated Commission Decision [1, 9, 10]:

- electric grid: $\eta_{el,r}$ = 45.2%, CO_2 equivalent emission = 0.531 $kgCO_2/kWh_{el}$, [11];
- boiler: $\eta_{th,r}$ = 90%, CO_2 equivalent emission = 0.20 $kgCO_2/kWh_p$; natural gas lower heating value = 9.59 kWh/Sm^3.

3.2. Summer season

For evaluation of the performance during summer season, outside air thermohygrometric conditions were assumed equal to the design values for Benevento: T=32 °C, ω=15 g/kg, relative humidity = 50 %, [12].

3.2.1. The MCCHP system

During summer, the hybrid AHU is switched-on, so also cooling energy is supplied to the final user.

The following parameters for some AHU components have been used (2,3):

- evaporative cooler saturation efficiency

$$\eta_{ec} = (T_1 - T_8) / (T_1 - T_{wb,1}), \quad (2)$$

where $T_{wb,1}$ is wet bulb temperature at point 1;

- cross flow heat exchanger efficiency

$$\eta_{cf} = (T_2 - T_3) / (T_2 - T_8). \quad (3)$$

The following typical values have been used for the two aforementioned parameters: η_{ec}=0.6; η_{cf}=0.5. Finally, also for the reference system, a by-pass factor of 17% for the cooling coil has been assumed [13], while a temperature increase of 10% has been assumed for process air flowing through the supply fan [14].

The nominal temperature and humidity ratio values that occur in different sections of the desiccant-based AHU are listed in Table 1 (Fig. 1). The temperature decrease of the regeneration air passing through the boiler heating coil, that is switched-off, has been neglected. Process air thermohygrometric conditions exiting the desiccant wheel have been provided by a simulation software of the rotor, considering outdoor air temperature and humidity ratio, regeneration air temperature and volumetric flow rate of process and regeneration air (800 m^3/h).

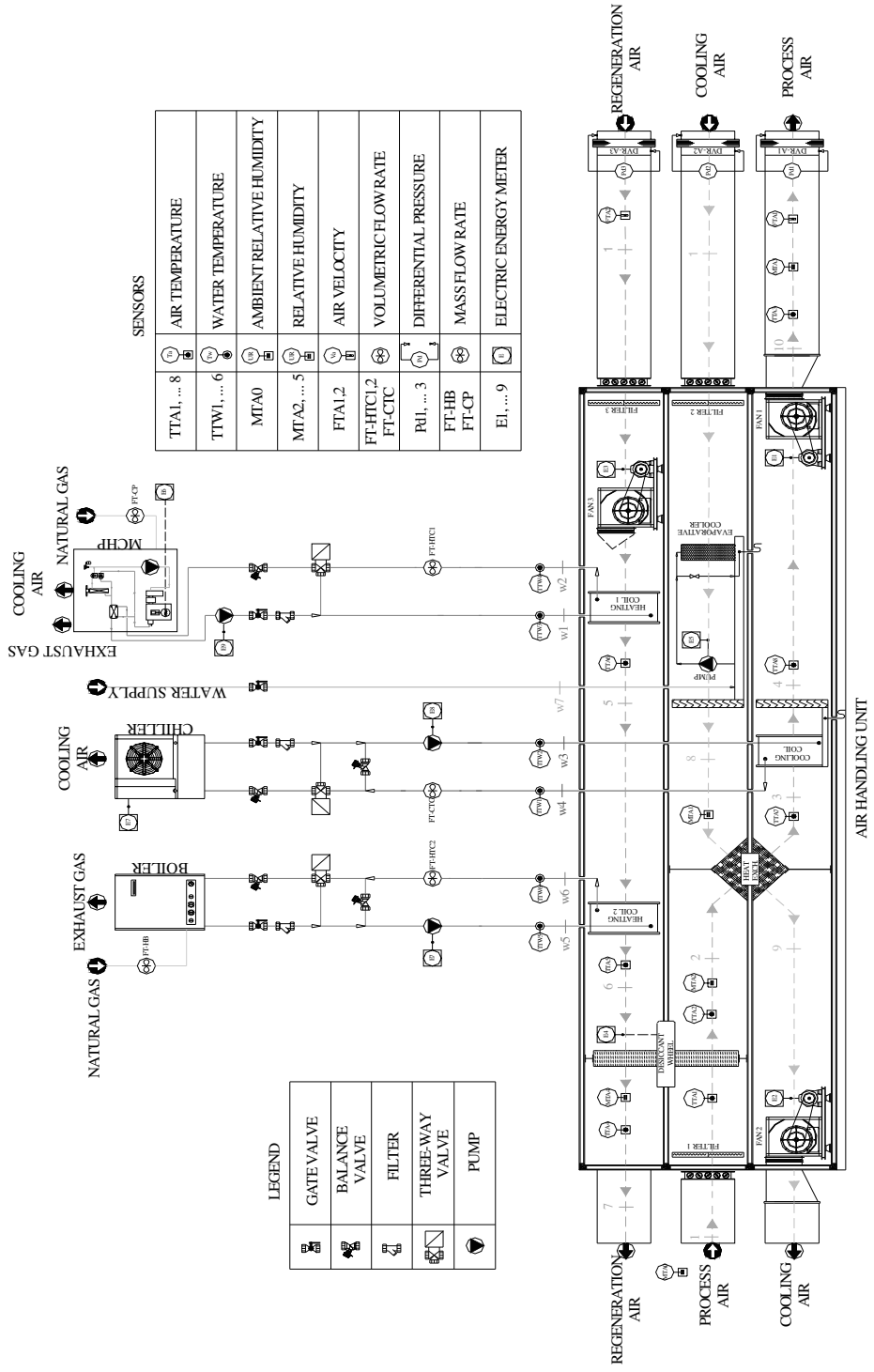

Fig. 1. The hybrid AHU layout

The cooling power provided by the cooling coil in the desiccant-based AHU can be evaluated as (4):

$$P_{cc} = \dot{m} \bullet (h_3 - h_4) = 5.30 \text{ kW}, \quad (4)$$

where $\dot{m}$ is the supply air flow rate (0.251 kg/s), equal to the regeneration one.

Table 1. Thermohygrometric air conditions in hybrid AHU.

		T [°C]	ω [g/kg]
Outdoor air	1	32.0	15.0
Process air at desiccant wheel outlet	2	49.8	9.35
Process air at cross-flow heat exchanger outlet	3	38.0	9.35
Process air at cooling coil outlet	4	17.3	9.35
Regeneration air at MCHP heating coil outlet	5	65.0	15.0
Regeneration air at desiccant wheel inlet	6	65.0	15.0
Cooling air at humidifier outlet	8	27.0	17.0
Process air at the fan outlet	10	19.0	9.35

In order to evaluate the net electric power supplied by the MCCHP system to the external electric appliances, the electric requirements of both the chiller and the AHU auxiliaries (fans, pumps…) must be accounted too. Electric requirement of the desiccant wheel motor can be neglected because it is smaller than 10 W.

The electric requirements of the chiller can be estimated with the following equation (5):

$$P_{el,ch} = P_{cc} / COP_M = 1.60 \text{ kW}, \quad (5)$$

where COP_M is the Coefficient Of Performance of the electric chiller interacting with the desiccant-based AHU, equal to 3.31.

AHUs based on chemical dehumidification have the advantage of reducing cooling energy demand, for the lack of cooling dehumidification, on which conventional air conditioning systems are instead based. In fact, the refrigeration unit can produce chilled water at higher temperatures, and consequently it operates with a higher COP. For these reasons, attention has been paid to the evaluation of the performance of the electric chiller in both the MCCHP system and the reference one: a detailed model, based on well known simulation software of inverse machines, allows to evaluate the performance of the air-cooled water chiller interacting with external secondary fluids, air and water [15, 16].

The AHU auxiliaries electric consumption, $P_{el,aux}$, due to the presence of three fans and two circulation pumps, is approximately 1.05 kW, so the net electric power supplied to external electric appliances is (6):

$$P_{el,n} = P_{el}^* - P_{el,ch} - P_{el,aux} = 3.13 \text{ kW}. \quad (6)$$

Thermal power to regenerate the desiccant wheel is fully supplied by the cogenerator and can be evaluated with the following expression (7):

$$P_{reg} = \dot{m} \bullet (h_5 - h_1) = 8.56 \text{ kW}. \quad (7)$$

The thermal power that can be used for domestic hot water production, P_{dhw}, is (8):

$$P_{dhw} = P_{th} - P_{reg} = 3.14 \text{ kW}. \quad (8)$$

Also during summer, MCHP primary power input is 20.8 kW.

The hybrid AHU can also be driven by separate electric and thermal "production": in that case the cogenerator is replaced by the electric grid to power the chiller, the auxiliaries and external electric devices (computers, lights…), and by a natural gas-fired boiler to supply thermal power to regenerate the desiccant wheel and to produce domestic hot water. Electric grid and natural gas boiler efficiencies are as defined in section 3.1.2.

The primary power input of the system can be evaluated with the following relation (9):

$$P_{p,sp} = P_{el}^* / \eta_{el,r} + (P_{reg} + P_{dhw}) / \eta_{th,r} = 25.8 \text{ kW}. \quad (9)$$

The desiccant-based AHU powered by separate production has a larger primary power consumption than the same AHU powered by the MCHP. Therefore, in the remaining of this work, only the latter is considered for the comparison with the following HVAC reference system.

3.2.2. The reference system

The reference system is an AHU with conventional cooling dehumidification and post-cooling of air (Fig. 2), that it is supposed to reach the same inlet conditions of the hybrid Air Handling Unit and to process the same air mass flow rate. The chiller, the AHU self-consumptions and electric appliances are supplied by the electric grid, while the post-cooling of air and domestic hot water production are obtained with a natural gas-fired boiler; their efficiencies are as defined in section 3.1.2. The nominal values of T and ω that occur in different sections of the reference AHU are listed in Table 2.

The cooling power supplied by the cooling coil can be calculated with the following relation (10):

$$P_{cc,r} = \dot{m} \bullet (h_1 - h_{2'}) = 7.77 \text{ kW}. \quad (10)$$

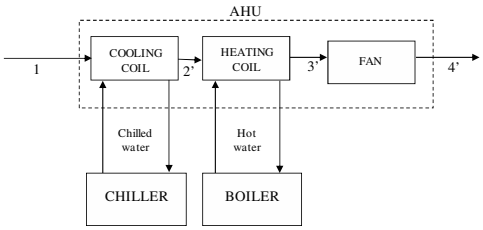

Fig. 2. AHU of the reference system

Thermal power supplied by the heating coil can be evaluated as (11):

$$P_{h,r} = \dot{m} \bullet (h_{3'} - h_{2'}) = 0.39\,\text{kW}. \quad (11)$$

Table 2. Thermohygrometric air conditions in AHU of the reference system.

		T [°C]	ω [g/kg]
Outdoor air	1	32.0	15.0
Process air at cooling coil outlet	2'	15.9	9.35
Process air at heating coil outlet	3'	17.3	9.35
Process air at fan outlet	4'	19.0	9.35

The auxiliaries electric power consumption in the reference system, $P_{el,aux,r}$, is about 0.59 kW, due to the presence of both chiller and boiler circulation pump and the one supply air fan.

So the primary power input to the system can be evaluated with the following relation (12):

$$P_{p,r,s} = \frac{P_{cc,r} / COP_r + P_{el,n} + P_{el,aux,r}}{\eta_{el,r}} + \frac{(P_{h,r} + P_{dhw})}{\eta_{th,r}} = 17.9\,\text{kW}, \quad (12)$$

where COP_r, equal to 3.0, is lower than COP_M because the chiller interacting with the reference system has both to dehumidify and to cool the process air, so it works with a lower chilled water temperature. In Fig. 3 all power flows in the summer conditions for the MCCHP and the reference system are shown.

The primary power input of the reference system, at nominal outdoor conditions, is lower than the MCCHP one: this result seems to discourage the employ of the trigeneration plant during the hot season. Nevertheless, there are operating conditions, in terms of outdoor air and supply air thermohygrometric conditions, in which the hybrid AHU energetically matched with a MCHP can obtain a primary power input lower than a conventional cooling AHU based on separate production, [7]. In order to estimate the effectiveness of the polygeneration system with respect to the conventional one, in a successive analysis the influence of the actual behavior of both outdoor and supply thermohygrometric conditions will be simulated on the basis of numerous experimental tests performed on the system, [8].

3.3. Annual energy performance

The heating period for Benevento is from 15 November to 31 March, [12], 10 hours a day, 5 days a week, so the winter operating hours for an office are about N_w=1,000 h. For the summer period, a value of N_s=650 h is assumed (from 1 June to 7 August and from 24 August to 15 September, 5 days a week, 10 hours a day).

The annual Primary Energy Saving, PES, of the MCCHP system with respect to the reference system is (13):

$$PES = 1 - \frac{P_p \bullet (N_w + N_s)}{P_{p,r,w} \bullet N_w + P_{p,r,s} \bullet N_s} = 8.30\,\%. \quad (13)$$

Winter operation has an higher effect on the annual PES than the summer one, both for the reduction of primary input power of the MCCHP and for the weight of winter operating hours [17].

4. Environmental analysis

The environmental performances of the MCCHP and reference systems are compared in terms of carbon dioxide equivalent emissions. To this aim, the equivalent CO_2 avoided emissions, on an annual basis, has been evaluated as follows (14):

$$\Delta CO_2 = 1 - \frac{CO_{2,M,w} \bullet N_w + CO_{2,M,s} \bullet N_s}{CO_{2,r,w} \bullet N_w + CO_{2,r,s} \bullet N_s} = 17.8\%. \quad (14)$$

where $CO_{2,M,w}$ (4.16 kg/h) and $CO_{2,r,w}$ (5.66 kg/h) are winter carbon dioxide equivalent emissions of the MCCHP system and the reference one, respectively, while $CO_{2,M,s}$ (4.16 kg/h) and $CO_{2,r,s}$ (4.13 kg/h) are the values during summer.

The two system have almost the same greenhouse-gas emissions during summer, while in winter the MCCHP can guarantee to avoid greenhouse-gas emissions with respect to the reference one.

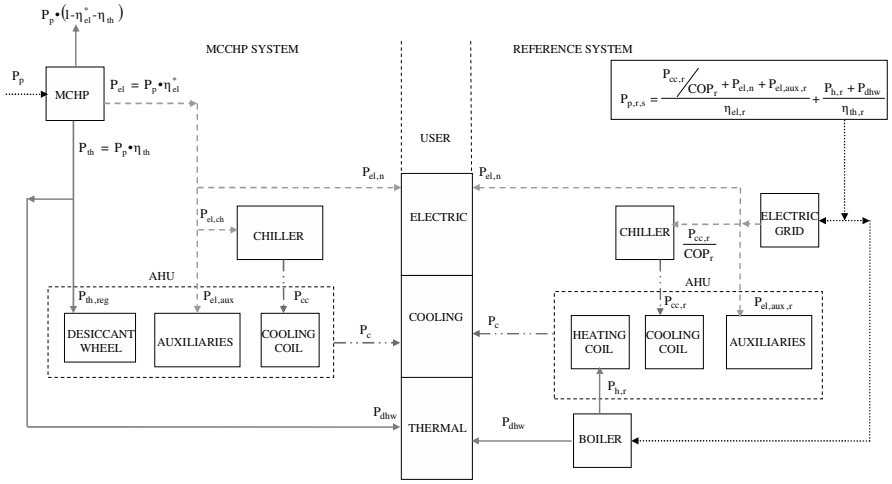

Fig. 3. Summer power flows in MCCHP and reference systems

5. Economic analysis

A simplified economic analysis of an innovative system, which usually requires high initial capital costs, plays a very important role in the assessment of its viability. In this feasibility study, the following assumption have been considered:

- unitary cost of electric energy equal to 0.17 €/kWh$_{el}$;
- unitary cost of natural gas equal to 0.50 €/Sm^3 for the cogenerator and 0.65 €/Sm^3 for the boiler in the reference system (natural gas employed in cogenerative application is subject to a lower taxation).

A simplified approach has been followed, evaluating the Simple Pay Back, SPB, (15):

$$SPB = \Delta IC \Big/ \left(AOC_r - AOC_M\right), \qquad (15)$$

where ΔIC is the Investment Cost difference between the MCCHP system with respect to the reference one, 20 k€, while AOC$_r$ (2.67 k€/y) and AOC$_M$ (1.79 k€/y) are the Annual Operating Costs of reference and MCCHP systems.

At the moment, the first cost of both the cogenerator and the desiccant wheel is very high to allow an acceptable economic return (SPB is greater than 20 years). However there are a great number of private and public subjects (gas utilities, manufacturers,…) involved in the definition of the economic variables concerning this type of system. For example, government grants along with attractive rates for electricity export to the grid may significantly encourage MCHP and desiccant dehumidification market penetration.

6. Conclusions

In this paper a MCCHP, consisting of an internal combustion engine cogenerator, a hybrid AHU incorporating a desiccant wheel and a chiller is numerically analyzed considering nominal outdoor and indoor air thermohygrometric conditions, nominal devices characteristics and assuming that the MCHP always works at full load. Such a system has been compared with a reference system, based on separate electric and thermal "production" and on a conventional cooling dehumidification AHU. The result is that in winter the MCCHP, working in cogeneration mode, can guarantee sensible savings in terms of primary energy consumption and significant reductions of greenhouse-gas emissions with respect to the reference system. In summer, on the other hand, the MCCHP primary energy consumption is higher than the reference system one, while their greenhouse-gas emissions are quite comparable. However, on an annual basis, PES and ΔCO_2 are both positive (8.30 % and 17.8 %, respectively).

In terms of economic viability, the high initial cost of both the MCHP and the desiccant wheel still determines a very long pay-back period, but government grants may significantly encourage MCHP and desiccant dehumidification market penetration.

Nomenclature

AOC	Annual Operating Cost, k€/y
CO_2	carbon dioxide equivalent emissions, kg/h
h	enthalpy, kJ/kg
IC	Initial Cost, k€
$\dot{m}$	mass flow rate, kg/s

P power, kW
T temperature, °C
N Number of operating hours, h
SPB Simple Payback Period, y
COP Coefficient Of Performance
PES Primary Energy Saving

Greek symbols

ω humidity ratio, g/kg
η efficiency

Subscripts and superscripts

aux auxiliaries
c cooling
cc cooling coil
cf cross flow heat exchanger
ch chiller
dhw domestic hot water
ec evaporative cooler
el electric
h heating
M MCCHP system
n net
p primary
r reference system
reg regeneration
s summer
sp separate production
th thermal
w winter
wb wet bulb
* MCHP effective electric power "production" and electric efficiency

References

[1] Chicco, G., and Mancarella, P., 2007, Trigeneration primary energy saving evaluation for energy planning and policy development, Energy Policy, 35 (12), pp. 6132-6144.

[2] Willis, H. L., and Scott, W. G., 2000, *Distributed power generation: planning and evaluation*, Marcel Dekker Inc., New York.

[3] Badami, M., and Portoraro, A., 2009, Performance analysis of an innovative small-scale trigeneration plant with liquid desiccant cooling system, Energy and Buildings, 41 (11), pp. 1195-1204.

[4] Jalalzadeh-Azar Ali, A., et al., 2005, Performance assessment of a desiccant cooling system in a CHP application incorporating an IC engine, International Journal of Distributed Energy Resources, 1(2), pp. 163-184.

[5] Schmitz, G., and Casas W., 2001, Experiences with a small gas engine driven desiccant HVAC-system, *Proc. 8th International IGRC Conference*, Amsterdam.

[6] Schmitz, G., and Casas, W., 2005, Experiences with a gas driven, desiccant assisted air conditioning system with geothermal energy for an office building, Energy and Buildings, 37 (5), pp. 493-501.

[7] Angrisani, G., et al., 2009, Experimental analysis of small scale polygeneration system based on a natural gas-fired Micro-CHP and a hybrid HVAC system equipped with a desiccant wheel, *Proc. 22nd International ECOS Conference*, Foz do Iguaçu, Paraná, Brazil, pp. 635-644.

[8] Angrisani, G., et al., 2010, Desiccant HVAC system driven by a Micro-CHP: experimental analysis, accepted for publication on Energy and Buildings.

[9] Directive 2004/8/EC of the European Parliament, Official Journal of the European Union, 21.02.2004.

[10] European Commission Decision of 21st December 2006, Official Journal of the European Union, 06.02.2007.

[11] Italian Environmental Ministry, www.minambiente.it

[12] National Italian Organization for Unification, norm UNI 10339:1995.

[13] Rossi, N., 2003, *Manuale del Termotecnico*, Ulrico Hoepli Press, Milano.

[14] Briganti, A., et al., 2001, *Manuale della Climatizzazione*, Tecniche Nuove Press, Milano.

[15] CoolPack, 2000, Software Package, Ver. 1.46, Department of Mechanical Engineering, Technical University of Denmark, Lyngby, Denmark.

[16] IMST-ART, 2009, Software Package, Ver. 3.20.02, Instituto de Ingeniería Energética, Universidad Politécnica de Valencia, Valencia, Spain.

[17] Li, H., Fu, L., et al., 2006, Energy utilization evaluation of CCHP systems, Energy and Buildings, 38 (3), pp. 253-257.

Acknowledgments: This work has been supported by Italian research project PRIN 2007 "Criteria and methodologies for the optimization of small/medium scale polygeneration systems".

An Analysis of Micro-CHP Systems for Residential Use

Dan Scarpete[a] and Krisztina Uzuneanu[b]

[a,b] *University "Dunarea de Jos" of Galati, Galati, Romania*

Abstract: In this paper, an analysis of different micro-CHP systems is made from the point of view of benefits and limitations of the operational and economic and environmental parameters of micro-CHP systems for residential use. The electric efficiency is better for micro-CHP systems with reciprocating engines, and Stirling engines are in the second place. The thermal efficiency is better for micro-CHP systems with Stirling engines followed by reciprocating engines. Stirling engines use an external heat source, which simplifies design, minimizes noise and vibration, and allow multi-fuel use. These features make the Stirling engine a promising alternative to the internal combustion engine.

Keywords: Combined heat and power, Residential, Prime mover, Electric and thermal efficiency.

1. Introduction

Cogeneration is an engineering concept involving the production of both electricity and useful thermal energy in one operation, thereby utilizing fuel more efficiently than if the desired products were produced separately [1].

Micro-cogeneration, also termed micro combined heat and power (Micro-CHP) or residential cogeneration, is an emerging technology with the potential to provide energy efficiency and environmental benefits by reducing primary energy consumption and associated greenhouse gas emissions [2].

Micro-CHP denotes the concept of smaller scale CHP systems suitable for a residential house [3]. A micro-CHP system can have different configurations ranging from simple to complex ones. Micro-CHP systems comprise a prime mover, which generates electricity, and the heat recovery and utilization components which use the heat rejected by the prime mover provide space heating, hot water, and/or even cooling. Figure 1 shows the structure of a micro-CHP system for residential application [4]. The system consists of a CHP plant, a storage tank and a back-up burner. The CHP plant which is driven by city gas is used to meet part of the electrical demand (including cooling load with the use of air conditioning), the deficiency is served by the utility grid.

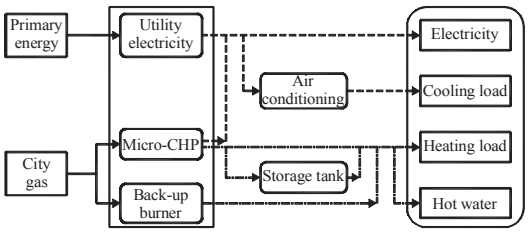

Fig. 1. Structure of a residential micro-CHP system [4].

Combined Heat and Power (CHP) systems can simultaneously deliver thermal and electric (or mechanical) energy services and thus use fuel very efficiently [5]. Reduced fuel use naturally reduces combustion emissions [6]. Today's small-scale CHP systems already provide heat, cooling and electricity at nearly twice the fuel efficiency of separate heat and power based on power remote plants, electric chilling, and onsite hot water and space heating [5]. CHP is an extremely efficient way of producing usable heat and electricity simultaneously at the point of use, offering an economic and environmentally friendly alternative for meeting thermal and electrical demands in many public sector applications [7]. In a CHP system, useful heat is delivered at a relatively high temperature, which results in less electricity being generated [8]. The balance of heat and electricity output is optimised to meet the particular site requirements.

Generally, CCHP (Combined Cooling, Heating and Power) indicates large-scale technologies that contain both improved conventional approaches, like steam turbines, reciprocating engines, combustion turbines and electric chillers, as well as relatively new technologies such as fuel cells, micro turbines, Stirling engines, absorption chillers and dehumidifiers [9]. Although steam turbine, reciprocating internal combustion engine and gas turbine that can be considered as the

conventional prime movers still make up most of the gross capacity being installed, micro gas turbine, Stirling engine and fuel cell present a promising future for prime movers in CCHP system [1,10].

The environmental benefits offered by CHP can assist public sector energy, estates and facilities managers to meet CO_2 emission reduction targets, such as the Kyoto Protocol and Agenda 21 [7]. Compared to generators which lack the system for utilizing waste heat, co-generation can reduce CO_2 emissions up to 30%; with a renewably fueled micro-CHP, a negative CO_2 balance can be created in comparison with heating by fossil fuel and pulling electricity from a fossil fuel burning electrical utility [11].

Recent indicators show the emergence of micro-CHP [3]. Market projections predict a world-wide market growth over 35% per year. High energy consumption, high energy expenditure, large spark-spread (i.e., difference between electricity and fuel costs), big square footage, and high income are the key conditions for market acceptance [3].

The micro-CHP systems applicable to domestic users in individual households still need further development to be widely acceptable [12]. Micro-CHPs are especially interesting due to their technical and performance features:

- A high overall energy conversion efficiency (e.g., in excess of 90% for Stirling engines).
- Low maintenance requirements equivalent to a domestic gas boiler.
- Very low noise and vibration levels for installation at home.
- Very low emissions of NO_x, CO_x, SO_x and particulates.

Micro-CHP systems powering up to approximately 10 kWe are considered as a future key technology for the energy supply of buildings and settlements from the viewpoints of both heating systems manufacturers and energy suppliers [13]; such CHP plants are based on different prime movers as: conventional diesel, gas or biomass engines, gas or steam turbines, as well as Stirling engines or fuel cells [3,13,14].

In this paper, an analysis of different micro-CHP systems is made from the point of view of benefits and limitations of the operational and economic and environmental parameters of micro-CHP systems for residential use. Since a prime mover in a micro-CHP generates electricity and the waste heat is recovered downstream, the analysis is focused on prime movers used in micro-CHP systems.

2. Technologies for micro-CHP systems

A prime mover in a micro-CHP system (fig. 2) generates electricity and the waste heat is recovered downstream [3].

Cogeneration technologies for residential, commercial and institutional applications can be classified according to their prime mover and from where their energy source is derived [14]. This section describes four micro-CHP prime movers. Each technology faces numerous challenges [5] detailed in the following. The prime movers to be evaluated include:

- Reciprocating engines.
- Stirling engines.
- Micro steam and gas turbines.
- Fuel cell systems.

2.1. Reciprocating engines

In micro-CHP systems with reciprocating engines, the conventional internal combustion engines (ICE) are coupled with a generator and heat exchangers to recover the heat of the exhaust gas and the cooling water and oil [5,15].

For micro-CHP applications, typically, spark ignition engines are used [16], due to their heat recovery system producing up to 160°C hot water or 20 bar steam output compared to diesel engines where the temperature is often lower, usually 85°C maximum [17].

Reciprocating engines have several advantages for micro-CHP [3]. First it is a mature and well-understood technology. It can be designed for different fuels including gasoline, diesel, natural gas or landfill gas, etc. [3,18]. The efficiency of the reciprocating engine is around 25-45%, which is higher than steam engines and current Stirling engines. Also reciprocating engines have a short startup time than external combustion engines.

The investment costs for micro CHP systems vary significantly depending on the kind of technology [15]. Furthermore there exists a high dependency of the specific investment costs from the electrical power output.

One of the limitations of reciprocating engines is the frequent maintenance [3]. In general, noise and emissions are two issues for the reciprocating engines. The NO_x emissions of small engines are fairly low, but still higher than the other technologies'.

2.2. Stirling engines

Compared to conventional internal combustion engine, Stirling engine is an external combustion device [5,19], where the heat is generated externally in a separate combustion chamber [15]. The cycle medium, generally helium or hydrogen, is not exchanged during each cycle, but within the device, while the energy driving the cycle is applied externally.

The Stirling engine itself is a heat recovery device, like the steam turbine [5]. Two types of Stirling engines show potential for residential cogeneration – kinematic Stirling and free-piston Stirling [20]. The free-piston Stirling does away with mechanical linkages, resulting in fewer moving parts, no need for a lubricant, low maintenance costs, and a longer life [5]. Kinematic Stirling engines are typically larger than their free-piston counterparts [20]. Electric capacities for kinematic Stirling units are between 5-500 kW, while the capacities for free-piston units are between 0.01 and 25 kW.

Due to the nature of external combustion, the Stirling engines can be operated on a wide variety of fuels, including all fossil fuels (e.g. natural gas [21]), biomass (biomass can be used many ways, including direct combustion, two-stage combustion, and (the cleanest) with a gasifer), solar, geothermal, and nuclear energy [5] [3]. The combustion can be controlled relatively easily and the emissions have the potential to be very low. The noise of the Stirling engine is lower than that of the IC engines [3]. The maintenance is also supposed to be low and the life is usually long.

The Stirling engines are 15-30% efficient in converting heat energy to electricity, with many reporting a range of 25 to 30% [20]. The goal is to increase the performance to the mid-30% range. The efficiency of modern Stirling generators is more than 40% [22]. On heating the working medium to 90°C, the total efficiency of a micro-CHP with Stirling engine is 95% [5,22]. Cogeneration systems based on natural-gas Stirling engines permit 40% reduction in fuel consumption relative to centralized power systems [22]. The cost of 1 kWh of power from a cogeneration system is 3–4 times less than for centralized power systems, and the heat generated is essentially free!

Stirling engines are more efficient than internal combustion engines in cogeneration systems on account of their thermal balance, i.e., the difference between the heat extracted by the spent gases and the heat extracted by the coolant liquid [22]. For Stirling engines, this difference is 30%. Taking account of their high efficiency, this permits the creation of compact and highly efficient cogeneration units.

A great advantage for the Stirling engine is that, in a micro-CHP, the heat from the burner that is not used by the Stirling engine can be readily used for hot water and space heating [3].

The major disadvantages of the Stirling engines include [3]:

- The high cost.
- The engine needs a few minutes to warm up.
- Durability of certain parts is still an issue.

Stirling engines are in between demonstration phases and marketing [16] being under development for deployment in residential CHP applications [23]. There are still field trials being carried out; but initial commercial products are already defined and on the verge of series production [16].

There are more than 20 Stirling engine manufacturers worldwide [3]. Currently Stirling engines have been used in various applications, which include residential [3,17,24]. But the total Stirling engine market is rather small [3].

2.3. Rankine cycle engine and micro gas turbines

Although typical Rankine cycle (RC) systems are in the order of MW or above, some small scale systems have capacity as low as 50 kWe [3]. The RC for micro-CHP is less expensive than most other prime mover technologies and is likely to be a competitive prime mover technology. There haven't been any RC engines in commercial sales for micro-CHP and more testing data are needed to really evaluate this promising technology [3].

The Organic Rankine Cycle (ORC) is similar to the cycle of a conventional steam turbine, except for the fluid that drives the turbine, which is a high molecular mass organic fluid [15]. The selected working fluids allow exploiting efficiently low

temperature heat sources to produce electricity in a wide range of power outputs.

The major disadvantage of the RC engines is that the efficiency is low (around 10%) [3].

Micro gas turbines are small gas turbines belonging to the group of turbo machines up to an electric power output of 300 kWe [15]. In order to raise the electrical output micro gas turbines are equipped with a recuperator.

The electric capacity of current micro-turbines, usually 25 kW or above, is too high to be in a residential micro-CHP unit [3]. Research is ongoing for systems with capacities less than 25 kW, e.g. 1 and 10 kW, which will be suitable for the single-family residential buildings [14].

For cogeneration applications, an overall efficiency of 80% and above can be achieved [14]. However, in the lower power ranges, reciprocating ICE have higher efficiency.

Micro-turbines offer a number of advantages when compared to reciprocating internal combustion engine based cogeneration systems [3,14]:

- Fast response.
- Compact size, low weight and lower noise.
- Lower NO_x emission.
- Low maintenance requirements.

Micro-turbines can use different fuels, including natural gas, hydrogen, propane or diesel and other biobased liquid and gas fuels [3,14].

The major disadvantages of this technology include the high cost, relatively shorter life and high O&M cost [3]. The efficiency of micro-turbines is not very high, although this is enough or more than enough for residential micro-CHP because of the high thermal/electric load ratio. Micro-turbine power output decrease with higher elevation and higher temperature [3,14].

2.4. Fuel cell

Fuel cells are electrochemical energy converters similar to primary batteries [15]. Fuel cell micro-CHP systems are either based on the low temperature proton exchange membrane fuel cell (PEMFC) which operate at about 80°C, or on high temperature solid oxide fuel cells (SOFC) working at around 800 - 1000°C [5,15].

Fuel cells normally run on hydrogen, but can also be used with natural gas or other fuels by external or internal reforming [25].

Fuel cells have several benefits. They have higher efficiency (up to 45% electric [5]) than most other prime movers [3]. Emissions are essentially absent [3,25] producing negligible amounts of pollution [5]. Because fuel cells have no moving parts, they are very quiet [5,25].

Fuel cells are still in the R&D stage [16]. The major problem of fuel cells is the short lifetime of the membrane [3], and their cost is very high [3,5].

There are no fuel cell based micro-CHP systems commercially available at this moment [3,5].

3. Prime mover evaluation

Because a micro-CHP unit is an important investment, to identify the best micro-CHP technology for a residential application, different cogeneration technologies presented above will be compared on the basis of different criteria. In general, three main groups of criteria are used [16]:

- Thermodynamic performance.
- Economic profitability.

Table 1. Characteristics of some available micro-CHP technologies [3,5,14-18,20,22].

Parameter range	ICE	Stirling engine	RC–ORC/Micro-turbine*	Fuel Cell
Electrical capacity (kWe)	1-10	1-10	0.5-10 25-80*	0.5-10
Electrical efficiency (%)	20-40	25-30 Curent 35-50 Possible	10-20 25-28*	30-50 PEMFC 40-50 SOFC
Thermal efficiency (%)	50-60	40-60	N.A.	40-60
Temperature of heat (°C)	85-100	200	70-90	80-100 PEMFC 950-1000 SOFC
Overall efficiency (%)	80-90	65-95	75-91*	70-90 PEMFC 70-95 SOFC
Thermal output (kWt)	3-30	3-15	85-150*	1-30
Availability (%)	85-98	85-90	N.A.	95
Part load performance efficiency	Good	Better	N.A.	Best
Maintenance cost (€/kWhe)	0.008-0.012	0.005-0.01	0.006–0.01 ($/kWhe)*	0.016-0.024
Emissions	Low	Lower	Low*	Lowest
Cost (€/kWe)	785-2200	2500-3500	1561-2516*	N.A.

- Environmental parameters.

Table 1 presents characteristics of the different available micro-CHP technologies.

The various prime mover technologies are evaluated using the metrics and weighting factors shown in Table 2 [3]. The weighting factors are assigned subjectively and are intended to provide a relative measure of the importance of each metric with respect to application in a CHP system.

Scores ranging from 0.1 to 2 are assigned to each prime mover technology for each metric, based on both quantitative and qualitative assessments, relative to application in a CHP system [3]. The weighted scores are shown in Figure 2. It can be seen that the reciprocating engines and the Stirling engines have higher scores, suggesting that they are more appropriate for the micro-CHP.

A comparison of residential micro CHP technologies related on prime mover can be made versus separate heat and power (SHP) [5]. Table 3 shows by which factor micro-CHP efficiencies exceed those of separate heat and power. The data from Table 3 indicate that the overall system efficiency has the best value for Stirling micro-CHP technology as well as for themal/electric ratio.

In [26], five commercial micro-CHP systems

Table 2. Micro-CHP prime mover evaluation metrics and weighting factors [3].

Evaluation Metric	Weighting Factor
Efficiency	0.5
Life	0.5
Low capital cost	2.0
Technology maturity	0.1
Scalable for residential	0.5
Customer acceptance	0.1
Low noise	0.5
Environmental friendly	0.1
Fast response	0.5
Large operating range	0.5
Easily couples with TAT	0.2
Source energy availability	0.1
Source energy flexibility	0.1
Maintenance cost	0.5
Fuel cost	0.5
Waste heat temperature	0.5

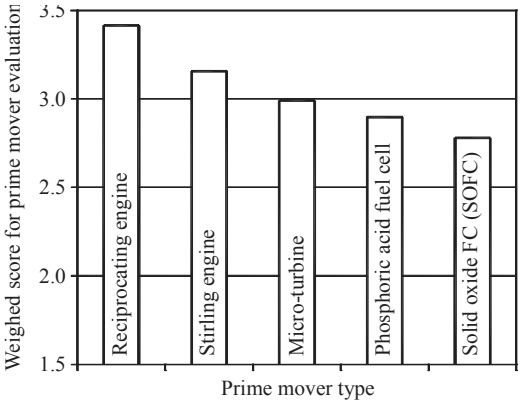

Fig. 2. The weighted scores for evaluation of different micro-CHP prime movers (adapted from [3]).

(<5 kW) are evaluated for use in residential applications by taking the viewpoint of a detached single family house (reference case). The studied micro-CHP technologies are (Table 4):

- Two gas reciprocating engines running on natural gas (ICE1 and ICE2).
- Two Stirling engines (SE1 and SE2).
- A fuel cell running on hydrogen gas with reforming of natural gas (FC).

Table 4. Power and efficiency of micro-CHP technologies [26].

CHP	P_e (kW)	η_e (%)	P_t (kW)	η_t (%)
ICE1	5.5	27	12.5	61
ICE2	4.7	25	12.5	65
SE1	2–9.5	24	8–26	72
SE2	1	12	4.9–8	80
FC	4	25	9	55

The data from Table 4 indicate that the electric efficiency is better for micro-CHP systems with reciprocating engines, and Stirling engines are in the second place. The thermal efficiency is better for micro-CHP systems with Stirling engines followed by reciprocating engines.

Based on a representative mixed housing development, a case study in [27] considers for illustrative

Table 3. Comparison of the main residential micro-CHP technologies to SHP [5].

1 kW unit	Electric η_e (%)	Thermal η_t (%)	Temperature range	System η (%)	T/E	SHP/CHP fuel
PEM Fuel Cell	29	46	80 - 100°C hot water	76	1.59	1.59
SOFC Fuel Cell	27	45	80 - 1000°C* hot water-high quality steam	82	1.67	1.51
IC Engine	25	56	90 - 120°C hot water, low-grade steam	81	2.24	1.59
Stirling engine	14	75	80 - 700°C* hot water-med. quality steam	89	5.36	1.48

*Depending on recuperation

η is the symbol used for thermodynamic efficiency calculated at higher heating value.

purposes a sample of 300 of the total stock, each with an individual annual thermal load of 20,000 kWh. The rationale applied in this case study is to aim for the implementation of the system which exploits the potential heat demand as fully as possible, with electricity production in capital plant amortisation, operating costs and pollutant emissions having no additional impact. Figure 3 presents a comparison of different electric& thermal technologies, both within a centralised system and with micro-CHPs. It can be note that the operating cost is minimum for micro-CHPs with Stirling engine.

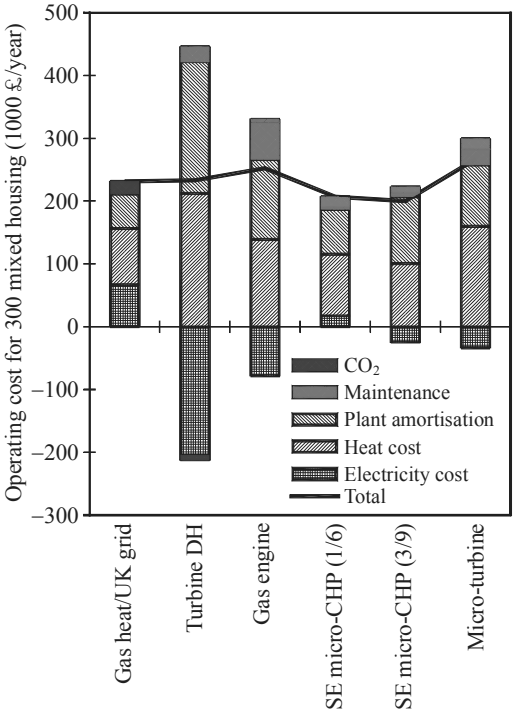

Fig. 3. Life cycle operation costs for residential CHP technologies (adapted from [27]).

An assessment of micro-CHP can be made on environment impact basis [28]. Figure 4 presents the annual CO_2 savings for micro-CHP prime movers compared to grid electricity and boiler alternatives. The best CO_2 savings are obtained for 1 kWe gas engine micro-CHP, followed by 1 kWe Stirling/Rankine engine (low efficiency) micro-CHP.

The annual financial savings through the use of CHP are analyzed in [26]: a comparison is made with the hypothetical situation in which all

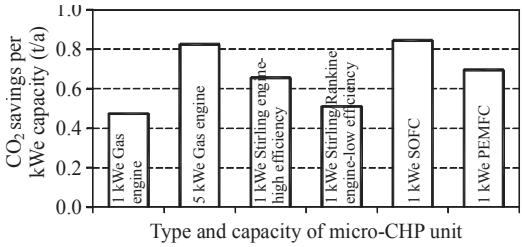

Fig. 4. Annual CO_2 savings for micro-CHP prime movers (adapted from [28]).

produced electricity can be valorized at the maximal (purchasing) price. For most CHP technologies, the annual savings in the actual situation turn out to be low, which is primarily due to the fact that the largest part (85–90%) of the produced energy is sold to the grid at very low prices. This makes the annual savings too low to return the investment cost in a reasonable amount of time.

4. Conclusions

Cogeneration is an engineering concept involving the production of both electricity and useful thermal energy in one operation, thereby utilizing fuel more efficiently than if the desired products were produced separately.

A prime mover in a micro-CHP system generates electricity and the waste heat is recovered downstream. The prime movers to be evaluated included: reciprocating engines, Stirling engines, micro steam and gas turbines, and fuel cell systems.

The evaluation of various prime mover technologies by using the metrics and weighting factors showed that the reciprocating engines and the Stirling engines have higher scores, suggesting that they are more appropriate for the micro-CHP.

A comparison of residential micro-CHP technologies focused on prime mover, made versus separate heat and power, indicates that the overall system efficiency has the best value for Stirling micro-CHP technology as well as for themal/ electric ratio.

An evaluation of five micro-CHP systems (<5 kW) for use in residential applications was made on power and efficiency basis. The electric efficiency is better for micro-CHP systems with reciprocating engines, and Stirling engines are in the second place. The thermal efficiency is better for micro-

CHP systems with Stirling engines followed by reciprocating engines.

The comparison of different electric&thermal technologies, both within a centralised system and with micro-CHPs, revealed that the operating cost is minimum for micro-CHPs with Stirling engine.

An assessment of micro-CHP made on environment impact basis indicated that the best CO_2 savings are obtained for 1 kWe gas engine micro-CHP, followed by 1 kWe Stirling/Rankine engine (low efficiency) micro-CHP.

The analysis of annual financial savings through the use of CHP pointed out that the annual savings are too low to return the investment cost in a reasonable amount of time.

As a final conclusion, regarding prime mover technology evaluation for producing electricity and heat for residential use, it can be stated that the micro-CHP units with Stirling engines are more appropriate for the micro-CHP having the best value for overall system efficiency.

Stirling engines use an external heat source, which simplifies design, minimizes noise and vibration, and allow multi-fuel use. These features make the Stirling engine a promising alternative to the internal combustion engine.

References

[1] Khaliq, A., 2009, Exergy Analysis of Gas Turbine Trigeneration System for Combined Production of Power Heat and Refrigeration, International Journal of Refrigeration 32, pp. 534-545.

[2] Dorer, V., and Weber, A., 2009, Energy and CO2 Emissions Performance Assessment of Residential Micro-Cogeneration Systems with Dynamic Whole-Building Simulation Programs, Energy Conversion and Management 50, pp. 648-657.

[3] Micro-CHP Systems for Residential Applications, 2006, Final Report, United Technologies Research Center, Contract No. DE-FC26-04NT42217.

[4] Ren, H., and Gao, W., 2010, Economic and Environmental Evaluation of Micro CHP Systems with Different Operating Modes for Residential Buildings in Japan, Energy Buildings, In press.

[5] Kaarsberg, T., et al., Combined Heat and Power for Saving Energy and Carbon in Residential Buildings, Building Industry Trends-10, DOE Scientific and Technical Information, pp. 149-159.

[6] Gans, W., Shipley, A. M., and Elliot, R. N., 2006, Survey of Emissions Models for Distributed Combined Heat and Power Systems, Report Number IE071, American Council for an Energy-Efficient Economy, New York.

[7] Northern Ireland trusts adopt DACHS mini-CHP as part of sustainable energy drive, http://www.cibse.org/pdfs/Arnold%20Teekaram%20BSRIA%20presentation.pdf

[8] A Developing Market for Cleaner Power, 2000, Electricity Association, Environmental Briefing, Combined Heat and Power, Number 9, Addendum April.

[9] Sathyakeerthi, B. R., Tri-Generation (CCHP) for a Pharmaceutical Company Whay Did Not Materialize? Mecon Ltd. Company, Bangalore, India, http://www.emt-india.net/announcements/issue25/winners_papers_Issue25/17_BSathyakeerthi.pdf

[10] Wang, J.-J., Zhang, C.-F., and Jing, Y.-Y., 2009, Multi-Criteria Analysis of Combined Cooling, Heating and Power Systems in Different Climate Zones in China, Applied Energy, In press.

[11] Lepisto, C., 2007, SenerTec Dachs: A 90% Efficient Power Plant for Your Home, Science & Technology (alternative energy), Berlin, http://www.treehugger.com/files/2007/03/senertec_dachs.php

[12] Kuhn, V., Klemeš, J., and Bulatov, I., 2008, MicroCHP: Overview of selected technologies, products and field test results, Applied Thermal Engineering 28, pp. 2039-2048.

[13] Matics, J., and Krost, G., 2008, Micro Combined Heat and Power Home Supply: Prospective and Adaptive Management Achieved by Computational Intelligence Techniques, Applied Thermal Engineering 28, pp. 2055-2061.

[14] Onovwiona, H.I., and Ugursal, V.I., 2006, Residential Cogeneration Systems: Review of the Current Technology, Renewable and Sustainable Energy Reviews 10, pp. 389-431.

[15] Simader, G. R., Krawinkler, R., and Trnka, G., 2006, Micro CHP systems: state-of-the-art, Final Report, Deliverable 8 (D8) of Green

Lodges Project (EIE/04/252/S07.38608), Austrian Energy Agency, Vienna.

[16] Aoun, B., 2008, Micro Combined Heat and Power Operating on Renewable Energy for Residential Building, Doctoral Thesis, Ecole Nationale Superieure des Mines de Paris.

[17] Knight, I., and Ugursal, I., 2005, Residential Cogeneration Systems: A Review of The Current Technologies, A Report of Subtask A of FC+COGEN-SIMISBN, ISBN No. M154-1/2005E, Catalogue No.: 0-662-40482-3.

[18] DACHS - Internal Combustion Engine, http://www.baxi.co.uk/products/DACHS.htm

[19] Wu, D. W., and Wang, R. Z., 2006, Combined Cooling, Heating and Power: A review, Progress in Energy and Combustion Science 32, pp. 459-495.

[20] Residential Micro-Cogeneration Using Stirling Engines, 2004, Emerging Technologies & Practices, ACEEE.

[21] Annual Social Report 2008, GasTerra B.V., Groningen, Nederland, www.gasterra.nl.

[22] Kirillov, N. G., 2008, Power Units Based on Stirling Engines: New Technologies Based on Alternative Fuels, Russian Engineering Research 28(2), pp. 104-110.

[23] Roth, K., Targoff, J., and Brodrick, J., 2008, Using Stirling Engines For Residential CHP, ASHRAE Journal, November, pp. 42-47.

[24] Market analysis micro CHP, 2007, RTD Project Name: Study "Use of Micro CHP Units in the Electrical Power Range 1 – 5 kWe for Berlin", Project No. 05 950, ProEcoPolyNet-Fact Sheet.

[25] Dorer, V., Weber, R., and Weber, A., 2005, Performance Assessment of Fuel Cell Micro-Cogeneration Systems for Residential Buildings, Energy and Buildings 37, pp. 1132-1146.

[26] De Paepe, M., D'Herdt, P., Mertens, D., 2006, Micro-CHP Systems for Residential Applications, Energy Conversion and Management 47, pp. 3435-3446.

[27] Options for Upgrading Residential CHP, http://www.microchap.info/COGEN%20options.pdf

[28] Slowe, J., MicroCHP to Increase Energy Efficiency: Emerging Technologies, Products and Markets, Delta Energy & Environment Affiliation, http://mail.mtprog.com/CD_Layout/Day_2_22.06.06/1400-1545/ID33_Slowe_final.pdf

Acknowledgments: The authors would like to acknowledge to EEA Financial Mechanism for financing the research on "Integrated micro CCHP – Stirling Engine based on renewable energy sources for the isolated residential consumers from South-East region of Romania (m-CCHP-SE)", under the contract No. RO-0054/2009.

Study the influence of cooling on the overall efficiency in mCCHP residential systems with fuel cell and additional heating system

Prof.PhD.eng. Nicolae BADEA, Prof.Assistance PhD.eng. Nelu CAZACU, Prof.Assistance PhD.eng. Ion VONCILĂ, Assistant eng. Ciprian VLAD, Junior Assistant eng. Ciprian BALANUȚĂ

„DUNĂREA DE JOS" University, Galati, Romania

Abstract: The paper is primarily aimed at highlighting the influence of cooling system - the chains used in trigeneration - the overall energy efficiency of these systems (mCCHP). The goal is to identify which topology of the CCHP system has a higher efficiency. The analysis undertaken, depending of the type cooling system used, shows that this influences radically the overall architecture of trigeneration residential system. The obtained results indicate total energy efficiency higher in case of mCCHP system with mechanical compression, for residential house.

Keywords: absorption, compression, fuel cells, mCCHP.

1. Introduction

An important concept in the energy area in the EU introduced by Directive 8/2004 is the promotion of cogeneration (CHP) by decentralization of the electric power and heat production. In the cogeneration – as a new feature - for meeting the quality and comfort criteria in residential buildings is remarkable the occurrence of trigeneration.

Trigeneration involves the use of heat for home heating in winter and the possibility of space cooling during the summer season. The cogeneration / trigeneration systems (CHP/CCHP) used in the residential sector should be developed and designed to be able to produce heat or cold and electricity simultaneously from a single source of energy. The development of CHP/CCHP systems in the EU is characterized by great diversity, both in terms of the scale and the nature of development.

In accordance with CE Directive no. 8/2004 of the Parliament of the European Council, concerning the promotion of cogeneration, the units of combined production, with the same electric power from a few kW to 50 kW are micro-CHP, between 50 and 1000 kW are medium power and between 1000 kW and maximum 10 MW are of great power. From the multitude of mCCHP systems, obtaining heat and electrical power, at European level is forecast a sharp increase of the research on systems with Stirling engines and fuel cells. The performance indicators of production of the trigeneration system - instead of separate heat and power (SHP) production - are: the ratio of electricity/heat (CHP index), the efficiency of electricity production in trigeneration, fuel economy, thermal efficiency, cold production efficiency, total effectiveness of energy. The mathematical relation of the total annual energy efficiency is [1]:

$$\eta_{chp} = 3{,}6\frac{E_{gen} + Q_{gen}}{mH_i} \quad (1)$$

where:

E_{gen} - annual production of electrical energy [kWh/year], Q_{gen} - annual heat production [kWh/year], m - annual fuel consumption [kg/year], H_i - low calorific value of the fuel [kJ kg^{-1}].

The percent fuel savings (PFS) of CCHP system in comparison with the separate heat and power SHP can be determined with the relation:

$$PFS = (\frac{\alpha_e}{\eta_e} + \frac{\alpha_Q}{\eta_Q} - 1)m \quad (2)$$

where:

α_e – electrical efficiency of the CCHP system, α_Q – thermal efficiency of the CCHP system, η_e – electrical efficiency of SHP system, η_Q – thermal efficiency of SHP system.

Corresponding Author: Prof.PhD.eng. Nicolae BADEA, Email: nicolae.badea@ugal.ro

2. The residential mCCHP system with fuel cells

The first performance indicator of the trigeneration production system is the index of cogeneration of CHP/CCHP system. On the base of ratio of electrical energy and useful heat of the location, ratio determined based on demand of the residential consumers, it is chose the structure of the realized CCHP system, as a result of comparison with the cogeneration index. The high variability hourly, monthly and seasonal of this factor involves the introduction of heating and energy storage systems to ensure household consumer requirements. The proposed CCHP system consist in a fuel cell that can track and ensure the electricity demand, a heat generation system which should cover the heat requirement in peak condition and a refrigeration plant. The refrigeration plant can be with mechanical compression or thermal compression. Whatever the refrigeration type is used, the refrigerant is the cold water at 3-5 °C pumped into the fans convectors. The latter makes the transfer of the cold in the living area. The fan convectors offer a dual operation cold water/hot water. The functional diagram of the CCHP system is represented in Fig. 1.

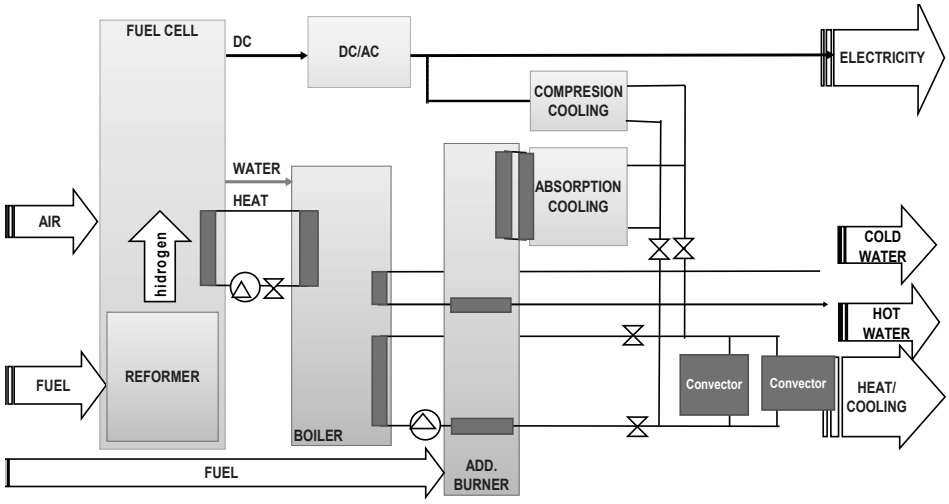

Fig. 1. Functional diagram of the proposed CCHP system

3. The components of CCHP system

3.1. The fuel cell

The fuel cells or cells transform the electrochemical energy by the hydrogen and oxygen conversion into electricity and heat in the presence of a catalyst [2]. The necessary hydrogen for a fuel cell can be obtained from the reforming of the methane gas.

The performance and the characteristics of the fuel cell are presented in the table 1 [4].

The fuel cell type PEMFC generates an amount of heat proportional with the demand of electricity. Ratio power to heat (index cogeneration) of fuel cells is 0.8÷1.1 [3]. For the analyzed mCCHP system was chosen a fuel cell type PEMFC with an electrical efficiency of 40% and cogeneration index 0.9.

3.2. The peak heat generation system

The low thermodynamic parameters of the fuel cell in heat generation makes the hot water from the boiler system to not be used for heating the residence building unless it's introduced in a intermediate system of central heating condensing type. The thermal heating produced is reused in the plant (Fig. 2). The efficiency of the additional burner is 0.95%.

Table 1. PEMFC type

Fuel cell type	Power	Type of electrolyte	Catalyst	Oxidizer	Fuel	Operating temp.	Efficiency
PEMFC	(1-250) kW	Polymer membrane	Platinum	Air or oxygen	Hydrocarbons or methanol	(50-70) ºC	(30-50) %

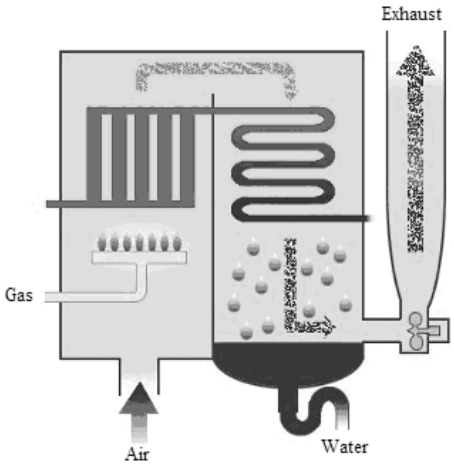

Fig. 2. Additional burner system

3.3. The cooling system

The cooling process takes place between two levels of pressure: vaporization and condensation. To determine the two levels of pressure we need to know the temperatures of vaporization and condensation of the cooling fluid. The current processes to produce the cold may be with:

- mechanical compression;
- thermal activation, witch can be with absorption or adsorption.

The procedure for obtaining the cold by absorption is the same like the one of vapor compression but has some significant differences [3]. The absorption process uses heat to vaporize the cooling fluid at high pressure, which is why it's called thermal compressor; its essential feature is that it has no moving parts.

In the case of refrigeration systems is defined the performance coefficient of cold production, COP, as the ratio between the energy needed to produce cold and the energy consumed. The performance of the cooling system is described by COP which has values between 2÷3 for the systems with mechanical compression and between 0.6÷0.8 for those with thermal activation. For simulation was used a value of mechanical compression COP=2.5 and for thermal compression COP=0.8.

3.4. The diagram of energy conversion in the mCCHP system

The functional diagram of the CCHP system presented in Fig. 1 is corresponding with the two energy diagrams presented in figure 3 and 4. The first is the energy distribution diagram where the refrigeration plant is with mechanical compression, and in the second diagram the refrigeration plant is with thermal compression. On the basis of individual performance components it's analyzed the total electrical efficiency of the CCHP system. The following relations belong - according with figures 3 and 4 - to the both cooling systems:

a) Mechanical compression system equations

$$\begin{cases} E_{cg} = E + \dfrac{C}{COP_c} \\ Q_{cg} = \dfrac{E_{cg}}{\gamma} \\ Q_b = Q_{cg} - Q_{hw} \\ Q_b + \eta_{ab} W_{peak} = Q_h \end{cases} \quad (3)$$

where:

E_{cg} – the electrical energy produced in cogeneration by the fuel cell [kWh], E – the electricity demand of the residence [kWh], C– the quantity of the cold[kWh], COP_c – the performance coefficient of mechanical compression, Q_{cg} – the heat quantity produced by the fuel cell [kWh], γ – the cogeneration index of the fuel cell, Q_b – the heat quantity of the boiler [kWh], Q_{hw} – the hot water consumption [kWh], η_{ab} – the efficiency of the additional heating system, W_{peak} – the fuel consumption of the additional heating system [kWh], Q_h – thermal load of the building [kWh].

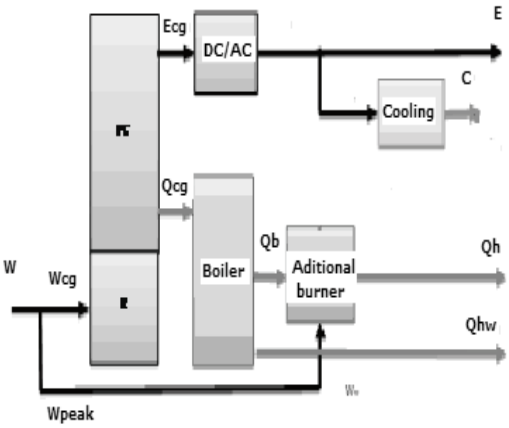

Fig. 3. Energy distribution diagram of the mCCHP system with compression

b) The thermal compression system equations

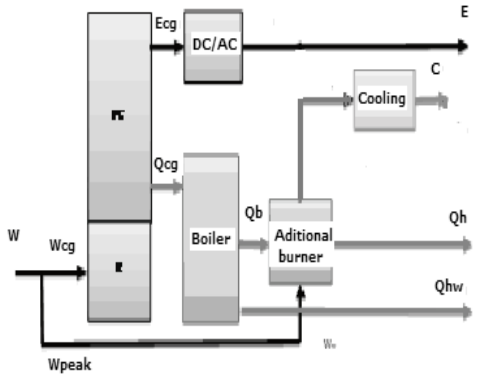

Fig. 4. Energy distribution variant of mCCHP system with absorption

$$\begin{cases} E_{cg} = E \\ Q_{cg} = \dfrac{E_{cg}}{\gamma} \\ Q_b = Q_{cg} - Q_{hw} \\ Q_b + \eta_{ab} W_{peak} = Q_h + \dfrac{C}{COP_a} \end{cases} \quad (4)$$

where:

COP_a – the performance coefficient of the system with absorption.

The performance indicators of production of the trigeneration system are the ratio of power/heat and the energy efficiency of the system. The analytical expressions of the two indicators are:

- *mCCHP system with compression*

Ratio power to heat:

$$\frac{E + \dfrac{C}{COP_c}}{Q_h + Q_{hw}} \quad (5)$$

The energy efficiency of the system:

$$\eta_{CCHP_{cc}} = \frac{E + Q_h + Q_{hw} + C}{\dfrac{E + \dfrac{C}{COP_c}}{\alpha_e} + \dfrac{Q_h + Q_{hw} - \dfrac{E + \dfrac{C}{COP_c}}{\gamma}}{\eta_{ab}}} \quad (6)$$

- *mCCHP system with absorption*

Ratio power to heat:

$$\frac{E}{Q_h + Q_{hw} + \dfrac{C}{COP_{ac}}} \quad (7)$$

The energy efficiency of the system:

$$\eta_{CCHP_{ab}} = \frac{E + Q_h + Q_{hw} + C}{\dfrac{E}{\alpha_e} + \dfrac{Q_h + Q_{hw} + \dfrac{C}{COP_a} - \dfrac{E}{\gamma}}{\eta_{ab}}} \quad (8)$$

Analytical relations (6) and (8) show that the mechanical compression system efficiency is higher than the thermal compression if:

$$COP_c > COP_a \eta_{ab} \left(\frac{1}{\alpha_e} - \frac{1}{\gamma \eta_{ab}}\right) \quad (9)$$

Where

- α_e – electrical efficiency of the fuel cell;
- γ – cogeneration index of the fuel cell;
- η_{ab}- additional burner efficiency

4. Case study of the simulation of the mCCHP system

4.1. Determination of the heat demand of the consumer

The colder the local climate is and the higher the indoor temperatures are, the higher is the heat demand for space heating. The space heat supply should compensate for heat transmission losses through walls and roofs and for heating supply air in mechanical or natural ventilation systems. The outdoor temperature is the most important variable in order to explain both the daily magnitude and variations from one year to another in the overall heat demand. The target area of the 32 countries contains locations where the annual average outdoor temperature varies from –2 to 19ºC, giving very different local conditions for space heating. The specific heat consumption is different, depending on the country (climate) but also according with the residential consumers.

The annual heating consumption of a residence can be determinate with the formula:

$$Q_h = U \cdot A \cdot \text{degree} - \text{days} \quad (10)$$

where:

Q_h is the heat added to or removed from the building per unit of time [Wh], U is the heat transfer coefficient of the building envelope, taking into account its components such as

glazing, insulation, exterior wall, etc. [W/m^{2}K], A is the external area of the building envelope [m^2].

Similar can be determinate the annual consumption of cold demand from the residence,

$$C = U \cdot A \cdot \text{cooling degree} - \text{days} \quad (11)$$

where the variation degree days for Galati area - Romania is presented in Fig. 5:

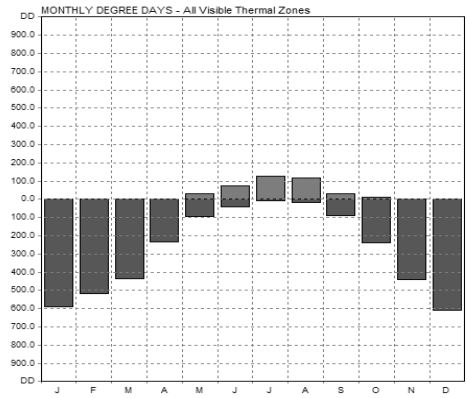

Fig. 5. Monthly degree-days annual variation

The data used to represent the distribution degree-days for the analysis were retrieved from the database of U.S. Department of Energy [6].

4.2. Hot water consumption

Preparation of hot water for domestic and other purposes is the second largest heat demand in the other sector after space heating. This heat demand is more pronounced in the residential sector compared to the service sector. A recent informative paper or report of the magnitude of average hot water consumption in European countries is however not available. Most hot water information is related to the design conditions for instantaneous and storage water heaters. The latest available survey information to be used is the (Eurostat, 1999) report about the energy consumption in households in the EU15 and some CEE countries. The average hot water consumption is estimated to be 50 l/day per capita.

Assuming a temperature difference of 50 ºC between the hot and cold water sides we can determine, based on the number of persons, the monthly quantity of heat required for domestic hot water.

$$Q_{hw} = N_p \cdot m \cdot c \cdot \Delta\theta \quad (12)$$

where:

- Q_{hw} – the energy needed to produce hot water [kWh],
- N_p – the number of persons,
- m – the water weight [kg],
- c – the heat capacity of water [kWh/kg ^{o}C],
- $\Delta\theta$ – the temperature difference [^{o}C].

4.3. The estimated demand of the electrical consumption

The inputs into the system are the energies required for residential consumers. Standardized data about energy consumption were taken from information's published by ANRE [5]. According to the Order of the President of ANRE no. 117/14.08.2008 on the household electrical are defined five standards consumers. Each category is characterized by the annual electricity consumption. The consumption of electricity in a residence is dependent on its endowment with domestic appliances. For each type of domestic user, the monthly consumption of electricity was considered stable.

Table 2. Electrical energy consumption – Source ANRE

Domestic end-users	Annual electricity consumption [kWh]	
	minimum	maximum
DA	⟨ 1000	
DB	1000	⟨ 2500
DC	2500	⟨ 5000
DD	5000	⟨ 15000
DE	≥ 15000	

4.4. The estimated distribution of energy consumption of a residential building

It is considered a residential building inhabited by 4 people, with floor area 144 m^2, volume 494.3 m^3, ground area 144 m^2, external wall area 144.6 m^2, window/wall=20% and an average U-value of 0.2238 W/m^{2}K (calculate by software VELUX for this building), in the south-eastern Romania. The estimated distribution of energy consumption was obtained with the software VELUX Visualizer Energy and Indoor Climate, and the results are given in Table 3, where was presumed a standard DC consumer of electricity from Romania.

Table 3. Monthly energy quantities required by the residential building

Month	heating degree-days	cooling degree-days	Electric energy E (kWh)	Local heating units Q_h (kWh)	Local cooling units C (kWh)	Domestic hot water Qhw (kWh)
JAN	589.7	0	268.5	1256	0	360
FEB	517.9	0	234.3	962.8	0	360
MAR	433.7	0	252.6	728.4	0	360
APR	232.7	2.8	246.3	235.6	0	360
MAY	96	29.3	267.9	0	0	360
JUN	40.3	74.6	245.9	0	243.2	360
JUL	7.7	124.9	260	0	464.3	360
AUG	17.1	116.4	260.2	0	440.7	360
SEP	90.2	32.7	246.4	0	0	360
OCT	240.4	12.6	268.4	240	0	360
NOV	440.7	0	246.6	764.1	0	360
DEC	610	0	252.8	1178	0	360

5. Simulation results

It was determined the total electrical efficiency of each type of trigeneration on the base of the residential energy (Fig. 3 and 4) and associated mathematical relations. The trigeneration plant with mechanical compression has a higher efficiency especially because of the COP, as well because the fuel cell control system follows the electric charge.

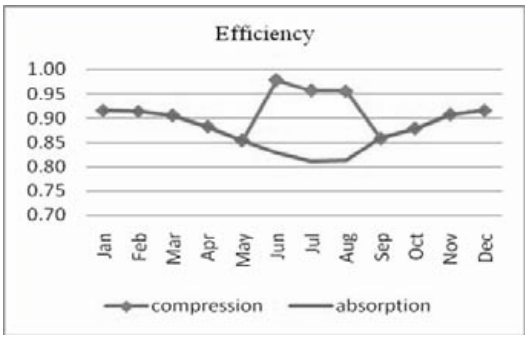

Fig. 6. The efficiency evolution of the mCCHP plant

The energy demand charts of the residence and the chart of the fuel cell are given in Fig. 7 and 8. Note that the cell ensures the demand of electricity, but can not provide the heat demand. The differences between the thermal energy requirement of the residential building and the fuel cell should be ensured by the additional heating system.

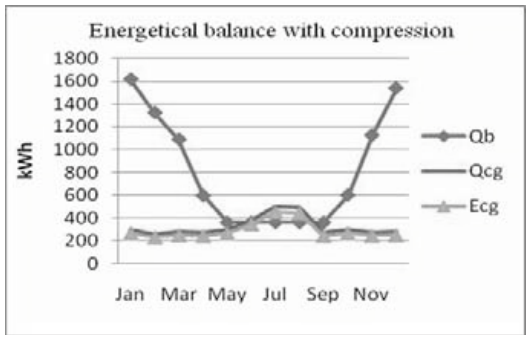

Fig. 7. Energetical balance of mCCHP system based on compression

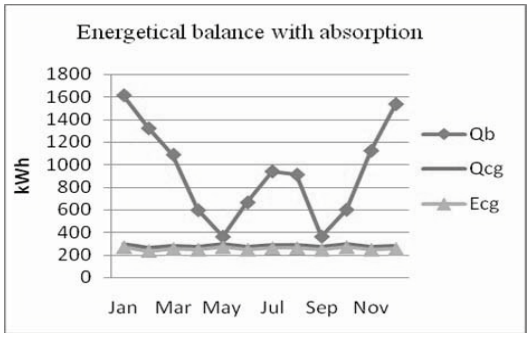

Fig. 8. Energetical balance of mCCHP system based on absorption

Note that the additional heating system consumes more energy in case of trigeneration system with absorption then in the case of the mechanical compression system (Fig. 9), because in the summer month's the heat is provided by the fuel cell.

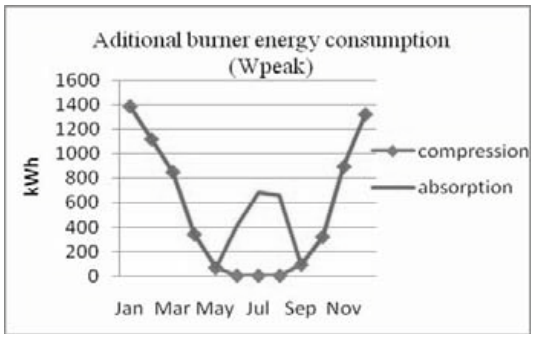

Fig. 9. Energy consumption evolution of the additional burner

The global energy consumption is bigger then in the trigeneration plant with absorption then in the case of the plant with mechanical compression.

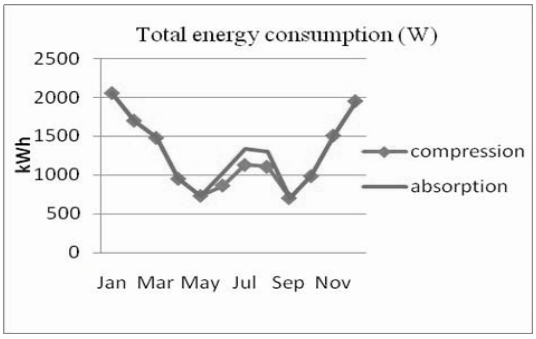

Fig.10. Total energy consumption of the mCCHP system

6. Conclusions

In winter period, the analysis of relations (5) - (8) and simulation results, we conclude that both systems have the same heat to power ratio and same overall efficiency.

In the summer period, heat to power ratio is influenced by the type of system cooling and its COP. Mechanical compression system has a higher ratio than that of the thermal compression, according to relations (5) and (7).

Efficiency of the two systems, as relations (6) and (8), depends on COP index cogeneration, cogeneration and additional burner efficiency. The COP of cooling system affects the system efficiency different.

Condition (9) specifies the relationship on how efficient the system is greater mechanical compression of the thermal compression. Efficiency value is obtained only from numerical simulation.

From the above analysis it can be concluded that:

- through their constructive and functional features the refrigeration plant influences radically overall behavior of trigeneration systems (CCHP).
- at the mCCHP systems – due the high energy efficiency of mechanical compression - fuel economy is substantial, when this method is used in comparison with the thermal compression.

References

[1] I. Zamora, et al., 2006, Cogeneration in Electrical Microgrids, International Conference on Renewable Energy and Power Quality, Spain.

[2] I. Pilatowsky, et al, 2007, Simulation of an Air Conditioning Absorption Refrigeration System in a Cogeneration Process Combining a Proton Exchange Membrane Fuel Cell, International Journal of Hydrogen Energy, pp 3174-3182.

[3] V. Dorer, R. Weber and A. Weber, 2005, Performance assessment of fuel cell micro-cogeneration systems for residential buildings, Energ Buildings, pp. 1132–1146.

[4] U.S. Department of Energy, 2004, *Fuel Cell Handbook*, Nacional Energy Technology Laboratory, B/T books.

[5] ANRE, Metodologie privind raportarea informatiilor referitoare la consumatorii de energie electrica, no.117/2008 , MO 644 /2008.

[6] U.S. department of energy, http://apps1.eere.energy.gov/buildings/energyplus/cfm /weather_data.cfm

Accuracy - This study is financially supported by Romanian PNCDI II grants, project nr.21063/2007.

Comparative Thermodynamic Performance of a Cogeneration Power Plant Using Plant Operational Data

Whitney Domigan[a] and Margaret Bailey[b]

[a] *Rochester Institute of Technology, Rochester, New York, USA*
[b] *Rochester Institute of Technology, Rochester, New York, USA*

Abstract: The John B. Rich Memorial Power Station, located in the United States, is an 88.4 MW cogeneration power plant with a unique relationship with its surrounding environment. The power station makes use of a plentiful and local byproduct of coal mining, called culm, as a feedstock. Culm is a low energy combination of anthracite coal and rock left over from the inefficient removal of rock from usable coal in the peak days of coal mining. For decades, culm deposits have leached pollution into groundwater and inhibited normal plant growth. By using culm, the power station removes a significant pollutant and eyesore from the area. Further, the power station is involved in a land reclamation program that covers land cleared of culm with topsoil and plant life. In order to process the culm, the power station utilizes two circulating fluidized bed (CFB) boilers. This work uses actual plant data to explore the thermodynamic performance of the plant. The first and second laws of thermodynamics are used to analyze the plant components, including the boilers, turbine, feedwater heaters, and condenser. The thermodynamic analyses are performed in part to determine properties through the plant, mainly mass flow rates that are not recorded during plant operation, and in part to characterize plant performance. Before the exergy analysis of the boilers can be performed, the streams into and out of each boiler must be characterized in terms of composition, mass, and exergy. Although the energy content of the culm is regularly measured by the power station, the exergy content must be determined based on the culm composition, which is provided by the plant. The exergy content of the flue gas is also determined based on the culm composition. The effects of sensor accuracy are briefly examined. The boiler performance is compared to other boiler technologies. A simple model of the plant with steam reheat is compared to the current plant configuration as well.

Keywords: Cogeneration, culm, exergy.

1. Introduction

The John B. Rich Memorial Power Station, in operation since the late 1980's, has pursued a unique fuel source (culm) and uses a relatively new boiler technology. Culm is a low-grade anthracite coal by-product with an energy content of 3224 kJ/kg, compared to 5160 kJ/kg for anthracite coal [1].

As more and more power sources options become available, it has become increasingly relevant to quantify the performance of a given technology. Since there are so many available technologies and power sources, it is necessary to quantify performance in a way that enables one to make informed decisions in terms of cost, reliability, practicality, and environmental impact. In this work, the performance of the plant will be quantified and the boiler performance will be examined alongside other technologies.

Work was previously performed on the power station [1, 2], but will be expanded and improved upon during this analysis in a number of ways. First, this analysis takes advantage of actual temperature, pressure, and flow rate data collected throughout the plant, whereas the previous analyses used estimated and analytical data only. Second, this work includes a more detailed examination of the boiler and the interactions between each of the major sub-systems of the plant. Finally, this work suggests and models possible plant improvements.

Corresponding Author: Domigan, Email: wdomigan@gmail.com

2. Background

2.1. Exergy

The thermodynamic analysis of the plant will include an energy analysis as well as an exergy analysis. Unlike energy, exergy is not conserved, but may be destroyed through irreversibility. Exergy is also a comparative value; all exergy measurements and analyses are performed with reference to a "dead state" or reference environment. The reference environment includes a uniform and unchanging temperature, pressure, and chemical composition [3].

2.2. Power station description

The power station in question delivers up to 88.4 MW of electricity to a local utility and 13,600 kg/h of steam to an adjacent correctional facility. On average, only about 4,939 kg/h of process steam is delivered from the plant.

The low operational temperature of CFB boilers (~860°C) cause two major emissions, NO_x and SO_x, to be much lower than a traditional pulverized coal power plant. NO_x emissions are reduced because the reactions which produce the most NO_x occur at temperatures above ~1480°C, which is much higher than CFB operational temperatures. The low CFB temperatures also allow limestone to be added to the combustion chambers, which effectively capture SO_2 formed during combustion, thereby reducing harmful SO_x emissions.

The cogeneration plant uses an 18-stage turbine. Steam is extracted at 5 locations through the turbine to be used elsewhere in the plant or off site to serve a local district heating load. The turbine isentropic efficiency and the generator efficiency are reported by the manufacturer as 80% and 95%, respectively [2].

The total plant feedwater path may be seen in Fig. 1. The labels shown in the diagram are used through the models in the following sections.

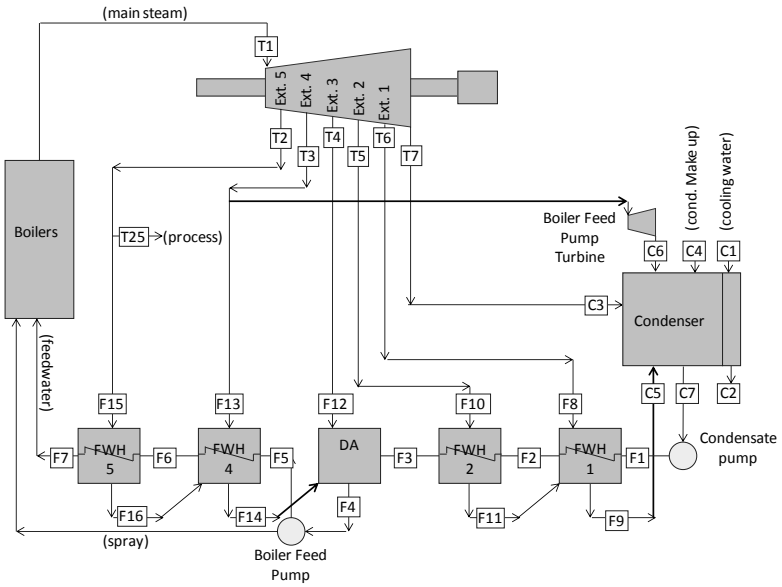

Fig. 1. Schematic of the feedwater path through the plant.

2.3. Operational data

Data is collected throughout the power plant to monitor both resource use and for safety considerations. This analysis takes advantage of 79 of the hundreds of temperature, pressure, and flow rate data collection points through the plant. Each sensor has an associated accuracy range that will be used to help gauge model error.

3. Thermodynamic models

A few basic assumptions are made across all the models described in this work. These assumptions include steady-state operations, negligible kinetic and potential energy effects, and ideal gas models for air and flue gas. Since exergy is with reference to a dead state, the environmental conditions are as realistic as possible. This work uses seasonal average temperatures and pressure at the plant elevation (0.961 bar, 267-192.5 K).

3.1. Boiler sub-system

A control volume approach is taken around the boiler combustion chamber. The feedwater tubes are taken to be outside the boiler control volume.

Two sources of heat transfer are considered: $\dot{Q}_{u,B}$ is the heat transfer from the combustion chamber to the feedwater, and $\dot{Q}_{l,B}$ is the heat loss through the boiler walls. A simplified boiler schematic may be seen in Fig. 2.

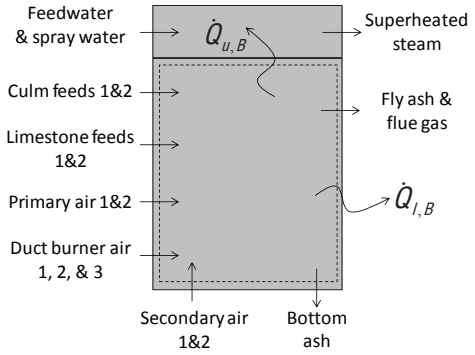

Figure 2. Schematic of boiler sub-system with control volume.

3.1.1. Combustion reactions

The boiler model assumes 120% theoretical air and 9% residue carbon (r=0.09) in the ash leaving the boiler. The reside carbon value is based on an analysis performed on the ash by the power plant. It should also be noted that the NO_x emissions are assumed to be all in the form of NO since NO is thermodynamically favoured over NO_2 at temperatures below 1480°C [4]. The opposite is true in traditional coal fired plants where boiler temperatures are well above the reaction temperature for NO_2 production [5].

The chemical reactions [4-6] within the boiler are given as:

$$C + 1.2(Air) \rightarrow (1-r)CO_2 + (0.2+r)O_2 + 4.512N_2 + rC \quad (1)$$

$$H + 1.2(Air) \rightarrow 0.5H_2O + 0.95O_2 + 4.512N_2 \quad (2)$$

$$S + 1.2(Air) \rightarrow SO_2 + 0.2O_2 + 4.512N_2 \quad (3)$$

$$CaCO_3 \rightarrow CaO + CO_2 \quad (4)$$

$$CaO + SO_2 + 1.2(Air) \rightarrow CaSO_4 + 0.7O_2 + 4.512N_2 \quad (5)$$

$$N + 1.2(Air) \rightarrow NO + 0.7O_2 + 4.512N_2 \quad (6)$$

$$O + 1.2(Air) \rightarrow NO + 1.2O_2 + 4.012N_2 \quad (7)$$

where $(Air) = (O_2 + 3.76N_2)$.

3.1.2. Boiler energy considerations

Neglecting the fan and pump work, an energy balance around each boiler is given as

$$\begin{aligned}\sum \dot{Q}_B &= \dot{m}_{FG}(h_f^o + \Delta h)_{FG} \\ &+ \dot{m}_{FA}(h_f^o + \Delta h)_{FA} + \dot{m}_{BA}(h_f^o + \Delta h)_{BA} \\ &- \dot{m}_{PA}(\underbrace{h_f^o}_{=0} + \Delta h)_{PA} - \dot{m}_{SA}(\underbrace{h_f^o}_{=0} + \Delta h)_{SA} \\ &- \dot{m}_{culm}\left(h_f^o + \Delta h\right)_{culm} - \dot{m}_{CaCO_3}\left(h_f^o + \Delta h\right)_{CaCO_3}\end{aligned} \quad (8)$$

where $\dot{m}_{PA}$ is the sum of the primary air streams, $\dot{m}_{SA}$ is the sum of the secondary and duct burner air streams, $\dot{m}_{culm}$ is the total culm used, $\dot{m}_{CaCO_3}$ is the total limestone into the boiler, and $\sum \dot{Q}_B = \dot{Q}_{l,B} + \dot{Q}_{u,B}$.

The energies associated with the formation of the flue gas and ashes are released or absorbed during the combustion process. Therefore, the enthalpy of formation values for the flue gas and ashes are included in the culm combustion energy release, described by the higher heating value of the fuel.

The change in enthalpy of the flue gas may be found with the ideal gas model, the ultimate and proximate analyses for culm, and the flue gas temperature [6]. The specific heat of flue gas model does not account for limestone addition, however, the effects of NO and SO_x reduction are only about 1% worst case [6] and so are neglected. The enthalpies of both ashes are calculated as functions of temperature [4]. The limestone term in (8) is determined based on the limestone reactions using the following format:

$$\dot{m}_{CaCO_3}(h_f^o + \Delta h)_{CaCO_3} = \sum_P \left[\dot{n}_P\left(\bar{h}_f^o + \Delta\bar{h}\right)_P\right] - \sum_R \left[\dot{n}_R\left(\bar{h}_f^o + \Delta\bar{h}\right)_R\right] \quad (9)$$

When a mass balance is performed on (4) and (5) it is found that $\dot{n}_{CaCO_3} = \dot{n}_{CO_2} = \dot{n}_{SO_2} = \dot{n}_{CaSO_4}$. The limestone temperature as it enters the boiler is approximated as the reference temperature, however, the formation of $CaSO_4$ occurs at the boiler chamber temperature. Therefore, the changes in enthalpy for the reactants in (9) cancel to zero, while the changes in enthalpy for the reactants do not. Equation (9) then becomes

$$\begin{aligned}\dot{m}_{CaCO_3}(h_f^o + \Delta h)_{CaCO_3} &= \dot{n}_{CaCO_3}\left[\left(\bar{h}_f^o\right)_{CaSO_4}\right. \\ &\left. + \left(\bar{h}_f^o + \Delta\bar{h}\right)_{CO_2}\right] - \dot{n}_{CaCO_3}\left[\left(\bar{h}_f^o + \Delta\bar{h}\right)_{CaCO_3}\right. \\ &\left. + \left(\bar{h}_f^o + \Delta\bar{h}\right)_{SO_2}\right]\end{aligned} \quad (10)$$

The change in enthalpy values are calculated using the assumption of constant specific heat, while the enthalpy of formation values are found from chemical property tables [8].

The useful heat transfer for each boiler describes the heat delivered into the feedwater. This value may be found by examining the change in enthalpy of the feedwater entering and exiting the boiler heaters.

$$\dot{Q}_{u,B} = \dot{m}_{FW}\left(h_{FW} - h_{SHS}\right) \tag{11}$$

The boiler heat loss may then be found by solving (8) for $\dot{Q}_{l,B}$:

$$\begin{aligned}\dot{Q}_{l,B} &= \dot{m}_{FG}\Delta h_{FG} + \dot{m}_{FA}\Delta h_{FA} + \dot{m}_{BA}\Delta h_{BA} \\ &- \dot{m}_{PA}\Delta h_{PA} - \dot{m}_{SA}\Delta h_{SA} - \dot{Q}_{u,B} \\ &- \dot{m}_{culm}(HHV) - \dot{m}_{CaCO_3}\left(h_f^o + \Delta h\right)_{CaCO_3}\end{aligned} \tag{12}$$

The boiler efficiency is given as the ratio between the energy content of the fuel and the heat transferred to the feedwater.

$$\eta_B = \frac{\dot{Q}_{u,B}}{\dot{Q}_{culm}} = \frac{\dot{Q}_{u,B}}{\dot{m}_{culm}(HHV)} \tag{13}$$

3.1.3. Boiler exergy considerations

The chemical exergy balance for the boiler may be used to find the exergy destroyed in the boiler:

$$\begin{aligned}\dot{E}_{d,B} &= \left(1 - T_o/T_{b,B}\right)\dot{Q}_{l,B} - \left(1 - T_o/T_c\right)\dot{Q}_{u,B} \\ &+ \dot{m}_{PA}e_{PA} + \dot{m}_{SA}e_{SA} + \dot{m}_{culm}e_{culm} \\ &+ \dot{m}_{CaCO_3}e_{CaCO_3} - \left[\dot{m}_{B10}e_{B10}\right. \\ &\left. + \dot{m}_{B9}e_{B9} + \dot{m}_{B8}e_{B8}\right]\end{aligned} \tag{14}$$

The flue gas exergy is calculated based on the flue gas temperature and the culm composition [6]. The culm exergy is also calculated based on the chemical composition of the fuel [7]. The exergetic efficiency for the boiler is given as the ratio between the useful exergy and the input exergy.

$$\varepsilon_B = \frac{\left(1 - T_o/T_c\right)\dot{Q}_{u,B}}{\dot{E}_{culm} + \dot{E}_{PA} + \dot{E}_{SA} + \dot{E}_{CaCO_3}} \tag{15}$$

3.2. Turbine, feedwater heaters, and condenser sub-systems

Although temperature and pressure data may be determined from plant data or using assumptions, the only flow rates recorded are the condensate makeup water (C4 on Fig. 1), steam out of boilers (T1 on Fig. 1), and the feedwater into the boilers (F7 on Fig. 1). By applying conservation of mass and energy balances to the feedwater heaters, the remaining mass flow rates may be found.

3.2.1. Feedwater heater analysis

It is assumed that heat loss is negligible for each feedwater heater. Using conservation of mass through the feedwater heaters in Fig. 1, it is readily seen that

$$\dot{m}_{F7} = \dot{m}_{F6} = \dot{m}_{F5} \tag{16}$$

$$\dot{m}_{F3} = \dot{m}_{F2} = \dot{m}_{F1} \tag{17}$$

$$\dot{m}_{F16} = \dot{m}_{F15} \tag{18}$$

$$\dot{m}_{F14} = \dot{m}_{F16} + \dot{m}_{F13} \tag{19}$$

$$\dot{m}_{F4} = \dot{m}_{F14} + \dot{m}_{F12} \tag{20}$$

$$\dot{m}_{F11} = \dot{m}_{F10} \tag{21}$$

$$\dot{m}_{F9} = \dot{m}_{F11} + \dot{m}_{F8} \tag{22}$$

Solving an energy balance around FWH 5 for the flow rate at F15 and substituting in (16) and (18) gives

$$\dot{m}_{F15} = \frac{\dot{m}_{F7}\left(h_{F7} - h_{F6}\right)}{\left(h_{F15} - h_{F16}\right)} \tag{23}$$

An energy balance around FWH 4 and substituting (16), (19), and (23) may be solved for the flow rate through F13

$$\dot{m}_{F13} = \frac{\dot{m}_{F6}\left(h_{F5} - h_{F6}\right) + \dot{m}_{F16}\left(h_{F16} - h_{F14}\right)}{\left(h_{F14} - h_{F13}\right)} \tag{24}$$

If a control volume is applied around the turbine, condenser, FWH 2, and FWH 1, it may also be found with conservation of mass that

$$\dot{m}_{F12} = \dot{m}_{T1} + \dot{m}_{C4} - \dot{m}_{F3} - \dot{m}_{F13} \tag{25}$$

An energy balance around FWH 2 along with (17), and (21) gives

$$\dot{m}_{F10} = \frac{\dot{m}_{F3}\left(h_{F2} - h_{F3}\right)}{\left(h_{F11} - h_{F10}\right)} \tag{26}$$

An energy balance around FWH 1 with (17), (21), and (26) gives

$$\dot{m}_{F8} = \frac{\dot{m}_{F2}\left(h_{F1} - h_{F2}\right) + \dot{m}_{F11}\left(h_{F11} - h_{F9}\right)}{\left(h_{F9} - h_{F8}\right)} \tag{27}$$

Using (16) - (27), all flow rates through the FWH system are now known. The turbine extraction flow rates may now be calculated thus:

Extraction 5: $\dot{m}_{T2} = \dot{m}_{F15} + \dot{m}_{T25}$ (28)

Extraction 4: $\dot{m}_{T3} = \dot{m}_{F13} + \dot{m}_{C6}$ (29)

where $\dot{m}_{C6}$ is found by applying an energy balance around the boiler feed pump to find the work input, and then using that work in an energy balance around the boiler feed pump turbine and solving for $\dot{m}_{C6}$.

Extraction 3: $\dot{m}_{T4} = \dot{m}_{F12}$ (30)

Extraction 2: $\dot{m}_{T5} = \dot{m}_{F10}$ (31)

Extraction 1: $\dot{m}_{T6} = \dot{m}_{F8}$ (32)

Turbine exhaust:

$$\dot{m}_{T7} = \dot{m}_{T1} - \dot{m}_{T2} - \dot{m}_{T3} - \dot{m}_{T4} - \dot{m}_{T5} - \dot{m}_{T6} \quad (33)$$

Finally, the missing flow rates through the condenser are found using conservation of mass:

$$\dot{m}_{C3} = \dot{m}_{T7} \quad (34)$$

$$\dot{m}_{C5} = \dot{m}_{F9} \quad (35)$$

$$\dot{m}_{C7} = \dot{m}_{C3} + \dot{m}_{C4} + \dot{m}_{C5} + \dot{m}_{C6} \quad (36)$$

3.2.2. Turbine energy considerations

Based on plant information, the turbine exhaust and extraction 1 flows are taken to be mixtures with respective qualities of 89% and 97%. The heat loss from the turbine is based on a heat loss curve provided by the plant; it is assumed that the turbine heat loss is 0.7% of the work produced by the turbine, or

$$\dot{Q}_{l,T} = -0.007\dot{W}_T \quad (37)$$

The work produced by the turbine may be calculated two ways. First, the generator efficiency may be applied to the generator export, which is carefully monitored by the plant. Second, an energy balance may be performed around the turbine using the calculated mass flow rates, assumed heat loss, and available temperature and pressure data. These work values will be referred to as $\dot{W}_{T,1}$ and $\dot{W}_{T,2}$, respectively, in the results section. Ideally these two values should be identical, however, because of assumptions and sensor errors, they are not.

An energy balance around the turbine gives

$$\dot{Q}_{l,T} - \dot{W}_T = \sum_{out} \dot{m}h - \sum_{in} \dot{m}h \quad (38)$$

When (37) is applied to (38), the turbine work may be solved for as

$$\dot{W}_T = -\left(\frac{1}{1.007}\right)\left[\dot{m}_{T1}h_{T1} - \left(\dot{m}_{T2}h_{T2} + \dot{m}_{T3}h_{T3} + \dot{m}_{T4}h_{T4} + \dot{m}_{T5}h_{T5} + \dot{m}_{T6}h_{T6} + \dot{m}_{T7}h_{T7}\right)\right] \quad (39)$$

The isentropic turbine efficiency is useful for comparative and validation purposes, and may be calculated using

$$\eta_{Ts} = \dot{W}_T / \dot{W}_{Ts} \quad (40)$$

where

$$\dot{W}_{Ts} = -\left(\frac{1}{1.007}\right)\left[\dot{m}_{T1}h_{T1} - \left(\dot{m}_{T2}h_{T2,s} + \dot{m}_{T3}h_{T3,s} + \dot{m}_{T4}h_{T4,s} + \dot{m}_{T5}h_{T5,s} + \dot{m}_{T6}h_{T6,s} + \dot{m}_{T7}h_{T7,s}\right)\right] \quad (41)$$

3.2.3. Turbine exergy considerations

The exergy destruction around the turbine is found from an exergy balance, which yields

$$\dot{E}_{T,d} = \left(1 - \frac{T_o}{T_{b,T}}\right)\dot{Q}_T - \dot{W}_T + \dot{m}_{T1}e_{f,T1} - [\dot{m}_{T2}e_{f,T2} + \dot{m}_{T3}e_{f,T3} + \dot{m}_{T4}e_{f,T4} + \dot{m}_{T5}e_{f,T5} + \dot{m}_{T6}e_{f,T6} + \dot{m}_{T7}e_{f,T7}] \quad (42)$$

The exergy efficiency compares the exergy of the desired output streams, meaning the turbine work, to the change in flow exergy across the turbine. The turbine exergy efficiency is then given as

$$\varepsilon_T = \frac{\dot{W}_T}{\dot{m}_{T1}e_{f,T1} - \dot{m}_{T7}e_{f,T7}} \quad (43)$$

3.2.4. Feedwater heaters and condenser

The heat transfer to the cooling water that passes through the condenser is found using an energy balance.

$$\dot{Q}_C = \dot{m}_{C7}h_{C7} - \left(\dot{m}_{C6}h_{C6} + \dot{m}_{C5}h_{C5} + \dot{m}_{C4}h_{C4} + \dot{m}_{C3}h_{C3}\right) \quad (44)$$

The exergy destroyed in the condenser and each of the feedwater heaters are found by applying exergy balances to give

$$\dot{E}_{d,C} = \left(1 - \frac{T_o}{T_{b,T}}\right)\dot{Q}_C - \dot{m}_{C7} e_{C7} + \dot{m}_{C6} e_{C6} + \dot{m}_{C5} e_{C5} + \dot{m}_{C4} e_{C4} + \dot{m}_{C3} e_{C3} \quad (45)$$

$$\dot{E}_{d,FWH-1} = \dot{m}_{F8} e_{F8} + \dot{m}_{F11} e_{F11} + \dot{m}_{F1}\left(e_{F1} - e_{F2}\right) - \dot{m}_{F9} e_{F9} \quad (46)$$

$$\dot{E}_{d,FWH-2} = \dot{m}_{F2}\left(e_{F2} - e_{F3}\right) + \dot{m}_{F10}\left(e_{F10} - e_{F3}\right) \quad (47)$$

$$\dot{E}_{d,DA} = \dot{m}_{F12} e_{F12} + \dot{m}_{F3} e_{F3} + \dot{m}_{F14} e_{F14} - \dot{m}_{F4} e_{F4} \quad (48)$$

$$\dot{E}_{d,FWH-4} = \dot{m}_{F13} e_{F13} + \dot{m}_{F16} e_{F16} + \dot{m}_{F5}\left(e_{F5} - e_{F6}\right) - \dot{m}_{F14} e_{F14} \quad (49)$$

$$\dot{E}_{d,FWH-5} = \dot{m}_{F15}\left(e_{F15} - e_{F16}\right) + \dot{m}_{F7}\left(e_{F7} - e_{F6}\right) \quad (50)$$

3.3. Total plant analysis

The total plant analysis pulls the subsystem analyses together to find the total performance of the plant. The total heat loss from the plant is given as the sum of the heat loss of each component

$$\dot{Q}_{l,P} = \dot{Q}_{\substack{l,B \\ total}} + \dot{Q}_{l,T} + \dot{Q}_{l,C} \quad (51)$$

where $\dot{Q}_{\substack{l,B \\ total}}$ is the sum of the heat losses from each boiler.

The work used internally for supporting the various pumps, fans, and lighting through the plant is found by taking the difference between the net power out of the plant, $\dot{W}_{P,net}$, and power output of the turbine, $\dot{W}_{gen}$.

$$\dot{W}_{P,in} = \dot{W}_{gen} - \dot{W}_{P,net} \quad (52)$$

The energy utilization factor (EUF) for the plant takes into account the energy within the process steam, the electrical energy exported from the plant, and the total heat input into the plant. The EUF is given as [9]

$$\mathrm{EUF} = \frac{\dot{m}_{T25}\left(h_{C4} - h_{T25}\right) + \dot{W}_{P,net}}{\dot{Q}_{\substack{culm \\ total}}} \quad (53)$$

where $\dot{Q}_{\substack{culm \\ total}}$ is the fuel energy added to the plant.

Since energy of the process steam is only a small fraction of the electrical energy, it may be neglected to find the plant thermal efficiency.

$$\eta_{th,P} = \dot{W}_{P,net} \Big/ \dot{Q}_{\substack{culm \\ total}} \quad (54)$$

The energy types in the numerator of (53) are of differing qualities, which makes the EUF a sub-ideal performance indicator. The exergetic efficiency, given below, is a better measure of the plant performance since exergy accounts for the different types of energy. The net exergy out of the plant is equal to $\dot{W}_{P,net}$.

$$\varepsilon_P = \frac{\dot{m}_{T25}\left(e_{f,C4} - e_{f,T25}\right) + \dot{W}_{P,net}}{\dot{E}_{P,in}} \quad (55)$$

where the exergy input is equal to

$$\dot{E}_{P,in} = \dot{m}_{culm}\left(e^{CH}_{culm}\right) \quad (56)$$

The total exergy destruction through the plant is given as the sum of the destruction in each subsystem

$$\dot{E}_{d,P} = \dot{E}_{\substack{d,B \\ total}} + \dot{E}_{d,T} + \dot{E}_{d,C} + \dot{E}_{d,F} \quad (57)$$

3.3.1. Turbine improvements

The moisture content at extraction 1 and the turbine exhaust will wear the turbine blades at a faster rate than if the steam was superheated. With this in mind, the addition of steam reheat, shown in Fig. 3, between extraction 3 and 2 is explored.

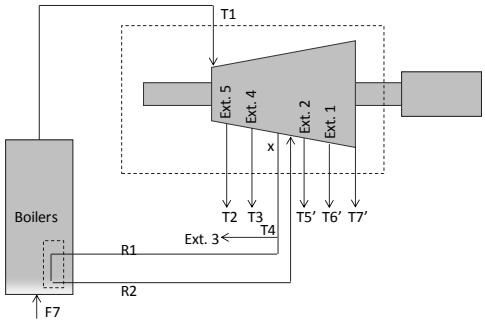

Figure 3. Schematic of simple turbine reheat scenario.

Table 1. Summary of significant energy values. NA indicates that data is not available.

Energy Parameter (MW)	Previous Analysis	Current Work Using $\dot{W}_{T,1}$	Current Work Using $\dot{W}_{T,2}$	With Turbine Reheat
$\dot{Q}_{l,B\ total}$	NA	73.45	73.45	NA
$\dot{Q}_{l,C}$	NA	112.65	112.65	NA
$\dot{Q}_{l,T}$	NA	0.63	0.54	0.60
$\dot{Q}_{l,P}$	NA	186.73	186.64	NA
$\dot{Q}_{process}$	8.53	4.08	4.08	4.08
$\dot{Q}_{culm\ total}$	309.5	304.88	304.88	332.42
$\dot{Q}_{u,B\ total}$	251	232.64	232.64	260.18
$\dot{W}_T$	NA	90.17	77.81	85.87
$\dot{W}_{gen}$	88.4	85.66	73.92	81.57
$\dot{W}_{P,i}$	7.25	7.94	7.94	7.94
$\dot{W}_{P,net}$	81.2	77.72	65.98	73.64

Table 2. Summary of significant exergy parameters. NA indicates that data is not available.

Exergy Parameter (MW)	Previous Analysis	Current Work Using $\dot{W}_{T,1}$	Current Work Using $\dot{W}_{T,2}$	With Turbine Reheat
$\dot{E}_{culm}$	NA	314.26	314.26	342.66
$\dot{E}_{PA} + \dot{E}_{SA}$	NA	5.77	5.77	NA
$\dot{E}_{CaCO_3}$	NA	0.002	0.002	NA
$\dot{E}_{in,total}$	NA	320.03	320.03	NA
$\dot{E}_{process}$	NA	1.66	1.66	1.66
$\dot{E}_{out,total}$	NA	79.34	67.64	75.3
$\dot{E}_{d,T}$	7.3	13.43	13.43	14.78
$\dot{E}_{d,C}$	NA	5.53	5.53	NA
$\dot{E}_{d,B\ total}$	146.3	452.22	452.22	NA
$\dot{E}_{d,FWH\ total}$	NA	15.78	15.78	NA
$\dot{E}_{d,total}$	NA	486.96	486.96	NA

An analysis of the reheat process is performed using averaged data and a number of assumptions. The temperature at T7' in Fig. 3 is assumed to be the temperature at T7 increased by 30°C to place it solidly in the superheated region. The temperatures upstream are back calculated from the T7' temperature based on the relationships between the temperatures in the operational data- for instance, the temperature decrease of 40% is observed in the operational data between T6 and T7, so the temperature at T6' will be found by applying a 40% increase from T7'. The pressures are assumed to remain unchanged from the no-reheat case.

Although the reheat will impact the feedwater heaters, condenser, and air and limestone addition to the boilers, this analysis will not go into such great detail. The heat required to increase the steam temperature and the necessary fuel use increase are both found. Since the overall efficiencies are based mainly on the fuel use and the power export, they may also be found.

4. Initial results

The analyses are performed using data collected at hourly intervals from Dec. 7- Dec. 30, 2009. These dates are chosen because of the even operation load throughout. Since the data used is from a winter month, the average winter reference conditions (0.961 bar, 267 K) will be used. The heat transfer and work parameters are listed in Tab. 1.Exergy parameters are in Table 2. Finally, the efficiency measures are given in Table 3.

Table 3. Summary of energy and exergy efficiencies. NA indicates that data is not available.

Efficiencies (%)	Previous Analysis	Current Work Using $\dot{W}_{T,1}$	Current Work Using $\dot{W}_{T,2}$	With Turbine Reheat
η_B	81	79.78	79.78	NA
η_{Ts}	~80	NA	82.19	79.82
η_{th}	26	25.63	21.74	22.15
EUF	29	26.98	23.10	23.38
ε_T	92.7	67.61	58.31	65.82
ε_B	NA	55.76	55.76	NA
ε_P	~34.5	25.40	21.63	22.18

The turbine reheat process requires an additional fuel use of 1.77 kg/s based on the additional energy transfer required to reheat the steam and the culm HHV.

5. Discussion

Of the two sets of outcomes from the current work, the first, based on the generator output, is more accurate for reasons outlined in the following section. It should be noted, however, that the reheat analysis should be compared to the second set of current work outcomes, based on the energy balance around the turbine. This is because the reheat analysis also depends on the energy balance method to determine the turbine work. Although the method is less accurate, the relative improvement of the reheat scenario may be seen and understood.

5.1. Accuracy

For the most part the results from this work and the previous work are within range. It may be noted, however, that there is a very large difference in the boiler exergy destruction rate. Because the previous analysis did not have a measurement of the culm exergy content, the methods in which they calculated the exergy destruction were very rough, whereas this work goes into detail about each exergy stream. The differences between the analyses have three major sources: actual data use, which includes effects of sensor accuracy, different reference conditions, and slightly different assumptions through the models.

The error between the two turbine work methods is found to be 13.7%. Although this is a high error, the accuracy errors of the sensors must be considered. Since 36 sensors are used in the calculation of $\dot{W}_{T,2}$, and only 1 sensor for $\dot{W}_{T,1}$, it is expected that $\dot{W}_{T,2}$ is less accurate than $\dot{W}_{T,2}$.

A range of turbine work can be established using the operational data and the corresponding sensor accuracies. An upper bound of 81.84 MW is found if all operational data is adjusted using the accuracies to yield the maximum turbine work, and a lower bound of 76.84 MW when the data is adjusted to yield the minimum turbine work. The sensor error therefore accounts for some of the turbine work error, but not all. The rest of the error between the two values may be attributed to assumptions used.

5.2. Comparisons

Although the picture given by the reheat to current comparison is incomplete, it does show how the overall plant performances increase when steam reheat is introduced. Since more energy overall will be entering the turbine, more power may be produced.

Energy and exergy analyses are performed on a number of non-CFB steam boilers [10]. It is found that the boiler energy efficiencies range from 72.46% for a boiler using nanofluids [10], to 84% for a boiler using sugarcane bagasse [11], to 93.76% for a boiler using heavy fuel oil [12]. Results found through this work, 79.8%, are well within this range.

Boiler exergy efficiencies have been given as 24.89% [10], 27.6% [11], and 43.8% [12]. The exergy efficiency for the boilers in this analysis, 55.8%, is higher than these analyses. These results suggest that CFB boilers using culm create less exergy destruction than a variety of other common steam boilers.

Although the efficiencies of the plant examined in this work may be better or worse than other plants, the environmental aspects of the plant are relatively desirable. There is little energy expended in the transport and preparation of culm as a fuel source. It is also notable that the culm deposits throughout mining country are harmful to the environment. When compared to the impact of a pulverized coal power station, the environmental impacts of the plant examined in this work are small. A traditional coal plant necessitates coal mining, transport, and pulverization, all of which take a great deal of energy, infrastructure, and labor.

5.3. Future work and conclusion

In order to have a better understanding of the environmental impact of the system, a more detailed examination of the combustion process and emissions in the boilers is needed. There are also many other plant improvements that will be quantified, such as the effects of increased process steam use and decreasing the residue carbon in the ash. Finally, the environmental impacts of the plant will be expanded and quantified through an externality analysis.

A thermodynamic analysis is performed on an 88 MW cogeneration power plant using actual operational data. The turbine is found to have an isentropic efficiency of 82.19% and an exergetic efficiency of 67.61%. The boiler is found to have energy and exergy efficiencies of 79.78% and 55.76%, respectively. The overall plant has a thermal efficiency of 25.63% and an exergetic efficiency of 25.40%.

Nomenclature

$h, \bar{h}$ enthalpy, kJ/kg, kJ/kmol

$h_f^o, \bar{h}_f^o$ enthalpy of formation, kJ/kg, kJ/kmol

r residue carbon, %

s entropy, kJ/(kg K)

$\dot{m}$ mass flow rate, kg/s

$\dot{n}$ molar flow rate, kmol/s

$\dot{E}_d$ exergy destroyed, MW

$\dot{Q}$ heat transfer, MW

$\dot{W}$ work, MW

Greek symbols

η energy efficiency

ε exergy efficiency

Subscripts and superscripts

c combustion chamber

FG flue gas

FA fly ash

BA bottom ash

FW feedwater

SHS super heated steam

T turbine

B boiler

F feedwater heaters

C condenser

P plant

gen generator

s isentropic

u useful

l loss

References

[1] Domigan, W., and Bailey, M., 2009, Exploring the Use of Exergy and Externality Parameters to Examine a Cogeneration Power Plant, *22nd International ECOS Conference Papers on Disc* [CD-ROM], ECOS, Foz du Iguaçu, Brazil.

[2] Bailey, M., et al., 2006, Exergetic, Thermal, and Externalities Analyses of a Cogeneration Plant, Journal of Solar Energy Engineering, 128(1), pp.98-103.

[3] Dewulf, J., et al., 2007, Exergy: Its Potential and Limitations in Environmental Science and Technology, Environmental Science and Technology, 42(7), pp. 2221-2232.

[4] Stultz, S., Kitto, J., 1992, *Steam: Its Generation and Use*, Babcock & Wilcox Company, 40th ed, Chap 9.

[5] Hill, S. C., 2000, Modeling of Nitrogen Oxides Formation and Destruction in Combustion Systems, Progress in Energy and Combustion Science, 26(4-6), pp. 417-458.

[6] Coskun, C., et al., 2009, A New Approach for Simplifying the Calculation of Flue Gas Specific Heat and Specific Exergy Value Depending on Fuel Composition, Energy, 34(11), pp. 1898-1902.

[7] Bilgen, S., Kaygusuz, K., 2008, The Calculation of the Chemical Exergies of Coal-Based Fuel by Using the Higher heating Values, Applied Energy, 85(8), pp. 776-785.

[8] Masterson, W., 1983, *Chemical Principles*, Harcourt Brace College Publishers.

[9] Kanoglu, M., Dincer, I., 2008, Performance Assessment of Cogeneration Plants, Energy Conservation and Management, 50(1), 76-81.

[10] Saidur, R., et al., 2009, Energy, Exergy, and Economic Analysis of Industrial Boilers, Energy Policy, In press.

[11] Cortex, L., Gomez, E., 1998, A Method for Exergy Analysis of Sugarcane Bagasse Boilers, Brazilian Journal of Chemical Engineering, 15(1).

[12] Aljundi, I., 2009, Energy and Exergy Analysis of a Steam Power Plant in Jordan, Applied Thermal Engineering, 29(2-3), pp. 324-328.

Simulation of a Motored Internal Combustion Engine Using an Improved CFD Model

C.D. Rakopoulos[a], G.M. Kosmadakis[a] and E.G. Pariotis[b]

[a] *Internal Combustion Engines Laboratory, Thermal Engineering Department, School of Mechanical Engineering, National Technical University of Athens, 9 Heroon Polytechniou St., Zografou Campus, 15780 Athens, Greece*

[b] *Laboratory of Naval Propulsion Systems, Section of Naval Architecture & Marine Engineering, Department of Naval Sciences, Hellenic Naval Academy, End of Hatzikyriakou Ave., Hatzikyriakio, 18539 Piraeus, Greece*

Abstract: The present work deals with the simulation of an internal combustion engine running under motoring conditions. The scope is to investigate, in what extent the incorporation of a new heat transfer formulation and a new phenomenological crevice model into an in-house CFD code improves the accuracy of the model. To do this, the measured heat flux at a specific location on the cylinder head of the engine, the in-cylinder pressure and the integral length scale are compared with the corresponding ones calculated from the in-house CFD model running with and without the improved heat transfer and crevice sub-models. As far as the engine configuration is concerned, two cases have been examined, one using a shrouded valve and another with an unshrouded one. The measured data are available from the literature, where extended measurements have been conducted concerning a CFR engine. For the turbulence phenomena the RNG k-ε turbulence model is used. Comparing the calculated data with the measured ones it is concluded that the heat fluxes are greatly underpredicted when using the standard law-of-the-wall heat transfer formulation, while they are adequately calculated when the improved wall-function formulation is used. Moreover, it has been shown through the simulation that using the crevice model, better matching between the calculated and experimental cylinder pressure traces during the whole closed part of engine cycle is achieved, while the effect on the calculated heat flux is low. On the other hand, comparing the calculated integral length scale with the measured one, only the trend of the measured values is captured. In general, it is shown that by incorporating the new wall heat transfer formulation and the new phenomenological crevice model into the CFD code, an overall better matching between the calculated and the measured heat flux and the mean cylinder pressure traces is achieved.

Keywords: Heat transfer, Crevices, Motoring, CFD model, Law-of-the-wall.

1. Introduction

One of the main physical processes affecting engine operation and exhaust emissions is the heat transfer inside the cylinder charge and through the cylinder boundaries. As engine simulation models are becoming major tools for engine design [1], many mathematical formulations have been proposed to adequately simulate the heat fluxes though the cylinder walls. This task is demanding due to the unsteady and highly inhomogeneous temperature distribution of the cylinder charge and the uncertainty existing in the determination of the initial and boundary conditions of this process. However, a proper estimation of the heat fluxes is a prerequisite especially for the computational fluid dynamic models (CFD), in order to provide valuable and reliable information regarding the interaction of engine design with engine efficiency, performance and emissions [2].

There are numerous experimental studies found in the literature concerning the measurements of heat fluxes on the cylinder walls, applied in diesel engines [3], spark-ignition engines [2,4], HCCI engines [5], and even in hydrogen-fueled engines [6]. Most of the aforementioned studies are followed by computer engine simulations, trying to develop numerical models that are capable of calculating reliably the heat flux through the cylinder boundaries [5,7,8].

On the other hand, the importance of taking into account the crevice volume by incorporating a detailed or a simple sub-model has already been established, and many research or commercial codes offer this option [9,10]. With a more detailed calculation of the trapped mass and its

Corresponding Author: G.M. Kosmadakis, Email: gkosmad@central.ntua.gr

variation during the engine's cycle, the engine performance and emissions are predicted in better terms, since the calculated pressure history is considered more reliable both in motoring [11] and firing conditions [12] and the calculated emissions, mainly HC and NOx are closer to the measured values [13,14].

The main objective of the present work is to further examine the developed heat transfer formulation [15] incorporated in an in-house CFD code, when a new phenomenological crevice model is also used [16], and to investigate in what extent the accuracy of the calculated results has been improved. For doing so, the measured heat fluxes at a specific location on the cylinder head and the pressure traces of an internal combustion engine running under motoring conditions are used for two inlet valves designs, i.e. one shrouded and one unshrouded. Also, the trend of the measured integral length-scale is compared to the calculated one, revealing the adequacy of the turbulence model used.

2. Experimental facilities

The measurements used in the present study are taken from [17], where experimental studies on a Cooperative Fuel Research (CFR) engine were conducted. It should be stressed at this point that all measurements shown and all the calculations conducted are under motoring conditions, so that attention is paid only to the heat transfer process and not to combustion. The measurement of surface temperatures at a specific location on the cylinder head (28.6 mm away from the cylinder axis) led to the determination of the local heat flux together with the integral length-scale for two inlet valve designs, one using a shrouded valve and another with an unshrouded one. The in-cylinder pressure for each case has been also recorded. The engine's specifications are given in Table 1. More details on the methodology followed for the implementation of the experimental measurements can be found in [17,18].

Table 1. CFR engine specifications.

	Unshrouded valve	Shrouded valve
Bore	83 mm	
Stroke	114.3 mm	
Compression ratio	6.3	10.5
Engine speed	600 rpm	1200 rpm
Connecting rod length	254 mm	
Intake valve opening	15 ^{0}CA BTDC	
Intake valve closing	50 ^{0}CA ABDC	
Exhaust valve opening	50 ^{0}CA BBDC	
Exhaust valve closing	15 ^{0}CA ATDC	

3. Numerical model

3.1. CFD model

The CFD code developed can simulate three-dimensional curvilinear domains using the finite volume method in a collocated grid. It incorporates the RNG k-ε turbulence model with some slight modifications to introduce the compressibility of a fluid in generalized coordinates, as described in [19]. It solves the following transport equations for the conservation of mass, momentum, energy and turbulence properties:

$$\frac{\partial(\rho\phi)}{\partial t} + \nabla\cdot(\rho\vec{u}\phi) = \nabla\cdot\left(\Gamma_\phi\nabla(\phi)\right) + S_\phi + S_{cr} \quad (1)$$

In Table 2 all the variables corresponding to the general transport property are shown.

Table 2. Variables that represent the generalized variable in Equation (1).

Generalized variable	Equation	Γ_φ
1	Continuity	0
u	u–momentum	μ_{eff}
v	v–momentum	μ_{eff}
w	w–momentum	μ_{eff}
h	Enthalpy	μ_{eff}/σ_h
k	Turbulent kinetic energy	μ_{eff}/σ_k
ε	Dissipation of turbulent kinetic energy	$\mu_{eff}/\sigma_\varepsilon$

While for the turbulence model, the source terms of the turbulent kinetic energy and its dissipation can be found in [16], where an extra term (S_{RNG}) has been added to this turbulence model [20]. Also, all the constants used in the RNG k-ε turbulence model and the enthalpy equation, are in accordance with [20]. These constants retain their values at all cases examined in this study.

The solution follows the PISO algorithm for the velocity-density-pressure coupling, according to the methodology found in [21], which is more robust than the SIMPLE algorithm [22]. For the present simulations, it has been observed that with the PISO algorithm the model converges within almost half the CPU time compared to the one needed, when the SIMPLE algorithm was used.

The spatial discretization is based on the hybrid-differencing scheme, while the temporal one on the backward second-order Euler scheme. The transport properties (specific heat capacity under constant pressure, thermal conductivity and laminar viscosity) are calculated from least-squares fits proposed by NASA [23].

Further details of the in-house CFD model used, its evaluation and validation, together with the mesh generation model used, can be found in previous published studies of the authors [15,16,24].

3.2. Heat transfer model

By investigating various heat transfer models described in [15], it has been shown that the developed wall-function formulation in the aforementioned work performs better than the most widely used formulations found in the literature, especially during the compression stroke. This formulation is based on a compressible version of the standard law-of-the-wall [25] and includes the unsteady pressure term, which has been also shown in [7,26] to give more accurate results. The new wall-function formulation is shown in (2), where the temperature profile and the non-dimensional temperature are given separately.

$$T^+ = \frac{1}{0.4767}\left[\ln\left(y^+ + \frac{1}{0.4767\,\mathrm{Pr}}\right) - \ln\left(40 + \frac{1}{0.4767\,\mathrm{Pr}}\right)\right] + 10.2384 + P^+\left(\frac{y^+ - 40}{0.4767 + 1/\mathrm{Pr}} + 117.31\right)$$

$$T^+ = \frac{\rho u_T c_p T}{q_W}\ln\left(T_W/T\right) \qquad (2)$$

where $y^+ = y u_T/\nu$ is the non-dimensional distance from the wall, $u_T = \sqrt{\tau_W/\rho} = C_\mu^{1/4}\sqrt{k}\,y/\nu$ is the friction velocity, and P^+ is the non-dimensional pressure term, given from (3).

$$P^+ = \frac{\left(dP/dt\right)\nu}{q_W u_T} \qquad (3)$$

The wall heat flux (in W/m^2), which is inserted in the source term of the energy equation (S_h) for the boundary cells, is shown in (4). This expression is used for every y^+.

$$q_W = \frac{\rho u_T c_p T \ln\left(T_W/T\right) - \frac{dP}{dt}\frac{\nu}{u_T}\left(\frac{y^+ - 40}{0.4767 + 1/\mathrm{Pr}} + 117.31\right)}{\frac{1}{0.4767}\left[\ln\left(y^+ + \frac{1}{0.4767\,\mathrm{Pr}}\right) - \ln\left(40 + \frac{1}{0.4767\,\mathrm{Pr}}\right)\right] + 10.2384} \qquad (4)$$

Further details concerning the development, implementation and validation of this new heat transfer model used in the in-house CFD, can be found in a previous work of the authors [15].

3.3. Crevice model

For the simulation of the crevices a quite simpler phenomenological model than the one found in [13] has been developed and incorporated into the in-house CFD code. The methodology followed is in accordance with the one presented in [13], but for the calculation of the mass flow rates between the crevice regions simpler expressions are used. The ring motion is neglected (axial and twist), as well as the flow through the ring grooves. For the calculation of the mass flow rates in every inter-ring region, isentropic compressible flow is assumed and an equivalent surface is introduced [27]. This approach is followed, since in very few cases the actual ring-pack dimensions of an engine are known and the initial conditions needed for the ring motion are questionable. Even if the engine's manual is available, where some characteristics of the rings and grooves are given, these are referred to the dimensions of the cold-state of the engine, without taking into consideration the thermal expansion of the piston and the rings. Moreover, in practical applications the ring-sets are sometimes replaced due to engine's maintenance and no specifications are available. Therefore, in most of the cases, estimations are used for the various dimensions required by the more detailed models [14] and in other cases the dimensions are calibrated within the tolerance of specifications of the rings and crevices, in order for the calculated pressure history to fit the measured one [28].

The crevice model developed by the authors, takes as an input only the number of the piston rings and the estimated/approximated dimensions of the crevice regions, which are actually the equivalent discharge surface and the volume of every inter-ring region. Fewer dimensions are needed than the model presented in [13], which makes the implementation of the present model easier. It should be stressed at this point that the implementation of this model can give reliable results, concerning mainly the variation of the in-cylinder mass. This parameter is actually of importance for in-cylinder simulations. However, for a detailed calculation of the pressures and mass flow rates within the ring regions during the

engine's cycle, a more detailed crevice model is needed.

Further details concerning the description, implementation and evaluation of this crevice model can be found in [16].

4. Results and discussion

4.1. Grid and time-step independence studies

To determine the time-step of the calculations and the size of the grid used for the simulations, grid and time-step independence studies have been realized. The grid independence study was conducted for the engine using the shrouded valve, because for high-swirl cases as the ones obtained with such valve geometry, the mesh should be as fine as possible. On the other hand, the time-step independence study was conducted only for the engine with the unshrouded valve, since it operates at lower rotational speed (600 rpm), and the requirements for a small time-step are higher.

Beginning with the grid-independence study, four different 3D meshes have been considered, with (10x10x20), (20x20x30), (30x30x40), and (40x40x50) grid lines along the x-, y- and z-axis, respectively, where the z- axis is the axial one. For every mesh the local heat flux was calculated at a specific location on the cylinder head using the heat transfer model developed in [15], where experimental measurements regarding the heat flux were also available. The calculated heat flux values at a specific location of the cylinder using the four alternative meshes are shown in Fig. 1.

As observed, the results obtained from the three finer meshes are very close, whereas the one corresponding to the coarser mesh differs significantly from the others. Also, the trend of the heat fluxes, when the mesh becomes finer, is in accordance to the one reported in [29]. Therefore, it is concluded that the accuracy provided from the mesh consisted by (30x30x40) grid lines along the three axis is adequate and this is used throughout this study.

As far as the time-step is concerned, four cases have been examined beginning with a very low value (0.25 ^{o}CA), which is very CPU demanding, but gives accurate results and gradually increasing it to 0.5, 1 and 2 ^{o}CA, where the accuracy is sacrificed for decreasing the computational time required. In all these cases examined the (30x30x40) grid has been used. Moreover, the time-step independence study has been conducted only for the case of low engine speed. Once the optimum time-step is determined, it is used for the high-speed case as well. The calculated local heat flux on the cylinder head using the different time-steps is shown in Fig. 2.

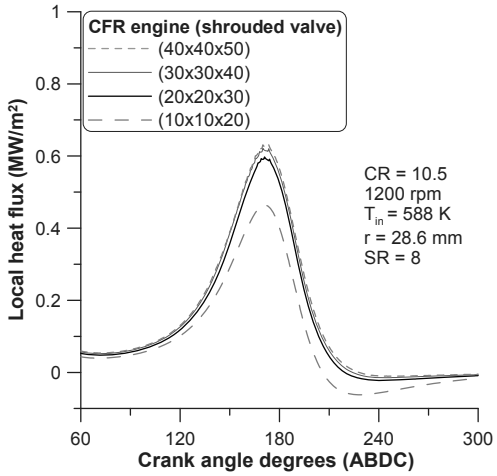

Fig. 1. Comparison of the local heat flux for different cell sizes (CFR engine with shrouded valve)

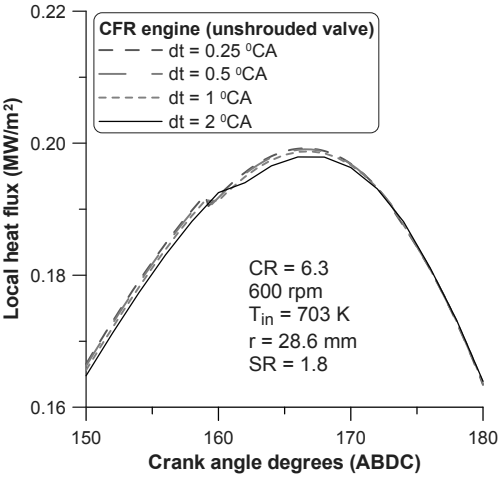

Fig. 2. Comparison of the local heat flux for different time-steps (CFR engine with unshrouded valve)

As observed, there is no significant difference in the results obtained using the three smaller time-steps. Therefore, the time-step chosen is 0.5 ^{0}CA, in order to have as detailed temporal calculations as possible and at the same time to keep the required CPU time at low levels.

4.2. CFR engine – Comparison of calculated with experimental results

In this section, the experimental results of [17] concerning the heat fluxes at a specific location on the cylinder head, 28.6 mm away from the cylinder axis, for two inlet valve designs (shrouded and unshrouded) are compared with the numerical results obtained with the in-house CFD model. The scope of this comparison is to investigate, in what extent the incorporation of the new heat transfer wall formulation and the phenomenological crevice model improves the accuracy of the in-house CFD model predictions. The operating conditions for the two inlet valve designs considered are shown in Table 3; while the calculated results correspond to three alternative CFD code configurations, as shown in Table 4.

Table 3. Engine operating conditions.

	Unshrouded valve	Shrouded valve
Rotational speed	600 rpm	1200 rpm
Swirl ratio	1.8	8
Inlet air temperature	703 K	588 K
Air temperature at IVC	747 K	630 K
Wall temperature	400 K	400 K
Rms velocity at IVC	5.9 m/sec	16.7 m/sec

Table 4. Theoretical cases examined.

Case	Heat Transfer formulation	Crevice sub-model
1	New [15]	Yes [16]
2	New [15]	No
3	Standard [25]	No

In Fig. 3 is shown the comparison of the calculated local heat fluxes with the measured one for the low-swirl case. The new wall-heat transfer formulation used is the one presented in a previous work by the authors [15]; while the crevice model is the one presented by the authors in [16]. Finally, the standard heat transfer formulation corresponds to the standard law-of-the-wall [25]. Comparing the calculated results between Case 1 and Case 2, the effect of the crevice model is depicted, while comparing the calculated results between Cases 2 and 3 the effect of the new wall heat transfer formulation becomes obvious.

As observed in this figure, taking into account the crevice regions does not actually influence the predicted heat flux on the cylinder head (Case 1 vs. Case 2). However, when the standard law-of-the-wall is used to simulate the heat transfer process, the heat fluxes are greatly underpredicted by a factor of almost two, as also stated by others researchers [7,8].

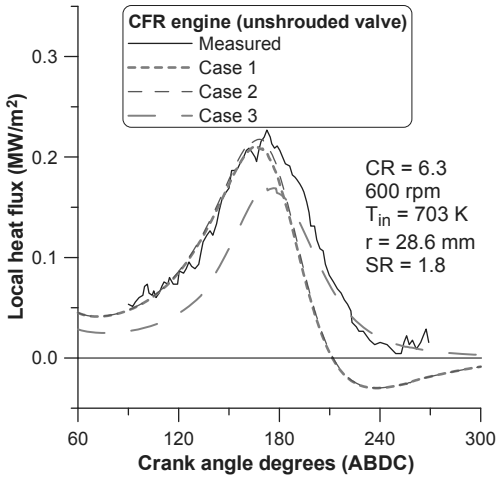

Fig. 3. Comparison of the local heat fluxes with experimental measurements [17] (CFR engine with unshrouded valve)

The measured heat flux approaches asymptotically the zero value after TDC [30], as is done also when the standard law-of-the-wall is used. On the other hand, the wall-heat transfer formulation (Cases 1,2) predicts negative heat fluxes beyond around 30 ^{0}CA ATDC. This is the only discrepancy observed, since during the compression stroke the matching between calculated and measured heat fluxes is quite good, and the value of the peak heat flux is well predicted together with its timing.

In order to better understand the importance of the simulation of the crevice regions, together with the use of an improved heat transfer formulation, the measured pressure traces are compared with the calculated ones using the three alternative CFD code configurations, for the low swirl mode, as shown in Fig. 4. It is obvious that by incorporating the new wall heat transfer formulation and the crevice sub-model (Case 1), the CFD code manages to predict quite good the cylinder pressure trace during the whole closed engine cycle, in contrast to what is observed for Cases 2 and 3, where the discrepancy between the measured and the calculated in-cylinder pressure becomes significant especially near the TDC.

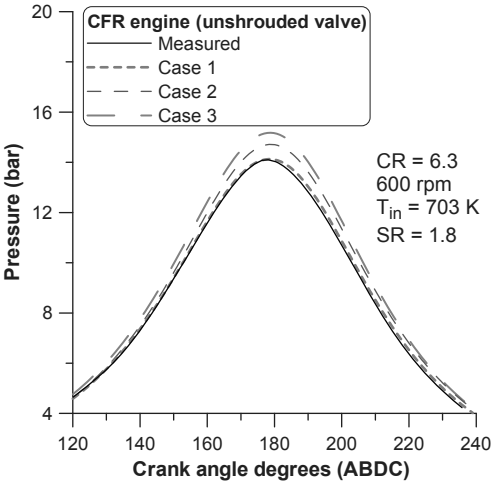

Fig. 4. Comparison of the predicted pressure with the measured one [17] (CFR engine with unshrouded valve)

Concerning the high-swirl case now, in Fig. 5, the measured heat fluxes at the same location on the cylinder head of the CFR engine are compared with the predicted ones (Cases 1-3) using the in-house CFD code.

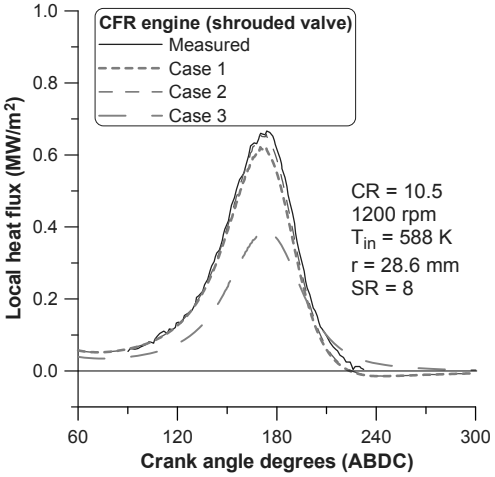

Fig. 5. Comparison of the local heat fluxes with experimental measurements [17] (CFR engine with shrouded valve)

As the rotational engine speed and the initial swirl ratio increase, the effect of the crevices on the peak heat flux is more intense (Case 1 vs. Case 2). Nevertheless, the trend during the compression and the expansion stroke is well captured for both CFD code configurations. The local heat fluxes using the standard law-of-the-wall (Case 3) are again significantly underpredicted, which support the conclusion of other researchers [7,8] that this formulation provides weak predictions of the heat transfer process.

Concerning the in-cylinder pressure traces for the high-swirl case, the comparison of the calculated with the measured ones is shown in Fig. 6.

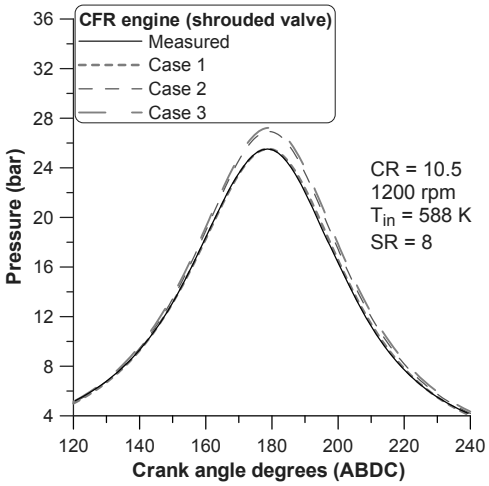

Fig. 6. Comparison of the predicted pressure with the measured one [17](CFR engine with shrouded valve)

When the simulation of crevices is omitted (Case 2), the peak pressure is overpredicted compared to the measured one, whereas the calculated pressure with the inclusion of crevices (Case 1) is almost identical to the measured one during the whole closed engine cycle. When the standard law-of-the-wall is used (Case 3), the peak in-cylinder pressure is slightly overpredicted. The discrepancy between the calculated and the measured cylinder pressure in this case is lower compared to the corresponding one at lower engine speed (Fig. 4), since in that case the calculated heat loss through the cylinder boundaries is low, forcing a steeper rise of the in-cylinder pressure.

For the high-swirl case there are also available measurements concerning the integral length-scale at the same location on the cylinder head (r=28.6 mm away from the cylinder axis). In Fig. 7 is shown the comparison between the measured and calculated integral length scale using the Case 1 CFD code configuration (new wall heat transfer formulation with crevice model). The calculated results using the other two CFD code

configurations (Cases 2 and 3) are not shown here, since identical numerical results are obtained.

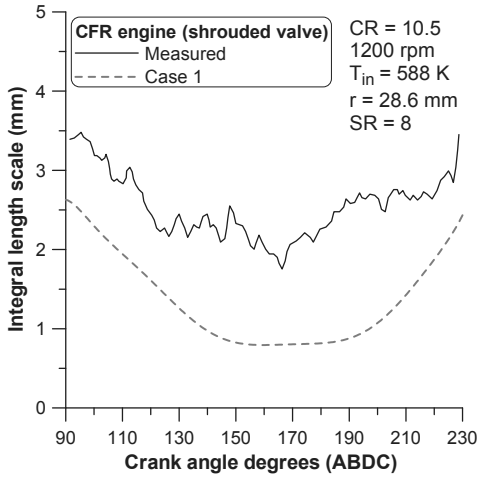

Fig. 7. Comparison of the local integral length-scale with experimental measurements [17] (CFR engine with shrouded valve)

As observed, the absolute value of the integral length-scale is not captured; however, qualitatively the predictions are correct. This discrepancy may be attributed to the fact that the integral length-scale has been measured at the wall, where the turbulence model used predicts a zero value. The calculated length-scale shown in Fig. 7 corresponds to the node adjacent to the wall on the cylinder head of the CFR engine. Nevertheless, the trend of the integral length scale is well captured, showing a minimum value just before TDC.

5. Conclusions

The present work identified in what extent the accuracy of an improved version of an in-house CFD code is enhanced, when a new wall heat transfer formulation together with a new crevice model are used. To achieve this, the measured local heat fluxes and the cylinder pressure traces for two inlet valve designs (shrouded and unshrouded ones) at two engine speeds are compared with the corresponding calculated ones for three CFD code configurations, i.e. Case 1, using the new wall heat transfer formulation with the new crevice model, Case 2, which is similar to the previous case, but without the crevice model, and Case 3 with a standard wall heat transfer formulation, but without crevice model.

The comparison revealed the necessity of using a detailed heat transfer model, such as the one proposed by the authors, since using the standard law-of-the-wall, the CFD model is not capable of reproducing neither the measured wall heat fluxes nor the measured pressure traces. It greatly under-predicts the former ones, while it over-predicts the latter one for all cases examined.

When the new wall-heat transfer formulation is used, both heat fluxes and pressure traces are calculated in much better terms, being much closer to the measured values.

The inclusion of a crevice model to the CFD code, although bringing a slight under-prediction of the heat fluxes, contributes in a great extent to the proper calculation of the in-cylinder pressure, during the whole engine cycle and especially near the TDC.

Moreover, the use of a detailed wall-heat transfer formulation and a crevice model do not actually influence the predicted integral length-scale, which follows the trend of the experimental one, although in absolute values high differences are observed.

Overall, using the new wall heat transfer formulation and the crevice sub-model proposed, a more fundamental description of the physical processes taking place inside the cylinder of an internal combustion engine is obtained, without affecting the computational time required for a simulation run, which is also a crucial parameter for multi-dimensional modeling. It is in the authors' plans to examine to what extent these new models improve the predictive accuracy of the in-house CFD code, when simulating IC engines under firing conditions.

Nomenclature

c_p specific heat capacity under constant pressure, J/kg/K

k turbulent kinetic energy (per unit mass), m^2/s^2

P pressure, N/m^2

Pr Prandtl number, -

P^+ non-dimensional pressure term, -

q_W wall heat flux, W/m^2

r distance from the cylinder axis, m

S_{cr} source term due to crevice flows

S_φ source term

t time, s

T temperature, K
T_{in} inlet air temperature, K
T_W wall temperature, K
T^+ non-dimensional temperature, -
u velocity along x-axis, m/s
u_T friction velocity, m/s
$\vec{u}$ velocity vector, m/s
v velocity along y-axis, m/s
w velocity along z-axis, m/s
y distance of the computational node from the wall, m
y^+ non-dimensional distance from the wall, -

Greek symbols

Γ_φ diffusion coefficient, kg/m/s
ε turbulent dissipation rate, m^2/s^3
ν kinematic viscosity, m^2/s
ρ density, kg/m^3
σ_h coefficient for the enthalpy equation, -
σ_k coefficient for the turbulent kinetic energy equation, -
σ_ε coefficient for the dissipation of turbulent kinetic energy equation, -
τ_W local wall shear stress, $kg/m/s^2$
ϕ generalized variable

Abbreviations

ABDC after bottom dead center
ATDC after top dead center
BBDC before bottom dead center
BTDC before top dead center
^{0}CA degrees of crank angle
CFD computational fluid dynamics
CPU central processing unit
CR compression ratio
HCCI homogeneous charge compression ignition
IVC inlet valve closure
PISO pressure implicit splitting of operators
rpm revolutions per minute
SIMPLE Semi-Implicit Method for Pressure Linked Equations
SR swirl ratio
TDC top dead center

References

[1] Komninos, N.P., 2009, Investigating the importance of mass transfer on the formation of HCCI engine emissions using a multi-zone model, Appl Energy, 86(7-8), pp. 1335-43.

[2] Alkidas, A.C., 1980, Heat transfer characteristics of a spark-ignition engine. Trans ASME, J Heat Transfer, 102(2), pp. 189-93.

[3] Dao, K., Uyehara, O.A., and Myers, P.S., 1973, Heat transfer rates at gas-wall interfaces in motored piston engine, SAE Paper no. 730632.

[4] Nijeweme, D.J.O., et al., 2001, Unsteady in-cylinder heat transfer in a spark ignition engine: Experiments and modeling, Proc Inst Mech Engrs, Part D, J Automob Eng, 215, pp. 747-60.

[5] Filipi, Z.S., et al., 2004, New heat transfer correlation for an HCCI engine derived from measurements of instantaneous surface heat flux, Trans SAE, J Engines, 113, pp. 1576-93 [SAE Paper no. 2004-01-2996].

[6] Demuynck, J., et al., 2009, Local heat flux measurements in a hydrogen and methane spark ignition engine with a thermopile sensor, Int J Hydrogen Energy, 34(24), pp. 9857-68.

[7] Han, Z., and Reitz, R.D., 1997, A temperature wall function formulation for variable-density turbulent flows with application to engine convective heat transfer modeling, Int J Heat Mass Transfer, 40(3), pp. 613-25.

[8] Angelberger, C., Poinsot, T., and Delhaye, B., 1997, Improving near-wall combustion and wall heat transfer modeling in SI engine computations, SAE Paper no. 972881.

[9] Goldsborough, S.S., and Potokar, C.J., 2007, The influence of crevice flows and blow-by on the charge motion and temperature profiles within a rapid compression expansion machine used for chemical kinetic (HCCI) studies, SAE Paper no. 2007-01-0169.

[10] Zhao, J.X., and Lee, C.F., 2006, Modeling of blow-by in a small-bore high-speed direct-injection optically accessible diesel engine, SAE Paper no. 2006-01-0649.

[11] Su, H., et al., 2007, Two-stage fuel direct injection in a diesel fuelled HCCI engine, SAE Paper no. 2007-01-1880.

[12] Jia, M., and Xie, M., 2007, Numerical simulation of homogeneous charge compression ignition combustion using a multi-dimensional model, Proc Inst Mech Engrs, Part D, J Automob Eng, 221, pp. 465-80.

[13] Namazian, M., and Heywood, J.B., 1982, Flow in the piston-cylinder-ring crevices of a spark-ignition engine: effect on hydrocarbon emissions, efficiency and power, Trans SAE, Section 1, 91, pp. 261-88 [SAE Paper no. 820088].

[14] Reitz, R.D., and Kuo, T-W., 1989, Modeling of HC emissions due to crevice flows in premixed-charge engines, Trans SAE, J Fuels Lubricants, 98, pp. 922-39 [SAE Paper no. 892085].

[15] Rakopoulos, C.D., Kosmadakis, G.M., and Pariotis, E.G., 2010, Critical evaluation of current heat transfer models used in CFD in-cylinder engine simulations and establishment of a comprehensive wall-function formulation, Appl Energy, 87(5), pp. 1612-30.

[16] Rakopoulos, C.D., et al., 2010, Investigating the effect of crevice flow on internal combustion engines using a new simple crevice model implemented in a CFD code, Submitted for publication in Appl Energy (February 2010).

[17] Boggs, D., and Borman, G., 1991, Calculation of heat flux integral length scales from spatially-resolved surface temperature measurements in an engine, Trans SAE, J Engine, 100, pp. 1242-58 [SAE Paper no. 910721].

[18] Boggs, D.L., 1990, Spatially-resolved measurements of instantaneous engine heat flux. Ph.D. Dissertation, University of Wisconsin-Madison.

[19] Demirdzic, I., et al., 1987, A calculation procedure for turbulent flow in complex geometries, Computer Fluids, 15(3), pp. 251-73.

[20] Han, Z., and Reitz, R.D., 1995, Turbulence modeling of internal combustion engines using RNG k-ε models, Combust Sci Technol, 106(4), pp. 267-95.

[21] Jennings, M.J., and Morel, T., 1988, Observations on the application of the k-ε model to internal combustion engine flows, Combust Sci Technol, 58(1), pp. 177-93.

[22] Ferziger, J.H. and Peric, M., 2002, *Computational methods for fluid dynamics*. Springer, Berlin.

[23] McBride, B.J., Gordon, S., and Reno, M.A., 1993, Coefficients for calculating thermodynamic and transport properties of individual species, NASA Technical Memorandum 4513.

[24] Rakopoulos, C.D., Kosmadakis, G.M., and Pariotis, E.G., 2009, Evaluation of a new computational fluid dynamics model for internal combustion engines using hydrogen under motoring conditions, Energy, 34(12), pp. 2158-66.

[25] Launder, B.E., and Spalding, D.B., 1974, The numerical computation of turbulent flows, Comput Methods Appl Mech Engrg, 3(2), pp. 269-89.

[26] Huh, K.Y., Chang, I.P., and Martin, J.K., 1990, A comparison of boundary layer treatments for heat transfer in IC engines, SAE Paper no. 900252.

[27] Keribar, R., Dursunkaya, Z., and Flemming, M.F., 1991, An integrated model of ring pack performance, Trans ASME, J Eng Gas Turbines Power, 113, pp. 382-89.

[28] Dursunkaya, Z., Keribar, R., and Richardson, D.E., 1993, Experimental and numerical investigation of inter-ring gas pressures and blowby in a diesel engine, SAE Paper no. 930792.

[29] Wu, H.W., and Perng, S.W., 2002, LES analysis of turbulent flow and heat transfer in motored engines with various SGS models, Int J Heat Mass Transfer, 45, pp. 2315–28.

[30] Yang, J., et al., 1988, Heat transfer predictions and experiments in a motored engine, Trans SAE, J Engines, 97, pp. 1608-22 [SAE Paper no. 881314].

Acknowledgments: G.M. Kosmadakis wishes to thank the Greek State Scholarships Foundation for granting him a Ph.D. research scholarship.

Optical Investigation in a GDI Engine Operating in Homogeneous and Stratified Charge Mixture Conditions Fuelled with Gasoline and Ethanol

Francesco Catapano[a], Paolo Sementa[b] and Bianca Maria Vaglieco[b]

[a] *Università di Napoli Federico II, Napoli, Italy*
[b] *Istituto Motori-CNR, Napoli, Italy*

Abstract: Imaging and UV-visible spectral measurements were carried out in optical spark ignition engine to investigate the spray characteristics and flame propagation of gasoline and ethanol fuel for two different engine conditions, homogeneous and stratified charge mixture. Measurements were performed in the optically accessible combustion chamber realized by modifying a real 4 strokes four cylinder high performance gasoline direct injection (G.D.I) engine. The cylinder head was modified in order to allow the visualization of the fuel injection and the combustion process using an endoscopic system coupled to a high spatial and temporal resolution ICCD detector. All the optical data were correlated to the engine parameters and to the exhaust emissions.

Keywords: Ethanol, GDI Engine, Optical Measurements.

1. Introduction

In these past few years strict regulations dealing with pollutant emissions of internal combustion engine as well as heavy concerns about the related health problems have been the impulse to search and use alternative/biological fuels with respect to fossil one. Ethanol can be considered one of these, because it can be used as a fuel extender for petroleum-derived fuels, an oxygenate, an octane enhancer, and a pure fuel. The start up to ethanol production in the mid 1970s was due to the need to develop alternative supplies of motor fuel in response to the oil embargoes in 1973 and 1979. Then, its use was focused on special markets such as in Brazil or Sweden [1-2].

Many differences between ethanol and gasoline are noted down as reported in Table 1. In particular, ethanol has a lower heating value (LHV), about 60% even if its stoichiometric air/fuel ratio is also smaller than gasoline one, and therefore, the amount of energy per kg of stoichiometric mixture is similar for both fuel. Moreover, ethanol has higher research octane number (RON). These parameters allow higher compression ratios, higher boost in turbocharged engines, and higher spark advances before knock limit. Ethanol also has a higher vaporization heat and in this way the available energy amount per kg of stoichiometric mixture to cool the charge is three times bigger (about 3.65). This provides higher densities in the intake that may increase volumetric efficiency mainly in naturally aspirated engines with port fuel injection (PFI) engines, or better cooling of the in-cylinder charge in naturally aspirated and turbo charged direct injection engines. This latter feature furthermore reduces the knock sensitivity. If direct fuel injection and turbo charging are two of the most effective indications in advancing the efficiency of gasoline engines, there is no doubt in the use of pure ethanol. In particular, the effect of inhibiting knock has been already tested thanks to the evaporative cooling from direct ethanol injection and its high octane rating [3-5]. The chemical composition of ethanol requires larger amounts of fuel to be injected, thus leading to the danger of oil dilution with direct-injected combustion concepts.

Direct injection and turbo charging may therefore optimize pure ethanol-fuelled engines to a level of performance that exceeds gasoline engine efficiency, taking full advantage of ethanol's higher octane number and vaporization heat.

In order to contribute to these improvements, some non intrusive measurements in the cylinder must be performed so that the related chemical and physical events can be assessed. Various experimental studies were carried out in optically accessible closed vessel, model combustion chamber, and rapid compression machines and only recently in optical engine in order to study the ethanol blends combustion process [6]. In particular, combined optical techniques were used in order to analyze the fuel spray distribution and evaporation, mixture preparation and self-ignition [7].

This paper deals with imaging and spectral measurements of the natural emissivity both in the visible and in the near UV inside an optically

accessible engine. Just few works have been carried out in SI ethanol fuelled engines whereas the ultraviolet-visible spectroscopy of gasoline engine has been widely studied [8].

Fuel property	Ethanol	Gasoline
Formula	C2H5OH	C4 to C12
Molecular weight	46.07	100–105
Density, kg/l, 15/15 °C	0.79	0.69–0.79
Boiling point, °C	78	27–225
Vapor pres., kPa at 38 °C	15.9	48–103
Specific heat, $kJkg^{-1}K^{-1}$	2.4	2
Viscosity, mPa s at 20 °C	1.19	0.37–0.44
Low. heating val., 10^3 kJ/l	21.1	30–33
Autoignition temp., °C	423	257
Flammability lim., Vol % *Lower/ Higher*	4.3/19	1.4/7.6
Stoichiometric air/fuel	9	14.7
Octane number	108.6	88-100

Table 1 Fuels chemical and physical properties

Simultaneous use of spectral emissivity and imaging measurements in UV-visible range have shown to be a powerful tool as well as high speed imaging of combustion process thanks to the presence in this region of the well-known "water bands" emitted by OH radical, CH, CN and C2, HCO. Moreover, carbonaceous material and CO-O can be observed in this spectral range [7].

2. Experimental Apparatus and Procedures

2.1 ENGINE

A spark ignition direct injection (DI), inline 4-cylinder, four stroke, displacement of 1750 cm^3, supercharged, high performance engine was used. It had a six holes nozzle on the injector tip, between the intake valves oriented at 45° angle with respect to the cylinder axis, and a valve timing variation in order to optimize intake and exhaust valve lift for all the engine speed. Further details are reported in Table 2.

Vol. cylinder, cm^3	435.5
Bore, mm	83
Stroke, mm	80.5
Turbine	Exh. gas turbocharger
Max boost press, bar	2.5
Valve timing	Ivo 31°,Ivc -1.5°,Evo -21°,Evc 39.5°
Vol.comp.ratio	9.5:1
Max power	147.1 kW at 5000 rpm
Max torque	320.4 Nm at 1400 rpm

Table 2 Engine specifications

A quartz pressure transducer was installed into the spark plug in order to measure the combustion pressure. The in-cylinder pressure, the rate of chemical energy release and the related parameters were evaluated on an individual cycle basis and/or averaged on 500 cycles [9].

An optical sapphire window (5 mm diameter) was installed in the engine head in the 4th cylinder. It allowed a view of the combustion chamber by an endoscopic probe. With this configuration, the endoscope field of view turned out to be exactly centered in the combustion chamber and was perpendicular to the axis of the cylinder, and then perpendicular to the plane of tumble motion. Using an endoscope with a viewing angle of 70°, it was therefore possible to classify an area that included the spark and the fuel injection.

2.2 OPTICAL APPARATUS

Imaging and polychromatic chemiluminescence measurements from ultraviolet (UV) to visible were performed by means of the optical experimental set-up shown in Figure 1.

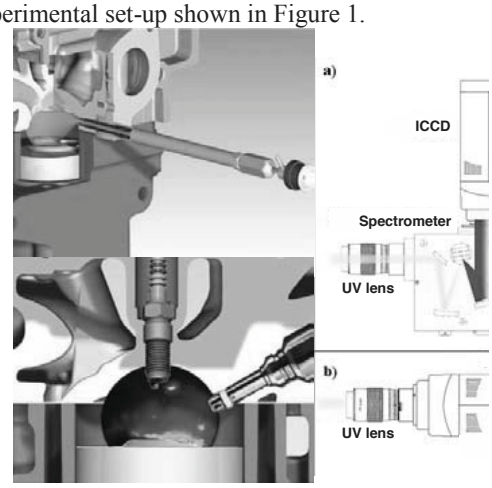

Figure 1 Sketch of the experimental setup for optical investigation and detail of the combustion chamber.

The injection and combustion phases were detected through an optical access on the head and an endoscopic probe coupled to a high spatial and temporal ICCD (Intensified Charge Coupled Device) camera. The camera had high sensitivity both in the UV and visible range; it had an intensified charge coupled device. In order to characterize the injection phase an intense strobe lamp was introduced in the spark location and Nitrogen gas flowed into the chamber. The images were recorded through an optical access on the engine head and an endoscopic probe.

Chemiluminescence signals, due to radical emission species, were detected in the central locations, between the sparkplug and the piston

bowl of the combustion chamber with high spatial resolution.
Chemiluminescence signals were collected and focused on the entrance slit of a spectrograph through an UV-Visible objective. Spectrograph was 15 cm focal length, f/4 luminous, and equipped with a grating of 300 g/mm, blazed at 300 nm, with a dispersion of 3.1 nm/mm. The spectral image formed on the spectrograph exit plane was matched with a gated intensified CCD camera. Data were detected with the spectrograph placed at two central wavelengths, 325 and 575 nm, respectively, and the intensifier-gate duration was set to 83 μs in order to have a good accuracy in the timing of the different investigated events. Engine synchronization with ICCD camera was obtained by the unit delay connected to the signal coming from the engine shaft encoder.
All experiments were made by measuring the in cylinder combustion pressure, exhaust emissions and performance.

3. Result and Discussion

All the tests presented in this paper were carried out at engine speed of 1000 rpm, minimum load and cold condition (T=323 K) using gasoline and ethanol. The absolute intake air pressure and temperature are fixed at 300 mbar and 303 K, respectively. The spark timing was fixed to operate in the MBT (Maximum Brake Torque) condition (12° BTDC). The fuel injection occurred always at fixed pressure of 30 bar.
Two different fuel injection strategies and two different fuels were tested. Initially, homogeneous charge condition (HC1) and stratified charge one (SC1) were taken into account and then the effect of ethanol injection was examined. In particular, by using ethanol the injection duration was longer to operate in stoichiometric condition due to the different ethanol stoichiometric air–fuel ratio as reported in table1.
For all the test cases, the injection duration was chosen to obtain stoichiometric equivalence ratio, as measured by a lambda sensor installed at the engine exhaust. More details about the engine operating conditions are reported in Table 3.
It is particularly important to note that the in cylinder pressure at SOI (Start Of Injection) was different for each conditions. In particular the SOI of SC2 condition was set to 60 CAD BTDC in order to achieve the best combustion stability in this engine condition.

test	Charge Condition	DOI [°ca]	SOI ATDC [°ca]	Pressure @ SOI [mbar]
HC1	Homogeneous	4.8	-265	295
SC1	Stratified	4.8	-70	680
HC2	Homogeneous	7.2	-265	295
SC2	Stratified	7.2	-60	920

Table 3 Engine operating conditions

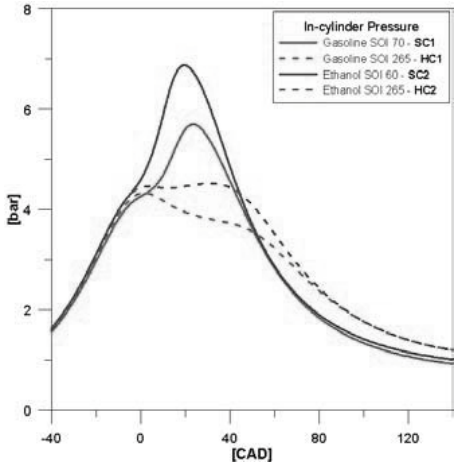

Figure 2 Pressure signal averaged on 500 consecutive cycles for the conditions of Table 3.

Figure 2 reports the pressure averaged curves for the selected conditions. The related Indicated Mean Effective Pressure (IMEP) and Coefficient of Variation (COV) are listed in Table 4. Data in Fig. 3 and Table 4 show an improvement in terms of combustion stability between homogeneous and stratified charge condition. Nevertheless, pressure measurements and derived engine parameters give global data and do not allow following locally the combustion process [10].

test	IMEP [bar]	COV IMEP [%]	CO [%]	HC [ppm]	Opacity [%]
HC1	0.8	19.34	0.4	170	2.5
SC1	0.8	8.4	1.4	1070	5.6
HC2	0.8	15	0.45	175	0.7
SC2	0.8	5.9	0.6	400	1.2

Table 4 Engine performance and exhaust emissions for both fuels investigated

For this purpose, optical techniques have been adopted in order to have detailed information on thermo and fluid dynamic phenomena that occur into the combustion chamber.

3.1 Injection Phase

Gasoline Injection

Figure 3 (a) reports a selection of images for the engine running in homogeneous charge condition at start of injection (SOI) 265°CA BTDC.
In this condition the spray shows a rapid vaporization of the fuel and a good homogenization of the charge due to the significant air motion in the cylinder. At the injection start, the intake valves are open and the piston is descending, the air motion is mainly determined by the intake duct shape that provides a strong tumble motion. The tumbling motions enhance fuel vaporization and fuel-air mixing. On the other hand, for stratified charge condition (SOI at 70° ca BTDC), the piston is in the compression phase, the intake valves are closed and the piston bowl causes the tumble motion in the opposite direction. In this condition the spray is led to the spark plug by the air motion and the bowl and a little amount of fuel impacts on the piston surface forming a fuel film not completely vaporized.

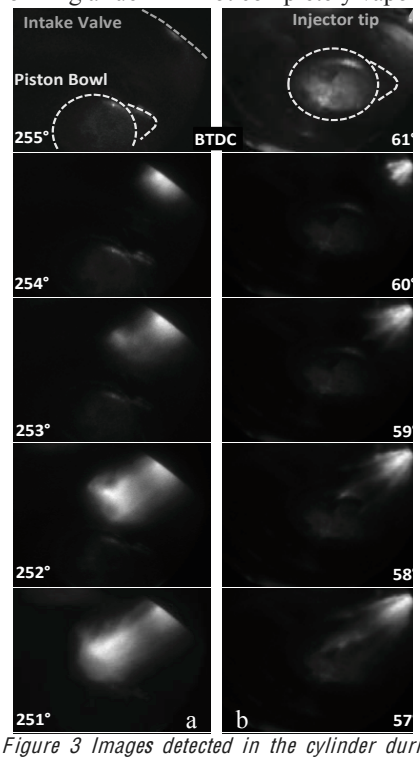

Figure 3 Images detected in the cylinder during the fuel injection phase for gasoline.

This creates fuel-rich regions with high density of low-volatile fuel compounds contributing to the higher level of HC measured at the exhaust than the homogeneous charge combustion condition. Moreover, these deposits of fuel generate locally fuel-rich zones that ignite when the normal flame front reaches them. (figure 5) When the flame front propagates up to the piston bowl region, it induces a diffusion-controlled flame that produces high soot concentration at the exhaust too. These results agree with literature data [11-12].

Ethanol Injection

A second series of images was obtained in the ethanol fuelled engine. The reduced image sequence reported in Figure 4 gives the spray evolution for HC2 (a) and SC2 (b).
The same effect was observed in the spray images as previously discussed.
Observation of the injection process has furthermore revealed that in the homogeneous charge conditions (0.2 bar of cylinder pressure) there were some fundamental differences in the ethanol and gasoline sprays.

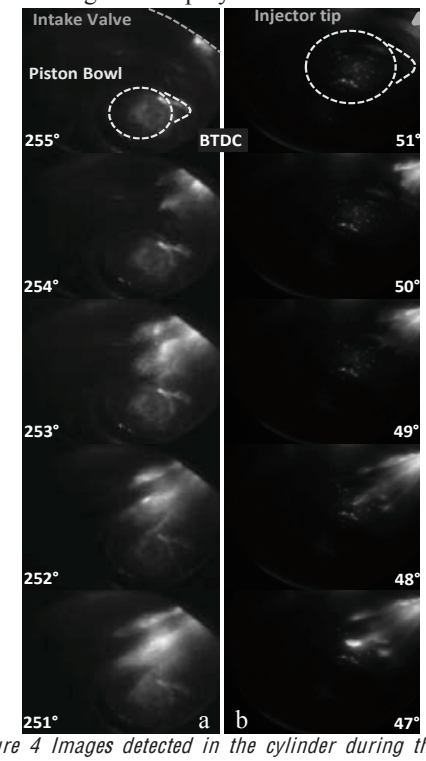

Figure 4 Images detected in the cylinder during the fuel injection phase for ethanol.

The different characteristics were evident on the ethanol images, which allowed the six individual plumes to be clearly seen in contrast to the gasoline one which shows a single cloud.
That originates probably from differences in the liquid properties of alcohol fuels compared to the hydrocarbons typically found in gasoline. Ethanol has a viscosity more than double when compared

to the main gasoline hydrocarbon components such as pentanes, octanes and xylenes [6].
Increasing the in cylinder pressure to 0.9 bar, at the SOI of stratified condition, the spray is less open than the ethanol homogeneous case (Fig. 4b). This means that the effect of liquid properties is less with respect to the gasoline injection at the same pressure.

3.2 Combustion Phase

Figure 5 shows a selection of images detected in the combustion chamber for the HC1 and SC1 engine conditions. The evidence of spark ignition is represented by a luminous arc near the spark plug. It occurs around 12 CAD BTDC. The spark luminosity persisted until 6 CAD BTDC when the flame kernel was well observable, even if its luminosity was much lower than the spark. Then the flame kernel moves from the spark plug with different trend due to the different distribution of air-fuel ratio in the two injection strategies. In the condition with SOI at 265 CAD the flame front moves with a radial like behaviour. While, for the strategy with SOI at 70 CAD, there is a strongly asymmetry in the flame front, the flame has a preferential propagation mode, since it reaches first the cylinder walls in the injector region.

The flame front propagation depends mainly on the turbulence and the air- PAH MOBK ; in particular it increases with the increase of turbulence and the AMA AK AOPMPLAN A can be assumed similar in the two investigated conditions, which differ only for the SOI, while, the AFR distribution is totally different. In the stratified combustion condition the injector sprayed the fuel through the piston bowl on the spark plug, and the air motion due to the piston bowl surface allows to a small amount of fuel to get into the exhaust valves region, this effect is amplified during the little time between the injection and the spark start. Therefore, the presence of rich mixture in the bowl region, near the injector, has direct effect on the flame evolution in terms of kernel propagation, velocity but also on the cyclic variability and flame stability [13] as shown in table 4. Figure 6 reports a selection of images obtained in the engine fuelled with ethanol for the injection strategies with SOI 265° and 60°ca BTDC, respectively. Also in this case it is possible to observe a different flame front evolution to confirm the different air-fuel ratio distribution.

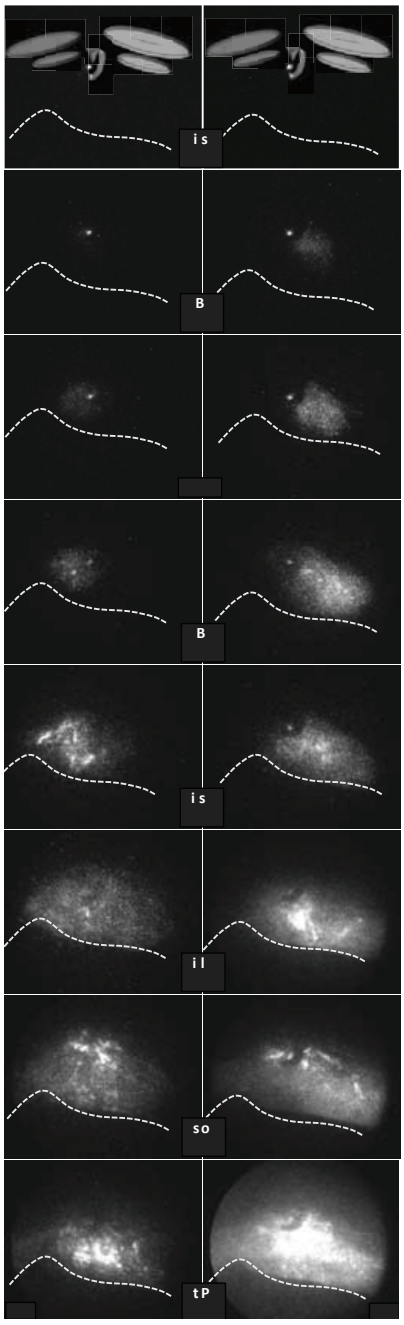

Figure 5 Images detected in the cylinder during the combustion phase for gasoline.

In particular, in the HC2 the flame front has a radial like behaviour, while, in SC2, it is asymmetric, with elongated shape in the injector direction. In this case the difference between the stratified and homogeneous flame front are less evident with respect to the gasoline one.

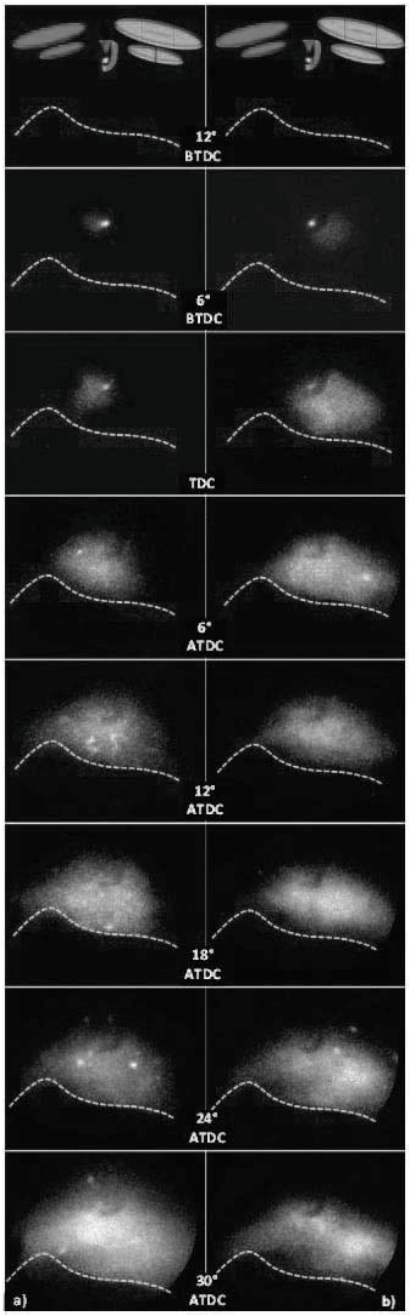

Figure 6 Images detected in the cylinder during the combustion phase for ethanol.

For the two fuels it is clear that the stratified flame front, in the first phase of combustion, spreads faster than the homogeneous case; this is due to the lower lambda in the piston bowl region. Then, around 12 CAD ATDC, the flame size becomes similar, and finally greater in the homogeneous case, probably because the mixture near the cylinder walls is richer than the stratified one.

Some clear differences, due to the fuel, can be seen in terms of presence of small diffusive flames. In the gasoline case, several bright spots were detected in the burned gas before the flame front reached the chamber walls. Bright spots were due to the ignition of the fuel-rich zones created by the fuel droplets stuck on the piston surfaces and near the valve. The ignition was induced by normal flame propagation.

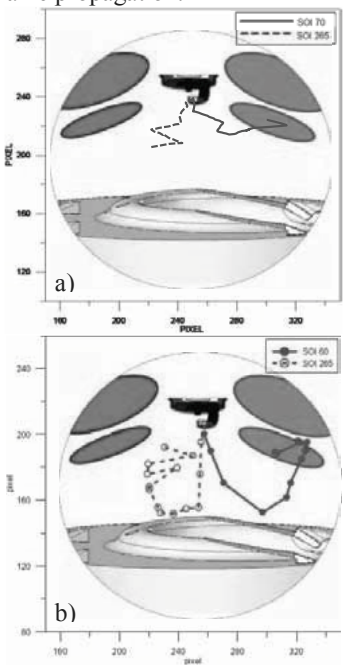

Figure 7 Centroid of luminosity for engine fuelled with gasoline (a) and ethanol (b).

A retrieving procedure of the optical data was realized to process each image. In this way it was possible to evaluate the luminous signal locally in each point of the combustion chamber and calculate the centroid of luminosity.

Figure 7 a and 7 b show the evolution of the centroid of luminosity in the two investigated conditions, for Gasoline and Ethanol respectively. It can be observed that, in the stratified condition, the flame front propagates rapidly to the right in the injector direction due to the charge stratification, while in the other condition the centroid of luminosity position is located near the cylinder central axis.

To confirm this result Figure 8 reports the heat release and heat release rate of the selected conditions. As you can see, combustion

performances are different for two injection strategies and for two fuels.

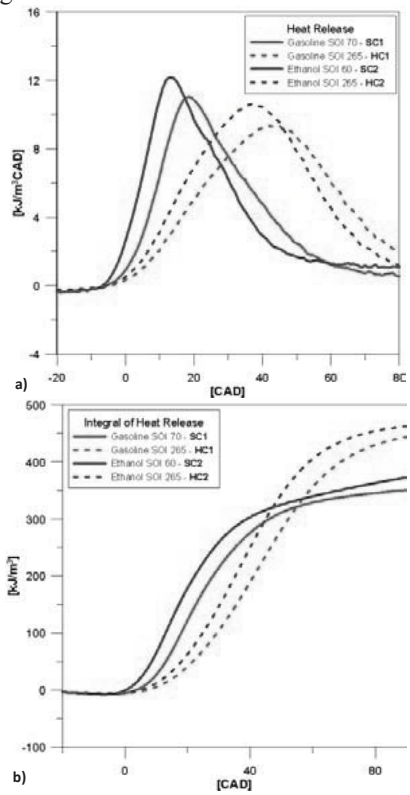

Figure 8 ROHR and HR averaged on 500 consecutive cycles for the conditions of Table 3

In the SC1 and SC2 case, higher pressure values and heat release were measured and evaluated until around 40°ca ATDC. At this time a crossing for the selected cycles was observed both in the pressure signals and heat-release curves, these signals remained lower than in the homogeneous one until the opening of the exhaust valves. This effect seems to indicate that in homogeneous charge combustion the process starts later but a higher amount of fuel and oxygen burns. Thus, the stratified strategy induces less efficient fuel consumption during the flame front propagation and more fuel is available to HC and soot production.

In terms of different behaviour between the two fuels Fig. 8 revealed that at ignition timing the ROHR for ethanol was lower, it is probably due to lower in-cylinder temperatures being higher injected quantity and cooling capacity. However, after ignition the ROHR rise was faster than gasoline.

The phasing of combustion defined by the location of peak pressure was faster and the peak pressure was higher by 1.5 bar for Ethanol.

Similar trends are shown (Figure 8) by the integral heat release.

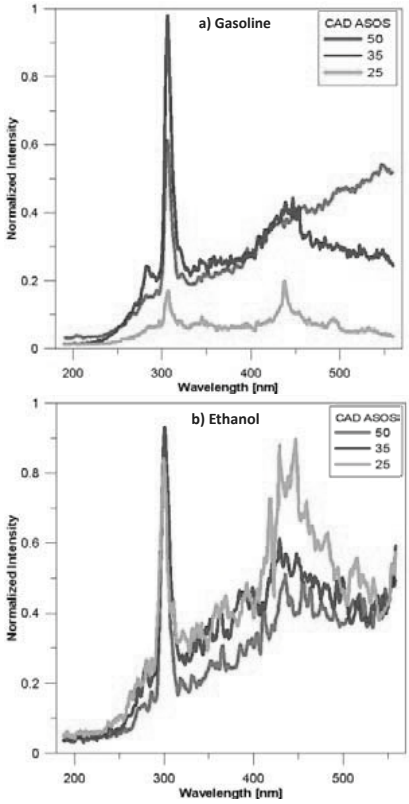

Figure 9 Spectra measured for homogeneous charge condition a) gasoline and b) ethanol.

In order to identify the chemical species that featured the flame, natural emission spectroscopy was applied in the combustion chamber. Figure 9 reports the spectra detected for gasoline and ethanol, for different crank angles.

It can be noted that the spectra showed two peak centered at 280 nm and 309 nm due to OH radical emission. Moreover, a broadband emission, from 250 to 500 nm, was detected only for gasoline. This band was due the convolution of HCO Vayda bands from 250 nm to 410 nm, and HCHO Emeleus bands from 340 nm to 523 nm [7]. Moreover, for the ethanol it seems to be absent any HCO band and it is always observed a strong peak centred at 431 nm due to the CH. In the late combustion phase (50 CAD ASOS) spectra measured were characterized, only for gasoline, by

a strong continuous contribution that increased with the wavelength in the visible range. This band, typical of blackbody emission is due to the soot particles. It is a confirmation of the higher exhaust emission, in terms of opacity value, for gasoline than ethanol.

Conclusions

The effects of the fuel and the injection strategies on the combustion process and on the pollutant formation in a real high performance GDI SI boosted engine were investigated. The engine was equipped with an endoscopic probe and light unit fiber in order to visualize the injection and the combustion. The engine worked at 1000 RPM, idle load, cold condition, and stoichiometric equivalent ratio.

The effect of different SOI, in order to obtain homogeneous and stratified charge mixture, was investigated and two fuels, gasoline and pure ethanol, were tested.

Gasoline spray was more sensible to air motion and changes in cylinder pressure. On the other hand ethanol spray plumes were thinner, more compact and not sensitive to change SOI (in cylinder pressure).

The effect of the different fuel injection strategies on the flame propagation, distribution and speed were evaluated.

In particular for both fuels the stratified flame front, in the first phase of combustion, spreads faster than the homogeneous case, due to the A/F ratio distribution, moreover the burning of fuel impinged on the piston bowl produces more soot and HC.

Ethanol showed the higher peak pressures and faster burning rates compared to gasoline.

The ethanol flames show a smaller number of bright spots than gasoline, may be associated with lower levels of soot.

The use of ethanol coupled to stratified charge strategies allowed the improvement in the performances stability and the reduction in the exhaust particulate matter and HC.

References

[1] Dickson, C., Northrop Grumman, Motor Gasolines, Summer 2006, Report No. NGMS248 PPS 2007/1, February 2007

[2] Gao, J., Jiang, D., Huang, Z., (2007) "Spray Properties of Alternative Fuels: A Comparative Analysis of Ethanol–gasoline Blends and Gasoline" Fuel 86, 1645–1650

[3] Heywood, J.B., *Internal Combustion Engine Fundamentals*., New York: McGraw-Hill 1988.

[4] American Petroleum Institute, Alcohols and Ethers: a Technical Assessment of Their Application as Fuels and Fuel Components, API Publication 4261, 3rd edition, June 2001

[5] Varde, K., Jones, A., Knutsen, A., Mertz, D., and Yu, P. (2007) "Exhaust Emissions and Energy Release Rates from a Controlled Spark Ignition Engine using Ethanol Blends" Proc. IMechE Vol. 221, N.8 Part D: J. Autom. Eng, 933-941.

[6] Aleiferis P.G., Serras-Pereira J., van Romunde Z., Caine J., Wirth M., "Mechanisms of spray formation and combustion from a multi-hole injector with E85 and gasoline" Combustion and Flame 157 (2010) 735–756

[7] Gaydon, A.G., *The Spectroscopy of Flames*, Chapman and Hall ltd., 1957.

[8] Zhao, H.,(2010) "Advanced Direct Injection Combustion Engine Technologies and Development" Vol.1:Gasoline and Gas Engines, Woodhead Publishing.

[9] Zhao, H., Ladommatos, N. (2001). Engine Combustion Instrumentation and Diagnostics. SAE Int., Inc.

[10] Witze, P. O. and Green, R. M. (1997) 'LIF and Flame-Emission Imaging of Liquid Fuel Films and Pool Fires in an SI Engine During a Simulated Cold Start' SAE Paper n 970866.

[11] Witze, P., Hall, M., Bennet, M. (1990). Cycle-resolved Measurements of Flame Kernel Growth and Motion Correlated with Combustion Duration. SAE paper n. 900023.

[12] Nogi, T., Ohyama, Y., Yamauchi, T. and Kuroiwa H. (1988) 'Mixture Formation of Fuel Injection Systems in Gasoline Engines' SAE Paper n. 880558.

[13] Bianco, Y., Cheng, W., Heywood, J. (1992). The Effects of Initial Flame Kernel conditions on Flame Development in SI Engines. SAE paper n. 912402.

Acknowledgments:

The authors are grateful to Mr. Carlo Rossi and Mr. Bruno Sgammato for the support in the experimental activities carried out.

Optical Characterization of the Thermo-Chemical Processes in a SI Small Engine for the Reduction in Fuel Consumption and Pollutants Emission

Cinzia Tornatore, Paolo Sementa and Simona Silvia Merola

Istituto Motori – CNR, via G. Marconi, 8 – 80125 Napoli (Italy)

Abstract: In the next future, small internal combustion engines still can be optimized in terms of combustion efficiency, of the cycle-to-cycle stability control, fuel consumption and pollutant exhaust emissions. To this aim it is necessary to better understand the fluid dynamic and thermo-chemical phenomena occurring in these complex systems. The objective of the present study is to analyze the effect of fuel injection mode on the in-cylinder mixture formation, combustion process and exhaust emission. In particular the change of phasing and the splitting of the fuel injection (double injection strategies) were tested. Specific fuel injection strategies were proposed as technological inexpensive key for the reduction in fuel film deposits and the improvement of the combustion process efficiency.
The cycle resolved visualization was used to study the flame kernel inception, to follow the flame front propagation and to investigate the in-cylinder pollutant formation and emission.

Keywords: Optical diagnostics; SI Small Engine; Fuel Consumption; Pollutants Emission.

1. Introduction

One of the most interesting innovation path for the reduction in fuel consumption and pollutants emission is shift from gasoline-powered vehicles to electric-powered vehicles. The shift would have several concrete benefits on the local air quality in the densely packed cities. This effect could be very important in some countries as China, India and other non-OECD countries that suffer pollutant and traffic problems caused by the rapid urbanization. Moreover the electric-powered vehicles would reduce the dependence on imported petroleum [1].

While the public transit systems are well reacting to the electric-power conversion, there are resisting forces in the two-wheel vehicle market, especially for scooters and motorcycles. The superior performance of gasoline-powered motorcycles is a powerful limiting factor. The growth in the EPV market is dependent on continuous improvement in battery cost and performance.

The role of the two-wheel vehicles in the above mentioned countries is fundamental because they represent the low-cost form of private transport in small and medium size cities where public transit service is limited or the city is geographically disperse. Moreover, future mobility analysis and transport trend studies demonstrated that in the next decade, the two-wheel vehicles and the small engine vehicles will be more and more widely used for transportation in urban areas [2, 3, 4]. Almost all these vehicles is equipped with port-fuel-injected (PFI) spark ignition (SI) engine. Processes in PFI engines were reasonably well understood thanks to synergy between the experimental diagnostics and numerical methodologies. On the other hand, still little work has been done for two-wheel vehicle engines. The optimization of the two-wheel vehicle engine efficiency especially at low speeds and high loads is required to satisfy the future emission and fuel consumption standards,. The proposal of low-cost solutions for this target would be desirable. For this goal the improvement in the basic knowledge of the thermo-fluid dynamic phenomena occurring during the injection and the combustion process is necessary.

The objective of the present study is the analysis of fuel injection mode effects on mixture formation, combustion process and exhaust emission. In this work, specific fuel injection strategies were suggested as technological inexpensive key for the reduction in fuel film deposits and for the improvement of the combustion process efficiency. In particular the phasing was changed and the fuel injection was split (DIS_Double Injection Strategy).

The experiments described in the paper are part of the research activities realized to optimize 4-stroke engines with low cost solutions [5, 6]. They can be useful in the future also for new generation engines for small urban vehicles.

2. Experimental Apparatus

The experimental investigations were performed on an optically accessible single-cylinder, PFI, four-stroke SI engine. The engine bore and stroke were 72 mm and 60 mm, respectively, and the geometric compression ratio was 11. The engine was equipped with the cylinder head of a commercial 250 cc motorcycles engine. A four-valve, pent-roof chamber engine was mounted on an elongated piston.

The engine reached a maximum speed of 5000 rpm. At 5000 rpm the maximum performance is: 7.9 kW and 14.7 Nm. These values are calculated considering a mechanical theoretical efficiency of 85%, since the real efficiency of experimental engines is lower than real engines because of higher friction losses.

The head had a centrally located spark plug and a quartz pressure transducer was flush-installed in the combustion chamber to measure the combustion pressure. The in-cylinder pressure, the rate of chemical energy release and the related parameters were evaluated on an individual cycle basis and/or averaged on 400 cycles [7]. A lambda sensor was installed at the engine exhaust for the measurement of the air/fuel ratio.

A special customized lube oil and coolant conditioning unit for transparent single cylinder engine application was used. The conditioning unit contains two pumps: one for oil and one for water. The oil pressure in the circuit can be adjusted through a pressure control valve (spill valve). A coolant heater, installed in the cooling water circuit, is foreseen to heat up engine coolant during engine operation as well as engine lube oil via the coolant/oil heat exchanger.

A section of the concentric flat-bottomed piston bowl was replaced with a sapphire window to enable the passage of optical signals coming from the combustion chamber. To reduce the window contamination by lubricating oil, the elongated piston arrangement was used together with self-lubricating Teflon-bronze composite piston rings in the optical section.

During the combustion process the emitted radiations passed through the sapphire window and they were reflected toward the optical detection assembly by a 45° inclined UV-visible mirror located at the bottom of the engine.

Cycle resolved flame visualization was performed using a 8-bit high speed CMOS (complementary metal-oxide semiconductor) camera. The camera was equipped with an extreme light sensitive image sensor and with a 50 mm focal Nikon lens. The resolution was 512x512 pixel with a speed of 5000 fps, the spectral range extended from 400 nm to 900 nm. A camera region of interest was selected (360 x 360 pixel) to obtain the best match between spatial and temporal resolution. This optical assessment allowed a spatial resolution around 0.25 mm/pixel and a frame rate of 7188 fps. The exposure time was fixed at 10 μs.

The Crank Angle Encoder signal synchronized the camera and the engine through a unit delay. AVL Indimodul recorded the TTL signal from the camera acquisitions together with the signal acquired by the pressure transducer. In this way, it was possible to determine the crank angles where optical data were detected.

Steady-state measurements of CO, CO_2, HC and NOx were performed in the undiluted exhaust. Gaseous emissions were measured by AVL Digas 4000 constituted by an electrochemical sensor for NOx and non-dispersive infrared (NDIR) analyzers for HC, CO and CO_2. Tests downstream a three-way catalyst were performed. The exhaust temperature was kept constant using a thermo-control device placed upstream of the catalyst.

3. Results and Discussion

All the tests presented in this section were carried out at an engine speed of 4000 rpm at wide open throttle. The intake air temperature was fixed at 298 K and the cooling water temperature was set at 333 K. Commercial gasoline was injected at 3 bar in the intake manifold.

Table 1. Selected engine conditions.

Test name	n. of injection	SOI [CAD vs TDC]	DOI [CAD]
CV	1	0	235
CV-OV	1	130	245
OV	1	-360	245
DIS	2	-360	112
		0	112

Different starts of injection or phasing were tested:

- fuel injection at intake valves closed (CV);
- fuel injection at intake valves open (OV);
- fuel injection at intake valves opening (CV-OV);
- fuel injection splitting (DIS_Double Injection Strategy).

The tested engine conditions were detailed in Table 1. The valve timing diagram is shown in Figure 1.

For each condition the fuel injection duration was fixed to obtain the same IMEP (Indicated Mean Effective Pressure) value averaged on 400 consecutive engine cycles. In particular the value of 7.0 bar with standard deviation lower than 0.1 bar was considered, as shown in Figure 2. The electronic spark timing was fixed to operate at the maximum brake torque.

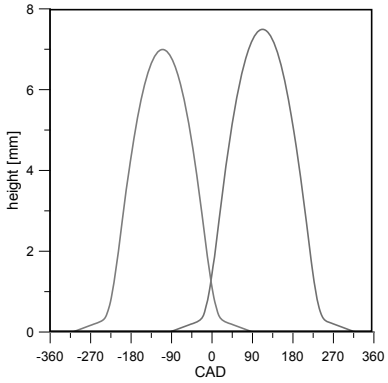

Figure 1. Valve-timing diagram

The thermal evolution and fluctuation of the pressure signal due to the cyclic variation was satisfactory, as reported in Figure 3. It shows the trend of the maximum combustion pressure value with the related standard deviation values reported as error bars. This result demonstrated that the heat transfer among the different components of the optical engine could be considered negligible.

Pressure measurements give useful and real-time cycle-resolved information on the combustion process. On the other hand they don't allow a local analysis that is necessary for detailing the thermal and fluid dynamic phenomena that occur in the combustion chamber. Optical techniques are powerful tools for this kind of investigation even if they are high-costs methodologies. They need specific engines and instrumentations and often are not user-friendly. In this work, optical techniques based on high spatial resolution and cycle resolved visualization were applied to characterize the combustion process for different injection modes.

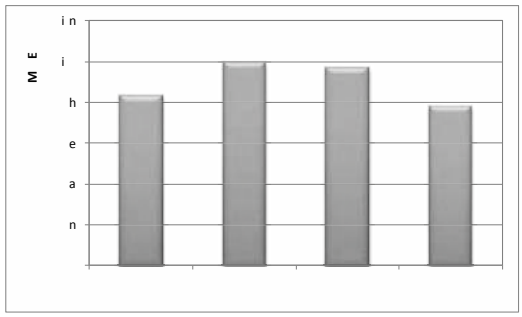

Figure 2. Standard deviation of IMEP measured in the combustion chamber and averaged on 400 consecutive engine cycles.

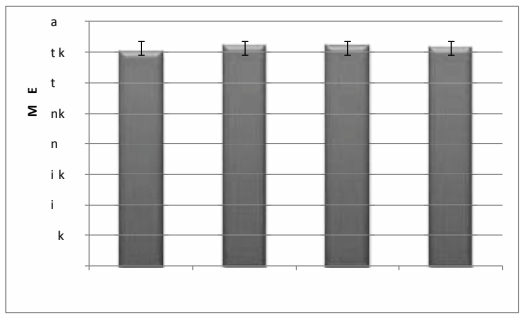

Figure 3. Maximum in-cylinder pressure signal averaged on 400 consecutive cycles. The error bars correspond to the standard deviations.

In a port-fuel-injected (PFI) engine, the fuel is generally injected at the backside of a closed intake valve to take advantage of the warm valve and port surfaces for vaporization. However, a large part of the injected spray is deposited on the intake manifold surfaces and form a layer of liquid film on the valve and port surfaces. The film needs to be re-atomized by the shearing airflow as the intake valves open. If these fuel layers are not well atomized they enter the cylinder as drops and ligaments [8 - 12]. These phenomena occur in varying degrees and depend upon the engine design, injector location and engine operation. Potentially, the fuel can enter the cylinder in a poorly atomized state, leading to increased unburned hydrocarbon emissions. This is particularly true during cold operation, when evaporation is low. In the small engines, such as scooter and small motorcycle engines, the fuel injection occurs in intake manifold smaller than

light-duty vehicle engines, increasing the criticism of fuel-wall interaction. Previous experiments in similar engine conditions demonstrated that the injector sprayed the fuel towards the plate between the intake valves and on the intake valves steams. The droplets impingement induced fuel deposits formation on the intake manifold walls. The fuel deposits were drawn by gravity on the valve head where they remained as film due to the surface tension. At TDC (Top Dead Centre), the intake valves lift is around 1 mm as shown in Figure 1. From this point, part of the droplets was carried directly into the combustion chamber by the gas flow. The droplets sucked in the combustion chamber stuck on the cylinder walls and on the piston surface.

The fuel film around the valves and the fuel droplets on the combustion chamber walls created fuel-rich zones that developed dynamically under the effect of the gas flow influencing the composition of the mixture and hence the combustion process [8, 13].

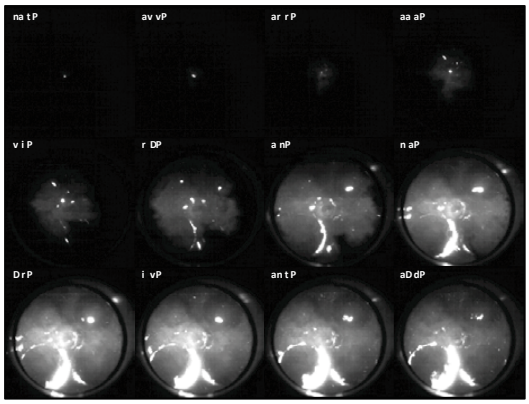

Figure 4. Cycle-resolved flame visualization detected for the CV condition.

To better understand this phenomenon, cycle resolved digital imaging of the combustion process was performed. Figure 4 reports the flame propagation detected in the combustion chamber for the CV condition. The evidence of spark ignition was represented by a luminous arc near the spark plug. It occurred around 21 CAD BTDC (Crank Angle Degrees Before Top Dead Centre) and it persisted until 17 CAD BTDC. At this time the flame kernel was already observable, even if its luminosity was very lower than the spark. Then the flame kernel was well resolvable and it moved from the spark plug towards the cylinder walls. Similar results were observed in the other selected engine conditions, as shown in Figures 5-7.

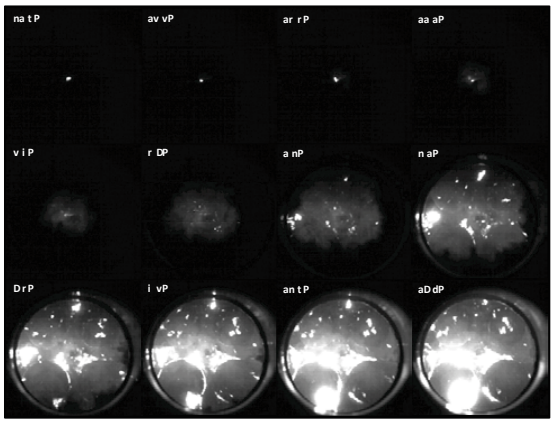

Figure 5. Cycle-resolved flame visualization detected for the CV_OV condition.

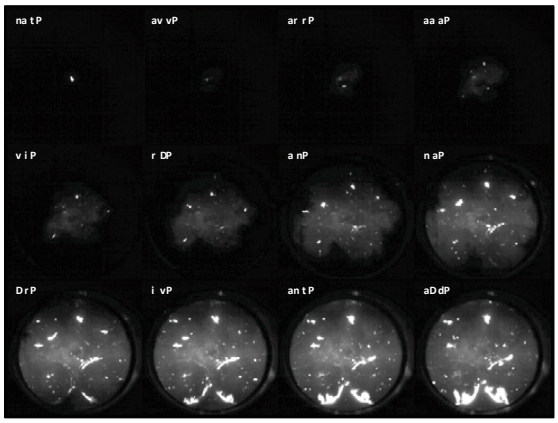

Figure 6. Cycle-resolved flame visualization detected for the OV condition.

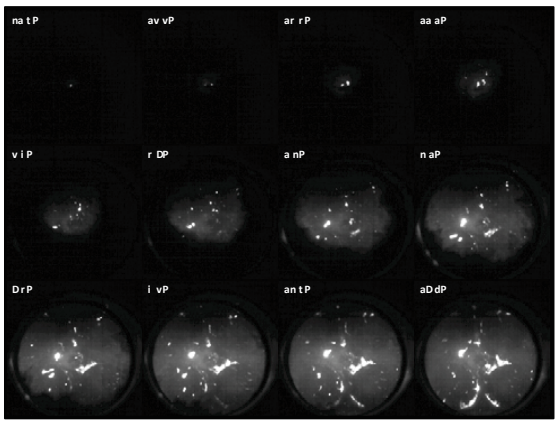

Figure 7. Cycle-resolved flame visualization detected for the DIS condition.

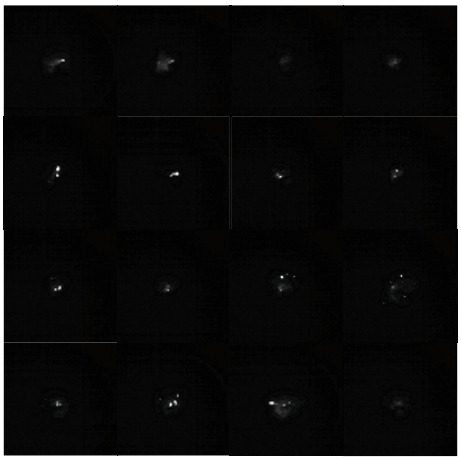

Figure 8. Flame emission detected at 11.1 CAD BTDC for four engine cycles.

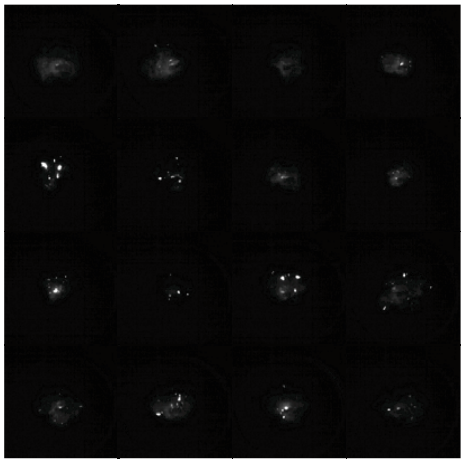

Figure 9. Flame emission detected at 7.8 CAD BTDC for four engine cycles.

In order to calculate the engine cycle variability of flame kernel, combustion images were acquired at the same crank angle for several consecutive cycles for each operating condition. Figures 8 and 9 report flame emission images detected at 11.1 and 7.8 CAD BTDC for four engine cycles. The integral luminosity measured at 7.8 CAD BTDC evaluated on 400 consecutive cycles is shown in Figure 10 together with the related standard deviation, the average deviation and the variance for each tested condition. The highest cycle-to-cycle variation was evaluated in the CV_OV condition; whereas the most stable kernels were the OV and DIS conditions. The kernel variability seems to be correlated to the wrinkling of the flame front outline due to the combustion reaction zone, as it can be observed in Figures 4-7. The negative curvatures in the flame front are due to non-homogeneous local distribution of the fresh mixture in the combustion chamber. This influenced the subsequent evolution of the flame propagation [14, 15]. In fact, around 4 CAD BTDC, the flame front shape showed more evident negative curvature and an asymmetry especially in the CV condition. This result is detailed in Figure 11 where the flame front outlines are evaluated by fixing a threshold according to the metric technique [16]. In the CV conditions, the flame reached first the cylinder walls in the exhaust valves region. This effect was due to the fuel film deposited on the intake valves that created fuel reach zones in the combustion chamber that slowed down the flame propagation.

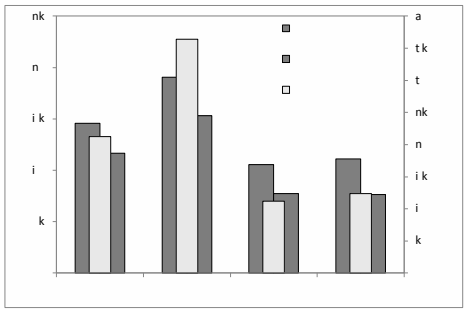

Figure 10. Percentage variation with respect to the mean value of the integral luminosity measured at 7.8 CAD BTDC on 400 consecutive cycles.

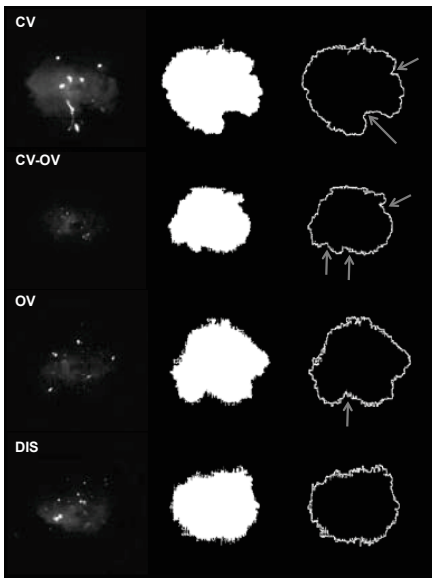

Figure 11. Flame front outlines evaluated at 4.5 CAD BTDC for the selected cycles.

Moreover, as clearly shown in Figures 4-7, several bright spots were detected in the burned gas before the flame front reached the chamber walls. As discussed in previous works [5, 6, 17] the bright spots were due to the fuel deposits on the sapphire window caused by the strip atomization of the fuel squeezing. The fuel deposits created fuel-rich zones with sub-millimeter size that ignited when reached by the normal flame front. When the fuel injection occurred totally or partially in open-valve condition the effect was enhanced by the partial carrying of the injected fuel droplets directly into the combustion chamber due to the gas flow. An amount of the droplets stuck on the cylinder walls and a part was deposited on the piston surface. The fuel injection splitting reduced the number of bright spots if compared to OV condition and their size if compared to the CV_OV condition. This result demonstrated a reduction in fuel droplets impingement on the piston surfaces.

An evident difference in the flame propagation for the tested engine conditions was observed around TDC. In fact, when the flame front reached the intake valves, an abnormal combustion took place and strongly luminous flames outlined the valves. Theses flames persisted well after the normal combustion event.

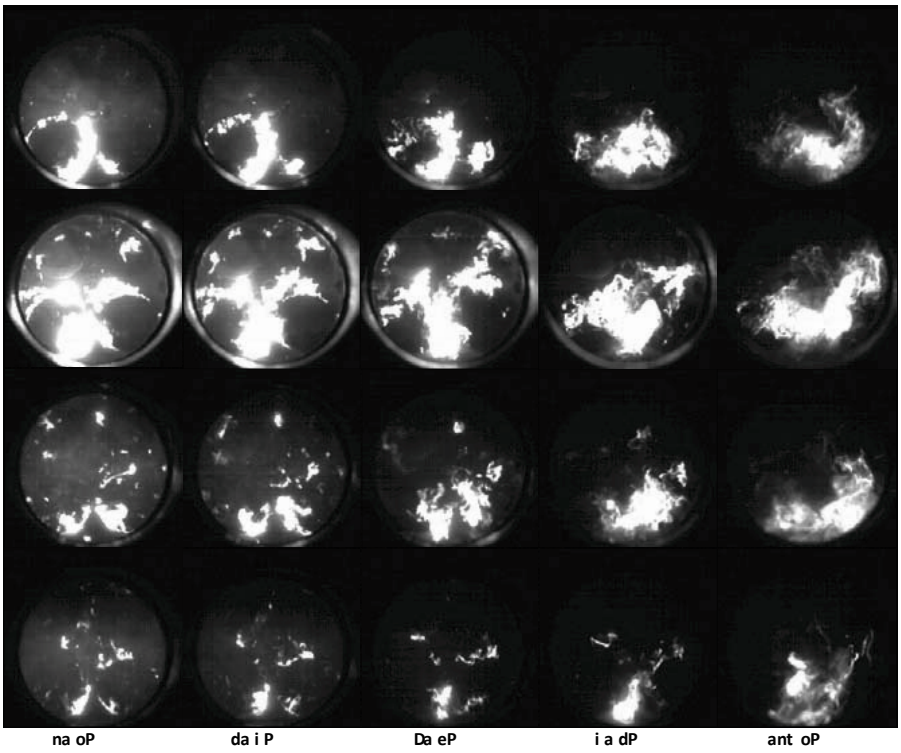

Figure 12. Cycle-resolved flame propagation detected in the late combustion phase.

The effect can be observed in Figure 12 that reports the last phase of the combustion process for the conditions shown in Figures 4-7. The abnormal combustion was correlated to the fuel film amount deposited on the intake valves. The fuel impinged on the intake manifold walls were drawn by gravity on the valve head where they remained as film due to the surface tension. The fuel layers were squeezed and only partially stripped. When the flame approached the intake valve region, the increasing heat exchange between the intake ports and the surrounding gas led to the fuel film evaporation. The residual fuel layers burned creating abnormal flames [18].

The higher fuel amount near the intake valves in the CV and CV_OV conditions induced more fuel-rich zones. When the fuel injection occurred at

open-valve, fuel deposition was reduced, some droplets were sucked in the combustion chamber, then they stuck on the cylinder walls and on the piston surface. During the CV_OV condition, the high level of micro-turbulence near the valve port gap was not able to induce a vaporization stronger than CV condition or a droplet flow towards the chamber as in OV. The droplets number increased because of the simultaneous effects of collision and coalescence. In the double injection strategy (DIS) the duration of interaction between air-flow and fuel droplets increased. The fuel vaporization improved and the fuel layer amount decreased. The reduction in mean droplets size also reduced the fuel deposits on the piston surfaces. The diffusion-controlled flame luminosity in DIS condition was lower than in single injection.

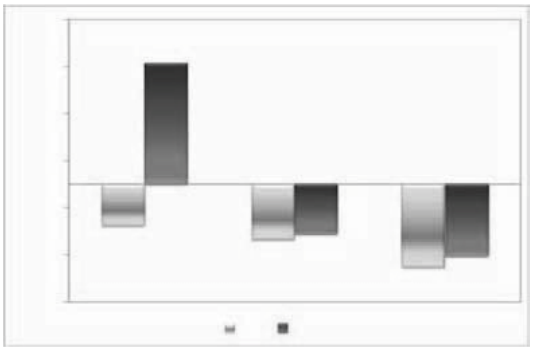

Figure 13. CO_2 and HC percentage variation with respect to CV condition measured at the exhaust averaged on 400 consecutives cycles.

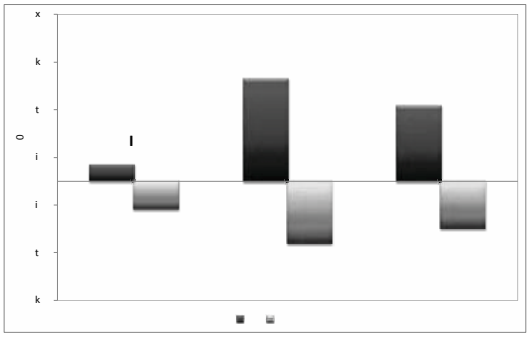

Figure 14. NOx and CO percentage variation with respect to CV condition measured at the exhaust averaged on 400 consecutives cycles.

Previous spectroscopic investigations proved that the abnormal combustion due to fuel film burning was characterized by diffusion-controlled flames. The flame spectra showed a strong continuous contribution that increased with the wavelength in the visible range, typical of carbonaceous structures and soot [19, 20]. Thus the abnormal combustion luminosity was associated with particulate and HC concentration in the combustion chamber. The in-cylinder results agree with exhaust measurements and with literature [8].

As shown in Figure 13, the highest HC level at the exhaust was measured for CV-OV condition while the lowest value was obtained in the double injection condition (DIS). The better fuel-air mixture that occurred in the open valve fuel injection strategy and in particular in the double injection case, reduced the CO_2 concentration. Since the IMEP value was the same for the tested conditions, these results demonstrated a reduction in fuel consumption in DIS case.

The typical trade-off between NO and CO was measured, as reported in Figure 14. NO decreases and CO increases together with the HC decrease for OV and DIS condition. This result can be caused by a reduction in thermal and prompt NO. Prompt NO is formed in the near-burner area by rapid reactions between hydrocarbon radicals and nitrogen that are relatively insensitive to temperature. It is assumed that HCN is formed through the reaction between the hydrocarbon fragment CH_2 and N_2. The product species, as HCN, are subsequently transformed into other species and in particular in CO.

Conclusions

The target of optimizing the small engines for urban cars and two-wheel vehicles needs the detailed knowledge of thermo-fluid dynamic phenomena occurring during the injection and the combustion process. In this work the effect of the fuel injection mode on mixture formation and combustion process was investigated. Cycle resolved visualization was used, it was supported by post-detection image procedures and by in-cylinder and exhaust conventional measurements. Different starts of injection were tested. Moreover a Double Injection Strategy (DIS) was studied and suggested as low-cost solution for the reduction in the wall wetting and fuel film deposits formation. The wall wetting makes a precise control of fuel delivery very difficult. The over-fuelling in port fuel injected gasoline engines is required to compensate for wall wetting and the poor evaporation process especially under cold starting

conditions. Since the diffusive flames used the oxygen not completely consumed after the normal flame front propagation, the exhaust evaluation of oxygen level and the lambda control strategies could be strongly misleading. The interaction between the flame front and the fuel film deposits on the intake valve and on the cylinder surfaces determined the inception of diffusion-controlled flames that persisted after the normal combustion event and caused the formation and emission of soot and unburned hydrocarbons. The fuel injection splitting induced a more homogeneous distribution of fuel-air charge. The effect was a reduction in HC and NOx emission at fixed engine performance. Moreover, CO_2 and fuel consumption reduction were measured.

References

[1] Weinert, J., Ogden, J., Sperling, D., Burke, A., 2008, The future of electric two-wheelers and electric vehicles in China, Energy Policy, 36, pp. 2544– 2555.

[2] Singh, S.K., 2006. Future mobility in India: implications for energy demand and CO2 emission, Transport Policy, 13, pp. 398–412.

[3] Iyer, N.V., Badami, M.G., 2007, Two-wheeled motor vehicle technology in India: Evolution, prospects and issues. Energy Policy, 35, pp. 4319–4331.

[4] Schipper, L., Ng, W.-S., 2007, Urban Transport Options in China: The Challenge to Choose EMBARQ., The WRI Center for Transport and Environment, Washington, DC.

[5] Merola, S.S, Sementa, P, Tornatore, C., Vaglieco, B.M., 2009, Effect of Fuel Injection Strategies on the Combustion Process in a PFI Boosted SI Engine, Int. J. of Automotive Technology, 10(50), pp. 545−553.

[6] Merola, S.S, Sementa, P, Tornatore, C., Carmignani, L., Di Palma, S., 2010, Fuel Injection Effect on In-cylinder Formation and Exhaust Emission of Particulate from a 4-Stroke Engine for 2-Wheel Vehicles, SAE Technical Paper n. 2010-01-0354.

[7] Heywood, J.B., 1988, *Internal Combustion Engine Fundamentals*, New York: McGraw-Hill.

[8] Henein, N.A., Tagomori, M.K., 1999, Cold-start hydrocarbon emissions in port-injected gasoline engines, Progress in Energy and Combustion Science, 25, pp. 563–593.

[9] Behnia, M., Milton, B.E., 2001, Fundamentals of fuel film formation and motion in SI engine induction systems, Energy Conversion and Management, 42(15-17), pp. 1751-1768.

[10] Costanzo, V.S., Heywood, J.B., 2005, Mixture Preparation Mechanisms in a Port Fuel Injected Engine, SAE Technical Paper n. 2005-01-2080.

[11] Gold, M.R., Arcoumanis, C., Whitelaw, J.H., Gaade, J., Wallace, S., 2000, Mixture Preparation Strategies in an Optical Four-Valve Port-Injected Gasoline Engine, Int. J. of Engine Research, 1(1), pp. 41-56.

[12] Nogi, T., Ohyama, Y., Yamauchi, T. and Kuroiwa H., 1988, Mixture Formation of Fuel Injection Systems in Gasoline Engines, SAE Technical Paper n. 880558.

[13] Meyer, R., Heywood, J.B., 1997, Liquid Fuel Transport Mechanisms into the Cylinder of a Firing Port-Injected SI Engine During Start Up, SAE Technical Paper n. 970865.

[14] Bianco, Y., Cheng, W., Heywood, J.B., 1992, The Effects of Initial Flame Kernel conditions on Flame Development in SI Engines, SAE Technical paper n. 912402.

[15] Witze, P., Hall, M., Bennet, M., 1990, Cycle-resolved Measurements of Flame Kernel Growth and Motion Correlated with Combustion Duration, SAE Technical paper n. 900023.

[16] Jain, A.K., 1989, *Fundamentals of Digital Image Processing*. Prentice-Hall.

[17] Merola, S.S. and Vaglieco, B.M., 2008, Optical investigations of fuel deposition burning in ported fuel injection (PFI) spark-ignition (SI) engine, Energy, 34, pp. 2108–2115

[18] Witze, P.O., Green, R.M., 1997, LIF and Flame-Emission Imaging of Liquid Fuel Films and Pool Fires in an SI Engine During a Simulated Cold Start, SAE Technical Paper n. 970866.

[19] Merola, S.S., Sementa, P., Tornatore, C., Vaglieco B.M., 2009, Spectroscopic Investigations and High Resolution Visualization of the Combustion Phenomena in a Boosted PFI SI engine, SAE International Journal of Engines, October 2009, 2(1), pp. 1617-1629.

[20] Merola, S.S., Sementa, P., Tornatore, C., Vaglieco, B.M., Carmignani, L., Di Palma, S., 2009, Optical Characterisation of the Combustion Process in a 4-Stroke Engine for 2-wheel vehicle, SAE Technical Paper n. 2009-24-0055.

Exergoeconomic Comparison between Spark-Ignition Engine and Compression-Ignition Engines with Hydrocarboneted and Renewable Fuels

Hugo L. Moreira[a] *and José J. Santos*[b]

[a] *Federal University of Rio Grande do Norte, Natal-RN, Brazil*
[b] *Federal University of Espírito Santo, Vitória-ES, Brazil*

Abstract: The plentiful of renewable energy in every part of the world, has created an expectation for rich and poor countries and especially for Brazil, because – as a developing nation – it must utilize its huge geographic and hydrographic potential in order to use this energetic alternative resource. The present work establishes an exergoeconomic comparison between internal combustion engines using ethylic alcohol and octane for Otto cycle engines,biodiesel and dodecane for Diesel cycle engines with power rating from 50 to 500 kW. A numeric simulation was implemented to calculate the thermodynamic and exergoeconomic parameters, considering the complete combustion with air-theoretical. The exergoeconomic analysis was based on the fuel-product methodology, which uses complementary equations necessary to calculate the exergetic cost of each flow. The expected results were very significant, because, despite of being a theoretical simulation it has used monetary values currently practiced by the market for the equipment and fuel price.

Keywords: Exergoeconomic, Thermoeconomic, Exergy, Internal Combustion Engine.

1. Introduction

Nowadays in Brazil, 60% of the generated energy comes from renewable sources, while other countries intend to reach 12% of them around 2010. Currently, 85% of the world energy is from fossil origin and 80% of this energy has their usage concentrated in about 10 countries. The expectation of Brazil being consolidated as the world main supplier of renewable fuel with high energetic content, becomes practicable thanks to its continental dimension placed in a tropical area, and for its plentiful hydro resources (22 to 24% of the whole sweet water of the planet), as well as its huge unoccupied areas.

In this scenery, biodiesel appears as an alternative to reduce the petroleum-derived fuel dependency as long as a new market for the oily-derived fuel, with the expectation to reduce pollution discharge. The introduction of biodiesel in the fuel market will represent a new dynamic for agroindustry, with its consequent multiplying effects in other segments of economy, involving vegetable oil, alcohol and diesel oil along with the resources and by-products of the ester vegetable production.

The PROBIODIESEL, is a program that comprehends integrated actions, in researching network, for the development of production technology and usage of biocombustion mixture, which aims the evaluation of its practicability and its technical, social-environmental and economic competitively for the Brazilian market and future exportation, along with its production and special distribution among the different regions of the country. It also involves researching actions and technological development, including field tests, in vegetable/diesel-oil addition, as well as specific technology that may implement the social-economic development of rural community settings by electricity and fuel production.

The competitively for ethanol national production in different regions of Brazil, the PROALCOOL program, the inner-structure for production and distribution already existing, the experience acquired and the performance of the technology developed for the productive chain of sugar cane, the automotive sector, the opportunity to substitute imported diesel oil and contribute for money saving, job and income generation, these are all synergy elements for the national biodiesel production.The PROALCOOL program had as a primary motivation, in its original conception, solve the discharge balance problem, due to the vertiginous uprising prices for diesel oil import.

Corresponding Author: Hugo L. Moreira, Email: hugolimabr@yahoo.com.br

The exergoeconomic (or thermoeconomic) methodology was created in order to support a thermal and economical analysis for thermal systems. These analysis aims to ratify the technical and economical viability of equipments and industrial plants, which have always produced reliable results. This new approach, also based on conservation concepts, enlarge the energetic analysis including the use of the Second Law and concepts of irreversibility and exergy.

2. Methodology

The exergoeconomic analysis have as a meaning objective, among others, determine the exergetics and monetary costs of all system components; allowing the knowledge and the comprehension of the forming process of these costs; promoting the optimization not only of the specific variables of each system component, but of the whole system.

This detailed analysis was obtained with the contribution of the Thermodynamics Second Law in conjunction with exergetic analysis, in which, according to [1], it would permit a better measurement to evaluate the magnitude of lost energy in relation to the amount of supplied energy under the form of energetic resource; it would also permit a better measurement of quality or loss from a thermodynamic point of view, thus becoming a good variable to define the reasonable efficiency for the energetic system.

2.1. Exergoeconomic Analysis

In [2], the author had synthesized this analysis based on the *Fuel – Product* concept, proposing a systemic approach in each component, with the purpose to generate auxiliary equations needed to calculate the exergetic costs of each flow. He had called this methodology of Exergoeconomic Analysis, which comprehends the following steps:

- Make an exergetic balance in each system component;
- Make an economic analysis of the subsystems;
- Obtain the costs balance of exergy flows in each component; and
- Calculate the parameters that would permit the analysis of the processes associated to each component.

The economic rating of the thermodynamic flows that perform one cycle, will be set up for the operational conditions later defined, always focusing the utilization of the available exergy from burning process of octane (C_8H_{18}), ethylic alcohol (C_2H_6O) for spark ignition engines, biodiesel ($C_{17}H_{33}CO_2CH_3$) and dodecane ($C_{12}H_{26}$) for Diesel cycle engine. The exergoeconomic method combines the exergetic and economic analysis, and was applied to Otto and Diesel Standard Cycles to reveal which one is thermoeconomically more efficient.

2.2. Exergetic Cost

The exergy balance gives the destruction value of exergy in each component of the system and this destruction is equal to the difference between incoming and out-coming exergy from the volume control. This happens because, in a real process, there will be always destruction and loss resulting in a bigger exergy in the entrance of the process, in relation to the product exergy. The exergetic cost of a product is therefore composed by the resources exergy, the external loss exergy and the irreversibility. As well shown in Fig. 1, the exergetic cost of the product will always be bigger than the resource.

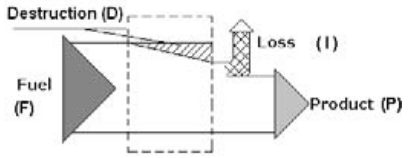

Fig. 1. Fuel (F), Product (P), Destruction (D) and Loss (I)

The exergetic balance in each component can be expressed as:

$$B_P = B_F - I - B_D \tag{1}$$

Starting from the concept of exergetic or reasonable efficiency, that is the relation between the product exergetic variation and the resource exergetic variation needed to the process, we can define the unitary exergetic cost as being the inverse relation, such as:

$$k = \frac{Exergy\ of\ \mathrm{Re}source}{Exergy\ of\ \mathrm{Pr}oduct} = \frac{B_{resource}}{B_{product}} = \\ = 1 + \frac{Loss(I) + Destruction(D)}{\mathrm{Pr}oduct(P)} = \frac{\mathsf{B}_\mathsf{i}^*}{\mathsf{B}_\mathsf{i}} \tag{2}$$

Where $\boldsymbol{k}$ is the unitary exergetic cost, B_i^* is the exergy expressed in (kW) necessary to conceive the desired product, and B_i is the minimum quantity of exergy expressed in (kW)

corresponding to the ideal process for the conception of the product. Obviously, ***k*** will be greater than or equal to the unity, and in an externally reversible process this factor will become equal to one.

In [3], the authors have formulated an endowment proceeding of exergetic costs, based only in thermodynamics precepts, such as:

- The exergetic cost of a flow (B^*), resource (F*), or product (P^*) is the real quantity of exergy needed to produce it;
- A detailed analysis of the global nature of the process and of the function of each subsystem in progressive formation of the final products, is the only requirement needed to solve the endowment problem of exergetic costs;
- The exergetic costs in the entrance of an equipment or component of the system should be rated with the flow that outcome from it.

Based on these postulates, a collection of proposition has been created and the systematic application on the equipments will permit us value the exergetic costs of the flows. These propositions will be set up in a general way, and afterwards will be applied in the systems to be considered.

- Proposition 1 – The exergetic cost is a conservative property:

$$\sum_{entrance} B_i^* - \sum_{exit} B_j^* = 0 \qquad (3)$$

- Proposition 2 – for a system or control of volume with more than one energetic resource, the outflows unitary exergetic costs must be equal to the inflows ones (resource rules). For a general system example as shown on Fig. 2, we have:

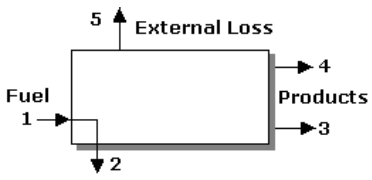

Fig. 2. General System Example

$$\frac{B_1^*}{B_1} = \frac{B_2^*}{B_2} \qquad (4)$$

- Proposition 3 – if a system has a product formed by various flows, the exergetic cost will be the same for each one of them (product rule). In the Fig. 2 example we have:

$$\frac{B_3^*}{B_3} = \frac{B_4^*}{B_4} \qquad (5)$$

- Proposition 4 – in the absence of value of an external loss flow, we shall admit a null exergetic cost. In this example we have:

$$\frac{B_5^*}{B_5} = 0 \qquad (6)$$

- Proposition 5 – in the absence of external value, the exergetic cost of the inflows in the system is equal to its exergy. In this example we have:

$$B_1^* = B_1 \qquad (7)$$

3. Energetic and Exergoeconomic Formulation of Engines

3.1. Energetic Analysis of Internal Combustion Engines

The energetic analysis of internal combustion engines involve chemical reaction, which include hydro-carbonated fuel combustion, and since we are mentioning a power generator device, the thermodynamic analysis of reagent systems are basically an extension of Thermodynamic First and Second Laws. Schematically, a surface of control involving our objective of study is shown on Fig. 3, characterizing the air and fuel inflows, and the outflows of exhaustion gases, heat and – mainly – work.

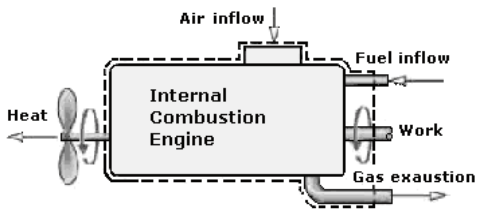

Fig. 3. Surface of control involving an internal combustion engine

During the combustion process, the mass of each element remains the same. This way, describing a chemical reaction basically implies on mass conservation of each composing element of the fuel and the oxidant. This way, we should consider the octane combustion with quantity of air theoretical, which is the minimum amount of air

needed to supply enough oxygen for a complete combustion of all carbon and hydrogen, as (8), Where *a, b, c* and *d* represent the number of moles of oxygen, dioxide of carbon, water and nitrogen respectively. In the first member we consider that 3,76 moles of nitrogen join each mole of oxygen. Applying the principle of mass conservation to carbon, hydrogen, oxygen and nitrogen respectively, we can obtain a system of four equations and four unknown members. Solving this system, the balanced chemical equation becomes as (8a).

In the same way, for the ethylic alcohol, dodecane and biodiesel combustion respectively, we should have (9), (10) and (11).

The energetic balance for reagent systems in permanent regime can be evaluated admitting the hypothesis that air-fuel combination and combustion products can be considered ideal gases, besides ignoring the effects of kinetic and potential energy, as shown in (12).

$$C_8H_{18} + a\,(O_2 + 3{,}76\,N) \longrightarrow b\,CO_2 + c\,H_2O + d\,N_2 \quad (8)$$

$$C_8H_{18} + 12{,}5(O_2 + 3{,}76\,N) \longrightarrow 8\,CO_2 + 9\,H_2O + 47\,N_2 \quad (8a)$$

$$C_2H_6O + 3(O_2 + 3{,}76\,N_2) \longrightarrow 2CO_2 + 3H_2O + 11{,}28N_2 \quad (9)$$

$$C_{12}H_{26} + 18{,}5(O_2 + 3{,}76N) \longrightarrow 12\,C\,O_2 + 13\,H_2O + 69{,}56\,N_2 \quad (10)$$

$$C_{17}H_{33}CO_2CH_3 + 27\,(O_2 + 3{,}76N_2) \longrightarrow 19CO_2 + 18H_2O + 101{,}52N_2 \quad (11)$$

$$\frac{\dot{Q}_{vc}}{\dot{n}_{vc}} - \frac{\dot{W}_{vc}}{\dot{n}_{vc}} = \sum_P n_s(\bar{h}^o_f + \Delta\bar{h})_s - \sum_R n_e(\bar{h}^o_f + \Delta\bar{h})_e \quad (12)$$

With these conceptions, the balance of mass and energy for a volume of control with various inflows and outflows becomes evident by (12), where $\dot{Q}_{vc}$ and $\dot{W}_{vc}$ are respectively the heat flow and the work flow (power) getting out of the volume of control; $\dot{n}_{vc}$ represents the molar fuel flow; the coefficient $\boldsymbol{n_s}$ e $\boldsymbol{n_e}$ correspond to the respective coefficient from (8.a) to (11) of the respective reaction, supplying the reagent moles and the products per mole of fuel; $\bar{h}^o_f$ is the enthalpy of formation of products and reagent and $\Delta\bar{h}$ symbolizes the difference of molar enthalpy of reagents and products in the inflow and outflow of the volume of control.

The fuel consumption denoted by $\dot{m}_f$ is well defined as the relation between the fuel masses outflow and its time unit. The mostly used parameter to relate the fuel flow to the power *(Pot)* is the fuel specific consumption (*sfc*) given by (13). For spark-ignition combustion engines, the fuel specific consumption according to [4] assumes values of 75 μg/J = 270 g/kWh. For compression-ignition engines this parameter assumes values of 55 μg/J = 200 g/kWh.

$$sfc = \frac{\dot{m}_f}{Pot} \quad (13)$$

For diesel engine using biodiesel, assuming a 40% efficiency with biodiesel having 36000 kJ/kg of heating power, the fuel specific consumption results in 250 g/kWh. In [5], the authors determined that *sfc* with a function of the engine speed, is higher in biodiesel than in diesel oil. Bench-test results previously reported showed that the average value of *sfc* for biodiesel is 17% greater that that of diesel oil.

3.2. Exergetic Analysis of Internal Combustion Engines

Exergy can be defined as the greater theoretical job possible to be obtained in relation to the state of reference to a temperature T_o and pressure P_o. The system exergy can be obtained by:

$$B = (E - U_o) + P_o(V - V_o) - T_o(S - S_o) \quad (14)$$

Where ***E*** (the sum of internal energy, potential and kinetic), ***V*** and ***S*** denote the energy, the volume and the system entropy respectively, while $\mathbf{U_o}$, $\boldsymbol{V_o}$,

and S_o are values of the same properties if the system were in the state of reference. There are several ways to calculate the exergy with a system of equation that must be specifically chosen for each case. We have, for example, the exergy due to the heat exchange that is defined by:

$$B_{heat} = \left(1 - \frac{T_o}{T}\right).\dot{Q}_{vc} \quad (15)$$

The chemical exergy is defined according to the type of process and chemical reactions of each process. In this case, the chemical exergy of the fuel in liquid form has been defined according to [6] by the product of coefficient β and the lower heat power, as follows:

$$B_{ch} = \beta.PCI \quad (16)$$

For hydro-carbonated liquid fuel, the coefficient β can be determined by (17):

$$\beta = 1{,}0506 + 0{,}0144.\frac{H}{C} \quad (17)$$

where H/C is the atomic relation between its elements. For liquid fuel since ethylic alcohol and biodiesel, the coefficient β can be determined by (18):

$$\beta = 1{,}0401 + 0{,}1728.\frac{Z_{H2}}{Z_C} + 0{,}0432.\frac{Z_{O2}}{Z_C} \quad (18)$$

where Z_{H2}/Z_C and Z_{O2}/Z_C is the mass fractions between its elements of the fuel.

In [7], the authors suggested for the calculation of chemical exergy of combustion gases of a hydro-carbonate type of C_mH_n an equation given in terms of Gibbs Function of the respective substance products of combustion, as follows:

$$B_{ch} = \begin{bmatrix} \bar{g}_{fuel} + \left(m + \frac{n}{4}\right).\bar{g}_{O_2} \\ -m.\bar{g}_{CO_2} - \frac{n}{2}.\bar{g}_{H_2O(gás)} \end{bmatrix}(T_O, P_O) + \\ + \bar{R}.T_O.\ln\left[\frac{(y_{O_2})^{m+n/4}}{(y_{CO_2})^m.(y_{H_2O})^{n/2}}\right] \quad (19)$$

where $\bar{g}_{fuel}$, $\bar{g}_{O_2}$, $\bar{g}_{CO_2}$ and $\bar{g}_{H_2O}$ are Gibbs functions for fuel, oxygen, dioxide of carbon and water steam, respectively. In the same way y_{O_2}, y_{CO_2}, y_{H_2O} are molar fractions of oxygen, dioxide of carbon and water steam, respectively.

Defined the equations to determine the exergy of each flow, we started from (3) and taking Fig. 3 as volume of control we can establish the exergetic balance for the internal combustion engine and apply particular equations to the case in study, obtained this way for the exergetic cost (B*) the following equation:

$$B^*_{fuel} + B^*_{air} - B^*_{power} - B^*_{heat} - B^*_{gases} = 0 \quad (20)$$

With the support of the complementary equations, previously defined by the propositions of cost endowment, we can establish a system of equations in order to define the exergetic cost for each flow. From the proposition 3 (products rule) we can assert that the unitary cost of heat is equal to the unitary cost of power, or:

$$\frac{B^*_{heat}}{B_{heat}} = \frac{B^*_{power}}{B_{power}} \quad (21)$$

From proposition 4 we can attribute a null exergetic cost for the gas exhaustion flow and for the air flow:

$$\frac{B^*_{gases}}{B_{gases}} = \frac{B^*_{air}}{B_{air}} = 0 \quad (22)$$

From proposition 5 we can attribute exergetic cost equal to exergy itself of the fuel:

$$B^*_{fuel} = B_{fuel} \quad (23)$$

3.3. Analysis of Monetary Parameters

The methodology to value the monetary costs is an application of a cost balance to a subsystem or equipment as shown on Fig. 4.

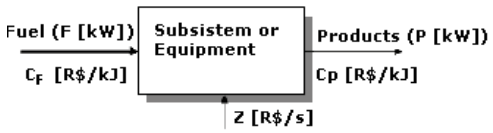

Fig. 4. Balance of Monetary Cost

The balance shown on Fig. 4 can be mathematically represented as follows:

$$C_P.B_P = C_F.B_F + Z \quad (24)$$

Where C_F and C_p represent the costs in monetary unit per exergy unit for the resource and the product respectively; in the same way B_f and B_p represent the amount of exergy for the resource and the product, and Z is the invested capital. In the particular case of a plant in operation and

already paid, we can take Z as a null value, although that's not the case, because the capital invested in each internal combustion engine is an important economic parameter for comparison. To determine Z, we shall consider:

$$Z_{(i)} = \frac{3600 * (A/P)}{t_{op}} * F_i \quad (25)$$

Where t_{op} represents the useful time life (in seconds); F_i represents the investment for each equipment or subsystem; (A/P) represents the capital recovering factor and will be calculated by (26), considering I the interest rate (varying from zero to 1); and N represents the reimbursement period (in years).

$$\left(\frac{A}{P}\right) = \frac{I*(1+I)^N}{(1+I)^N - 1} \quad (26)$$

4. Results and Discussions

These results were obtained from the numeric simulation in EES educational platform, attempting to the thermodynamic modeling established on the third section, where the parameters of entrance were established for power rating from 50 to 500 kW.Other parameters of entrance were obtained from literature as shown on Table 1; the monetary values of the equipment (diesel and gasoline engines) and the fuel were researched and obtained from values currently practiced by market.

The Table 2 and Table 3 summarize the thermodynamic properties at various points at the power operating conditions. The exergy analysis of the system and its components are carried out using fuel-product relationships and (14) – (19).

Table 1. Entrance Data for Numeric Simulation

Entrance Parameter	Otto Engine	Diesel Engine
Power [kW]	50 to 500	50 to 500
Air Temperature [K]	298	298
Fuel Temperature [K]	298	298
Exhaustion Gas Temperature [K]	1800	1800
Fuel specific consumption [kg/kWs]	0.000075	0.000055
Initial Investment [R$]	45.000,00	60.000,00
Hydro-carbonate Fuel Price [R$/m^3]	2.500,00	1.750,00
Renewable Fuel Price [R$/m^3]	900,00	1000,00
Useful Life Time - (10 years) [s]	315360000	315360000

Table 2. Thermodynamic Properties (Exergy and Exergetic Cost) at Octane and Dodecane Fuel

Power [kW]	$B_{inC8H18}$ [kW]	$B_{inC12H26}$ [kW]	$B_{outC8H18}$ [kW]	$B_{outC12H26}$ [kW]	$B_{heatC8H18}$ [kW]	$B_{heatC12H26}$ [kW]	$B^*_{heatC8H18}$ [kW]	$B^*_{heatC12H26}$ [kW]
50	178,8	130	2841	1930	0,6242	0,2695	2,204	0,697
100	266,6	193,9	4237	2878	1,294	0,5125	3,405	0,9886
150	399,9	290,8	6355	4317	2,911	1,153	7,613	2,219
200	533,2	387,8	8473	5757	5,175	2,05	13,45	3,934
250	666,5	484,7	10592	7196	8,086	3,203	20,88	6,132
300	799,8	581,6	12710	8635	11,64	4,613	29,88	8,807
350	933,1	678,6	14828	10074	15,85	6,278	40,42	11,96
400	1066	775,5	16947	11513	20,7	8,2	52,47	15,58
450	1200	872,5	19065	12952	26,2	10,38	66	19,67
500	1333	969,4	21183	14391	32,35	12,81	80,99	24,22

The Table 4 and Table 5 shows results obtained from the exergoeconomic analysis of the system for hydro-carbonate and renewable fuels at engine correspondent. The exergoeconomic analysis of the system and its components are carried out using fuel-product relationships and (20) – (26).

Table 3. Thermodynamic Properties (Exergy and Exergetic Cost) at Ethylic Alcohol and Biodiesel Fuel

Power [kW]	$B_{inC2H6O}$ [kW]	$B_{inBiodiesel}$ [kW]	$B_{outC2H6O}$ [kW]	$B_{outBiodiesel}$ [kW]	$B_{heatC2H6O}$ [kW]	$B_{heatBiodiesel}$ [kW]	$B^*_{heatC2H6O}$ [kW]	$B^*_{heatBiodiesel}$ [kW]
50	83,34	94,88	86,65	81,37	0,2418	0,1825	0,2418	0,1825
100	166,7	189,8	173,3	162,7	0,9645	0,7286	0,9645	0,7286
150	250	284,6	259,9	244,1	2,164	1,636	2,164	1,636
200	333,4	379,5	346,6	325,5	3,836	2,903	3,836	2,903
250	416,7	474,4	433,2	406,9	5,976	4,528	5,976	4,528
300	500,1	569,3	519,9	488,2	8,582	6,507	8,582	6,507
350	583,4	664,2	606,5	569,6	11,65	8,84	11,65	8,84
400	666,7	759	693,2	651	15,17	11,52	15,17	11,52
450	750,1	853,9	779,8	732,4	19,14	14,56	19,14	14,56
500	833,4	948,8	866,5	813,7	23,57	17,94	23,57	17,94

Table 4. Results of Exergoeconomic Analysis for Operating Conditions with Hydro-Carbonated Fuel

Power [kW]	$B^*_{powerC8H18}$ [kW]	$B^*_{powerC12H26}$ [kW]	$C_{Fuel\text{-}C8H18}$ [R$/kJ]x$10^6$	$C_{Fuel\text{-}C12H26}$ [R$/kJ]x$10^6$	$C_{powerC8H18}$ [R$/kJ]	$C_{powerC12H26}$ [R$/kJ]	$Pr_{powerC8H18}$ [R$/s]	$Pr_{powerC12H26}$ [R$/s]
50	176,6	129,3	52,45	37,02	0,00843	0,01109	0,4215	0,5543
100	263,2	192,9	52,45	37,02	0,004261	0,005567	0,843	1,109
150	392,3	288,6	52,45	37,02	0,002887	0,003735	1,264	1,663
200	519,7	383,8	52,45	37,02	0,0022	0,002819	1,686	2,217
250	645,6	478,6	52,45	37,02	0,001788	0,00227	2,107	2,771
300	769,9	572,8	52,45	37,02	0,001514	0,001903	2,529	3,326
350	892,7	666,6	52,45	37,02	0,001317	0,001642	2,95	3,88
400	1014	759,9	52,45	37,02	0,00117	0,001445	3,372	4,434
450	1134	852,8	52,45	37,02	0,001056	0,001293	3,793	4,989
500	1252	945,2	52,45	37,02	0,000964	0,001171	4,215	5,543

Table 5. Results of Exergoeconomic Analysis for Operating Conditions by Renewable Fuel

Power [kW]	$B^*_{powerC2H6O}$ [kW]	$B^*_{powerBiodiesel}$ [kW]	$C_{Fuel\text{-}C2H6O}$ [R$/kJ]x$10^6$	$C_{Fuel\text{-}Biodiesel}$ [R$/kJ]x$10^6$	$C_{powerC2H6O}$ [R$/kJ]	$C_{powerBiodiesel}$ [R$/kJ]	$Pr_{powerC2H6O}$ [R$/s]	$Pr_{powerBiodiesel}$ [R$/s]
50	83,1	94,7	37,75	28,86	0,004184	0,00555	0,2092	0,2775
100	165,7	189	37,75	28,86	0,002123	0,002802	0,4184	0,555
150	247,9	283	37,75	28,86	0,001437	0,001886	0,6276	0,8324
200	329,5	376,6	37,75	28,86	0,001093	0,001428	0,8368	1,11
250	410,7	469,9	37,75	28,86	0,0008871	0,001154	1,046	1,387
300	491,5	562,8	37,75	28,86	0,0007498	0,0009706	1,255	1,665
350	571,8	655,3	37,75	28,86	0,0006517	0,0008397	1,464	1,942
400	651,6	747,5	37,75	28,86	0,0005781	0,0007416	1,674	2,22
450	730,9	839,4	37,75	28,86	0,0005208	0,0006653	1,883	2,497
500	809,9	930,9	37,75	28,86	0,000475	0,0006042	2,092	2,775

The entrance exergy in the volume of control of each fuel is obtained from (16). The fuel mass flow will always be a function of power and specific consumption as well defined by (12). Figure 5 shows that the exergy of each fuel is a linear function of the power. The exergy produced by the heat demonstrated in (15) associated to the solution demonstrated in (12) gives us the amount of exergy produced by heat. The exergoeconomic parameters were compared, based on the exergetic costs (B_i^*) of the fuel as shown in Fig. 6.

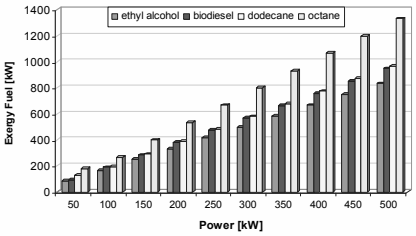

Figure 5. Fuel Exergy in function of the Power

The monetary cost per energy is obtained from the cost balance shown in Fig. 4, once the resource is equal to the fuel and the product is equal to the power, as already defined by (22). Figure 7 demonstrates that diesel engines are more expensive than gasoline ones, although this cost tends to decrease with the raise of the power.

The monetary cost per time unit is obtained dividing the energy monetary cost by the power itself. Figure 8 demonstrates that diesel engines revealed more expensive performances.

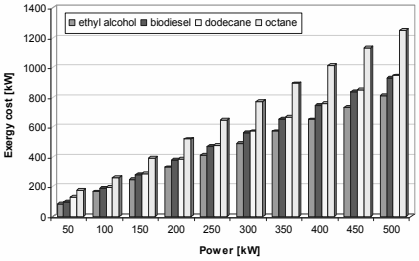

Fig. 6. Exergetic Cost of Fuel in function of the Power

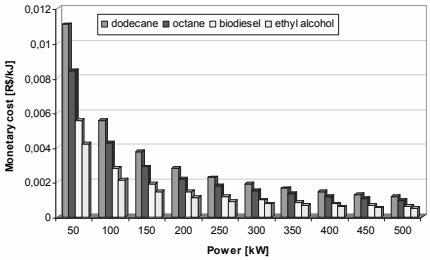

Fig. 7. Monetary Cost of the Power

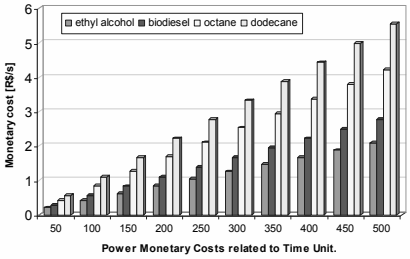

Fig. 8. Power Monetary Costs related to Time Unit

5. Conclusion

The simulation has demonstrated that, although renewable fuels engines have revealed a higher thermal performance than hydro-carbonated engines, the flows of exergetic and monetary costs of the power in hydro-carbonated engines are more expensive than in bio-fuel ones; this is due to the fact that ethanol exergy is greater and initial capital of investment – in Otto engines – is lower than in Diesel engines.

References

[1] Tsatsaronis, G., 1993, Thermoeconomic Analysis and Optimization of Energy Systems, Energy Combust, Vol. 19, pp. 227-257.

[2] Tsatsaronis, G., 1994, Invite Papers on Exergoeconomic, Energy Special Issue, Vol. 19, nº 3.

[3] Valero, A., et al., 1986, General Theory of Exergy Saving, *ASME WAM*, *AES*, Vol. 2-3, pp. 1-21.

[4] Heywood, J.B., 1988, *Internal Combustion Engine Fundamentals*, Ed. McGraw-Hill Book Company, São Paulo, Brazil, 930p.

[5] Carraretto, C., et al., 2004, Biodiesel as alternative fuel: Experimental analysis and energetic evaluation, Energy, Article in press.

[6] Szargut, J., et al., 1988, *Exergy Analysis of Thermal, Chemical, and Metallurgical Processes*, Hemisphere Publishing Corporation, New York, U.S.A., 330p.

[7] Moran, M. J., and Shapiro, H. N., 2004, *Fundamentals of Engineering Thermodynamics*, 5th ed, John Wiley & Sons, New York.

Experimental comparison of the brake performance of a spark ignition engine fuelled with gasoline and LPG

Massimo Masi[a]

[a] *Department of Mechanical Engineering, University of Padova, Italy*

Abstract: The use of LPG as alternative fuel to gasoline is common practice in spark ignition internal combustion engines. In the past, the main reason for the use of LPG as fuel was merely due to the lower cost for the final user in comparison with gasoline. However, there are theoretical reasons to consider LPG as a very attractive fuel for internal combustion engines. Nowadays, there is a continuously increasing stock production of dual-fuel (gasoline-LPG) passenger car models. Despite of that, doubts about the real performance worsening in LPG operation still exist. The paper deals with the theoretical advantages of using LPG as fuel for spark ignition internal combustion engines. Brake performance derived from experimental analyses at the test bed of a passenger car engine fed either with gasoline and LPG are analysed and compared. The engine designed to operate with gasoline has been equipped with one of the more recent standard kit for the dual-fuel engine operation. The performance decrease in LPG operation are discussed both in steady state and transient condition.

Keywords: LPG, dual-fuel SI engine, gaseous LPG injection, LPG ICEs performance.

1. Introduction

Liquefied petroleum gas (LPG) is a mixture of hydrocarbons, mostly propane (C_3H_8) and butane (C_4H_{10}) isomers. The composition of LPG depends on its final use and varies greatly according to seasons, countries, properties of the supply crude oil/gas used and refining processes. Today's European LPG is a by-product derived almost equally from natural gas (NG) extraction (55%) and petroleum refineries (45%). The commercially available LPG for the automotive market has to comply with a standard [1] that does not define compositions, but limits fuel properties only. As a rule of thumb, countries having relatively cold climates tend to use a higher propane percentage, while warmer countries mostly use butane (see Table 1).

Although the LPG derived from refineries contains a very small sulphur amount, LPG (with NG) is considered as the most ecological fossil fuel because it has a low carbon-hydrogen ratio, high purity, no toxicity, no corrosive activity, and does not contain aromatic hydrocarbons. Many studies attest that the emissions from LPG powered vehicles are lower than those from the gasoline fuelled equivalents. Besides the obvious reduction in carbon dioxide (CO_2) emission, Snelgrove at al. [2] report lower emissions of hydrocarbons (HC, -40%) and of carbon monoxide (CO, -60%) over the European Test Cycle at 25°C. The emissions of nitrogen oxides (NO_x) from LPG fuels measured by Newkirk et al. [3] are lower than those from gasoline.

The advantages of LPG fuelling in burn rate, lean mixture limit, anti-knock performance and pollutants emission have been studied by Campbell et al. [4]. They present the results of an experimental campaign carried out on a 1.4 litre four cylinder four stroke spark ignition engine modified to run with one cylinder fed with gaseous LPG. Moreover the authors clearly explain the basic design of a common LPG conversion system for gaseous fuel operation: an heavy gauge steel tank equipped with a pressure relief valve and a safety fill stop device stores the saturated liquid LPG in equilibrium with its vapour.

Table 1. LPG composition as automotive fuel in Europe (source Urban 1982).

Country	Propane- Butane (% by volume)
Belgium	50 – 50
Denmark	50 – 50
France	35 – 65
Greece	20 – 80
Ireland	100 – 0
Italy	25 – 75
Netherlands	50 – 50
Spain	30 – 70
Sweden	95 – 5
United Kingdom	100 – 0
Germany	90 – 10

LPG at very low quality flows through the non-return valve of an evaporating device, driven by LPG vapour pressure itself, and completes the phase change. In this process, superheating is preferably restrained to the minimum extent and the minimum pressure value required for a satisfactory operation of the delivery system must be guarantee. Finally, a gaseous LPG–air mixing device provides the reactant mixture to cylinder intake. The performance of a recent OEM evaporator-pressure reducer device is studied by Price et al. [5] both theoretically and experimentally.

The early generation LPG mixers, conventional Venturi-controlled devices similar to gasoline carburettors, has been surpassed by gas electro-injectors actuated by an ECU sensing the feedback of the exhaust oxygen probe.

The up-to-date commercially available LPG feeding systems (OEM and aftermarket gaseous LPG injection systems) are the so-called "third generation" systems. These systems perform a gaseous LPG sequential multi-point port fuel injection managed by a "slave" ECU, which is in turn controlled by the main gasoline ECU. The opening time pulses of the gasoline injectors generated by the main gasoline ECU are acquired by the LPG ECU, which multiplies them by a factor that accounts for the different duty cycle of the LPG injectors. Corradini and Togninelli [6] report the details of different techniques and strategies to operate gaseous LPG delivery systems. Moreover, they describe how the need of two ECUs can be avoided by introducing a pressure regulation device on the injectors rail in order to tune gas pressure to the value which makes the injectors duty cycle of gasoline and gas equal.

During the last ten years more and more researchers have investigated liquid LPG injection by means of both numerical calculations and experimental tests (see, e.g., Watson and Phuong [7]). Boretti and Watson [8] have recently presented a computer model for the analysis of LPG fuelled, and compressed natural gas (CNG) fuelled, direct injection engines. They consider both the homogeneous stoichiometric spark ignited and the jet controlled lean stratified jet ignited concepts. In spite of the advantages, they find that the major challenge is the development of adequate LPG injectors. Cipollone and Villante [9] consider liquid-phase injection as one of the most important aspects of LPG fuelled SI engines and use a 1-D mathematical model to study the transient phenomena occurring in a LPG injection system, focusing the attention on the air-fuel ratio and liquid-phase control.

Lee et al. [10] have analysed the penetration and evaporation characteristics of LPG sprays using the Schlieren and Laser Induced Fluorescence (LIF) methods. Combustion has been visually examined and numerical calculations have been performed using KIVA-3 to simulate various spray and combustion conditions.

The great interest about liquid injection, the continuously increasing stock production of dual-fuel (gasoline-LPG) passenger car models equipped with gaseous LPG delivery systems, and the commercial publications claiming that gasoline and LPG have almost the same performance, all these facts seem to attest that an high optimisation degree of gaseous LPG systems has been achieved. Nevertheless, doubts about the actual performance gap between LPG and gasoline operation still exist.

The paper presents the first step of a research on the real performances of the up-to-date gaseous LPG port injection systems. After a brief discussion about the theoretical advantages and drawbacks of fuelling SI internal combustion engines with LPG, the brake performance of a passenger car engine fed with gasoline and LPG are experimentally measured at the test bed and compared. Engine design has been converted to dual-fuel operation with one of the more recent commercial kit. The lower performance obtained using LPG instead of gasoline is discussed in both steady state and transient operation.

2. LPG as SI engines fuel

Engine torque output for a given SI engine only depends on the mean effective pressure (*mep*). This is defined as [12]:

$$mep = \eta_{ter,id}\ \eta_{ind}\ \eta_v\ \rho_a\ \frac{F}{A}\ H_u\ \eta_m\,. \qquad (1)$$

The terms in eq. 1 are the ideal cycle thermal efficiency $\eta_{ter,id}$, the indicated efficiency η_{ind}, the volumetric efficiency η_v, the air density of the engine breathing environment ρ_a, the fuel to air ratio F/A, the fuel lower heating value (LHV) H_u and the mechanical efficiency η_m, respectively.

Thus, the performance with the two different fuels (gasoline and LPG) is different if and only if at least one of the terms defining *mep* in eq. 1 varies.

The discussion that follows is limited to gaseous LPG injection, since this is the case considered in the present analysis.

For a given engine, the thermal efficiency ($\eta_{ter,id}$) of the ideal air-fuel cycle slightly increases with LPG because of its specific heat ratio which decreases the overall fuel-air mixture ratio with respect to gasoline.

The indicated efficiency (η_{ind}) could theoretically increase with LPG due to a faster flame speed (which maintains the pressure at combustion TDC and during the expansion stroke higher and reduces the heat losses). However Campbell et al. [4] state that the burn rates measured for the two fuels are not sufficiently different to justify a spark advance rescheduling for close-to-stoichiometric engine operation.

Volumetric efficiency (η_v), i.e. the parameter which mostly affect power output, is worsened by gaseous LPG injection. For stoichiometric mixtures and for a given cylinder volume, Watson and Phuong [7] refer that induced air decreases because the 4.03% of air is displaced by LPG vapours compared to the 1.65% of fully vaporized gasoline. Moreover, gasoline vaporization heat helps decrease the temperature, so that the air-fuel mixture introduced in the cylinders is denser than that in the LPG case.

Assuming as a first instance that mechanical efficiency (η_m) is independent from fuel (however, the higher inlet manifold pressure in LPG part load operation reduces the pumping losses), the product of air density (ρ_a), fuel to air ratio (F/A), and fuel LHV (H_u) has to be discussed. If F/A is the stoichiometric ratio, this product is the maximum thermal energy that can be released from the mixture that contains a unit volume of air at reference conditions. This value is almost the same, about 3.5 MJ/m^3 at ambient pressure and 15°C, for gasoline and LPG (being slightly higher for LPG).

However, LPG offers the following advantages (in addition to the very remarkable feature of reducing usual pollutants emissions):

a) it improves the three-way catalyst efficiency and durability (absence of unburnt deposits, sulphur and other poisoning substances);
b) it reduces benzene, toluene and xylene emissions;
c) it reduces engine maintenance and wear (it does not interfere with cylinder lubrication and increases spark plug life).

In view of this discussion, it is theoretically demonstrated that gaseous LPG injection in a gasoline engine (without other changes) reduces power output, mostly because of volumetric efficiency deterioration, also in the case of equal optimisation level of both the fuel delivery systems.

A non-optimised LPG injection systems can augment power output deterioration for one or both the two following reasons:

1) an excess of LPG superheating further reduces intake air density;
2) a non accurate LPG metering always reduces power output and, in the case of rich mixtures, increases emissions and lowers global thermal efficiency.

3. Engine test facility

The SI engine used for this research is tested in an acoustic-insulated cell equipped with an intake air fan, which supplies air for engine breathing, exhaust extractors, which remove combustion gases from the room, and a variable speed centrifugal fan, which preserves the engine thermal regime (see Fig. 2).

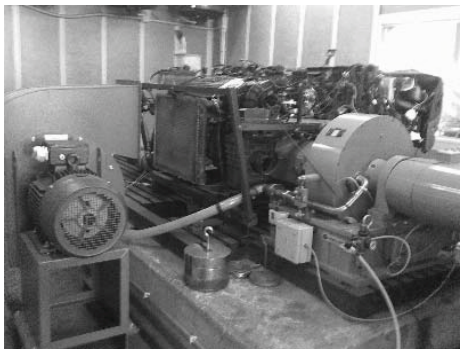

Fig. 2. The engine at the test bed.

3.1. Engine

A four stroke five cylinder 2 litres engine has been recovered from the final dismantling of a passenger car. This power unit motored with minor modifications different vehicle models

manufactured by FIAT group S.p.A from 1994 until 2001. The major specifications of the original engine are summarised in Table 2.

The engine has been transformed for dual-fuel operation by an up-to-date aftermarket kit which does not differs substantially from most of the OEM LPG fuel systems equipping passenger cars of many worldwide manufacturers. The LPG kit is a sequential multi-point port fuel electronic injection system which delivers the LPG in gaseous phase in the intake manifolds upstream to the gasoline injectors. System basic operation and components do not differ from the brief description presented in the paper introduction.

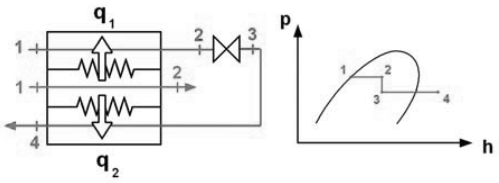

Fig. 1. Evaporator device: heat exchange scheme (left); LPG thermodynamic states (right).

Some additional notes are needed for the evaporator, which is one of the most critical components of the system. This device has actually multiple functions since it provides:

1) a partial evaporation in the first passage of a LPG–engine coolant heat exchanger (1–2 red path in Fig. 1).

2) a pressure reduction obtained by an orifice-plate system (2–3 red path in Fig. 1).

3) evaporation completion (with superheating) in the second passage of the same LPG–engine coolant heat exchanger (3–4 red path in Fig. 1).

In order to assure the hot flux at the heat exchanger sections (1–2 blue path in Fig. 1), the evaporator device is mounted on a water circuit in parallel to the passengers heating water circuit. Thus engine coolant is kept upstream to the thermostatic valve which adjusts the coolant flow to the main engine heat exchanger. Fig. 1 summarises the heat transfer in the evaporator device (on the left): q_1 and q_2 are the first and the second stadium heat fluxes, respectively, and the corresponding LPG thermo-dynamic states are drawn on the right.

LPG metering is controlled by an ECU which corrects by a constant factor the duty cycle of gasoline injectors. The electro-injectors act like chocked flow orifices. In this operating condition their mass flow rate (w) follows the well-known equation:

$$w = A\, p_0 \sqrt{\frac{2}{R T_0}} \left(\frac{2}{\gamma + 1} \right)^{\frac{1}{\gamma - 1}} \sqrt{\frac{\gamma}{\gamma + 1}}, \qquad (1)$$

where A is throttle section area, p_0 and T_0 are the total pressure and temperature in the injectors rail, γ is the specific heats ratio and R is the gas constant. Thus, in this operation scenario the evaporator device should cope with the other two following fundamental functions:

1) assuring that p_0 is always high enough to guarantee the chocked flow condition in the injectors.

2) assuring that p_0 is kept constant.

Rail pressure is mechanically managed by this evaporator device through a metal spring which acts on the orifice plate. The steel spring is partly balanced by the action of the manifold absolute pressure (MAP) deriving from an adequate linkage between the evaporator and the air intake manifold.

The amount of LPG delivered cycle by cycle and for any engine operating condition is corrected by the feedback of the exhaust oxygen sensor (which is actually designed to optimise the amount of injected gasoline).

Table 2. Engine technical data sheet.

Parameter	Value
Model	FIAT 838 A1.000
Type	4 stroke 5 cylinder inline SI
Fuel	Gasoline
Swept volume	1998 cm^3
Maximum torque	185 N x m @ 4500 rpm
Maximum power	107 kW @ 6100 rpm
Stroke	75.6 mm
Bore	82 mm
Combustion chamber	Pent-roof 4 valves
Compression ratio	10
Distribution	Double over-head camshaft (DOHC) with intake and exhaust variable timing device.
Fuel metering	Multi-point port fuel sequential electronic injection
Exhaust treatment	3-way catalyst with lambda sensor

3.2. Instrumentation

The engine is coupled with an eddy current electromagnetic dynamometer Borghi-Saveri mod. FE-260S (the accuracy is ±2.8 Nm for torque and ±16 rpm for revving speed measurements). Torque and other performance parameters derived from torque have been corrected following the ISO 3046-1 standard [11] (to this end, sensors for ambient air temperature, pressure and humidity have been adopted). Fuel consumption is obtained by a weight measure. The fuel tank is arranged on a load cell (digital balance KERN mod. CB24K1N) with a 24 kg full scale reading, a resolution of 0.001 kg and a maximum linearity error of 0.003 kg. The engine thermal regime is monitored by 3 temperature sensors located at the engine heat exchanger inlet and outlet sections and in the lubricant slump. The sampling frequency for all these data is 1 Hz.

The experimental apparatus also provides an absolute pressure sensor for the MAP acquisition, and 4 temperature and 4 pressure transducers for the measure of the thermo-dynamic state of the LPG and the engine coolant at evaporator device inlet and outlet sections, respectively (stations 1 and 4 of the red path and stations 1 and 2 of the blue path in Fig. 1). Finally an amperometric clamp which capture the ECU pulse sent to cylinder 1 ignition coil (its resolution is 1 rpm) is used to link the evaporator measures with dynamometer data. The sampling frequency for this data set is 1 kHz.

The adopted temperature sensors are K type thermocouples with grounded hot junction and compensated cables. According to the manufacturer, the uncertainty on temperature measurements is 2.5 K.

The total data amount is captured by two National Instruments® acquisition boards and is managed by the software LabView® version 6.2.

3.3. Experimental campaign

The performance of LPG fuelled engines is affected by the evaporator device in two similar ways:

1) Different climate conditions alter the heat exchange between LPG and engine coolant, affecting both the degree of LPG superheating and ambient air density.
2) Different heat exchange (i.e. different extension of the evaporator heated surfaces) alter the degree of LPG superheating without modifying ambient air density.

Three different test condition has been set to take this into account:

- A standard condition T_{med}, referring to engine operation in Italian middle season (temperature of the LPG upstream the evaporator equal to 25.6°C);
- A more demanding condition T_{hot}, referring to engine operation in Italian summer season (temperature of the LPG upstream the evaporator equal to 31.5°C);
- A different evaporator heat exchange condition T_{cold}, referring to engine operation in Italian summer season but with an evaporator device with a less heated surface (the temperature of the LPG upstream the evaporator equal to 12.7°C and ambient air temperature is equal to 30°C).

More than 150 tests have been performed taking into account 4 different loads and 5 different engine rotational speed for any test condition.

At the time of writing technical troubles have invalidated some of the more demanding test, in particular with reference to the T_{cold} condition.

Table 3 shows the summary of the valid steady-state acquisitions.

Table 3. Summary of the steady-state test campaign.

Test condition	Load	Gasoline	LPG
T_{med}	100%	27	**7**
T_{med}	75%	0	**7**
T_{med}	50%	1	6
T_{med}	25%	2	5
T_{hot}	100%	0	7
T_{hot}	25%	0	7
T_{cold}	100%	0	5
T_{cold}	50%	0	2
T_{cold}	25%	0	6

3. Results

Figure 3 shows the full load brake torque and power curves for gasoline operation and the 3 LPG test conditions. Maximum torque and power result lower than those declared by the manufacturer (this depends partly from stock dispersion and partly from wear), and a very notable performance deterioration appears for all the LPG operation condition. In particular, the brake torque (i.e. the mep) obtained in LPG operation at T_{med} (that is the best performance LPG fuelled engine condition tested) is more than 20% lower that that obtained in gasoline operation. This exceeds the

performance reduction expected theoretically because of the volumetric efficiency drop.

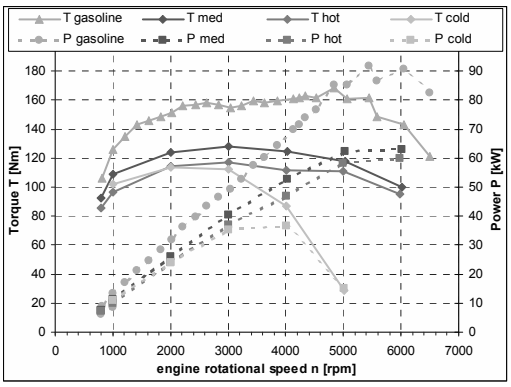

Fig. 3. Full load brake torque (solid lines) and power (dotted lines) in gasoline (green) and LPG operation (blue = T_{med}, red = T_{hot}, cyan = T_{cold}).

In order to check the reliability of fuel metering without a direct measurement of volumetric efficiency, some considerations can be drawn from the fuel consumption diagrams in Fig. 4. The full load fuel mass flow rate (*c*) and the specific fuel consumption (*sfc*) roughly confirm that the LPG delivered by injectors is sufficiently correct, especially at the low-to-medium regimes in which specific fuel consumption indicates a high energy conversion efficiency. Since the relation between *sfc* and global thermal efficiency (η_{ter}) of an engine is:

$$\eta_{ter} = 1/(sfc\ H_u) \qquad (3),$$

both *sfc* values (which are not higher than similar gasoline fuelled engines) and the LPG LHV (greater than gasoline) ensure that the full load thermal efficiency of the tested engine never falls below 0.3 during LPG operation (except for idle regime). The behaviour is less clear at high rotational speeds (above 5000 rpm). The simultaneous decrease in fuel mass flow rate and *sfc* matches with a volumetric efficiency drop hypothesis and seems to confirm the reliability of fuel metering. However, the excessively low values of specific fuel consumption (i.e. the high thermal efficiency) could be interpreted as an insufficient fuel delivery masked by the well-known wide range tolerated by LPG lean combustion (see e.g. [4]).

Fig. 3 also shows a gradual and continuous increase of the gap between full load brake torque curves in LPG (T_{med} condition) and gasoline operation. This trend can be explained by an increase of volumetric efficiency deterioration in LPG operation as engine rotational speed increases. This relationship is clearly shown in Fig. 5, in which manifold pressure relative to ambient condition is plotted in different engine operating condition. The negative pressure values quantify the pressure losses in the intake system upstream the injectors.

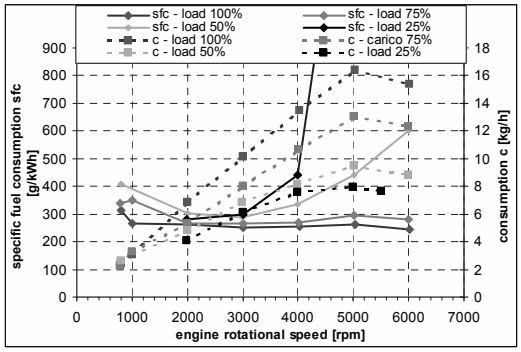

Fig. 4. Brake specific fuel consumption (solid lines) and fuel consumption (dotted lines) in LPG operation at different loads.

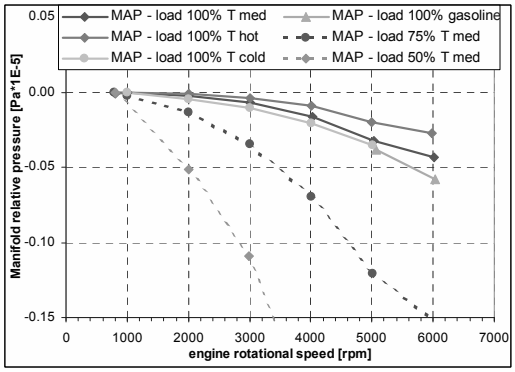

Fig. 5. Manifold pressure (relative to ambient) for all the full load test conditions and for the part loads (T_{med} condition).

As is well known, the general form of pressure losses Δp in fluid flows is:

$$\Delta p = \zeta\ \rho \frac{v^2}{2} \qquad (4).$$

the mean fluid velocity (*v*) depends on the volumetric flow rate that is, in turn, on engine rotational speed. On the other hand, the overall pressure loss coefficient (ζ) depends on piping geometry and throttle position. Thus, the reduction of the fresh

charge density (ρ) make the volumetric efficiency decrease progressively for given throttle position and rotational speed when the engine switches from gasoline to LPG fuelling, or when it operates with LPG at T_{cold}, T_{med}, and T_{hot} in this order.

The excessive superheating occurring in the LPG evaporator device in the T_{hot} operating condition clearly appears in Fig. 6 (above), which shows the change in LPG thermodynamic state operated by the evaporator. A satisfactory regulation of the reduced pressure, which seems roughly constant, is performed, but the device delivers to the injectors a gaseous LPG that is at least 10°C hotter than the very low quality LPG entering the device. This happens even at high rotational speeds, when the heat exchange with engine coolant becomes more difficult.

The unattended poor results obtained with LPG operation at T_{cold} need a further discussion. The worst brake torque obtained in this operating condition seems inconsistent with the volumetric efficiency, which is probably higher than in the other LPG test conditions. The main reason of this behaviour is explained in Fig.6 (below). Because of the low temperature of the small supply tank that is peculiar of the T_{cold} tests, the LPG saturation pressure in the tank is too low, so that a high quality two-phase flow enters the evaporator device becoming:

- too much superheated (the heat flux required to complete the vaporisation is too low);
- badly metered (total pressure in the injectors rail is too low).

Some transient measures are now presented about a simple test performed both in gasoline and in LPG operation. The engine has been forced to abruptly change from idling to wide open throttle while the load applied by the dynamometer increases with the square of the rotational speed. This test simulates the unreal scenario of a passengers car engine loaded by a mass-less virtual vehicle provided with a given aerodynamic drag but without any inertia other than that of the engine.

The transient shows that LPG operation causes a performance deterioration greater than that observed in the steady-state tests. The time history of brake torque and engine speed is plotted in Fig. 7. The steady-state is achieved after about 6s in gasoline operation. Both torque and engine speed reach their maximum values roughly 1s later in LPG operation (engine reaction is more than 15% slower). Moreover, both torque and engine speed maximum values are considerably smaller than the corresponding values in gasoline operation. Power output is heavily penalised as it is almost halved in LPG operation.

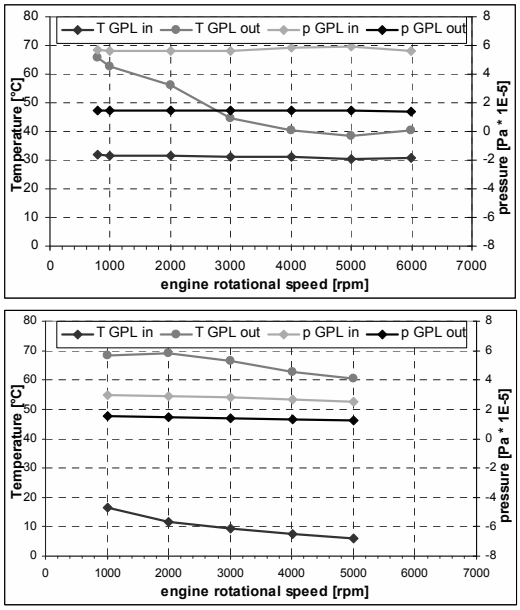

Fig. 6. LPG thermodynamic states before and after the evaporator device in full load operation at T_{hot} (above) and T_{cold} (below). ("in" and "out" indicate red sections 1and 2 of Fig. 1).

4. Conclusions

The first step of a research on the actual performances of an up-to-date gaseous LPG port injection systems has been presented. Theoretical reasons about the performance reduction of SI engines designed for gasoline operation when fuelled with gaseous LPG has been discussed. A SI internal combustion engine of a passenger car has been converted to dual-fuel operation with one of the more recent commercial kits and has been experimentally tested. The steady-state global performance results lead to the major conclusion that the noticeable performance deterioration in LPG operation is mainly due to a deterioration of volumetric efficiency, which appears to get worse than the theoretical expectation because of an excessive LPG superheating. This consideration has been confirmed by the acquisition of LPG thermodynamic state upstream and downstream the evaporator-pressure reducer device. These measures show that:

a) the coolant flow rate into the evaporator (or alternatively the heat exchanger surface of the evaporator device) is too large for low-to-medium engine rotational speeds. The superheating overcompensate the cooling of gaseous LPG due to the pressure reduction section of the device;

b) For medium-to-high rotational speeds the superheating following gas cooling due to pressure reduction keeps the LPG temperature across evaporator-pressure reduced device almost constant;

c) For the high rotational speeds the device causes an overall cooling of the gaseous LPG which should be the most favourable operation condition in relation to volumetric efficiency. However, the performances are globally worse, probably because of a scarce delivery of LPG to combustion chambers.

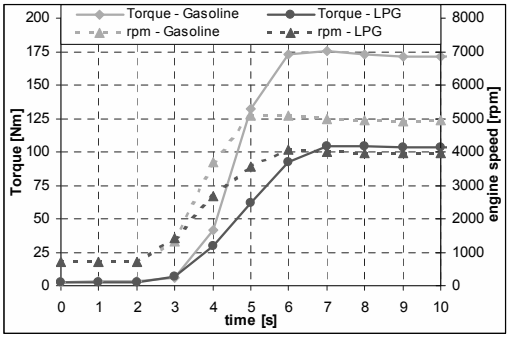

Fig. 7. Transient performance : brake torque and engine speed. Comparison between gasoline (green) and LPG (blue) operation.

Despite to the unrealistic conditions of the transient tests performed, the results clearly show a very noticeable deterioration of engine performance in LPG operation.

The presented analysis is far to be completed and in many cases the obtained results indicate nothing more than trends. However, it can be stated that there is still a lot of work to do in order to optimise the performance attainable by SI engines equipped with the up-to-date gaseous LPG port injection systems.

References

[1] EN 589: 2008, Automotive Fuels – LPG – Requirements and Test Methods.

[2] Snelgrove, D. G., Dupont, P., and Bonetto, R., 1996, An investigation into the influence of LPG (Autogas) composition on the exhaust emissions and fuel consumption of 3 bi-fuelled Renault vehicles, SAE Paper 961170.

[3] Newkirk, M. S., et al., 1996, Reactivity and exhaust emissions from an EHC-equipped LPG conversion vehicle operating on butane/propane fuel blends, SAE Special Publications, 1208, pp.-195-206.

[4] Campbell, M., Wyszynski, P., and Stone, R., 2004, Combustion of LPG in Spark-Ignition Engine, SAE Paper 2004-01-0974.

[5] Price, P., Shengmin, G., and Hirschmann, M., 2004, Performance of an evaporator for a LPG powered vehicle, Applied Thermal Engineering, 24, pp.1179-1194.

[6] Corradini, F., and Togninelli, M., 2003, Gas Pressure Regulation to Drive LPG/CNG Systems with Standard Gasoline ECU, SAE Paper 2003-01-0709.

[7] Watson, H. C., and Phuong, P. X., 2007, Why Liquid Phase LPG Port Injection has Superior Power abd Efficiency to Gas Phase Port Injection, SAE Paper 2007-01-3552.

[8] Boretti, A. A., and Watson, H. C., 2009, Development of a Direct Injection High Flexibility Cng/Lpg Spark Ignition Engine, SAE Paper 2009-01-1969.

[9] Cipollone, R., and Villante, C., 2000, A/F and Liquid-Phase Control in LPG Injected Spark Ignition ICE, SAE Paper 2000-01-2974.

[10] Lee, S., Kusaka, J., and Dalsho, Y., 2003, Mixture formation and combustion characteristics of directly injected LPG spray, JSAE Paper 20030009.

[11] ISO 3046-1, 2002, Reciprocating internal combustion engines – performance.

[12] Heywood, J. B., 1988, *Internal Combustion Engine Fundamentals*, McGraw-Hill Book Co., Singapore.

Acknowledgments: The author gratefully acknowledge Andrea Lazzaretto and Andrea Toffolo for their precious suggestions, and Federico Pavin and Antonio Sturniolo for the help in the instrumentation setup.

Predicting the Annual Performance of an Engine Trigeneration System – Electricity, Hot Water and Chilled Water – Through a Computational Simulation Analysis

Denilson Boschiero do Espirito Santo and Johnathan Flores Arteaga
Mechanical Engineering Faculty - Energy Department
State University of Campinas - SP - Brazil - denilson@fem.unicamp.br

Abstract: The efficient use of natural resources is an important contribution for the construction of a more sustainable world. Decentralized electricity production through cogeneration systems can save primary energy if it operates with high energy utilization factor (EUF). High EUF is obtained when the system produces electricity and a substantial amount of the energy rejected by the prime mover is used to meet site thermal demands. Energy consumption in buildings varies as activity, climate and occupancy changes at the different day hours, weekdays and weather seasons. The cogeneration case study should be done considering the performance of the system at different energy demands profiles and climatic profiles. In this paper an annual analysis of an engine cogeneration system is developed as an integrated thermal system (ITS) through a computational simulation program. The thermal system integration simulation considers characteristics of the system, characteristic of the individual equipment, design considerations and parameters, the dynamic of off design operating conditions, energy demands profiles of the site and climatic data to evaluate the performance of the cogeneration plant in an annual basis. The results can contribute in the implementation decision process and in the optimization of the solution

Keywords: integrated thermal system, cogeneration, trigeneration, simulation, software, iterative procedures, engine, absorption chiller.

1. INTRODUCTION

A more sustainable use of natural resources is an important contribution to reduce the environmental impact of human activities. In the electricity generation field the use of renewable technologies should be prioritized but the impacts and implications of their large use should be better evaluated. Renewable forms of electricity generation cannot attend the world electricity demand, then the use of fossil fuel power plants will continue to have an important contribution. Thermal plant efficiencies are being raised by advances in engineering fields such as materials, manufacturing process, fluid flow, heat transfer, combustion, and others. Cogeneration system take advantage of the engineering advances and incorporates them into the equipment, but a site energy demand analysis and the system simulation play an important role in achieving coincident energy demands that can be met by the cogeneration system and in the evaluation of design parameters in the optimization of the system.

In commercial buildings energy demands varies as the activity, climate and occupancy changes at the different day hours, weekdays and weather seasons. Cogeneration systems technical analysis is developed through different methodologies. Load duration curves (LDC) was utilized by Orlando [1], the mixed integer linear programming (MILP) was utilized by Chinese et al [2] while Renedo et al [3] developed a case study utilizing monthly electricity consumptions and three periods (winter, spring-autumm and summer) thermal consumptions to evaluate the performance of a given cogeneration system.

The analysis of cogeneration performance can be done based on the first law of thermodynamics [4] and on the second law of thermodynamics [5-6]. The gas emission associated with the combustion is also a concern when comparing prime movers solutions [7]. Depending on the energy flows produced by the cogeneration plant it can be referenced as trigeneration or poligeneration [8]. The use of cogeneration systems utilizing biofuels can also be considered.

In this paper a software [9] (COGMCI) is used to evaluate the performance of an engine cogeneration system, producing electricity, hot water and chilled water (cooling load). The software does the evaluation of the performance of the system considering an hourly daily profile of energy demands and climatic data. Energy demands of a Brazilian university hospital were utilized as a case study. Climatic profiles of the hospital region were also utilized.

The computational methodology considers the system as an integrated thermal system (ITS) where the performance of the individual equipments affects the operation of the complete system. The methodology combines curve fitting from literature and manufacturer's data, mathematical representations of physical phenomena, energy demands, design parameters and thermodynamic properties.

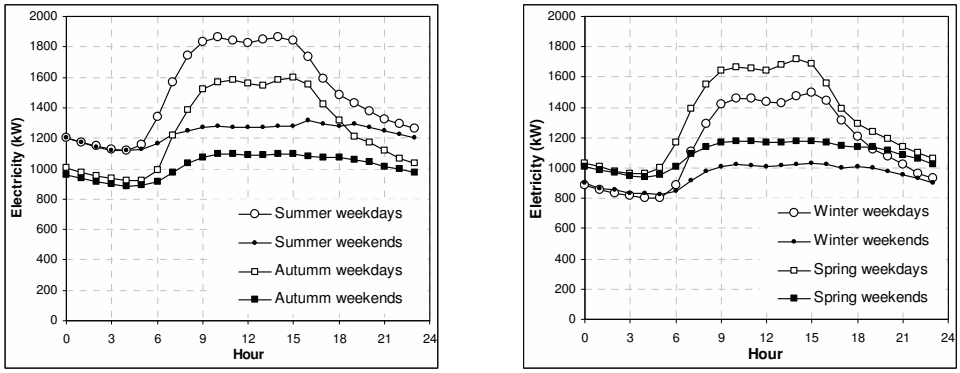

a) summer and autumn *b) winter and spring*

Figure 1 – Hospital electricity demand (kW)

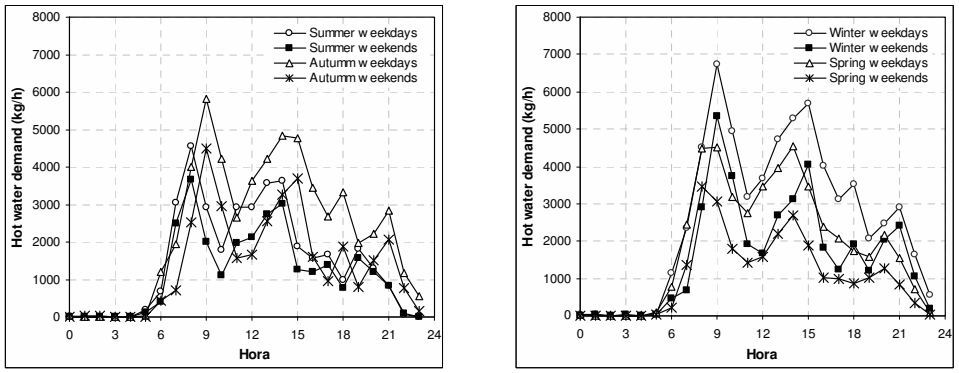

a) summer and autumn *b) winter and spring*

Figure 2 – Hospital hot water demand (kg/h)

2. CASE STUDY: HOSPITAL

In this study, loads of a local university hospital is assessed. Actually the hospital buy electricity from the electrical grid, produces steam at combustible oil fueled steam generator, hot water in steam boilers and produces chilled water at two water cooled screw compressor chillers.

The energy demand profiles were obtained through a data acquisition system that was installed to register the energy demands of the hospital. The data acquisition system is monitoring the total hospital electricity demand, sanitary use hot water, steam and the electrical demand of the electrical chillers at a one-hour time interval. A software displays the data in a computer and store them in files. The energy and weather profiles were obtained during the year of 2006. Mean energy demands daily profiles were grouped at eight different groups that were assumed to have similar values: i) summer weekdays (60 days), ii) summer weekends/holidays (29 days), iii) autumn weekdays (65 days), iv) autumn weekends/holidays (28 days), v) winter weekdays (67 days), vi) winter weekends/holidays (27 days), vii) spring weekdays (60 days) and viii) spring weekends/holidays (29 days). Climatic data were grouped in mean daily profiles as a function of the weather station.

Figure 1 shows the mean electricity demand profiles. Figure 2 shows the mean demand profile of hot water for sanitary purposes (50°C). Figure 3 shows the mean cooling load (air conditioning) profile. Figure 4 is the mean weather profile obtained at a climatic monitoring station located at the university campus.

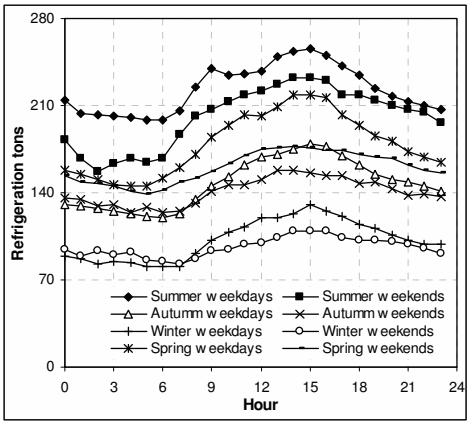

Figure 3 – Hospital cooling load (refrigeration tons)

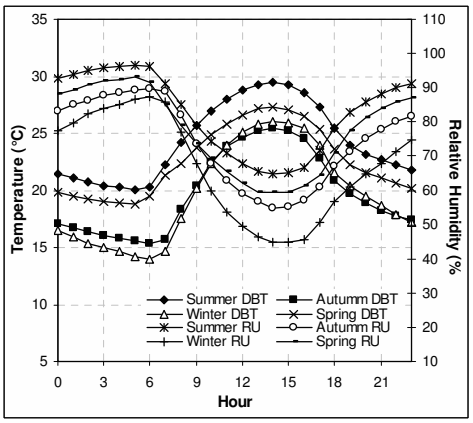

Figure 4 – Climatic data

3. METHODOLOGY

The results presented here were obtained by mean of a software (COGMCI) consisting of Fortran engineering programs and a Delphi interface. Graphical results are generated by a spreadsheet (Excel) that imports data from result files. The Fortran programs is composed of one main algorithm and more than 20 subroutines dealing with (i) five different engines, (ii) water and steam properties, (iii) exhaust gas properties, (iv) absorption chiller selection, (v) absorption chiller simulation, (vi) heat recovery steam generator (HRSG) simulation, (vii) pre-heater design, (viii) pre-heater simulation, (ix) exhaust gas heat exchanger design, and (x) exhaust gas heat exchanger simulation, among others.

The main program controls data entry, results and all calculations. Calculation procedures use polynomial curve fitting (engine and absorption chiller performance); deterministic modeling or mathematical representations of physical phenomena (heat transfer and pressure drops); and physical properties (water and exhaust gases). A computational algorithm involving several iterative procedures was developed, constituting an integrated thermal system, i.e., considering all pieces of equipment as operating as a single system. It produces results as a function of demands, energy supplied by engine, design parameters, equipment performance, and simplified hypothesis. The hourly profile analysis simulation applied here approximates the dynamic nature of energy consumption in buildings and the dynamics of thermal equipment performance in an integrated system by a series of quasi-steady-state operating conditions with one-hour time-steps, as used by Lebrun (1999) [10].

The software was previously utilized to develop others case studies [11-18].

At this case study the computational algorithm is executed eight times, to predict the performance of the system at weekdays and weekends at the four different seasons of the year, as explained at section 2.

4. COGENERATION CONFIGURATION

Figure 5 shows the cogeneration configuration evaluated here. Flows are identified in the text by brackets. The cogeneration system is formed by one internal combustion engine, primary and secondary hot water circuits, one exhaust gas heat exchanger (EGHE), one hot water single stage absorption chiller, and auxiliary equipment (pumps, cooling towers, heat exchangers, etc). The secondary circuit recovers energy from the engine oil radiator and intercoolers and uses it to warm water for sanitary purposes at HE2. The primary circuit recovers energy from the engine jacket, the water is reheated utilizing the energy of the engine exhaust gas, after it is directed to the absorption chiller for chilled water production. If there is energy excess in the primary circuit water it can be

used to warm water for sanitary purposes at HE1 (after recovery at secondary circuit).

The engine performance is based on the Jenbacher J320 GS C85 [19], the engine has an electric power of 1060 kWe at full load. Figure 6 presents the energy balance of the engine and figure 7 the exhaust gas flow and temperature as a function of the engine load. The maximum engine mechanical efficiency (40.3%) is found at full load, at this condition 39% of the engine energy is converted into electricity. Design temperatures of hot water at the primary and secondary circuits are based on values defined by the manufacturer. Correction for atmospheric pressure (not applicable in this study) assumes a 0.7% loss of power for each 100 meters above 500 meters. Correction for dry bulb temperature assumes a 0.5% loss of power for each degree Celsius above 25°C.

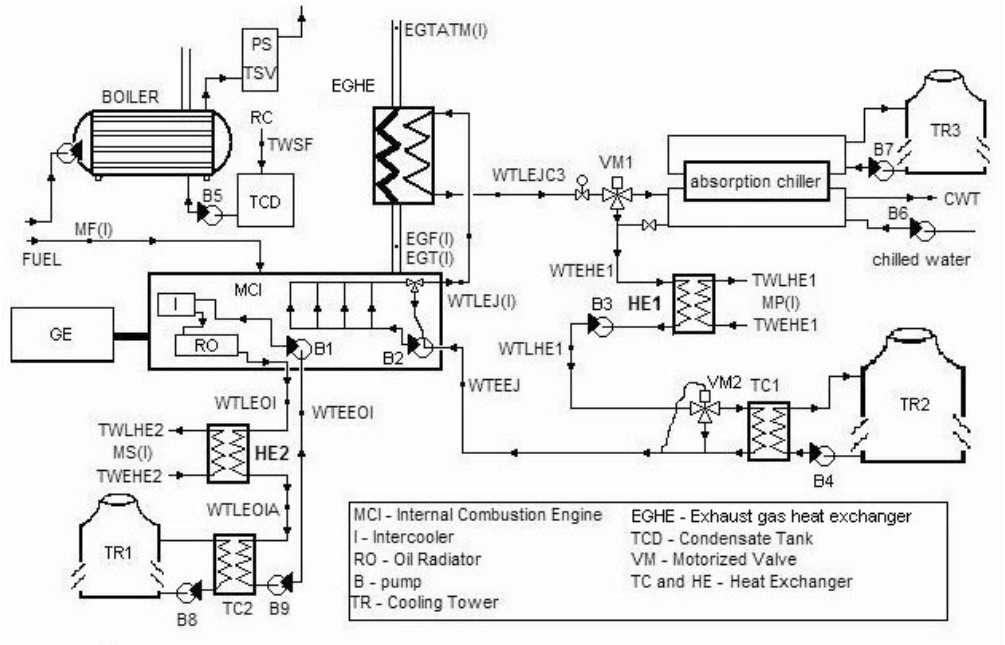

Figure 5 – Cogeneration Scheme

The absorption chiller (AC) selection and simulation is based on performance curves from a manufacturer (Trane Company, 1989) [20]. The selected absorption chiller has a nominal capacity of 520 tons (1774 kW) based on saturated steam at 184 kPa as the heat source, chiller water being produced at 7.2°C (5.5°C temperature difference) and water entering the condenser at 29.4°C. The program selects the AC based on the primary circuit water flow and temperature difference. At this study it was selected considering that hot water enters the AC generator at 119°C and leaves it at 75°C, chilled and condensed water temperatures are as defined at the nominal capacity condition (these represents the design condition of the chilled water plant at the hospital). The water flow at the condenser and absorber is as required by the manufacturer. The AC avoids electricity demand at the electrical chillers by a rate of 0.8 kW/ton.

The exhaust gas heat exchanger (EGHE) is simulated according to the methodology proposed by Ref. [21]. A heat loss of 1% was assumed. Exhaust gas composition is assumed to be constant, and properties are evaluated at its mean temperature at the EGHE. The exhaust gases temperature leaving the EGHE is designed to be 17°C higher then the primary circuit hot water temperature entering the EGHE (approach point).

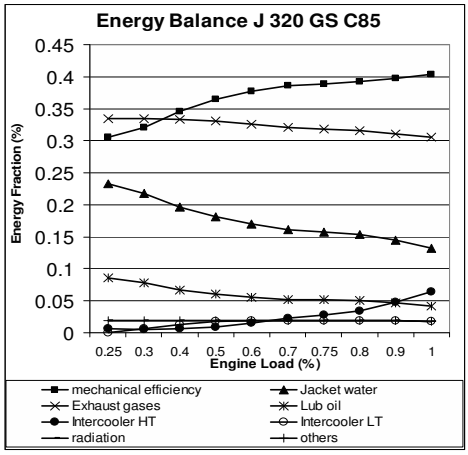

Figure 6 – Engine Energy Balance

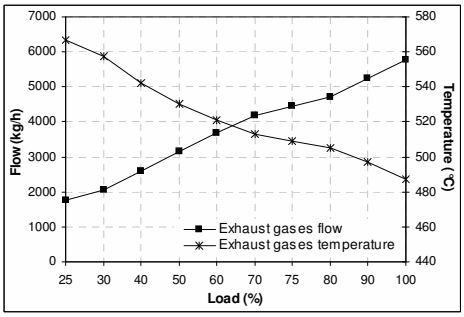

Figure 7 – Exhaust gas flow and temperature

At design condition, secondary circuit hot water enters the engine [WTEEOI] at 35°C (fixed) and leaves it [WTLEOI] at 55°C, while primary circuit hot water enters the engine [WTEEJ] at 75°C and leaves it [WTLEJ(I)] at 90°C. Water flows at primary and secondary circuits are designed considering the energy at the circuit and the design temperature difference (constant flow).

Heat exchangers HE1 and HE2, which recover energy from the primary and secondary circuits (hot water for sanitary purpose), were designed and simulated utilizing the NTU (number of thermal units) method. The design sanitary use flow is 6000 Kg/h for both heat exchangers. HE2 is designed considering water entering at 22.2°C and leaving at 50°C and HE1 is designed to receive sanitary use hot water at 30°C and to warm it to 50°C (design condition). Sanitary use hot water recovers energy at HE2 and HE1 in a series arrangement [MS(I) = MP(I)] and its demands varies accordingly with figures 2.

Cooling towers and auxiliary heat exchangers are responsible for rejecting unused energy, preventing the engine from operating under unsafe conditions. These equipment will not be simulated, i.e., it is assumed that they can reject the energy as needed.

The total produced electricity is 3% higher than the net engine power, taking into account the use of electricity in auxiliary equipment (parasitic load). No heat loss is assumed at the exhaust gas ducts and hot water pipes.

Since the revenue electricity value for exceeding electricity transferred to the grid in Brazil is very low compared with the natural gas price, it is considered that the engine operates at electrical dispatch (following the electricity demand curve) and surplus electricity is imported from the grid as necessary.

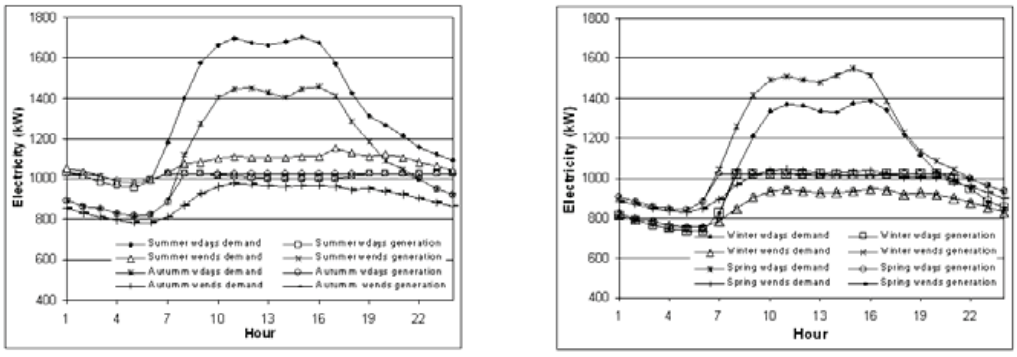

a) summer and autumn *b)winter and spring*

Figure 8 – Electricity demand and generation

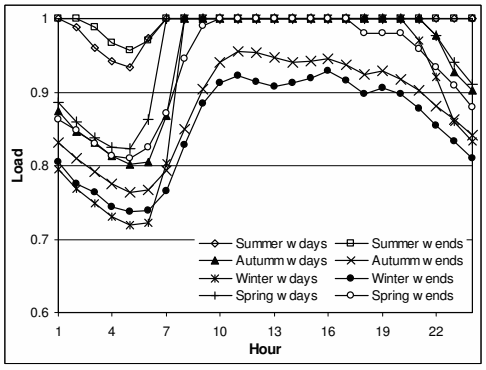

Figure 9 – Engine load

5. TECHNICAL RESULTS

6.1 Electricity

Figure 8 shows the electricity balance obtained through the simulation analysis, the hospital electricity demand and the engine production can be compared. The electricity demand presented at figure 8 are different from the values presented in figure 1, since at these figures the electricity demand is corrected due to the avoided electricity replaced by the use of the absorption chilled instead the electrical chillers.

In summer the engine operates at part load during the night (between 2 and 6 am). In the remaining hours the engine operates at full load and surplus electricity should be bought from the grid. In autumn the results are different for weekdays and weekends. At weekdays the engine operates at part load between 10 pm and 7 am and at full load in the remaining hours. In the weekends the engine operates at part load all the day. In winter the engine is expected to operate at part load between 9 pm and 7 am and at full load in the remaining hours. In the weekends the engine operates at part load all the day. In spring the engine is expected to operate at part load between 10 pm and 6 am in the weekdays and between 6 pm and 9 am in the weekends. In the remaining hours it operates at full load.

The mean engine load factor can be seen in figure 9. The lower engine load factor is close to 0.72 and a mean engine load of 0.94 is expected to occur during a one year period of operation.

6.2 Absorption chiller (AC) / cooling load

The AC capacity and the hospital cooling load can be compared at figures 10. In summer weekdays the electrical chillers needs to operate between 9 am and 11 pm and in weekends between 10 am and 10 pm. It also can be noted that when the engine operates at full load the absorption chiller can produce about 210 tons (738 kW), at this condition hot water enters the absorption chiller generator at 119°C and leaves at 76°C. Since the design temperature of the primary circuit water returning to the engine is 75°C, there is energy to be recovered at HE1 or rejected at cooling tower (TR2).

In autumn and winter the absorption chiller is expected to attend the cooling load, while in spring the electrical chillers is expected to operate at the weekdays complementing the absorption chiller capacity. A part of the energy of the primary circuit (including the recovery of the energy of the exhaust gases) is rejected when the absorption chiller real capacity is higher than the cooling load. This occurs mainly in summer weekends and in the remaining of the year.

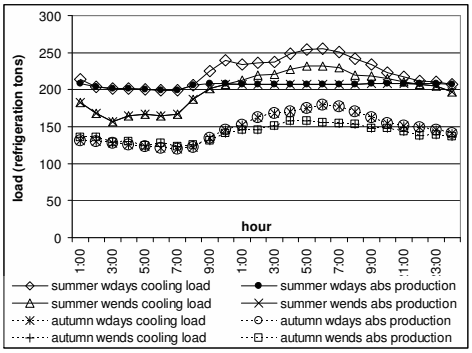

a) summer and autumn

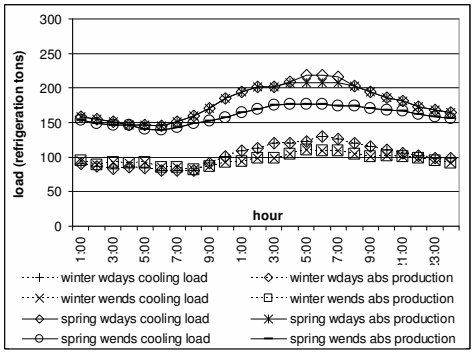

b) winter and spring

Figure 10 – Absorption chiller real capacity (refrigeration tons)

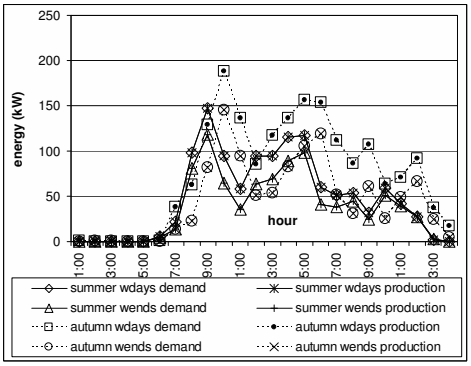

a)summer and autumn

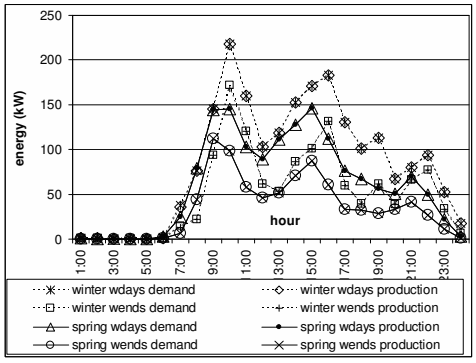

b) winter and spring

Figure 11 – Hot water demand and production (kW)

6.3 Hot water for sanitary purpose

Hot water is produced recovering energy from the engine secondary circuit (oil radiator, low and high temperature intercooler – figure 5). When the engine operates at full load about 12% of the engine energy is available at the secondary circuit (~ 320 kW). This energy is capable to attend the hospital sanitary hot water demand, but at the hours the engine load factor are low, the secondary circuit water leaving the engine can be lower then 50°C (sanitary use hot water design temperature). At these hours energy from the primary circuit can be recovered to reach the design temperature.

Hot water demand and production can be compared at figures 11. It can be seen that the hot water demand is attended mainly by the engine secondary circuit (HE2) (hot water demand are coincident with the production values) but if necessary the primary circuit energy can be utilized (HE1).

7. Energy Utilization Factor (EUF)

The EUF is calculated as the sum of the energy products of the cogeneration system (electricity, hot water and chilled water) divided by the engine energy consumption. The results can be seen in figure 12. The net electricity contribution to EUF varies between 35.8% (5 am winter) and 37.8% with engine at full load. Hot water contribution to EUF is 0% at hours there is no hot water demand and has a maximum value of 8% in winter 10 am. The chilled water production at the absorption chiller contributes between 10.5% in winter 7 am and 27.5% in summer 4 pm (figures not shown). A mean annual EUF of 61.8% was obtained (66% in summer, 59.9% in autumn, 54.2% in winter and 62.8% in spring).

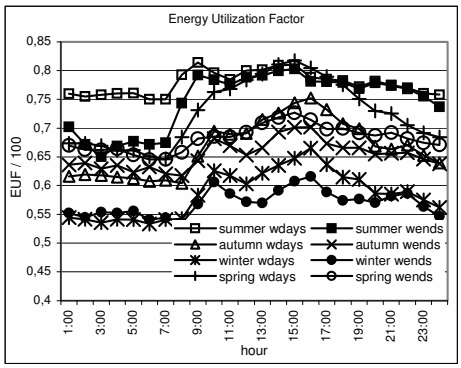

Figure 12 – Final EUF

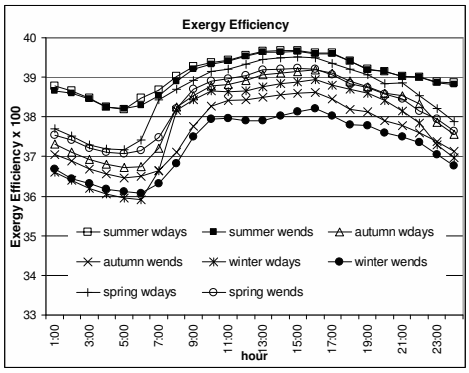

Figure 13 – Exergy efficiency

8. Exergy Efficiency

The exergy efficiency of the cogeneration system is show at figure 13 [22-24]. It is defined as the sum of the net exergy flows of the cogeneration system divided by the chemical exergy of the fuel

consumed by the engine. The lower heating value (LHV) of the fuel is utilized.

Better results is obtained in summer weekdays, a maximum value of 39.7% was calculated. The annual mean exergy efficiency was calculated as 38.3% (39.1% in summer, 38% in autumn, 37.6% in winter and 38.5% in spring).

When the engine operates at full load the electricity contribution to exergy efficiency is 37.8%. Chilled water contribution has a maximum value of 1.7% (absorption chiller operating at full load) and hot water contributes with a maximum of 0.4% at winter 10 am.

9. Daily Energy Analisys

At table 1 the seasonal electricity, hot water and steam consumption of the hospital can be predicted based on the mean demands profiles (figures 1 to 3). Considering that steam and hot water are produced with an efficiency of 80% and electricity is produced with an efficiency of 38% the daily energy consumption of the hospital can be estimated (last line of table 1). Multiplying them by the number of days at each season (weekdays and weekends) and doing the sum the annual energy consumption can be estimated as 30,456,524.1 kWh/year.

The simulation of the proposed cogeneration system revealed that surplus electricity will be bought from the grid, steam will continue to be produced at the existing steam generators, hot water demand will be completely met by the cogeneration system and additional chilled water will be produced at the existing screw compressor chillers. Table 2 reveals the energy consumption of the hospital considering the implementation of the proposed cogeneration solution. In line 4 the natural gas consumption of the engine can be checked. Considering the efficiency production of electricity, steam and hot water the seasonal energy consumption of the hospital can be estimated (last line of table 2) and the annual energy consumption can be estimated as 25,454,851.2 kWh/year. The implementation of the cogeneration system represents a primary energy savings of 16.4%.

10. Conclusions

A simulation methodology utilizing mean profiles of energy demands and climatic data for weekdays and weekends for the different season of the year was developed to predict the performance of a cogeneration solution.

Due to the low steam demand, an engine cogeneration configuration producing electricity, hot water and chilled water was proposed. Better result was obtained at the summer months, since a higher amount of the engine energy is recovered (mainly due to higher loads of the absorption chiller). An annual mean EUF equal to 61.8% and a mean exergy efficiency equal to 38.3% were calculated. A primary energy savings of 16.4% was obtained comparing the proposed cogeneration solution with the assumed actual situation (80% efficiency for steam and hot water production and 38% thermal efficiency for electricity production).

A detailed analysis of the engine primary and secondary circuit hot water temperatures were not presented in this study, but a complete energy balance were developed by the simulation program. A more detailed analysis can be done considering mean energy profiles for each year month, also considering weekdays and weekends.

Utilizing the data of tables 1 and 2 it is estimated that the proposed cogeneration solution can be competitive with thermal plants with thermal efficiency as high as 47.5%.

TABLE 1 – DAILY ENERGY CONSUMPTION

Without Cogeneration	Summer		Autumn		Winter		Spring	
	wdays	wends	wdays	wends	wdays	wends	wdays	wends
Electricity consumption (kWh/day)	35,973	29,542	30,126	24,320	27,521	22,776	31,682	26,113
Steam consumption (kWh/day)	4,152.75	3,839.38	2,807.21	3,020.24	2,524.08	3,162.49	2,994.82	3,474.48
Hot water consumption (kWh/day)	1,174.28	903.50	1,791.71	1,088.03	2,024.51	1,244.16	1,483.39	843.99
Daily energy consumption	101,324.58	83,670.71	85,027.60	69,135.34	78,109.42	65,445.16	88,971.44	74,116.51

TABLE 2 – DAILY ENERGY ANALYSIS

With Cogeneration	Summer		Autumn		Winter		Spring	
	wdays	wends	wdays	wends	wdays	wends	wdays	wends
Grid electricity consumption (kWh/day	7811.93	1521.68	4117.26	0.00	3188.48	0.00	4863.75	137.94
steam consumption (kWh/day)	4152.75	3839.38	2807.21	3020.24	2524.08	3162.49	2994.82	3474.48
hot water consumption (kWh/day)	0.00	0.00	0.00	0.00	0.00	0.00	0.00	0.00
Natural gas consumption (kWh/day)	58841.04	59009.25	56808.90	53690.23	55104.09	52262.74	57254.43	56249.72
electricity production (kWh/day)	24953.92	25042.98	23888.63	22266.95	23052.73	21556.66	24121.48	23593.58
daily energy consumption (kWh/day)	84589.68	67812.89	71152.80	57465.53	66649.93	56215.85	73797.28	60955.83

REFERENCES

[1] Orlando, J. A. Cogeneration Design Guide. Ashrae, 1996.

[2] Chinese D., Meneghetti A., Nardin G. and Simeoni P.; "From Hospital do Municipal Cogeneration Systems: An Italian Case Study". International Journal of Energy Research 2007; 31:829-828.

[3] Renedo C. J., Ortiz A., Manana M. Silió D. and Pérez S., "Study of different cogeneration alternatives for a Spanish hospital center". Energy and Buildings 38 (2006) 484-490.

[4] Panno D., Messineo A. and Dispenza A. "Cogeneration plant in a pasta factory: Energy saving and environmental benefit". Energy 32 (2007) 746-754.

[5] Balli O., Aras H. and Hepbasli A., 2008, "Exergoeconomic analysis of a combined heat and power (CHP) System". International Journal de Energy Research, Vol. 32, pp. 273-289.

[6] Rosen M. A., Le M. N. and Dincer I., 2005, "Efficiency Analysis of a Cogeneration and District Energy System". Applied Thermal Engineering, Vol. 25, pp.147-159.

[7] Serra L.M., Lozano M. A., Ramos J., Ensinas A. V. and Nebra S.A. "Polygeneration and efficient use of natural resources". Energy, 34 (2009), 575-586.

[8] Canova A., Chicco G., Genon G. and Mancarella P., 2008, "Emission Characterization and Evaluation of Natural Gas-fueled Cogeneration Microturbines and Internal Combustion Engines". Energy Conversion and Management, Vol 49, pp. 2900-2909.

[9] Espirito Santo, D. B. 2009. "COGMCI – Internal combustion engine cogeneration software evaluator". available at www.sisterm.com.br and ftp://ftp.fem.unicamp.br/pub/COGMCI.

[10] Lebrun Jean, Bourdouxhe Jean-Pascal and Grodent Marc, 'A Toolkit for Primary HVAC System Energy Calculation – ASHRAE 1999'. Laboratoire de Thermodynamique, Université di Liège.

[11] Espirito Santo, D. B. "Simulation of Internal Combustion Engines Cogeneration Systems: Four Different Engines Sizes with Hot Water Absorption Chiller". Ecos'2005, Norway, 2005, vol. 1, p. 1113-1120.

[12] Espirito Santo, D. B. "Evaluating and Electricity Base Load Engine Cogeneration System – Electricity, Steam and Hot Water – Trough a Computational Simulation Methodology". Ecos'2006, Greece, 2006, vol. 3, p. 1169-1176.

[13] Espirito Santo, D. B., "Comparing Two Engines of 425 kWe with the Same Cogeneration Configuration through a Computational Simulation Methodology". IJoT - International Journal of Thermodynamics, December 2006, vol. 9 (n° 4), p. 171-179.

[14] Espirito Santo, D. B., "Evaluating an Electricity Base Load Engine Cogeneration System - Electricity, Steam, Hot Water and Chilled Water - Through a Computational Simulation Methodology". ECOS 2007, Padova, Italy, 2007.

[15] Espirito Santo, D. B., "Simulation of an Internal Combustion Engine Cogeneration System: One Engine of 590 kWe with HRSG, Economizer and Heat Exchangers". Brazilian Conference on Mechanical Engineering, COBEM 2007, Brasilia - DF - Brazil.

[16] Espirito Santo, D. B., 2008, "Evaluating an Electricity Base Load Engine Cogeneration System – Electricity, Steam, Hot Water and Chilled Water – Through a Computational Simulation Methodology". ECOS 2008, Krakow, Poland.

[17] Espirito Santo, D. B., "Performance evaluation of an electricity base load engine cogeneration system". International Journal of Energy Research 2009, DOI: 10.1002/er.1592.

[18] Espirito Santo, D. B. and Arteaga, J. A. F., 2008, "Comparing Operational Strategies of an Internal Combustion Engine Cogeneration System". ECOS 2009, Foz do Iguaçú, Brazil.

[19] Jenbacher J320 GS C85, Energy Balance, 2003.

[20] The Trane Company. "Single Stage Absorption Cold Generator 101 to 1660 Tons". March 1989.

[21] Ganapathy, V. Waste Heat Boiler Deskbook. Fairmont Press, Lilburn:1991.

[22] Bejan A., Tsatsaronis G. and Moran M., "Thermal Design and Optimization". John Wiley and Sons, Inc, 1996.

[23] Moran M. J. and Shapiro H. N., "Fundamentals of Engineering Thermodynamics". John Wiley and Sons, Inc, 1995.

[24] Kotas T. J., "The Exergy Method of Thermal Plant Analysis" 2nd ed. Malabar, FL, Krieger: 1995.

.

Thermodynamic Optimisation of the Otto / Stirling Combined Cycle

Barry Cullen[a], Michel Feidt[b], Jim McGovern[a], Stoian Petrescu[c]

a. Dublin Energy Lab, Dublin Institute of Technology, Bolton Street, Dublin 1, Ireland
b. L.E.M.T.A., U.R.A.C.N.R.S.7563, University "Henri Poincare" of Nancy 1, Avenue de la Foret de Haye, 54504, Vandouevre-les-Nancy, France
c. Department of Engineering Thermodynamics, University Politehnica of Bucharest, Splaiul Independentei, 313, 060042 Bucharest, Romania

Abstract: Combined cycle systems are an established method for increasing primary energy efficiency of power generation systems. Some ongoing research is concerned with investigating the novel combined cycle system involving the Otto and Stirling thermodynamic cycles. The Otto cycle is to act as the topping cycle, with the Stirling cycle acting to recover heat from the exhaust for the purpose of additional power generation.

The present work investigates the thermodynamic optimisation of the combined cycle system for the case of the engines operating under two imposed parametric constraints: 1) imposed heat addition to the Otto cycle, and 2) imposed maximum cycle temperature of the Otto cycle. These conditions are analogous to a specified fuel consumption of the engine and the metallurgical limit of the operating components respectively. The optimum work output for each scenario is analysed with respect to the particular physical constraints of the Stirling cycle heat exchangers – effectiveness, NTU, heat transfer coefficient and heat transfer area. Only interactions between the engine and the external source and sink are considered in this treatment. Regeneration within the cycle, as would typically be used within the practical engine, is considered as perfect.

The existence of an optimum power output for the combined system is proven analytically. A numerical study is then presented to further investigate the performance for each of the parameters named above.

Keywords: Combined Cycles, Otto Cycle, Stirling Cycle, Thermodynamic Optimisation

1. Introduction

Combined cycle power generation systems are an established method for increasing primary generation efficiency. An established technology that have benefitted from several decades of development, they are more typically associated with large scale centralised generation systems, and almost exclusively involve turbine plant operating on Brayton / Rankine combinations. Current thinking, however, favours development towards Distributed Generation (DG) networks in an effort to increase energy efficiency for both environmental and security reasons [1-5]. Arising from this is an interest in small-scale combined cycle systems involving reciprocating engines such as gas fired Otto cycle and Diesel cycle engines. These engines traditionally dominate this smaller scale (<5MW) power systems market as Combined Heat and Power (CHP) generators, renewable gas prime movers and standby generators [6, 7]. Some recent work has focused on use of the Rankine cycle as a heat recovery device on a reciprocating internal combustion engine. Gambarotta and Vaja [8] investigated the Organic Rankine Cycle (ORC) as a bottoming cycle on an Otto Cycle spark ignition engine. Badami et al [9] investigated the standard Rankine cycle

Corresponding Author: Barry Cullen, Email: barry.cullen@dit.ie

Nomenclature

$\dot{C}$	Heat Capacitance Rate, = $\dot{m}C_p$, W/K
C_p	Specific Heat at Constant Pressure, J/kgK
K_L	Heat loss conductance, W/K
K_o	Otto cycle entropy constraint parameter
K_s	Stirling cycle entropy constraint parameter
$\dot{m}$	Mass flowrate, kg/s
$\dot{Q}$	Heat, W
R_v	Otto cycle compression ratio
S	Entropy, J/K
T	Temperature, K
ε	Heat exchanger effectiveness

Subscripts

1,2,3,4	Otto cycle state points
H	Stirling Source temperature
C	Stirling Sink temperature
amb	Ambient
o	Otto Cycle
s	Stirling Cycle

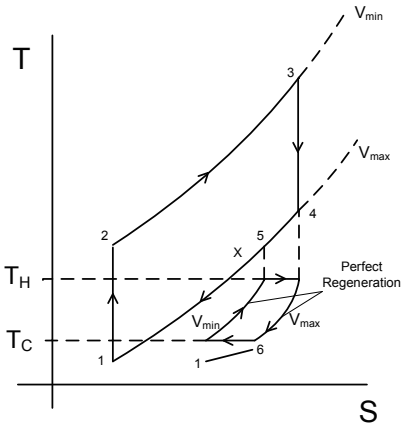

Figure 1: The Combined Cycle represented on the T-S plane

bottoming an Otto cycle for use as a CHP generator. Endo et al [10] have investigated the exergy gains possible from utilising a Rankine cycle as a bottoming cycle on an automotive internal combustion engine. Similar work has been conducted by Chammas and Clodic [11].

Use of the Stirling cycle as a bottoming cycle has been studied also by several different parties, for example [12-15]. Use of the Stirling cycle as a bottoming cycle is of interest due to the high theoretical output and efficiency that could be attained, in addition to potentially smaller plant footprint and quiet operation. Some ongoing work [16-18] has been investigating this alternative combined cycle utilising a Stirling cycle engine as a bottoming cycle on an Otto cycle engine. Whereas these previous works have dealt with the modelling and simulation of the combined cycle for use in instances such as stationary and vehicular power generation, the present work seeks to contribute to the general model by developing an optimised thermodynamic model of the system considering parameters concerning the Stirling engine source and sink heat exchangers: effectiveness (ε) and NTU. This further implies the opportunity to study the optimal heat exchanger area (A) and overall heat transfer coefficient (U). The optimisation procedure can be considered as being in terms of Finite Dimension Thermodynamics (FDT) [19], as the performance of the cycles is considered with regard to the physical characteristics of the heat exchangers.

2. The Combined Cycle

In the combined cycle analysis, the thermodynamic cycles are considered with the Stirling cycle as the bottoming cycle on the Otto cycle. The combined system is depicted on the T-S plane in Fig. 1. Of interest is the optimisation of the combined power output and efficiency under two operating conditions: 1) fixed heat input to the Otto cycle and 2) fixed maximum cycle temperature in the Otto engine. These conditions are analogous to specified fixed fuel consumption of the engine and a metallurgical limit on the system components respectively. The coupling of the two relies on

correct specification of the heat exchanger inventory between both the Stirling cycle source – the Otto cycle exhaust stream, and sink – a water cooling circuit.

The following section details the basic relationships of the mathematical model. Section 4.0 analyses the optima in terms of a fixed heat addition. Section 5.0 provides a similar analysis for the case of imposed maximum cycle temperature in the Otto cycle.

3. Basic Mathematical Model

Depicted in Fig. 1 is the air standard Otto/Stirling combined cycle. The power output of the air standard Otto cycle is readily expressed as:

$$-\dot{W}_{otto} = \left|\dot{Q}_{in} + \dot{Q}_{out}\right| \quad (1)$$

$$-\dot{W}_{otto} = \dot{C}_o[(T_3 - T_2) - (T_4 - T_1)] - K_L(T_3 - T_{amb}) \quad (2)$$

Where K_L is a generalised heat conductance term to account for global losses from the cycle that can not otherwise be accomodated in the analysis. Similarly, the power output of the Stirling cycle can be expressed as:

$$-\dot{W}_{stirling} = \varepsilon_H \dot{C}_o(T_4 - T_H) + \varepsilon_C \dot{C}_s(T_1 - T_C) \quad (3)$$

Where $\dot{C}_o$ and $\dot{C}_s$ are the minimum heat capacitance rates of the Stirling cycle source and sink heat exchangers respectively:

$$\dot{C}_o = \dot{m}_o C_{v,o} \quad (4)$$

$$\dot{C}_s = \dot{m}_s C_{p,s} \quad (5)$$

The entropy balance of the Otto engine, with inclusion for the heat transfer to the Stirling cycle, can be expressed as:

$$\oint \frac{\delta\dot{Q}_{combustion}}{T} + \frac{\delta\dot{Q}_{heat\ transfer}}{T} + \frac{\delta\dot{Q}_{exhaust}}{T} + d\dot{S} = 0 \quad (6)$$

This can be reduced to:

$$\int_{T_2}^{T_3}\frac{dT}{T} + \int_{T_4}^{T_5}\frac{dT}{T} + \int_{T_5}^{T_1}\frac{dT}{T} = -\frac{\dot{S}}{\dot{C}_o} \quad (7)$$

giving the entropy generation constraint for the Otto cycle:

$$K_o = e^{-\frac{\dot{S}}{\dot{C}_o}} = \frac{T_1 T_3}{T_2 T_4} \quad (8)$$

This entropy constraint would permit analysis with inclusion for internal irreversibilities, with $0 < K_o \leq 1$. Under the endoreversible conditions, $K_o = 1$. A similar condition exists for the endoreversible Stirling cycle:

$$\frac{T_{amb}}{T_C} = K_S - \frac{\varepsilon_H \dot{C}_o T_4}{\varepsilon_C \dot{C}_s T_H} \quad (9)$$

Where

$$K_S = 1 + \frac{\varepsilon_H \dot{C}_o}{\varepsilon_C \dot{C}_{sc}} - \frac{\dot{S}_{I,S}}{\varepsilon_C \dot{C}_{sc}} \quad (10)$$

It can be seen from equation (10) that for the endoreversible case, $K_s > 1$. Study of the cycles in the present work is limited to the endoreversible case; however the inclusion of both $K_o$and K_S in the analysis permits investigation with inclusion for irreversibilities.

3.1 Case of Imposed Heat Addition

The objective function of the combined cycle is ultimately the work output. We can achieve an optimum scenario by considering cycle temperatures. The optimum combined work output may most simply be expressed as:

$$-\dot{W}_{TOTAL} = -\dot{W}_{otto} - \dot{W}_{stirling} \quad (11)$$

In order to complete the optimisation, we must specify the constraints to be imposed. In this first scenario, the heat addition to the Otto cycle – and therefore the combined cycle as a whole, is to be fixed. The heat added to the Otto cycle is:

$$\dot{q}_o = \dot{C}_o(T_3 - T_2) - K_L(T_3 - T_{amb}) \quad (12)$$

This serves as the first constraint. This equation expresses the cycle heat addition as that admitted to the engine less a cooling loss term between the engine and the surroundings. This term accounts for non-adiabatic operation of the engine. The other constraints to be considered relate to the endoreversibility criteria. For the Otto cycle:

$$\frac{T_{amb} T_3}{K_o} - T_2 T_4 = 0 \quad (13)$$

For the Stirling cycle, equation (6) acts as the entropy generation constraint.

With these constraints, the objective function therefore becomes:

$$-\dot{W}_{TOTAL} = \dot{q}_o - K_L T_3 + K_L T_{amb} + \dot{C}_o T_{amb} - \dot{C}_o T_4 + \varepsilon_H \dot{C}_o T_4 - \varepsilon_H \dot{C}_o T_H + \varepsilon_C \dot{C}_S T_{amb} - \frac{\varepsilon_C \dot{C}_S T_{amb}}{\left[K_S - \frac{\varepsilon_H \dot{C}_o T_4}{\varepsilon_C \dot{C}_S T_H}\right]} \quad (14)$$

This function represents the combined work output of the combined cycle plant and can be optimised to determine expressions for the optimal cycle temperatures that will maximise the work output. For the condition of imposed heat addition, maximum work output corresponds to maximum efficiency also.

Performing the optimisation provides the optimum temperature relationships detailed in the following.

The temperature at the end of expansion and immediately before exhaust, $T_4{}^*$ can be determined by numerical solution of the polynomial:

$$\frac{(\dot{q}_o + K_L T_{amb}) K_L T_{amb} K_o}{(\dot{C}_o + K_L)(K_o T_4 - \dot{C}_o T_{amb})^2} = \frac{\varepsilon_H}{K_S}\left[\frac{\varepsilon_H \dot{C}_o}{\varepsilon_C \dot{C}_S} + \sqrt{\frac{T_{amb}}{T_4}}\right] \quad (15)$$

The temperature after initial compression of the working gas, $T_2{}^*$ is computed from:

$$T_2{}^* = \frac{\dot{q}_o T_{amb} - K_L T_{amb}{}^2}{[K_o T_4 \dot{C}_o + K_o T_4 K_L - \dot{C}_o T_{amb}]} \quad (16)$$

And the optimum temperature after combustion $T_3{}^*$is determined from:

$$T_3{}^* = \frac{\dot{C}_o T_2{}^* - T_{amb} K_L + \dot{q}_o}{\dot{C}_o + K_L} \quad (17)$$

The optimum temperatures of the Stirling source can be described by:

$$T_H{}^* = \frac{1}{K_S}\left[\frac{\varepsilon_H \dot{C}_o}{\varepsilon_C \dot{C}_S} T_4 + \sqrt{T_{amb} T_4}\right] \quad (18)$$

The corresponding sink temperature can then be derived from equation (10). Power output of the combined cycle can therefore be calculated by substituting the preceding optimal temperatures into equation (11):

$$-\dot{W}_{TOTAL,q}{}^* = \dot{q}_o - K_L T_3{}^* + K_L T_{amb} + \dot{C}_o T_{amb} - \dot{C}_o T_4{}^* + \varepsilon_H \dot{C}_o T_4{}^* - \varepsilon_H \dot{C}_o T_H{}^* + \varepsilon_C \dot{C}_S T_{amb} - \frac{\varepsilon_C \dot{C}_S T_{amb}}{\left[K_S - \frac{\varepsilon_H \dot{C}_o T_4{}^*}{\varepsilon_C \dot{C}_S T_H{}^*}\right]} \quad (19)$$

And efficiency can be calculated in the usual manner:

$$\eta_T{}^* = \frac{-\dot{W}_{TOTAL,q}{}^*}{\dot{q}_o} \quad (20)$$

The preceding analysis offers expressions for power output and efficiency for the combined cycle when the heat supplied to the total system is fixed as an imposed parameter. It is also useful to examine the optimisation of the combined system with a maximum cycle temperature in the Otto cycle used as an imposed constraint. This is given in the next section.

3.2 Case of Imposed Maximum Cycle Temperature

In this scenario, it is assumed that a maximum cycle temperature is to be imposed. This is a common optimisation constraint for thermal power plant and allows consideration of the engine in terms of real metallurgical limits.

In this case, the first imposed constraint becomes:

$$T_3 = T_{max} \quad (21)$$

And the Otto cycle entropy constraint becomes:

$$\frac{T_{amb} T_{max}}{K_o} - T_2 T_4 = 0 \quad (22)$$

Temperature $T_2{}^*$ is computed from the entropy constraint given in equation (22):

$$T_2{}^* = \frac{T_{max} T_{amb}}{K_o T_4{}^*} \quad (23)$$

The optimum heat requirement to the cycle is free to vary subject to the maximum temperature constraint:

$$\dot{q}_{SH}{}^* = \dot{C}_o(T_{max} - T_2{}^*) + K_L(T_{max} - T_{amb}) \quad (24)$$

$T_2{}^*$ is a function of $T_4{}^*$, the optimum temperature after expansion in the Otto cycle. To determine this temperature, the objective function can again be optimised for maximum power and efficiency under the given constraints. Temperature $T_4{}^*$ can therefore once again be calculated by solution of a polynomial:

$$\frac{\dot{C}_o T_{amb} T_{max}}{K_o {T_4}^2} = \dot{C}_o(1-\varepsilon_H) + \frac{\varepsilon_H \dot{C}_o}{K_S}\left[\frac{\varepsilon_H \dot{C}_o}{\varepsilon_C \dot{C}_S} + \sqrt{\frac{T_{amb}}{T_4}}\right] \quad (25)$$

The optimum temperatures for the Stirling cycle are computed as before. This is possible as the source temperature, ${T_H}^*$ is a function of the optimum ${T_4}^*$ for the given constraints. The power output of the combined cycle under the given constraints can therefore be expressed in terms of the optimal temperature values as:

$$-\dot{W}_{TOTAL,T}{}^* = \dot{C}_o\left[T_{max} - \frac{T_{amb}T_{max}}{K_o {T_4}^*} + T_{amb} - {T_4}^*\right] + \varepsilon_H \dot{C}_o({T_4}^* - {T_H}^*) + \varepsilon_C \dot{C}_S T_{amb}\left[1 - \frac{1}{\left(K_S - \frac{\varepsilon_H \dot{C}_O {T_4}^*}{\varepsilon_C \dot{C}_S {T_H}^*}\right)}\right] \quad (26)$$

And the efficiency under these constraints becomes:

$$\eta_T{}^* = \frac{-W_{TOTAL,T}{}^*}{\dot{q}_o{}^*} \quad (27)$$

3.3 Study of Heat Exchanger Parameters: NTU, Heat Transfer Coefficient, Heat Transfer Area

The model equations presented in the foregoing sections offers expressions for the optimal work output as a function of the heat exchanger effectiveness, ε. More direct analysis in terms of physical characteristics of the system can be completed by analysis in terms of the heat exchanger Number of Transfer Units (NTU). The effectiveness-NTU relationship used in the present work is [20]:

$$\varepsilon = 1 - \exp(-NTU) \quad (28)$$

The NTU value is a dimensionless quantity that includes for the heat exchange area, A, the overall heat transfer coefficient, U and the heat capacitance rate, C:

$$NTU = \frac{UA}{\dot{C}} \quad (29)$$

The total NTU for the Stirling cycle engine is considered as the sum of the source and sink heat exchanger NTU values:

$$NTU_T = NTU_H + NTU_C \quad (30)$$

This permits an expression for the heat transfer area distribution for the engine:

$$\left(\frac{A_H}{A_T}\right) = \left(\frac{U_T}{U_H}\right)\left(\frac{\dot{C}_o}{\dot{C}_T}\right)\left[1 - \frac{NTU_C}{NTU_T}\right] \quad (31)$$

This equation allows study of the optimal heat exchanger area distribution in terms of the ratio of the overall heat transfer coefficients, $\left(\frac{U_C}{U_H}\right)$ the ratio of the heat capacitance rates, $\left(\frac{\dot{C}_o}{\dot{C}_S}\right)$ and the NTU ratio $\frac{NTU_C}{NTU_T}$.

4. Results

The optimised system is represented in the following figures for the two cases of imposed heat addition and maximum cycle temperature constraint. The two cases of imposed heat addition and imposed maximum cycle temperature are analysed in section 3.1 and 3.2 respectively. Within each scenario, performance is analysed against heat exchanger effectiveness and NTU separately.

4.1 Imposed Heat Addition

In this scenario, the following parameters were imposed: $\dot{Q}_{in} = 27kW$, $\dot{C}_o = 10W/K$, $\dot{C}_s = 15W/K$, $T_1 = 300K$, $K_L = 0.5W/K$

4.1.1 Heat Exchanger Effectiveness Analysis

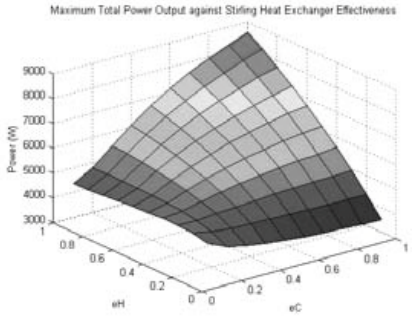

Figure 2. Total Power Vs Heat Exchanger ε

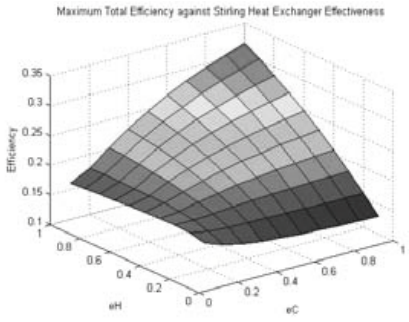

Figure 3. Total Efficiency Vs Heat Exchanger ε

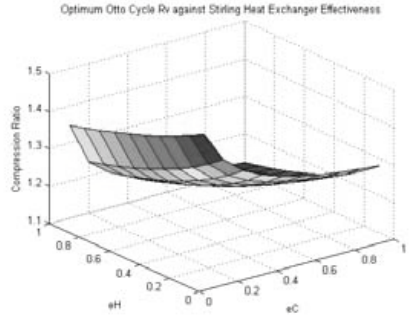

Figure 4. Otto Cycle Optimum Compression Ratio Vs Heat Exchanger ε

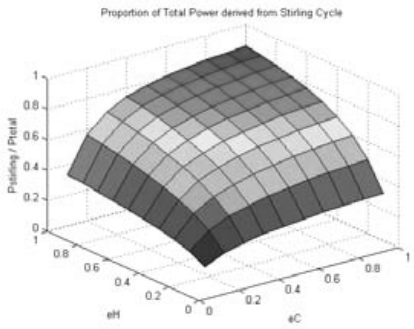

Figure 5. Proportion of Total Power Contributed by Stirling cycle

It is possible also to express the model results against the heat exchanger NTU. This offers the advantage of allowing analysis in terms of the physical inventory of the heat exchangers. It can be seen that an expression in terms of NTU yields a clearer optimum point for Power output and Efficiency, as may be seen in Fig. 6 and Fig. 7.

4.1.2 Heat Exchanger NTU Analysis

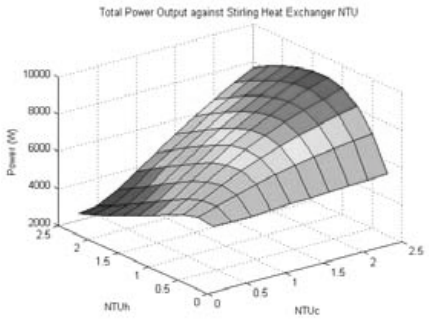

Figure 6. Total Power Vs Heat Exchanger NTU

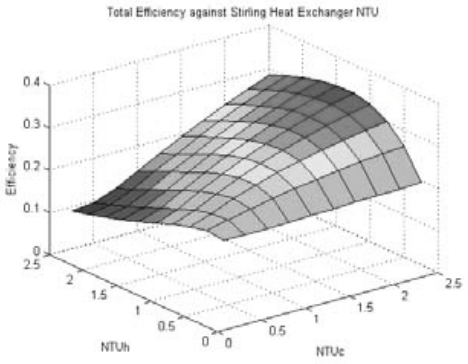

Figure 7. Total Efficiency Vs Heat Exchanger NTU

4.2 Maximum Cycle Temperature

In this scenario, it was desired to investigate the system optimisation considering a maximum cycle temperature of the Otto cycle to be an imposed constraint. The constrained temperature parameter imposed was: $T_3 = T_{max} = 3000K$,

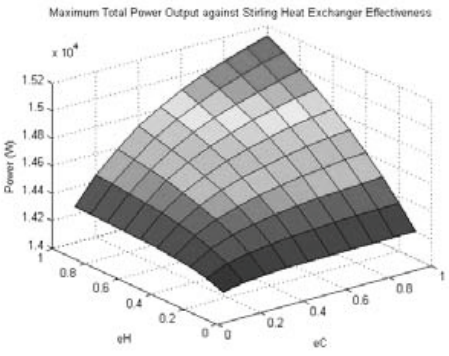

Figure 8. Total Power Vs Heat Exchanger ε

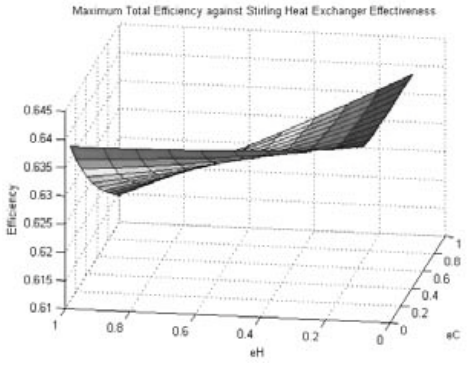

Figure 9. Total Efficiency Vs Heat Exchanger ε

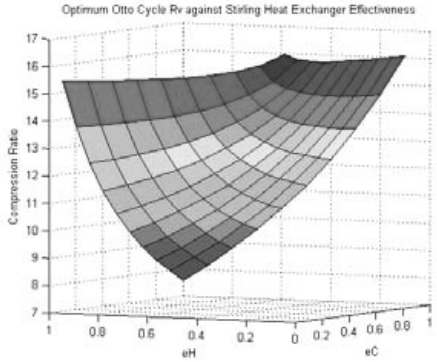

Figure 10. Otto Cycle Optimum Compression Ratio Vs Heat Exchanger ε

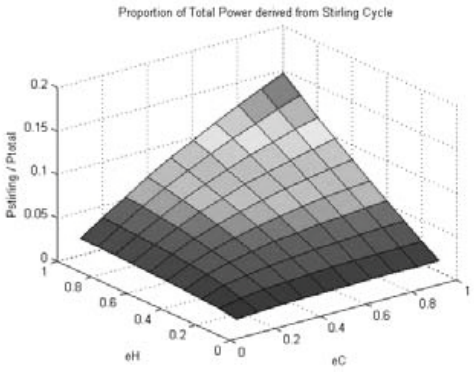

Figure 11. Proportion of Total Power Contributed by Stirling cycle

4.3 Comments

Figures 2 to 11 present the results of the model presented in section 3. Figures 2 to 5 show the results of the analysis for the condition of imposed heat addition to the combined cycle. It is evident from Fig. 2 that maximum power is achieved for the case of maximum heat exchanger performance. Similarly, efficiency increases to a maximum for perfect heat exchange. It is notable though that in order to maximise the total combined output for this constraint, the Otto cycle compression ratio is reduced considerably below typical expected values. This has the net effect of increasing the temperature available at the Stirling source and thereby increasing the power output and efficiency of the Stirling bottoming cycle. These trends are visible in Fig. 4 and Fig. 5. In Fig. 5 it is notable that the Stirling cycle dominates the total power output, accounting for over 80 % of the total output. Figures 6 and 7 show the total combined power output and efficiency as a function of the NTU of each of the Stirling cycle heat exchangers. This method has the advantage of demonstrating a clearer optimum than the case of the heat exchanger effectiveness values. It also permits a clearer analysis in terms of the physical characteristics of the heat exchangers.

Results for the case of imposed maximum temperature in the Otto cycle are presented in Fig. 8 to 11. It is seen that maximum power is achieved at maximum heat exchanger effectiveness, whilst efficiency is minimised at these conditions. As in the case of imposed heat input, it is seen in Fig. 10 that for maximum power conditions, the Otto cycle compression ratio is reduced, although in this instance it remains in the range of that expected for a real engine. This is a consequence of the temperature limitation placed on the cycle. Figure 11 demonstrates that, at most, the Stirling bottoming cycle produces approximately 15% of the total power output.

It is clear from the results presented in section 4 that clear optima exist for each of the analysed constraints. As regards thermodynamic design of a power plant, it is evident that for the case of imposed heat, maximum power and maximum efficiency coincide. To achieve this, the effectiveness of the Stirling heat exchangers must be maximised. For the case of maximum imposed temperature, maximum power and efficiency are not coincident. Maximum efficiency occurs for the case of the Otto cycle acting alone. In this instance, the efficiency gain from the increased compression ratio of the Otto cycle appears to overcome that from the addition of the bottoming cycle, as to increase the power and efficiency of the Stirling cycle the compression ratio is reduced to raise the

temperature of the exhaust, which acts as the thermal source for the Stirling cycle.

5. Conclusions

A thermodynamic model of the combined Otto / Stirling cycle is presented and optimised for maximum total power output, with the Otto exhaust acting as the thermal source to the Stirling cycle. The optimisation is performed for two different imposed criteria. The first imposed constraint is a fixed heat input to the Otto cycle. The second scenario investigated was the case of an imposed maximum cycle temperature for the Otto cycle, T_3. In both scenarios the optimum temperatures in each cycle are presented. Calculation of the optimum temperatures allows calculation of the optimum work in each case.

The novel hybrid system described here, that of the Otto/Stirling combined cycle, is of interest to the power generation industry. Attention is currently being given to the use of Organic Rankine cycle (ORC) systems as bottoming cycles on natural gas fired Otto engines. The Stirling cycle is pertinent as an alternative bottoming cycle due to its high theoretical efficiency, its quiet operation, its compact construction and modest footprint.

References

1. Lopes, J. A. Peças, et al., *Integrating distributed generation into electric power systems: A review of drivers, challenges and opportunities.* Electric Power Systems Research, 2007. **77**(9): p. 1189-1203.
2. Chicco, Gianfranco and Pierluigi Mancarella, *Distributed multi-generation: A comprehensive view.* Renewable and Sustainable Energy Reviews, 2009. **13**(3): p. 535-551.
3. Pepermans, G., et al., *Distributed generation: definition, benefits and issues.* Energy Policy, 2005. **33**(6): p. 787-798.
4. Bayod-Rújula, Angel A., *Future development of the electricity systems with distributed generation.* Energy, 2009. **34**(3): p. 377-383.
5. Rourke, Fergal O., Fergal Boyle, and Anthony Reynolds, *Renewable energy resources and technologies applicable to Ireland.* Renewable and Sustainable Energy Reviews, 2009. **13**(8): p. 1975-1984.
6. Fraser, Peter *Distributed Generation in Liberalised Electricity Markets.* OECD/IEA 2002.
7. Cullen, Barry and Jim McGovern, *The Quest for More Efficient Industrial Engines: A Review of Current Industrial Engine Development and Applications.* ASME Journal of Energy Resources Technology, 2009. **131**(2).
8. Gambarotta, Agostino and Iacopo Vaja, *Internal Combustion Engines bottoming with Organic Rankine Cycles. A thermodynamic analysis.*, in *21st International Conference on Efficiency, Cost, Optimization, Simulation and Environmental Impact of Energy Systems*. 2008, AGH University of Science & Technology, The Silesian University of Technology: Cracow-Gliwice, Poland.
9. Badami, M., et al., *Design and performance evaluation of an innovative small scale combined cycle cogeneration system.* Energy, 2008. **33**(8): p. 1264-1276.
10. Endo, T., et al., *Study on Maximizing Exergy in Automotive Engines*, in *2007 SAE World Congress*. 2007, SAE International: Detroit, Michigan.
11. Chammas, Rody El and Denis Clodic, *Combined Cycle for Hybrid Vehicles*, in *2005 SAE World Congress*. 2005, SAE International: Detroit, Michigan.
12. Yaguchi, H., Sawada,D. , *Exhaust Heat Recovery Apparatus*, United States Patent Office, Editor. 2003, Toyota Jidosha Kabushiki Kaisha: United States.
13. Sawada, D., Yaguchi, H., Mitani, S., *Exhaust Heat Recovery Apparatus*, World Intellectual Property Organisation, Editor. 2007, Toyota Jidosha Kabushiki Kaisha.
14. Mori, M., *Power Device Equipped with Combustion Engine and Stirling Engine*, E.P. Office, Editor. 2004, Honda Motor Co. Ltd.

15. Johansson, Lennart, *Exhaust Gas Alternator System*, U.S.P. Office, Editor. 2003, STM Power Inc.: United States of America.
16. Cullen, Barry, Jim McGovern, Stoian Petrescu, Michel Feidt, *Preliminary Modelling Results for an Otto Cycle / Stirling Cycle Hybrid-Engine-Based Power Generation System*, in *ECOS 2009: 22st International Conference on Efficiency, Cost, Optimization, Simulation and Environmental Impact of Energy Systems*. 2009: Foz do Iguacu, Brazil. p. 2091-2100.
17. Cullen, Barry and Jim McGovern, *Proposed Otto Cycle / Stirling Cycle Hybrid Engine Based Power Generation System*, in *ASME Power 2008*. 2008, ASME Orlando, Florida.
18. Cullen, Barry and Jim McGovern, *Energy system feasibility study of an Otto Cycle / Stirling Cycle hybrid automotive engine.* Energy, 2010. **35**(2): p. 1017-1023.
19. Feidt, Michel, *Optimal Thermodynamics - New Upperbounds.* Entropy, 2009(11): p. 529-547.
20. Incropera, Frank P. and David P. DeWitt, *Fundamentals of Heat and Mass Transfer*. Fifth ed. 2002: John Wiley & Sons.

THERMOECONOMIC OPTIMIZATION FOR AN IRREVERSIBLE HEAT ENGINE MODEL

M. A. Barranco-Jiménez [a], *N. Sánchez-Salas* [b] *F. Angulo-Brown* [b]

[a] *Departamento de Ciencias Básicas, Escuela Superior de Cómputo del IPN Av. Juan de Dios Bátiz s/n. Esq. Miguel Othón de Mendizábal, Col. Lindavista. CP 07738, México D. F*

[b] *Depto. de Física, Escuela Superior de Física y Matemáticas, Instituto Politécnico Nacional, UP Zacatenco, Edif. 9, 2º. Piso, Col. Lindavista. CP 07738, México D. F.*

Abstract: Within the context of Finite Time Thermodynamics(FTT) we study a model of an irreversible thermal engine in terms of the performance cost and the investment cost. Our study is made by the maximization of objective functions defined as the ratio of the power output and the ecological function and the total performing costs respectively. In this work we study the thermoeconomics of an irreversible heat engine with losses due to heat transfer across finite time temperature differences, heat leak and internal irreversibilities in terms of a parameter that is added to Clausius inequality. We calculate the optimal thermal efficiencies under both the maximum power and the maximum ecological function conditions in terms of a economical parameter which is associated to the fractional fuel cost. We show that under ecological conditions the plant dramatically reduces the amount of heat rejected to the environment, and a lost of profits is translated in to an usage of fuels that dramatically reduces the heat rejected towards the environment respect to that of a maximum power regime.

Keywords: Finite Time Thermodynamics, Thermoeconomics Optimization, Irreversible heat engines

1. Introduction

In 1995, De Vos [8] studied the thermoeconomic optimum performance of a nuclear heat engine model, this model was proposed previously by Novikov and Chambadal [10, 5]. The configuration of the engine consists of two heat reservoirs: one at the high temperature T_H and the another at the low temperature T_L, both temperatures are constant. Between the two reservoirs are two components:

- first, a reversible Carnot heat thermal engine,
- second, one irreversible component, a thermal conductor g. (see Fig. 1(a)).

Novikov assumed that hotter side of the Carnot engine is at some variable temperature T_X, if T_X equals to T_H, the engine converts heat into work at its maximum efficiency, *i.e.* at Carnot efficiency, $\eta_C = 1 - T_L/T_H$, but, then the energy conversion occurs infinitely slow and thus, none power, W, is produced. Therefore, Novikov proposed not to maximize the efficiency, η, but rather the power production rate W. He demonstrated that this happens when T_X equals $\sqrt{T_H T_L}$. The conversion efficiency η is lower than de Carnot value and equals to $1-\sqrt{T_L/T_H}$. A few years after, Curzon and Ahlborn (CA) [7] introduced a model for a power plant, with two thermal conductors α and β, see Fig. 1(b), their engine model has two intermediate temperatures, T_X and T_Y. The CA scheme reduces to the Novikov model if the thermal conductance β tends to infinity. It is remarkable that the CA generalization of the Novikov model leads to the same result for the maximum power efficiency, that is,

$$\eta_{CA} = 1 - \sqrt{\frac{T_L}{T_H}}$$

, a value often referred to in the literature as the Curzon-Ahlborn efficiency. In the work published by De Vos[8] he proposed an endoreversible power plant optimized with respect to economical exploitation, the objective function now called profits, are defined by,

$$q = \frac{W}{C}, \tag{1}$$

where W is the power output and C are the running costs of the plant, they consist of two parts:

- a capital cost assumed to be proportional to the investment and, therefore, proportional to the size of the plant, and

Corresponding author: Barranco-Jiménez, Email: mbarrancoj@ipn.mx

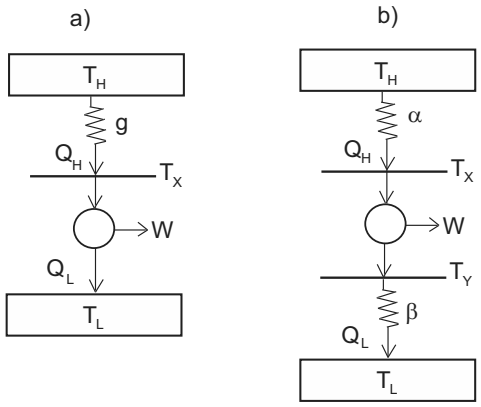

Figure 1: Endoreversible engines. a) Novikov model; b) Curzon-Ahlborn engine.

- a fuel cost that is proportional to the fuel consumption and, therefore, to the heat flows Q_H (see Fig.1).

De Vos assumed that, $Q_{max} = g(T_H - T_L)$, *i.e.* the maximum heat it can be extracted from hot reservoir without supplying work, is an appropriate measure for the size of the plant. Thus, the running costs C of the plant exploitation could be given by

$$C = aQ_{max} + bQ_H, \tag{2}$$

where the coefficients a and b both have the dimension ecu/J.

In his paper, De Vos demonstrated that the efficiency under optimum thermoeconomic conditions, η_{opt}, is between the maximum power value (CA efficiency) and the Carnot efficiency, that is,

$$\eta_{CA} < \eta_{opt} < \eta_C \tag{3}$$

On the other hand, Sahin and Kodal [12], as De Vos did, analyzed an endoreversible heat engine (see, Fig. 1(b) in finite time thermoeconomic context. They defined a new profits as

$$F_P = \frac{W}{C_i + C_f}, \tag{4}$$

where C_i and C_f refer to annual investment and fuel consumption costs, respectively. The investment cost of the plant is assumed to be proportional to the size of the plant, in the same manner as De Vos did, but, Sahin and Kodal assumed that size of the plant can be taken as proportional to the total heat transfer area. Thus, the annual investment cost of the system can be given as,

$$C_i = a(A_H + A_L) \tag{5}$$

now, a, the proportionality coefficient for the investment cost, is equal to the capital recovery factor times investment cost per unit heat transfer area, and its dimension is $ncu/(year\ m^2)$. The unit *ncu* stands for the national currency unit. The annual fuel consumption cost is proportional to the heat rate input, as in the Novikov model, *i.e.*

$$C_f = bQ_H, \tag{6}$$

where, b, is equal to the annual operation hours time price per unit heat input, and its dimension is $ncu/yearkW$.

Recently, Barranco-Jiménez and Angulo-Brown [3, 4], also studied the Novikov model and Curzon and Ahlborn model in the context of thermoeconomic optimization but they proposed as objective function a criterion known as ecological function [1, 9], this criterion also provides an optimum thermal efficiency between CA efficiency and Carnot efficiency and has been proved that the engine operation under this criterion reduces the entropy production. In this work, following the analysis presented by Sahin and Kodal [13], we analyze a thermoeconomic optimization of a irreversible thermal heat engine. In this work we study the thermoeconomics of an irreversible heat engine with losses due to heat transfer across finite time temperature differences, heat leak and internal irreversibilities in terms of a parameter that comes from the Clausius inequality. We calculate the optimal thermal efficiencies under both the maximum power and the maximum ecological function conditions in terms of a economical parameter which is associated to the fractional fuel cost.

2. Theoretical model

The theoretical model considered is shown in Fig. 2, the irreversible heat engine operates between a heat source of temperature T_H and a heat sink of temperature T_L. A T-S diagram of the model including heat leakage, finite time heat transfer and internal irreversibilities is also shown in Fig. 2(b). During the isothermal expansion of the working fluid, the fluid has T_X, the same happens for isothermal compression, in that branch the working fluid gets a T_Y temperature. In this model we considered that the rate of heat flow $\dot{Q}_H$ from the hot source to the heat engine is given by,

$$\dot{Q}_H = U_H A_H (T_H - T_X), \tag{7}$$

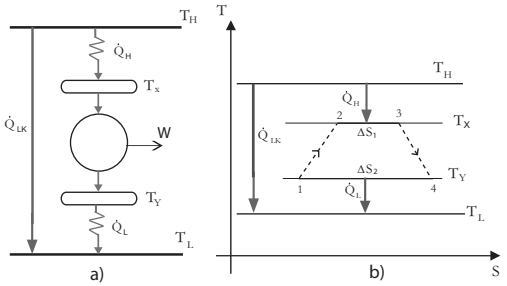

Figure 2: Schematic diagram of the irreversible heat engine and its $T-S$ diagram.

and in the same way for heat flow from working substance to heat sink.

$$\dot{Q}_L = U_L A_L (T_Y - T_L), \tag{8}$$

where U_H and U_L are the heat transfer coefficients, and A_H and A_L are the heat transfer areas of the hot-side and cold-side heat exchangers, respectively. Also it is considered a heat loss from heat interchange between hot thermal source and cold thermal sink directly, the rate of this heat leakage $\dot{Q}_{LK}$ from the hot reservoir at temperature T_H to the cold reservoir at temperature T_L given by,

$$\dot{Q}_{LK} = C_I (T_H - T_L) = \xi U_H A_H (T_H - T_L), \tag{9}$$

where C_I is the internal conductance of the heat engine and ξ denotes the percentage of the internal conductance with respect to the hot-side convection heat transfer coefficient and heat transfer area, that is, $\xi = \frac{\gamma}{U_H A_H}$. Then the total heat rate $\dot{Q}_{HT}$ transferred from the hot reservoir is, $\dot{Q}_{HT} = \dot{Q}_H + \dot{Q}_{LK}$ and the total heat rate $\dot{Q}_{LT}$ transferred to the cold reservoir is $\dot{Q}_{LT} = \dot{Q}_L + \dot{Q}_{LK}$. Applying the first law of thermodynamic, the power output is given by,

$$\begin{aligned} \dot{W} &= \dot{Q}_{HT} - \dot{Q}_{LT} = \dot{Q}_H - \dot{Q}_L \\ &= U_H A_H (T_H - T_X) - U_L A_L (T_Y - T_L). \end{aligned} \tag{10}$$

On the other hand, applying the second law of thermodynamic to the internal part of the model we get,

$$\oint \frac{dQ}{T} = \frac{\dot{Q}_H}{T_X} - \frac{\dot{Q}_L}{T_Y} < 0. \tag{11}$$

One can rewrite the inequality in 11, as,

$$\frac{\dot{Q}_H}{T_X} = R \frac{\dot{Q}_L}{T_Y}, \tag{12}$$

where R is the so-called nonendoreversibility parameter [6, 11]. Substituting 1, and 2, into 12, a relationship between T_Y and T_X is obtained as,

$$\frac{T_Y}{T_L} = \frac{1}{1 - \frac{\psi A_R}{R}\frac{(1-\theta)}{\theta}}; \tag{13}$$

where $\psi = \frac{U_H}{U_L}$, $A_R = \frac{A_H}{A_L}$ and $\theta = \frac{T_X}{T_H}$. The efficiency for this heat engine is given by

$$\eta = 1 - \frac{\dot{Q}_{LT}}{\dot{Q}_{HT}} = \frac{\dot{Q}_H - \dot{Q}_L}{\dot{Q}_H + \dot{Q}_{LK}}; \tag{14}$$

A thermoeconomic analysis of power plants consists in to optimize a profit function defined as the quotient of the appropriate functions (the power output [12, 13, 8] and ecological function [2, 3, 4]), and the annual investment cost taking account both investment and fuel consumption costs. In the same sense as in 4, the profit function in terms of ecological function is given by,

$$F_E = \frac{W - T_L \sigma}{C_i + C_f} \tag{15}$$

where σ is the total entropy production for the engine. Applying the second law to engine (see Fig. 2) σ can be written as

$$\sigma = -\frac{\dot{Q}_H}{T_H} + \frac{\dot{Q}_H}{T_X} - \frac{\dot{Q}_L}{T_Y} + \frac{\dot{Q}_L}{T_L} - \frac{\dot{Q_{LK}}}{T_H} + \frac{\dot{Q_{LK}}}{T_L} \tag{16}$$

By using 4-9, 15 and 16, it is possible to obtain the normalized profit functions, the objective function associated to the power output is given by, $\overline{F}_P = \frac{aF_P}{U_H T_L}$ and the expression for the objective function associated to the ecological function is given by, $\overline{F}_E = \frac{aF_E}{U_H T_L}$, after some manipulations they can be written as:

$$\overline{F}_P = \frac{1 - \left(\frac{\tau}{R\theta - A_R \psi (1-\theta)}\right)}{\left(\frac{1-f}{f}\right)\left(\frac{A_R+1}{U_H T_H A_R (1-\theta)}\right) + 1 + \xi\left(\frac{1-\tau}{1-\theta}\right)} \tag{17}$$

$$\overline{F}_E = \frac{1 + \tau - \left(\frac{2\tau}{R\theta - A_R\psi(1-\theta)}\right) + \left(\frac{1}{R} - 1\right)\frac{\tau}{\theta} + \xi(\tau - 1)\frac{1-\tau}{1-\theta}}{\left(\frac{1-f}{f}\right)\left(\frac{A_R+1}{U_H T_H A_R (1-\theta)}\right) + 1 + \xi\left(\frac{1-\tau}{1-\theta}\right)} \tag{18}$$

where $\tau = \frac{T_L}{T_H}$ and the parameter f, is the relative investment cost of the hot size heat exchanger and cold side, defined as

$$f = \frac{a}{a+b} \tag{19}$$

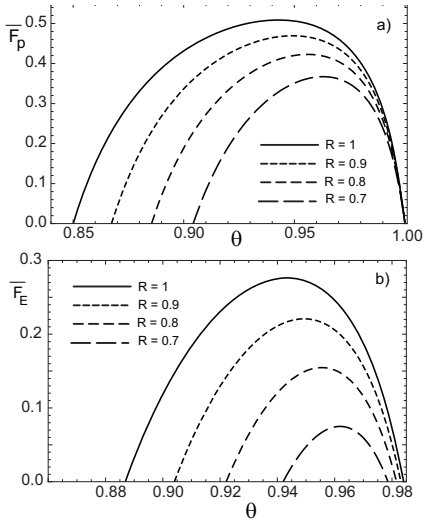

Figure 3: Performance of profits functions a) Associated to power output and b) associated to ecological function, versus θ for several values of R (T_H = 1200 K, T_L = 400 K, A_R = 1, f = 0.7, ψ = 0.5 and ξ = 0.02)

By using, 7, 8, 12 and 14, after some algebra an expression for thermal efficiency can be written as:

$$\eta = \frac{1 - \frac{\tau}{R\theta - \psi A_R(1-\theta)}}{1 + \frac{\xi(1-\tau)}{1-\theta}}. \tag{20}$$

In Fig. 3 we show the profits function ($\overline{F}_P$ and $\overline{F}_E$) respect to independent variable, $\theta = T_X/T_Y$, for several values of R, as we can observe from Fig. 3 there is a critical value for T_X that maximize the profits function, for different values of ψ and f. Then, it is possible to optimize both normalized profits functions (17 and 18) respect to θ. This procedure will be numerically implemented in section 3.

In Fig. 4, for the case of power output, we show the behavior of profits function versus the thermal efficiency of heat engine model, as can be observed it presents a loop paths, distinctive for models with heat leakage.

As can be observed from Fig. 4(a), the profits increases as f increases and the thermal efficiency is independent of this parameter. In Fig. 4(b) the global performance curves are presented for several values of the parameter of internal irreversibility R.

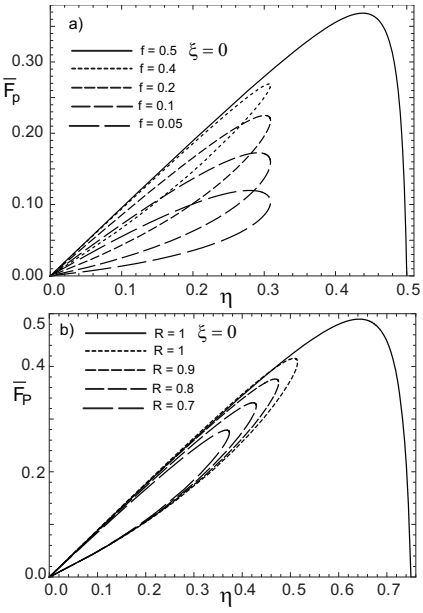

Figure 4: Performance of profits functions associated to power output vs. η, for severals values of a) f and, b) several values of R (T_H = 1200 K, T_L = 400 K, A_R = 1, f = 0.7, ψ = 0.5 and ξ = 0.02).

We also observed that both the profits and the thermal efficiency at optimum thermoeconomical conditions decrease as R increases.

3. Performance Optimization

In Figs. 3(a) and 3(b), we observed that the maximum values for profits function associated to power output and ecological functions, respectively, decrease as R, the internal parameters of internal irreversibility, increases. That is, there is a critical value for θ that maximizes both profits functions. The critical value θ^* that gives maxima values of objective functions, 17 and 18, are obtained by solving numerically the next equations:

$$\left.\frac{d\overline{F}_P}{d\theta}\right|_{\theta^*} = 0, \tag{21}$$

$$\left.\frac{d\overline{F}_E}{d\theta}\right|_{\theta^*} = 0. \tag{22}$$

In Fig. 5, it is shown the numerical solutions for θ^*, the quotient of hot-side temperatures, for optimum profits function associated to the power output (see Fig. 5(a)) and the optimum profits function associated to the ecological function (see Fig. 5(b)). In Fig. 6, we show the optimal thermal efficiencies in

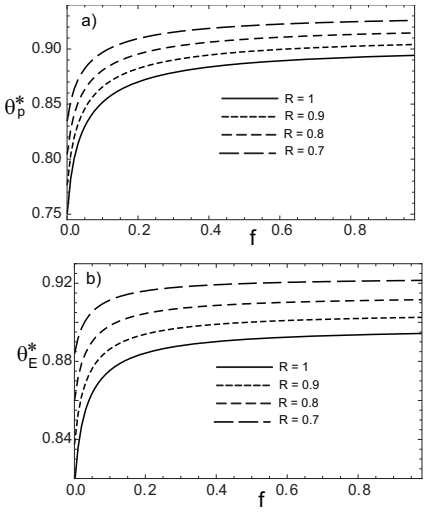

Figure 5: Critical relative temperatures (θ^*) vs. economical parameter f for several values of R. a) For maximum power outpu and b) for maximum ecological function($T_H = 1200\ K$, $T_L = 400\ K$, $A_R = 1$, $\psi = 0.5$ and $\xi = 0.02$).

terms of parameter f, for several values of R. As it can be observed, for all values of f, next inequality is satisfied,

$$\eta_{CA} < \eta_{opt}^{mp} < \eta_{opt}^{me} < \eta_C. \tag{23}$$

Previously, this result has been obtained for optimization of endoreversible heat engines with different heat transfer laws at the thermal couplings [2, 4, 3].

On the other hand, by using the second law of thermodynamics in the heat engine model presented in Fig. 2, we obtain

$$Q_L = \frac{1}{1 - \frac{A_R U_H}{R U_L}\left(\frac{1-\theta}{\theta}\right)} - 1 + \xi \frac{U_H}{U_L} A_R(\tau - 1) \tag{24}$$

being, Q_L the heat flow away to thermal heat sink for the irreversible engine model. Thus, if the heat engine works at MP regime,

$$Q_L^P = \frac{1}{1 - \frac{A_R U_H}{R U_L}\left(\frac{1-\theta_P^*}{\theta_P^*}\right)} - 1 + \xi \frac{U_H}{U_L} A_R(\tau - 1) \tag{25}$$

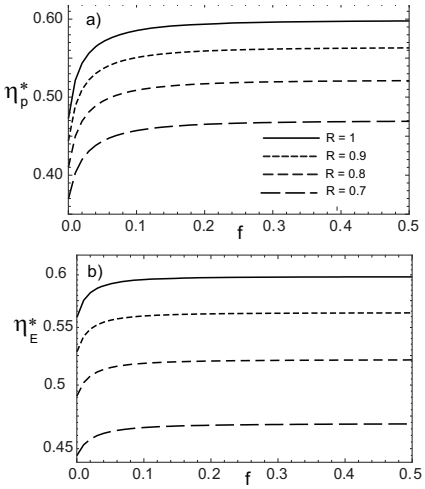

Figure 6: Performance of optimal efficiencies en terms of f for several values of R, a) At maximum power output and b) maximum ecological functions ($T_H = 1200\ K$, $T_L = 400\ K$, $A_R = 1$, $\psi = 0.5$ and $\xi = 0.02$).

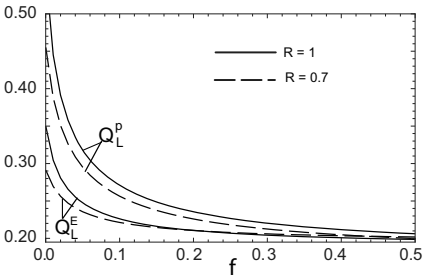

Figure 7: Heat flows give away to cold thermal source at maximum profits function associated to power output and ecological functions respect to f.

Analogously, if the heat engine works at ecological regime,

$$Q_L^E = \frac{1}{1 - \frac{A_R U_H}{R U_L}\left(\frac{1-\theta_E^*}{\theta_E^*}\right)} - 1 + \xi \frac{U_H}{U_L} A_R(\tau - 1) \tag{26}$$

From 25 and 26, it is possible to calculate the heat rejected to cold thermal sink for every value of f, at both MP and ME regimes, and as can be seen in Fig. 7, next inequality is satisfied,

$$Q_L^E < Q_L^P \tag{27}$$

4. Conclusions

In this work, we presented a thermoeconomic performance analysis for an irreversible heat engine model, taking into account the heat leak loss between the external heat reservoirs, and internal dissipation of the working fluid by means of a parameter that comes from the Clausius inequality. We calculated the optimal temperatures of working fluid and, the optimum efficiencies of thermal heat engine in terms of design parameters and another economical parameter associated to investment cost and to the heat transfer areas of the heat exchanger. The effects of the major irreversibilities and the the relative fuel cost parameter on the general and optimal conditions are analyzed and discussed. We obtained that the global performance curves ($\overline{F}$ vs. η), have closed loop shape if there is a heat leakage irreversibility, a typical behavior observed for this kind of irreversibles heat engines. We also presented the analysis of environment impact of the thermal heat engine by means of the heat rejected to cold thermal source, when the engine operates at both optimum profits function associated to the power output and associate to the ecological function, respectively. Our results show that at maximum power output the "waste" energy to environment is bigger than at maximum ecological regime, this same result was previously reported for the case of endoreversible heat engines.

References

[1] F. Angulo-Brown. An ecological optimization criterion for finite-time heat engines. *Journal of Applied Physics*, 69(11):7465–7469, 1991.

[2] M. A. Barranco-Jiménez. Finite-time thermodynamic optimization of a non endoreversible heat engine model. *Revista Mexicana de Física*, 55(3):211–220, 2009.

[3] M. A. Barranco-Jiménez and F. Angulo-Brown. Thermoeconomic optimisation of endoreversible heat engine under maximum modified ecological function. *Journal of the Energy Institute*, 80(4):232–238, 2007.

[4] M. A. Barranco-Jiménez and F. Angulo-Brown. Thermoeconomic optimisation of novikov power plant model under maximum ecological conditions. *Journal of the Energy Institute*, 80(2):96–104, 2007.

[5] P. Chambadal. Les centrales nucleaires. *Armand Colin*, pages 41–58, 1957.

[6] J. Chen. The maximum power output and maximum efficiency of an irreversible carnot heat engine. *Journal of Physics D: Applied Physics*, 27:1144–1149, 1994.

[7] F.L. Curzon and B. Ahlborn. Efficiency of a carnot engine at maximum power output. *American Journal of Physics*, 43(1):22–24, 1975.

[8] A. De Vos. Endoreversible thermoeconomics. *Energy Conversion and Management*, 36(1):1–5, 1995.

[9] L. A. Arias Hernández and F. Angulo-Brown. A general property of endoreversible thermal engines. *Journal of Applied Physics*, 81(7):2973–2979, 1997.

[10] I. I. Novikov. The efficiency of atomic power stations (a review). *Atomimaya*, 3:409–, 1957.

[11] S. Ozcaynak, S. Goktan, and H. Yavuz. Finite-time thermodynamics analysis of a radiative heat engine with internal irreversibility. *Journal of Physics D: Applied Physics*, 27:1139–1143, 1994.

[12] B. Sahin and A. Kodal. Performance analysis of an endoreversible heat engine based on a new thermoeconomic optimization criterion. *Energy Conversion and Management*, 42(9):1085–1093, 2001.

[13] B. Sahin and A. Kodal. Finite time thermoeconomic optimization for irreversible heat engines. *International Journal of Thermal Sciences*, 42(8):777–782, 2003.

Acknowledgments: This work was supported in part by COFAA and EDI-IPN-México.

Nature-inspired Design of a Polymer Electrolyte Fuel Cell

Signe Kjelstrup[a], Marc-Olivier Coppens[b], John Pharoah[c] and Peter Pfeifer[d]

[a] *Norwegian University of Science and Technology, Trondheim*
[b] *Howard P. Isermann Department of Chemical and Biological Engineering, Rensselaer Polytechnic Institute, Troy, N.Y., US*
[c] *Fuel Cell Research Centre, Kingston, Ontario, Canada*
[d] *Department of Physics and Astronomy, University of Missouri, Columbia, US*

Abstract: We apply the condition of uniform entropy production over the membrane area to design a polymer electrolyte membrane fuel cell. The gas supply and water outlet systems, designed to produce entropy uniformly, have a fractal structure inspired by the human lung. The tree-like gas distributor carved into the bipolar plates can eliminate the need for porous transport layers. The amount of catalyst needed is optimized, by reducing the possibility for rate-limiting mass transfer. A numerical example indicates that a fourfold reduction in catalyst material and more than 10 % improvements in the energy efficiency are feasible.

Keywords: Energy efficiency, Diffusional losses, Equipartition of entropy production, Catalyst saving

1. Introduction

The performance of a fuel cell can be diagnosed from its polarization curve, the relation between the electric potential and the current density in the cell, see Fig.1. This curve shows that a large portion of the total energy available for work is dissipated as heat in the cell. The losses vary with the current density. There are always losses connected with the electrode overpotential(s), and with the ohmic resistance loss. But at large current densities, additional losses may occur from mass transfer limitations [1]. The overpotential obtains then contributions from concentration polarization. We will show how these last contributions can be minimized, through optimization of the second-law efficiency and better catalyst utilization [2-4].

The procedure for minimization of entropy production is a rigorous methodology that was already successfully applied to process units like heat exchangers, chemical reactors, and distillation towers. An interesting property emerged from these studies [2]: If the process can take place with sufficient degrees of freedom, the optimal process will follow a trajectory of thermodynamic states, a so-called highway in state-space, characterized by constant local entropy production. Surprisingly, the human lung functions accordingly [3]. The lung has a fractal structure with two distinct scaling regimes: the bronchi where flow dominates transport, and the space-filling acini lined by alveoli, where diffusion dominates transport. It was shown [3] that the entropy production is uniformly distributed in both regimes. These observations are now prompting us to pose the following question related to fuel cell design: Given that constant local entropy production is beneficial to some process units, even to Nature, can we take advantage of this as a guiding principle for fuel cell design? Which gas supply system do we find when the fuel cell is designed using this principle from the outset?

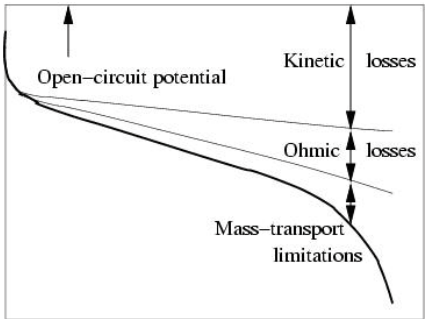

Fig. 1. A typical fuel cell polarization curve, showing the potential losses and their origin

Corresponding author: Signe Kjelstrup Email: signe.kjelstrup@chem.ntnu.no

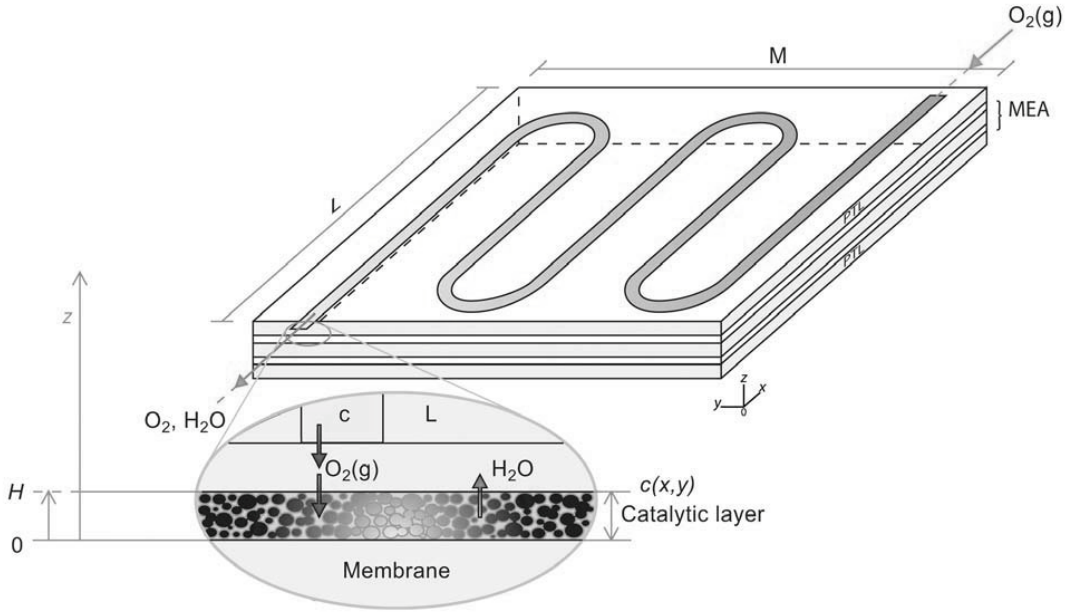

Fig. 2. A typical polymer electrolyte fuel cell membrane electrode assembly (labeled MEA), with porous transport layers (labeled PTL) and serpentine gas supply system for oxygen or air.

In order to answer these questions and obtain numerical insight, we shall use a single PEMFC operating on hydrogen and oxygen or air at 1 bar and 80 ^{o}C. Consider therefore the cell in Fig.2. The catalytic layers are nanoporous, but they appear homogeneous on the micrometer scale. The close-up in the bottom of the figure shows the uniformly packed nanoporous material. The catalytic layers are connected to electric current collectors at the sides of the layers (not shown in the figure).

The rectangular membrane sheet has the area $L \times M$. A point on the planar membrane surface has coordinates (x, y). The catalytic layers on each side of the membrane are of a height H, typically 10-20 μm. This height, measured along the z-axis with the membrane-catalyst interface at position $z = 0$

(see Fig.2, bottom) is one design variable in the

study. The other variable is the macroporosity field ε(x,y), where the macroporosity ε is the fraction of free volume in the layer.

The catalytic layers are supplied with oxygen (air) and hydrogen gas. The oxygen (air) supply system is sketched in Fig.2 as a serpentine channel. There are numerous flow-field designs for the gas supply system [5], and their large impact on the cell performance is well established. Serpentine channels or parallel pathways are most frequent in PEMFC. The flow-field is machined as channel(s) into the so-called bipolar plates. The bipolar plates are clamping the membrane-electrode assembly.

The solution to the questions of higher energy efficiency with minium amount of catalyst, shall be found by redesigning the gas supply system and introducing an appropriate macroporosity field ε(x,y) and heigth H of the catalytic layer.

2. Theoretical Considerations

The aim is to find a local design that results in the optimal global performance of the fuel cell.

On the local scale, we consider an area element $\Delta x\ \Delta y$ of the electrode area on each side of the membrane sheet. The membrane sheet is coarse-grained, such that it can be considered pseudo-homogeneous and continuous, without phase changes. In this coarse-grained representation, the electrodes are subdivided into small areas Δx

Δy around points (x,y) where Δx and Δy are substantially larger than any pore channel diameter in the catalytic layer, but smaller than L,M. When the cell potential, E, across the membrane is measured between these two points and the reaction refers to one Faraday transferred, its value is:

$$E(x,y) = -\Delta G(x,y)/F - R\, j(x,y)\, \Delta x\, \Delta y - \eta^c \qquad (1)$$

Here F is Faraday's constant, R is the total cell resistance, $j(x,y)$ is the electric current density, and η^c is the overpotential of the cathode (the anode overpotential is small). The reaction Gibbs energy is ΔG. The total entropy production of the cell is related to the last two terms. The origins of the potential loss are ohmic resistance, the reaction overpotential, in particular at the cathode, and diffusional losses due to mass transfer limitations [6]. The overpotential is frequently more than 0.4 V out of the theoretical 1.23 V, available at 298 K. The variables in (1) refer to the average concentrations in $\Delta x\, \Delta y$.

Concentration gradients can develop in the z- as well as in the x,y-directions in the catalytic layer, in the porous transport layer, as well as in the nanoporous layer [1], and variations up to 0.2 (0.1) V has been observed perpendicular to (parallel to) the membrane, from such gradients. The production of electric current can thus be diffusion limited.

The total electric current, I, the integral of the local current density $j(x,y)$ over the membrane area, is considered constant, and the oxygen consumption is $J^0 = I/4FLM = j/4F$. In the absence of mass transfer limitations, the Butler-Volmer equation relates the current density at the cathode to the cathode overpotential. The cathode reaction has then been observed to follow first-order kinetics with respect to oxygen giving:

$$J^0 = k_0\, H\, c \qquad (2)$$

where k_0 is the intrinsic kinetic coefficient of the forward reaction (in s^{-1}) and c (in kmol m^{-3}) is the concentration of oxygen gas. [2] showed numerically that processes with a constant demand on the production and with sufficient degrees of freedom, obtained their optimum thermodynamic efficiency when the process was operated along a path with constant uniform entropy production (equipartition of entropy production). In the fuel cell, the process path consists of a series of five steps. The first step is the diffusion of oxygen and water through the porous transport layer (PTL) at the cathode. The next step is the electrochemical reaction and transport in the electrocatalytic layer. The third step is the proton and water transport between the anode and cathode. The fourth and fifth steps are the reaction at the anode and the transport through the PTL on the anode side. Each of these steps should have constant entropy production according to the highway hypothesis [2]. There is one constraint, namely that of constant total electricity production, I from the area $L \times M$ The local electricity production $j(x,y)$ is free in the outset. Under these conditions, an optimal state can be postulated for the fuel cell, with constant local entropy production, having

$$\nabla p(x,y) = C_1 \qquad (3)$$

where p is the pressure and C_1 is a constant. [3] found that this was obeyed in the bronchial tree of the human lung. In the electrocatalytic layers, uniform entropy production means that the overpotential is the same everywhere, or that

$$j(x,y) = j = C_4 \text{ and } c(H) = c^0 \qquad (4)$$

When the current density is the same everywhere, the concentration at $z = H$ is constant. In the ideal case, the concentration is equal to the one at the inlet to the flow system, c^0. The consequences of these criteria for the fuel cell design shall now be discussed.

3. An optimal cell design

3.1. The gas supply system

According to (3,4) the gas supply system must deliver gas as uniformly as possible to all positions (x,y,H) at time t, and likewise remove water as uniformly as possible from all positions (x,y,H). In addition, the steady rate of supply per

unit membrane area, J^0 , must match the rate of consumption, $j/4F$.

The gas supply system for the fuel cell should be compared to the first part of the bronchial tree. According to the statements above, a tree-like channel structure, with the channels only open at the tips of all branches, will obey the conditions stated. Such a structure will deliver the reactant with the same concentration to all positions (x,y). While the gas supply system in the lung is three-dimensional, however, the gas supply system of the fuel cell is preferably quasi-two-dimensional, even though this is not mathematically required. This is because it is practical to give the distributor channels the same height, so that the closed channels can be machined into planar bipolar plates. A proposal that matches these considerations is illustrated in the upper part of Fig. 3, which shows a fractal gas supply system for oxygen. There are several outlets for oxygen. Note that in each fractal distributor the distance between inlet and outlet is identical, leading to uniform distribution or collection conditions. So, the gas is delivered as uniformly as possible over the membrane area and products are collected likewise, to conform with conditions (3,4).

Four generations of branches are shown in Fig.3. This is an example. Two considerations are important for the number of branches. The tips should reach out to most of the membrane area. A large number of branches is favorable from this point of view. On the other hand, it should not be too difficult to manufacture the system. Space limitations and construction complications may thus limit the number. Also, the pressure drop increases with the number of generations. Right angles were chosen in the illustration in Fig.3 for reasons of simplicity. The particular form of branching of the fractal tree, and in particular the angle of a branch with the inlet tube could give uneven pressure reductions at large gas velocities. This is not critical here, because the entropy production in the gas distributor is negligible. The main purpose of the structure is not so much to minimize the entropy production in the structure itself, but rather to provide boundary conditions for the membrane electrode assembly that produce minimum entropy in the next step of the process path.

We can now return to Eq. (3), and see the role of the PTL in view of the above design. If the supply and removal systems are carved into the bipolar plates, these plates can in principle be put directly on to the catalytic layer. Whether this is feasible depends on the number of outlets. With present ways to machine on the micrometer level, this may not be a limiting factor. It may then be an advantage to eliminate the porous transport layer, as its performance depends on operating conditions. A PTL will under many conditions lead to mass-transfer limitations, and produce an extra diffusional regime. With a gas distributor system carved into the bipolar plate, on the other hand, one has pressure-driven flow all the way up to the catalytic layer. This prevents the establishment of diffusional layers much better than the design shown in Fig.2.

The single fuel cell in Fig.3 is thus drawn without the porous transport layer. The total height of the single cell is therefore smaller than that in Fig.2, making concentration gradients less likely than in Fig.2.

3.2. The catalytic layer

We next address the question; which local macroporosity, $\varepsilon(x,y)$, and layer height, H, lead to the highest value of the total cell potential, when cells are compared for the same oxygen consumption, or electric current density cf. (4). The close-up in Fig.3 illustrates the situation we want to optimize. The diameter of the

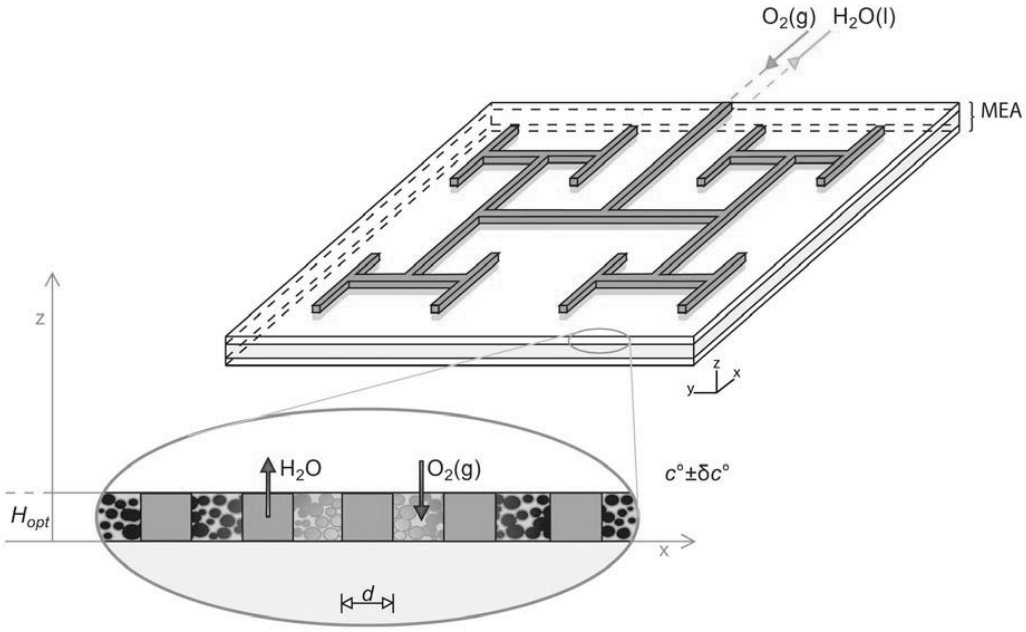

Fig. 3. A polymer electrolyte fuel cell design that minimizes diffusional losses, and saves on catalyst material by introducing macropores in the catalytic layer.

macropores is denoted by *d*, and the width of the columns in the layer that contain the nanoporous catalyst agglomerates by *w*. The two parameters are related via the macroporosity.

How can the reactants gain easier access to the active sites in the catalytic layer than is pictured in Fig.2, given that conditions (3,4) apply? Given a uniform concentration of gases at $z = H$, a sufficient macroporosity should be introduced in this layer, hereby reducing the amount of catalyst needed, while keeping up the same production of electricity.

Consider therefore a nanoporous catalytic layer penetrated by macropores as sketched in the insert of Fig.3. The remaining part of the layer contains columns of nanoporous material with dispersed Pt. The design variables are: (1) the height of the catalytic layer, *H*, and (2) the macroporosity, ε. We have shown that the Lagrangian of the constrained optimization problem is:

$$f = (1-\varepsilon)\, H + \lambda[c^o (Dk\,(\varepsilon-\varepsilon^2))^{1/2} \tanh H\,[(k/D)((\varepsilon-1)/\varepsilon)]^{1/2} - J^o] \quad (5)$$

Here λ is a Lagrange parameter and *D* is the oxygen diffusion constant in bulk pores. The function *f* is minimized with respect to ε, in order to minimize the amount of catalytic material in the volume $V=(1-\varepsilon)HLM$, for a given oxygen flux J^o. The intrinsic rate constant *k* is constant in the optimization. The value of the constant is the one compatible with the (hypothetically valid) Butler-Volmer equation and the current density in question. (5) has a physical solution if there exists a pair (ε, *H)* such that the following flux condition is satisfied:

$$J^o \leq c^o (\mathrm{Dk})^{1/2}/2 = J^{\max} \quad (6)$$

This states that sufficient system resources (c^o, *D, k*) must be available to produce the desired flux. Clearly, not much oxygen reacts if these variables are minuscule. If (6) is fulfilled, then there is a unique solution obtained from the Lagrangian given by:

$$\begin{aligned} \varepsilon_{\mathrm{opt}} &= 0.5 \\ H_{\mathrm{opt}} &= (\mathrm{D/k})^{1/2} \tanh^{-1}(J^o/J^{\max}) \\ d_{opt} &= w_{opt} \end{aligned} \quad (7)$$

Remarkably, the optimal catalyst structure is always given by the macroporosity $\varepsilon_{opt} = 1/2$. Furthermore, H_{opt} depends only on system variables. This means that each MEA should best be designed with a tailored height and a uniform macroporosity of 1/2. This optimum was also found by [8], even though their constraints were different. [8] maximized the yield using a constant volume, rather than minimized the amount of catalyst with a constant production.

The water transport problem in the fuel cell can now be addressed in view of the above findings. It follows from the solution to the optimization (3,4, 7), that water transport out of the cell will be greatly enhanced in the new situation where macropores are introduced in the catalytic layer. Water is produced in the nanoporous layer, and the biggest problem now is connected to water clogging of the nanopores near the catalytic site [1,6]. Facilitated water and oxygen transport are two aspects of the same issue. From the perspective of water removal only, a thick porous transport layer like in Fig.2 is a disadvantage as documented by many authors [9], and we propose that it is eliminated in a first test. The further removal system for water out of the cell should then look similar to the gas supply system. The water outlet system could be shifted upwards or downwards of the oxygen or air outlet system in the bipolar plates.

4. Numerical example

In order to obtain numerical insight, consider the familiar standard E-TEK Elat/Std/DS/V2 gas diffusion electrode, as studied for instance by [10].

We shall need the relation between the overpotential and the current density in (1) under conditions of zero mass transfer limitation. This relation is given by the Butler-Volmer equation, or its representation, the Tafel equation in the high current density regime. The Butler-Volmer equation for the cathode overpotential is

$$j = j_o \left[\exp\left(\alpha\eta/RT\right) - \exp\left((1-\alpha)\eta/RT\right)\right] \qquad (8)$$

where j_o is the equilibrium exchange current density, α is the transfer factor for the overall reaction, R is the universal gas constant and T is the temperature.

Table 1. Predicted change in optimal height of catalyst layer using air as feed at the cathode at 353 K, for the case explained in the text, section 4.

Current density / A m^{-2}	500	15000	15000
Transfer factor α	1.0	1.0	0.8
Overpotential /V	0.238	0.342	0.427
Rate coeff. / s^{-1}		577	2760
Optimal height, H_{opt}/ μm		20	4.1

A typical height of the catalytic layer is 10 μm. In order to assess a possible benefit of introduction of macropores in this catalytic layer, the procedure is a follows.

Determine the intrinsic rate coefficient, k_o, using (8) for a current density which does not imply that diffusional losses are present, and (2) for the oxygen consumption. A typical current density is 500 A m^{-2} membrane (see Table 1) In the presence of air, k_o = 19 s^{-1}, when the equilibrium exchange current density is j_o = 0.2 A m^{-2} membrane, a reasonable value [6], and the transfer factor α=1.0. The ratio catalyst area/ membrane area is taken from [10].

Determine the coefficient k corresponding to a current density in a regime which has diffusional losses, typically 15 kA m^{-2} (cf. Table 1) The outcome of the calculation gives the overpotentials and the rate coefficients listed in Table 1, depending on the transfer factor that we choose.

The maximum oxygen consumption from (6) is more than one order of magnitude larger than the consumption corresponding to the current density, using an oxygen diffusion constant of D= 5.6x 10^{-6} m^2/s [1]. Therefore there is a potential to reduce mass transfer limitations.

It follows from (7) that the optimal height of the layer is 20 μm when the transfer factor α is unity, but 4.1μm if this value changes to 0.8. In the first case, there is no need to introduce any macropores, as the layer height will double, cf. Table 1 (the same

amount of catalyst is needed since the macroporosity is 0.5). In the second case, the height is considerable reduced, and since Pt is absent in the macropores, the saving of catalyst is more than 75%.

The pore diameter size is not part of the solution, but an upper limit on the diameter can be given of 0.05 μm, a realizable number [12].

5. Discussion and conclusion

This work has given the principles of a method to design optimal catalytic layers and gas supply systems in fuel cells, inspired by the geometry of the lung and governed by the principle of equipartition of entropy production [2,7]. The detailed mathematical derivations will be documented in a forthcoming paper. We were able to combine principles previously used in reactor and catalyst design [4,8] and present a new, systematic procedure for energy and material cost reductions. The two optimization methods have been utilized before, but only separately, and for different systems. Chemical reactors and other process units have been optimized with the entropy production as objective function [2,7] and catalyst reduction methods have been studied in reactors and catalyst design [4,8]. This is the first time that both methods are applied in combination, and applied to fuel cells.

The numerical example of application for the standard E-TEK electrode is promising. We have found that the amount of catalyst can be lowered by a factor of four, using published values for the standard E-TEK electrode. This electrode has a loading of 0.5 mg/cm^2, but more efficient electrodes are now available, making coatings of 0.2 mg/cm^2 more typical. From the present optimization method we therefore see that the target set by the U.S. DOE of 0.03 mg/cm^2 becomes within reach. According to this work, the way to achieve this goal is to introduce proper macropores into the catalytic layer.

We have thus presented a method which predicts that the catalyst saving potential can be large. It is reassuring to find that the optimal solution for the catalytic layer is the same as that obtained in other contexts [4,8]. This adds credibility to the present results, in spite of the boundary conditions being somewhat different here. Special here is that the intrinsic kinetic constant is a function of the overpotential.

In order to calculate the optimal height of the catalytic layer, we need to know the diffusion coefficient, the oxygen concentration, the oxygen demand, and the rate constant cf. (7). The last two parameters vary, but their variation is limited in the relevant range. It can be shown that the solution is not so sensitive to the variables.

Bio-inspired flow channel designs have been proposed by others [11]. Also these authors argued that a more uniform distribution be used of gases over the membrane sheet, without formulating a physical reason for it, however. Their results are promising in the present context. Their leaf and lung designs gave a 30 % improvement in energy performance of the PEM fuel cells. The present work, not only explains why this is so, but also gives a mathematical procedure for further improvements, resulting from a rational, nature-inspired design procedure, rather than from an empirical, biomimetic procedure.

Results on water clogging and its detrimental effects on the performance of fuel cells [9], can now be seen in new light. Modeling as well as experimental results show that clogging of such pores is responsible for significant performance losses, of the order of 10 % of the total potenial, see [9] and references therein. By introducing macropores in the catalytic layer, one enhances the possibility for water to escape greatly. And this possibility to escape is further enhanced, because we may avoid the porous transport layer altogether. On top of that, we can also tailor the water removal channels, that mimicks the supply gas distributor of Fig.3, by making the walls hydrophobic.

The question of cell lifetime can be addressed on the background of the condition set, that of uniform distribution of entropy production or energy dissipation. More uniform conditions across the cell represent less stresses on the catalyst and the transport system. It is therefore expected that also the cell lifetime, will benefit from the new design.

Heuristically, it follows that a stack is optimal in the thermodynamic sense when all single cells obey optimal conditions. The constants may differ between the cells in a stack if the oxygen

condition at the inlet varies from one cell to the next. But they may be the same, if all cells are fed by the same supply. Construction of cell stacks can thus be made following the same guidelines.

The conclusions reached above, have been based on theoretical considerations. It now remains to validate the results experimentally by building a cell, proving that better energy efficiencies can indeed be realized in practice for the proposed structure. The present results, supported by [11], indicate that this may be worthwhile, as the gains seem to be significant.

Acknowledgements: The authors are grateful to the Center for Advanced Study at The Norwegian Academy of Science and Letters for extraordinary sabbatical stays.

References

[1] Harvey, D., Pharoah, J.G., and Karan, K., 2008, A comparison of different approaches to modeling the PEMFC catalyst layer, J. Power Sources 179, pp. 209-219.

[2] Johannessen, E. and Kjelstrup, S., A highway in state space for reactors with minimum entropy production, 2005, Chem. Eng. Sci. 60, pp. 3347-3361.

[3] Gheorghiu, S. et al., 2005, In: *Fractals in Biology and Medicine*, Vol IV (G.A. Losa, D. Merlini, T. F. Nonnenmacher, E.R. Weibel, Eds), Birkhäuser Verlag, Basel, pp.31-42.

[4] Wang, G. et al., 2007, Optimizing transport in nanostructured catalysts: A computational study, Chem. Eng. Sci. 62 pp. 5110-5116.

[5] Li, X., and Sabir, I., 2005, Review of bipolar plates in PEM fuel cells: Flow-field designs. Int. J. Hydrogen Energy 30, pp. 359-371.

[6] Eikerling, M., and Kornyshev, A.A., 1998, Modelling the performance of the cathode catalyst layer of polymer electrolyte fuel cells, J. Electroanal. Chem. 453, pp. 89-106.

[7] Kjelstrup, S., Bedeaux, D., and E. Johannessen, E., 2007, *Elements of irreversible thermodynamics for engineers*, 2nd. Rev. ed. Tapir Academic Publishers, Trondheim.

[8] Johannessen, E., Wang, G., Coppens, M.-O., 2007, Optimal distributor networks in porous catalyst pellets. I. Molecular diffusion, Ind. Eng. Chem. Res. 46, pp. 4245-4256.

[9] Ihonen, J., Mikkola, M., Lindbergh, G., 2004, Flooding and gas diffusion backing in PEFCs. Physical and chemical characterisation. J. Electrochem. Soc. 151, pp. A1152-A1161.

[10] Meland, A.-K., Kjelstrup, S., Bedeaux, D. 2006, Rate-limiting proton hydration in the anode of the polymer electrolyte fuel cell, J. Mem. Sci. 282, pp. 96-108.

[11] Kloess, J.P. et al., 2009, Investigation of bio-inspired flow channel designs for bipolar plates in proton exchange membrane fuel cells, J. Power Sources 188, pp. 132-140.

[12] Wang, G. and Coppens, M.-O., 2008, Calculation of the optimal macropore size in nanoporous catalysts and its application to $DeNO_x$ catalysis, Ind. Eng. Chem. Res. 47, pp. 3847-3855.

A Parametric Study of a PEMFC Flow Field using a Constructal Radial Design

I. Pérez-Raya, A. Hernández-Guerrero, F. Elizalde-Blancas, D. Juárez-Robles
Department of Mechanical Engineering, University of Guanajuato
Salamanca, Gto., Mexico

Abstract: This work presents the results of a parametric study for the flow field of a PEMFC with a radial configuration. The parametric study is based on the constructal theory with a geometrical variation of the number and length of the flow deflectors. The objective of the study is to find the optimal geometry that distributes in a more efficient way the reactant gases that produces a lower pressure drop and the most uniform current density distribution. The proposed design on this work shows an improvement on the cell performance, with a better use of the reaction area compared with previous designs. The results also show that the effect of channeling the flow inside of these radial configurations helps to improve the cell performance.

Keywords: Fuel Cell Performance, Constructal, Power, Polarization Curves.

1. Introduction

In a conventional PEM fuel cell the reactant gases flow through the flow channels. The distribution of gases to the cell reaction area is the main function of the channels, allowing the reactant gases to diffuse into the catalyst layer through the gas diffuser layer (GDL), and then take part in the electrochemical reactions.

A significant amount of investigations has been carried out on flow channel design, finding that the fuel cell performance strongly depends on the design of these flow channels. The channels not only form the shape of the bipolar plates, they also supply the reactant gases to the fuel cell active area. Water management and gases distribution depend greatly on the channel design.

Significant differences on the performance between each design have been reported in the literature. Some reported configurations of the flow field include: i) Parallel, ii) Serpentine, iii) Fractal, iv) Interdigitated, v) Spiral, vi) Bifurcation, vii) Radial configuration.

Voss et al. [1] presented one of the first radial configurations for a fuel cell, see Figure 1. In their configuration the inlet of the reactant gases is at the center of the cell, then the flow is oriented through triangular arrangements that form radial channels. These channels are distributed in a radial form throughout the fuel cell reaction area.

Due to the fact that the reactant gases flow through the less blocked channels, the water accumulates at the zones with the lower flow of gases. For this reason, the fuel cell presented by [1] has a low efficiency. This configuration has an inadequate water management.

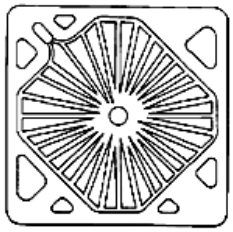

Figure 1. Radial design with triangular elements [1].

In order to improve water management [2] proposed a better design applying the flow interdigitated concept, see Figure 2.

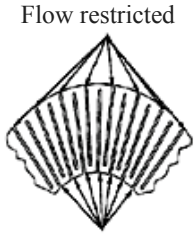

Figure 2. Interdigitated radial design [2].

In the interdigitated radial design, the gases flow in a radial direction through the channels. At the end of the channels the gases are forced to flow into the diffusion layer. Flooding disappears in

Corresponding Author: A. Hernandez-Guerrero, e-mail: abelh@salamanca.ugto.mx

these regions and a better mass transport into the fuel cell is produced.
Cano et al. [3] proposed a radial design with the gases entrance located also at the center of the cell, from which the gases are distributed through the radial channels. The design proposed by [3] has the characteristic of producing a high current density near the gases inlet. However, overall, the current production in the cell is non-uniform, due to the lower uniform species distribution along the channels. Figure 3 shows the channel flow design proposed by [3].

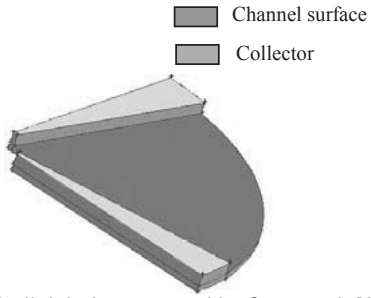

Figure 3. Radial design proposed by Cano et al. [3].

This work presents the results of a parametric study of a new design of bipolar plates (see Figure 1). The parameterization is represented by equation 1, and has the control of the length and number of elements in contact in the proposed design.

The new configuration has been created in order to improve the performance of the cell and to observe the effect of flow orientation through the radial channels. The principles of the constructal theory are used as a base to optimize the fuel cell performance. This theory aims to determine the most relevant architectures that maximize the performance of a phenomenon [4]. For instance, Wechsatol et al. [5] varied the radial geometry of a microchannel network in order to dissipate heat from a circular plate minimizing the pressure drop.

2. Model description

Showing in Figure 4 is a sketch of the design of the base case considered in the presented study model. An analysis about the effect of the number of rows and the length was performed. The length of the elements $_j$ was parameterized as:

$$L_i \quad F\_{o}^{n} \quad 1 \quad i \quad n \qquad (1)$$

F is a parameter chosen in such a way that:

$$\sum_{i\ 1}^{n} L_i \quad F \sum_{i\ 1}^{n} \_{o}^{n} \quad 2.25 \quad 0.5(n \quad 1) \ mm \qquad (2)$$

Table 1, shows the range of the n and $_0$ parameters that was analyzed. The width of the rectangular elements considered in the present study, shown in Figure 4, is 0.5 mm. The number of elements in each row was determinate by the restriction that the distance between two adjacent elements could not be less than 0.4 mm. At the same time, the length of the elements could not be less than 0.4 mm. The reason of the previous restrictions is because of the necessity to make geometries that could be machinated in usual manufacture laboratories. In that case for the parameterized analysis there were geometries that not were built. The number of elements considered in each row is shown in Table 1.

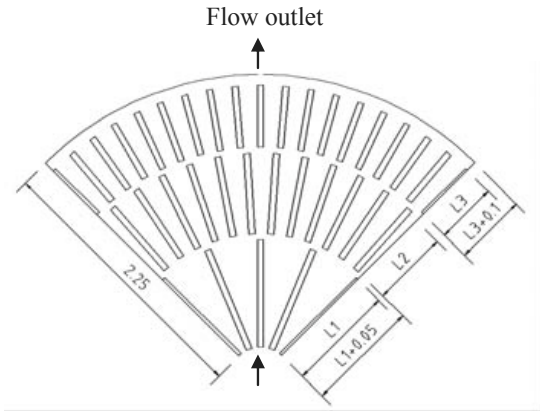

a) 2D sketch showing the length of the elements in the parameterization (dimension in cm).

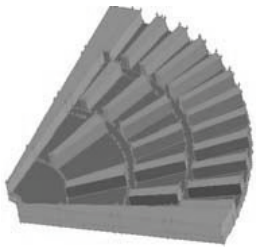

b) 3D representation of the computational domain.

Figure 4. Radial design proposed in the present study for the flow field.

Table 1. Analyzed geometries.

N	φ_0 Values					Elements number in the n_i row
	0.25	0.5	0.75	1	1.25	
1						16
2						48
3						72
4						70
5						70
6						70

The geometry has 16 inlets, 4 outlets, and different number of elements in each row equally distributed.

3. Computational model

This section provides the information considered on the model that was used for the present analysis.

3.1 Numerical model

Figure 5 shows the three-dimensional sketch of a fuel cell. Hydrogen and air at 100 % relative humidity are used as reactant gases for the anode and cathode side, respectively. A value of 0.79/0.21 was taken for the relation Nitrogen/oxygen.

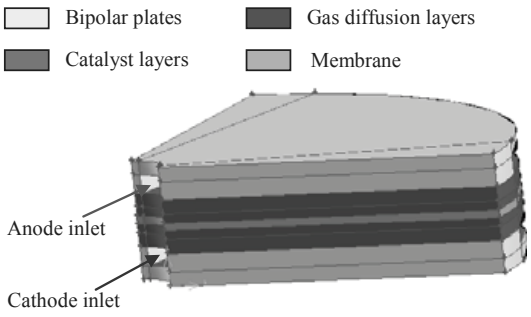

Figure 5. Components of the fuel cell.

Table 2 shows the dimensions and properties used in the current model. The only difference between the models is the flow field geometry, in order to compare the results obtained for each model.

The reference current density has been taken as 1 A/cm^2, for both models. The inlet velocities of the fuel and the oxidant were kept constant in all the cases. It is considered that the hydrogen oxidation reaction and the oxygen reduction reaction only occur at the catalyst layer/membrane interface.

Table 2. Dimensions and properties used in the analysis.

Description	Value
Channel length ($L_{channel}$)	22.5 mm [3]
Channel height at the inlet ($H_{channel}$)	1 mm [3]
Channel width at the inlet (W)	1 mm [3]
GDL thickness (H_{GDL})	0.5 mm [3]
CL thickness (H_{CL})	0.025 mm [3]
Membrane thickness (H_{mem})	0.128 mm [3]
GDL porosity (ε_{GDL})	0.4 [6]
CL porosity (ε_{CL})	0.4 [6]
GDL Electrical conductivity (σ_{GDL})	53 $\Omega^{-1}m^{-1}$ [6]
CL Electrical conductivity (σ_{CL})	53 $\Omega^{-1}m^{-1}$ [6]
Reference exchange current density at the anode side ($j_{0,a}^{iref}$)	1.0 x 10^9 A m^{-3} [7]
Reference exchange current density at the cathode side ($j_{0,c}^{iref}$)	3 x 10^5 A m^{-3} [7]

3.2 Model assumptions

A computational three-dimensional model is built for the geometry presented in Figure 4. A computational model is used to analyze the electrochemical reactions occurring at the catalyst layer/membrane interface (for both, anode and cathode side). In other zones, such as the gas diffusion layer, no chemical reactions occur. The assumptions used in the model are:

1. Steady state.
2. The reactant gases are considered as ideal gases.
3. Constant temperature inside the cell.
4. Laminar flow.
5. Constant thermal properties.
6. Isotropic materials.

3.3 Governing equations

The model solves the energy, mass conservation, species transport and electric potential equations. The coupled governing equations are solved using a software based on the finite volume technique, Fluent®, which already includes the source terms.

$$\nabla \cdot (\rho \bar{u}) = S_i \quad (3)$$

$$\bar{u}\nabla \cdot (\rho \bar{u}) = -\nabla P + \nabla \cdot (\mu \nabla \bar{u}) + S_p \quad (4)$$

$$\bar{u} \cdot \nabla \cdot (\varepsilon \rho Y_{H_2}) = \nabla \cdot \bar{J}_{H_2} + S_{H_2} \quad (5)$$

$$\bar{u} \cdot \nabla \cdot (\varepsilon \rho Y_{O_2}) = \nabla \cdot \bar{J}_{O_2} + S_{O_2} \quad (6)$$

$$\bar{u} \cdot \nabla \cdot (\varepsilon \rho Y_{H_2O}) = \nabla \cdot \bar{J}_{H_2O} + S_{H_2O} \quad (7)$$

$$\nabla \cdot (\sigma_{sol} \phi_{sol}) + S_{sol} = 0 \quad (8)$$

$$\nabla \cdot (\sigma_{mem} \phi_{mem}) + S_{mem} = 0 \quad (9)$$

The terms added to the governing equations, better known as source terms, see Table 3, take into account the electrochemical effects occurring in the cell.

Table 3. Source terms.

Volume	Source term	
Anode catalyst	$S_{H_2} = -\frac{M_{H_2}}{2F} R_a$	(10)
	$S_i = S_{H_2} + S_{H_2O}$	(11)
	$S_{sol} = -R_a$	(12)
	$S_{sol} = +R_a$	(13)
Cathode catalyst	$S_{O_2} = -\frac{M_{O_2}}{4F} R_c$	(14)
	$S_{H_2O} = -\frac{M_{H_2O}}{2F} R_c$	(15)
	$S_i = S_{O_2} + S_{H_2O}$	(16)
	$S_{sol} = +R_c$	(17)
	$S_{mem} = -R_c$	(18)
GDL	$S_p = -\frac{\mu}{\beta} \bar{u}$	(19)

The source terms are non-zero at the specified zone or volume; otherwise their value is zero. S_a and S_c represent the current density at the anode and cathode side, respectively, defined as:

$$S_a = j_a^{ref} \left(\frac{[H_2]}{[H_2]_{ref}} \right)^{\gamma_a} \left(e^{\alpha_a F \eta_a / RT} - e^{-\alpha_c F \eta_a / RT} \right) \quad (20)$$

$$S_c = j_c^{ref} \left(\frac{[O_2]}{[O_2]_{ref}} \right)^{\gamma_c} \left(- e^{\alpha_a F \eta_c / RT} + e^{-\alpha_c F \eta_c / RT} \right) \quad (21)$$

The driving force the kinetics is the local surface over-potential, η, also known as the activation loss. It is given by:

$$\eta_a = \phi_{sol} - \phi_{mem} \quad (22)$$

The gain in electrical potential from crossing from the anode to the cathode side is taken into account by subtracting the open-circuit voltage V_{oc} on the cathode side.

$$\eta_c = \phi_{sol} - \phi_{mem} - V_{OC} \quad (23)$$

The open circuit voltage is reported in [8] as:

$$V_{oc} = 0.0025T + 0.2329 \quad (24)$$

In the transport species equation, the mass diffusion flux, $J_{i,\xi}$, is defined as:

$$J_{i,\xi} = -\rho D_i \frac{\partial Y_i}{\partial \xi} \quad (25)$$

Um et al. [7] define D_i, as:

$$D_i = \varepsilon^{1.5} D_i^0 \left(\frac{P_0}{P} \right) \left(\frac{T}{T_0} \right)^{3/2} \quad (26)$$

Where D_i^0 is the diffusivity of the specie i at the reference temperature and pressure. Nguyen and White [9] proposed the calculus of the water diffusion coefficient, D_w, as

$$D_w = 5.5 \times 10^{-11} n_d \exp\left[2416 \left(\frac{1}{303} - \frac{1}{T_s} \right) \right] \quad (27)$$

The driving force for the water transport is defined as:

$$\alpha(x, y) = n_d(x, y) - \frac{F}{I(x, y)} D_w(x, y) \frac{C_{wc} - C_{wa}}{t_a} \quad (28)$$

where n_d represents the electro-osmotic drag coefficient, that is a function of the water activity at the anode side. It is calculated using the follow equation:

$$n_d(x, y) = 0.0049 + 2.02 a_a - 4.53 a_a^2 + 4.09 a_a^2$$
$$a_a \le 1$$
$$n_d(x, y) = 1.59 + 0.159(a_a - 1)$$
$$a_a > 1 \quad (29)$$

The water concentration at the anode and cathode side, C_{wa} y C_{wc}, respectively, is calculated by:

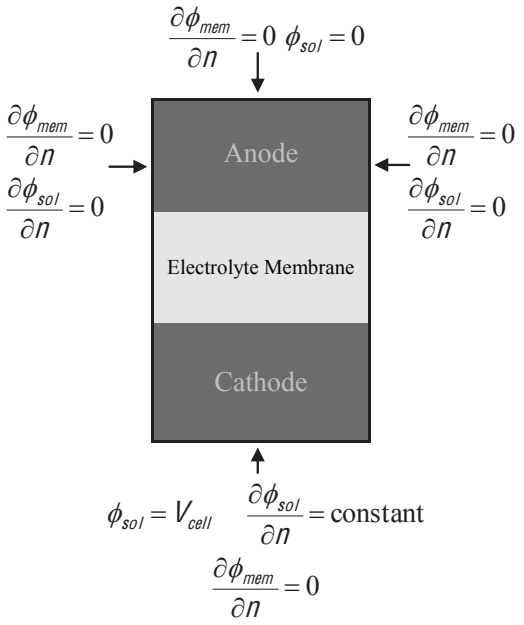

Figure 6. External boundary conditions.

$$C_{w,k}(x,y) = \frac{\rho_{m,dry}}{M_{m,dry}}(0.0403 + 17.8a_k - 39.8a_k^2 + 36a_k^3)$$
$$a_k \le 1$$
$$C_{w,k}(x,y) = \frac{\rho_{m,dry}}{M_{m,dry}}\left(14.0 + 1.4(a_k - 1)\right) \quad (30)$$
$$a_k > 1$$

The k subscript represents the anode and cathode sides, and $\rho_{m,dry}$ and $M_{m,dry}$ are the density and molecular weight, respectively, of the dry membrane. The water activity is defined as:

$$a_k = \frac{X_{w,k}(x,y)P(x,y)}{P_{w,k}^{sat}} \quad (31)$$

where, $X_{w,k}$ represents the molar fraction of water in the anode and cathode. The saturation pressure of water [10-11] is calculated by:

$$\log_{10} P_{w,k}^{sat} = -2.1794 + 2.953\times10^{-2}(T - 273.15) + 9.1837\times10^{-5}(T - 273.15)^2 + 1.4454\times10^{-7}(T - 273.15)^3 \quad (32)$$

Springer [12] defines the membrane conductivity, σ_{mem}, as:

$$\sigma_{mem} = \varepsilon(0.514\lambda - 0.326)e^{1268\left[\frac{1}{303} - \frac{1}{T}\right]} \quad (33)$$

where λ represents the water content, defined as:

$$\lambda = 0.043 + 17.18a_a - 39.85a_a^2 + 36.0a_a^2$$
$$a_a \le 1$$
$$\lambda = 14.0 + 1.4(a_a - 1)$$
$$a_a > 1 \quad (34)$$

3.4 Boundary conditions

The boundary conditions are defined at the inlet, outlet, walls and at the interfaces between consecutive layers. At the outlet, the gauge pressure is defined equal to zero, considering that the gases are discharged to the environment. The principal boundary conditions around the computational domain are shown in Figure 6.
At the interface between the flow channels and the bipolar plates, the velocity and the mass flow are equal to zero. At the interface between the flow fields ant the GDLs the velocity, mass flux, species concentration and species flux are all continuous, and it was considerate like porous jump. At the interface between GDLs and the CLs, the velocity and concentration conditions are similar to those at the interface between the flow fields and the GDLs. At the interface between the CLs and the membrane the mass flow is zero because the hydrogen cannot pass through the membrane.

The inlet flow rates for the anode and cathode has been defined using the stoichiometric flow ratio, ζ, which is defined as the quantity of reactant fed to the fuel cell, divided by the required quantity in the electrochemical reaction. Thus:

$$\zeta_C = X_{O_2,in}\vartheta_{c,in}\frac{P_C}{RT}\frac{4F}{I_{ref}A} \quad (35)$$

$$\zeta_a = X_{H_2,in}\vartheta_{a,in}\frac{P_a}{RT}\frac{2F}{I_{ref}A} \quad (36)$$

4. Results

The numerical results are validated with the study of [8]. They carried out an analysis of a straight channel for a PEM fuel cell. Their geometry presents the advantage of being a simple model as compared with other experimental analyses. Um et al. [8] obtained an experimental polarization curve for the straight channel at the Penn State Electrochemical Engine Center (ECEC).

The operating conditions for the validation of the model are presented in Table 4.

Table 4. Operating conditions of the cell [8].

Description	Value
Cell temperature (°C)	70
Operating pressure (atm)	2
Relative humidity for the fuel entrance (%)	100
Reference current density (A cm^{-2})	1
Stoichiometric ratio for the anode	1.5
Relative humidity of the air at the inlet (%)	100
Stoichiometric ratio for the cathode	2
Nitrogen/oxygen mole fraction at the inlet	0.79/0.21

Figure 7 shows the comparison between the present numerical model and the experimental results of the polarization curve for the fuel cell of [8]. The comparison shows a small variation at high current densities, due to the assumptions considered in the model. However, the differences are minimal and the results present a similar behavior.

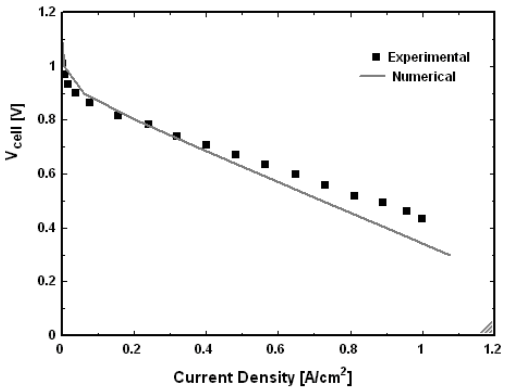

Figure 7. Comparison of the polarization curves between numerical and experimental results.

The fuel cell global performance can be explained by the polarization curves. The polarization curves represent the cell operation voltage versus the current production and it represents the principal irreversibilities on the fuel cell. Figure 8 shows the polarization curves for some geometries which have the same value for the parameter φ_0 and a different value for the variable n. As it can be seen in Figure 8, the activation losses for all the geometries are similar at low current densities. The concentration losses present at high current densities tend to increase conform n decreases. It is because low n values do not have as much uniformity concentration distribution as with high values of the parameter n.

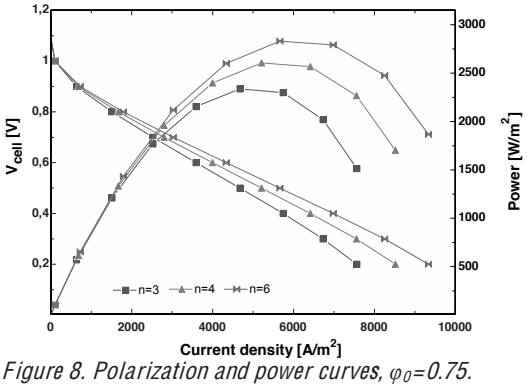

Figure 8. Polarization and power curves, φ_0=0.75.

The species concentration distribution for the extreme models is presented in Figure 9. There is a significant difference between these models. The geometry with the lowest n value (n=3) presents a fastest fuel consumption whereas the geometry with the highest n value (n=6) has a more uniform distribution on the reaction area. Flow outlets define the tendency of the flow; however, Figure 9 also shows that the proposed geometry does not have zones with a significant difference in concentration species.

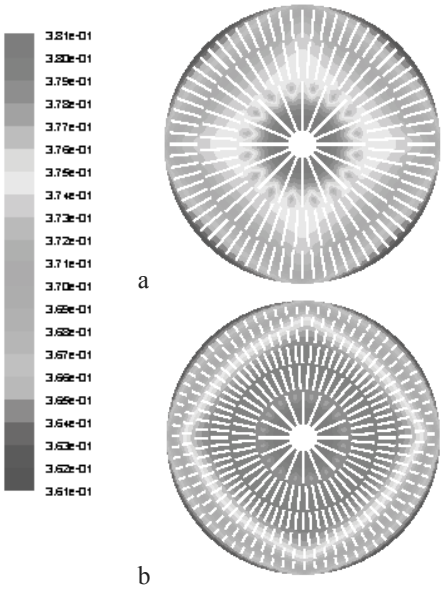

Figure 9. Distribution of the molar fraction of hydrogen for a) n=3, φ_0=0.75 b) n=6, φ_0=0.75.

The effect (, ($_0$ can be shown by the polarization and power curves for the geometries that have a same value of the n parameter, see Figure 10. A similar trend as in the previous case occurs, the higher the value of $_0$, the lower the concentration losses, and much more power is generated. It is important to note the low power developed for n=3 and $_0$=0.25, caused by the inefficient flow distribution of this geometry.

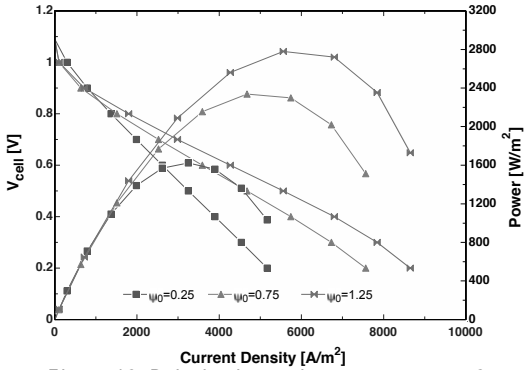

Figure 10. Polarization and power curves, n=3.

In order to compare the parameters, n and $_0$, Figure 11 shows a comparison of the effect of both parameters at the average current density obtained at 0.6 V. The effect of the variation of the parameter $_0$ has a stronger effect on the current density than the number of rows (n). This result also shows that the highest value of the number of rows does not have the better distribution flow field; in that case it is necessary to compare the models that showed the highest average current density.

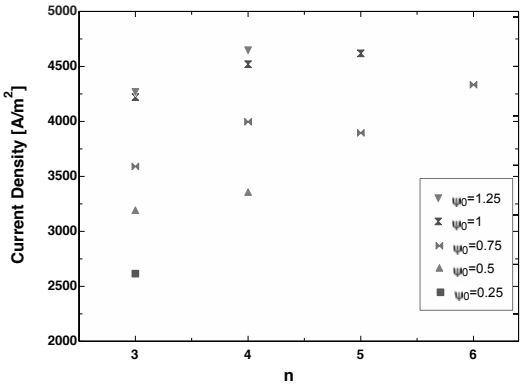

Figure 11. Average current density for the studied models, V_{cell}=0.6 V.

Figure 12, shows the power curves for the above mentioned cases. The geometry with the larger number of channels is not the case with the more power generated. The production power capacity for the geometries n=5 and n=4 is almost the same and both of them show more power generated than the geometry n=6. The geometry with n=4 has a little more power production than the geometry with n=5, and it presents the best cell performance.

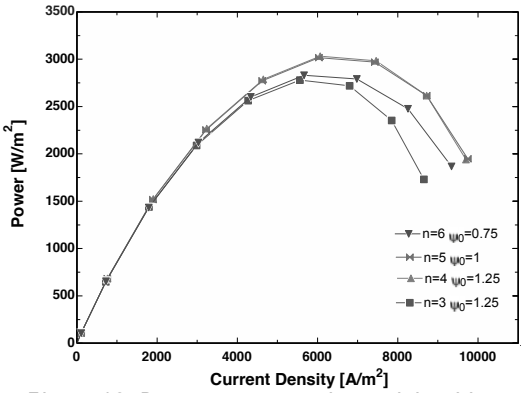

Figure 12. Power curves for the models with a high average current density.

5. Comparison

In order to compare the obtained results, two different radial geometries were built, one of them was proposed for Cano et al [3] and the other one was proposed by Perez et al [13]. Both geometries were simulated under the same model considered in the present study. These geometries were chosen because they have the same active area as the present geometry.

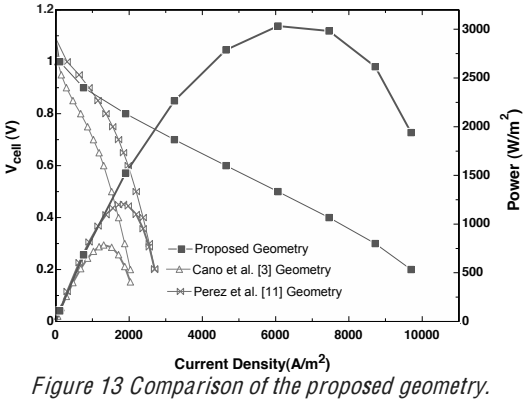

Figure 13 Comparison of the proposed geometry.

Figure 13 shows the power curves for the three geometries. An important improvement on the fuel cell performance is obtained under the

proposed geometry. As it can be seen the proposed geometry does not have high concentration losses. It results on having a more uniform distribution than the two compared geometries. At the same time the proposed geometry presents a higher power generation.

6. Conclusions

A parametric study of a radial configuration for the bipolar plates of PEM fuel cells is carried out in this work. The proposed 3D model is able to predict the cell performance. The study aimes to determine the geometry that maximizes the current density -in a more uniform way- enhancing the fuel cell performance. The performed analysis, which is based on the constructal theory, shows the effect of guiding the gases through the cell, getting a better performance for a special geometry. This study also shows the importance of the design on the fuel cell flow channels. In that case the geometry must be focusing on the design that increases the uniformity on the species concentration.

For this parameterization the variation of the n parameter does not have as much effect as the variation of the φ_0 parameter. In a specific manner, the geometry with n=4 and φ_0=1.25 is the model that has the best performance increasing the power and the current density uniformity. This geometry will also reduce the cost and the manufacturing time because of the simpler geometry in comparison with the other analyzed cases.

Nomenclature

a_k	Activity of water on stream k [dimensionless]
C_i	Concentration of the specie i (mol m^{-3})
D_i	Mass diffusivity of specie i (m^2 s^{-1})
F	Faraday constant (97487 C mol^{-1})
H	Height (mm)
I	Local current density (A m^{-2})
j^{ref}	Volumetric reference exchange current density (A m^{-3})
j_i	Mass flow of the species i
L	Length (mm)
M_i	Molecular weight of the specie i (kg kmol^{-1})
n	Row level
P	Total pressure (Pa)
P_0	Reference pressure (101325 Pa)
R	Universal gas constant (8.314 J mol^{-1}K^{-1})
S	Source term in the transport equations
T	Temperature (K)
T_s	Surface temperature at the anode (K)
T_0	Reference temperature (300 K)
$\bar{u}$	Velocity vector (m s^{-1})
W	Width (mm)
X_i	Mole fraction of the i specie
Y_i	Mass fraction of the i specie

Greek symbols

α	Net flux of water by proton
β	Permeability (m^2)
ϕ	Electrical potential (V)
γ	Concentration coefficient
ε	Porosity of the medium (dimensionless)
ζ	Stoichometric flux ratio
η	Overpotential (V)
ϑ	Volumetric flux in the inlet (cm^3 s^{-1})
λ	Water content
μ	Dynamic viscosity (kg s m^{-2})
ρ_m	Mixture density (kg m^{-3})
$\rho_{mem,dry}$	Dry membrane density (kg m^{-3})
σ	Electrical conductivity (Ω^{-1} m^{-1})

Superscripts

Ref	Reference value
Sat	Saturated

Subscripts

a	Anode
c	Cathode
CL	Catalyst layer
GDL	Diffusion layer
k	Species
mem	Membrane
sat	Saturated
sol	Solid
W_a	Water in the anode side
W_c	Water in the cathode side

References

[1] Voss H.H, Chow C.Y. Coolant Flow Field Plate for Electrochemical Fuel Cells. US Patent No. 5,230,966, 1993.
[2] Gurau V, et al. US Patent No. 6,551,736, 2003.

[3] Cano-Andrade S., Hernandez-Guerrero A. von Spakovsky M. R.[2], Damian-Ascencio C. E., Current Density Curves for Radial Configuration PEMFCs, accepted, Energy, The International Journal, 2009.
[4] Xavier Daguenet-Frick, Jocelyn Bonjour, Rémi Revellin, Constructal Microchannel Network for Flow Boiling in a Disc-Shaped Body, IEE Transactions on Components and Packaging Technologies, 2009.
[5] W. Wechsatol, S. Lorente, A. Bejan. Optimal tree-shaped networks for fluid flow in a disc-sahped body, Int J. Heat Mass Transfer, vol. 45, no. 25, pp. 4911-4924, 2002.
[6] W.M. Yan, H.C. Liu, C.Y. Soong, F. Chen, H.S. Chu, Numerical study on cell performance and local transport phenomena of PEM fuel cells with novel flow field designs; Journal of Power Source, vol. 161, pp. 907-919, 2006.
[7] Sukkee Um, C.Y. Wang, Three-dimensional analysis of transport and electrochemical reactions in polymer electrolyte fuel cells; Journal of Power source, vol. 125, pp 40-51, 2004.
[8] Um S., Wang C.Y., Chen K.S.; Computational fluid dynamics modeling of proton exchange membrane fuel cells; J. Electrochemical Soc., vol. 147, pp. 4485-4493, 2000.
[9] Nguyen T., White R.; A water and heat management model for proton – exchange – membrane fuel cells; J. Electrochemical Soc., vol. 140, pp. 2178-2186, 1993.
[10] H.C. Liu, W.M. Yan, C.Y. Soong, F. Chen, Effects of baffle-blocked flow channel on reactant transport and cell performance of a proton exchange membrane fuel cell, J. Power Sources 142 (2005) 125–133.
[11] H.C. Liu,W.M.Yan, C.Y. Soong, F. Chen, H.S. Chu, Reactant gas transport and cell performance of proton exchange membrane fuel cells with tapered flow field design, J. Power Sources 158 (2006) 78–87.
[12] Springer T.E., Zawodzinski T.A., Gottesfeld S., Polymer Electrolyte Fuel Cell Model, J. Electrochem Soc., Vol. 138, (1991) 2334-2341.
[13] Perez Raya I., Hernandez Guerrero A., Juarez Robles D., Gutierrez Rivera M., Rubio Arana J. New Radial Based Flow Configurations for PEMFCs, P. of ASME IMECE2009-12202, 2009.

Simulation Model of a High Temperature PEM Fuel Cell Based Cogeneration System

Nicola Zuliani, Rodolfo Taccani

Department of Mechanical Engineering
University of Trieste
Trieste - Italy

Abstract: This paper focuses on the development of an energy simulation model of a high temperature PEM fuel cell based cogeneration system. The system is composed of a steam reforming unit that can be operated with different fuels such as LPG and methane. The balance of plant is modeled using a commercial industrial process simulation software, Aspen Plus®. Components such as burner and chemical reactors are simulated using existing modules available in the software library. The fuel cell performance is predicted by means of a zero dimensional semi-empirical model implemented in Fortran and then integrated in the Aspen Plus process simulation. This choice allows to analyze the performance of the system taking into account for the CO influence on the fuel cell. The fuel cell model is validated using experimental data available in the literature and from tests carried out by the authors. The overall model is then used to perform a preliminary efficiency analysis that allows to asses the difference with low temperature PEM fuel cell based systems.

Keywords: High Temperature PEM Fuel Cells, Simulation Model, Steam Reforming.

1. Introduction

Fuel cells are attractive energy production devices that promise high primary energy savings, low pollutants emissions with compact and low weight size. But thinking of fuel cells as the replacement to the actual energy production systems is unpractical due to the limited hydrogen availability. This problem affects mostly Low Temperature PEM fuel cell (LTPEM), which require very pure hydrogen as feed fuel. Indeed, hydro-carbons fuels, as methane, natural gas or GPL, are normally available and do not imply major safety issues. From this point of view, the possibility to convert and use efficiently hydrocarbon based fuels in hydrogen, could turn fuel cells in a very attractive energy devices additionally because they allow co-production of heat. Fuels conversion to hydrogen can be carried out through different well known processes, including steam reforming, partial oxidation and auto thermal reforming. Steam reforming is generally the preferred reaction as it produces higher concentration of hydrogen [1]. Large hydrogen production plants are already commercialized, however, for small scale applications, the need for high purity fuel with low CO content (lower than 40 ppm) affects reformer complexity, cost and system performance. Literature presents different examples of small fuel processors coupled with low temperatures PEM fuel cells: a description of a practical application and simulation of a 4 kW electric power system can be found in [2]. The prototype presented has a net electric efficiency of 18% and a 30% thermal efficiency (LHV basis). However, according to the authors, an optimized design could allow higher efficiencies. In [3], where a 1 kW_{elec} LTPEM system fueled with methane is described, the gross electric efficiency of the system is more than 30% in the load range considered when the anode-off gas is re-circulated.

Problems related to CO tolerance and water management can be avoided using High Temperature PEM (HTPEM). In this kind of FC operating temperature can be 180°C reducing CO negative effects and therefore simplifying the design of the reformer: CO concentration up to 2% can be tolerated with negligible negative effects on performance. On the other hand conversion efficiency of HTPEM is lower than LTPEM. Testing and evaluation of a HTPEM fuel cell can be found in [4] while in [5] different PBI based technologies are characterized. Regarding the long term performance in [6] a study on the degradation behavior of the PBI membrane is described. Only few works regarding coupling of an HTPEM stack

Corresponding Author: Nicola Zuliani, Email: nzuliani@units.it

to an hydrogen generator can be found: in [7] an integration of a HTPEM stack with a methanol reformer is presented, while in [8] a simulation study of a micro CHP based on a HT PEM stack is described. The theoretical analysis shows that global efficiency in the range of 40% can be achieved. With the aim of a preliminary analysis on the efficiency differences with LTPEM fuel cells, this paper focuses on the development of an energy simulation model of a HTPEM fuel cell based cogeneration system.

2. Simulation model description

The simulation model has been implemented as part of a research project aimed to the design and development of a small cogenerative HTPEM system fuelled with methane or LPG. Therefore all the modeled components are already available even if a complete operational characterization has not been yet completed. The general schematic of the system includes two subsystems: fuel processing and HTPEM stack.

2.1. Fuel processing subsystem

The reformer modeled, produced by WS Reformer, is a steam methane reformer with a thermal output of 3.5 kW, and gas composition (dry basis) of H_2 75% - 79%, CO_2 20% - 23%, CH_4 < 1%, CO < 1% [9]. The reformer can use both methane or LPG. In the presented data methane has been chosen. Referring to Fig. 1, the process methane is mixed with vapor and introduced in the Steam Reforming Reactor (SRR). The overall product gas is a mixture of H_2, CO_2, CO, together with unconverted CH_4 and steam. The SRR products pass through an heat exchanger (Ex-2) where they are cooled down to the Water Gas Shift Reactor (WGSR) temperature. This purification process reduces the CO concentration to less than 1%. After the WGSR, the gas mixture, now containing about 55% of H_2, 20 % of CO_2, water and less than 1% of CH_4 and CO, goes to the HTPEM stack. Process water evaporation takes place by recovering heat from:

- the combustion chamber flue gas, by means of heat exchanger Ex-1;
- cooling down the reformate products of the SRR;
- the exothermic water gas shift reaction.

In the flow sheet, the last 2 recovering processes are modeled using only a single heat exchanger module, named Ex-2, in which the heat duty of the SRR product gas and the heat duty of the WGSR are taken into account.

2.1.1. Steam reformer reactor

The steam reformer reactor performs the reforming reaction of methane and the associated water gas shift reaction:

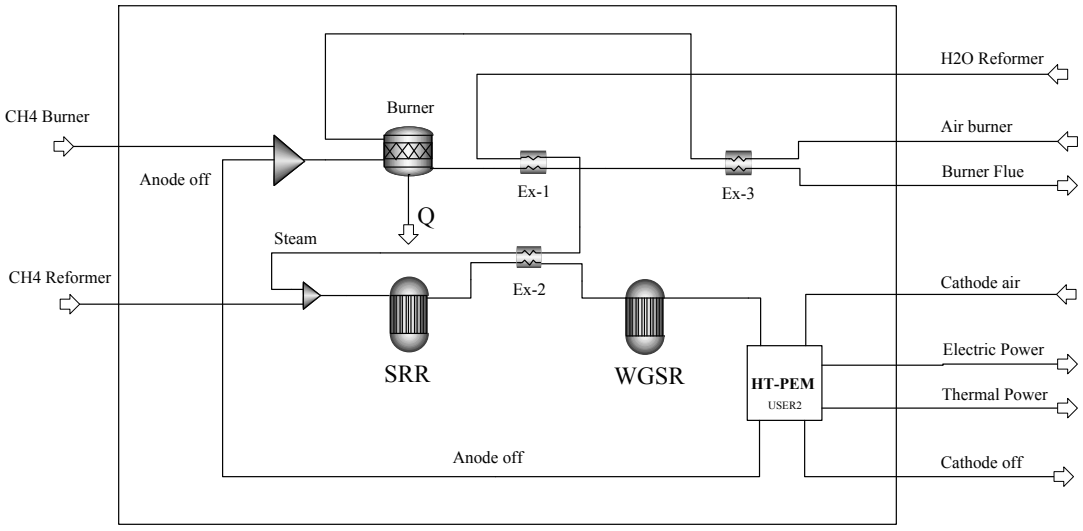

Fig. 1. Process flow sheet of the overall system.

$$CH_4 + H_2O \rightarrow CO + 3H_2 \quad (1)$$

$$CO + H_2O \rightarrow CO_2 + H_2 \quad (2)$$

The reactor has been supposed to be isothermal and heat is supplied by a CH_4 burner. The variables that affect the product gas composition are: reactor temperature, pressure, feed composition, steam to carbon ratio and type of catalyst used. The two reactions are assumed to be near equilibrium as supposed in [10]. On these basis, the reactor has been modeled as an Aspen Plus equilibrium reactor and operating temperature is 750°C in order to ensure an optimum methane conversion [1].

2.1.2. Water gas shift reactor

According to the considered reformer design [9] only a single stage purification unit has been modeled, where the water gas shift reaction (2) takes place. The process is moderately exothermic, and heat can be recovered to evaporate the input water. The water gas shift reactor has been modeled as an Aspen Plus® equilibrium reactor.

2.1.3. Heat exchangers

Heat management has a crucial role in order to achieve the maximum conversion efficiency. It has been assumed that heat exchangers have two functions: recovering the heat to evaporate the process water, and minimize the heat losses from the burner flue gas. As above mentioned, referring to Fig. 1, water evaporation takes place by means of heat exchangers Ex-1 and Ex-2 while Ex-3 recovers heat from the combustion chamber flue gas. Ex-1 and Ex-3 are modeled as Aspen Plus MHeatX modules while Ex-2 is composed by two Aspen Plus HeatX modules. The latter allows the simultaneous heat recover from cooling down the reformate output an from tempering the water gas shift reactor to 250°C. At the design point, the hot gas exit temperature for Ex-2 is equal to the WGSR temperature, while the hot gas exit temperatures for Ex-1 and Ex-3 are set to 400°C and 200°C respectively.

2.1.4. Burner

The Aspen Plus predefined reactor RGibbs is used to model the burner. The reactor performs gas phase chemical equilibrium through Gibbs free energy minimization. Outlet gas temperature is set to 700°C.

2.1.5. Reformer process hypothesis

Reformate gas composition and fuel processor efficiency depend on reactors temperatures and on steam to carbon ratio (S/C) used. Reactors temperatures are already defined above while the steam to carbon ratio is 3.5 at design point. This value has been chose as suggested in [9].

For the SRR and WGSR it has been assumed that the size of the catalyst bed is sufficient to approach equilibrium. The overall losses are the sum of several factors which are related to the design and mode of operation [11]:

- evaporation enthalpy of excess water;
- wall heat losses;
- exhaust gas enthalpy;
- reformate gas enthalpy.

In this work wall heat losses have been neglected. The fuel processor has been designed to produce 1.5 m^3/h (STP) of hydrogen, in order to meet the requirements for a stack of 1 kW_{elec}. For achieving the maximum efficiency from the system a preliminary design specification has been imposed: fuel consumption at the burner has been calculated as the minimum value in order to allow a SRR temperature of 750°C.

2.2. The fuel cell model

In literature most of the simulation models presented regard low temperature fuel cell (i.e. T < 100°C), while a limited number of papers focus on HTPEM (T > 160°C). For instance [12] and [13] do not consider the CO poisoning effects on the catalyst surface. While in [14] the influence of CO in the fuel has been taken into account and for this reason it has been chosen as reference for the development of the zero dimensional model used in this work. In the following are presented the main assumption while more details can be found in the original paper [14]. The parameters values used in the model are reported in Appendix.

2.2.1. Cathode model

Cathode is modelled with a semi-empirical equation:

$$U = U_0 - \frac{RT}{4\alpha_c F}\ln\left(\frac{i+i_0}{i_0}\right) - R_{ohmic} i - \frac{R_{conc} i}{\lambda - 1} \quad (3)$$

U is the cell voltage, U_0 is the open circuit voltage as measured in the experimental tests. The second term represents the Tafel equation

and includes the charge transfer coefficient α_c, the current density i and the exchange current densities i_0. The third term is related to the ohmic loss. In the last term the resistance associated with the concentration losses is related to the cathode stoichiometry λ. In (3) the variables i_0, R_{ohmic}, α_c and R_{conc}, are made temperature dependant through suitable regressions [14] (see Appendix).

2.2.2. Anode model

Anode model accounts for losses due to the CO poisoning effect on the catalyst layer. The anode overpotential η_a is related to the current density i and to θ_{H_2}, the fraction of catalyst sites with adsorbed H_2, assuming a Butler-Volmer kinetics with a symmetry factor α=0.5:

$$\eta_a = \frac{RT}{\alpha F}\sinh^{-1}\left[\frac{i}{2k_{eh}\vartheta_{H_2}}\right], \quad (4)$$

where k_{eh} is the hydrogen oxidation rate. In [14] θ_{H_2} is calculated using the model developed in [15] where four processes, described by the (5-8), express the interfacial kinetics of the adsorption, desorption and electro-oxidation processes of hydrogen and carbon monoxide on the catalyst surface:

$$CO + M \underset{b_{fc}(\theta_{CO})k_{fc}}{\overset{k_{fc}}{\rightleftharpoons}} (M-CO) \quad (5)$$

$$H_2 + 2M \underset{b_{fh}k_{fh}(\theta_{CO})}{\overset{k_{fh}(\theta_{CO})}{\rightleftharpoons}} 2(M-H) \quad (6)$$

$$(M-H) \xrightarrow{k_{eh}} H^+ + e^- + M \quad (7)$$

$$H_2O + (M-CO) \xrightarrow{k_{ec}} M + CO_2 + 2H^+ + 2e^- \quad (8)$$

In steady state conditions, the expressions used to calculated the CO and H_2 coverage can be formulated as function of the current density as [14]:

$$\rho\frac{d\theta_{H_2}}{dt} = 0$$

$$k_{fh}y_{H_2}p\left[1-\theta_{H_2}-\theta_{CO}\right]^n - b_{fh}k_{fh}{\theta_{H_2}}^n - i = 0 \quad (9)$$

$$\rho\frac{d\theta_{CO}}{dt} = 0$$

$$k_{fc}y_{CO}p\left[1-\theta_{H_2}-\theta_{CO}\right] - b_{fc}k_{fc}\theta_{CO} - \frac{ik_{ec}\theta_{CO}}{2k_{eh}\theta_{H2}} = 0 \quad (10)$$

The final expression of the semi-empirical fuel cell model is:

$$U = U_0 - \frac{RT}{4\alpha F}\ln\left(\frac{i+i_0}{i_0}\right) - R_{ohmic}i - \frac{R_{conc}i}{\lambda-1} - \eta_a \quad (11)$$

The model is zero-dimensionally, therefore no spatial variation of its physical properties is considered. The number of cells is 100 in order to achieve an electric power of 1 kW at 0.5 V single cell voltage. The stack operating temperature has been assumed equal to 160°C. Stack electric power is calculated as:

$$P_{elec} = V_{cell} * I * n_{cell} \quad (12)$$

where V_{cell} is the single cell voltage calculated by the model, I is the stack current, n_{cell} is the number of cells in the stack. The stack energy balance is used to evaluated the stack thermal power output. The fuel cell model is implemented in Fortran and then integrated in the Aspen Plus® flow sheet.

2.2.3. Fuel cell model validation

Model results were initially validated with the experimental data collected with a single fuel cell fed with pure hydrogen at 160°C [16].

Furthermore the fuel cell model results have been compared to the experimental data collected feeding the cell with a synthetic gas mixture that simulate a steam methane reformate composition H_2 55.77% - CO 0.48% - CH_4 0.55% - CO_2 43.2% vol. As shown in Fig. 2, there is a good agreement between the model and the experimental data. In the same figure a CO sensitivity analysis is presented (0.2% and 1%).

3. Results and discussion

In this work, the fuel processor efficiency is defined as:

$$\eta_{fp} = \frac{(\boldsymbol{n}_{H_2} * LHV_{H_2})_{ref}}{(\boldsymbol{n}_{CH_4} * LHV_{CH_4})_{ref} + (\boldsymbol{n}_{CH_4} * LHV_{CH_4})_{burner}} \quad (13)$$

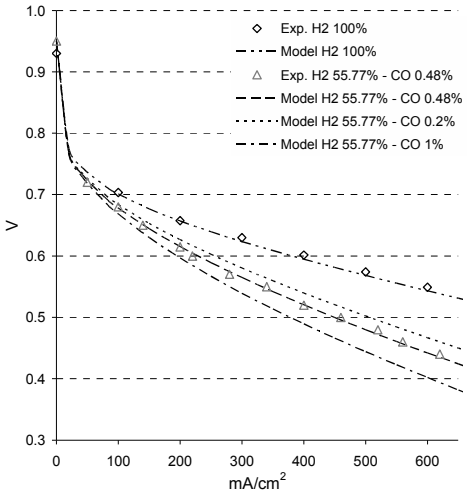

Fig. 2. Comparison between fuel cell model and experimental data. Cell fed with hydrogen and mixture H_2 55.77% - CO 0.48% - CH_4 0.55% - CO_2 43.2% vol. Cell temperature 160°C.

Where $\boldsymbol{n}$ is the mole flow rate, LHV_{H_2} is the low heating value of hydrogen (241 kJ/mol) and LHV_{CH_4} is that of methane (801 kJ/mol). The fuel cell stack electric efficiency, is defined as:

$$\eta_{fc} = \frac{P_{elec}}{(\boldsymbol{n}_{H_2} * LHV_{H_2})_{ref}} \quad (14)$$

The total electric efficiency is:

$$\eta_{elec} = \frac{P_{elec}}{(\boldsymbol{n}_{CH_4} * LHV_{CH_4})_{ref} + (\boldsymbol{n}_{CH_4} * LHV_{CH_4})_{burner}} \quad (15)$$

The thermal efficiency is defined as:

$$\eta_{therm} = \frac{P_{therm}}{(\boldsymbol{n} * LHV_{CH_4})_{ref} + (\boldsymbol{n} * LHV_{CH_4})_{burner}} \quad (16)$$

The choice of defining the efficiency in terms of LHV has been done to use a means of comparison widely used in conventional distributed cogeneration system such as internal combustion engines and gas turbine. P_{therm} is the thermal power that ideally could be recovered from the stack and is equal to $1-\eta_{elec}$. Table 1 reports system model results in the base case: no anode-off gas recirculation, hydrogen reformer output 3.5 kW (thermal) and HTPEM stack with 100 cells at 0.5V. The gas composition at fuel processor outlet given by the simulation model is comparable to the technical specification (see par. 2.1) of the considered commercial reformer. Fuel processor efficiency (77%) is comparable with the efficiency of a steam reformer unit of similar thermal power [3]. At a cell voltage of 0.5V, the HTPEM efficiency is 32% while the total electric efficiency is 24%. Obviously stack efficiency can be improved shifting the operating point to higher voltage. For instance, operating at 0.6 V stack efficiency is 36% and the total electric efficiency is 28%.

Table 1. System model results for the base case (no anode off gas recirculation).

Burner Feed		
Flow rate (methane)	0.108	kg/h
Thermal power	1.49	kW
LHV (methane)	801	kJ/mol
Water		
S/C	3.5	
Flow rate	0.851	kg/h
Steam temperature	378	°C
Air to burner		
Flow rate	2.394	kg/h
Reformate Composition (dry basis)		
H_2	79.20	% vol.
CO	0.52	% vol.
CH_4	0.87	% vol.
CO_2	19.4	% vol.
H_2 thermal power	3.44	kW
Fuel cell stack		
Number of cells	100	
Load	22	A
Total voltage	50	V
Single cell voltage	0.5	V
Stack Electric Power	1.093	kW
Stack Thermal Power	1.663	kW
Fuel utilization	0.73	
Cell efficiency	32	%
Fuel processor efficiency	77	%
Total electric efficiency	24	%

3.1. Influence of anode off-gas recirculation

In system real operation it is important to analyze the effect of part load operation on efficiency. Fig. 3 shows the effect of stack load variation on electric and thermal efficiency in a system without anode off gas recirculation. It is important to underline that in the presented data

the reformer does not follow the cell load request, and therefore the fuel utilization varies with the load. At 100 % stack load (0.5V) cell efficiency is 32% and total electric efficiency is 24%, if load is reduced to 70% cell and system efficiencies are respectively 25% and 19%.

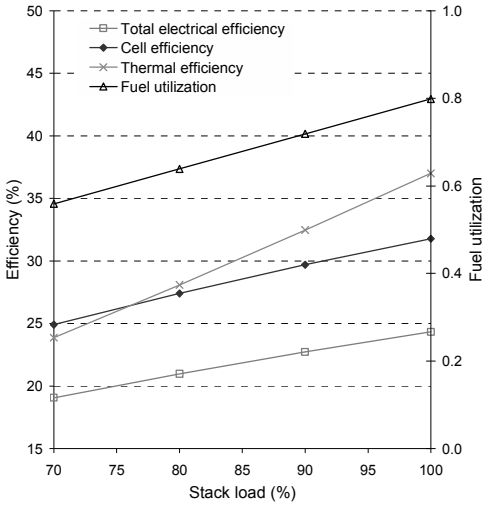

Fig. 3. Effect of stack load variation on total electric efficiency, thermal efficiency, fuel utilization and cell efficiency. No anode off gas recirculation.

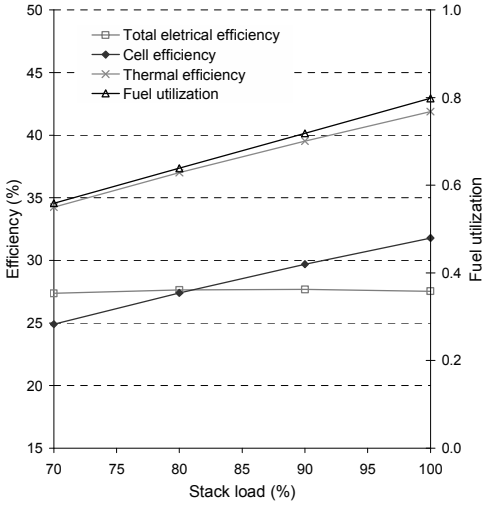

Fig. 4. Effect of stack load variation one total electric efficiency, thermal efficiency, fuel utilization and cell efficiency considering anode off gas recirculation.

In Fig. 4 are shown the results if the anode off gas is recirculated to the reformer. As load decreases fuel utilization decreases, and the thermal content of the recirculated anode-off gas flow is higher, decreasing the burner energy supply requirements. The total electric efficiency remains almost constant, being about 27% for all stack loads. Furthermore the thermal efficiency is increased from less than 25% to 34% at 70% stack load and from 34% to 42% at 100% stack load. Therefore recirculation, even if requiring a more complex BOP, is important to achieve high efficiency in particular in case of slow dynamic response of reformer. These theoretical results have to be validated with the actual performance of a real system, where the recirculation benefits are related to the combustion chamber capability to efficiently burn fuel blends with different calorific values (i.e. methane and anode-off gas with H_2O, CO and CO_2).

3.2. Influence of CO content at reformer outlet

Fuel processor transient and partial load operation can affect CO content at reformer outlet. Table 2 shows the cell efficiency variations with the CO content. Results highlight how cell efficiency decrease only to some extent: from 31.51%, at 0.4% CO, to 27.98% for CO concentrations of 1.2%. These results have to be compared with LTPEM fuel cell based systems, where small CO concentrations could dramatically affect stack performance and also stack life.

Table 2. Effect of CO content on cell efficiency.

CO (% vol.)	cell efficiency (%)
0.46	31.51
0.81	30.11
1.27	27.98

4. Conclusions

A simulation model of an HTPEM cogeneration system has been developed. A preliminary efficiency analysis shows that a system electric efficiency of 27% could be achieved. This value is only 10% lower than LTPEM based systems of similar size [3].

With respect of load variation on system efficiency two cases have been considered:

system without anode off gas recirculation and system with recirculation. It has been shown that recirculation, even if requiring a more complex BOP, is important to achieve high efficiency in particular in case of slow dynamic response of reformer. In transient operation, even high content of CO in the reformer output, the performance and durability of the stack is not compromised. Higher levels of thermal integration, investigable with the presented simulation model, could lead to higher efficiencies, as well as higher stack operating temperatures. Indeed the latter could negative affect the membrane degradation behavior. The next steps of the research will focus on experimental activity finalized to validate the simulation model.

Nomenclature

F faraday's constant, C mol^{-1}

I current, A

M vacant catalyst site

P power, kW

R universal gas constant, J mol^{-1} K^{-1}

T cell temperature, K

U cell voltage, V

i cell current density, A cm^{-2}

i_0 exchange current density, A cm^{-2}

n mole flow rate, mol s^{-1}

n_{cell} cell numbers

p pressure, bar

y_{H2},y_{CO} molar fraction, hydrogen, CO

Greek symbols

θ_{H2}, θ_{CO}, fractional coverage, hydrogen, CO

η_a anode activation losses, V

ρ density, kg m^{-3}

Subscripts and superscripts

n - order of anode kinetic model

elec - electric

ref - reformate

therm - thermal

BOP - Balance of Plant

References

[1] Gunther, K., 2008, *Fuel Processing for Fuels Cells*, WILEY-VCH Verlag GmbH & Co. KGaA, Weinheim, Germany.

[2] Gigliucci, G., et al., 2004, Demonstration of a Residential CHP System Based on PEM Fuel Cells, Journal of Power Sources, 131(1-2), pp.62-68.

[3] Heinzel, A., Roes, J., Brandt, H., 2005, Increasing the Electric Efficiency of a Fuel Cell System by Recirculating the Anodic Off Gas, Journal of Power Sources, 145(2), pp.312-318.

[4] Etim U. U., 2009, Testing and Evaluation of a High Temperature PBI Membrane Based PEM Fuel Cell, ECS Trans., 17(1), pp. 277-284.

[5] Q.F. Li, et al., (2010), Properties, Degradation and High Temperature Fuel Cell Test of Different Types of PBI and PBI blend membranes, Journal of Membrane Science, 347, pp. 260–270.

[6] Moçotéguy, (2009) P., Long-Term Testing in Dynamic Mode of HT-PEMFC H_3PO_4/PBI Celtec-P Based Membrane Electrode Assemblies for Micro-CHP Applications, Fuel Cells, 10(2), pp. 299-311.

[7] Chao, P., et al., 2005, Integration of High Temperature PEM Fuel Cells with a Methanol Reformer, Journal of Power Sources, 145(2), pp. 392-398.

[8] Korsgaard, R.A., Nielsen, P.M, Kaer, K.S., 2008, Part one: A Novel Model of HTPEM-Based Micro-Combined Heat and Power Fuel Cell System, International Journal of Hydrogen Energy, 33(7), pp. 1909-1920.

[9] WS Reformer, 2008, Compact C1, Technical Datasheet, WS Reformer GmbH, D-71272 Renningen, Germany .

[10] Godat, J., Marechal, F., 2003,Optimization of a Fuel Cell System Using Process Integration Techniques, Journal of Power Sources, 118(1-2), pp. 411-423.

[11] Schmid, H.P., Wünning, J.A., 2004, Flox Steam Reforming for PEM Fuel Cell Systems, Fuel Cells 2004, 4(4).

[12] Scott, K., Pilditchl, S., Mamlouk1, M., 2007, Modelling and Experimental

Validation of a High Temperature Polymer Electrolyte Fuel Cell, Journal of Applied Electrochemistry, 37(11), pp. 1245-1259.

[13] Cheddie, D.F., Munroe, N.D.H., 2006, Three Dimensional Modeling of High Temperature PEM Fuel Cells, Journal of Power Sources, 160(1), pp. 215-223.

[14] Korsgaard, R. A., et al., 2006, Modeling of CO Influence in PBI Electrolyte PEM Fuels Cells, *Proceedings of 4th International ASME Conference on Fuel Cell Science, Engineering and Technology, FUELCELL 2006*; New York, USA, pp. 61-65.

[15] Springer, T. E., et al., 2001, Model for Polymer Electrolyte Fuel Cell Operation on Reformate Feed: Effects of CO, H2 Dilution, and High Fuel Utilization, Journal of the Electrochemical Society, 148(1), pp. 11-23.

[16] Taccani, R., et al., 2009, Performance Analysis of a HT PEM Fuel Cell, *Proceedings of the 3rd European Fuel Cell technology & Applications EFC09*, Rome, Italy, pp. 85-86.

Acknowledgments: This research work was supported by Regione Autonoma Friuli Venezia Giulia – Italy.

Appendix

Expressions and parameters values used in model calculations are shown in Table 3. The parameters values are the same as in [14] expect for a_3 and k_{eh}.

Table 3 Expressions and parameters values used in the fuel cell model.

Expressions used in equation (1)		
Charge transfer coefficient, α_c	a_0T+b_0	
Exchange current densities, i_0	a_3e^{-b3T}	A/cm^2
Ohmic losses, R_{ohmic}	a_1T+b_1	Ω
Concentration losses, R_{conc}	a_2T+b_2	Ω
Values used for cathode model		
Charge transfer constant, a_0	2.761×10^{-3}	K^{-1}
Charge transfer constant, b_0	-0.9453	-
Ohmic loss constant, a_1	-1.667×10^{-4}	ΩK^{-1}
Ohmic loss constant, b_1	0.2289	Ω
Diffusion limitation constant, a_2	-8.203×10^{-4}	ΩK^{-1}
Diffusion limitation constant, b_2	0.4306	Ω
Limiting current constant, a_3	30.3×10^{3}	A
Limiting current constant, b_3	-0.04368	-
Open circuit voltage, U_0	0.95	V
Pre-exponential factors used for anode model		
CO desorption rate, b_{fc}	8.817e12	bar
H_2 desorption rate, b_{fh}	2.038e6	bar
CO electrooxidation rate, k_{ec}	3.267e18	$A\ cm^{-2}$
H_2 electrooxidation rate, k_{eh}	25607	$A\ cm^{-2}$
CO adsorption rate, k_{fc}	94.08	$A\ cm^{-2}\ bar^{-1}$
H_2 adsorption rate, k_{fh}	2.743e24	$A\ cm^{-2}\ bar^{-1}$
Activation energy values used for anode model		
CO desorption rate, b_{fc}	127513	kJ/kmol
H_2 desorption rate, b_{fh}	47904	kJ/kmol
CO electrooxidation rate, k_{ec}	196829	kJ/kmol
H_2 electrooxidation rate, k_{eh}	3550	kJ/kmol
CO adsorption rate, k_{fc}	19045	kJ/kmol
H_2 adsorption rate, k_{fh}	1.899e5	kJ/kmol

ANALYSIS OF POWER AND ENERGY IN AN ELECTROCHEMICAL POWER SYSTEM APPLIED TO A ROBOTIC DEVICE

Elisângela Martins Leal, Rogerio Rodrigues dos Santos

Vale Soluções em Energia, Energy Technological Center, São José dos Campos, SP, Brazil.

Abstract: Electrochemical power generation is an incredibly diverse and sophisticated field, and several major research initiatives throughout the world are racing for the ultimate electrochemical power solution. From the robotic perspective high torques may be avoided, due to mechanical limitations of joints and links. It can be achieved by reducing the weight of the robots and/or adjusting their speed of operation. In this paper, an analysis of an electrochemical system used in a robotic device is performed using a Ragone plot. In the following, an optimal control strategy for a serial manipulator is proposed. A contribution of the control strategy is the efficient usage of the limited power resource. The consideration of energy supplier curves for the determination of the control law is shown as an effective way to improve power consumption and overcome torque limitations of small devices. The resulting methodology can be useful to the design and path planning of small portable manipulators. Numerical results show the viability of the proposed methodology.

Keywords: Electrochemical power, power density, energy density, robot path planning, control strategy.

1. Introduction

The field of mobile robotics places stringent demands on the power system. Energetic autonomy, or the ability to function for a useful operation time independent of any tether, refueling, or recharging, is a driving force in a robot designed for a field application. A graphical technique which contributes to the intuitive understanding of the performance of a power system is the Ragone plot. This plot is useful for graphically comparing the merits of different power systems for a wide range of operation times. They plot the specific power versus the specific energy of a system on logarithmic scales.

Information on the basic fundamentals of batteries [1] and fuel cell systems [2, 3] can be found in the literature. Batteries and fuel cells are electrochemical devices that convert chemical energy into electrical energy by electrochemical oxidation and reduction reactions, which occur at the electrodes. The basic physical structure of batteries and fuel cells is an electrolyte layer sandwiched by an anode (negative electrode) and cathode (positive electrode) on either side. In a cell, the reactions occur at the electrode surfaces. In generalized terms, the reaction at the electrodes and the overall reaction can be represented by, respectively [1]:

$$\mathrm{Ox} + z\,\mathrm{e}^{-} \leftrightarrow \mathrm{Red} \tag{1}$$

The change in the standard free energy (ΔG^0), i.e. the maximum electric energy that can be delivered by the chemicals that are stored within or supplied to the electrodes in the cell, is expressed as [1, 2]:

$$\Delta \mathrm{G}^0 = -n_e\,\mathrm{F}\,\mathrm{E}^0 \tag{2}$$

When the conditions are other than the standard state (0.101 MPa and 298 K), the voltage E_0 of a cell is given by the Nernst equation [4]:

$$\mathrm{E}_0 = \mathrm{E}^0 - \frac{\mathrm{R\,T}}{n_e\,\mathrm{F}} \ln\left[\frac{a_{\mathrm{C}}^{c}\,a_{\mathrm{D}}^{d}}{a_{\mathrm{A}}^{a}\,a_{\mathrm{B}}^{b}}\right] \tag{3}$$

In the case of a fuel cell, the maximum work available from a fuel source is also related to the free energy of reaction (ΔG_R), whereas the enthalpy of reaction (ΔH_R) is the pertinent quantity for a heat engine [2]:

$$\Delta \mathrm{G}_{\mathrm{R}} = \Delta \mathrm{H}_{\mathrm{R}} - \mathrm{T}\Delta \mathrm{S}_{\mathrm{R}} \tag{4}$$

As shown in Eq. (4), the difference between ΔG_R and ΔH_R is proportional to temperature and to the change in entropy (ΔS_R).

Electrode reactions are characterized by both chemical and electrical changes and are

heterogeneous in type. They may be as simple as the reduction of a metal or the overall process may be relatively complex, involving several steps. Before the electron transfer step, electroactive species must be transported to the electrode surface by migration or diffusion. The electroactive species needs to be adsorbed by the electroactive material either before the electron step or after it. These behaviours lead to losses and prevent some chemical energy from being converted to useful electric work during cell discharge. To determine actual cell performance, three losses must be subtracted from the Nernst potential: (1) activation polarization, (2) concentration polarization, and (3) Ohmic polarization. When connected to an external load (R), the cell voltage V can be expressed as [1]:

$$\mathrm{V} = \mathrm{E}_0 - i\left(\eta_{\mathrm{act}} + \eta_{\mathrm{conc}} + R_i\right) = \mathrm{E}_0 - i\,R_t \qquad (5)$$

The Nernst equation characterizes the ability of the reactants to diffuse in the electrolyte from the bulk fluid flow and limits the current generation in the device. The activation polarization characterizes the energy needed to start the reaction. Activation losses are a function of the charge transfer kinetics of the electrochemical processes and are predominant at small current density. On the other hand, concentration polarization adjusts for the diffusion gradient into the active sites and is dominant when the cell is operating at high current density. Ohmic polarization is directly related to the internal resistance of the cell. It follows Ohm's law and describes the thermal losses caused by resistive heating that occur when a current passes through an electrolyte and through electrodes.

2. Fuel cells

A fuel cell generates electricity directly through electrochemical reactions. Fuel is transformed at the anode, and oxygen is transformed at the cathode. The transformations release electrons that are available to drive a load, and ions that are preferentially transported through an electrolyte. Assuming that the weight of the fuel cell stack ($\mathrm{W_{FC}}$) is a function of the power (P) delivered to the load, it follows [5]:

$$\mathrm{W_{FC}} = \mathrm{P}\, f_{\mathrm{FC}} / i\, \mathrm{V} \qquad (5)$$

The factor f_{FC} can be related to the weight and total area of the electrodes in the stack. Similarly, assuming the weight of the reactant subsystem ($\mathrm{W_{RS}}$) is a function of the energy (E) delivered by the device [5]:

$$\mathrm{W_{RS}} = \mathrm{E}\, f_{\mathrm{RS}} / \mu\, F\, \mathrm{V} \qquad (6)$$

For a fuel cell, the gravimetric energy density (ED) is a measure of the total energy available in the device per unit mass and it is determined by the voltage of the cell and the amount of charge that can be stored in the fuel. Typical units for gravimetric energy density are Wh/kg and it can be calculated by [6]:

$$\mathrm{ED} = \frac{\mathrm{E}}{\mathrm{W_{RS}}} = \frac{\mu\, F\, \mathrm{V}}{f_{\mathrm{RS}}} \quad \text{or} \quad \mathrm{V} = \frac{\mathrm{ED}\, f_{\mathrm{RS}}}{\mu\, F} \qquad (7)$$

Gravimetric power density (PD) is the total power available in the device per unit mass (W/kg). It is related to the gravimetric energy density (PD = ED/t) at a given discharge rate, and indicates how rapidly the cell can be discharged and how much power can be generated. It can be given by [6]:

$$\mathrm{PD} = \frac{\mathrm{P}}{\mathrm{W_{FC}}} = \frac{i\, \mathrm{V}}{f_{\mathrm{FC}}} \qquad (8)$$

Substituting Eq. (5) and (7) in Eq. (8) yields:

$$\mathrm{PD} = \frac{\mathrm{E}_0^2}{R_t\, f_{\mathrm{FC}}} \left[\frac{\mathrm{ED}\, f_{\mathrm{RS}}}{\mu\, F\, \mathrm{E}_0} - \left(\frac{\mathrm{ED}\, f_{\mathrm{RS}}}{\mu\, F\, \mathrm{E}_0} \right)^2 \right] \qquad (9)$$

Defining $q_0 = \mu\mathrm{F}$ as the maximum available capacity of the reactant (when $\mu = 1$), the maximum electrical energy that can be obtained by electrochemical conversion of the reactant is $q_0\mathrm{E}_0$. Substituting this in Eq. (9) gives:

$$\mathrm{PD} = \frac{\mathrm{E}_0^2}{R_t\, f_{\mathrm{FC}}} \left[\frac{\mathrm{ED}\, f_{\mathrm{RS}}}{q_0\, \mathrm{E}_0} - \left(\frac{\mathrm{ED}\, f_{\mathrm{RS}}}{q_0\, \mathrm{E}_0} \right)^2 \right] \qquad (10)$$

3. Batteries

In addition to fuel cell-based electrochemical power, an intense research and development effort is currently underway in batteries. The principal focus is lithium batteries. In their simplest form, batteries consist of two dissimilar electrode materials (positive electrode or cathode and negative electrode or anode) that are separated by an ionic conductor, which may be liquid, polymer, or solid phase. The characteristic performance of a battery is dictated by the type of electrode material and electrolyte (ionic phase that is usually held in a porous matrix that is often referred to as the separator). Because the electrolyte must be compatible chemically and electrochemically with the electrode materials, the combination of electrolytes and electrodes are limited.

Lithium-ion batteries have specific energies of around 160 Wh/kg and are expected to show substantial near- and mid-term increases in capacity, rate capability, and stability. According to McLarnon *et al.* [7] the energy density-power density relationship for batteries is:

$$\mathrm{PD} = \frac{\mathrm{E}_0^2}{R_t}\left[\left(\frac{\mathrm{ED}}{q_0\,\mathrm{E}_0}\right)^{0.5} - \frac{\mathrm{ED}}{q_0\,\mathrm{E}_0}\right] \qquad (11)$$

It is interesting to note that the form of Eq. (11) is similar to that for Eq. (10), differing in the exponents and in the inclusion of the factors f_{FC} and f_{RS}, which are related to the characteristics of the fuel cell stack and the reactant subsystem.

4. Ragone Plots

A very useful graphical technique for comparing some power devices is the Ragone plot. The diagram is a log-log plot, which allows a significant spectrum of gravimetric power density (kW/kg) and gravimetric energy densities (kWh/kg) to be plotted compactly. Figure 1 shows a Ragone plot for the direct methanol fuel cells listed in Table 1 and Figure 2 exhibits a Ragone plot for the batteries listed in Table 2. As the system power increases, less energy can be extracted. The highest gravimetric energy density batteries can only provide miniscule levels of power.

Table 1. Specifications for commercial (or to be) direct methanol fuel cells.

Company/ Product	Power [W]	Size (mm)	Weight (kg)
Ball Aerospace & Technology Corp	100	109 x 203 x 254	6,16
Hydrogenics Corp./HyPORT C	500	533x330x406	35
IdaTech Company/FCS 1200	850	740 x 690 x 640	84
Smart Fuel Cell/SFC A25	25	465 x 290 x 162	9,7
Toshiba	12	275 x 75 x 40	1,02
Voller Energy Ltd/Portapack VE 100	100	330 x 330 x 160	11,65

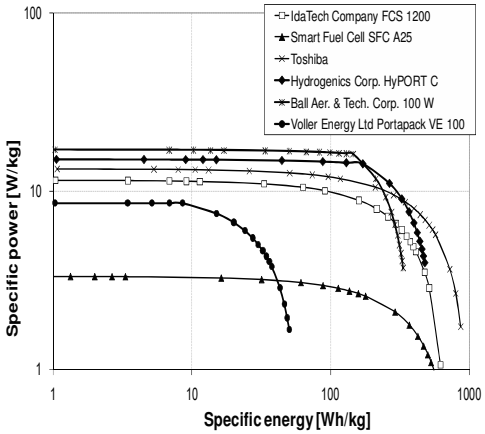

Figure 1. Ragone plot for the direct methanol fuel cells listed in Table 1.

Table 2. Specifications for commercial Li-ion batteries.

Company	Weight (kg)	Mid-discharge voltage [1] (V)	Discharge capacity at *C*/5 (Ah)	Polarization resistance [2] (Ω cm²)
Sony	0.60	3.50	1.18	213
NEC Moli	0.48	3.75	1.30	189
A & T	0.50	3.75	1.45	54
Sanyo	0.45	3.75	1.30	118
Matsushita	0.40	3.75	0.82	50

1: Theoretical voltage of 4.2 V; 2: at rates above 1*C*.

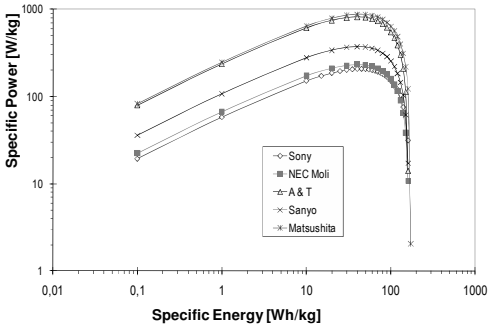

Figure 2. Ragone plot for the batteries listed in Table 2.

5. Robot Kinematics

To describe both the workspace and geometrical position of the robot in the same reference system it is necessary to establish the robot direct kinematics.

Given the joint coordinates q of a serial manipulator, the transformation matrix that represents the geometrical elements of the robot are described by using homogeneous transformations such as:

$$A_i = \begin{bmatrix} \mathbf{R}_{i-1}^{i} & \mathbf{d}_{i-1}^{i} \\ 0 & 1 \end{bmatrix} \quad (12)$$

where $\mathbf{R}(\mathbf{q})$ is a rotational matrix and $\mathbf{d}(\mathbf{q})$ is a translational vector. Using this concept, the kinematics characteristics of a serial robot manipulator with n degrees of freedom is completely defined by the transformation:

$$\mathbf{T}_0^n = A_1(q_1) \cdot A_2(q_2) \cdots A_n(q_n) \quad (13)$$

Using the Denavit-Hartenberg representation [8], each homogeneous transformation A_i is obtained as a result of four basic transformations:

$$A_i = Rot_{z,\theta} \cdot Trans_{z,d} \cdot Trans_{x,a} \cdot Rot_{x,\alpha} \quad (14)$$

where a (*length*), α (*twist*), d (*offset*) and θ (*angle*) are the associated parameters.

As $\mathbf{T}$ matrix is defined according to Equation (13) for a specific manipulator, given a Cartesian reference point $\mathbf{P}_{base}$, the end-effector Cartesian position for each joint coordinate $\mathbf{q}(d, \theta)$ is obtained from:

$$\mathbf{P}_{end} = \mathbf{T}(d, \theta) \,.\, \mathbf{P}_{base} \quad (15)$$

This procedure is called direct kinematics computation. Given the reference point $\mathbf{P}_{base}$ and the end-effector point $\mathbf{P}_{end}$, the procedure that lead to the determination of the corresponding joint coordinate $\mathbf{q}(d, \theta)$ is called inverse kinematics computation.

Using Equation (15) it is possible to describe the Cartesian position of an arbitrary serial robot manipulator. The kinematics determination is of main importance in the manipulability analysis, as presented in the following.

6. Mechanical Power

The consideration of the dynamics behavior of a serial manipulator is of great importance in its path planning. This information allows a detailed analysis and consequently the development of a precise control specification.

Many efficient schemes have been proposed to model the dynamics of rigid multi-body mechanical systems [8].

The dynamics model can be obtained explicitly through algebraically computation, or numerically through iterative computation.

The techniques based on the Newton-Euler method starts from the dynamics of all individual parts of the system. They look at the instantaneous or infinitesimal aspects of the motion, using vector quantities as Cartesian velocities and forces.

Alternatively, the Euler-Lagrange based methods starts from the kinetic and potential energy of the total system, considering the states of the system during a finite time interval. This approach works with scalar quantities, the energies.

Independent of the approach, the generalized forces at the end are determined as described by the equation:

$$\mathbf{Q}(\mathbf{q}(t))\ddot{\mathbf{q}}(t) + \mathbf{C}(\dot{\mathbf{q}}(t), \mathbf{q}(t)) + \mathbf{G}(\mathbf{q}(t)) = \mathbf{u}(t) \quad (16)$$

Where: $\mathbf{q}(t)$, $\dot{\mathbf{q}}(t)$ and $\ddot{\mathbf{q}}(t)$ are the joint position, velocity and acceleration, respectively. $\mathbf{Q}(\mathbf{q}(t))$ is the joint space mass matrix and $\mathbf{C}(\dot{\mathbf{q}}(t), \mathbf{q}(t))$ is the vector of Coriolis and centrifugal forces. The vector $\mathbf{G}(\mathbf{q}(t))$ is the vector of gravitational forces and $\mathbf{u}(t)$ is the generalized force vector.

The energy that is necessary to move the robot is an important design issue, because in real applications energy supply is limited and any energy demand reduction leads to smaller operational costs. Due to the relationship that exists between energy and force, the minimal energy can be estimated from the generalized force $u_i(t)$ that is associated to each joint i at time instant $t_0 \le t \le t_f$.

The interval between the initial time (t_0) and the final time (t_f) is discretized in N steps. Then, the mechanical power (P_M) is used for design purposes as defined by:

$$P_M = \sum_{i=1}^{N} \left[u_i^T(t)\, \dot{q}_i(t) \right]^2 \quad (17)$$

This expression represents well the phenomenon under study because it considers both the kinematics and the dynamical aspects of the trajectory, simultaneously [9].

7. Dynamics model of Robotic Manipulator

Physical characteristics of a two degree of freedom robotic planar manipulator are presented by means of Denavit-Hartenberg parameters shown in Table 3.

Table 3. Denavit-Hartenberg parameters, (*) joint variable.

Joint	A (m)	α (rad)	d (m)	θ (rad)
1	a_1	0	0	θ_1^*
2	a_2	0	0	θ_2^*

Link lengths are $a_1=1\ m$, $a_2=1\ m$, and link masses are $m_1=1\ kg$ and $m_2=1\ kg$, respectively.

By developing Euler-Lagrange equation and using the Lagrangian the explicit equations of the system dynamics are obtained [8].

For a robotic planar manipulator with two degrees of freedom ($n = 2$) the elements of matrix **Q**, **C** and **G** (Eq. 16) are:

$$Q_{11} = (1/3)\, m_1 a_1^2 + (1/3)\, m_2 a_2^2 + m_2 a_1^2 + m_2 a_1 a_2 \cos(q_2) \quad (18a)$$

$$Q_{12} = (1/3)\, m_2 a_2^2 + 0.5\, m_2 a_1 a_2 \cos(q_2) \quad (18b)$$

$$Q_{21} = (1/3)\, m_2 a_2^2 + 0.5\, m_2 a_1 a_2 \cos(q_2) \quad (18c)$$

$$Q_{22} = (1/3)\, m_2 a_2^2 \quad (18d)$$

$$C_{11} = -m_2 a_1 a_2 \sin(q_2)\, q_1' q_2' - 0.5\, m_2 a_1 a_2 \sin(q_2)\, (q_2')^2 \quad (18e)$$

$$C_{21} = 0.5\, m_2 a_1 a_2 \sin(q_2)\, (q_2')^2 \quad (18f)$$

$$G_{11} = -0.5\, m_1 g\ a_1 \cos(q_1) - 0.5\, m_2 g\, a_2 \cos(q_1+q_2) - m_2 g\, a_1 \cos(q_1) \quad (18g)$$

$$G_{21} = -0.5\, m_2 g\, a_2 \cos(q_1+q_2) \quad (18h)$$

where $g = 9.81\ m/s^2$ is the gravity. As a result, the system dynamics is presented according to Eq. 16.

A further development is required to compute the system dynamics by means of a standard numerical procedure.

By defining the state variables as $x_1 = q_1$, $x_2 = q_2$, $x_3 = \dot{q}_1$ and $x_4 = \dot{q}_2$, and the notation $\mathbf{w}_1 = (x_1\ \ x_2)^T$ and $\mathbf{w}_2 = (x_3\ \ x_4)^T$, the second order system is converted to the equivalent a first order system:

$$\dot{\mathbf{w}}_1 = \mathbf{w}_2 \quad (19)$$

$$\dot{\mathbf{w}}_2 = \mathbf{Q}^{-1}(\mathbf{u} - \mathbf{C} - \mathbf{G}) \quad (20)$$

In the current study the maximal value of the torque is minimized. The required concepts of optimal control are summarized in the following.

8. Optimization of Discrete Dynamic Systems

A discrete dynamic system [10] is described by means of a state vector $\mathbf{w}(i)$ of dimension n in each step i. The choice of a control vector $\mathbf{u}(i)$ of dimension m enables the transition of the system to the state $\mathbf{w}(i+1)$ through the relation:

$$\mathbf{w}(i+1) = f[\mathbf{w}(i), \mathbf{u}(i), i] \quad (21)$$

where:

$$\mathbf{w}(0) = x_0 \quad (22)$$

Given a number of steps N, the general optimization problem for such class of system is to find the best control vector $\mathbf{u}(i)$, $i=0, ..., N-1$ which minimizes the performance index:

$$J = \phi[\mathrm{w}(N)] + \sum_{i=0}^{N-1} L[\mathrm{w}(i), u(i), i] \quad (23)$$

subject to Eqs. (21) and (22), where N, $\mathbf{w}_0$ and f are given. This is a parametric optimization problem with equality constraints, and can be solved by means of a nonlinear programming methodology [11, 12] if the control vector $\mathbf{u}(i)$ is understood as design vector [10].

For a given value of $\mathbf{u}(i)$, the state vector $\mathbf{w}(i)$ is computed by the optimization of J.

The extension of the formulation for a discrete system with terminal constraints requires the computation of $\mathbf{u}(i)$ that minimize:

$$J = \phi[\mathbf{w}(N)] \quad (23)$$

Subject to:

$$\mathbf{w}(i+1) = f[\mathbf{w}(i), \mathbf{u}(i), i], \quad \mathbf{w}(0) = \mathbf{w}_0 \quad \text{and} \quad \psi[\mathbf{w}(N)] = 0,\ i = 0, \ldots, N-1 \quad (24)$$

9. Numerical Result

The next numerical result was computed before the optimization process, and obtained through the dynamic system (Eq. 24) of a planar manipulator with two degree of freedom. The optimization was carried out by using Eq. 19.

The initial Cartesian position of the manipulator end-effector was $x = 2\ m$ and $y = 0m$ (and corresponding joint configuration $q_1(t_0) = 0\ rad$ and $q_2(t_0) = 0\ rad$, respectively) and the final positon $x = 0\ m$ and $y = 2\ m$ (corresponding joint configuration $q_1(t_f) = \pi/2\ rad$ and $q_2(t_f) = 0\ rad$, respectively). A cubic *spline* interpolation applied to joint coordinates was used to compute the movement between initial and final configurations.

The total travelling time as fixed in 1 s ($t_0 = 0\ s$ and $t_f = 1\ s$) and the corresponding interpolation equation of the first joint P_1 satisfies bound constraints $P_1(t_0) = 0\ rad$ and $P_1(t_f) = \pi/2\ rad$, at initial and final time, respectively. Furthermore, in the interpolation equation of the second joint P_2 the constraints $P_2(t_0) = 0\ rad$ and $P_2(t_f) = 0\ rad$ are accomplished.

Additional constrains were included to ensure that $\dot{P}_1(t_0) = \dot{P}_1(t_f) = \dot{P}_2(t_0) = \dot{P}_2(t_f) = 0$. Joint velocities (the position derivatives) at the initial and final times ensure a rest to rest motion. By solving the differential equation that describes the dynamics effect of the system (Eq. 24) by using $\mathbf{q}, \dot{\mathbf{q}}$ and $\ddot{\mathbf{q}}$ given by the interpolation equation P_j, the torque u_{ij} associated to each joint $j=1,2$ is obtained, in the time instants $i=1,...,N-1$.

The corresponding physical movement resulting from initial *spline* interpolation is presented in Figure 3.

When the movement presented in Figure 3 is performed, the maximum torque value is u_{max} = *19.6200 Nm*. The interpolated value of the control $\mathbf{u}(i)$ is used as initial guess of the optimization process. The optimal design of position, velocity and acceleration $\mathbf{q}, \dot{\mathbf{q}}$ and $\ddot{\mathbf{q}}$, decrease the performance index to u_{max} = *10.1092 Nm*.

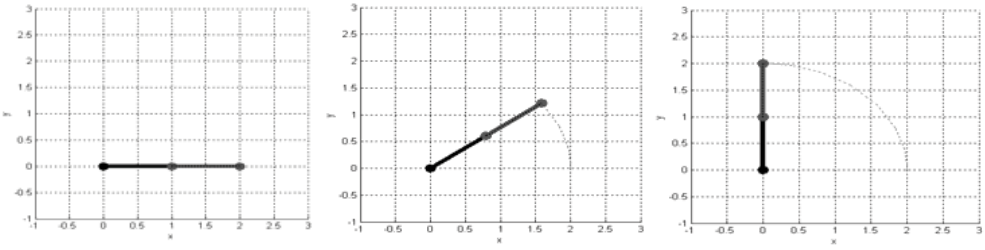

Figure 3. Robot movement before optimization.

Figure 4 presents the torque value required to perform the given movement before the optimization (dot line) and after the optimization (solid line). Results of the first joint and second joint are presented.

By comparing initial and final values a higher nonlinearity of the optimal design is observed. It is justified by the use of inertia effects to improve the general performance.

On the other hand, torque values were increased at the last phase of the movement as shown in Figure 4, aiming achieve the final position goal.

The comparison between the initial (F_{max} = *19.6200 Nm*) and final (F_{max} = *10.1092 Nm*) performance indexes demonstrate the effective improvement of the objective index.

The optimization process was carried out by means of a finite set of reference points. As a result, smoothness is not ensured between time step transitions. Optimal data was processed through a *spline* interpolation to obtain the smooth design presented.

Figure 5 shows a sequence of images given by the optimal design.

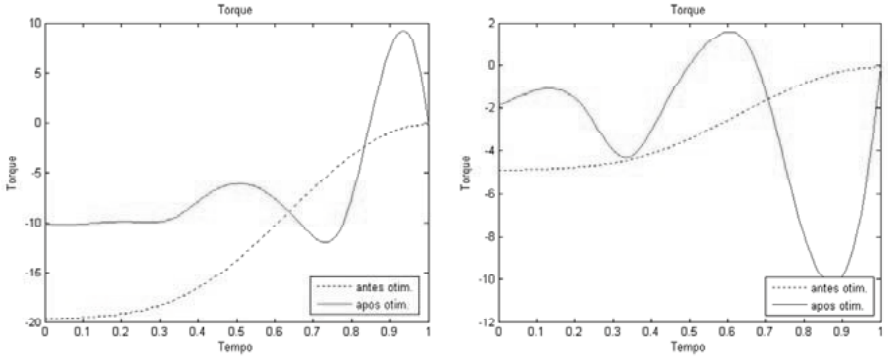

Figure 4. Torque applied to each joint before (dot line) and after (solid line) the optimization.

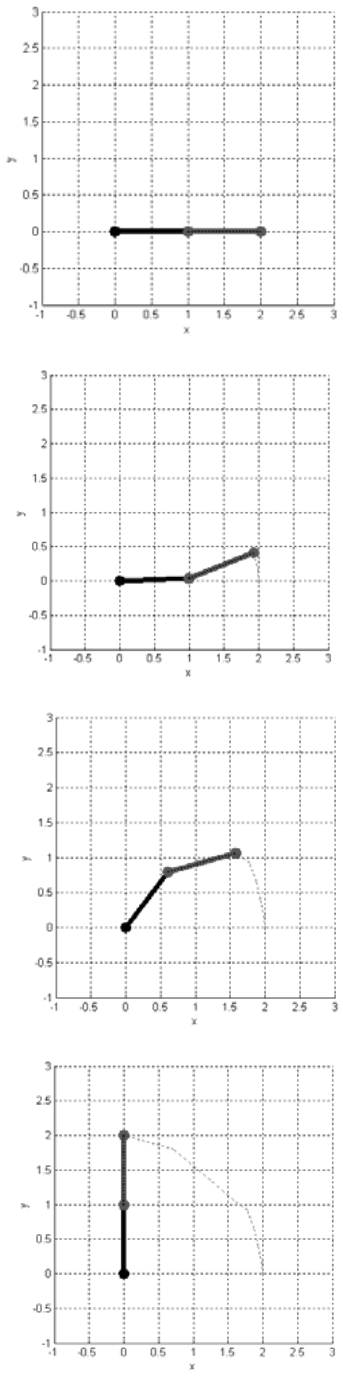

Figure 5. Robot movement after optimization

10. Conclusions

As mentioned earlier, the energy necessary to move a robot is an important design issue and the consideration of the dynamics behavior of a serial manipulator is of great importance in its path planning.

The optimized mode shows a lesser energy demand. This energy demand can be supplied by an electrochemical device. The use of this portable power source motivated the improvement of control strategies aiming to transform robotic manipulators in portable and/or autonomous devices.

By using Euler-Lagrange formalist, dynamic equations of two degrees of freedom manipulator were shown and robotic kinematics and dynamics were addressed.

The complexity involved in the system dynamics grows when a robot with more sophisticated geometry is considered. At this point, the choice of matrix representation presented here is the recommended tool to deal with robot of arbitrary complexity.

A numerical result shows the effectiveness of the proposed methodology in reducing the torque peak. With the change of the power consumption profile, fuel cells became an attractive power supplier to robotic devices.

As a result, the coupled analysis of battery and fuel cell technologies and robot consumption is a challenging field that will enable the build of portable and smart general purpose robots.

The next step of this research is the consideration of different mechanical and geometric constraints on robotic joints, coupled with the use of mechanical inertia as a power recharger. Besides, the coupling of the electrochemical equations with the power and energy required by the robotic device will also be considered.

Results currently obtained by authors motivate the use of this methodology and the coupled analysis in more complex scenarios.

Nomenclature

a_i activity of relevant species

F Faraday constant (96,487 C/mol)

E^0 Standard potential at 0.101 MPa and 298 K (V)

n_e number of electrons participating in the reaction

R Gas constant (kJ/kg)

T Absolute temperature (K).

i current density ($A.cm^{-2}$)

R_i internal resistance of the cell ($\Omega.cm^2$)

f_{FC} weight factor for the fuel cell device (kg/cm^2).

f_{RS} factor that is a function of the amount of reactants (number of equivalents) and the weight of the auxiliary components (weight/equivalent of stored energy).

q robotic joint angle (rad).

u generalized force (Nm).

Q joint space mass matrix.

C Coriolis and centrifugal forces.

G gravitational forces.

Greek symbols

η_{act} impedance due to activation losses ($\Omega.cm^2$)

η_{conc} impedance due to concentration losses ($\Omega.cm^2$).

μ energy conversion efficiency

References

[1] Linden D. and Reddy, T. B. (eds). *Handbook of batteries*. 3rd ed. New York: McGraw-Hill; 2001.

[2] EG&G Services Parsons, Inc. *Fuel Cell Handbook*. U.S. Department of Energy, Office of Fossil Energy, National Energy Technology Laboratory, Under Contract No. DE-AM26-99FT40575, 2000.

[3] Hoogers G. (ed) *Fuel Cell Technology Handbook*. Danver, MA: CRC Press, 2002.

[4] Delpierre G. R., Sewell, B. T, 2002, *Standard electrode potentials*. Available at http://www.physchem.co.za/Data/Electrode%20Potentials.htm.

[5] Kinoshita, K., Landgrebe, A. R., 1993, *Analysis of power and energy for fuel cell systems*, Journal of Power Sources, Vol. 47, pp. 159-175.

[6] Pell, W. G., Conway, B. E, 1996, *Quantitative modeling of factors determining Ragone plots for batteries and electrochemical capacitors*, Journal of Power Sources, Vol. 63, pp. 255 – 266.

[7] McLarnon, F.R., Cairns, E.J., Landgrebe, A.R., 1988, *Estimation of power-energy plots for secondary batteries*. In: Proceedings of the 33rd International Power Sources Symposium, Cheny Hill, NJ, June 13-18, The Electrochemical Society, Inc., Pennington, NJ, USA, p. 410.

[8] Craig, J. J., 1989. *Introduction to robotics: Mechanics & control,* second edition. Reading, MA: Addison-Wesley.

[9] Saramago, S. F. P.; Steffen, V. Jr., Optimization of the Trajectory Planning of Robot Manipulators Taking Into-Account The Dynamics of the System. *Mechanism and Machine Theory*, 33 (7), 883-894, 1998.

[10] Bryson, A. E. Jr., 1999, *Dynamic Optimization*. Addison Wesley Longman, Inc.

[11] Vanderplaats, G. N., 1999, *Numerical Optimization Techniques for Engineering Design*. 3rd edition, VR&D Inc.

[12] Luenberger, B. G., 1984, *Linear and Non-Linear Programming*. 2nd edition, Addison-Wesley.

EFFECT OF COMBINED HEAT TRANSFER ON THE THERMOECONOMIC PERFORMANCE OF AN IRREVERSIBLE HEAT ENGINE MODEL

M. A. Barranco-Jiménez [a] *, N. Sánchez-Salas* [b] *and F. Angulo-Brown* [b]

[a] *Escuela Superior de Cómputo del IPN, Distrito Federal, México*
[b] *Escuela Superior de Física y Matemáticas del IPN, Distrito Federal, México*

Abstract: In the present paper, we study the thermoeconomic optimization of an irreversible heat engine by using finite-time/finite-size thermodynamic theory. In our study we take into account losses due to heat transfer across finite time temperature differences, heat leakage and internal irreversibilities in terms of a parameter which comes from the Clausius' inequality. In the considered heat engine model, the heat transfer from the hot reservoir to the working fluid is assumed to be simultaneous radiation and conduction modes and the heat transfer to the cold reservoir is assumed of the conduction type. In this work, the optimum performance and two design parameters have been investigated under two objective functions: the power output per unit total cost and the ecological function per unit total cost. The effects of the technical and economical parameters on the thermoeconomic performance have been also discussed under the aforementioned three criteria of performance.

Keywords: Thermoeconomic performance, irreversible, Solar-driven heat engine, optimization.

1. Introduction

In 2000, Sahin [15] studied the thermoeconomic performance of an endoreversible solar-driven heat engine. In this study, he considered that the heat transfer from the hot reservoir to the working fluid is given by radiation, while the mode of heat transfer from the working fluid to the cold reservoir is given by a Newtonian heat transfer law. Sahin [15], calculated the optimum temperatures of the working fluid and the optimum efficiency of the engine operating at maximum power conditions. Later, Sahin and Kodal [16], applied this procedure to study the termoeconomics of an endoreversible heat engine in terms of the maximization of a profit function defined as the quotient of the power output an the annual investment cost. Recently, Barranco-Jiménez et al [6], studied the optimum operation conditions of an endoreversible heat engine with different heat transfer laws at the thermal couplings but operating under maximum ecological function conditions, and more recently, Barranco-Jiménez et al [7] also studied the thermoeconomic optimum operation conditions of a solar-driven heat engine. In these studies, Barranco-Jiménez et al considered three regimes of performance: The Maximum Power Regimen (MPR) [10, 8, 11], the maximum efficient power [20] and the maximum ecological function regime (MER) [1, 3]. In our study we use two regimens of performance: The maximum power regime, and the so-called ecological function regime. In this work following the Ust's procedure [19], we study the thermoeconomics of an irreversible heat engine with losses due to heat transfer across finite time temperature differences, heat leakage between thermal reservoirs and internal irreversibilities in terms of a parameter which comes from the Clausius inequality. In the considered heat engine model, the heat transfer from the hot reservoir to the working fluid is assumed to be simultaneous radiation and conduction modes and the heat transfer to the cold reservoir is assumed of the conduction type. In our study we use two regimens of performance: The maximum power regime, and the so-called ecological function regime

2. Theoretical model

The considered irreversible solar-driven heat engine operates between a heat source of temperature T_H and a heat sink of temperature T_L (see Figure (1a)). The temperatures of the working fluid exchanging heat with the reservoirs at T_H and T_L are T_X and T_Y, respectively. A T-S diagram of the model including heat leakage, finite time heat transfer and internal

Corresponding author: Barranco-Jiménez, Email: mbarrancoj@ipn.mx

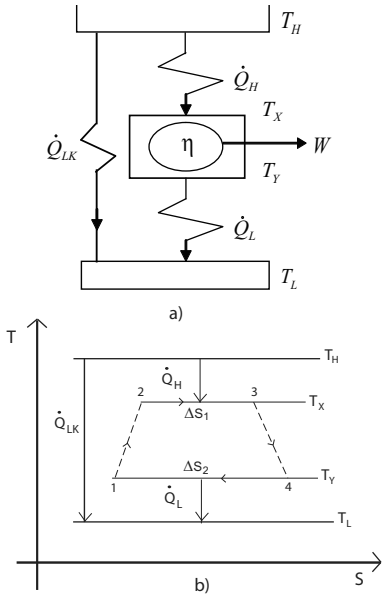

Figure 1: Schematic diagram of the irreversible heat engine and its $T-S$ diagram [18].

irreversibilities is also shown in Figure (1b). Heat transfer from the hot reservoir is assumed to be simultaneously conduction and radiation modes. The net heat flow rate $\dot{Q}_H$ from the hot reservoir to the heat engine can be written as [19],

$$\begin{aligned}\dot{Q}_H &= \dot{Q}_{HC} + \dot{Q}_{HR} \\ &= U_{HC}A_H\left(T_H - T_X\right) + U_{HR}A_H\left(T_H^4 - T_X^4\right),\end{aligned} \tag{1}$$

where U_{HC} and U_{HR} are the heat transfer coefficients for conduction and radiation heat transfer modes, respectively, and A_H is the heat transfer area of the hot-side heat exchanger. On the other hand, conduction heat transfer is assumed to be the main mode of the heat transfer to the low temperature reservoir and therefore the heat flow rate $\dot{Q}_L$ from the heat engine to the cold reservoir can be written as,

$$\dot{Q}_L = U_{LC}A_L\left(T_Y - T_L\right) \tag{2}$$

where U_{LC} is the cold side heat transfer coefficient and A_L is the heat transfer area of the cold-side heat exchanger. The rate of heat leakage $\dot{Q}_{LK}$ from the hot reservoir at temperature T_H to the cold reservoir at temperature T_L with thermal conductance γ is given by,

$$\dot{Q}_{LK} = \gamma\left(T_H - T_L\right) = \xi U_H A_H\left(T_H - T_L\right), \tag{3}$$

where γ is the internal conductance of the heat engine and ξ denotes the percentage of the internal conductance with respect to the hot-side conduction heat transfer coefficient and heat transfer area, that is, $\xi = \frac{\gamma}{U_H A_H}$. Then the total heat rate $\dot{Q}_{HT}$ transferred from the hot reservoir is,

$$\dot{Q}_{HT} = \dot{Q}_H + \dot{Q}_{LK}, \tag{4}$$

and the total heat rate $\dot{Q}_{LT}$ transferred to the cold reservoir is,

$$\dot{Q}_{LT} = \dot{Q}_L + \dot{Q}_{LK}. \tag{5}$$

Applying the first law of thermodynamic, the power output is given by,

$$W = \dot{Q}_{HT} - \dot{Q}_{LT} = \dot{Q}_H - \dot{Q}_L \tag{6}$$

By using Eqs. (1), (2) and (6), we get a normalized expression for the power output $\overline{W} = \frac{W}{U_{HC}A_H}$, given by,

$$\overline{W} = \left(T_H - T_X\right) + \beta\frac{\left(T_H^4 - T_X^4\right)}{T_H^4} - \psi A_R\left(T_Y - T_L\right), \tag{7}$$

where $\beta = \frac{U_{HR}}{U_{HC}}T_H^3$, $\psi = \frac{U_{LC}}{U_{HC}}$ and $A_R = \frac{A_L}{A_H}$. Applying the second law of thermodynamic to the irreversible part of the model we get,

$$\oint \frac{dQ}{T} = \frac{\dot{Q}_H}{T_X} - \frac{\dot{Q}_L}{T_Y} < 0. \tag{8}$$

One can rewrite the inequality in Eq. (7) as,

$$\frac{\dot{Q}_H}{T_X} = R\frac{\dot{Q}_L}{T_Y}, \tag{9}$$

where R is the so-called nonendoreversibility parameter [9, 14, 2]. This parameter, which in principle is within the interval $0 < R \leq 1$ ($R = 1$ for the endoreversible case), can be seen as a measure of the departure from the endoreversible regime [9, 14, 2]. Substituting Eqs. (1) and (2) into Eq. (9), a relationship between T_Y and T_X is obtained as,

$$\frac{T_Y}{T_L} = \frac{R\psi A_R}{R\psi A_R - \frac{(1-\theta)}{\theta} - \beta\frac{(1-\theta^4)}{\theta}}, \tag{10}$$

where $\theta = \frac{T_X}{T_H}$. On the other hand, the thermal efficiency of the irreversible heat engine is,

$$\eta = 1 - \frac{\dot{Q}_{LT}}{\dot{Q}_{HT}} = \frac{\dot{Q}_H - \dot{Q}_L}{\dot{Q}_H + \dot{Q}_{LK}}. \tag{11}$$

In thermoeconomic analysis of power plant models, an objective function is defined in terms of a characteristic function (power output [17, 18, 13, 12], ecological function [1, 5, 6, 7, 4] and the cost involved in the performance of the power plant. In his early paper on this issue, De Vos [12] studied the thermoeconomics of a Novikov power plant model in terms of the maximization of an objective function defined as the quotient of the power output and the performing costs of the plant. In that paper [12], De Vos considered a function of costs with two contributions: The cost of the investment which is assumed as proportional to the size of the plant and the cost of the fuel consumption which is assumed to be proportional to the quantity of heat input in the Novikov model. Analogously, Sahin and Kodal [16] made a thermoeconomic analysis of a Curzon and Ahlborn [10] model in terms of an objective function which they defined as power output per unit total cost taking into account both the investment and fuel costs [16], but assuming that the size of the plant can be taken as proportional to the total heat transfer area, instead of the maximum heat input previously considered by De Vos [12]. Following the Sahin et al. procedure [18], the objective function has been defined as the power output per unit investment cost, due to a solar driven heat engine does not consume fossil fuels. In order to optimize power output per unit total cost, the objective function is given by [18],

$$F = \frac{W}{C_i}, \tag{12}$$

where C_i refers to annual investment cost. The investment cost of the plant is assumed to be proportional to the size of the plant. The size of the plant can be proportional to the total heat transfer area. Thus, the annual investment cost of the system can be written as [18],

$$C_i = aA_H + bA_L, \tag{13}$$

where the investment cost proportionality coefficients for the hot and cold sides a and b respectively are equal to the capital recovery factor times investment cost per unit heat transfer area, and their dimensions are $ncu/(year \cdot m^2)$, ncu being the national current unity. In analogous way to Eq. (12), we define another objetive function in terms of the ecological function and the unit total cost,

$$F_E = \frac{E}{C_i} = \frac{W - T_L\Sigma}{C_i}, \tag{14}$$

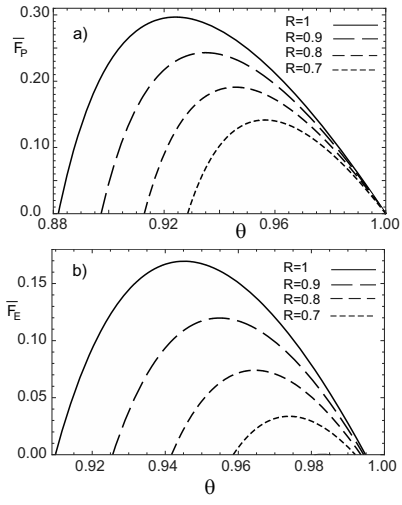

Figure 2: Variation of the thermo-economic objective functions respect to $\theta = \frac{T_X}{T_H}$, for several values of the parameter R, under a) power output conditions and under b)ecological function conditions.

where Σ is the total entropy production of the irreversible heat engine model. If we apply the second law of thermodynamic to the model of Fig. 1, the total entropy production Σ can be expressed as,

$$\Sigma = -\frac{\dot{Q}_H}{T_H} + \frac{\dot{Q}_H}{T_X} - \frac{\dot{Q}_L}{T_Y} + \frac{\dot{Q}_L}{T_L} - \frac{\dot{Q}_{LK}}{T_H} + \frac{\dot{Q}_{LK}}{T_L}. \tag{15}$$

Using Eqs. (1)-(3), (7), (12) and (13), we get a normalized expression for the objective function ($\overline{F}_{mp} = \frac{\dot{W}}{C_i}$) associated to the power output given by,

$$\overline{F}_{mp} = \frac{\tau\left((1-\theta) + \beta\left(1-\theta^4\right)\right) - \psi A_R\left(\frac{T_Y}{T_L} - 1\right)}{A_R\left(\frac{1-f}{f}\right) + 1}, \tag{16}$$

where $\tau = \frac{T_H}{T_L}$ and the parameter f, is the relative investment cost of the hot size heat exchanger and is defined as [18],

$$f = \frac{a}{a+b}. \tag{17}$$

In Fig. 2a, we depict the objective function given by Eq. (16) versus θ, for several values of the parameter R. In Fig. 2b we show the function F_{mp} for several values of the parameter A_R.

Analogously to Eq. (16), by using Eqs. (1)-(3) and (13)-(15), we can obtain a normalized objective

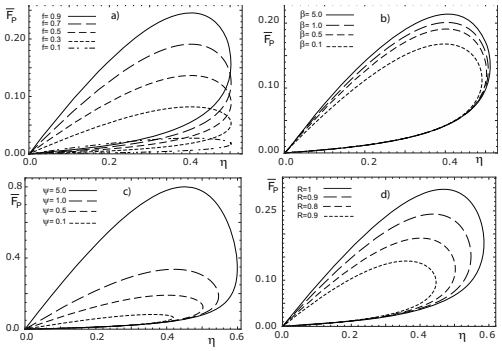

Figure 3: Variation of the dimensionless thermoeconomic objective function $\overline{F_{mp}}$ with respect to thermal efficiency for several a)R, b) β, c) A_R and d) f values, respectively. ($\xi = 0.02$).

function ($\overline{F}_E = \frac{aF_E}{U_{HC}T_L}$) associated to the ecological function, this objective function is given by,

$$\overline{F}_E = \frac{\Lambda\left((1-\theta)+\beta\left(1-\theta^4\right)\right)-\xi\tau\left(1-\frac{1}{\tau}\right)^2}{A_R\left(\frac{1-f}{f}\right)+1}, \quad (18)$$

where $\Lambda = \tau + 1 - \frac{1}{\theta} + \frac{1}{R}\left(\frac{T_L}{T_Y} - 2\right)$. On the other hand, by using Eqs. (1), (2), (3) and (11) the thermal efficiency, η_{th}, of the irreversible heat engine can be expressed by,

$$\eta_{th} = \frac{1 - \frac{\psi A_R}{\tau R\psi A_R\theta-(1-\theta)-\beta\left(1-\theta^4\right)}}{1+\frac{\xi\left(1-\frac{1}{\tau}\right)}{(1-\theta)+\beta\left(1-\theta^4\right)}}. \quad (19)$$

In Fig. (2b), we depict the objective function given by Eq. (18) versus θ, for several values of the parameter R. The dimensionless thermoeconomic objective functions (Eqs. (16) and (18)), can be plotted with respect to the thermal efficiency (Eq. (19)) for given values of f β ψ and A_R as shown in Figs. 3(a)-3(d) and Figs. 4(a)-4(d) for the cases of the maximum power output and maximum ecological function conditions respectively. In all cases we use $\tau = 4$, as in [18], where $T_L \approx 300$K and therefore $T_H \approx 1200$K, this value of τ is for comparison with [18], however a more realistic value of T_H could be of the order of 431K [11], which is the effective sky temperature stemming from the dilution of solar energy. As it could be seen from Figs. (2a) and (2b), there is a value of θ that maximizes the objective functions for given f, ψ and τ values.

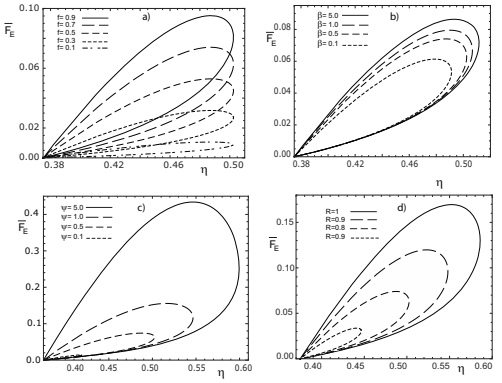

Figure 4: Variation of the dimensionless thermoeconomic objective function $\overline{F_E}$ with respect to thermal efficiency for several a)R, b) β, c) A_R and d) f values, respectively. ($\xi = 0.02$).

Since the two objective functions and thermal efficiency depend on the working fluid temperatures (T_X, T_Y), the objective functions given by Eqs. (16) and (18) can be maximized with respect to T_X or T_Y, that is, we calculate $\frac{dF}{d\theta}|_{\theta=\theta^*} = 0$, for Eqs. (16) and (18), the θ^* values obtained give us the maximum values for $\overline{F}_{mp}$ and $\overline{F}_E$ functions, respectively. This optimization procedure has been numerically carried out in the next section.

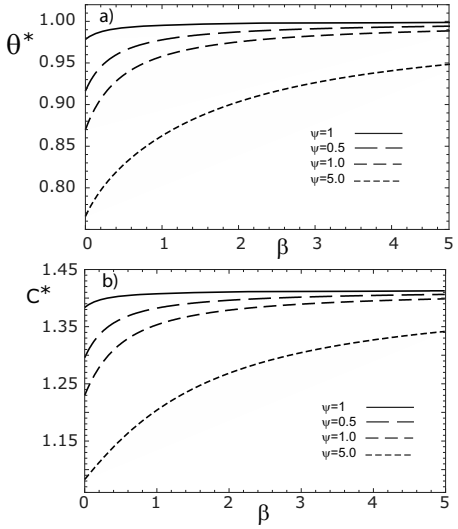

Figure 5: Optimum temperature variations at maximum power conditions of a) $\theta^* = \frac{T_X^*}{T_H}$ and b) $C^* = \frac{T_Y^*}{T_L}$ with respect to β for various ψ values ($T_H = 1200K$, $T_L = 300K$, $A_R = 1$, $f = 0.7$, $R = 0.8$ and $\xi = 0.02$).

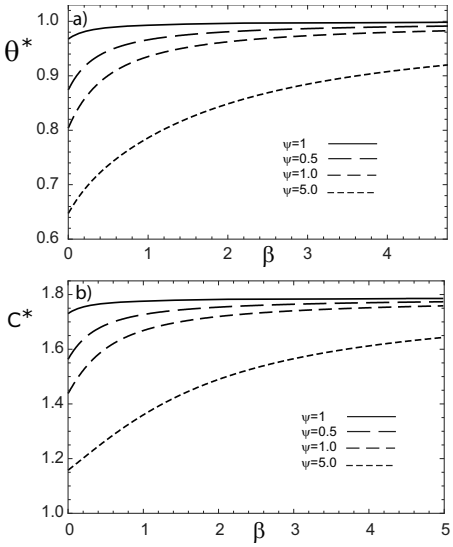

Figure 6: Optimum temperature variations at maximum ecological function conditions of a) $\theta^* = \frac{T_X^*}{T_H}$ and b) $C^* = \frac{T_Y^*}{T_L}$ with respect to β for various ψ values ($T_H = 1200K$, $T_L = 300K$, $A_R = 1$, $f = 0.7$, $R = 0.8$ and $\xi = 0.02$).

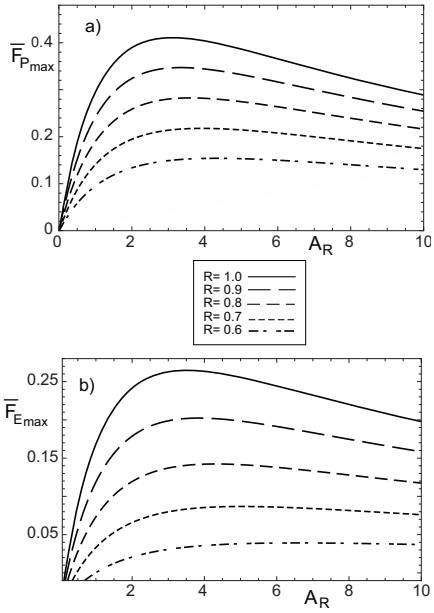

Figure 7: Variation of the maximum thermoeconomic objetive functions $\overline{F}$ respect to A_R, for several values of the parameter R under a) maximum power conditions and b) maximum ecological function conditions.

3. Numerical results and discussion

We can observe from Figs. (2a) and (2b), that the maximum thermo-economic objective functions ($\overline{F}_{mp}$ and $\overline{F}_E$) diminish while the corresponding optimum hot working fluid temperatures shift towards T_H when the internal irreversibility parameter R decreases. On the other hand, the thermo-economic objective function at MER is lesser than the thermoe-conomic objective function at MPR. In Figs. (3) and (4), for both MPR and MER cases, the variation of the dimensionless thermo-economic objective functions with respect to thermal efficiency for several values of R, β, ψ, and f are presented. From figures 3(a)-(d) and 4(a)-(d), we see that the loop curves become smaller as f, β and ψ decrease. We can also see that the maximum thermal efficiency is independent of f values, while the maximum $\overline{F}_{mp}$ (or $\overline{F}_E$), decreases for decreasing f values (see Figs. (3a) and (4a)). In Figs. 5 and 6, we show the variations of optimal temperatures T_X and T_Y with respect to β for different values of ψ and for both maximum power and maximum ecological function conditions, respectively. We observe in Figs. (5) and (6), that for smaller values of ψ and higher values of β, the ratio of the optimum temperatures T_X and T_Y to the source temperature T_H and T_L is generally higher. We can also see when the radiation β increases, $\frac{T_X^*}{T_H}$ increases and approaches to 1. This means that the optimal temperature gets closer to the source tmeperature T_H as radiation increases. We can also observe in Figs. 5 and 6 that, the effect of β on T_X^* and T_Y^* is more important in the interval $0 < \beta < 2$. In Figs. 7 and 8, we show the variation of the maximum dimensionless thermo-economic objective functions ($\overline{F}_{max}$, for both MPR and MER cases) with respect to the ratio $A_R = \frac{A_L}{A_H}$ for different values of the parameter R (see Fig. (7a) and (8a)) and for several values of the temperature ratio $\tau = \frac{T_H}{T_L}$ (see Figs. (7b) and (8b)). We can observe en Figs. 7 and 8, for both MPR and MER, as A_R increases, $\overline{F}_{max}$ increases to its peak value, an then decreases smoothly. We can also observe that $\overline{F}_{max}$ increases and the optimal A_R value decreases considerably for increasing R and τ values.

4. Conclusion

In this work, following the Ust procedure, a thermoeconomic performance analysis using finite time/finite size thermodynamics has been carried out for an irreversible heat engine model in terms of

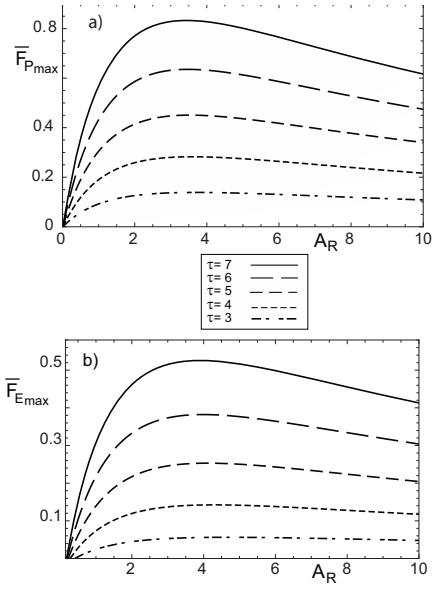

Figure 8: Variation of the maximum thermoeconomic objetive functions $\overline{F}$ respect to A_R, for several values of the parameter τ under a) maximum power conditions and b) maximum ecological function conditions.

the maximization of two objective funtions. The objective functions have been defined as the quotient between power output and the ecological function per unit total investment cost, respectively. By means of the maximization of these objective funtions, the optimum thermoeconomic performance and the corresponding best design parameters of the solar-driven heat engine were determined. In this context, the effects of the economic parameter, f, and the ratio of heat transfer areas, A_R, on the optimal thermoeconomic performance have been investigated. For the model here studied we have considered at the superior thermal coupling simultaneous conduction and radiation modes as in ref [19] and the heat transfer to the cold reservoir is assumed of the conduction type.

4.1. Acknowledgements

This work was supported by COFAA and EDI-IPN-México.

References

[1] F. Angulo-Brown. An ecological optimization criterion for finite-time heat engines. *Journal of Applied Physics*, 69(11):7465–7469, 1991.

[2] F. Angulo-Brown, G. Ares de Parga, and L. A. Hernández. A variational approach to ecological-type optimization criteria for finite-time thermal engine models. *Journal of Physics D: Applied Physics*, 35(10):1089–1093, 2002.

[3] L. A. Arias-Hernández, M. A. Barranco-Jiménez, and F. Angulo-Brown. Comparative analysis of two ecological type modes of performance for simple energy converters. *Journal of the Energy Institute*, 82(4):223–227, 2009.

[4] M. A. Barranco-Jiménez. Finite-time thermodynamic optimization of a non endoreversible heat engine model. *Revista Mexicana de Física*, 55(3):211–220, 2009.

[5] M. A. Barranco-Jiménez and F. Angulo-Brown. Thermoeconomic optimisation of novikov power plant model under maximum ecological conditions. *Journal of the Energy Institute*, 80(2):96–104, 2007.

[6] M. A. Barranco-Jiménez, N. Sánchez-Salas, and F. Angulo-Brown. On the optimum operation conditions of an endoreversible heat engine with different heat transfer laws in the thermal couplings. *Revista Mexicana de Física*, 54(4):284–292, 2008.

[7] M. A. Barranco-Jiménez, N. Sánchez-Salas, and F. Angulo-Brown. Thermoeconomic optimum operation conditions of a solar-driven heat engine model. *Entropy*, 11:443–453, 2009.

[8] A. Bejan. *Advanced Engineering Thermodynamics*. Addison Wesley, New York, 1988.

[9] J. Chen. The maximum power output and maximum efficiency of an irreversible carnot heat engine. *Journal of Physics D: Applied Physics*, 27:1144–1149, 1994.

[10] F. L. Curzon and B. Ahlborn. Efficiency of a carnot engine at maximum power output. *American Journal of Physics*, 43(1):22–24, 1975.

[11] A. De Vos. *Endoreversible Thermodynamics of Solar Energy Conversion*. Oxford University Press, New York, 1992.

[12] A. De Vos. Endoreversible thermoeconomics. *Energy Conversion and Management*, 36(1):1–5, 1995.

[13] A. Koyun. Performance analysis of a solardriven heat engine with external irreversibilities under maximum power and power density condition. *Energy Conversion and Management*, 45(11):1941–1947, 2000.

[14] S. Ozcaynak, S. Goktan, and H. Yavuz. Finite-time thermodynamics analysis of a radiative heat engine with internal irreversibility. *Journal of Physics D: Applied Physics*, 27:1139–1143, 1994.

[15] A. Z. Sahin. Optimum operating conditions of solar driven heat engines. *Energy Conversion and Management*, 41(13):1335–1343, 2000.

[16] B. Sahin and A. Kodal. Performance analysis of an endoreversible heat engine based on a new thermoeconomic optimization criterion. *Energy Conversion and Management*, 42(9):1085–1093, 2001.

[17] B. Sahin and A. Kodal. Finite time thermoeconomic optimization for irreversible heat engines. *International Journal of Thermal Sciences*, 42(8):777–782, 2003.

[18] B. Sahin, Y. Ust, Y. Tamer, and I. A. AkcayKoyun. Thermoeconomic analysis of a solar driven heat engine. *Renewable Energy*, 31(7):1033–1042, 2006.

[19] Y. Ust. Effects of combined heat transfer on the thermo-economic performance of irreversible solar-driven heat engines. *Renewable energy*, 32:2085–2095, 2007.

[20] T. Yilmaz. A new performance criterion for heat engines: efficient power. *Journal of the Energy Institute*, 79(1):38–41, 2006.

A Multi-Stage Optimal Renewal Planning of an Energy Supply System for an Office Building from an Economic Viewpoint

Shu Yoshida [a], Koichi Ito [b], Yoshiharu Amano [b], Keigo Matsuo [c], Takumi Hashizume [b], Daniel Favrat [d] and François Marechal [d]

[a] *Energy Use Research and Development Center, Kansai Electric Power Co., Inc., Osaka, Japan.*
[b] *Research Institute for Science and Engineering, Waseda University, Tokyo, Japan.*
[c] *NTT Energy and Environment Systems Laboratories, Tokyo, Japan.*
[d] *Industrial Energy System Laboratory, École Polytechnique Fédérale de Lausanne, Switzerland.*

Abstract: A multi-stage optimal renewal planning problem for the energy supply system is studied by evaluating the long-term economics based on the annualized cost method. This problem is mathematically expressed as a mixed integer-linear programming formula, and a numerical study is carried out for an office building using the GAMS/CPLEX solver. Decision variables are the renewal year and the system's configuration at each of the renewal multi-stages together with the system's operational strategy for hourly changing energy demands. By taking the deterioration of the existing equipment of the system into account, the renewal system is assumed to be composed by adding the same and new types of equipment with technologically improved performance. The present planning year is set as 10 years after the system's initial construction, and the evaluation period is assumed to be 20 years from present, with the system renewed twice during this period. The main results are as follows: From the economic standpoint, the optimal first and second renewal years are the 10th and 22nd years after the system's initial construction. Comparing this optimal solution with the reference renewal plan, which renews the system using the same configuration only once, 15 years after the initial construction, the average annual total cost can be reduced 4.89 %.

Keywords: Energy supply system, Multi-stage optimization, Office building, Renewal planning.

1. Introduction

As the lifetimes of buildings are much longer than those of their energy supply systems for space heating and cooling, the latter must be renewed several times through the lifetimes of the former. In the renewal planning problems of the above systems, it is important to comprehensively take into account several factors such as energy demands, the structure of the existing system together with the capacities and costs of component equipment, future performance improvements of candidate equipment which may be installed at each renewal stage, the performance deterioration of the existing and newly installed equipment, the total system's operational policy, etc. Up to the present, several studies have been done by authors on the renewal planning problems of systems based on the mathematical optimization approach [1-4].

In this study, for the purpose of investigating the system's renewal planning problem over a relatively long term, multi-stage renewal planning is formulated as a mathematical optimization problem, and the economic aspects of the optimal renewal system is investigated numerically for the system installed into an office building. As a sensibility study, the influence is analysed on the optimal renewal plan of the construction cost ratio necessary to install new equipment.

2. A multi-stage optimal renewal planning problem

2.1. Framework of problem

The multi-stage optimal renewal planning method proposed here can make rational decisions by determining multi-stage renewal years, respective renewal system structures, equipment capacities and systems operational strategies so as to minimize the long-term total cost of the objective energy supply system. From the standpoint of practical computing time limitations to derive the optimal solution, the number of renewal stage is set as two in this paper, and the framework of the optimal renewal planning problem is shown in Fig. 1. Here, the horizontal axis t is the year variable, and the initial system, say $\boldsymbol{X}_0$, is constructed at t = 0 y. The present planning year

Corresponding Author: S. Yoshida, Email: yoshida.shuu@e2.kepco.co.jp

is set as $t = t_p$, and the system will be evaluated economically during the period from $t = t_p$ to $t = t_p + T$. In other words, T is the total evaluation period of the system in this multi-stage planning problem. For the sake of simplicity, the legal lifetime of all equipment is set to be equal to each other by denoting κ, the initial system $\boldsymbol{X}_0$ will be renewed to the first renewal system $\boldsymbol{X}_1$ at $t = \tau_1$ ($t_p \le \tau_1 \le \kappa$). In this renewal stage, equipment set $\boldsymbol{X}_{0,1}$ is determined to be undiscarded from $\boldsymbol{X}_0$, but equipment set $\boldsymbol{X}_{0,2}$ is discarded from $\boldsymbol{X}_0$ as shown in Fig. 1. In addition, from the candidate equipment set $\boldsymbol{Y}_1$ of possible additions to the system, $\boldsymbol{Y}_{1,1}$ is selected as the set of installing equipment, but $\boldsymbol{Y}_{1,2}$ is not selected as the installing equipment. Namely, the first renewal system $\boldsymbol{X}_1$ is composed by combining $\boldsymbol{X}_{0,1}$ and $\boldsymbol{Y}_{1,1}$. This $\boldsymbol{X}_1$ will be renewed once again at the second renewal year $\tau = \tau_2$ ($\kappa \le \tau_2 \le t_p + T$) to the second renewal system $\boldsymbol{X}_2$ as shown in Fig. 2. Theoretically, it is possible to renew the initial system $\boldsymbol{X}_0$ twice before $t = \kappa$, i.e., $\tau_2 < \kappa$, but this case is omitted to avoid the complication of the present planning problem.

2.2. Mathematical formulation

Let us briefly explain here the mathematical formulation of the planning problem and its solution method.

2.2.1. Decision variables and constraints

Decision variables that will be determined by the optimization problem are composed of continuous or binary variables which are defined at each multi-stage renewal years, τ_1 and τ_2, the selection

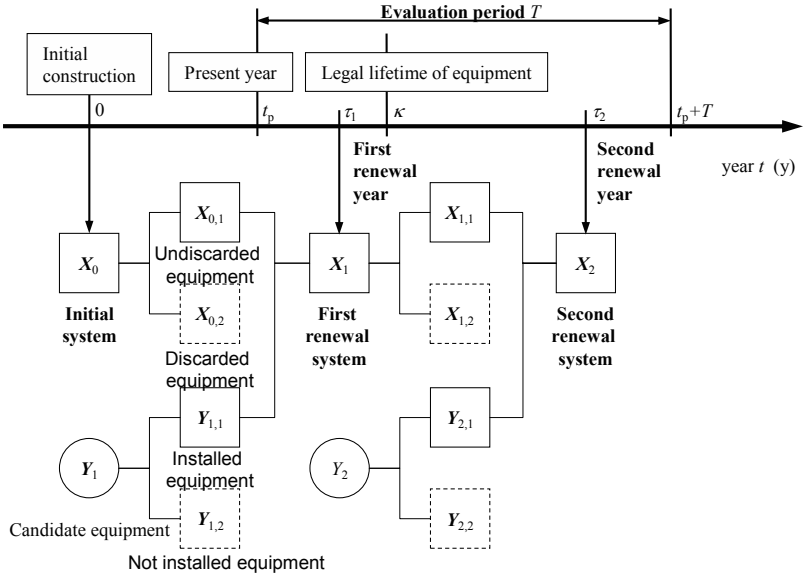

Fig. 1 Framework of the multi-stage renewal planning problem.

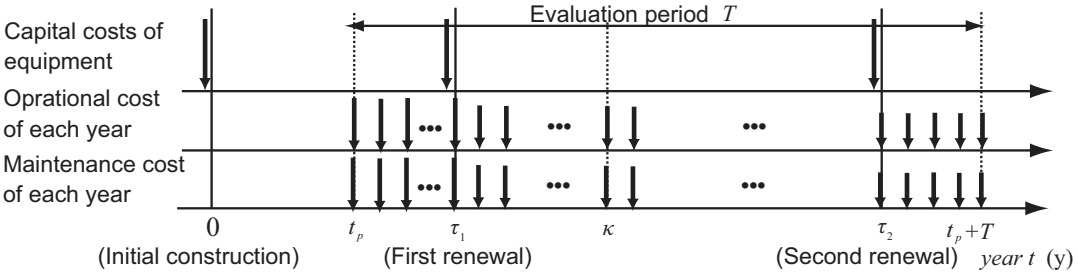

Fig. 2 Economic evaluation of renewal system.

of equipment to be discarded from the old system, i.e., $\boldsymbol{X}_{0,2}$ and $\boldsymbol{X}_{1,2}$ in Fig. 1, and the selection of newly installed alternative equipment, i.e., $\boldsymbol{Y}_{1,1}$ and $\boldsymbol{Y}_{2,1}$, that are defined together with their capacities, the selection of utility rates and utility maximum contract demands. The operational variables are those of relating the system's evaluation period. In this study, energy demands are assumed to be changed hourly and seasonally, but for the simplicity of the analysis, their patterns will be fixed yearly through the system's evaluation period. However, as the system's structure changes at each of the renewal stages, and the performance characteristic of the existing equipment deteriorates year by year, the system's operational policy must be changed yearly through the system's evaluation period. In this study, performance improvement and deterioration are expressed by rates α and β %/year for each piece of equipment, and performance characteristics rise and decrease linearly year by year according to these rates. This fact makes the total number of decision variables very large for this optimization problem, and of course it makes it difficult to derive the optimal numerical solution practically. Concerning the determination of optimal renewal years, say $\tau_1 = \tau_1^*$ and $\tau_2 = \tau_2^*$, they are not derived directly by the mathematical optimization algorithm. Namely, by assuming all sets of possible values of their combination *a priori*, their corresponding values from the objective function are compared to each other, and the best ones are chosen as the optimal values.

Next, as constraints of the optimization problem, the first sets of equations consist of the performance characteristics of each kind of equipment and the upper and lower limits of its capacity. The performance characteristics are formulated as relations between the input and output energy flow rates. As explained previously in this section, it is important to notice that the relations of performance characteristics of equipment change year by year due to deterioration. The second set of equations consists of the relationship between the energy consumption and maximum contract demands and the selection of utility rates. The third set of constraints consists of energy balance and supply demand relationships, formulated by linear relationships among the energy flow rates at each energy flow junction. The first to third sets of equations are formulated for each energy demand pattern throughout the year.

2.2.2. Objective function

The objective function to be minimized is the average annual total cost from the long-term economic viewpoint. This is evaluated as the sum of the annual capital, operational and maintenance costs based on the annualized costs method [5] during the period from the present year t_p to the end of the evaluation year $t = t_p + T$.

As shown in Fig. 2, in the calculation of the above-mentioned cost, it is necessary to take into account the construction and disposal costs of equipment at each renewal stage, expressed by multiplying the construction and disposal cost ratio, say γ and μ, for each equipment cost.

It is of course necessary to consider the interest rate i %/year and the residual cost of equipment at the end of the total evaluation period $t = t_p + T$. Concerning the latter, the residual cost ratio at the end of the legal lifetime is set as ε, and its value is simply assumed to be equal for all equipment. As the operational cost changes year by year, the average value of the annual total cost, i.e., the mathematical formulation of the objective function to be minimized, becomes relatively complex. Lastly, it is assumed here that each piece of equipment can be used after its legal lifetime κ though its maintenance cost rises $(1 + \theta)$ times higher step wisely, where θ is the ascent rate of maintenance costs after the legal lifetime of the equipment.

2.2.3. Solution method

From sections 2.2.1 and 2.2.2, the multi-stage renewal planning problem for the energy supply system can be expressed mathematically as a mixed-integer linear programming problem. This problem includes large numbers of continuous and binary unknown decision variables with many constraint equations. To derive the numerical optimal solution, the GAMS with CPLEX solver (version 10) is adopted here, developed by combining the branch and bound method with the simplex one [6].

3. Numerical study

3.1. Input data

By using the optimization method proposed in the previous section, a numerical study is carried out

on the renewal planning problem of the energy supply system for an office building with total floor area of 15 000m^2. This energy system supplies electricity and heat for space cooling and heating by purchasing electricity, natural gas and water. These energy demands are estimated at each 24-hour sampling time on representative average days of the four seasons in addition to summer and winter peak demand days. As an example, average hourly energy demands on four seasons are shown in Fig. 3. The initial system studied here is composed of only a gas-fired absorption refrigerator (RG) of 2708kW as shown in Fig. 4. The economic and performance characteristic values of this system are shown in Table 1. The present renewal planning year is set as t_p = 10th year, and both sets of candidate equipment newly installed at the first and second renewal years τ_1 and τ_2 are proposed equally as shown in Fig. 5; i.e., cooling tower (CT), electric compression refrigerator (RE), chilling unit (water type) (CH), brine electric heat pump (HB), ice storage tank for HB (IHB), gas engine (GE), waste heat absorption refrigerator (GL), gas-fired absorption refrigerator (RG), steam boiler (BS), and heat exchangers from brine to water (HEB), from water to water (HEH) and from steam to water (HES). Their performance characteristic values are shown in Table 2 together with their performance improvement and deterioration rates, and the respective capital and maintenance unit costs of the equipment. Rates for purchased electricity, natural gas and water are shown in Table 3. The evaluation period of the system, T, is set as 20 years, and the values of miscellaneous other parameters are shown in Table 4. The primary energy consumption of purchased electricity and natural gas are 4.8 MJ/kWh and 45 MJ/m^3, respectively. The coefficients of CO_2 emission of purchased electricity and natural gas are assumed to be 0.356 kg-CO_2/kWh and 2.29 kg CO_2/m^3, respectively, based on data from the Kansai area, Japan.

3.2 Numerical results

3.2.1 Comparative reference renewal plan

Before calculating the optimal solution for the input data explained in 3.1, we calculated the reference renewal plan as a standard plan. In this plan, the initial reference renewal plan for the $\boldsymbol{X}_0$

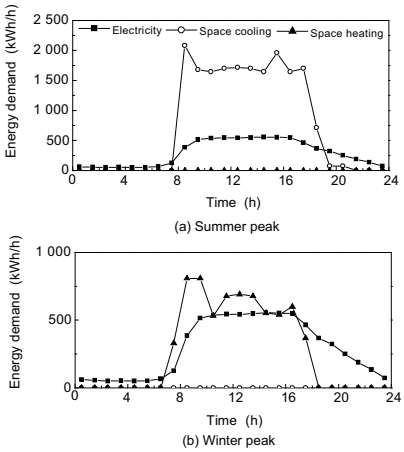

Fig. 3 Example of hourly energy demands.

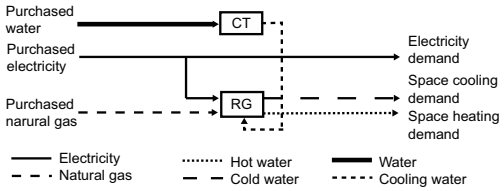

Fig. 4 Structure of initial system.

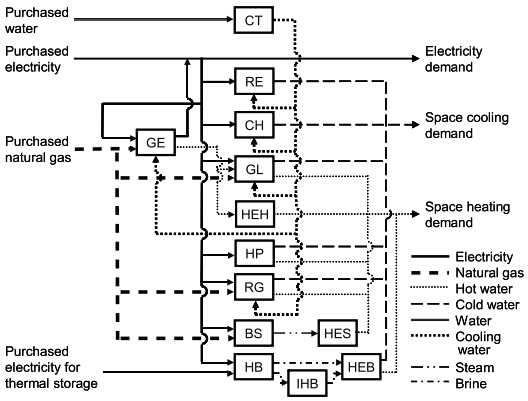

Fig. 5 Alternative equipment.

will be renewed only once at t =τ_1=15th year, and the renewal system consists of equipment equal to the initial system. In this case, the average annual total cost is 52.78×10^6 yen/year, which is the sum of the annual capital, operational and maintenance costs of 4.16, 44.47 and 4.15×10^6 yen/year, respectively.

The average amounts of primary energy consumption and CO_2 emission during the evaluation period T are also calculated and their

Table 1. Economic and performance values of initially existing equipment.

Equipment	Capital unit cost $a \times 10^3$ yen/kW + $b \times 10^6$ yen		Maintenance unit cost	Capacity	Performance characteristic value	
	a	b				
RG	10.6	6.72	1 534 yen/(kW·y)	2 708 kW	COP* (Space cooling) Thermal efficiency (Space heating)	1.01 0.84

*COP=Coefficient of performance

Table 2. Economic and performance values of initially existing equipment newly installed.

	Performance characteristic value		Performance improvement rate of equipment α %/y	Performance deterioration rate of equipment β %/y	Capital unit cost $a \times 10^3$ yen/kW + $b \times 10^6$yen		Maintenance unit cost yen/(kW·y)
					a	b	
GE	Power efficiency Thermal efficiency	0.40 0.34	0.0	0.5	220	6.60	3.20 yen/kWh
RE	COP	6.41	1.0	0.5	12.7	13.6	1 230
CH	COP	5.77	1.0	0.5	14.9	0.937	1 883
HP	COP (Space cooling) COP (Space heating)	4.50 3.66	1.5	0.5	37.9	0	1 422
HB	COP (Brine for direct supply) COP (Brine for thermal storage) COP (Space cooling) COP (Space heating)	3.63 2.97 3.63 3.11	1.5	0.5	52.2	12.3	2 161
IHB	Maximum rate (Ice making) Maximum rate (Space cooling)	0.14 0.20	–	–			
RG	COP (Space cooling) Thermal efficiency (Space heating)	1.35 0.88	0.75 (Space cooling) 0 (Space heating)	1.5 (Space cooling) 0.25 (Space heating)	13.2	7.33	1 534
GL	COP (Space cooling: Natural gas usage) COP (Space cooling: Waste heat) Thermal efficiency (Space heating)	1.33 1.81 0.88	0.75 (Space cooling) 0 (Space heating)	0.75 (Space cooling) 0.25 (Space heating)	15.4	8.56	1 600
BS	Thermal efficiency	0.82	0.0	0.25	4.37	0.112	706

Table 3. Rates of purchased electricity and natural gas (Kansai area).

Utility	Unit cost		
	Customer charge	Demand charge	Energy charge
Electricity	—	1.66×10^3 yen/(kW · month)	(July～Sept.) 11.15 yen/kWh (Other months) 10.13 yen/kWh
Electricity for thermal storage	—	—	(22:00～8:00) 4.20 yen/kWh
Natural gas	37.8×10^3 yen/month	(Apr.～Oct.) 1.38×10^3 yen/(month · m^3/h) (Other months) 2.77×10^3yen/(month · m^3/h)	(Apr.～Oct.) 42.69 yen/m^3 (Other months) 46.80 yen/m^3
Water	—	—	550 yen/m^3

Table 4. Values of miscellaneous parameters.

Item	Symbol	Value
Present renewal planning year	t_p	10th year
Evaluation period	T	20 years
Legal lifetime of equipment	κ	15 years
Interest rate	i	3%/year
Residual cost ratio of equipment at the end of legal lifetime	ε	0

Item	Symbol	Value
Construction cost ratio	γ	0.2
Surplus rate of system's capacity of facility	λ	0.3
Disposal cost ratio	μ	0.1
Ascent rate of maintenance cost after legal lifetime of equipment	θ	0.2

values are 16.6 GJ/year and 1069.1 t-CO_2/year, respectively.

3.2.2 Optimal solution for renewal planning problem

Before determining the optimal renewal years of both $\tau_1 = \tau_1^*$ and $\tau_2 = \tau_2^*$, we only determined τ_2 which minimizes the objective function by changing τ_1 year by year from the 10th year to the 15th year. Fig. 6 shows a detailed comparison of several renewal plans and Fig. 7 shows the equipment capacity of the renewal system. As an example, when the first renewal year is set to be τ_1 = 10th year, the optimal second renewal year is determined as t_2 = 22nd year. Fig. 6 shows that the optimal renewal years are respectively $\tau_1 = \tau_1^*$ = 10th year and $\tau_2 = \tau_2^*$ = 22nd year which minimize the average annual total cost for the multi-stage renewal planning problem discussed here. In this figure, the result is also shown for the comparative reference renewal plan. The average annual total cost of the optimal solution is 4.89 % lower than that of the reference plan. As shown in Fig. 6, the economic effect of the system's renewal decreases from 4.89 % to 3.24 % with a delay of the first renewal year τ_1 from the 10th to 15th year. In Fig. 6, the average amount of CO_2 emission is also shown for each renewal plan, and the value increases from 967.1 to 1006.1 t-CO_2/year according to τ_1 = 10 ~ 15th year.

In Fig. 7, the left and right columns show the respective capacities of each piece of equipment in the first and second renewal systems, respectively. The result of this figure shows that from an economic point of view it is better to discard the deteriorated RG and to install an improved RG together with the HB and IHB. The reason to install the HB seems to be that its performance efficiency is higher than that of the gas-fired absorption refrigerator RG. Concerning the equipment capacity values, those of HB and IHB decrease according to the delay of τ_1, but that of RG shows the contrary tendency. It is also interesting that the optimal second renewal year is almost τ_2 = 22 y except one case. In this renewal stage, only a small scale HP is installed to back up the deterioration of the already existing equipment. It is notable that τ_2 almost equal to 22nd year becomes optimal, because if τ_2 is later, the benefit of installing this equipment becomes relatively small. These obtained results seem to be difficult to explain based only on engineering and inference.

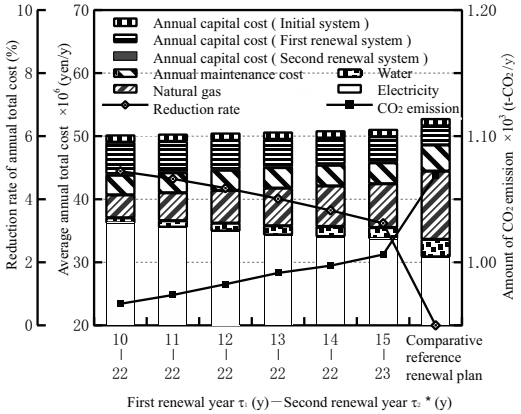

Fig. 6 Detailed comparison of several renewal plans by changing the first renewal year τ_1 (γ = 0.2).

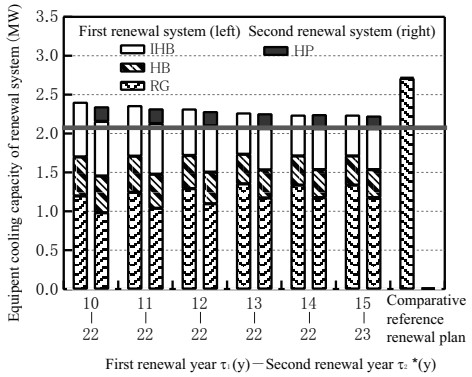

Fig. 7 Equipment capacities of renewal systems (γ = 0.2).

3.2.3 Sensitivity analysis on the value of construction cost ratio

Table 5 shows the results of the sensitivity analysis on the value of the construction cost ratio, γ, to the optimal solution. It shows the capacities of each piece of equipment for the optimal renewal solution by changing γ = 0.2, which is the reference value, to 1.25. It also shows that the types of equipment to be discarded and installed don't change for γ = 0.2 and 0.5 at each of the optimal renewal stages. However, when γ becomes 0.75, the CH is installed at the second renewal stage instead of the HP. When γ becomes more than 1, these types of equipment change to other ones, but from a practical economic standpoint, the value of γ doesn't exceed more than 0.5 in Japan.

Table 5. Equipment capacities of renewal systems (kW).

		Construction cost ratio γ				
		0.20	0.50	0.75	1.00	1.25
	First renewal year τ_1	**10**	**10**	**10**	**12**	**15**
	Second renewal year τ_2	**22**	**21**	**20**	**20**	**23**
First renewal system	**Existing system**					
	RG	dis.*	dis.*	dis.*	2220	2099
	Equipment installed newly				0	0
	GE	0	0	0	0	0
	HE	0	0	0	0	0
	RE	0	0	0	0	0
	CH	0	0	0	0	231
	HP	0	0	0	152	0
	HB	502	375	375	0	0
	IHB**	702	525	525	0	0
	RG	1197	1414	1387	0	0
	GL	0	0	0	0	0
	BS	0	0	0	0	0
Second renewal system	**Existing system**					
	CH	0	0	0	0	222
	HP	0	0	0	146	0
	HB	472	354	356	0	0
	IHB**	702	525	525	0	0
	RG	982	1180	1179	dis.*	dis.*
	Equipment installed newly				0	0
	GE	0	0	0	0	0
	HE	0	0	0	0	0
	RE	0	0	0	0	0
	CH	0	0	242	449	0
	HP	186	216	0	0	0
	HB	0	0	0	0	0
	IHB**	0	0	0	0	0
	RG	0	0	0	1751	2053
	GL	0	0	0	0	0
	BS	0	0	0	0	0

* dis. = discarded ** kWh

4. Conclusion

A multi-stage optimal renewal planning method is proposed for an energy supply system installed into a building from a long-term economic viewpoint. Through the numerical study for an office building with total floor area of 15 000 m^2, the following main results wete obtained:

1. From an economic standpoint, the optimal first and second renewal years are the 10^{th} and 22^{nd} years after the system's initial construction.
2. Comparing the optimal solution with the reference renewal plan, which renews the system only once, 15 years after the initial construction, the average annual total cost can be reduced 4.89 %.
3. In the optimal renewal planning, all the deteriorated equipment installed initially is discarded and a brine electric heat pump is installed together with a gas-fired absorption refrigerator at the first renewal stage. At the second renewal stage, only a small scale electric heat pump is installed to back up the supply shortage caused by the deterioration of existing equipment
4. As a sensitivity analysis, the construction cost ratio of each piece of equipment increases up to 6.25 times the standard value. In the region of γ<1.0, no obvious influence is observed on the optimal configuration of the renewal equipment and renewal first and second years.

Nomenclature

a, b Coefficients of capital units cost of equipment
i Interest rate, %/year
t Year variable, year
T Total evaluation period of the system, year
t_p Present renewal planning year, year
$\boldsymbol{X}_0$ Initial system
$\boldsymbol{X}_1$, $\boldsymbol{X}_2$ First and second renewal systems, respectively
$\boldsymbol{X}_{0,1}$, $\boldsymbol{X}_{1,1}$ Sets of equipment un-discarded at first and second renewal stages, respectively
$\boldsymbol{X}_{0,2}$, $\boldsymbol{X}_{1,2}$ Sets of equipment discarded at first and second renewal stages, respectively
$\boldsymbol{Y}_1$, $\boldsymbol{Y}_2$ Sets of candidate equipment installed newly at first and second renewal stages, respectively
$\boldsymbol{Y}_{1,1}$, $\boldsymbol{Y}_{2,1}$ Sets of selected equipment installed newly at first and second renewal stages
$\boldsymbol{Y}_{1,2}$, $\boldsymbol{Y}_{2,2}$ Sets of equipment not installed at first and second renewal stages, respectively
α Performance improvement rate of equipment, %/year
β Performance deterioration rate of equipment, %/year
ε Residual cost ratio of equipment at the end of legal lifetime
γ Construction cost ratio
μ Disposal cost ratio
τ_1, τ_2 First and second renewal years, respectively, year
θ Ascent rate of maintenance cost after legal lifetime of equipment
BS Steam boiler
CH Chilling unit (water type)
CT Cooling tower
GE Gas engine
GL Waste heat absorption refrigerator
HB Brine electric heat pump
HEB Heat exchanger from brine to water
HEH Heat exchanger from water to water
HES Heat exchanger from stem to water
HP Electric heat pump
IHB Ice storage tank for HB
RE Electric compression refrigerator
RG Gas-fired absorption refrigerator

Reference

[1] Yoshida S., Gamou S., Ito K., Enokido T., Yokoyama R. An Optimal Renewal Planning of Energy Supply System from Economic Viewpoint. In Proceedings of Int. Conf. on Power Engineering (ICOPE) 2005; Part B: 1477-1483.

[2] Yoshida S., Ito K., Amano Y., Hashizume T. Multi-Objective Renewal Planning of Energy Supply Systems for Buildings from Economic and Environmental Viewpoints. In Proceeding of ECOS2008, Vol. III: 1545-1552

[3] Amano Y., Ito K., Yoshida S., Matsuo K., Hashizume T., Favrat D., Marechal F. Impact Analysis of Carbon Tax on the Renewal Planning of Energy Supply System for an Office Building. Energy 35 (2010) 1040-1046.

[4] Yoshida S., Ito K., Amano Y., Matsuo K., Hashizume T., Ueta K. A Multi-Stage Optimal Renewal Planning for Energy Supply System from Economic Viewpoint. In Proceedings of Int. Conf. on Power Engineering (ICOPE) 2009, Vol.3: 173-178

[5] Witte L.C., Schmidt P.S., Brown D.R. Industrial Energy Management and Utilization. Hemisphere Publishing, 1988, 68-69.

[6] Broke A., Kendric D., Meerraus A. GAMS Release 2.25– A User's Guide. GAMS Development Corp., 1996.

Acknowledgments: The authors would like to thank members of working group on total energy supply systems in the Committee of Building Electric Power Utility for their support and cooperation.

Feasibility Analysis of Micro-CHP Systems for Residential Building Applications

Margherita Cadorin, Pier Ruggero Spina, and Mauro Venturini

Engineering Department, University of Ferrara, Italy

Abstract: In this paper, an energy and economic analysis of micro-CHP systems is presented, to evaluate their feasibility as an alternative to household boilers. The considered CHP systems are based on innovative technologies, already available, but not yet widespread and industrialized, or available in the short-term. The considered technologies are external combustion systems, such as the ones based on Stirling engines, micro Rankine cycles and thermo-photovoltaic generators.
With reference to these three typologies of micro-CHP systems, analyses are carried-out in order to evaluate the energy performance and the payback period, with reference to natural gas and electric energy tariffs in the present European market scenario. In particular, since these CHP systems are intended as an alternative to household boilers, the heat that has to be produced (and used) and, consequently, the operating hours of the CHP systems, are determined. This allows the estimation of investment payback time of these technologies with respect to traditional household boilers.

Keywords: cogeneration, distributed generation, boiler, energy performance of residential buildings, energy tariffs, micro-CHP, investment payback period.

1. Introduction

The ever increasing demand for energy all over the world is mainly satisfied through the use of fossil fuels [1]. Due to the shortage of these resources and to the fact that they are responsible for most of CO_2 emissions in the atmosphere, increasing economical resources have been dedicated worldwide to find an environmentally-friendly solution for power generation. Combined heat and power (CHP) is a technology which allows high primary energy savings [2] and, therefore, limits CO_2 emissions. While industrial applications of CHP systems are fairly widespread, the applications for residential heating systems are limited by several technical [3-5], environmental [6], economic [7] and legislative [8] problems, especially for small- and micro- electric power sizes. The main difficulty for residential applications can be attributed to the fact that the CHP technologies available at present cannot always combine high efficiency, low cost, silent operation, low pollutant emissions and reduced maintenance [3].

The aim of this paper is to evaluate the capability of micro-CHP systems based on innovative technologies as an alternative to traditional household boilers with a size up to approximately 35 kW of thermal power. The considered micro-CHP systems are the ones based on Stirling, micro Rankine cycle and thermophotovoltaic (TPV) technologies, which are already available but not yet widespread and industrialized, or available in the short-term. All these micro-CHP systems are external combustion systems characterized by high reliability, low noise and a potentially high value of the overall CHP efficiency.

An energy analysis was preliminarily carried out to evaluate the energy production in terms of the ratio between thermal and electric energy. Then, the investment payback period of these micro-CHP systems was estimated, as a function of the tariff scenario in Europe, and building energy requirements. For this analysis, the payback period to recover only the additional costs of the CHP technology was evaluated with respect to a traditional boiler. In fact, the considered micro-CHP systems are intended as an alternative to traditional household boilers, and, consequently, all the costs related to the boiler can be avoided.

2. Novel micro-CHP technologies

The considered micro-CHP systems are intended as an alternative to household boilers. Thus, they should be characterized by the same level of noise, pollutant emissions and maintenance as common household boilers. The considered innovative

Corresponding Author: Mauro Venturini, Email: mauro.venturini@unife.it

micro-CHP systems are the ones based on Stirling, micro Rankine cycle and TPV technologies. They are all external combustion systems (so, pollutant emission levels are comparable to those of boilers), characterized by high reliability, low noise, and potentially high values of the overall CHP efficiency. In fact, even if electric efficiencies are low (from some percentage points of the TPV prototypes, to about 25 % of Stirling CHP systems), the potential overall CHP efficiency is usually higher than 80 % and can approach 100 % in condensing systems [3]. The electric power sizes of the units available on the market, even if at a prototype level only, range from 1 to 10 kW, with thermal power of 5 to 45 kW [3]. Thus, these technologies could represent a promising alternative to household boilers up to about 35 kW of thermal power.

Since all these CHP technologies are not currently industrialized and widespread on the market (some of them are not likely to be available in the short-term), a well-established market price is difficult to estimate and the current specific cost of the prototypes is very high.

2.1. Stirling engines

The micro-CHP Stirling systems up to 10 kW of electric power size available on the market, which are mostly prototypes, range from 1 to 9 kW of electric power size, with corresponding thermal power size from 5 to 25 kW, which may represent a good alternative to household boilers. The electric efficiency ranges from 13 to 25 % with the CHP efficiency higher than 80 % [3], which may even go beyond 95 %.

2.2 Micro Rankine cycles

The micro-CHP systems based on the Rankine cycles (which use water or an organic fluid (ORC) as working fluid) up to 10 kW of electric power size available on the market, most of them at a prototype level only, range from 2 to 10 kW of electric power size, with corresponding thermal power size from 11 to 44 kW, which, also in this case, may represent a good alternative to household boilers. The electric efficiency ranges from 6 to 19 %, with potential overall CHP efficiency always higher than 90 % [3,9].

2.3 Thermophotovoltaic (TPV) generators

The TPV-based micro-CHP systems can be obtained by converting a condensing boiler with a surface radiant burner (which is widespread as a household boiler), by adding PV cells inside the combustion chamber [3,10,11]. All heat not converted into electric energy by PV cells (such as heat removed from cells by the PV cell cooling system) is usefully recovered. Thus, the extra-fuel supplied for electric energy production with respect to the simple boiler can be considered fully converted into electric energy. Although the electric efficiency of TPV CHP systems is low (approx. 2-5 % of available prototypes, and, however, less than 10 %), the potential CHP efficiency is always higher than 90 % [3].

With respect to Stirling engines and micro Rankine cycles, the TPV generators are characterized by (i) electric efficiency almost independent of machine load and (ii) no moving parts, so that noise and vibrations are very low. However, they still require remarkable technological development, both for component design and for their integration.

3. European scenario for distributed CHP in residential buildings

3.1. European regulation on energy performance of buildings

The overall primary energy demand for domestic users can be estimated by means of the parameter (Energy Performance *EP*) reported in (1):

$$EP_{\mathrm{ov}} = EP_{\mathrm{H}} + EP_{\mathrm{W}} + EP_{\mathrm{C}} + EP_{\mathrm{light}}, \qquad (1)$$

where the different contributions account for "space heating", "hot water" production, "air conditioning" and "lighting", and usually refer to household surface area and time (i.e. kWh/(m^2 yr)).

As regards the primary energy required for both "heating" and "hot water" production, it results:

$$EP_{\mathrm{H,W}} = \frac{Q_{H,W}}{A}\frac{1}{\eta_{H,W}} = \frac{q_{H,W}}{\eta_{H,W}}, \qquad (2)$$

The annual energy demand $Q_{\mathrm{H,W}}$ (and, as a consequence, $EP_{\mathrm{H,W}}$ values) mainly depends on (i) climatic zone, (ii) building shape, (iii) heat transferred by transmission and ventilation and (iv) internal and solar heat gains [12].

The Energy Performance of Buildings Directive (EPBD) 2002/91/EC [13] sets the basic principles and requirements of the energy performance of buildings; the Concerted Action (CA) EPBD [8]

provides an overview of the implementation of this EU legislation. According to [8], the required energy performance limits for residential buildings (by only considering the contributions of heating and hot water production, $EP_{H,W}$) starting from 1 January 2010 are reported in Fig. 1 for some EU countries.

Data in Fig. 1 highlight the lowest and highest allowable $EP_{H,W}$ (e.g., by considering the most and least favourable climatic zone, respectively), and the average value calculated accordingly. In one case (Belgium), only one value was available. It can be observed that the range of variation of $EP_{H,W}$ is considerably large, ranging from approximately 10 to 300 kWh/(m^2 yr). Therefore, if a CHP system with a thermal power of 0.15 kW$_t$/m^2 is considered, a $q_{H,W}$ equal to 300 kWh/(m^2 yr) corresponds to 2,000 annual equivalent operating hours.

3.2. Tariff scenario in Europe

The considered tariff scenario refers to the second semester of 2007. These tariffs do not account for 2008/2009 worldwide financial crisis, and so they can be considered more representative of a mid-term energy market scenario.

Figure 2 shows the specific consumer tax-included price for household users of natural gas and electric energy respectively. For instance, only the values for band D2 (annual consumption of natural gas between 20 and 200 GJ, i.e. between 525 and 5254 Sm^3) and band DC (annual consumption of electric energy between 2500 and 5000 kWh) of some EU countries are reported.

It can be highlighted that there are considerable differences among the different EU countries. For this reason, the EU27 tariff has also been reported, to highlight how each European country compares to the average European tariff. More generally, by considering the whole range of variation in natural gas price (bands D1, D2 and D3) and electric energy cost (bands DA, DB, DC, DD and DE) for household users, the following ranges of variation can be reasonably assumed:

- c_{NG}: 0.20 – 1.50 €/Sm^3;
- c_{EE}: 0.05 – 0.50 €/kWh.

Therefore, the feasibility of the considered micro-CHP systems has to be evaluated for each country, by also taking into account the expected building energy performance (Fig. 1).

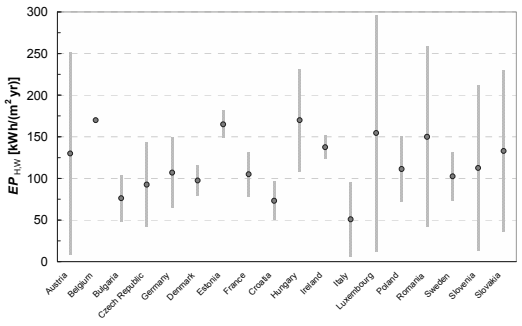

Fig. 1. Energy Performance (EP) limits for residential buildings starting from 1 January 2010 [8].

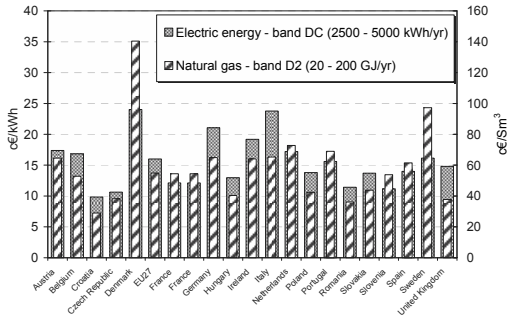

Fig. 2. Household consumer tax-included price of natural gas and electric energy [14].

4. Methodology

4.1. Energy conversion system modelling

A systemic approach was used to simulate CHP operation. In particular the CHP system was modelled as in Fig. 3, under these assumptions:

- Losses in the combustion system were accounted for through combustion efficiency η_c.
- The possibility that a fraction of combustion heat bypasses the energy conversion system and is directly used to produce useful heat (as in the case of Stirling and micro Rankine cycle technologies) was accounted for by means of the coefficient ε.
- The energy conversion system was modelled by means of its efficiency η_{ES}.
- The produced electric power P_e was evaluated through the overall electric efficiency η_e, which is defined in:

$$\eta_e = \eta^* \eta_{ES} \varepsilon \eta_c , \quad (3)$$

where the efficiency η^* takes into account the following contributions, depending on the CHP technology:

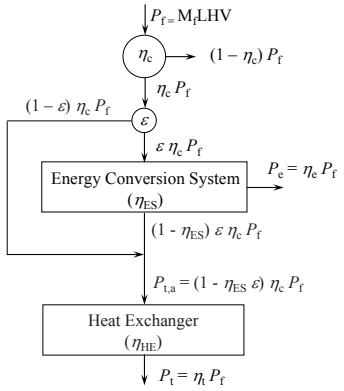

Fig. 3. Energy system model.

- Stirling and micro Rankine cycle: η^* is given by the product of the mechanical efficiency η_m, of the electric generator efficiency η_{eg} and of the efficiency η_{aux} accounting for auxiliaries. A typical value of η^* for Stirling and micro Rankine cycle technologies is approx. 0.75 [3].
- TPV: η^* is the efficiency of DC/AC converter η_{ec} (i.e. $\eta^* = \eta_{ec}$). A typical value of DC/AC converter efficiency is 0.90 [3].

• The heat $P_{t,a}$ that can be converted into useful heat is the sum of the heat discharged by the energy conversion system and the combustion heat that bypassed the energy conversion system itself. The useful thermal power recovered by the CHP system P_t was evaluated through the thermal efficiency η_t, which is expressed in (4):

$$\eta_t = \eta_{HE}\left(\eta_c - \eta_{ES}\varepsilon\eta_c\right) = \eta_{HE}\left(\eta_c - \eta_e/\eta^*\right) \qquad (4)$$

The values of the electric efficiency and thermal efficiency η_e and η_t depend on the energy conversion system considered and on ambient and load conditions as well. In this paper annual average values of these efficiencies were considered, and sensitivity analysis was performed on these values.

4.2. Thermo-economic analysis

The economic analysis consists of the determination of the period to pay back the additional costs of the CHP technology with respect to a traditional boiler. In fact, the considered micro-CHP systems are intended as an alternative to household boilers, so that CHP installation avoids all costs (both installation and operating costs) related to the traditional boiler. As the considered micro-CHP systems are not yet industrialized or widespread in the market, and therefore a well-established market price is difficult to estimate, a parametric analysis was carried out on the additional costs of the CHP technology.

The payback period (PBP) was evaluated as the period which makes the Net Present Value (NPV), defined in (5), equal to zero.

$$NPV = -I + \sum_{i=1}^{N} \frac{F_i}{(1+r)^i}, \qquad (5)$$

where I is the investment cost ($I = c_{add} \cdot P_f$) and r is the discount rate (assumed equal to 5 %).

For the calculation of the cash flows F_i, first the number of annual hours of operation for the micro-CHP systems is needed, and can be estimated as in (6)

$$YH = \frac{q_{H,W} A}{P_t}. \qquad (6)$$

Then, the cash flow for each i-th year F_i can be obtained as expressed in (7):

$$F_i = \left(P_e YH\right)\left(c_{EE} - c_{main}\right) - \left[\left(P_f - \frac{P_t}{\eta_{HE}\eta_c}\right)YH\right]c_{NG}, \qquad (7)$$

The electric energy produced annually (i.e. $P_e YH$) allows a net specific revenue (i.e. c_{EE}-c_{main}), which takes into account the specific cost for micro-CHP system maintenance c_{main} (in the paper c_{main} = 0.01 €/kWh). Then, the cash flow has to be lowered, by considering the cost of natural gas, due to the additional fuel used to feed the micro-CHP system with respect to the boiler only.

4.3. Assumptions

A reference micro-CHP system with the following features was considered as the base case:

η_e = 10.0 %
η_{HE} = 93.0 %
η^* = 75.0 %
η_c = 99.5 %

According to (4), it results that:

η_t = 80.1 %
η_{CHP} = 90.1 %

The assumed efficiency values have to be considered as annual average values and are representative of micro-CHP systems based on Stirling engine and micro Rankine cycle

technologies [3]. The assumed heat exchanger efficiency η_{HE} = 93 % is the typical annual average efficiency of a condensing boiler [15].

To perform sensitivity analysis on efficiency values, the ranges of variation reported in Tab. 1 were considered. The assumed electric efficiency values are representative of a wide range of micro-CHP systems up to 10 kW of electric power size. In particular, CHP systems based on TPV technology can be represented by electric efficiency values η_e up to 10 % (with η^* = 90 %) [3,11]. Otherwise, for CHP systems based on Stirling and micro Rankine cycle technologies, η_e typically varies in the range 5 – 25 % (but with η^* = 75 %) [3].

For the base case, the additional purchase cost of CHP technology with respect to a traditional boiler was assumed equal to c_{add} = 100 €/kW$_f$, i.e. the additional cost was referred to the fuel input power of the CHP system. Since the considered micro-CHP systems are not yet industrialized and widespread on the market, a well-established market price is difficult to estimate, and consequently the CHP technology additional cost was varied in the range c_{add} = 50 - 200 €/kW$_f$.

A CHP system size equal to 0.15 kW$_t$/m^2 (i.e. 15 kW of thermal power per 100 m^2 of household surface) was considered, since it was assumed that the existing boiler would be replaced by a CHP system with the same thermal power size in order to fulfill the same thermal energy demand.

The annual electric energy produced by the CHP systems, operated in heat-led mode, was considered lower than the annual electric energy required by the users. This assumption is verified when the ratio C between electric and thermal energy demands of the users is higher than C values reported in Tab. 2, which depend on the considered CHP technologies.

Even though the annual electric energy produced by the micro-CHP system was lower than that required by the users, the electric energy production (which is simultaneous with thermal energy production) is usually *not simultaneous* with user electric energy consumption. In fact, electric energy is overproduced during winter months (when thermal requirements are higher), while the highest electric energy consumption from the grid usually occurs during summer months due to air cooling. In order to balance this mismatch, in many countries "*compensation*" mechanisms exist between the electric energy sent to the grid and that purchased from the grid on a time basis (such as the so-called "net metering"), to properly reward the production of electric energy from distributed sources. Therefore, for the sake of simplicity, it was assumed that all the electric energy produced and consumed over one year could be rewarded at the electric energy consumer price purchase cost c_{EE}.

Table 1. Efficiency ranges for sensitivity analysis

η_e [%]	2.5 – 10.0	5.0 - 25.0
η^* [%]	90.0	75.0
η_{HE} [%]	93.0	93.0
η_c [%]	99.5	99.5

Table 2. Efficiencies and electric to thermal energy ratio "C" of the considered CHP technologies.

η^* [%]	η_e [%]	η_t [%]	η_{CHP} [%]	$C = E_e/E_t$
90.0	2.5	90.0	92.5	0.028
	5.0	87.4	92.4	0.057
	10.0	82.2	92.2	0.122
75.0	5.0	86.3	91.3	0.058
	10.0	80.1	90.1	0.125
	15.0	73.9	88.9	0.203
	20.0	67.7	87.7	0.295
	25.0	61.5	86.5	0.407

5. Results and discussion

5.1. Feasibility analysis

For the reference base case defined in para. 4.3, the period to pay back the additional costs of the CHP technology with respect to a traditional boiler was evaluated as a function of the European tariff scenario (Fig. 2: natural gas - band D2; electric energy - band DC) and of building energy demand for heating and hot water production $q_{H,W}$.

In Fig. 4, the PBP trends are reported for some European countries. The results allow the identification of the period required to pay back the additional costs of the CHP technology with respect to a traditional boiler. It should be noticed that the results are strongly influenced by the considered tariffs. As an example, owing to high Italian tariffs for both electric energy and natural gas, the CHP system payback period is less than 13 years when the D2/DC tariff scenario is assumed, with $q_{H,W}$ equal to 120 kWh/(m^2 yr). Otherwise, if the D2/DB tariff scenario is considered, the CHP system payback period is always greater than 15 years, even though $q_{H,W}$ is almost tripled (i.e. 300 kWh/(m^2 yr)).

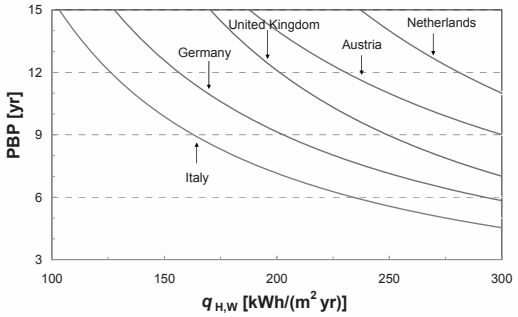

Fig. 4. Payback period vs. annual energy demand for some European countries.

5.2. Influence of CHP system parameters

Due to the large variation that may affect CHP system parameters (as building energy demand, efficiencies, CHP technology costs and tariff scenario), sensitivity analysis has been carried out to provide a useful and easy-to-read tool, which should allow the evaluation of the profitability of the micro-CHP system as a function of:

- building energy demand for heating and hot water production $q_{H,W}$, according to the range of EP_{HW} reported in Fig. 1;
- electric efficiency, mainly depending on the considered micro-CHP technology;
- additional purchase cost of the CHP technology with respect to a traditional boiler;
- tariff scenario (c_{NG} and c_{EE}), mainly depending on the country and on oil price.

A PBP of 10 years was imposed, since this can be considered a cut-off point to evaluate the actual potential of CHP technology for residential building applications. For the calculation of PBP, a discount rate equal to 5 % was assumed.

In Fig. 5 the curves of building energy demand for heating and hot water production $q_{H,W}$ allowing a PBP of 10 years are reported as a function of the additional purchase cost of the CHP technology with respect to a traditional boiler and of the electric efficiency of the CHP system, for two tariff scenarios: Italy and Sweden. In particular, these two European countries were chosen since they strongly differ in climate and tariffs. In fact, it can be seen in Fig. 2 that the cost of natural gas in Sweden is almost 50 % more than in Italy, while electric energy is about 30 % cheaper. Moreover, it should be noted that in Fig. 5 the micro-CHP systems are differentiated as a function of system efficiency, as explained in para. 4.3 (Tab. 1). In particular, the two different values of η^* (90 %, for TPV systems and 75 % for Stirling and micro Rankine cycle technologies) have an effect on the slope of the curves at constant $q_{H,W}$ value.

It can be shown that, in order to achieve a given payback period, an increase of the additional purchase cost of the CHP technology requires a higher electric efficiency, for any given $q_{H,W}$ value. In other terms, for a given micro-CHP system characterized by a given electric efficiency and a given purchase cost, the profitability can be reached in a shorter time if the energy demand for heating and hot water production $q_{H,W}$ is higher. Moreover, a higher additional purchase cost is allowed by higher η^* values, in correspondence of the same η_e.

As a result of the different energy tariffs, the same micro-CHP system is more profitable in Italy than in Sweden, even though the average energy demand in Sweden is almost twice the average energy demand in Italy (i.e. in Fig.1, average values of 100 against 50 kWh/(m^2 yr)).

The difference between the tariffs also translates into the fact that, while for Italy the curves at constant value of $q_{H,W}$ are very close to each other for the two different η^*, the same two curves for Sweden are very far from each other, i.e. a much higher η_e is required to counterbalance the decrease of η^*.

In Fig. 6a and 6b the curves of building energy demand $q_{H,W}$ allowing a PBP of 10 years, are reported as a function of electric energy and natural gas costs (c_{NG} and c_{EE}), for two different CHP technologies (Fig. 6a: η_e = 5 % and η^* = 90 %; Fig. 6b: η_e = 15 % and η^* = 75 %), and a additional purchase cost equal to 100 €/kW$_f$.

For any given value of $q_{H,W}$, the lines have a positive slope, since a higher electric energy cost (which is an avoided cost, and so contributes to the saving) is counterbalanced by a higher natural gas cost. As regards the comparison between the two different technologies, it can be highlighted that, for any given energy tariff scenario (i.e. c_{NG} and c_{EE}), a CHP technology with η_e = 15 %, η^* = 75 % (Fig. 6b) allows the same payback period as a CHP technology with η_e = 5 %, η^* = 90 % (Fig. 6a), but with a lower building energy demand $q_{H,W}$, owing to the combination of effects of the respective efficiency values. Moreover, it can be noted that a CHP technology with η_e = 5 % and η^* = 90 % (Fig. 6a) is more sensitive to the natural

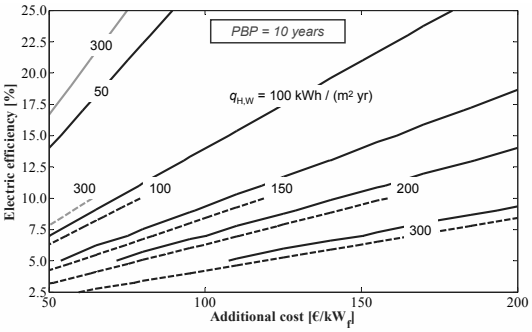

Fig. 5. Annual energy demand $q_{H,W}$ vs. additional purchase cost and electric efficiency, to achieve PBP = 10 years (Italy (black line), Sweden (copper line) - dashed line: $\eta^* = 90$ %; continuous line: $\eta^* = 75$ %).

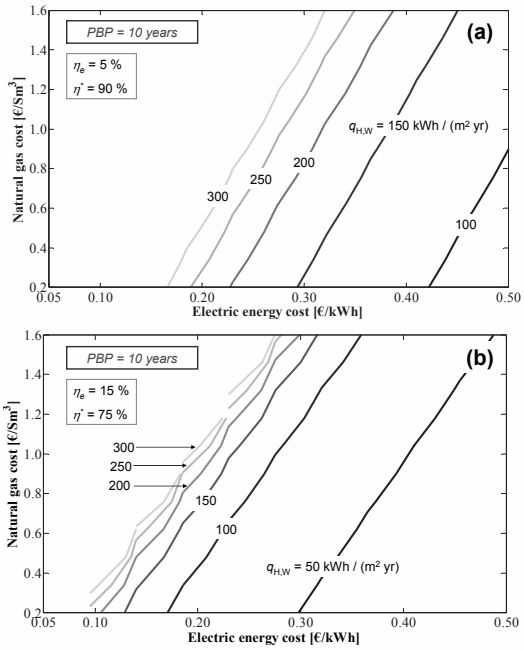

Fig. 6. Annual energy demand $q_{H,W}$ vs. electric energy and natural gas costs, to achieve PBP = 10 years @ c_{add} 100 €/kW$_f$.

gas and electricity costs than a CHP technology with η_e = 15 % and η^* = 75 % (Fig. 6b). This is due to the fact that the electric power P_e and the power of the extra-fuel supplied for electric energy production with respect to the simple boiler (factors which multiply *YH* in (7)) are both low when η_e is low. Therefore, by varying natural gas and electricity costs, a same annual cash flow value (F_i) can only be obtained by means of large variations of *YH*, which correspond to large variations of building energy demand $q_{H,W}$.

6. Conclusions

In this paper, an energy and economic analysis of micro-CHP systems was carried out, to evaluate their feasibility as an alternative to household boilers. The considered CHP systems are the ones based on Stirling engines, micro Rankine cycles and thermo-photovoltaic generators.

The result of this paper is an easy-to-use tool, which allows the evaluation of the feasibility of the considered micro-CHP system as a function of (i) efficiency parameters, (ii) European natural gas and electric energy tariff scenario, (iii) building energy requirements and (iv) additional costs of the CHP technology with respect to a traditional boiler.

As an example, under the Italian tariff scenario, a CHP system based on Stirling or micro Rankine cycle technologies, with an electric efficiency of about 10 %, can have a payback period lower than 10 years, if the additional purchase cost with respect to a traditional boiler is lower than 100 €/kW$_f$ and the building thermal energy demand is higher than 150 kWh/(m^2 yr).

Nomenclature

A	household surface area, m^2
C	E_e/E_t (defined in [2])
c	specific cost, €/kWh or €/Sm^3
E	energy, kWh
EP	energy performance, kWh/(m^2 yr)
F	cash flow, €/yr
I	investment, €
i	index
M_f	fuel mass flow rate, kg/s
N	number of years for *NPV* calculation, yr
NPV	net present value, €
P	power, kW
PBP	payback period, yr
q	annual energy demand per unit household surface area, kWh/(m^2 yr)
Q	annual energy demand, kWh/yr
r	discount rate
YH	annual hours of operation, hr/yr

Greek symbols

η	efficiency
η^*	efficiency equal to $\eta_m \cdot \eta_{eg} \cdot \eta_{aux}$ (Stirling and micro Rankine cycle) or to η_{ec} (TPV)

ε fraction of energy which directly produces useful heat bypassing the energy conversion system

Subscripts and superscripts

a available
aux auxiliaries
add additional
c combustion
C air conditioning
CHP combined heat and power
e electric
EE electric energy
ec DC/AC converter
eg electric generator
ES energy conversion system
f fuel
H heating
HE heat exchanger
light lighting
m mechanical
main maintenance
NG natural gas
ov overall
t thermal
W domestic hot water

References

[1] Shafiee, S., and Topal, E., 2010, A long-term view of worldwide fossil fuel prices, *Applied Energy*, 87, pp. 988-1000.

[2] Directive 2004/8/EC of the European Parliament and of the Council.

[3] Bianchi, M., et al., 2009, Le tecnologie innovative ed efficienti nei sistemi di generazione in assetto co-trigenerativo e nei sistemi integrati con unità a pompa di calore nelle applicazioni industriali e del terziario, Report RSE/2009/18 (in Italian), http://192.107.92.63/index.php/component/docman/doc_download/19-sistemi-integrati-di-co-trigenerazione-.html.

[4] Mago, P. J., et al., 2006, "Modeling of Micro-Cooling, Heating, and Power (Micro-CHP) for Residential or Small Commercial Building Applications", ASME IMECE2006-13558.

[5] Bertani, A., et al., 2006, "Management of Low Voltage Grids with High Penetration of Distributed Generation: concepts, implementations and experiments", Proc. of CIGRE, Paris.

[6] Peacock, A.D., and Newborough, M., 2005, "Impact of micro-CHP systems on domestic sector CO2 emissions", Applied Thermal Engineering, vol. 25, pp. 2653–2676.

[7] Gullì, F., 2006, "Small Distributed Generation Versus Centralized Supply: a Social Cost-Benefit Analysis in the Residential and Service Sectors", Energy Policy, 34, pp. 804-832.

[8] EPBD Buildings Platform, Country Reports 2008, ISBN 2-930471-29-8.

[9] Leibowitz, H., et al., 2006, "Cost Effective Small Scale ORC Systems for Power Recovery from Low Grade Heat Sources", ASME IMECE2006-14284.

[10] Coutts, T. J., 2001, "An overview of thermophotovoltaic generation of electricity", Solar Energy Materials & Solar Cells 66, pp.443-452.

[11] Cadorin, M., et al., 2010, Thermoeconomic Analysis of MicroCHP Thermophotovoltaic (TPV) Systems, Submitted to *Proc. of ECOS 2010*, Lausanne, Switzerland.

[12] ISO 13790:2008.

[13] Directive 2002/91/EC of the European Parliament and of the Council.

[14] http://epp.eurostat.ec.europa.eu/

[15] Persson, T., and Ronnelid, M., 2007, Increasing solar gains by using hot water to heat dishwashers and washing machines App. Therm. Eng., 27, pp. 646-657.

Acknowledgments: The work was carried out with the support of the Italian Ministry of Education, University and Research (PRIN 2007 national research project).
Authors gratefully acknowledge Mirko Morini PhD for his precious support in performing the simulations.

Gas turbines for polygeneration? A thermodynamic investigation of a fuel rich gas turbine cycle

Burak Atakan [a]

[a] *Thermodynamics, IVG, Department of Engineering, University of Duisburg-Essen, Duisburg, Germany*

Abstract: Gas turbines as used nowadays are working far in the fuel lean regime, which is most reasonable for mobile applications, since the formation of pollutants and soot are avoided while the temperatures remain low enough to avoid damage of the turbine. However, from a thermodynamic point of view the exergy utilization is far from optimum at such conditions.
For stationary conditions a different approach may be worth a second thought: the use of gas turbines as chemical reactors for hydrogen and carbon monoxide production in combination with power generation and the utilization of the exhaust enthalpy stream. A gas turbine model cycle is analyzed using complex equilibria including radicals and chemical exergies. Chemical exergies were calculated from equilibrating the gas mixtures at different points in each process with a large excess of moist air. Methane was studied as an exemplary fuel; it can be viewed as an important representative of natural gas and of biogas.

Comparing the exergy losses of the idealized gas turbine process, the losses for the fuel rich stoichiometry are lower than at the lean stoichiometry used in gas turbines nowadays. The exact values of the exergetic efficiency depend on the pressure ratio, which was studied in the range of 10 to 30. The hydrogen to carbon monoxide ratio would be typically near 2.2, while the adiabatic flame temperature would be in a range, which either would cause no damage to typical gas turbines or could be handled with carbon fiber reinforced carbon. The composition of the gases is likely to change within the turbine, where temperature and enthalpy drops. This was considered in additional calculations where chemical equilibration of the gas mixture in the turbine is considered. Such a process would combine a partial oxidation with an energy conversion process. The possibility to produce syngas mixtures would add an additional flexibility to the gas turbine process, which seems to be worth to be considered.

Keywords: Polygeneration, turbine, chemical exergy

1. Introduction

Gas turbine processes are important devices used in stationary systems to convert the combustion enthalpy of a fuel into electrical power. In aeroplanes they are used as an engine so the propulsion is the aimed effect. The thermal efficiency is restricted by the upper temperature limit which can be used at the turbine entrance in order to avoid the degradation of the steels or super alloys. In order to reduce the combustion temperature they are nowadays mainly run in a very lean combustion regime, aiming to hold the gas phase and surface temperatures low. This also has the side effect that the nitric oxide formation, which is strongly coupled to temperature, may be partially avoided. Similarly, soot formation is also of minor importance in the lean regime. Generally, the thermal efficiency can be increased significantly if the hot exhaust gases are used in combined gas and steam power plants. Recently, Yamamoto et al. proposed a combined cycle where one of two gas turbines is run in a fuel rich mode, leading to increased total efficiency [1]. One important idea behind this work was that carbon-fibre-reinforced-carbon composites (C/C) may be used as a construction material for turbines in the fuel rich regime, since they survive much higher temperatures in a reducing atmosphere.

Fossil fuels like natural gas are also the starting point for the production of base chemicals like methanol, syngas (H_2/CO) or hydrogen. At the same time, the production processes often consume a considerable amount of exergy even though the reactions for their formation show that theoretically this would not be necessary. Thus, for example Jin et al. studied the possibilities of using several fuels for the simultaneous production of base chemicals and power [2, 3], combining known processes in a rational but complex way. Polygeneration or multigeneration, as the

production of several energetic products is mostly called, often is regarded as a kind of optimization process where existing technologies are combined in a more or less complex way [4-6]. However, the possibility of heaving relatively simple processes capable of providing several useful products, including mechanical power, has to our knowledge not been studied yet. Combustion processes run in an unusual mode may be one possible choice. This way, the large knowledge of the scientific combustion community may be used.

The present thermodynamic investigation was performed as a starting point in order to see if gas turbine processes may be used in principle for the polygeneration of syngas and electrical power or shaft work, generally assuming that the exhaust gases are further used either for heating or for further energy conversion processes like a steam cycle. If a gas turbine cycle is used (also) as a chemical reactor, the properties of the gas mixture expanding in the turbine will be quite different from a typical lean exhaust gas mixture. Also, since the temperatures in the turbine are generally quite high, chemical reactions will take place while the gas mixture expands and due to this the chemical composition may change in the turbine. Due to the high temperatures, the equilibrium concentrations of atoms and radicals in the mixture may be substantial, thus influencing temperatures and enthalpies. The equilibrium of a complex mixture can be evaluated by minimization of the free enthalpy. The chemical equilibrium calculation procedures used in the present work are well established and freely available[7].

In order to analyze a poly-generation gas turbine process, the chemical exergy flows are analyzed together with the energy flows as a function of different parameters. The main parameters were the stoichiometry, the pressure ratio and also the possibility of chemical equilibration in the turbine, while the temperature is reduced.

2. Modeling

The modeled process is depicted in Fig. 1. The methane fuel and the air are compressed separately, mixed and burned in the combustor. The combustion products are expanded in the turbine. All steps are modeled as adiabatic processes for different stoichiometries, varying the air mass flow rate $\dot{m}_3$. Since it was aimed to study the thermodynamic optimum, the turbine and the two compressors were first assumed to be reversible (*rev*). In later calculations, isentropic efficiencies of 90% for the turbine and 75% for each compressor were assumed (*irr*). Pressure losses in the lines or the combustor were neglected.

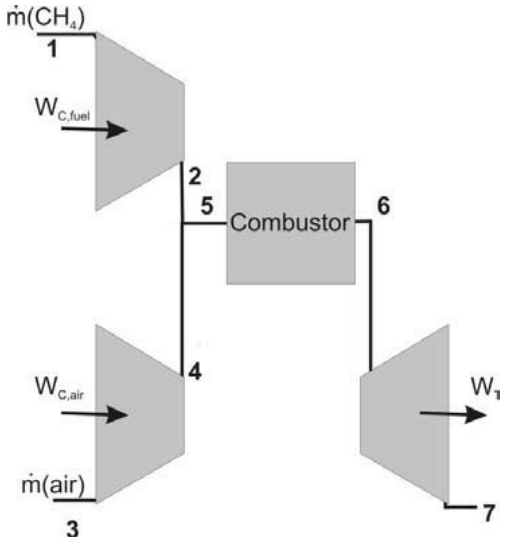

Fig. 1 Scheme for the modeled process, all parts are assumed to be adiabatic.

All species and mixture properties were calculated using the Cantera library [7] within Python, which also provides procedures for equilibrating a multi-species gas phase mixture for two constant parameters like temperature and pressure, enthalpy and pressure or entropy and pressure by minimizing the free enthalpy at constant elemental composition. In addition, the possibility of carbon (soot) formation was investigated by calculating a two phase equilibrium, consisting of a complex gas phase and a pure graphite solid phase. The thermodynamic data were taken from the established data base of the GRI 3.0 mechanism [8] and the gas phase was assumed to behave as a mixture of ideal gases. No assumptions regarding constant heat capacities were made. The program evaluates the enthalpies h, entropies s and further thermodynamic properties of the mixture. However, the calculation of (chemical) exergies had to be implemented. Pure air (mole fractions: O_2: 0.209421, N_2: 0.78084, Ar: 0.00934, CO_2: 0.00038, H_2O: 0.013) was taken as the dead state of the surrounding at 1.013 bar and 300 K, this appeared to be most reasonable for the present

purpose. To calculate exergies, it was deemed most appropriate and easiest to calculate the initial enthalpy and entropy of a given mixture in a certain thermodynamic state (Index: *i*) and to equilibrate it chemically and reversibly (Index: *eq*) with a large excess of air (mass ratio: r=10^5:1, Index: *air*) at ambient condition. From the differences in enthalpy and entropy, the exergy e is calculated per mass of the initial mixture (m_i), or per kg of initially added methane, which was used as surrogate for natural gas:

$$e_i = \frac{E}{m_i} = \left[(r \cdot h_{air} + h_i) - (r+1) h_{eq} \right] - T_0 \left[(r \cdot s_{air} + s_i) - (r+1) s_{eq} \right] \quad (1.1)$$

The specific properties as used here are always enthalpy per kg of the given mixture (either air, fuel or fuel/air) or the equilibrated state starting with 1 kg of fuel or fuel/air mixture and 10^5 kg of air. The ratio r was checked for a range of values, at values above 10^4 the calculated exergy per kg of initial mixture was no longer dependent on the exact value. The procedure was checked for a few species like methane and produced results very near to the values given in the literature. All work terms were taken as pure exergy as usual. The initial exergy of methane is evaluated here to be 51.86 MJ/kg (829.75 kJ/mol).

After separated adiabatic compression of methane (state 2) and air (state 4), an adiabatic mixing process was regarded (state 5), followed by an adiabatic isobaric chemical equilibration (state 6). This equilibrated gas mixture was then expanded to ambient pressure isentropically in the turbine. Here two cases were studied, first the chemical composition in the turbine was frozen and the isentropic state at ambient pressure was calculated. However, the temperatures are high enough in most calculations so that this can only be regarded as one thermodynamic limit with frozen chemistry. Therefore a second calculation for the turbine was performed with chemical equilibration and constant entropy at ambient pressure. In some cases, this leads to considerable changes in the exhaust composition. The real state will be somewhere in between; this can only be evaluated using a kinetic model, which was not performed in the present work but will be addressed in future.

In order to evaluate the sensitivity of the investigated processes to irreversibilities in the turbine and the compressor, isentropic efficiencies of 90%, and 75%, respectively, were assumed in a further series of calculations. The states behind the compressors and the turbine were calculated the usual way. For the turbine, the exhaust enthalpy was calculated from the initial enthalpy of the entering fluid and the isentropic specific work $w_{t,s=const}$ times the isentropic efficiency:

$$h_7 = h_6 + w_{t,s=const} \eta_{s,T} \quad (1.2)$$

The isentropic work was calculated from the final enthalpy after equilibration at the given exhaust pressure and initial entropy. The state at this final enthalpy and pressure was recalculated for the non-isentropic case either with frozen composition or with equilibration, as described above. The calculations for the compressors w_c were similar, only the isentropic work was divided by the isentropic efficiency and constant compositions were assumed.

Exergetic efficiencies for the state behind the turbine were calculated from the sum of the absolute value of the net work (w_{net}) and the exergy at this state divided by the entering exergy of the fuel:

$$\xi_7 = \frac{|w_{net}| + e_7}{e_{fuel,1}} \quad (1.3)$$

For the other states, the input of the compressor work is taken as an exergy inflow:

$$\xi_i = \frac{e_i}{w_c + e_{fuel,1}} \quad (1.4)$$

Thermal efficiencies η were calculated from the absolute value of the net work output related to the specific enthalpy of combustion (lower heating value $\Delta_{r,CH_4} h^0$) of methane:

$$\eta = \frac{|w_{net}|}{\Delta_{r,CH_4} h^0} \quad (1.5)$$

In the diagrams, the ratio of actual mass flow of air to fuel relative to the stoichiometric value, called theoretical air, are shown as independent variable:

$$\lambda = \frac{\dot{m}_{air} / \dot{m}_{fuel}}{\dot{m}_{air} / \dot{m}_{fuel}\ _{stoich}} \quad (1.6)$$

This is the inverse of stoichiometry.

For the comparison of the products hydrogen and carbon monoxide, the number of moles at a certain

state were normalized by the number of moles of methane in the initial mixture ($n(CH_4)_5$) as present in state 5. This choice avoids misinterpretations of non-normalized mole fractions. These values were calculated using the mass fraction of methane at state 5 and the mass fraction (y) of species i at a certain position and converted to mole fractions with the molecular mass (M):

$$\frac{n_i}{n_{CH_4,5}} = \frac{y_i / M_i}{y_{CH_4,5} / M_{CH_4}} \qquad (1.7)$$

3. Results and Discussion

3.1. Overview: A Pressure ratio of 10

First the results for a pressure ratio ($=p_1/p_2$) of 10 leading to a maximum pressure of 1.013 MPa shall be discussed, as shown in Fig. 2. The λ values were varied in the range from 0.25 to 4. The adiabatic combustion temperatures (T_6) vary between 1090 and 2400K and are only slightly increased due to irreversibilities in the compression. It should be emphasized that these temperatures are resulting from the equilibrium calculation, and give an overview over the parameter range from the rich to the lean stoichiometry, although the higher temperatures around the stoichiometric conditions are not useful for practical applications. The difference between a reversible and an irreversible compression gets more pronounced with increasing λ value, since more air has to be compressed per kg of methane.

The same trend is also seen for the temperature T_7 behind the turbine. If chemical equilibration in the turbine is included, the temperatures differ only at small λ values, because the gas mixture forms more CO_2 instead of CO in this regime, leading to a higher temperature at a given enthalpy. It should be remembered that all species mole fractions were related to the initial methane mole fraction in the mixture, state 5.

For clarity, only the target species hydrogen and CO are included to Fig. 2 together with the mostly unwanted CO_2, although the complex equilibrium was calculated. As can be seen, between 1.54 and 1.71 mole hydrogen is predicted per mole of initially provided methane and the stoichiometry range for this is quite narrow. The predicted CO mole fraction peak is relatively flat and per mole methane 0.63 - 0.88 mole CO is present in equilibrium after combustion. The hydrogen mole fraction is only slightly influenced by chemical equilibration of the mixture in the turbine or by irreversibilities in the compressors and the turbine. In contrast, the CO mole fraction is strongly influenced by chemical equilibration, the relative mole fraction values drops from 0.9 to around 0.63. However, the higher temperatures due to non-reversible compressors and turbine help in the formation of larger amounts of CO and after chemical equilibration the value rises to 0.7, depending on the exact stoichiometry. The temperatures of adiabatic combustion lie between 1485 and 1809 K in the interesting λ range, which is well accessible with the C/C materials and in part be accessible with conventional gas turbine blades (1723-1773K) [1, 9].

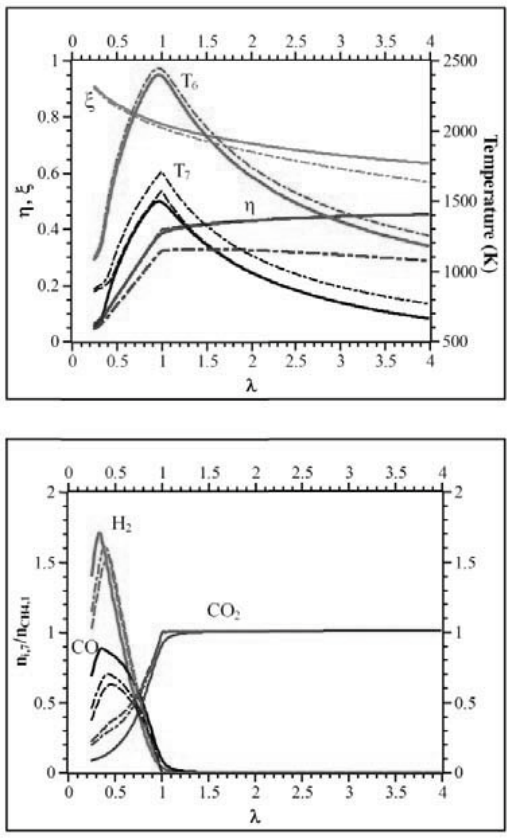

Fig. 2 Gas turbine cycle with a compression ratio of 10 calculated for various stoichiometries. Solid lines show the results for the isentropic case, dashed lines for the isentropic case with equilibration in the turbine and the dashed-dotted lines for the non-isentropic case with equilibration.

If gas turbines without blade cooling are used λ could be further reduced, e.g. to a value of 0.35. This would lead to a turbine entrance temperature of 1300K and H_2 and CO values of 1.7 and 0.9 per mole of methane, respectively, in the irreversible case at an exergetic efficiency of 87%. This case will not be discussed in detail further to avoid confusion due to too many discussed cases, however, such conditions seem also to be reasonable and the results are included in the figures throughout.

Table 1 summarises the main results at two 3 . . . 1 9 . the maximum hydrogen yield was chosen, as well as a slightly leaner for comparison. The thermal efficiencies in the interesting stoichiometry range between λ=0.4 and λ=0.5 seems to be disappointing at first sight with values around 10% (see also Table 1). They were calculated from the relation between the net work output, w_{net}, and the lower heating value of methane. However, this is relativised if the exergetic efficiencies are regarded and the purpose of the process, i.e. producing power and base chemicals, is remembered.

Table 1. Properties, work and efficiencies for some states for the process with non-reversible turbine and compressors and chemical equilibration in the turbine.

λ	0.395	0.506	0.427	0.506
p_{max} (MPa)	1.01	1.01	3.04	3.04
$\|w_{net}\|$(MJ/kg_{CH4})	4.33	6.58	6.44	8.48
w_c (MJ/kg_{CH4})	3.19	3.91	5.90	6.80
$\|w_t\|$ (J/kg_{CH4})	7.52	10.5	12.3	15.3
$\eta_{thermal}$	0.09	0.13	0.13	0.17
ξ_{2+4}	0.99	0.99	0.99	0.99
ξ_5	0.99	0.98	0.98	0.98
ξ_6	0.87	0.85	0.88	0.87
ξ_7	0.86	0.84	0.86	0.85
T_5 (K)	623	629	836	845
T_6 (K)	1485	1809	1761	1983
T_7 (K)	959	1159	935	1041
$n(H_2)_7/n(CH_4)_1$	1.62	1.30	1.54	1.36
$n(CO)_7/n(CH_4)_1$	0.700	0.676	0.622	0.614

The exergetic efficiencies in this λ range are between 85-87% and are reduced only very slightly with the introduction of irreversible turbines and compressors. If this value is compared with the exergetic efficiency of 65% at a lean stoichiometry of λ=3 an important improvement is recognized. This difference is even more pronounced with turbines and compressors having an isentropic efficiency below 1; in the example calculated here, the exergetic efficiency in the lean range is further reduced to values below 61%, which should be an important argument to consider the fuel rich stoichiometry regime. The main exergy losses take place in the combustion process as can be seen from Table 1, while the exergy losses in the other parts are of minor importance. However, the exergy loss in stoichiometric and lean adiabatic combustion is much higher [10, 11] than in the investigated rich regime.

In the high temperature regime some radicals like atomic hydrogen and the hydroxyl radical (OH) are present in a considerable amount as seen in Fig. 3. The (relative) equilibrium concentrations of these radicals may be in the percent regime at high temperatures, as it is seen for OH, but they only play a minor role after passing the turbine and equilibration takes place at reduced temperatures. However, if the chemical equilibration in the turbine is not performed, the concentrations would remain unrealistically high, again being an argument for considering the chemical equilibration in the turbine.

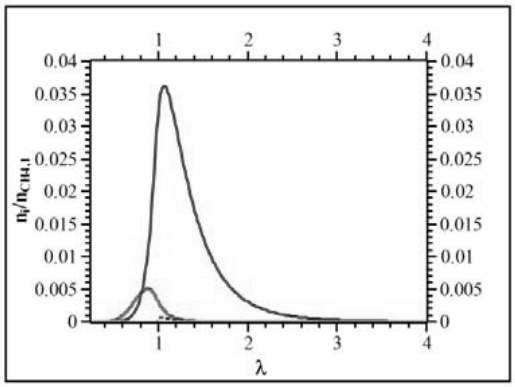

Fig. 3 Equilibrium H (red) and OH (blue) mole fractions at the turbine entrance (state: 6) both divided by the initial methane mole fraction, as a function of λ at the turbine entrance (solid lines) and equilibrated behind the turbine (dashed lines) shown for a reversible turbine with an inlet pressure of 1.013MPa.

3.2. Influence of the pressure ratio

The compression ratio is known to be an important parameter for gas turbine cycles. With increasing pressure ratio, , the thermal efficiency increases.

Thus, it was interesting to investigate higher pressure ratios. Some results for = 30 are presented; the calculations were performed again for totally reversible compressors and turbine (*rev*) as the limiting case and for the above given isentropic efficiencies (*irr*). Some results from the latter are included in Table 1, while the results are compared in Fig. 4.

From Fig. 4 it is seen that the amount of hydrogen produced in the fuel rich regime is nearly unaffected by the pressure ratio, it is slightly reduced to 1.54 mole hydrogen per mole methane initially added. Also, the maximum is shifted towards a higher λ value of 0.43. The CO formed per CH_4 0 . 0 0
10 leading to values of slightly above 0.62. The exergetic efficiency at $\lambda = 0.4$ slightly increases to 87-88% for the irreversible case. Regarding the thermal efficiency, the effect of is more pronounced: it reaches a value of 13 % for the which gives the highest hydrogen yield, compared % ,

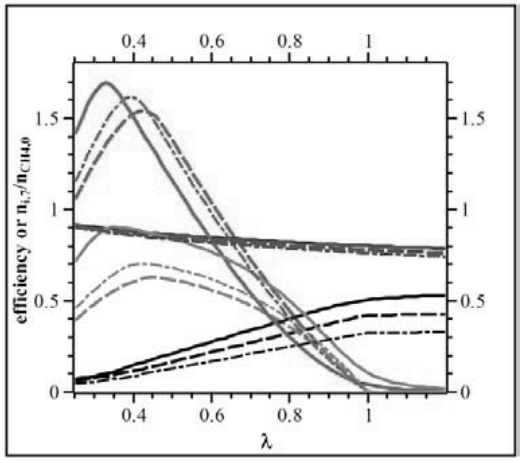

Fig. 4 Comparison of the results for = 30 with = 10. Solid lines: = 30, rev, no equilibration in the turbine; dashed lines: = 30, irr; dashed-dotted lines: = 10, irr. The latter two were both calculated with equilibration in the turbine. Red: H_2, grey: CO, blue: exergetic efficiency, black: thermal efficiency.

If the λ value is increased to 0.51, the thermal efficiency rises to 17%, while the exergetic efficiency is at 87%, meaning that there is some amount of flexibility in the preferred products. However, there is also a drawback: due to the higher pressure ratio, the adiabatic combustion temperatures rise from 1485-1809 K at = 10 to 1761-1983 K at = 30 for the λ values given in Table 1. Temperatures above 1800 K would be far too high as turbine entrance temperature for conventional turbine blades, thus the pressure ratio may be restricted by the maximum temperature also in the fuel rich regime. However, if C/C turbine blades can be used, the temperature levels would be acceptable.

3.3. Carbon formation

Another question which arises and may prevent the development of fuel rich gas turbine processes is the possible formation of carbonaceous matter, meaning mainly soot. In order to check this possibility two-phase equilibria, with an ideal gas phase and a solid pure graphite phase, were investigated. Again the gas phase considered all the species present in the GRI mechanism. The amount of graphite produced per methane input was calculated as a function of temperature and stoichiometry for initial air-methane mixtures covering the λ range between 0 and 1.

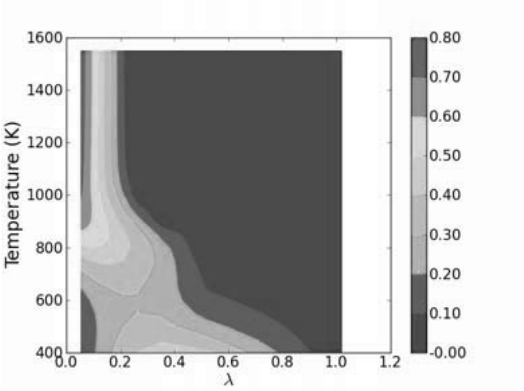

Fig. 5 The molar amount of graphite formation in equilibrium per mole of initially present methane calculated at 1 bar.

These calculations were performed for 1, 10 and 30 bar; since the 1 bar case turns out to be most critical, only the results for this pressure are shown in Fig. 5. At low temperatures and low λ values methane is stable, if λ is near 1 the formation of CO_2 and CO is predominant, while at λ values around 0.4 graphite maybe formed at temperatures of around 800 K and ambient pressure. This can be avoided at slightly higher λ values, thus the results for λ=0.51 are also shown in Table 1. However, if the calculated turbine exit temperatures T_7 are regarded (see Fig. 2) it is seen that the temperature

level is predicted to be above 800 K for the λ range of interest, even at λ values of 0.35. However, the risk of solid carbon or soot formation remains if in a subsequent cooling step, e.g. in a heat exchanger, chemical equilibration is established. Thus the subsequent cooling should be a fast process, probably introducing further irreversibilities. Investigations of the chemical kinetics of these systems are needed in order to judge the rate of equilibration and possible formation of carbonaceous matter while cooling takes place. This was not the aim of the present thermodynamic investigation.

4. Conclusions

A simple fuel-rich gas turbine process running with methane as fuel was investigated and has been shown to be thermodynamically favourable for the polygeneration of base chemicals like hydrogen or syngas together with mechanical power. In the present work, only the basic conversion process was studied without considering the subsequent processes, such as the utilization of the exhaust enthalpy stream as input for a steam power cycle and perhaps also for heating purposes. Also the separation of the product gases was not considered here, which surely will lead to some further exergy losses. But this also holds for any other partial oxidation without power generation. Nevertheless, from this study it is seen that this proposed process may be favourable with quite small exergy losses, if hydrogen or syngas is needed for other industrial processes or as fuel for hydrogen fuelled cars. Predicted thermal efficiencies of 9-17% are clearly small, but this is to be expected if the fuel is not mainly burned to carbon dioxide and water; thus, this is an intrinsic limitation of incomplete conversion. Also, the known possibilities of recuperatively heating the compressed gases (state 5) by the turbine exhaust gases, which generally leads to higher thermal efficiencies, may be worth further investigation.

Regarding the temperature levels at the turbine entrance, C/C materials would be most interesting. But also the thermal behaviour of nickel based high temperature alloys should be studied under these fuel rich conditions, since the gas mixture is now much less corroding, due to the absence of excess air.

A thermodynamic study can only lead to conclusions whether a process is principally possible and rational. This seems to be the case for the polygeneration of syngas, mechanical or electrical power and possibly also of heat. The possible problems of soot formation and the details of combustion, the rate of equilibration of the product gases in the turbine and in a following cooling process have to be studied in addition by experimental methods and kinetic modeling. Such studies seem to be worth being performed, in order to use gas turbines as chemical reactors. Also, different fuels which may come from regenerative sources like organic alcohols may be interesting in future studies. The advantage could also be a relatively simple but flexible process, avoiding further exergy losses, which arise in coupling numerous flow devices and machines in a complex way.

Nomenclature

e specific exergy, kJ/kg
h enthalpy, kJ/kg
$\dot{m}$ mass flow rate, kg/s
M molecular mass, kg/mol
n number of moles, mol
p pressure, Pa
r ratio of excess air to fuel for exergy calculation,-
s specific entropy, kJ/(kg K)
T temperature, K
T_0 temperature of the surrounding, K
w work per unit mass of fuel, kJ/kg
y mass fraction, -

Greek symbols

η thermal efficiency, -
λ inverse of stoichiometry, -
π pressure ratio
ξ exergetic efficiency, -

Subscripts

c compressor
eq equilibrium state
i state number i
s=const isentropic
stoich stoichiometric

t turbine

th thermal

References

[1] Yamamoto T., Lior N., Furuhata T., Arai N., 2007, A novel high-performance low-NO alpha fuel-rich/fuel-lean two-stage combustion gas and steam turbine system for power and heat generation, Proceedings of the Institution of Mechanical Engineers Part a-Journal of Power and Energy. 221, pp. 433-46.

[2] Jin H. G., Han W., Gao L., 2007, Multifunctional energy system (MES) with multifossil fuels and multiproducts, Journal of Engineering for Gas Turbines and Power-Transactions of the ASME. 129, pp. 331-37.

[3] Jin H. G., Sun S., Han W., Gao L., 2009, Proposal of a Novel Multifunctional Energy System for Cogeneration of Coke, Hydrogen, and Power, Journal of Engineering for Gas Turbines and Power-Transactions of the ASME. 131, pp.

[4] Chicco G., Mancarefla P., 2009, Distributed multi-generation: A comprehensive view, Renewable & Sustainable Energy Reviews. 13, pp. 535-51.

[5] Liszka M., Ziebik A., 2009, Economic optimization of the combined cycle integrated with multi-product gasification system, Energy Conversion and Management. 50, pp. 309-18.

[6] Piacentino A., Cardona F., 2008, An original multi-objective criterion for the design of small-scale polygeneration systems based on realistic operating conditions, Applied Thermal Engineering. 28, pp. 2391-404.

[7] Goodwin D. G., 2003, An open-source, extensible software suite for CVD process simulation, Chemical Vapor Deposition XVI and EUROCVD. 14, pp. 2003-08.

[8] Smith G. P., Golden D. M., Frenklach M., et al., 2000, [www-document], http://www.me.berkeley.edu/gri_mech/.

[9] Yamamoto T., Kobayashi N., Arai N., Tanaka T., 1997, Effects of pressure on fuel-rich combustion of methane-air under high pressure, Energy Conversion and Management. 38, pp. 1093-100.

[10] Caton J. A., 2000, On the destruction of availability (exergy) due to combustion processes - with specific application to internal-combustion engines, Energy. 25, pp. 1097-117.

[11] Dunbar W. R., Lior N., 1994, Sources of Combustion Irreversibility, Combustion Science and Technology. 103, pp. 41-61.

Acknowledgement: This work was inspired by a fruitful discussion with Ulrich Maas (KIT) which is gratefully acknowledged.

Fuel Cell-Based Cogeneration System Covering Data Centers' Energy Needs

Giuseppe Leo Guizzi [a], *Michele Manno* [a]

[a] *Dipartimento di Ingegneria dell'Impresa, Università degli studi di Roma Tor Vergata, Italy*

Abstract: The Information and Communication Technology industry has gone in the recent years through a dramatic expansion, driven by many new online (local and remote) applications and services. Such growth has obviously triggered an equally remarkable growth in energy consumption by data centers, which require huge amounts of power not only for IT devices, but also for power distribution units and for air-conditioning systems needed to cool the IT equipment.
Following a previous work where the authors analyzed energy and cost savings that could be achieved in the energy management of data centers by means of a conventional combined cooling, heating and power system based on an internal combustion engine and a LiBr/H_2O absorption chiller, this paper is dedicated to the economic and energy performance assessment of a CHP system based on a natural gas membrane steam reformer producing a pure hydrogen flow for electric power generation in a polymer electrolyte membrane fuel cell (PEMFC). Heat is recovered from both the reforming unit and the fuel cell in order to supply the needs of an office building located near the data center. In this case, the cooling energy needs of the data center are covered by means of a vapor-compression chiller equipped with a free-cooling unit.
Since the fuel cell's output is direct current (DC), rather than alternate current (AC) as in electric generators driven by internal combustion engines, the possibility of further improving data center's energy efficiency by the adoption of DC-powered data center equipment is also discussed.

Keywords: Data Center, Cogeneration, Energy Efficiency, District Heating, Hydrogen, PEMFC, Membrane Reformer

1. Introduction

In recent years, the rapid growth of the Information and Communication Technology (ICT or, more simply, IT) industry has brought about a strong worldwide expansion of energy use by data centers, which lie at the core of the industry. Recently, a study [1] has estimated that electric energy consumption by data centers in the world has more than doubled in the period from 2000 to 2005; furthermore, it showed that in 2005 it represented 1% of world total electric energy consumption. This growth is estimated to continue on this exponential trend at least in the near future [2].
More specifically, Fig. 1 shows that energy consumption for cooling purposes, combined with energy losses due to the power distribution units (including UPS), is indeed remarkable if compared to the energy really absorbed by the IT equipment in the data center: with current technologies, the ratio between IT equipment power and total facility power can be on average estimated as 0.5. This ratio has been designated as DCiE (Data Center Infrastructure Efficiency) by The Green Grid, an organization grouping several major IT companies and promoting efficiency in IT industry; DCiE, along with its reciprocal PUE (Power Usage Effectiveness), are recommended by this organization as useful metrics in order to assess data center efficiency [3].

The value of 0.5 is indeed the figure used in [1] in constructing its estimate, represented in Fig. 1, and also found valid in [4], but the situation can be even worse in particular occasions: for example, [5] found a DCiE of 0.29 for the relatively small data center analyzed, while in [6] values of 0.5 and 0.26 for two different data centers located in Singapore are reported, and, finally, in [7] the energy performance of 22 data centers is reviewed, with DCiE values ranging from 0.33 to 0.75, with an average value of 0.57.
In order to further emphasize the importance and relevance of the subject, it is worth mentioning that US Congress, through Public Law 109-431,

Corresponding author: Michele Manno, Email: michele.manno@uniroma2.it

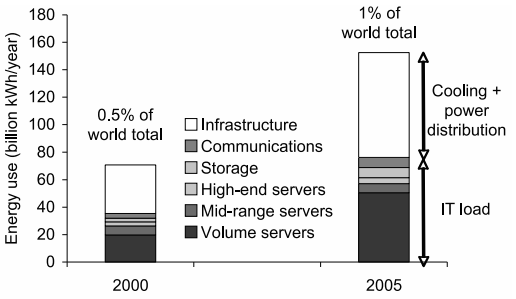

Figure 1: Total electricity use for data centers in the US in 2000 and 2005, including cooling and auxiliary equipment [1]

requested the Environmental Protection Agency to "analyze the rapid growth and the energy consumption of computer Data Centers", as well as to evaluate possible standards for increasing energy efficiency in the industry. The report [8] clearly points out the following technologies and solutions for energy-efficiency improvement: using high-efficiency power distribution and UPS units; using state-of-the-art cooling equipment; monitoring power in real time; using combined heat and power, with on-site generation with the electric grid as backup.

Currently, data centers rely on the electric grid for energy supply, with conventional HVAC systems providing the cooling power required, which thus produce a further consumption of electric energy, still drawn from the grid (power consumption for cooling purposes can be 25% or more of the total data center power [2]). A UPS unit is always present in order to ensure the necessary level of security and protection for the electronic devices, both towards dangerous effects of electric disturbances (transient over-voltages or drops in voltage, voltage peaks, frequency variations) and towards grid interruptions (micro-interruptions or black-outs). Finally, an emergency electric generator (usually based on a diesel internal combustion engine) can be optionally included, with the only task of guaranteeing data center's service during prolonged grid interruptions, when the continuity of service is particularly important.

In a previous paper [9] the authors analyzed energy and cost savings that could be achieved by means of a CCHP system based on an internal combustion engine that supplies the electric power to the data center facility, coupled to a single-stage absorption chiller driven by the engine's discharge heat in order to meet the cooling power requirements.

In this paper another distributed generation plant, based on the integration of a methane membrane reformer and of a polymer electrolyte fuel cell, is considered as an alternative to the conventional thermal engine analyzed in the previous paper. A vapor-compression chiller equipped with free-cooling units is used to meet the cooling load of the data center rather than an absorption chiller, due to the particularly high electric efficiencies that can be achieved in this case, and also because a significant part of heat is recovered in the CHP plant at low temperature.

Furthermore, in order to improve the data center's own efficiency, a power distribution system based on high voltage direct current is considered instead of the conventional one based on alternating current: recent studies [10, 11] have demonstrated the potential of direct current systems for reducing overall power consumption in data centers thanks to the elimination of several AC/DC conversion steps. The direct current layout is also particularly suited to be integrated with the CHP system, which delivers direct current through its PEM fuel cell, as well as with renewable sources such as photovoltaic modules.

2. Conventional data center energy scenario

2.1. Data center energy requirements

The electric load generated in the conventional scenario has been evaluated with reference to the data published in [8] and represented in Table 1. In this table, average PUE values (equipment power to IT power ratio) for the different equipments of a data center are given, according to several scenarios taken into account in the EPA report. In this paper data from the "improved operation" scenario have been considered, since in this case the overall PUE of 1.7 (corresponding to a DCiE of 0.59) is the closest to current values found in the literature [1, 2, 4, 5, 6, 7].

Therefore, according to Table 1 and taking into account an average IT power consumption $P_{el,IT}$ = 100 kW, 27 kW are required by the UPS, the transformer and the lighting equipment; 13 kW are needed to operate the HVAC auxiliaries; finally, 30 kW are required by the chiller unit. The total load is therefore $P_{el,tot}$ = 170 kW.

These data can also be used to determine the ac-

		Site Infrastructure						
	IT Equipment	Transformer Losses	UPS Losses	Chilled Water	Fans	Lighting	Total	Rounded Value
Historical	1.00	0.05	0.17	0.54	0.16	0.08	2.00	2.00
Current Trends	1.00						1.90	1.90
Improved Operations	1.00	0.05	0.20	0.30	0.13	0.02	1.70	1.70
Best Practice	1.00	0.03	0.10	0.10	0.03	0.02	1.28	1.30
State of Art	1.00	0.03	0.05		0.04	0.02	1.14	1.20

Table 1: Estimate of PUE contribution by equipment per scenario used in the EPA Report [12]

tual cooling load generated by the data center: with the assumption that all power absorbed by the IT equipment and lighting is ultimately transformed into heat, and that the power losses by UPS and transformer are also turned into waste heat, the cooling load is therefore $P_{fr} = P_{el,base} = 127\,\text{kW}$.
In order to evaluate the overall energy consumption of the data center, two further assumptions are made:

- the load is almost constant throughout both the day and the year (data center's equivalent operating hours $h_{eq,IT} = 8\,760\,\text{h}$). This can indeed be the case for data centers housing critical IT equipment (servers, storage and network systems) that need to be always operating;
- the cooling load is not affected by ambient temperature fluctuations, so that the cooling power required is also almost constant throughout the day and the year. This assumption is correct for many data centers that indeed have minimal surface exposure to the outside and are confined within an air-conditioned facility [6, 13], but obviously should be checked case by case.

The electrical energy annually required in this scenario is therefore:

$$E_{el} = P_{el,tot} h_{eq,IT} \tag{1}$$

Annual operating costs related to the electrical energy consumption are calculated by means of the following equation (current electric energy cost in Italy can be estimated as $c_{EE} = 16$ c€/kWh):

$$C = c_{EE} E_{el} \tag{2}$$

Since this energy scenario is to be compared to a cogeneration one, the average grid efficiency used to calculate the primary energy consumption is taken from the Italian Energy Authority deliberations regulating cogeneration facilities. The resulting value for a power plant with rated power lower than 1 MW fueled by natural gas is $\eta_{el,ref} = 38.28\%$, taking an average efficiency $\eta_{el,grid} = 40.0\%$ and transport losses over the grid for a medium-voltage grid connection accounting for a 4.3% penalty (AEEG deliberations n. 42/2002, updated by n. 296/2005 and n. 307/2007). Thus:

$$E = E_{el} / \eta_{el,ref} \tag{3}$$

Finally, annual CO_2 emissions related to this scenario are calculated on the basis of specific emissions by thermoelectric power plants ($e_{CO_2,EE} = 496\,\text{g/kWh}$) indicated by the Italian utility ENEL [14]:

$$m_{CO_2} = e_{CO_2,EE} E_{el} \tag{4}$$

2.2. Thermal load definition

In this case study, beside the data center electric and cooling loads discussed in the previous section, the heating load of an office building housing the data center is added to the energy scenario. The heating load is determined, according to Italian regulations, as follows:

$$E_{th} = (\varepsilon_{wh} + \varepsilon_{th}\delta)\, V \tag{5}$$

where ε_{wh} is the volumetric thermal energy required for water heating, ε_{th} is the volumetric thermal energy required for proper heating purposes for each *heating degree day* (δ), and V is the office building volume. The heating degree day index is defined as the sum of the positive differences between the reference temperature of 20 °C and the daily average ambient temperature over a given reference heating period. The values of annual heating degree days for any Italian city is regulated by DPR n. 412/1993; for the three locations considered in this paper these values are: 2404 for Milan, 1415 for Rome, 751 for Palermo. In order to evaluate the monthly distribution of the thermal load, the number of heating degree days is then distributed over the year according

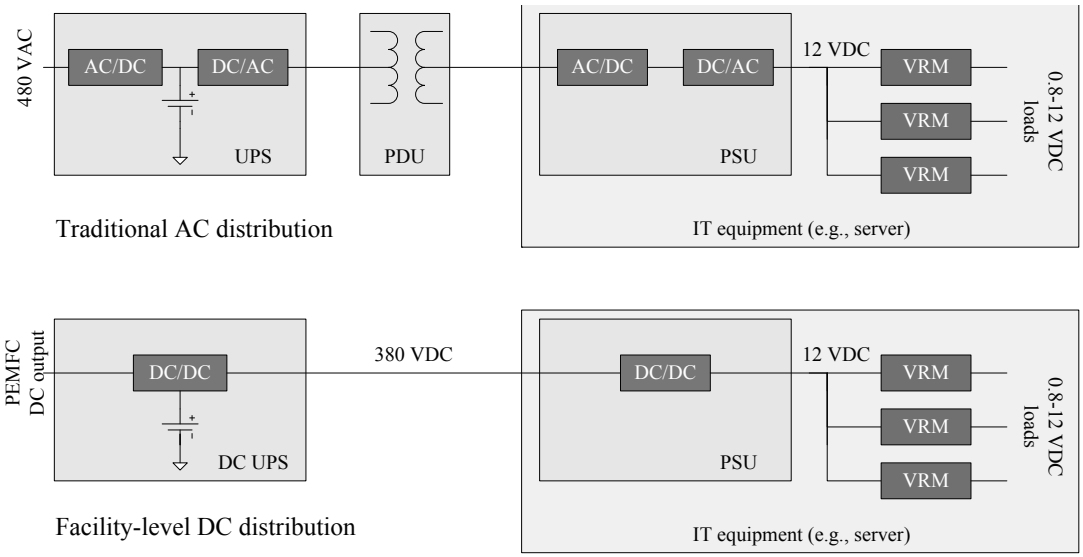

Figure 2: Data center power distribution systems: traditional AC (top) and high-voltage DC (bottom)

to the definition of heating degree days given above, taking into account the average ambient temperature for these cities, measured at the meteorological stations located at Linate (Milan), Ciampino (Rome) and Punta Raisi (Palermo) airports.

The assumptions made in this case study are:

- specific heat loads in 5: $\varepsilon_{th} = 10.83\,\mathrm{Wh\,m^{-3}\,K^{-1}}$ and $\varepsilon_{wh} = 1.0\,\mathrm{kWh\,m^{-3}}$;
- office building volume: $15\,000\,\mathrm{m^3}$.

The resulting annual heat load is thus 405.5 MWh for Milan, 244.9 MWh for Rome and 137.0 MWh for Palermo. In order to calculate the primary energy consumption related to these thermal loads, it is necessary to introduce the thermal efficiency of conventional boilers $\eta_{th,civ} = 0.80$ (this value is again indicated by the Italian Energy Authority as reference for non-industrial appliances), so that total primary energy consumption is:

$$E = \frac{E_{el}}{\eta_{el,ref}} + \frac{E_{th}}{\eta_{th,civ}} \tag{6}$$

Natural gas consumption is calculated as follows, taking into account a lower heating value $\Delta h_{LHV,\mathrm{CH_4}} = 802.3\,\mathrm{kJ\,mol^{-1}} = 35.79\,\mathrm{MJ/m^3_n}$:

$$\dot{V}_{n,\mathrm{CH_4}} = \frac{E_{th}}{\eta_{th,civ}\Delta h_{LHV,\mathrm{CH_4}}} \tag{7}$$

Total operating costs and CO_2 emissions are thus evaluated according to the following equations:

$$C = c_{EE}E_{el} + c_{NG}\dot{V}_{n,NG} \tag{8}$$

$$m_{\mathrm{CO_2}} = e_{\mathrm{CO_2},EE}E_{el} + e_{\mathrm{CO_2},NG}\dot{V}_{n,NG} \tag{9}$$

with natural gas cost estimated as $c_{NG} = 46$ c€/$\mathrm{m^3_n}$ with reference to the Italian market, and specific CO_2 emissions $e_{\mathrm{CO_2},NG} = 2.75\rho_{n,NG} = 1.963\,\mathrm{kg/m^3_n}$ with the simplifying assumption that natural gas composition is 100% methane.

3. Proposed data center energy scenario

3.1. Direct current power delivery system

The architecture of a typical data center power delivery system, shown on top of Fig. 2, is currently based on AC power, distributed to the facility at 480 V. An UPS is used to isolate equipment from power interruptions or other disturbances and to provide emergency backup energy storage usually by means of batteries: therefore inside the UPS, AC power is first converted to DC which is then converted back to AC for the facility distribution grid and routed to power distribution units (PDUs) for distribution to equipment in racks [11]. Inside the servers and other IT equipment such as storage or networking units, power supply units (PSUs) convert AC (at 120 V AC) to 12 V DC voltage as needed by the digital equipments. Further conversions may be required and performed by dedicated voltage regulator modules (VRMs) inside the electronic device.

A DC power distribution architecture (Fig. 2 bottom) can be used to avoid several electric power

conversion stages, thus eliminating the associated power losses. Indeed, direct current data centers have been set up and tested in order to assess the energy efficiency gains that could be achieved [10, 11], with rather good results: an end user could obtain an improvement of 4-6% efficiency points over well designed efficient AC systems currently available [10]. Based on these estimates, since in the reference "improved operation" scenario of Table 1 the power losses of UPS and PDU combined are 0.25 W for 1 W of IT power, in the alternative energy scenario these losses have been reduced to 0.15 W for 1 W of IT power. Furthermore, the reduction of power losses in the conversion stages is doubly beneficial because it also reduces the cooling load on the HVAC system, so that base electric power and cooling load have been reduced to $P_{fr} = P_{el,base} = 117\,\mathrm{kW}$.

3.2. Membrane reformer

The steam reforming unit must accomplish the conversion of the fuel input (in this case a stream composed of 100% methane) to hydrogen, through the methane-steam reforming reaction:

$$CH_4 + H_2O \rightleftarrows CO + 3H_2 \tag{10}$$

and the water-gas shift reaction:

$$CO + H_2O \rightleftarrows CO_2 + H_2 \tag{11}$$

In a conventional fuel processor, the steam reforming unit is composed of several reactors. The first one is the main reformer, where high temperatures ($800 \div 850\,^\circ\mathrm{C}$) are maintained in order to shift the endothermic ($\Delta_r H^0 = 206.17\,\mathrm{kJ\,mol^{-1}}$) methane-steam reforming reaction to the right, thus increasing hydrogen's yield. The reformate stream is then fed into two water-gas shift reactors maintained at lower temperature ($\sim 400\,^\circ\mathrm{C}$ and $\sim 200\,^\circ\mathrm{C}$) where the exothermic ($\Delta_r H^0 = -41.17\,\mathrm{kJ\,mol^{-1}}$) reaction 11 is catalytically promoted in order to increase hydrogen production and to remove CO (poisonous for the PEM fuel cell) from the stream. Finally, the last component is a low-temperature ($\sim 100\,^\circ\mathrm{C}$) PROX (Preferential Oxidation) unit, where the remaining CO is catalytically burned with oxygen in order to reduce CO concentration in the reformate stream at values acceptable for the operation of a PEM fuel cell.

A membrane reactor differs from a conventional one under several points of view. The fuel input is fed, together with water vapor, to the reformer (Fig. 3), which usually consists of a first section where methane and water react at high temperature according to equilibrium reactions 10 and 11, immediately followed (inside the same component) by a section where a hydrogen-selective membrane divide the feed area, where the reformate stream flows on a catalyst bed promoting the steam reforming reaction, from a permeate area, where hydrogen permeated across the membrane is collected. The heat input necessary to sustain the reactions is supplied by hot gases, resulting from the combustion of the "retentate", flowing outside the reactor (Fig. 3), which still contains significant amounts of hydrogen, methane and carbon monoxide (Table 3).

The main advantage of this configuration is that both reactions 10 and 11 are shifted to the right mainly by the subtraction of one product (H_2) from the stream, so that the reformer temperature can be significantly lower than in conventional reformers (high temperatures are however favorable, being the overall process endothermic), with obvious benefits in terms of process efficiency [15, 16, 17].

Many different membrane types have been subjected to extensive research and experimentation, but in this paper palladium-based dense membranes are considered for their good compromise between permeance and selectivity [15].

Hydrogen permeation through a Pd-based membrane involves seven sequential steps [17], but the diffusion of atoms through the bulk membrane is usually the rate determining step [17], so that hydrogen permeation through the membrane can be expressed by Richardson's law [15]:

$$J = \frac{k}{t}\left(p_{H_2,f}^{0.5} - p_{H_2,p}^{0.5}\right) \tag{12}$$

where k is the permeability of the membrane, t its thickness, $p_{H_2,f}$ and $p_{H_2,p}$ hydrogen's partial pressures on the feed side and on the permeate side, respectively. Membrane's permeability depends on temperature according to an Arrhenius expression:

$$k = k_0 \exp\left(\frac{-E_a}{RT}\right) \tag{13}$$

A lumped-parameter model has been set up in order to evaluate the membrane area required to obtain a specified hydrogen recovery factor, which is defined as the ratio of hydrogen permeated through the membrane to the amount of hydrogen that could be theoretically obtained if reactions 10 and 11 would

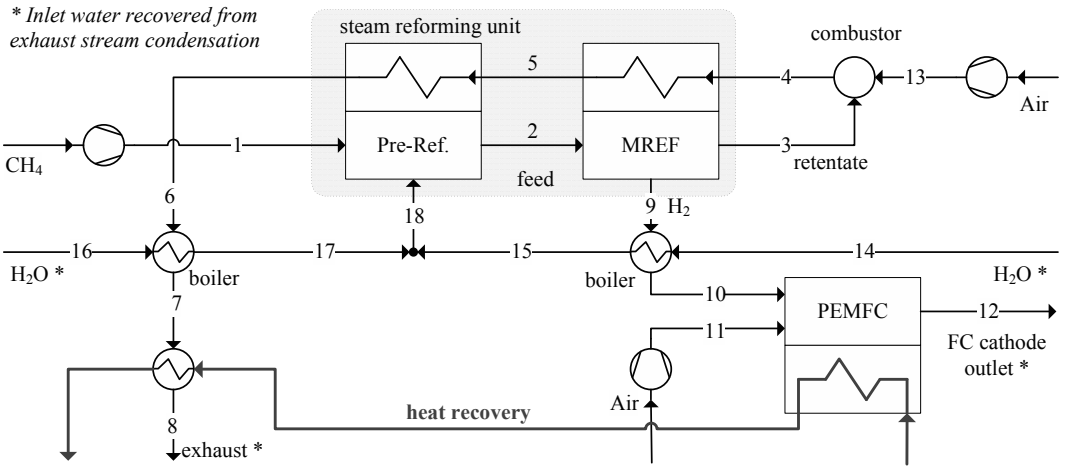

Figure 3: Layout of the cogeneration system

proceed to completion. For a fuel input composed only by methane, it is thus defined as:

$$\gamma = \frac{\dot{n}_{H_2,p,out}}{4\dot{n}_{CH_4,in}} \tag{14}$$

The reactor has been considered isothermal and subdivided in a sequence of N_{cv} control volumes; inside each control volume the stream coming from the previous one reacts according to 10 and 11 reaching equilibrium conditions. For the i^{th} control volume, hydrogen flux J^i through the membrane is then evaluated according to hydrogen's partial pressure by using Richardson's law 12, and the membrane area is finally calculated taking into account a constant amount of hydrogen permeated in each control volume: $A_m^i = \dot{n}_{H_2,p,out} / \left(N_{cv} J^i\right)$. The hydrogen permeated is then subtracted from the stream on the feed side of the reactor, which is fed to the following control volume, so that $\dot{n}_{H_2,f}^{i+1} = \dot{n}_{H_2,f}^{i} - J^i A_m^i$. The temperature in the steam reformer unit (Table 2) has been taken as high as possible, the upper limit being close to the maximum temperature allowable by the Pd membrane ($\sim$ 650 °C [15]), because high temperatures shift the equilibrium reactions to the right, thus increasing hydrogen's partial pressure on the feed side and consequently hydrogen's flux J, resulting in a lower membrane area required for a given hydrogen recovery factor. Increasing feed total pressure is equally beneficial for reducing membrane area, but membrane's mechanical strength must be taken into account on this respect (furthermore, it also increases methane's compressor power consumption). Pressure on the permeate side is determined by the fuel cell's operating conditions. In order to increase hydrogen's permeation across the membrane, a sweep stream on the permeate side could have been used so as to decrease hydrogen's partial pressure, but the resulting hydrogen's dilution would have been detrimental for the fuel cell's performance, as shown by 17.

Table 2: Membrane reformer parameters

Parameter	Value
t	50 μm
k_0	1.97×10^{-7} mol s^{-1} m^{-1} Pa$^{-0.5}$ [16]
E_a	13 810 J mol^{-1} [16]
γ	0.65
T	600 °C
$p_{f,in}$	9.0 bar
$p_{p,out}$	1.2 bar

Finally, a most important parameter for the steam reforming process is the "steam-to-carbon" ratio, defined as the ratio between the molar flows of water vapor and methane into the reformer:

$$\sigma = \frac{\dot{n}_{H_2O,in}}{\dot{n}_{CH_4,in}} \tag{15}$$

For a conventional steam reforming unit, increasing values of σ yield higher hydrogen conversion factors [18], because both equilibrium reactions 10 and 11 are shifted to the right, at the cost of a larger thermal input required for producing the necessary amount of water vapor.

In a membrane reforming unit, instead, increasing the steam-to-carbon ratio has two opposed effects

Table 3: Stream data for relevant points of the cogeneration system of Fig. 3

Point	T [°C]	p [bar]	n^* [$\frac{\text{mol}}{\text{mol}_{CH_4}}$]	CH_4	CO	CO_2	H_2	H_2O	O_2	N_2
				mol %						
2	600.0	8.91	5.10	11.7	1.4	6.4	30.0	50.4	0.0	0.0
3	600.0	8.64	3.35	5.2	2.9	21.7	18.0	52.2	0.0	0.0
4	1326.9	1.20	8.00	0.0	0.0	12.5	0.0	33.8	4.4	49.4
6	687.7	1.16	8.00	0.0	0.0	12.5	0.0	33.8	4.4	49.4
7	180.6	1.14	8.00	0.0	0.0	12.5	0.0	33.8	4.4	49.4
8	70.0	1.12	8.00	0.0	0.0	12.5	0.0	33.8	4.4	49.4
9	600.0	1.22	2.60	0.0	0.0	0.0	100.0	0.0	0.0	0.0
10	70.0	1.20	2.60	0.0	0.0	0.0	100.0	0.0	0.0	0.0
18	370.0	9.00	3.30	0.0	0.0	0.0	0.0	100.0	0.0	0.0

on the membrane area required to achieve a given value of hydrogen recovery factor: on the one hand, higher values of σ are beneficial for the same reason detailed above for conventional reforming units (both equilibrium reactions are shifted to the right); on the other hand, though, hydrogen's partial pressure on the feed side $p_{H_2,f} = \dot{n}_{H_2,f}/\dot{n}_f p$ decreases with σ, since both $\dot{n}_{H_2,f}$ and $\dot{n}_f$ increase with σ, but the first less rapidly than the second, so that, taking into account Richardson's law 12, the permeation through the membrane decreases with σ. In this situation an optimum value of steam-to-carbon ratio may be found, and indeed this is what is shown in Fig. 4, which illustrates the influence of the steam-to-carbon ratio on total membrane area calculated with the model described above, with reference to a unit input flow of methane (operating conditions are summarized in Table 2): the minimum is found for $\sigma \cong 3.3$, which is thus taken as a further operating condition in the simulations concerning the whole data center energy scenario discussed in the following sections.

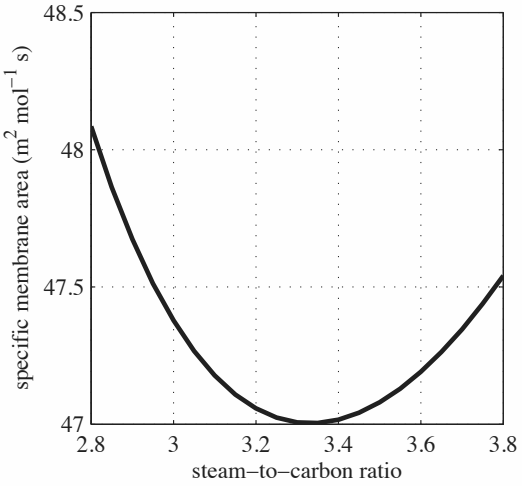

Figure 4: Influence of steam-to-carbon ratio on specific membrane area (with reference to 1 mol s^{-1} *of* CH_4 *input)*

3.3. PEM fuel cell

In this work a PEM fuel cell is considered for its high power density, fast start-up capability and relatively low-cost materials [15].
Figure 5 shows typical cell voltage and efficiency values for a PEM fuel cell included in a small mobile system [19], which is here considered as a reasonable (and conservative) reference system for the stationary fuel cell required by the proposed CHP plant. The polarization curve (cell voltage *vs* current density) can be expressed in the following analytical form (empirical coefficients are listed in Table 4):

$$V_{cell} = E^{rev} - \frac{RT}{\alpha n_e F} \log \frac{i}{i_0} - ri - m \exp(ni) \quad (16)$$

where E^{rev} is the reversible cell potential:

$$E^{rev} = E^0 + \frac{RT}{n_e F} \log \left(\frac{a_{H_2} a_{O_2}^{1/2}}{a_{H_2O}} \right) \quad (17)$$

The theoretical cell voltage at standard temperature and pressure E^0 is related to the change in molar Gibbs' free energy of formation $\Delta_f g^0$:

$$E^0 = \frac{-\Delta_f g^0}{n_e F} \quad (18)$$

For the reaction $H_2 + O_2 \rightarrow H_2O_g$, $\Delta_f g^0 = -228.6\,\text{kJ mol}^{-1}$ so that $E^0 = 1.1848$ V; if air is used

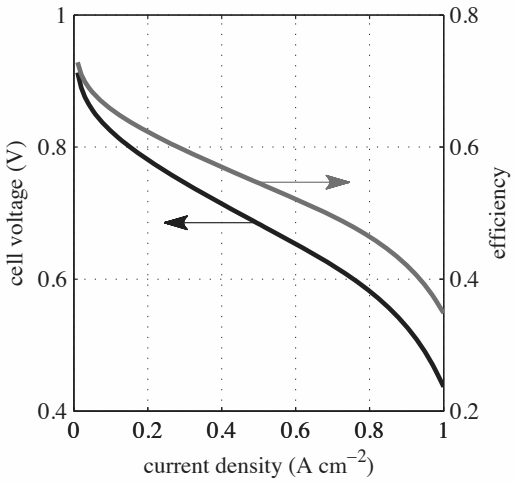

Figure 5: Cell voltage and efficiency

Table 4: Empirical coefficients in the analytical expression of the polarization curve 16

Coefficient	Value
α	0.3629
i_0	6.257×10^{-6} A cm^{-2}
r	0.1752 Ω cm^2
m	1.879×10^{-4} V
n	6.887 A^{-1} cm^2

as oxidant ($x_{O_2} = 0.21$), the reversible cell potential is thus $E = 1.1733$ V at the fuel cell operating temperature of 70 °C.
The cell efficiency is then evaluated with reference to the change in molar enthalpy of formation at standard temperature and pressure, which for the above mentioned reaction is $\Delta_f h^0 = -241.8$ kJ mol^{-1} if hydrogen's lower heating value is considered:

$$\eta_{FC} = \frac{n_e F V_{cell}}{-\Delta_f h^0} \tag{19}$$

The fuel cell in this plant layout can work in a dead-end configuration because of hydrogen's high purity resulting from the membrane separation process, so that the fuel utilization factor can be considered equal to 1, leaving aside very small quantities of hydrogen leaked to the environment due the periodical purging of accumulated inerts [15].

3.4. CHP plant data

The fuel cell must be sized so as to supply, at rated conditions, a net power output $P_{el,net} = 170$ kW: taking into account power losses related to DC/DC converters, fuel cell's auxiliary units and natural gas and air compressors, calculated according to the data presented in Table 5, the necessary stack power output is $P_{el,stack} = 187.1$ kW. If a current density $i = 0.30$ A cm^{-2} at rated operating conditions is chosen, rated cell voltage and efficiency are, respectively, $V_{cell} = 0.746$ V and $\eta_{FC} = 0.595$. With $N_s = 2$ stacks of $N_c = 1000$ cells connected in parallel (a reasonable value for this power size [20]) the overall stack voltage at rated power would therefore be $V = 746.0$ V, and consequently the total current would be $I = P_{el,stack}/V = 251.4$ A. The resulting cell area is thus $A_{cell} = I/(N_s\, i) = 419.0$ cm^2, a size that is acceptable for the stationary power plant here considered.
In order for the fuel cell to be able to supply the required power output, the hydrogen flow must be $\dot{n}_{H_2,p,out} = P_{el,stack}/(-\Delta_f h^0 \times \eta_{FC}) = 1.30$ mol s^{-1}; therefore, the steam reforming unit must be supplied with a methane input flow $\dot{n}_{CH_4,in} = \dot{n}_{H_2,p,out}/(4\gamma) = 0.50$ mol s^{-1}. The necessary membrane area thus results $A_m = 23.64$ m^2, while the overall plant net electric efficiency at rated conditions is:

$$\eta_{el,CHP} = \frac{P_{el,net}}{\dot{n}_{CH_4,in}\,\Delta h_{LHV,CH_4}} = 42.29\% \tag{20}$$

Thermal efficiency is shown to be particularly high thanks to the recovery of latent heat from both the exhaust streams (which is beneficial not only because it increases heat recovery but also because it makes the plant self-sufficient with respect to water supply, a most important issue both from an environmental and an economic point of view [21]). At rated operating conditions heat recovery amounts to $P_{th,CHP} = 252.0$ kW (low-temperature heat recovery particularly suitable for a heat distribution system using radiant panels), so the value of thermal efficiency is:

$$\eta_{th,CHP} = \frac{P_{th,CHP}}{\dot{n}_{CH_4,in}\,\Delta h_{LHV,CH_4}} = 62.68\% \tag{21}$$

As a concluding remark about the membrane reforming unit, the steam reforming efficiency obtained is 76.45% (based on the lower heating value), its definition being:

$$\eta_{SR} = \frac{\dot{n}_{H_2,p,out}\,\Delta h_{LHV,H_2}}{\dot{n}_{CH_4,in}\,\Delta h_{LHV,CH_4} + P_{aux,SR}} \tag{22}$$

In this scenario, a state-of-the-art vapor compression chiller with free-cooling capabilities is used to meet the cooling load. The chiller taken as reference is the HITEMA ECFS 150 model, with rated power output 150 kW. Annual energy consumption is thus evaluated on a monthly basis, taking into account average COP and free-cooling power output of the chiller as functions of the ambient temperature (calculated according to data available on the manufacturer's web site):

$$E = \sum_{i=1}^{12} \left[\frac{P_{el,base} + P^i_{el,chiller}}{\eta^i_{el,CHP}} h^i + \frac{\max\left(E^i_{th} - E^i_{th,rec}\right)}{\eta_{th,civ}} \right] \tag{23}$$

with

$$P^i_{el,chiller} = \frac{P_{fr} - P^i_{freecooling}}{COP^i} + P^i_{aux} \tag{24}$$

being the chiller's monthly electric power consumption, and

$$E^i_{th,rec} = \eta^i_{th,CHP} \frac{P_{el,base} + P^i_{el,chiller}}{\eta^i_{el,CHP}} \tag{25}$$

being the thermal energy that can be recovered by the CHP plant. In the above equations, h^i is the total number of hours for each month, while P^i_{aux} is the electric power required by chiller auxiliaries (pump, fans). The cooling and electric loads (P_{fr} and $P_{el,base}$) have been estimated as 117 kW in section 3.1. Net electric efficiency $\eta^i_{el,CHP}$ may vary due to variations in the overall electric load, which in this analysis may take place only with reference to the chiller's performance (in terms of COP and free-cooling power output), whereas the base IT electric load is assumed constant throughout the year.
Finally, annual operating costs and CO_2 emissions can be calculated as follows:

$$C = c_{NG} \frac{E}{\Delta h_{LHV,\mathrm{CH_4}}} \tag{26}$$

$$m_{\mathrm{CO_2}} = e_{\mathrm{CO_2},NG} \frac{E}{\Delta h_{LHV,\mathrm{CH_4}}} \tag{27}$$

4. Results and discussion

The results of the calculations described in the previous section are reported in Fig. 6 for a data center located in Rome, in terms of primary energy, operating costs and CO_2 emission savings that could be obtained with the proposed CHP plant with reference to the conventional data center energy scenario described in section 2. Table 6 shows the same results in absolute values.

Table 5: Simulation assumptions

Parameter	Value
DC/DC converter efficiency	97.5% [19]
FC auxiliary consumption	1.5%
compressor polytropic efficiency	0.70
reformer pressure loss	4%
heat exchangers pressure loss	2%
combustor pressure loss	4%

In particular, Fig. 6 shows the contribution of the four energy-saving methods discussed in this paper, i.e. , from bottom to top: the conversion of the data center to a direct current architecture (labeled AC→DC); the adoption of a high-performance chiller, with particular reference to its free-cooling capabilities (free-cool.); the adoption of an efficient power plant instead of the grid to supply the required electrical power (CHP_{el}); finally, supplying the required thermal energy (section 2.2.) by means of heat recovered from the CHP plant (CHP_{th}). The results clearly point out that significant energy, economic and environmental benefits can arise from the efficient energy management of a data center.
The direct current architecture and the adoption of free-cooling both contribute to reduce data center's electric power requirement, so that their weight on the overall savings is the same for energy, costs and CO_2 emissions.

Furthermore, the particularly high electric efficiency, which can be achieved by the CHP plant thanks to the membrane reformer unit, makes possible to attain remarkable savings by substituting the electric grid with the CHP plant as the data center's power source, particularly in the case of operating costs, because of the substantial difference between electric energy and natural gas costs, at least in Italy (on an energy basis, the former costs approximately 4.44 c€/MJ, while the latter costs 1.30 c€/MJ).
Finally, the availability of heat recovered from the CHP plant makes for another energy and cost saving opportunity, if an office or residential building is located close to data center's premises (in this case, under the particular assumptions made about the thermal load, and specifically about the office building volume, heat recovery from the CHP plant

Table 6: Annual results for the reference data center located in Rome

	Conventional DC	CHP DC	CHP savings
Primary energy consumption / GWh	4.196	3.109	1.087
Operating costs / k€	252.4	143.9	108.5
CO_2 emissions / t	799.1	613.9	185.2

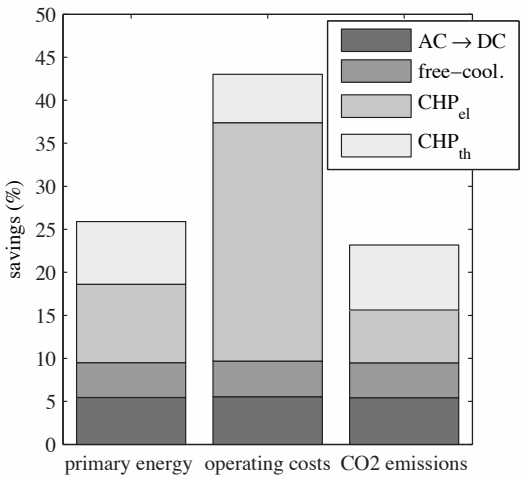

Figure 6: Primary energy, operating costs and CO_2 emission savings for the reference data center located in Rome

is always sufficient to meet the required thermal load).

The influence of the electrical energy to natural gas cost ratio is described in Fig. 7. With current cost values, the ratio is approximately 3.46 on an energy basis. The data reported in Fig. 7 have been obtained holding the electrical energy cost constant for different natural gas costs. Obviously, the higher the cost ratio, the larger the cost savings in the CHP scenario; anyway, it must be observed that these savings are substantial for a wide range of cost ratios, and that it is generally possible to assume that electric energy and natural gas cost variations will be more or less interrelated.

The influence of data center geographical localization is finally described in Fig. 8, which reports the results obtained for the reference data center located in Milan (MI), Rome (RM) and Palermo (PA). It can be seen that the colder the place, the better the performance of the CHP plant. Indeed, lower average temperatures produce more free-cooling output and higher thermal loads (besides higher chiller efficiencies). Fuel cell performance, on the contrary, is not significantly affected by ambient temperature.

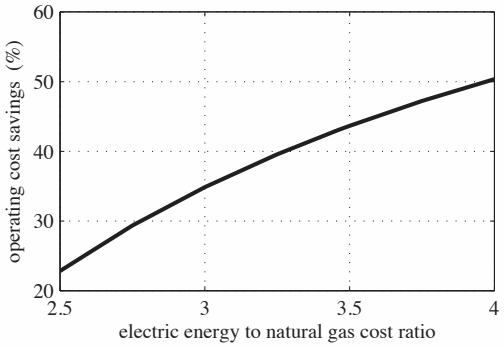

Figure 7: Influence of electric energy to natural gas cost ratio on operating cost savings

5. Conclusions

This paper discussed and analyzed annual energy consumption, operating costs and CO_2 emissions related to the operation of a data center with an IT equipment electric power consumption of 100 kW located in Italy, taking first into account current typical energy efficiency values for this particular type of building, then an advanced data center energy management system based on a direct current architecture, with cooling provided by a state-of-the-art vapor compression chiller equipped with a free-cooling unit, and with the main power supply provided by a CHP plant based on a membrane reformer unit and a PEM fuel cell. The CHP unit also supplies thermal energy to an office building located close to the data center facility.

The simulations have demonstrated that the adoption of advanced energy management technologies can bring about remarkable energy, cost and emission savings in the operation of a data center: in particular, annual energy costs can be cut by more than 100 k€, (representing a 43.0% cost reduction) when the thermal energy from the CHP system can be usefully recovered. Such remarkable savings must obviously be weighted against investment costs and durability performance for the membrane reformer

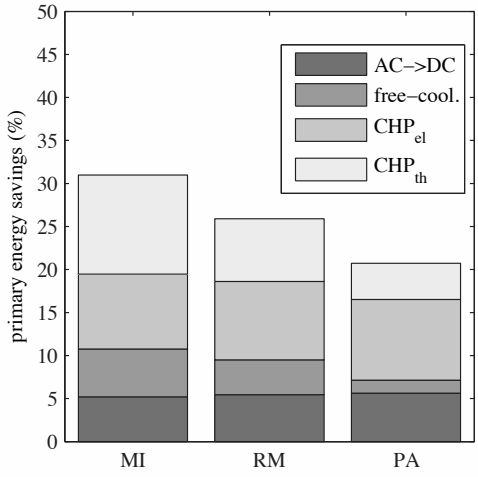

Figure 8: Primary energy savings for the reference data center located in Milan, Rome or Palermo

and the PEM fuel cell that are currently not yet fully satisfactory. It must be noted, however, that great effort is being put on both these research topics, due to the promising results achievable. For example, a demonstration membrane reformer unit has been recently set up and tested [22], obtaining encouraging results in terms of system efficiency, footprint, hydrogen purity and production rate (up to 40 m^3_n/h).
The innovative data center energy management system can also offer substantial savings from an environmental point of view, even if less remarkable than cost savings due to the electricity to natural gas cost ratio in Italy. The electric to natural gas cost ratio is obviously an important factor in determining the economic results achievable by the CHP system; anyway, even though cost savings decrease with increasing natural gas costs, good results can still be obtained for a wide range of electric to natural gas cost ratios. Therefore, since electricity and natural gas cost fluctuations are obviously not independent on each other, the economic results of a CHP system are not going to be significantly altered by possible future price oscillations.
Finally, due to the influence of ambient temperature on thermal load and on free-cooling power output, the localization of the data center is a significant factor for the CHP plant's performance, with considerably higher energy and cost savings obtained in colder climates.

Nomenclature

a	activity
A	area, m^2
e	specific emissions, kg/kWh or kg/m^3_n
E	energy, J or Wh, or cell potential, V
F	Faraday's constant, 96 480 C mol^{-1}
g	molar Gibbs' free energy, J mol^{-1}
h	molar enthalpy, J mol^{-1}
k	membrane permeability, mol s^{-1} m^{-1} $Pa^{-0.5}$
i	current density, A cm^{-2}
I	current, A
m	mass, kg, or coefficient in 16, V
n	coefficient in 16, A^{-1} cm^2
$\dot{n}$	molar flow rate, mol s^{-1}
p	pressure, bar
P	power, kW
r	fuel cell's area-specific resistance, Ω cm^2
R	universal gas constant, 8.3145 J mol^{-1} K^{-1}
t	membrane thickness, m
T	temperature, K
V	voltage, V, or volume, m^3
$\dot{V}$	volumetric flow, m^3 s^{-1}

Greek Letters

α	coefficient in 16
γ	hydrogen recovery factor
δ	heating degree day, K
ε	specific heat load, Wh m^{-3} (K^{-1})
η	efficiency
σ	steam-to-carbon ratio

Subscripts and superscripts

a	activation
$cell$	related to a single FC cell
cv	control volumes
e	electrons
el	electric
f	feed, formation
m	membrane

p permeate

rev reversible

SR steam reforming unit

th thermal

Acronyms

AC Alternating Current

CHP Combined Heat and Power

COP Coefficient Of Performance

DC Data Center, Direct Current

DCiE Data Center infrastructure Efficiency

FC Fuel Cell

HVAC Heating, Ventilation and Air Conditioning

IT Information Technology

LHV Lower Heating Value

PDU Power Distribution Unit

PSU Power Supply Unit

UPS Uninterruptible Power Supply

References

[1] J.G. Koomey. Woldwide electricity used in data centers. *Environmental Research Letters*, 3:034008, 2008.

[2] K. Kant. Data center evolution. *Computer Networks*, 53:2939–2965, 2009.

[3] C. Belady et al. The Green Grid data center power efficiency metrics: PUE and DCiE. http://www.thegreengrid.org/~/media/WhitePapers/White_Paper_6_-_PUE_and_DCiE_Eff_Metrics_30_December_2008.ashx?lang=en, 2007.

[4] J. Mitchell-Jackson et al. Data center power requirements: measurements from Silicon Valley. *Energy*, 28:837–850, 2003.

[5] J.F. Karlsson and B. Moshfegh. Investigation of indoor climate and power usage in a data center. *Energy and Buildings*, 37:1075–1083, 2005.

[6] H.S. Sun and S.E. Lee. Case study of data centers' energy performance. *Energy and Buildings*, 38:522–533, 2006.

[7] S. Greenberg et al. Best practices for data centers: Lessons learned from benchmarking 22 data centers. In *Proceedings of the 2006 ACEEE Summer Study on Energy Efficiency in Buildings*, Pacific Grove, CA (USA), 2006.

[8] U.S. Environmental Protection Agency. EPA report to congress on server and data center efficiency. http://www.energystar.gov/index.cfm?c=prod_development.server_efficiency_study, 2007.

[9] G.L. Guizzi et al. Comparative analysis of combined cooling, heating and power systems covering data centers energy needs. In *Proceedings of the 22nd International Conference on Efficiency, Cost, Optimization (ECOS 2009)*, Foz do Iguaçu, Paraná, Brazil, September 2009.

[10] L. Simmons. Peer review of Lawrence Berkeley National Laboratory (LBNL) study on direct current in the data center. http://hightech.lbl.gov/dc-powering/pubs/Peer_Review_of_LBNL_Study.pdf, 2008.

[11] M. Ton et al. DC power for improved data center efficiency. http://hightech.lbl.gov/documents/DATA_CENTERS/DCDemoFinalReport.pdf, 2007.

[12] Silicon Valley Leadership Group. Data center energy forecast. Final report. http://svlg.net/campaigns/datacenter/docs/DCEFR_report.pdf, January 2008.

[13] N. Rasmussen. Calculating total cooling requirements for data centers. http://www.apcmedia.com/salestools/NRAN-5TE6HE_R2_EN.pdf, 2007.

[14] ENEL. Environmental report (in italian). http://www.enel.it/azienda/it/investor_relations/bilanci_documenti/doc/2007RAPPAMB/rapporto_ambientale_2007.pdf, 2007.

[15] S. Campanari et al. Innovative membrane reformer for hydrogen production applied to pem micro-cogeneration: Simulation model and thermodynamic analysis. *International*

Journal of Hydrogen Energy, 33:1361–1373, 2008.

[16] A. Bottino et al. Steam reforming of methane in equilibrium membrane reactors for integration in power cycles. *Catalysis Today*, 118:214–222, 2006.

[17] A. Li et al. Staged-separation membrane reactor for steam methane reforming. *Chemical Engineering Journal*, 138:452–459, 2008.

[18] A.E. Lutz et al. Thermodynamic analysis of hydrogen production by steam reforming. *International Journal of Hydrogen Energy*, 28:159–167, 2003.

[19] G.L. Guizzi et al. Hybrid fuel cell-based energy system with metal hydride hydrogen storage for small mobile applications. *International Journal of Hydrogen Energy*, 34:3112–3124, 2009.

[20] J. Larminie and A. Dicks. *Fuel Cell Systems Explained (Second Edition)*. John Wiley & Sons, 2nd edition, April 2003.

[21] J.R. Lattner and M.P. Harold. Comparison of conventional and membrane reactor fuel processors for hydrocarbon-based PEM fuel cell systems. *International Journal of Hydrogen Energy*, 29:393–417, 2004.

[22] Y. Shirasaki et al. Development of membrane reformer system for highly efficient hydrogen production from natural gas. *International Journal of Hydrogen Energy*, 34:4482–4487, 2009.

Analysis and optimization of fuel cell cogeneration systems for application in single-family houses

F. Cardona[a], A. Piacentino[a], V. Alterio
[a] DREAM, Department of Energetic and Environmental Researches, University of Palermo, Viale delle Scienze, 90128, Palermo

Abstract: The world's demand of energy is projected to double by 2050 in accordance with population growth and with the industrialization of developing countries. The supply of fossil fuel could be limited and even worse is concentrated in a few regions of world, while demand is growing everywhere. One promising alternative to fossil fuel is hydrogen which is abundant and generously distributed through the world without regard for national boundaries. The aim of this paper is to explore this early market opportunity for fuel cell cogeneration systems in buildings and to determine the conditions under which they might compete with the alternative of purchased power. It is suitable to identify and to provide solutions for problems encountered in adapting these systems to buildings through a process which involve three steps:

- Determination of buildings energy annual demand compiled by a data acquisition system or logged daily by operators
- Characterization of a specific fuel cell in terms of amount of heat flow available and its temperature level, based on the power output of the system
- Calculation of annual energy costs (natural gas fuel and possibly purchased electrical energy) for providing power, heat and air conditioning and comparison with operating costs of existing buildings. The energy cost savings provided by the various cogeneration systems were used to provide estimates of what capital costs for each of these systems might be economically justified

A numerical model is developed to perform a fuel cell cogeneration system, coupled with a Thermal Energy Storage (TES), in accordance with energy requirements of a single-family residence. The objective of the mathematical model is to calculate the energy allocation for each system component and to determine fuel use of the system on hour basis. The operation of the cogeneration system is dependent on the temperature of TES (T_{TS}) which varies during the hours. If the tank is hot enough ($T_{TS} \geq T_{hwx}$ temperature limit for electric domestic water heating) it can supply the entire domestic water load, otherwise if the tank is too hot ($T_{TS} \geq T_{fcx}$ temperature limit for external heat rejection from the fuel cell) the heat transfer from the fuel cell will be limited.
Two conventional systems connected to public grid are investigated as alternatives to the cogeneration ones.

Keywords: Fuel cell, Cogeneration system, Building application.

1. Introduction

Cogeneration System systems based on renewable energy sources, such as geothermal, wind, and solar energy and systems based on fossil fuels, such as diesel generators and fuel cells are only a few of the possibilities for small scale residential applications. A fuel cell based Cogeneration System represents a particularly promising system for a residence due to its high efficiency, excellent part load performance, small-scale applicability, and quiet operation. A fuel cell system generates approximately the same amount of thermal energy as electrical energy. The available thermal energy can be used in different ways, such as space heating, space cooling and water heating. The design (Fig. 1) studied consists of a fuel cell system (**FCS**) and a vapour compression Heat Pump (**HP**).

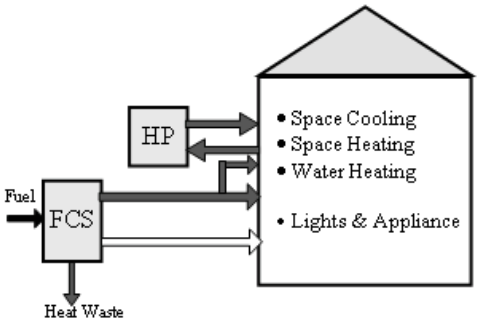

Fig. 1. Fuel cell system and heat pump, with heat recovery for water and space heating

The thermal energy from the FCS is used for water and space heating. The heat pump provides space cooling electrically. The heat pump also satisfies the portion of the heating requirement that exceeds the thermal energy available from the FCS.

The FCS provides electricity for lights, appliances, and the heat pump. For better use of the available thermal energy, a thermal storage tank [1] is added to the system.(Fig. 2)

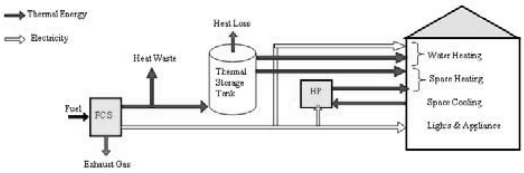

Fig. 2. Cogeneration system with fuel cell, heat Pump, and thermal storage

In this scheme thermal energy from the fuel cell system is transferred to the thermal storage tank. The stored energy can supply domestic water and space heating demands, otherwise they must be supplied electrically.

2. Problem description

The objectives of this research are:

- establishing the energy requirements for a single-family residence;
- modelling the performance of a fuel cell based *Cogeneration System*, in accordance with energy requirements [2], [3];
- evaluating system energy use characteristics for various climatic conditions.

The residence discussed throughout the research is a detached, single-family residential building selected as a "typical" residence.

The size and characteristics of the house are based on the data available from previously studied residential energy load characteristics from literature [4]. The average lights, appliance load, and domestic hot water use profiles are obtained from the available literature for a 200 m² residence occupied by 4 people.

The design characteristics of the residence are based on current residential building codes and the space heating and cooling loads are obtained from available literature (by applying the building energy simulation program).

2.1 Analysis

In order to analyze the proposed residential cogeneration system, the energy requirements for a representative residential building are established and a mathematical model is developed to relate the response of the fuel cell to the building thermal and electrical loads. Finally, the model is applied to investigate the performance of the cogeneration system in different climatic conditions and to evaluate the significance of key design decisions.

Energy is used in a residence for domestic water heating, space heating and cooling, lights and appliances.

In accordance with the cogeneration system considered in this research, thermal energy can be used for domestic water heating and space heating. However, thermal energy from the fuel cell system may not be sufficient at all times.

An electric resistance heater supplies the domestic water heating, while an electric vapour-compression heat pump supplies the space heating.

During the cooling season, electricity is used to operate the heat pump in air conditioning (AC) mode. The lights and appliances must be powered by electricity at all times.

2.2. Domestic hot water energy use

The main factors in determining the energy use for water heating are:

- the consumption profile,
- the heater efficiency,
- the design hot water temperature,
- the incoming city water temperature.

In order to calculate the theoretical energy required for the hot water load, the heating equipment efficiency will not be included in this section. The equipment efficiency will later be included in the cogeneration system model as a design parameter (K_{DW}) and the design hot water temperature is assumed to be 60°C.

City water temperature (T_{CW}), which depends on air, water reservoirs and ground temperature, shows geographic and seasonal variations. For sufficiently long water pipes, city water temperature would be the same as the ground temperature at the depth of the pipes.

2.3. Electric load for lights and appliances

Data for electricity use by lights and appliances (excluding water heating) has been determined by

statistical surveys conducted on European population [5]. The report was prepared for european "non heat ventilation and air condition" (HVAC) electric load profiles for use in simulating the performance of residential cogeneration system and it gives a mean daily profile for the electricity consumption by lights and appliances, which can be used for every day of the year.

Lights and appliances data, presented in Fig. 3, are average electric loads on hour basis.

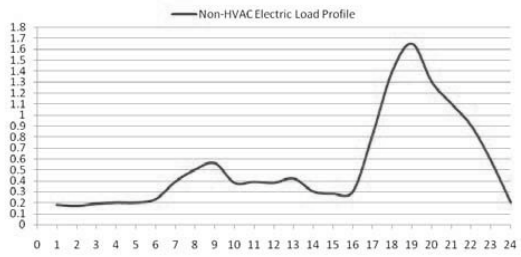

Fig. 3. Average electric loads for lights and appliances on hour basis

Actual peak electric loads will be higher than those indicated. It is probably not economical (and may not be feasible) to use the fuel cell to meet peak power requirements imposed by transient effects such as motor starts. Therefore, a battery pack is used to supply power for transients. It is assumed that the battery has sufficient capacity to level the electrical loads to the average values presented in Fig. 3. The capacity and peak output of the battery pack [6] can be determined by investigating the electricity demand of a residence. For this reason, equipment specifications are considered and the peak power demands of residential appliances are shown in Fig. 4 for transition period as small as 1 sec.

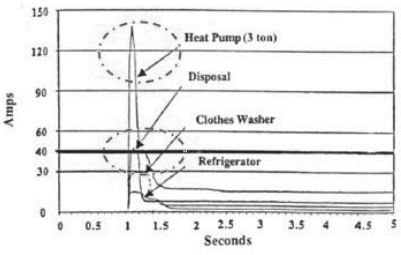

Fig. 4. Starting requirements for selected residential appliances

It is observed that the compressor of the heat pump has the highest power demand. In order to be able to start the heat pump, the cogeneration system should be sized to deliver high peak electrical power for a couple of seconds [7].

As result, the battery pack must have sufficient power output to supply these peak power demands. In addition, the battery pack must have sufficient storage capacity to meet low electrical power requirements over consecutive hours in a residence.

By Analysing the electric load characteristics (Fig.3), it shows that in the absence of space heating and cooling loads the electric demand is lower than 0.3 kW for 7 consecutive hours during the night. Therefore, meeting this low power load with the fuel cell will probably not be feasible.

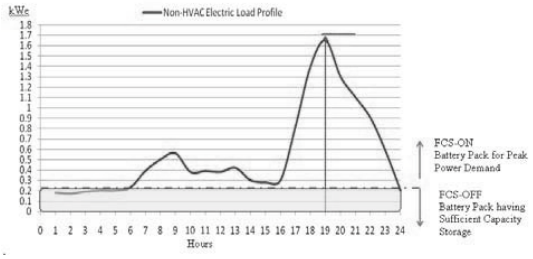

Fig. 5. Operation of battery pack for covering average electric of loads for lights and appliances on hour basis

The battery pack should have a minimum capacity to supply low electric loads until a significantly higher electric power is demanded for consecutive hours. Usually this value, for typical fuel cell such as PEM, included between 0.5 kW and 3 kWh, hence a battery pack with 3kWh capacity is suggested.

2.4. Energy requirements for space heating and cooling

The energy requirements for space heating and cooling are determined by heating and cooling loads and they depend on the building properties:

- Geographical location (and corresponding weather conditions)
- Infiltration
- Internal factors such as the operation of lights and appliances, occupancy, and internal mass.

The building properties used in the model are typical for new energy efficient construction.

Infiltration refers to the unintentional introduction of outside air into the conditioned space. Air leaks into all buildings. The air inflow rate is typically

sufficient to completely replace the air in the building 0.3 to 1.6 times per hour. Infiltration values, corresponding to buildings with medium air-tight construction, are selected for the residence. During cooling season lights and appliances present an additional load for cooling, since electricity supplied to these devices is ultimately dissipated in terms of thermal energy. During heating season**,** the demand is reduced due to lights and appliances. The lights and appliances load is assumed to follow the profile described in section 2.3

For the purpose of this research, it has been assumed that 4 people occupy the house during the evenings and nights and 2 people remain in the house during the day.

The internal mass of the building represents inertia against sudden changes in the temperature of the building. Considering the weight of the floor, appliances, and the furniture, the internal mass for this residential building has been estimated as 78 kg/m^2.

2.4.1. Energy use by heating and cooling equipment

The space heating and cooling system is based on vapour compression heat pump [8].

During heating hours, the indoor coil operates as a condenser and the outside coil as an evaporator, and vice versa during cooling hours.

During the heating cycle, five components of the heat pump system use electricity and the compressor is the major user of electricity.

Supplemental electric resistance coils located next to the indoor coil use electricity to satisfy the space heating demand that cannot be supplied by the heat pump cycle. Electricity is used for the outdoor coil fan and the supply fan.

The factors that affect the coefficient of performance (COP) and the operation of the heating system are the outdoor dry-bulb temperature and the part load ratio.

A typical heating COP for a heat pump is 3.10 at 8.3 °C for a medium priced heat pump.

Both the heating COP and the heating capacity for the heat pump can be modelled as quadratic functions of the outdoor dry bulb temperature.

For the cooling cycle heat pump also provides space cooling. The operating conditions that affect the efficiency and the capacity of the cooling cycle are the outdoor dry-bulb temperature, indoor dry- and wet-bulb temperatures, and the sensible and total cooling part load ratios. Since both heating and cooling performance depend on part load ratio, the size of the equipment must be known before the performance at any load condition can be evaluated. For warmer climates, the heat pump is sized to meet the maximum space-cooling load.

Once the building properties, internal factors, and the HVAC system characteristics are fixed, the model can be run for the selected geographic locations and the appropriate weather data.

2.5. Energy requirements except for heating and cooling space

The following section presents the load requirements at peak heating and cooling days.

The peak-heating day graphs (Fig. 6) include:

- the hourly average space heating requirement,
- the hourly domestic water heating requirement,
- the hourly the lights/appliances/supply fan electric loads.

The peak-cooling day graphs (Fig. 7) show:

- the hourly average electric loads for space cooling,
- the hourly domestic water heating requirement,
- the hourly lights/appliance/supply fan electric loads, and
- the hourly total electric loads.

The total electric load presents the sum of the loads for air conditioning , lights, appliances, and supply fan.

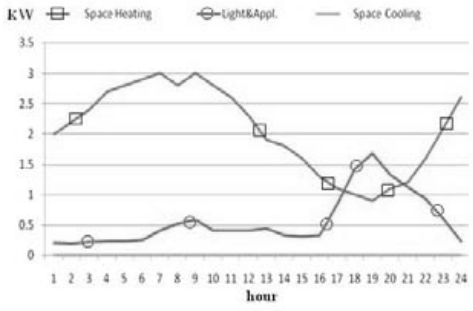

Fig. 6. Demand on hour basis during peak heating day

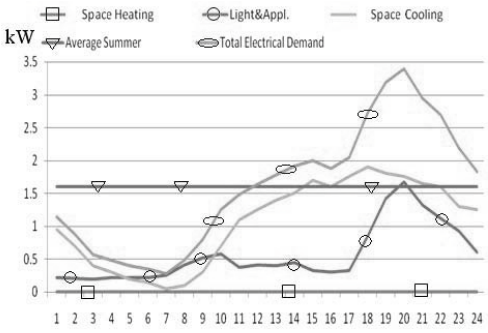

Fig. 7 Demand on hour basis during peak cooling day

The average summer electrical power demands of the residence are 1.6 kW.

The thermal space heating loads are much higher in a colder climate, and the electric space cooling loads are higher in a warmer climate. The length of the space cooling and heating seasons will affect the operation and the thermal energy utilization of the cogeneration systems.

The monthly energy use is plotted in Fig. 8

In cold climates, more thermal energy available from the fuel cell system (FCS) will be used during the long winters, and less heat will be rejected to the environment during the short summer season. In warmer climates, however, due to the length of the cooling season and the high electric loads for space cooling, a significant fraction of the thermal energy available from the FCS cannot be used in the residence and must be rejected to the environment.

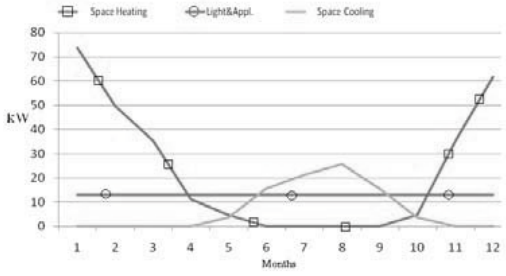

Fig. 8. Demand on month basis

Therefore, the fuel and thermal energy utilization efficiencies are expected to be lower in warmer climates.

3. System description

A fuel cell based cogeneration system supplies both the electric and thermal demands of the residence. A scheme of the cogeneration system is shown in Fig. 9.

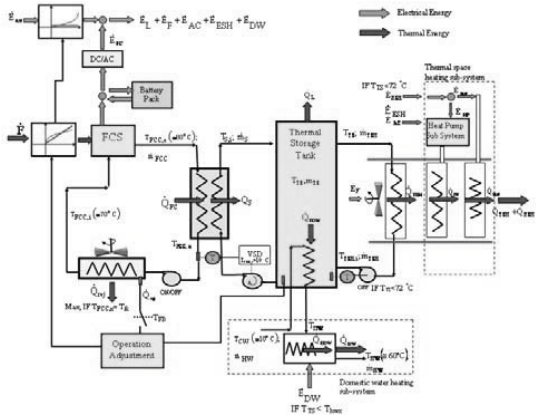

Fig. 9. Scheme of cogeneration system

The system can be divided into the following sub-systems:

- Fuel cell sub-system
- Thermal storage tank sub-system
- Domestic water heating sub-system
- Thermal space heating sub-system
- Heat pump sub-system.

The cogeneration system/PEMFC is designed to be an electric load following system, therefore a Control Feedback System is introduced and performance comparison is described.

4. Operating regimes

The mathematical model developed for the cogeneration system calculates the energy use during each hour of the year.

The input data for the model are the following ones:

- the hour numbers (from 1 to 8760)
- the outdoor dry-bulb temperature for every hour of the year
- the space heating demand for the residence for every hour of the year
- the electric load due to the lights and appliances for every hour of the year
- the electric load due to the space cooling for every hour of the year

- the electric load due to the supply fan for every hour of the year
- the incoming domestic water temperature for every hour of the year
- the amount of domestic water used for every hour of the year.

For the selected geographical locations and for every hour of the year these data are available from load calculations. The objective of the mathematical model is to calculate the energy distribution for each system component and to determine fuel consumption of the system for every hour.

The desired results for every hour are as follows:

- The thermal space heating supplied from thermal storage (TS) expressed in kW
- The thermal domestic water heating supplied from the TS (kW)
- The heat loss term from the TS (kW)
- The thermal energy supplied by the fuel cell sub-system to the TS (kW).

At the end secondary results for every hour will also be known:

- The heat which cannot be stored and has to be rejected from the fuel cell coolant line to the outdoors for proper operation of the FC sub-system (kW)
- The electricity used for the heat pump sub-system during heating hours (kWh)
- The electricity required for domestic water heating (kWh),
- Electricity produced by the fuel cell sub-system (kWh)
- The thermal output of the fuel cell sub-system (kW)
- The fuel use of the fuel cell sub-system (kW).

The operation of the cogeneration system is dependent on the temperature of the thermal storage tank (T_{TS}), which varies during the hour. If the tank is hot enough ($T_{TS} \geq T_{hwx}$), it can supply the entire domestic water load. If the tank is too hot ($T_{TS} \geq T_{fcx}$) the heat transfer from the fuel cell will be limited. Finally, preference is given to use thermal energy to heat domestic water because a heat pump can supply space heating while supplemental water heating is obtained using electric resistance heat.

Thus, if the temperature drops below a set point ($T_{TS} < T_{TSL}$) then thermal energy will not be applied to space heating but rather stored for domestic water heating. Values for the temperature set points T_{hwx}, T_{fcx} and T_{TSL} are determined in the following paragraphs based on heat exchanger calculations for the domestic water and fuel cell coolant and on an energy balance on the hot water storage tank. A system diagram for the hot water storage tank is illustrated in Fig. 10

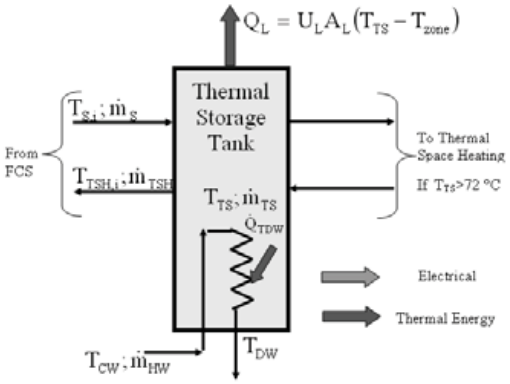

Fig. 10 Diagram for the Thermal Energy Storage tank

4.1 Limiting Variable T_{hwx}

The temperature T_{hwx} is the minimum thermal storage tank temperature (T_{TS}) required to heat the domestic hot water flow rate ($\dot{m}_{HW}$) up to the design hot water temperature (T_{HW} about 60°C).

For T_{TS} values lower than this calculated target, additional electric heating of the domestic water will be required. The efficiency of the domestic water heat exchanger is given by:

$$\varepsilon = \frac{T_{HW} - T_{CW}}{T_{hwx} - T_{CW}} \quad (1)$$

Finally, if we have a single-stream exchanger (where only one fluid changes temperature), it results:

$$\varepsilon = 1 - \exp\left[-\frac{UA}{\dot{m}_{HW} \cdot C_P}\right] \quad (2)$$

Combining (1) and (2), it results:

$$\varepsilon = \frac{T_{HW} - T_{CW}}{T_{hwx} - T_{CW}} = 1 - \exp\left[-\frac{UA}{\dot{m}_{HW} \cdot C_P}\right] \quad (3)$$

which can be solved for the temperature T_{hwx}:

$$T_{hwx} = T_{CW} + \frac{T_{HW} - T_{CW}}{1 - \exp\left[-\frac{UA}{\dot{m}_{HW} \cdot C_p}\right]} \quad (4)$$

The UA value for the heat exchanger is determined by geometrical shape, T_{HW} and T_{CW} at the maximum water flow rate. This maximum flow rate, which is used for system sizing, exceeds the average hourly flow rate, which is used for estimating energy use.

4.2 Limiting Variable T_{fcx}

The temperature T_{fcx} indicates the maximum T_{TS} at which the specified thermal output of the fuel cell sub-system $\dot{Q}_{FC}$ can be completely transferred into the thermal storage tank ($\dot{Q}_{FC} = \dot{Q}_S$).

The rate of energy transfer to the thermal storage tank, $\dot{Q}_S$, results by applying the First Law of Thermodynamics

$$\dot{Q}_S = \dot{m}_S \cdot C_p (T_{Si} - T_{TS}) \quad (5)$$

The mass flow rate can be increased to accommodate higher heat output from the fuel cell subsystem or to balance higher tank temperature.

However, since the fuel cell output temperature, $T_{S,i}$ is assumed to be constant, once the maximum mass flow rate ($\dot{m}_{S,max}$) is reached, further the tank temperature increasing causes $\dot{Q}_S$ to decrease linearly with T_{TS}. T_{fcx} is the tank temperature above, which $\dot{Q}_S$ drops linearly and can be found from:

$$T_{fcx} = T_{S,i} - \frac{\dot{Q}_{FC,t}}{\dot{m}_{S,max} \cdot C_P} \quad (6)$$

where $\dot{Q}_{FC,t}$ is the maximum heat available from the fuel cell for a particular hour.

The denominator can be found from the maximum design conditions for the heat transfer loop:

$$\dot{Q}_{S,dsn} = \dot{m}_{S,max} \cdot C_P (T_{S,i} - T_{TS,dsn}) \quad (7)$$

Where $T_{TS,dsn}$ is the design T_{TS} at which the maximum fuel cell heat can be transferred to the tank and $\dot{Q}_{S,dsn}$ is the maximum heat transfer that can be provided by the fuel cell ($\dot{Q}_{S,dsn} = \dot{Q}_{FC,max}$).

Combining (6) and (7) results:

$$T_{fcx} = T_{Si} - \frac{\dot{Q}_{FC,(t)}}{\dot{Q}_{S,dsn}} (T_{Si} - T_{TS,dsn}) \quad (8)$$

which must be evaluated for each hour since $\dot{Q}_{FC,(t)}$ varies with each hour.

4.3 Limiting Variable T_{TSL}

T_{TSL} is the minimum value of T_{TS} under which space heating from the storage tank is not allowed.

This temperature is set in order to (in absence of space heating), the thermal storage tank can supply the maximum domestic water load for an hour without heat addition from the fuel cell subsystem.

An energy balance on the thermal storage tank (in the absence of space heating and heat addition from the fuel cell) determines:

$$-\dot{Q}_{HW} - U_L A_L (T_{TS} - T_{zone}) = m_{TS} \cdot C_p \frac{dT_{TS}}{dt} \quad (9)$$

Equation 9 indicates that T_{TSL} increases with decreasing thermal storage tank size. Since the heat loss term is very small compared to the domestic water load, it is adopted as constant and (9) can be expressed as a linear equation.

The temperature drop for the tank over an hour is specified as the temperature difference between T_{TSL} and the maximum $T_{hwx,max}$

$$\frac{dT_{TS}}{dt} = \frac{T_{TSL} - T_{hwx,max}}{1hr} \quad \text{and} \quad T_{TS} = T_{hwx,max}$$

This relationship determines the following equation for energy balance

$$m_{TS} \cdot C_p \frac{T_{TSL} - T_{hwx,max}}{1hr} = \dot{Q}_{HW,max} + U_L A_L (T_{TS} - T_{zone}) \quad (10)$$

and the following expression for T_{TSL}:

$$T_{TSL} = T_{hwx,max} + \frac{\left(\dot{Q}_{HW,max} + U_L A_L (T_{hwx,max} - T_{zone})\right) 1hr}{m_{TS} \cdot C_p} \quad (11)$$

In order to eliminate mathematical problems in the model, T_{TSL} is limited to be less than 72°C.

This approach guaranties that TTSL will be always higher than $T_{hwx,max}$ and minor than T_{fcx} calculations.

4.4. Variable T_{TS} versus 3 limiting variables (T_{hwx}, T_{fcx}, T_{TSL})

The relation of the tank temperature (T_{TS}) to the 3 limiting variables ($\mathbf{T_{hwx}}$, $\mathbf{T_{fcx}}$, $\mathbf{T_{TSL}}$) in accordance with season (heating or cooling) determines the operating regime of the thermal management (Table 1)

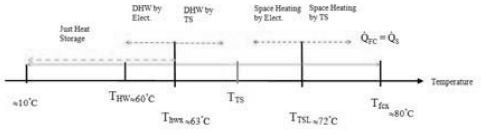

Table 1 Operating Regimes for the Cogeneration System

Routine N.	Season	TS Tank Temperature	Description
1	Cool.	$T_{TS} < T_{hwx}$	1. Electric water heating, 2. Full heat transfer from the fuel cell sub-system
2	Cool.	T_{hwx} , $T_{TS} < T_{fcx}$	1. No electric water heating, 2. Full heat transfer from the fuel cell sub-system
3	Cool.	T_{fcx} , T_{TS}	1. No electric water heating, 2. Limited heat transfer from the fuel cell sub-system
4	Heat.	$T_{TS} < T_{hwx}$	1. Electric water heating, 2. Full heat transfer from the fuel cell sub-system, 3. Electric space heating only
5	Heat.	T_{hwx} , $T_{TS} < T_{TSL}$	1. No electric water heating, 2. Full heat transfer from the fuel cell sub-system, 3. Electric space heating only
6 special	Heat.	$T_{TS} = T_{TSL}$	1. No electric water heating, 2. Full heat transfer from the fuel cell sub-system, 3. Balanced thermal and electric space heating
6	Heat.	$T_{TSL} < T_{TS} < T_{fcx}$	1. No electric water heating, 2. Full heat transfer from the fuel cell sub-system, 3. Thermal space heating only
7	Heat.	T_{fcx} , T_{TS}	1. No electric water heating, 2. Limited heat transfer from the fuel cell sub-system, 3. Thermal space heating only

5. Analysis of Operating Regimes

The calculations in each regime focus the energy balances on the components of the cogeneration system presented before. The specific equations used in each subroutine of the MATLAB code will be showed in detail in an other paper. In this one is showed only routine 2 with relative equations. The calculation procedure for the complete cogeneration system model is illustrated in Fig 11 and 12. Model outputs are calculated for all hours during a typical year, starting with January 1st, as hour 1 (i = 1) since to December 31st, hour 24 (i = 8760). For every hour, the space-heating requirement is evaluated. However, an Additional Control System (if active) limits E_{FC} in case Q_{rej} exceed 10% of Q_{FC} and electricity will be supplied by E_{net} (Energy supplier)

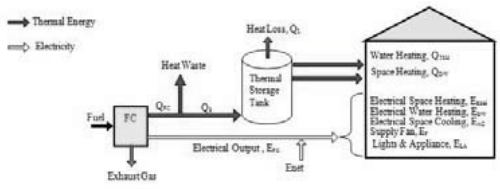

Fig. 11. Total Energy System Diagram for Energy Balances

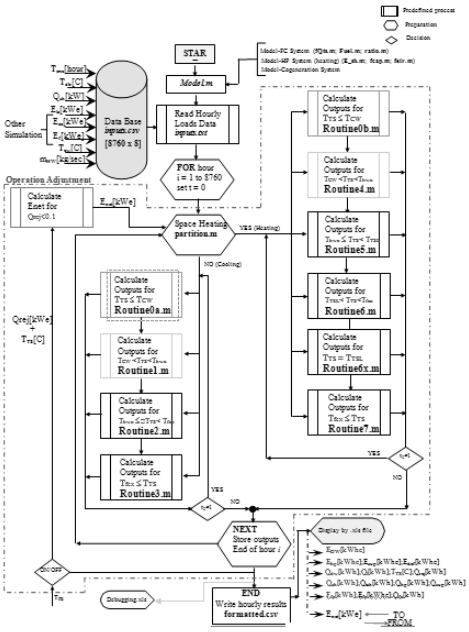

Fig. 12. Calculation chart for the complete Cogeneration System

5.1. Routine 2: calculations

This regime is used for the cooling season when thermal storage tank temperatures are higher than T_{hwx} but less than T_{fcx}. The domestic water is completely heated with thermal energy from the tank. In absence of thermal space heating, an energy balance on the storage tank gives

$$\dot{Q}_S - \dot{Q}_{DW} - \dot{Q}_L = m_{TS} \cdot C_p \frac{dT_{TS}}{dt} \qquad (12)$$

Since electricity is not used for water heating or space heating, the fuel cell power is given by:

$$\dot{Q}_{FC} = r_{TE} \cdot \dot{E}_{FC}$$

then

$$\dot{Q}_S = \dot{Q}_{FC} = r_{TE}\left(\dot{E}_{LA} + \dot{E}_{AC} + \dot{E}_F + \dot{E}_{net}\right) \qquad (13)$$

where the terms on the right side are known.

The heat available from the fuel cell sub-system is given by:

$$\dot{Q}_{DW} = \dot{m}_{HW} \cdot C_p (T_{DW} - T_{CW}) \quad (14)$$

The heat loss from the thermal storage tank is given by:

$$\dot{Q}_L = U_L A_L (T_{TS} - T_{ZONE}) \quad (15)$$

Combining equations (12) – (15) it results the following energy balance,

$$r_{TE} \cdot \dot{E}_{FC} - \dot{m}_{HW} \cdot C_p (T_{DW} - T_{CW}) - U_L A_L (T_{TS} - T_{ZONE}) = m_{TS} \cdot C_p \frac{dT_{TS}}{dt} \quad (16)$$

Equation 12 can be put in the form

$$\alpha - \beta T_{TS} = m_{TS} \cdot C_p \frac{dT_{TS}}{dt} \quad (17)$$

where:

$$\alpha = r_{TE} \cdot \dot{E}_{FC} - \dot{m}_{HW} \cdot C_p (T_{HW} - T_{CW}) - U_L A_L T_{ZONE} \quad (18)$$

$$\beta = U_L A_L \quad (19)$$

Solving this differential equation it results the tank temperature as a function of time t1<t<t2 [0<t<1hr]

$$T_{TS,t_2} = \frac{\alpha}{\beta} + \left(T_{TS,t_1} - \frac{\alpha}{\beta} \right) \exp\left[\frac{-3600\beta}{m_{TS} C_P} (t_2 - t_1) \right] \quad (20)$$

Equation 20 can be modified in order to obtain the time required to reach a particular tank temperature, $T_{TS,t2}$;

$$t_2 = t_1 + \frac{m_{TS} C_P}{3600\beta} \ln \frac{T_{TS,t_1} - \frac{\alpha}{\beta}}{T_{TS,t_2} - \frac{\alpha}{\beta}} \quad (21)$$

System operation is modelled by calculating the temperature at the end of the hour from Eq. (16) and comparing it to the limits of Routine 2 (T_{hwx} and T_{fcx}). If the calculated T_{TS} is within the limits, it is kept and $t_2 = 1$, to indicate the end of the hour.

However, if T_{TS} exceeds the upper limit or is less than the lower limit, then the time, t_2, is determined using Eq. (21) for $T_{TS} = T_{fcx}$ or, $T_{TS} = T_{hwx}$, respectively. In all cases, the equations of Routine 2 (derived below) are used to calculate the outputs from its activation, t_1, to its termination, t_2.

The program passes to the appropriate routine through the Partitioner code using the last calculated tank temperature and t_2 as the initial values for the next subroutine.

The individual outputs calculated in this Routine 2 are:

- The thermal energy for domestic water heating (QDW)
- Electricity output of the fuel cell sub-system (EFC)
- Fuel use (FFC)
- The thermal energy output of the fuel cell sub-system (QFC).

The heat transfer from the thermal storage tank to the domestic water is calculated with the following expression:

$$Q_{DW} = Q_{TDW} = \dot{m}_{HW} \cdot C_p (T_{HW} - T_{CW})(t_2 - t_1) \quad (22)$$

The required fuel cell sub-system net electric output, thermal output, and fuel use can be calculated as follows:

$$E_{FC} = \left(\dot{E}_{LA} + \dot{E}_{AC} + \dot{E}_F + \dot{E}_{net} \right)(t_2 - t_1) \quad (23)$$

$$\dot{Q}_{FC} = r_{TE} \cdot \dot{E}_{FC} \quad (24)$$

$$F_{FC} = \frac{E_{FC}}{\eta} \quad (25)$$

5.2. Conventional Energy System Regimes

The energy uses for conventional residential energy systems are calculated by addition of two special subroutines. These subroutines use some of the functionality of the cogeneration system routines. However, the thermal to electric ratio, r_{TE}, is set to zero, to indicate the unavailability of thermal energy to the system and the energy available from the thermal storage tank is set to zero. The conventional system are the following:

- Conventional System – all-electric
- Conventional System – electric cooling / gas heating

In the first one the regime is used to simulate a conventional system using only electricity as an

energy source (electric vapour compression heat pump and electric water heater), while in the second one the regime is used for the calculations of the conventional system with natural gas heating (a natural gas furnace for space heating, a natural gas water heater and an electric air conditioning unit for space cooling).

6. Results

6.1. Cogeneration System

The following sections discuss the design considerations and energy use characteristics of the cogeneration system. The effects of the heat pump and fuel cell sub-system performances on the cogeneration system are also presented. Therefore the energy savings relative to conventional systems are presented.

6.2 Cogeneration Control Strategy

The residential fuel cell cogeneration system is installed in replace of the conventional hot water supply heater. The electricity generated is used to supply appliances, with the added benefit of the heat given off during power generation being used to heat water for baths and showers. Therefore, three control strategies are presented to identify the most efficient way to use a cogeneration system (FC based) for a single family house:

1. Operation adjustment for every hour power demand, Minimum F_{FC} (Fuel), (Electrical Demand Management ED-M)
2. Operation adjustment for every hour power demand, Minimum F_{FC} (Fuel) while T_{TS} = 60 °C always (if $T_{TS} \geq 60$ °C then $Q_{DW} > 0$)
3. Operation adjustment for every hour power demand, Minimum F_{FC} (Fuel) and Minimum Q_{rej} (Limited Electrical Demand with Limited Thermal Waste Management LED-LTW-M).

In the following paragraphs are illustrated the EDM and LED-LTW-M management and the comparison with conventional systems.

6.3 Electrical Demand Management (EDM)

The net electric power, provided from the fuel cell sub-system (FCS), must be sufficient to meet the maximum hourly averaged demand, as predicted by the system model (Fig. 13). Short duration loads, such as motor starts, are supplied from batteries, which are part of the power conditioning system.

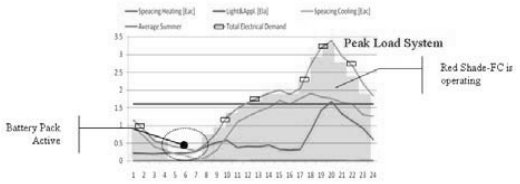

Fig. 13. Energy demand supplied from FCS in EDM mode

The electricity generated (Minimum F_{FC}) is used to supply the total electric demand (curve with box in Fig. 13). The maximum yearly electric and thermal output from FCS are presented in Table 2.

Table 2 Energy consumption of FCS

1 Year (for i=0 to i=8760)	HP (COP=3)
Lights, appl and Fan, [E_{LA}+E_F] (kWhe)	4986.3
Space cooling [E_{AC}] (kWhe)	2556
Electric space heating, [E_{ESH}] (kWhe)	2333.2
Electric water heating, [E_{DW}] (kWhe)	39.8
TOTAL Electricity [E_{FC}] (kWhe)	**9915.3**
Thermal space heating, [Q_{TSH}] (kWh)	969.8
Thermal water heating, [Q_{DW}] (kWh)	4137.2
Heat rejected, [Q_{rej}] (kWh)	2041.1
Heat loss from T_S,[Q_L] (300l) (kWh)	899.9
TOTAL HEAT, [Q_{FC}] (kWh)	**8045.6**
FUEL ENERGY, [F_{FC}] (kWh)	**25539.2**
Cogeneration System efficiency (%)(E_{FC}+ Q_{FC})/F_{FC} (%)	70.3%

In the following tables there is an example of displaying file "Formatted.csv" and "Debugging.xls". The Regimes of Table 5 represent the routines of operating (regime 6,5 = routine 6 bis of Table 1)

Table 3. Example of file input.txt

h	T_{db} [C]	Q_{Sh} [kW]	E_{la} [kWe]	E_{ac} [kWe]	E_f [kWe]	Tcw [C]	m_{HW} [kg/sec]
1	9	3	0.18	0	0.03	14	2.36
2	8	3.2	0.17	0	0.03	14	1.31
3	7	3.4	0.19	0	0.03	14	0.46
4	6	3.7	0.2	0	0.03	14	0.46
5	6	3.8	0.2	0	0.03	14	0.53
6	7	3.9	0.23	0	0.03	14	3.83
7	8	4	0.39	0	0.03	14	14.96
8	9	3.8	0.5	0	0.03	14	20.48
9	10	4	0.56	0	0.03	14	18.9
10	11	3.8	0.38	0	0.03	14	17.33
11	12	3.6	0.39	0	0.03	14	15.59
12	13	3.3	0.38	0	0.03	14	13.02
13	14	2.9	0.42	0	0.03	14	11.55
14	15	2.8	0.3	0	0.03	14	10.66
15	13	2.6	0.28	0	0.03	14	9.35
16	12	2.3	0.3	0	0.03	14	9.45
17	12	2.1	0.82	0	0.03	14	10.87
18	11	2	1.4	0	0.03	14	14.7
19	11	1.9	1.65	0	0.03	14	17.39
20	11	2.1	1.3	0	0.03	14	17.48
21	10	2.2	1.1	0	0.03	14	15.49
22	10	2.6	0.9	0	0.03	14	13.13
23	9	3.1	0.58	0	0.03	14	10.87
24	9	3.6	0.2	0	0.03	14	6.83

Table 4. Example of file formatted.csv

h	E_{dw}	E_{light}	E_{app}	E_{EC}	Q_{FC}	Q_{TSH}	Q_{TSh}	Q_{TW}	Q_{TWR}	Q_{dw}	Q_L	Tts	Efficiency	η_{FC}
	kWe	kWe	kWe	kWe	kW	kW	kW	kW	kW	kW	kW	C	N/A	N/A
1	0	0.79	0	0.997	2.483	0.761	0	3	0.537	2.475	0	0.127	0.107	73.324	0.405	0.763
2	0	0.84	0	1.039	2.573	0.795	0	3.2	0.618	2.502	0	0.07	0.107	73.324	0.404	0.766
3	0	0.89	0	1.109	2.758	0.855	0	3.4	0.725	2.877	0	0.025	0.107	73.324	0.402	0.77
4	0	0.98	0	1.212	3.034	0.942	0	3.7	0.87	2.89	0	0.025	0.107	73.324	0.398	0.777
5	0	1.01	0	1.239	3.106	0.966	0	3.8	0.83	2.97	0	0.025	0.107	73.324	0.398	0.779
6	0	1.06	0	1.316	3.317	1.033	0	3.9	0.72	3.18	0	0.206	0.107	73.324	0.397	0.785
7	0	1.18	0	1.596	4.102	1.289	0	4	0.376	3.821	0	0.803	0.107	73.324	0.389	0.808
8	0	1.16	0	1.686	4.357	1.374	0	3.9	0.168	3.622	0	1.096	0.107	73.324	0.387	0.815
9	0	1.15	0	1.742	4.515	1.429	0	4	0.307	3.693	0	1.014	0.107	73.324	0.385	0.82
10	0	1.11	0	1.519	3.881	1.216	0	3.8	0.179	3.621	0	0.93	0.107	73.324	0.391	0.801
11	0	1.02	0	1.442	3.666	1.146	0	3.6	0.305	3.398	0	0.807	0.107	73.324	0.393	0.795
12	0	0.91	0	1.319	3.325	1.036	0	3.3	0.23	3.07	0	0.699	0.107	73.324	0.397	0.785
13	0	0.78	0	1.229	3.079	0.957	0	2.9	0.25	2.87	0	0.82	0.107	73.324	0.399	0.778
14	0	0.76	0	1.09	2.707	0.838	0	2.9	0.139	2.841	0	0.572	0.107	73.324	0.403	0.769
15	0	0.72	0	1.027	2.542	0.786	0	2.6	0.177	2.423	0	0.502	0.107	73.324	0.404	0.765
16	0	0.68	0	0.982	2.423	0.748	0	2.3	0.134	2.166	0	0.507	0.107	73.324	0.405	0.762
17	0	0.52	0	1.365	3.453	1.077	0	2.1	0.387	1.713	0	0.503	0.107	73.324	0.395	0.789
18	0	0.42	0	1.647	4.256	1.333	0	2	0.636	1.364	0	0.799	0.107	73.324	0.388	0.83
19	0	0.37	0	2.081	5.443	1.671	0.04	1.9	0.668	1.212	0	0.944	0.107	73.298	0.377	0.815
20	0	0.51	0	1.837	4.796	1.519	0	2.1	0.451	1.649	0	0.938	0.107	73.324	0.382	0.828
21	0	0.55	0	1.662	4.345	1.37	0	2.2	0.432	1.768	0	0.831	0.107	73.324	0.387	0.815
22	0	0.66	0	1.593	4.092	1.286	0	2.6	0.474	2.126	0	0.705	0.107	73.324	0.389	0.807
23	0	0.84	0	1.449	3.687	1.153	0	3.1	0.462	2.638	0	0.583	0.107	73.324	0.393	0.796
24	0	0.99	0	1.223	3.065	0.952	0	3.6	0.478	3.122	0	0.367	0.107	73.324	0.399	0.779

Table 5. Example of file debugging.xls

Time	Efc [kW]	REGIME	h
1	0.997	6.5	1
1	1.039	6.5	2
1	1.109	6.5	3
1	1.212	6.5	4
1	1.239	6.5	5
1	1.316	6.5	6
1	1.596	6.5	7
1	1.686	6.5	8
1	1.742	6.5	9
1	1.518	6.5	10
1	1.442	6.5	11
1	1.319	6.5	12
1	1.229	6.5	13
1	1.09	6.5	14
1	1.027	6.5	15
1	0.982	6.5	16
1	1.365	6.5	17
1	1.647	6.5	18
0.05817	1.68	7	19
0.10629	2.262	5	19
0.05817	1.68	7	19
0.10629	2.262	5	19
0.05817	1.68	7	19
0.10629	2.262	5	19

0.05817	1.68	7	19
0.10629	2.262	5	19
0.05817	1.68	7	19
0.10629	2.262	5	19
0.05817	1.68	7	19
0.10629	2.262	5	19
0.0152	1.68	7	19
0.0377	1.973	5	20
0.96223	1.829	6.5	20
1	1.682	6.5	21
1	1.393	6.5	22
1	1.449	6.5	23
1	1.223	6.5	24

Hour 19 is executed in 13 steps because T_{ts} changing between Regime 5 and 7, while hour 20 is executed in two steps because T_{ts} changes between Regime 5 and 6.5.

In the following Table 6 is showed a comparison between the cogeneration system in ED-M operation and two conventional systems (all electric and electric with natural gas).

Table 5 Energy use in residences and energy saving with cogeneration system

1 Year (for i=0 to i=8760)	HP (COP=3)
Conv. all-electric [kWh] (efficiency 45%)	33962.88
Conv. electric AC and natural gas heating [kWh] (Elect. efficiency 45%)	26725.86
Cogeneration System [kWh]	25539.2
% Energy Savings (Cogeneration System vs. All-electric)	≈ 25%
% Energy Savings (Cogeneration System vs. Electric and NG)	≈ 5%

6.4 Limited Electrical Demand with Limited Thermal Waste Management (LED-LTW-M)

In Fig 14 and in Table 6 are illustrated the management of FCS in LED-LTW-M mode and the energy consumption of FCS.

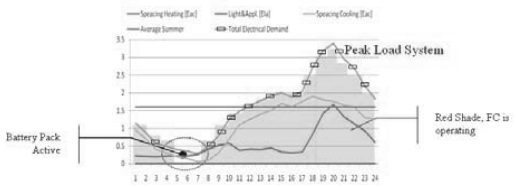

Fig. 14. Energy demand supplied from FCS in LED-LTW-M mode

The net electric power, provided by the fuel cell sub-system (FCS), must be sufficient to supply the maximum hourly averaged demand, as predicted by the system model, and minimum amount of Q_{rej}. Short duration loads are supplied by batteries system.

Table 6. Energy consumption of FCS

1 Year (for i=0 to i=8760)		HP (COP=3)
Lights, appl and Fan, [E_{LA}+E_F]	(kWhe)	4986.3
Space cooling [E_{AC}]	(kWhe)	2556
Electric space heating, [E_{ESH}]	(kWhe)	2334.1
Electric water heating, [E_{DW}]	(kWhe)	39.8
Energy From Network, [E_{net}]	(kWhe)	1348.19
(Enet with Elect.Trans. efficiency 45%)	(kWhe)	2995.99
TOTAL Electricity [E_{FC}] (kWhe)		**8568.4**
Thermal space heating, [Q_{TSH}]	(kWh)	966.6
Thermal water heating, [Q_{DW}]	(kWh)	4137.2
Heat rejected, [Q_{rej}]	(kWh)	683.9
Heat loss from T_S [Q_L] (300l)	(kWh)	899.9
TOTAL HEAT, [Q_{FC}]	**(kWh)**	**6678.9**
FUEL ENERGY, [F_{FC}]	**(kWh)**	**21593.3**
Cogeneration System efficiency (%) (E_{FC}+ Q_{FC})/F_{FC} (%)		70.6%

Then a comparison between FCS and two conventional systems (all electric and electric with natural gas) is evaluated.

Table 7. Energy use in residences and energy saving with cogeneration system

1 Year (for i=0 to i=8760)	HP (COP=3)
Conv. all-electric [kWh] (Elect. efficiency 45%)	33962.88
Conv. electric AC and natural gas heating [kWh] (Elect. efficiency 45%)	26725.86
Cogeneration System [kWh]	24589.29
% Energy Savings (Cogeneration System vs. All-electric)	≈28%
% Energy Savings (Cogeneration System vs. Electric and NG)	≈8%

7. Conclusions

This work has established a generalized system design and performance evaluation procedure for a building cogeneration system.. The research indicates that it can be suitable in alternative to conventional grid connected energy systems in residential sector.

Table 8 Performances of FCS in accordance with different control strategies

1 Year (for j=0 to j=8760)		FC (3.5 kW) HP (COP=3) EDM	FC (3.5 kW) HP (COP=3) EDM and T_{TS} = 60 °C	FC (3.5 kW) HP (COP=3) LED-LTW-M
Lights, appl and Fan, [E_{Lk}+E_F]	(kWhe)	4986.3	4986.3	4986.3
Space cooling [E_{AC}]	(kWhe)	2556	2556	2556
Electric space heating, [E_{SHe}]	(kWhe)	2333.2	2333	2334.1
Electric water heating, [E_{DW}]	(kWhe)	39.8	0	39.8
Energy to Network, [E_{ntd}]	(kWhe)	0	98.83	0
Energy from Network, [E_{ntd}]	(kWhe)	0	0	1348.19
TOTAL Electricity [F_{FC}]	**(kWhe)**	**9915.3**	**9974.4**	**8568.4**
(with Elect. effic. 45%)	**(kWhe)**	**0**	**0**	3995.99
Thermal space heating, [Q_{TSH}]	(kWh)	969.8	969.8	966.6
Thermal water heating, [Q_{DW}]	(kWh)	4137.2	4176.9	4137.2
Heat rejected, [Q_{rej}]	(kWh)	2041.1	2041.9	683.9
Heat loss from T_{ts} [Q_L] (3000)	(kWh)	899.9	911.8	899.9
TOTAL HEAT, [Q_{FC}]	**(kWh)**	**8045.6**	**8077.2**	**6678.9**
FUEL ENERGY, [F_{FC}]	**(kWh)**	**25539.2**	**25699.6**	**21503.3**
MAX FC Output	**(kWh)**	**3.5**	**3.5**	**2.0**
FC System efficiency (%) (E_{AC}+ Q_{FC})/F_{FC} (%)		70.30%	70.30%	70.60%
Wasted Heat %= Q_{rej}/Q_{FC}		25.5%	25%	**10%**
% Energy Savings (Cogeneration System vs. All-electric)		25%	25%	28%
% Energy Savings (Cogeneration System vs. Electric and NG)		5%	5%	8%

The most efficient control strategy is resulted LED-LTW-M, in fact FCS could achieve 70,60 % of efficiency and just 10% of heat wasted, which is close to the practical cogeneration efficiency. Therefore in LED-LTW-M mode the maximum fuel cell output is approximately 2 kWe and the fuel cell size can be reduced with respect to original 3,5 kWe.

The cogeneration system simulation (LED-LTW-M) confirmed that more than 90 % of the thermal energy generated in the FCS can be used to provide domestic water heating and space heating. This indicates the thermal and electric load requirements of a residence are a good match with the outputs of FCS; of course, the fuel utilization efficiency of the cogeneration system can be further increased if other low temperature thermal loads, such as swimming pools, are present.

Additionally, further design considerations have been taken into account for the optimum size of the thermal storage tank which was obtained for a 300 - 310 litre, in accordance with load profile adopted and with the maximum thermal energy utilization (Q_{tsh} Q_{dw}). For both smaller and larger thermal storage tank sizes, more fuel is necessary to supply the residence demand.

At the beginning of the research a heat pump with COP=3 was selected for the cogeneration system. The residence considered has low space cooling loads and during the heating season, the heat pump works when the thermal energy available from the cogeneration system is not enough. Hence, the additional first cost of a more efficient heat pump is not compensated by the energy savings over its life cycle and the selected heat pump seemed to be the best choice.

Then FCS in LED-LTW-M mode introduces about 28% primary energy savings over conventional residential energy systems (and 8% over conventional system electric-natural gas) and seems quite attractive in northern locations due to high space heating.

The research was very successful in assessing the suitability of fuel cell based residential cogeneration systems. It represents a particularly promising system due to its high efficiency, excellent part load performance, small-scale applicability and quiet operation.

Nomenclature

Symbols	Specification	Unit
A	Area	m^2
As	Annual surface swing, °C	kJ/kg K
Cp	Specific heat	
COP	Coefficient of performance for heat pump	
D	diameter	m
E	Energy	kWh
$\dot{E}$	Electrical power	kW
F	Fuel use	MJ
EER	Energy efficiency ratio for heat pump	
EIR	Electric input ratio for heat pump	
K	thermal conductivity	W/m K
m	Mass	kg
$\dot{m}$	Mass flow rate	kg/sec
r_{TE}	Fuel cell thermal to electric ratio	
Q	Heat transfer	kWh
$\dot{Q}$	Heat transfer rate	kW
t_0	Phase constant (day of minimum surface temperature)	days
SEER	Seasonal energy efficiency ratio	
T	Temperature	°C

U	Overall heat transfer coefficient	$kW/m^2 K$
V	Volume	liters
$\dot{V}$	Volume flow rate	m^3/sec
α	Thermal diffusivity	m^2/sec
ε	Heat exchanger effectiveness	
ρ	Density	kg/m^3

Subscripts and superscripts

avg Average
AC Air conditioning
CW Cold water from the city water line
cap Capacity
db dry-bulb (temperature of outside air)
defdefrost
DW Domestic water
e Exit
ESH Electric space heating
F Supply fan
f_{cx} Limit for external heat rejection from the FC
g Ground
hp Heat pump
FC Fuel cell
FCC Fuel cell coolant
HW Hot water
h_{wx} Limit for electric domestic water heating
i Inlet
L Lights and appliances
m Mean earth temperature
r_{ej} Heat rejection to the environment
s Soil
S Loop between the thermal storage and the heat exchanger (to the fuel cell)
SH Space heating
T_{si} Temperature of water entering TS from FC heat exchanger
sup Supplemental heating
TS Thermal storage
T_{SH} Thermal space heating
T_{SL} Limit for thermal space heating
$T_{S,dsn}$ Maximum (design) temperature of TS in order to transfer the maximum possible waste heat from the FC to the TS
T_{SL} limit for thermal space heating
$T_{S,dsn}$ Maximum (design) temperature of TS in order to transfer the maximum possible waste heat from the FC to the TS
w water
zone controlled zone
HVAC building's heating, ventilating, and air conditioning

References

[1] Piacentino, A. et al., 2006, Optimal sizing and operation of thermal energy storage devices for trigeneration systems, *Proc. Energy: production, distribution and conservation,* SGEditoriali, Milano, vol. 1, pp. 203-215

[2] Krist, K. et al., 1999, SOFC-based Residential Cogeneration Systems, *Proc. Electrochemical Society* Proceedings 99, Iss. 19 107-115

[3] Mehmet Burak Gunes "Investigation of a Fuel Cell Based Total Energy System for Residential Applications", Virginia Polytechnic Institute and State University

[4] Darrow, K. et al., 1993, Analysis of Residential and Small Commercial Cogeneration Technology, Gas Research Institute, GRI-93/0168

[5] IEA Annex 42 report "European and Canadian non-HVAC Electric and DHW Load Profiles for Use in Simulating the Performance of Residential Cogeneration Systems"

[6] Peterson et al., 1999, Operational Experience of a Residential Photovoltaic Hybrid System, Solar Energy 65, Iss. 4 pp. 227-235.

[7] Scrivano, G. et al., Experimental characterization of PEM fuel cells by micro-models for the prediction of on-site performance, *Renewable Energy* (2008), doi:10.1016/j.renene.2008.05.034

[8] Pontikakis, N., Ruth Douglas, 1994, W., *Electrical Residential Water Heating: A Consumption and Conservation Survey*, ASHRAE Transactions 100, Iss. 2 pp. 74-91

Stirling Engine in Generating Electricity Systems

Dan Scarpete[a], Krisztina Uzuneanu[b] and Nicolae Badea[c]

[a,b,c] *University "Dunarea de Jos" of Galati, Galati, Romania*

Abstract: TIn this paper, an analysis of different generating electricity systems with Stirling engine is made from the point of view of benefits and limitations, both operational and economic and environmental. Stirling engine has the ability to work at low temperatures, and can also use all fossil fuels and biomass, to realize an environmentally friendly electrical energy production. The Stirling engines are 15-30% efficient in converting heat energy to electricity, with many reporting a range of 25 to 30%. The goal is to increase the performance to the range of 30-40%. The major disadvantages of the Stirling engines include: the high cost and durability of certain parts is still an issue.

Keywords: Biomass, Fossil fuels, Generating electricity system, Solar, Stirling engine.

1. Introduction

The Stirling engine was patented in 1816 by Robert Stirling [1,2], and the first solar application of record was by John Ericsson in 1872 [2].

NV Philips initiated a comprehensive research program to develop the Stirling engine in Sweden [3]. Thirty years later, in 1968, United Stirling AB (USAB) was licensed by Philips to continue research on Stirling engine. United Stirling began the design and development of the Mark I Stirling engine in 1975, based on a revised concept. In this design, the engine had a "U" configuration that simplified its design and manufacture. This configuration allowed the engine's power to be controlled through variable pressure operation.

The free-piston Stirling engine was invented and patented by William Beale in 1971 [4]. RE-1000 is the first mature free-piston Stirling engine designned and built for 1 kW brake power output [4,5].

Since its invention, prototype Stirling engines have been developed for automotive purposes; they have also been designed and tested for service in trucks, buses, and boats [2]. The Stirling engine has been proposed as a propulsion engine in passenger ships, and road vehicles such as city buses [2,3]. The Stirling engine has also been developed as an underwater power unit for submarines, and the feasibility of using the Stirling engine for high-power space-borne systems has been explored by NASA. However, the Stirling cycle engine is well suited for stationary power [6].

Until recently, autonomous power systems based on traditional internal combustion engines were consistent with available technology, fuel and energy reserves, and ecological conditions [7]. At the present time Stirling engines are again coming to the scene because of their advantages on a fossil fuel shortage context [8].

Stirling engines can be operated on a wide variety of fuels, including all fossil fuels, biomass, solar, geothermal, and nuclear energy [9], with external combustion that facilitates the control of the combustion process and results in low air emissions, low noise and more efficient process [10]. In addition, best in class machines fewer moving parts compared to conventional engines limit wear on components and reduce vibration levels [10].

The most outstanding feature of the Stirling engine is its ability to work at low temperatures, namely below the temperature of boiling water [11]. More precisely, even the temperature of the human body is sufficient to put the engine into motion. Such a kind of an engine can use low temperature energy sources that are widespread in nature: the hot water from flat solar collectors, geothermal water, and hot industrial wastes.

Stirling motors are often used in the electricity-generating condensing boilers [12]. The Stirling engines are 15-30% efficient in converting heat energy to electricity, with many reporting a range of 25 to 30% [13]. Since these engines show high thermal efficiencies they are most suitable for applications where thermal requirements are significant [14], e.g. for CCHP (Combined Cooling, Heating and Power) or CHP (Combined Heat and Power) systems (fig. 1).

Development of Stirling engines is proceeding world-wide in spite of their admittedly higher cost

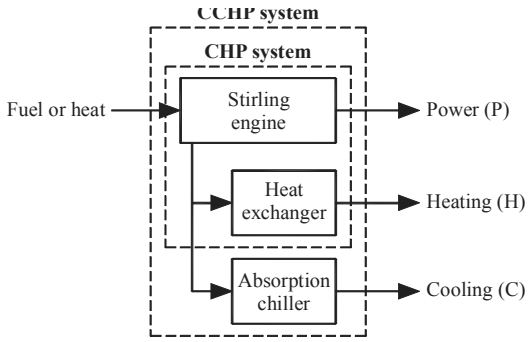

Fig. 1. A schematic representation of a CCHP/CHP system with Stirling engine (adapted from [15]).

because of their high efficiency, particularly at part load, their ability to use any source of heat, their quiet operation, their long life and their non-polluting character [16].

In this paper, an analysis of different generating electricity systems with Stirling engine is made from the point of view of benefits and limitations, both operational and economic and environmental.

In reviews of energy conversion, the Stirling engine is regarded as the most promising for further development in generating electricity systems for local use.

2. The Stirling engine

The ideal Stirling cycle combines four processes, two constant-temperature processes and two constant-volume processes [2]. Because more work is done by expanding high-pressure, high-temperature gas than is required to compress low-pressure, low-temperature gas, the Stirling cycle produces net work, which can drive an electric alternator.

In the ideal Stirling engine cycle [2], a working gas is alternately heated and cooled as it is compressed and expanded. The working fluid is contained in the motor and the mass of the fluid remains constant [14]. Gases such as helium and hydrogen, which permit rapid heat transfer and do not change phase, are typically used in the high-performance Stirling engines [2,14]. Also, air is used as working fluid [14,17]. Hydrogen, thermodynamically a better choice [2], is more conductive and has a lower viscosity and therefore lower flow losses than helium [18]; generally results in more efficient engines that does helium [2,18]. However, hydrogen is more hazardous, is more difficult to contain, and probably causes hydrogen embrittlement [18]. Helium, on the other hand, has fewer material compatibility problems and is safer to work with [2]. Helium is an environmentally benign gas [19] having an ODP and GWP of zero [20].

All Stirling engines fall into one of the following two basic categories [9,13,14,21]:

- Kinematic Stirling engines have a crank arrangement to convert the reciprocal piston motion to a rotational output, say to drive a generator. The displacer is actuated through some form of mechanical linkage.
- Free-piston Stirling engines have no rotating parts. In the majority of cases, output power is taken from a linear (usually permanent magnet) alternator attached to the piston, while the displacer is actuated by the pressure variation in the space beneath the piston.

In theory, the Stirling engine is the most efficient device for converting heat into mechanical work [2]. The efficiency of thermal conversion cycle/engine is limited by the Carnot cycle (ideal engine) efficiency derived from the second law of thermodynamics: the higher the temperature of thermal energy input, the higher the engine efficiency.

As it is expected, the nature and pressure of the working fluid influence the power performance of the Stirling engine.

Results obtained at various temperatures of heat source (700-1000°C) using air and helium (pressure range of 1-4.5 bar), for a gamma type Stirling engine with 276 cc swept volume, are shown in Figure 2 [17]. It is seen that an increase in the heater temperature results in an increase in power output. Comparison of curves for helium and air at the same conditions shows that for helium the engine power output is about twice that of air.

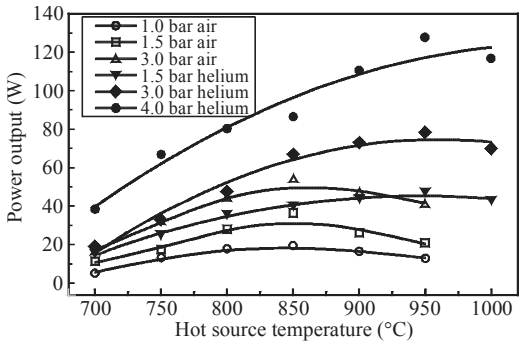

Fig. 2. Variation of brake power with heat source temperature [17].

Several firms are mass-producing Stirling engines that outperform internal combustion engines and gas-turbine engines, with an efficiency of 40% even at 600-700°C [7]. In the best designs, the mass/power ratio is 1.2-3 kg/kW, while the efficiency is 40-45%. Since Stirling engines show high thermal efficiencies they are most suitable for applications where thermal requirements are significant, for example in geographical regions with a high annual heating demand [14].

3. Stirling converters

Stirling devices are usually developed for cogeneration and power generation units [14].

Kinematic Stirling engines rely on a separate electric generator or alternator to convert the mechanical power into gas electricity, while free-piston Stirling engines integrate the alternator into the engine [2]. The resulting engine/alternator with its ancillary equipment is often called a converter or a power conversion unit.

Electric capacities for kinematic Stirling units are between 5-500 kW [13], while the capacities for free-piston units are between 0.01 and 25 kW [13,22]. The last can immediately produce grid compatible AC electricity [23].

Larger sizes of free-piston Stirling units are feasible but unlikely to be commercially viable, as alternator volumes become excessive [22]. A solution long recognized but not as yet put into practice is the coupling of the free-piston engine to a pump and turbine [22]. The Stirling driver is comprised of two conventional, displacer type, free-piston engines configured as a dynamically balanced opposed pair. Each engine drives a simple single-acting blower (or low pressure ratio gas pump), using the outer end of its power piston. The single turbine/generator is separate from the engines and connected by ductwork. The engines and turbines utilize the same helium working fluid. This arrangement is shown schematically in Figure 3 (*a*). Both the engine/blowers and the turbine/generator are hermetically sealed within pressure vessels. The net output of the system is 7 kWe. A schematic of one half of the Stirling driver is shown in Figure 3 (*b*). Power control is accomplished by variation in the size of the turbine nozzle.

The electrical efficiency of generating electricity systems with Stirling engine is about 12-20%, with the target of higher efficiencies than 30% [14]. In higher value micro-CHP applications, electric efficiencies of more than 40% and system overall efficiencies of more than 95% have been achieved [9]. Table 1 [24] reports the main parameters of micro-CHP systems with Stirling engines. The high electrical efficiency of the large Stirling engine leads to the lowest GHG emissions [25].

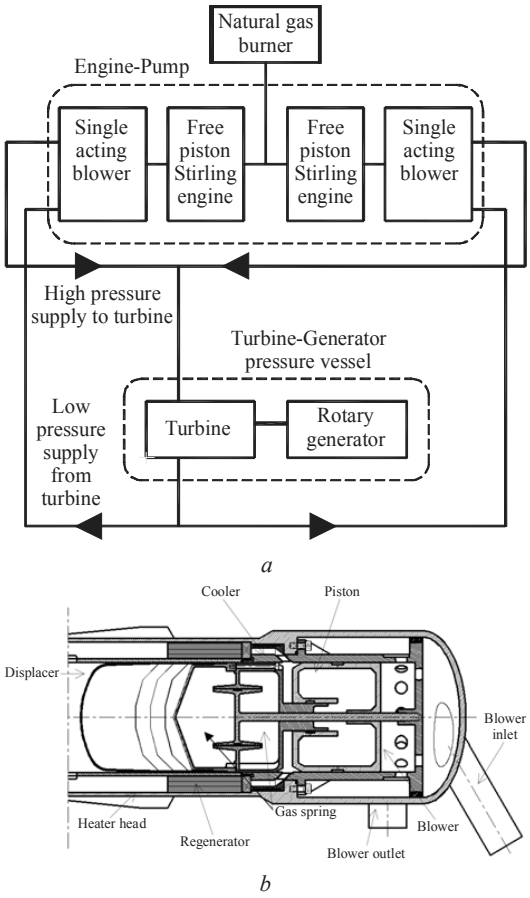

Fig. 3. System schematic (a) and single engine and blower (b) [22].

Table 1. Characteristics of the various types of micro-CHP devices [24].

Energy conversion device	Energy source	Conversion efficiency range (%)	
		Electric	Thermal
Internal combustion engine	Liquid fuel, natural gas	30-38	45-50
Fuel cell	Hydrogen, hydrocarbon	30-40	40
Stirling engine	Any type of fuel, solar radiation	10-35	60-90
Rankine cycle engine	Any type of fuel, solar radiation	10-20	70-85

4. Stirling systems on biomass

The Stirling cycle engine can use different types of renewable sources of energy including biomass, solar and geothermal energy [6].

Biomass needs to undergo several processes so that it can be widely used as a source of energy [26]. These processes will transform its accumulated energy (carbon and hydrogen) into solid, liquid and gaseous fuels or into electricity. Fig. 4 displays the details of three kinds of conversion processes: physical, thermo-chemical and biological.

The problems concerning utilisation of biomass fuels in connection with a Stirling engine are concentrated on transferring the heat from the combustion of the fuel into the working gas [27]. The temperature must be high in order to obtain an acceptable specific power output and efficiency, and the heat exchanger must be designed so that problems with fouling are minimised.

Currently, given the exhaustion of organic-fuel reserves and the rising prices of oil and natural gas, the mass production of 3-500 kW power generators with modification of the Stirling engine for local fuel is of considerable interest [7]. Possible fuels include peat, ground coal, shale, agricultural wastes, and wood chips. Stirling engines fueled by wood chips are already in production.

Another option that may have merit is to consider fuel switching between biogas and natural gas with a Stirling engine which is a good concept applicable in the waste water treatment plants [28]. The biogas can be also obtained from the dairy facilities [29].

To analyze the potential technological option for the conversion of biomass into electricity, available technologies and their technical and comercial maturity should be taken into account [26]. The biomass energy technologies having the high and medium technological maturity and economic feasibility are the steam cycle, gasification with internal combustion and Stirling engine and biodiesel/internal combustion engines. For small power systems (5–200 kW), the situation is critical as they are not available technologies with high technological maturity and economical feasibility (Table 2).

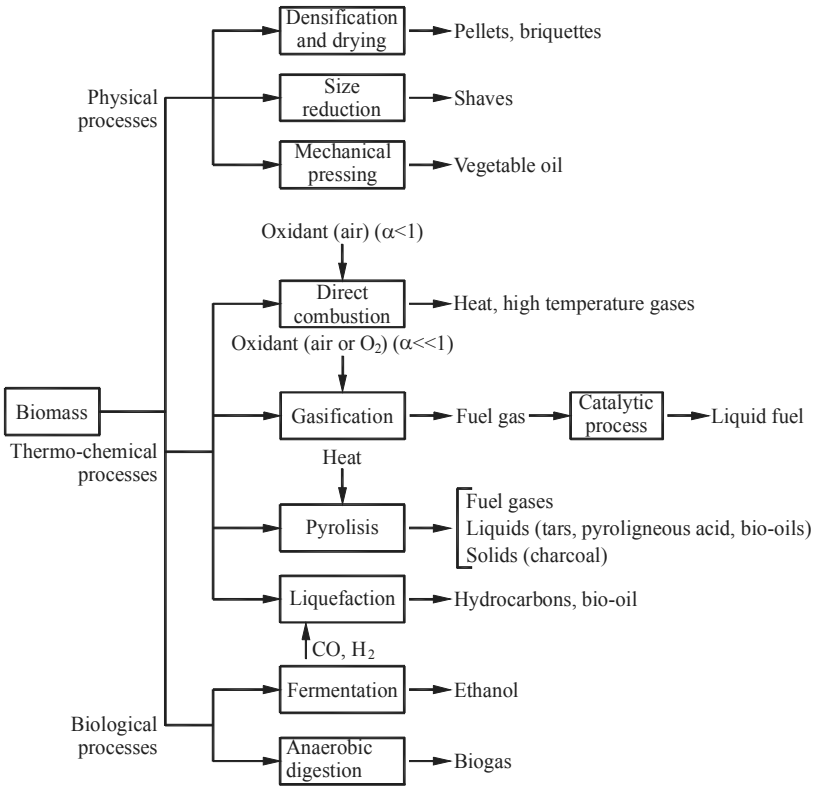

Fig. 4. Biomass energy conversion routes [26].

Table 2. Available technologies for electricity generation out of biomass for 5–200 kW power range [26].

Technology*	Technological maturity			Commercial feasibility			Comments
	H	M	L	H	M	L	
Gasification/ICE		X			X		Few commercial options and successful projects
Biodiesel/ICE		X			X		Initial commercialization. Biodiesel quality problems
Gasification/SE		X				X	Ongoing research projects
Combustion/SE	X				X		Commercial/demonstration units
Combustion/SC	X				X		High cost and low efficiency conversion
Gasification/GMT			X			X	Ongoing research projects
Gasification/FC			X			X	Ongoing research projects

* ICE-internal combustion engine, SE-Stirling engine, SC-steam cycle, GMT-gas micro-turbine and FC-fuel cell.

4. Stirling systems on solar

Existing and emerging solar thermal electric technologies are being positioned to provide a significant portion of the new electrical generation capacity that will be added around the world, particularly in regions where there is an abundance of sunshine [30].

Solar thermal electric power generating systems incorporate three different design architectures relative to concentrating solar systems [2,31]:

- Line-focus systems that concentrate sunlight onto tubes running along the line of focus of a parabolic shaped reflective trough.
- Point-focus central receiver (power tower) systems that use large fields of sun-tracking reflectors (heliostats) to concentrate sunlight on a receiver placed on top of a tower.
- Point-focus dish systems that use parabolic dishes to reflect light into a receiver at the dish's focus.

The most efficient solar thermal power plants on the ground are currently based on Stirling engines located at the focus of a parabolic dish solar concentrating mirror [32], although Bryton and organic-Rankine cycle engines have been used with dishes [31]. Stirling engines are preferred for these systems because their high efficiencies (thermal-to-mechanical efficiencies in excess of 40% have been reported) [31,32] and their high power densities (50 kW/liter for solar engines) [31].

A dish/Stirling system comprises a parabolic dish concentrator, a thermal receiver, and a Stirling engine/generator located at the focus of the dish [2,31].

Exceptional performance has been demonstrated by dish/Stirling systems, which belong to the third design architecture using a 25 kWe Stirling engine, which converted sunlight to electrical energy with 29.4% efficiency [2].

During the test period of a Stirling dish solar electric power system, temperature differences as high as 100 to 130°C of the Stirling engine working fluid (hydrogen gas) were observed [3]. These differences were usually the results of clods, uneven dirty mirrors, winds, etc. To maintain a constant hot gas temperature when the receiver high tube temperature varies, hydrogen gas is added to or removed from the cold section of the Stirling engine (Fig. 5). In contrast to pressure control, Stirling engines for dish/Stirling systems can be provided with a hydraulically-actuated variable swash plate to control piston stroke, and therefore engine power [18].

The size of collectors employed by today's dish/Stirling systems ranges from approximately 7.5 m for a system which will produce 7 kWe under optimal sunshine conditions (1000 W/m^2) up to 11 m for a 25 kWe system [30].

Thermal energy storage systems are required for continuous operation of advanced space power systems that use solar energy and Stirling engines [33]. Storage systems have been designed to use the latent heat of fusion of metals or salts. Energy is stored during the heating and melting of phase-change material in the sunlit portion of the orbit.

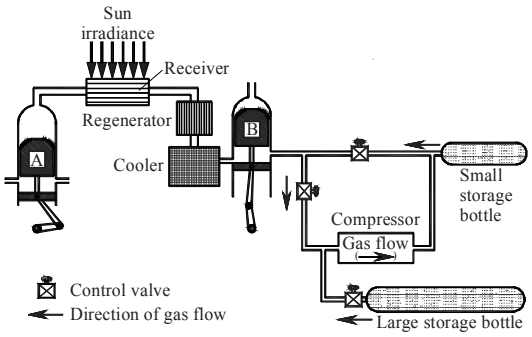

Fig. 5. Description of USAB 4-95 Stirling engine operation [3].

5. Stirling systems on other fuels

Stirling engines can operate on almost any fuel (gasoline, alcohol, natural gas or butane), with external combustion that facilitates the control of the combustion process and results in low air emissions, low noise and more efficient process [10].

Autonomous power units with Stirling engines (Stirling generators) are irreplaceable in the oil and gas industry, on introducing new fields; power is required here for prospecting, drilling, welding, and other uses [7]. In these conditions, possible fuels are unpurified natural gas, by-product gas extracted together with the oil, and gas condensate. Power units with 3-8 kW Stirling engines are expedient for automation, communications, and cathode-protection systems at gas pipelines, while more powerful systems (from 100 kW to 1 MW) are irreplaceable for marine and land drilling systems in the oil and gas industry.

In the longer term, once high efficiency and reliability have been demonstrated, the coal diesel may become the preferred option for small, low-emission coal-fueled power (below 50MW plant size) [34]. Among other advanced coal-power technologies, Stirling engine, indirectly fired with coal combustor, will compete with the direct coal-fired diesel for these future opportunities.

To convert the heat generated in a 7.5 kW(th) 90 Sr radioisotopic heat source to electricity for a space-isotope power project, the following systems were studied: Stirling, Brayton Cycle, three organic Rankines, and an organic Rankine plus thermoelectrics [35]. The Stirling engine system is a 1 kWe, free-piston Stirling engine (Fig. 6). Helium is the working fluid, and electricity is generated with a linear alternator. Stirling engine have the highest efficiency of any of the considered systems. If what is desired is a high efficiency system for whatever temperature heat source is designed, the Stirling engine is the best choice. The main uncertainty in the Stirling engine is in its reliability.

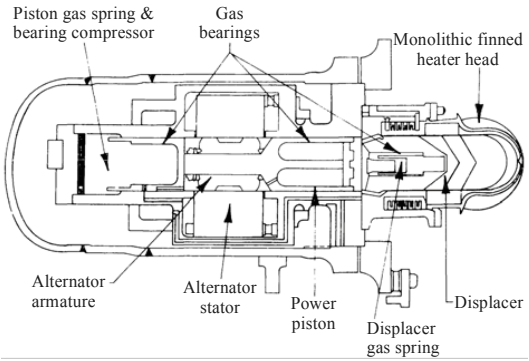

Fig. 6. Schematic of free-piston Stirling engine [35].

A generator which will be man-portable, which will produce 10 W of electrical power was successfully developed [36]. This system is designed for an operating lifetime of five years without maintenance or refueling. A small Radioisotope Stirling Generator has been developed. The energy source of the generator is a 60 W plutonium-238 fuel clad developed for space applications. A free piston Stirling engine drives a linear alternator to convert the heat to power. Although the authors demonstrated only 18.5% conversion efficiency, they expect, with further improvements in controlling heat loss, to approach the goal of 20% conversion efficiency.

Power sources capable of supplying tens of watts are needed for a wide variety of applications including portable electronics, sensors, micro aerial vehicles, and mini-robotics systems [37]. The utility of these devices is often limited by the energy and power density capabilities of batteries. A small combustion engine using liquid hydrocarbon fuel could potentially increase both power and energy density by an order of magnitude or more. Although other engine designs perform better at macro-scales, the Stirling engine cycle is better suited to small-scale applications due to:

- High heat transfer rates that are inherent with miniature devices.
- Combustor and engine can be scaled and optimized semi-independently.
- Continuous combustion that minimizes issues with flame initiation and propagation.

Today it is generally presumed that commercial geothermal power-plants work only with high temperature steam, while geothermal water is applicable only for direct use [11]. As a contrast to that, the new development of the Stirling engine showed that the low temperature geothermal sources can also be successfully used for the conversion of heat into the mechanical work and then into electric power.

6. Conclusions

Stirling engines can be used for primary power generation and as a bottoming cycle utilizing waste heat for power generation. Stirling engine

has the ability to work at low temperatures, and can also use all fossil fuels and biomass, to realize an environmentally friendly electrical energy production.

The two types of Stirling engines, kinematic Stirling and free-piston Stirling, show potential for generating electricity systems. Electric capacities for kinematic Stirling units are between 5-500 kW, while the capacities for free-piston units are between 0.01 and 25 kW.

To increase the electric capacity of free-piston Stirling generators, a solution long recognized but not as yet put into practice is the coupling of the free-piston engine to a pump and turbine.

The Stirling engines are 15-30% efficient in converting heat energy to electricity, with many reporting a range of 25 to 30%. The goal is to increase the performance to the mid-30% range or even more than 40%.

Autonomous power units with Stirling generators are irreplaceable in the oil and gas industry, where power is required for prospecting, drilling, welding, and other uses. In these conditions, possible fuels are unpurified natural gas, byproduct gas extracted together with the oil, and gas condensate.

Stirling engines have been identified as a promising technology for the conversion of concentrated solar energy into usable electrical power due to their high efficiency and high power densitiy.

The major disadvantages of the Stirling engines include: the high cost, the engine needs a few minutes to warm up and durability of certain parts is still an issue.

In reviews of energy conversion, the Stirling engine is regarded as the most promising for further development in generating electricity systems for local use.

References

[1] Brandhorst Jr., H. W., 2007, Free-Piston Stirling Convertor Technology for Military and Space Applications, Indo-US Workshop on Power & Energy, New Delhi.

[2] Stine, W. B., and Diver, R. B., 1994, A Compendium of Solar Dish/Stirling Technology, Contract No. 67-3678, Sandia National Laboratories, Albuquerque.

[3] Lopez, C. W., and Stone, K. W., 1993, Performance of the Southern California Edison Company Stirling Dish, Contract DE-AC04-94AL85000, Sandia National Laboratories, Albuquerque.

[4] High Performance Free-Piston Stirling Engines, 2005, Sunpower Inc., www.sunpower.com.

[5] Schreiber, J. G., Geng, S. M., and Lorenz, G. V., 1986, RE-1000 Free-Piston Stirling Engine Sensitivity Test Results, NASA, Lewis Research Center, Cleveland.

[6] Corria, M. E., Cobas, V. M., and Lora, E. S., 2006, Perspectives of Stirling Engines Use for Distributed Generation in Brazil, Energy Policy 34, pp. 3402-3408.

[7] Kirillov, N. G., 2008, Power Units Based on Stirling Engines: New Technologies Based on Alternative Fuels, Russian Engineering Research 28(2), pp. 104-110.

[8] Scollo, L., Valdez, P., and Baron, J., 2008, Design and construction of a Stirling engine prototype, International Journal of Hydrogen Energy 33, pp. 3506-3510.

[9] Kaarsberg, T., et al., Combined Heat and Power for Saving Energy and Carbon in Residential Buildings, Building Industry Trends-10, pp. 149-159.

[10] Wu, D. W., and Wang, R. Z., 2006, Combined Cooling, Heating and Power: A review, Progress in Energy and Combustion Science 32, pp. 459-495.

[11] Kolin, I., Koscak-Kolin, S., and Golub, M., 2000, Geothermal Electricity Production by Means of the Low Temperature Difference Stirling Engine, Proc. World Geothermal Congress 2000, Kyushu - Tohoku, Japan, pp. 3199-3203.

[12] Annual Social Report 2008, GasTerra B.V., Groningen, Nederland, www.gasterra.nl.

[13] Residential Micro-Cogeneration Using Stirling Engines, 2004, Emerging Technologies & Practices, ACEEE.

[14] Florette, M. (Chairman), 2006, Utilizations, Report on Working Committee 5, Triennium 2003-2006, France.

[15] Li, H., et al., 2006, Energy Utilization Evaluation of CCHP Systems, Energy and Buildings 38, pp. 253-257.

[16] Martini, W. R., 1983, Stirling Engine Design Manual, Second Edition, Lewis Research Center, Grant NSG-3194.

[17] Cinar, C., et al., 2005, Beta-type Stirling engine operating at atmospheric pressure, Applied Energy 81, pp. 351-357.

[18] Andraka, C. E., et al., Solar Heat Pipe Testing of the Stirling Thermal Motors 4-120 Stirling Engine, Sandia National Laboratories, Albuquerque, USA

[19] Fischer, S., and Labinov, S., 2000, Not-In-Kind Technologies for Residential and Commercial Unitary Equipment, Oak Ridge National Laboratory, Oak Ridge, Tennessee.

[20] Energy Efficient Alternatives to Chlorofluorocarbons (CFCs)-Final Report, Contract No. DE-AC01-91ER30155-H1, Washington, 1993.

[21] Harrison, J., Micro Combined Heat & Power, EA Technology.

[22] Wood, J. G., Lane, N. W., and Beale, W.T., 2001, Preliminary Design of a 7 kWe Free-Piston Stirling Engine with Rotary Generator Output, Sunpower, Inc. Athens, Ohio, USA.

[23] Monteiro, E., Moreira, N. A., and Ferreira, S., 2009, Planning of micro-combined heat and power systems in the Portuguese scenario, Applied Energy 86, pp. 290-298.

[24] Thiers, S., Aoun, B., and Peuportier, B., 2010, Experimental characterization, modeling and simulation of a wood pellet micro-combined heat and power unit used as a heat source for a residential building, Energy Buildings, In press.

[25] Praetorius, B., and Schneider, L., 2006, Micro Cogeneration: Towards a Decentralized and Sustainable German Energy System?, 29th IAEE International Conference, Potsdam.

[26] Lora, E. S., and Andrade, R. V., 2009, Biomass as energy source in Brazil, Renewable and Sustainable Energy Reviews 13, pp. 777-788.

[27] Obernberger, I., Carlsen, H., and Biedermann, F., 2003, State-of-the-Art and Future Developments Regarding Small-Scale Biomass CHP Systems with a Special Focus on OCR and Stirling Engine Technologies, International Nordic Bioenergy 2003 Conference.

[28] Clifton, N., Whitman, E. J., and Zughbi, J. A., 2003, RP-5 Renewable Energy Project, Quarterly Technical Report, DOE Award No. DE-FC26-02NT41475, IEUA, Fontana, CA, USA.

[29] Clifton, N., Whitman, E. J., and Zughbi, J. A., 2007, RP-5 Renewable Energy Project, Final Technical Report, DOE Award No. DE-FC26-02NT41475, IEUA, Chino, CA, USA.

[30] Strachan, J. W., Diver, R. B., and Estrada, C., Overview of an Emerging Commercial Solar Thermal Electric Technology, To be presented at 1995 Annual Meeting of the Mexican Solar Energy Association.

[31] Mancini, T. R., 1997, Solar-Electric Dish Stirling System Development, Report number SAND-97-2924C, Sandia National Laboratories, Albuquerque, USA.

[32] Bennett, C. L., 2007, Persistent Monitoring Platforms, Final Report, LDRD Project Tracking Code: 03-ERD-076, Lawrence Livermore National Laboratory, Livermore, USA.

[33] Wilson, D. F., DeVan, J. H., and Howell, M., 1990, High-Temperature Thermal Storage Systems for Advanced Solar Receivers. Materials Selection, Contract DE-AC05-84OR21400, Oak Ridge National Laboratory, Oak Ridge, Tennessee.

[34] Little, A. D., 1989, Conceptual design of coal-fueled diesel system for stationary power applications-Topical report, Contract AC21-88MC25124, Cambridge, Massachusetts.

[35] Thayer, G. R., and Mangeng, C. A., 1995, An Assessment of Dynamic Energy Conversion Systems for Radioisotope Heat Sources, Los Alamos National Laborator, Los Alamos, New Mexico.

[36] Tingey, G. L., Sorensen, G. C., and Ross, B. A., 1995, Isotope Powered Stirling Generator for Terrestrial Applications, 12th Symposium on Space Power and Propulsion Conference, Albuquerque, New Mexico.

[37] Haroldsen, B. L., et al., 2005, Design and Fabrication of a Meso-Scale Stirling Engine and Combustor, Sandia National Laboratories, Albuquerque, New Mexico.

Acknowledgments: The authors would like to acknowledge to EEA Financial Mechanism for financing the research on "Integrated micro CCHP – Stirling Engine based on renewable energy sources for the isolated residential consumers from South-East region of Romania (m-CCHP-SE)", under the contract No. RO-0054/2009.

Combined Heat and Power Solar Stirling Engine

S. Petrescu[a], G. Tirca – Dragomirescu[a], M. Feidt[b], A. Dobrovicescu[a], M. Costea[a], C. Petre[a], C. Dobre[a]*

[a]*University "POLITEHNICA" of Bucharest, Department of Engineering Thermodynamics, Bucharest, Romania*
[b]*L.E.M.T.A., U.M.R. C.N.R.S. 7563, University "HENRI POINCARE" of Nancy 1, France*

Abstract: A thermodynamic model for accurately predicting the overall efficiency and power output of a solar assembly with cogeneration, using a Stirling engine is presented. An analytical method for calculating pressure losses, such as those due to finite speed, friction and throttling, and losses due to regeneration in Stirling engine combined with an analytical method for predicting their effect on engine performance in terms of efficiency and power output has been achieved. The influence of different parameters on the Efficiency and Power has been studied, such as Speed of the piston, Diameter of the Mirror, Emissivity of the Concentrated Solar Radiation Receiver, Reflectivity of the Mirror material, diurnal and seasonal insolation. This study could be used for a better design of the Combined Heat and Power Solar Stirling engines.

Keywords: Solar Stirling Engine, Optimization, Finite Speed Processes, Internal and External Irreversibilities, Regenerator Losses, Receiver Design.

1. Introduction

Cogeneration systems suitable for residential and small-scale commercial applications like hospitals, hotels or institutional buildings are available, and many new systems are under development. These products are used or aimed for meeting the electrical and thermal demands of a building for space and domestic hot water heating, and potentially, absorption cooling [1]. The performance of Stirling engines meets the demands of the efficient use of energy and environmental security and therefore they are the subject of much current interest. Especially solar-powered Stirling engines working with relatively low temperature with air or helium as working fluid are potentially attractive engines of the future [2]. Recently, a 10 kW_{el} Eurodish dish/Stirling unit became operational at CNRS-PROMES laboratory in Odeillo, France. Its thermal model [3] is also available and it consists of a radiation transfer model for the cavity, which is coupled to the solar flux distribution, and on a thermodynamic model for the Stirling engine.

This paper presents an original scheme of computation for a Solar Stirling Engine with Cogeneration. For the Sunmachine Stirling Engine [developed by Sunmachine GmbH] [4] we have adapted the scheme of Computation and Optimization previously developed [5-8]. It is based on the First Law of Thermodynamics for processes with Finite Speed and uses the Direct Method. The First Law expression includes the effect of the pressure losses due to finite speed of the piston, friction and throttling and it also provides the method for calculating all the pressure losses as a function of the average piston speed. The Direct Method consists of integrating the mathematical expression of the First Law for each thermodynamic process with Finite Speed in an irreversible cycle. In this way, one obtains the equations of the irreversible processes and also the equations of the Heat and Work in each process of the cycle, in a similar way to the Classical Reversible Thermodynamics. The essential difference here is that in all these equations the Finite Speed of the Process generating irreversibilities appears as a parameter.

Combining the results of this systematic thermodynamic analysis, applied to an irreversible Solar Stirling Engine cycle with Cogeneration, an analytical method was developed for the study and optimization of the system performances.

The proposed method has practical applicability to the design of the Solar Dish – Stirling Engine systems in terms of selection of elements dimensions, such as piston size and speed, regenerator size and its thermal configuration (wire diameter and path), the selection of the most appropriate working gas for some desired operating conditions for the Stirling engine and also in terms of the receiver cavity size for Solar Stirling Engines that use dish concentrators.

An important element of the model is that the performances (Power and Efficiency of the irreversible cycle) are computed as a function of solar insolation E. By using this method we are able to predict the Performances of a Solar Stirling

Corresponding Author: Tirca – Dragomirescu Georgiana, Email: georgianatirca@gmail.com

systems operating at any hour, day of the year and in any geographical location on the earth.
The Solar Concentrated Radiation Receiver is designed to be adapted for the Sunmachine Stirling Engine [4], (Fig.3). As an example for using the developed method here, the values of the Efficiency and Power have been estimated for 45° North latitude, in the four seasons of the year. The energy balance for the whole system with combined heat and power configuration is used.

2. Performances of Solar Stirling Engine calculations

The aim of the model is to determine the Efficiency and the Power output of Solar Stirling Engines over a range of operating conditions.
The thermal efficiency of the Stirling engine is expressed as a product of the Carnot cycle efficiency and a second law efficiency [8,9]:

$$\eta_{SE} = \eta_{CC,g} \cdot \eta_{II,irrev} = \left(1 - \frac{T_{L,g}}{T_{H,g}}\right) \cdot \eta_{II,irrev} \quad (1)$$

where the second law efficiency is expressed as a product between the efficiency regarding losses due to imperfect Regeneration (X) and the efficiency regarding the pressure losses (Δp)[10].

$$\eta_{II,irrev} = \eta_{II,X} \cdot \eta_{II,\Delta p} \quad (2)$$

The power of the Stirling engine is given by:

$$P_{SE} = z \cdot \eta_{SE} \cdot m_g \cdot R \cdot T_{H,g} \cdot \ln(\varepsilon_v) \cdot \frac{w_p}{2 \cdot S} \quad (3)$$

where: z is an adjusting coefficient with the value $z = 0.45$.This value of z has been validated for 12 Stirling Engines (and 16 Regimes of functioning) with high performances (with Efficiencies up to 41% and Powers up to 55 kW), using H_2 or He as a working fluid [6,8,11,14].
Incomplete regeneration represents a major loss in the Stirling engines. This loss is expressed by using a coefficient of regenerative losses, *X*. An analysis for determining this loss has been made, obtaining the Second Law Efficiency due to imperfect regeneration [10-13]:

$$\eta_{II,X} = \frac{1}{1 + \frac{X \cdot c_v}{R \cdot \ln \varepsilon_v} \cdot \left(1 - \frac{T_{L,g}}{T_{H,g}}\right)} \quad (4)$$

with

$$X = X_1 \cdot y + X_2 \cdot (1 - y) \quad (5)$$

where y is an adjusting coefficient of this model. The value of y has been determined from experimental data of 4 solar Stirling ensembles. Setting y = 0.27 provided the best fit between analytical results and experimental ones [6,8].
The other terms are:

$$X_1 = \frac{1 + 2 \cdot M + e^{-B}}{2 \cdot (1 + M)}; X_2 = \frac{M + e^{-B}}{1 + M} \quad (6)$$

with

$$M = \frac{m_g \cdot c_{v,g}}{m_R \cdot c_R}; B = (1 + M) \cdot \frac{h \cdot A_R}{m_g \cdot c_{v,g}} \cdot \frac{S}{w_p} \quad (7)$$

in which the convection coefficient *h* is computed as [10-11,13-15]:

$$h = \frac{0.395 \cdot \left(\frac{4 \cdot p_m}{R \cdot T_L}\right) \cdot w_p^{0.424} \cdot c_p(T_m) \cdot \nu(T_m)^{0.576}}{(1 + \tau) \cdot \left[1 - \frac{\pi}{4 \cdot \left[\left(\frac{b}{d}\right) + 1\right]}\right] \cdot D_H^{0.576} \cdot \mathrm{Pr}^{\frac{2}{3}}} \quad (8)$$

where T_m is the mean gas temperature.
The expression of the Second Law Efficiency due to the pressure losses is [9,10,12]:

$$\eta_{II,\Delta p} = 1 - \frac{\frac{w_p}{w_{S,L}} \cdot \gamma \cdot \left(1 + \tau^{\frac{1}{2}}\right) \cdot \ln \varepsilon_v + 5 \cdot \left(\frac{w_g}{w_{S,L}}\right)^2 \cdot N_s}{\tau \cdot \eta_{CC} \cdot \eta_{II,X} \cdot \ln \varepsilon_v} - \frac{\frac{3 \cdot (0.94 + 0.045\, w_p) \cdot 10^5}{4 \cdot p_1}}{\tau \cdot \eta_{CC} \cdot \eta_{II,X} \cdot \ln \varepsilon_v} \quad (9)$$

where: w_{SL} is the speed of sound:

$$w_{S,L} = \sqrt{\gamma \cdot R \cdot T_{S,L}} \quad (10)$$

τ – gas temperature ratio, ε_v – volume ratio and γ – adiabatic exponent.
The piston speed w_p, is directly connected to the rotation speed n_r [rpm]:

$$w_p = \frac{2 \cdot S \cdot n_r}{60} \quad (11)$$

The gas in the Stirling Engine is Nitrogen [4].
The regenerator parameters have been determined based on its dimensions and material characteristics. A Copper regenerator with the interior composed by a matrix of screens is used [16].
The hydraulic diameter of the regenerator is given by the expression:

$$D_H = D_{ext} - D_{\mathrm{int}} \quad (12)$$

Taking into account that the regenerator has the shape of a cylindrical annulus, its equivalent diameter D_R is given by the formula:

$$D_R = \sqrt{D_{ext}{}^2 - D_{\text{int}}{}^2} \quad (13)$$

where D_{ext} and D_{int} are the exterior and interior diameters of the regenerator.

The mass m_R and the heat transfer area A_R of the Regenerator are given by the expressions (14) and (15):

$$m_R = \frac{1}{16} \cdot \pi^2 \cdot D_R{}^2 \cdot L_R \cdot d \cdot \frac{\rho}{b+d} \quad (14)$$

$$A_R = \frac{1}{4} \cdot \pi^2 \cdot D_R{}^2 \cdot \frac{L_R}{b+d} \quad (15)$$

where: L_R – width of the regenerator and ρ – Copper density.

The gas speed that is circulating through the regenerator is:

$$w_g = w_p \left(\frac{D}{D_R} \right)^2 \quad (16)$$

The above analysis shows that the pressure losses and their effect on efficiency and power output of the engine depend on the mean piston speed and hence the engine rotation speed.

2.1. Performances of Solar Stirling Engine

The analyzed solar assembly is composed of a solar radiation concentrator (a dish parabolic mirror), a solar concentrated radiation Receiver, a Stirling Engine and an Electric Generator [6,8,15].

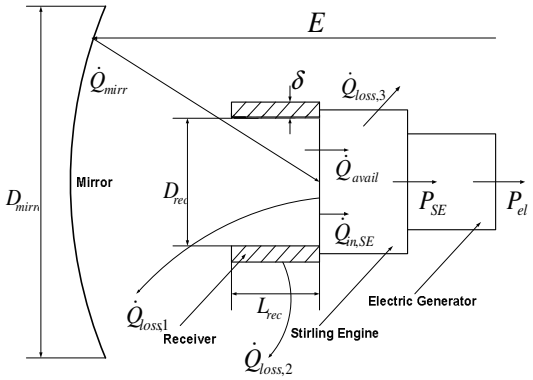

Fig. 1: A solar assembly: Parabolic Dish Mirror, Radiation Receiver, Stirling Engine, Generator.

The analytical expression for the electric power output of the solar assembly is:

$$\begin{aligned} P_{el} &= E \cdot A_{mirr} \cdot \eta_{conc} \cdot \eta_{rec} \cdot \eta_{SE} \cdot \eta_{EG} \\ P_{el} &= P_{SE} \cdot \eta_{EG} \end{aligned} \quad (17)$$

where the mirror area is:

$$A_{mirr} = \frac{\pi \cdot D_{mirr}^2}{4} \quad (18)$$

The electric power output and the total power of the solar Stirling engine are predicted as a function of the solar insolation E.

In order to make estimations as close as possible to the reality, we have to take into account that the solar radiation striking the surface of the mirror is not entirely arriving in the solar receiver.

The first factor that we have to consider is the shadow made by the receiver on the surface of the mirror. Subtracting from the total surface of the mirror this shadowed part we obtain the actual surface that reflects the radiation towards the receiver:

$$A_{mirract} = A_{mirr} - A_{recshadow} \quad (19)$$

where:

$$A_{recshadow} = \frac{\pi \cdot (D_{rec} + 2 \cdot \delta)^2}{4} \quad (20)$$

Then the geometrical efficiency of the mirror is calculated as:

$$\eta_{mirract} = \frac{A_{miract}}{A_{mirr}} \quad (21)$$

Another factor that has to be taken into account is that the surface of the mirror is not perfect and this affects also the amount of radiation reflected towards the solar receiver. The material from which the mirror is manufactured is also very important.

A total efficiency of the concentrator may be determined as:

$$\eta_{conc} = R_{mirr} \cdot \eta_{\text{int}\,erception} \cdot \eta_{mirract} \quad (22)$$

By applying the First Law, the cylindrical Radiation Receiver efficiency is given by the formula [6,8,15,17]:

$$\begin{aligned} \eta_{rec} = \alpha_{cav} \cdot \Bigg[1 - \frac{\varepsilon_m}{\alpha_{cav}} \cdot \frac{\sigma \cdot T^4}{\eta_{mirr} \cdot E \cdot C} - \\ - \left(\frac{A_{ext} \cdot h_{ext} \cdot (T_{ext} - T_0)}{\alpha_{cav} \cdot \eta_{mirr} \cdot E \cdot C \cdot A_{cav}} + \right. \\ \left. + \frac{A_{\text{int}} \cdot h_{\text{int}} \cdot (T - T_0)}{\alpha_{cav} \cdot \eta_{mirr} \cdot E \cdot C \cdot A_{cav}} \right) \Bigg] \end{aligned} \quad (23)$$

where the geometrical concentrator factor is:

$$C = \left(\frac{D_{mirr}}{D_{rec}} \right)^2 \quad (24)$$

and the geometrical sections are computed from the geometric characteristics:

$$A_{ext} = \pi \cdot (D_{rec} + 2 \cdot \delta) \cdot (L_{rec} + \delta) \quad (25)$$

$$A_{\text{int}} = \pi \cdot D_{rec} \cdot L_{rec} + \frac{\pi \cdot D_{rec}^2}{4} \quad (26)$$

$$A_{cav} = \frac{\pi \cdot D_{rec}^2}{4} \quad (27)$$

Also:

$$T_{ext} = \frac{\frac{k}{\delta} \cdot A_m \cdot T + A_{ext} \cdot h_{ext} \cdot T_0}{\frac{k}{\delta} \cdot A_m + A_{ext} \cdot h_{ext}} \quad (28)$$

where: T_{ext} is the external temperature of the Solar Receiver and A_m is the average area:

$$A_m = \frac{A_{\text{int}} + A_{ext}}{2} \quad (29)$$

In order to optimize the heat transfer process, the following condition is imposed: the rate at which the heat is transferred to the engine equals the rate at which heat is received by the mirror times the receiver efficiency. Assuming a stationary state, this condition is:

$$\dot{Q}_{avail} = \eta_{rec} \cdot \dot{Q}_{mirr} = \eta_{rec} \cdot \eta_{conc} \cdot E \cdot A_{mirr} \quad (30)$$

Hence, this heat transfer rate is not more than the Stirling engine requires for operation at a particular piston speed.

The optimum engine rotation speed is then:

$$n_r = \frac{60 \cdot \dot{Q}_{avail}}{z^{'} \cdot m \cdot R \cdot T_{H,g} \cdot \ln \varepsilon_v} \quad (31)$$

where $z^{'}$ is another adjusting coefficient. The numerical value of $z^{'}$ was determined [6,8] in a similar manner to the determination of the coefficient y; that is based on experimental data from operating solar Stirling engines, using their real operating parameters and conditions [18].

The total efficiency of the Solar/Dish Stirling engine assembly is:

$$\eta = \eta_{conc} \cdot \eta_{rec} \cdot \eta_{SE} \cdot \eta_{EG} \quad (32)$$

This is a function of the solar insolation E, through the Receiver Efficiency expression (23).

3. Results

The flux diagram is computed with maximum value of E=1000 W/m^2 (Fig. 2 and 4), [19,20]. It is important to remark the significant value of Q_{cogoen} = 4987 W, in comparison with Electrical Power produced P_e = 1843 W.

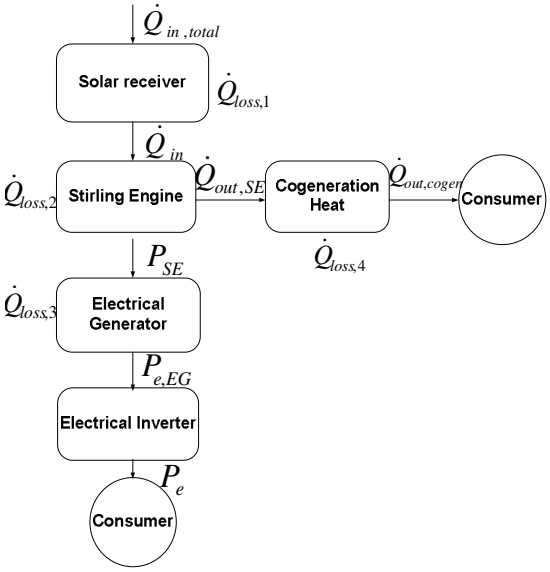

Fig. 2: Flux diagram for the Stirling/Dish assembly

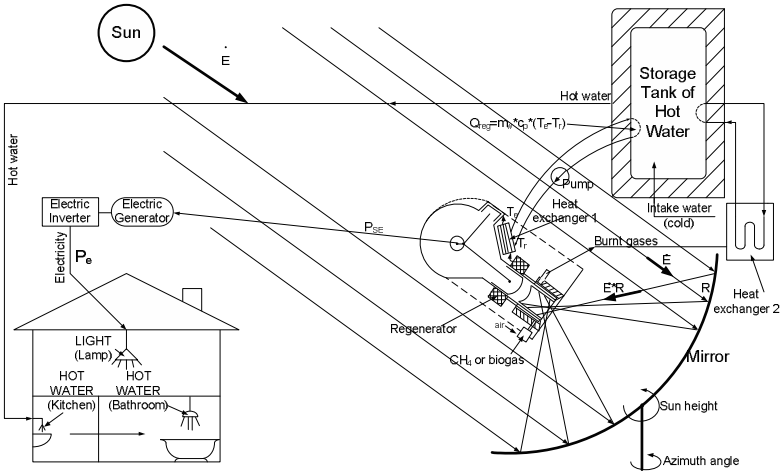

Fig. 3. Solar Stirling/Dish Engine with Cogeneration

Adopting Cogeneration will improve the total efficiency of the Solar System from 22 % (producing only electricity and no heat cogenerated) to 59 % (which takes into account both electricity production and heat production).
The results obtained with the mathematical model for the performances of the Stirling engine are similar with those stated by the producer experimental data [4] (see Table 1).
For this Stirling Engine [4] we have determined a new value for the adjusting parameter for z, denoted Z_N=0.2875 (N subscript from Nitrogen). One expected smaller performances regarding heat transfer in the Receiver in the case of using Nitrogen instead of Hydrogen or Helium, as in the case of high performance engines. In addition, for this engine [4], the power goes up to 3 kW for an average pressure of 33 bar, which are smaller values in comparison with those high performance engines, for which z=0.45[11,14].

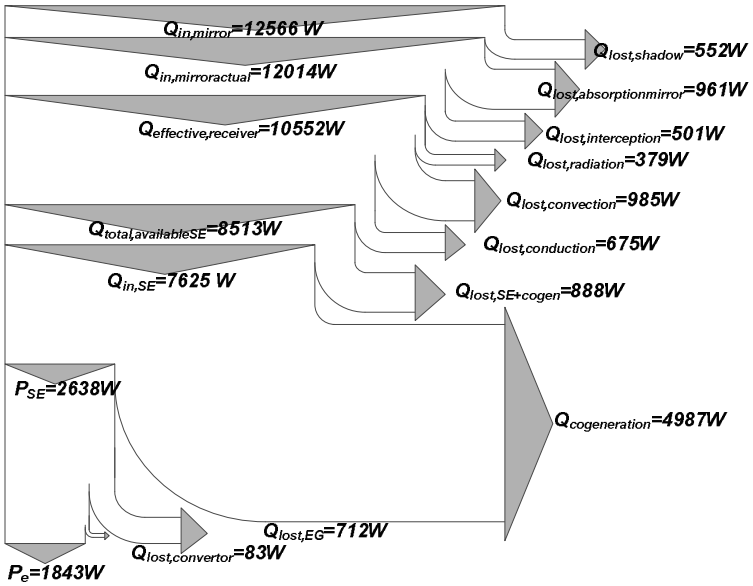

Fig. 4: Sankey Diagram for the Solar/Dish/Stirling assembly. It is important to remark the significant value of Q_{cogoen}=4987 W, in comparison with Electrical Power produced P_e=1843 W.

In the next graphs (Fig.6-14), the influence of different parameters on the Efficiency and Power have been studied, (Speed of the piston, Diameter of the Mirror D_{mirr}, Emissivity of the Concentrated Solar Radiation Receiver, Reflectivity of the Mirror material R, diurnal and seasonal insolation E).
The results obtained with the analytical model for the performances of the Stirling engine are similar with those experimentally stated by the producer [4].

Table 1. Performances of the Stirling engine:

	Speed	Power	Efficiency
Mathematical model	0.87 m/s	1.57 kW	34.08 %
	1.73 m/s	2.86 kW	33.17 %
Producer (Experimental)	0.87 m/s	1.5 kW	36 %
	1.73 m/s	3 kW	33 %

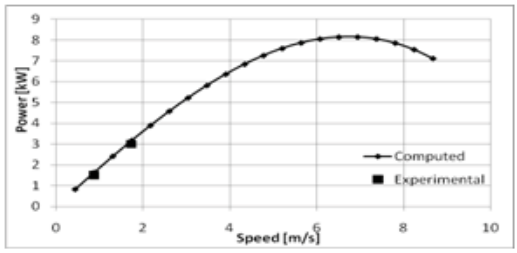

Fig. 6. Power of the Stirling Engine

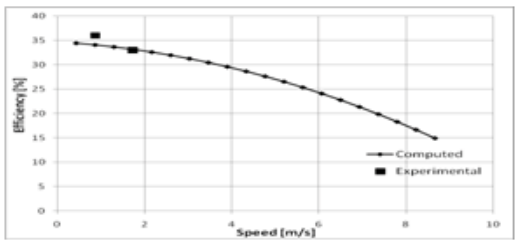

Fig. 7. Efficiency of the Stirling Engine

One of the most important parameters that influence the performance of a solar Stirling engine is the direct insolation E. Unfortunately this quantity does not have a constant value. It depends upon location (latitude, altitude), hour and season. It strongly influences the performances of the solar ensemble as illustrated in Fig. 8 and 9. As expected, that the best performances are reached during summer and the worst during winter.

$$E = S \cdot \cos Z \quad (33)$$

where E= insolation, S~1000 W/m^2 , Z = zenith angle [20,21]

$$Z = \cos^{-1} \cdot \left(\sin \Phi \sin \delta + \cos \Phi \cos \delta \cos H\right) \quad (34)$$

where Φ= latitude, H = hour angle = 15^o x (time - 12) , δ= solar declination angle

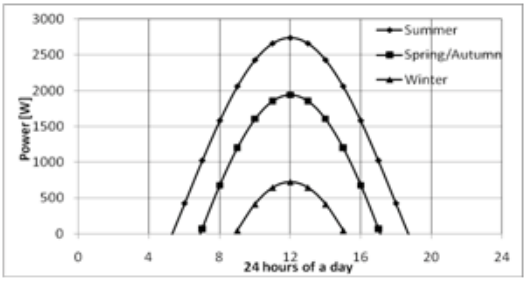

Fig. 8. Power of the Stirling Engine on a day long for various insolation values depending on season

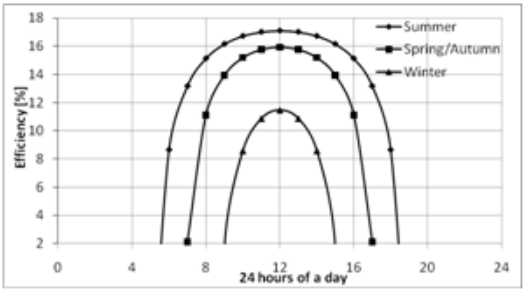

Fig. 9. Efficiency of the Stirling Engine on a day long for various insolation values depending on season

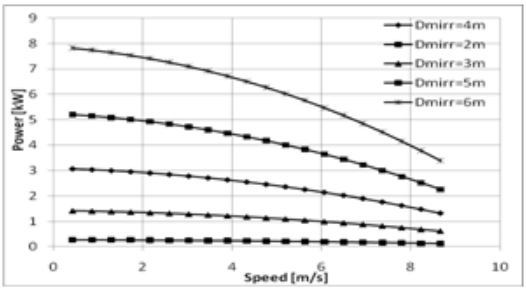

Fig. 10. Power of the Solar/Dish Stirling for emissivity=0.2 and the D_{mirr}=2…6m

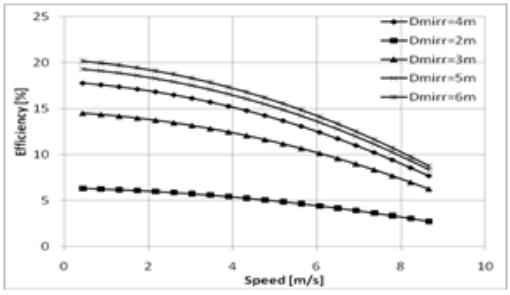

Fig. 11. Efficiency of the Solar/Dish Stirling for emissivity=0.2 and the D_{mirr}=2…6m

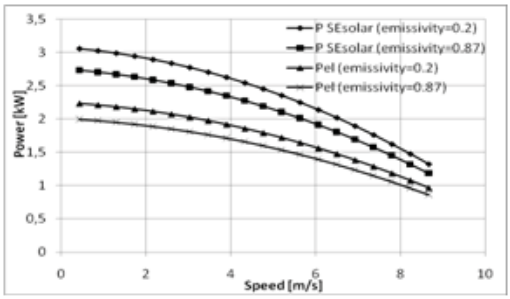

Fig. 12. Comparison between the electrical and total power of the Solar/Dish/Stirling engine for emissivity=0.2 and emissivity=0.87

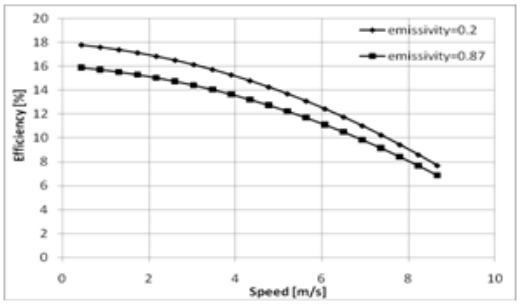

Fig. 13. Comparison between the efficiencies of the Solar/Dish/Stirling engine for emissivity=0.2 and emissivity=0.87

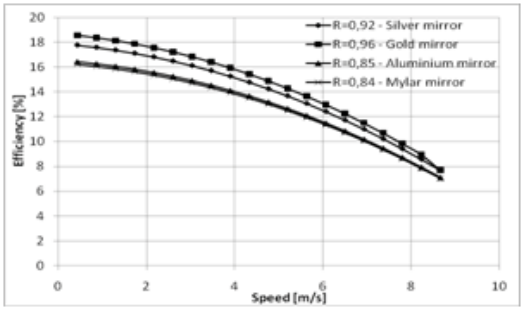

Fig. 14. Efficiency of the Dish/Stirling assembly for different values of the reflectivity

4. Conclusion

The objective of this approach was to closely simulate the operation of actual Solar/Dish/Stirling engines with cogeneration without losing insight to the mechanisms that generate the irreversibilities (internal and external). Losses generated by finite speed of the actual processes were computed, based on the first Law of Thermodynamics for Processes with Finite Speed.

This technique of computation for Stirling engine processes has been combined with a losses analysis and efficiency computation of the Solar Concentrated Radiation Receiver system for the Solar/Dish/Stirling engine. The result is a technique of computation and optimization of the performances of such systems. The influence of different parameters on the Efficiency and Power have been studied, (Speed of the piston, Diameter of the Mirror D_{mirr}, Emissivity of the Concentrated Solar Radiation Receiver, Reflectivity of the Mirror material R, diurnal and seasonal insolation E). This study could be used for better design of Combined Heat and Power Solar Stirling engines. It has applicability to the design of the engine in terms of selection of elements such as piston size and speed, regenerator size and its internal configuration, and the properties of the working gas. The results also have applicability to the design of the Solar Receiver of the Stirling Engine, in terms of size of the Receiver cavity and more generally to the design of the Receivers for any Stirling engines that use solar dish concentrators.

Nomenclature

A area, m^2
b distance between wires (in regenerator), m
C geometric concentration factor
c specific heat, J/(kg K)
D diameter, m
d wire screen diameter (in regenerator), m
E solar radiation density, W/m^2
h convection heat transfer coeff., $W/(m^2 K)$
k thermal conductivity, W/ (m K)
m mass of the working gas, kg
N_s number of screens of the regenerator
n_r revolutions per minute, 1/s
p pressure, Pa
Δp pressure loss, Pa
Pr Prandtl number
R gas constant, J/ (kg K)
S piston stroke, m
T temperature, K
V volume, m^3
w piston speed, m/s
X coefficient of regenerative losses
y, z, z' adjusting coefficients

Subscripts

avail available
cav receiver cavity
conc concentrator
CC Carnot cycle
EG electrical generator
ext receiver external wall
g working gas
H hot end
int receiver internal wall
L cold end
m mean value
mirr mirror
p at constant pressure or piston
R regenerator
rec receiver
S,L sound speed at sink temperature
SE Stirling engine
II,irrev second law efficiency
v at constant volume
X incomplete regeneration
1 initial state (inlet condition)

Greek symbols

α global absorbtivity of receiver
δ insulation depth, m
ε_v volumetric ratio
ε_m global emissivity of receiver
ρ mirror global reflectivity
γ specific heat ratio
η efficiency
σ Stefan – Boltzmann constant, $W/(m^2 K^4)$
υ viscosity of the working gas, m^2/s
τ ratio of the gas extreme temperatures

References

[1] Onovwiona, H.I., and Ugursal, V.I., 2006, Residential Cogeneration Systems: Review of The Current Technology, Renewable and Sustainable Energy Reviews, 10(5), pp. 389-431.

[2] Thombare, D.G., and Verma, S.K., 2008, Technological Development in the Stirling Cycle Engines, Renewable and Sustainable Energy Reviews, 12(1), pp. 1-38.

[3] Nepveu, F., Ferriere, A., Bataille, F., 2009, Thermal Model of a Dish/Stirling Systems, Solar Energy, 83(1), pp. 81-89.

[4] Technical specification Sunmachine http://www.sunmachine.com.

[5] Petrescu, S., Zaiser, J., Petrescu, V., 1996, *Lectures on Advanced Energy Conversion,* vol. I, Bucknell University, Lewisburg, USA.

[6] Petrescu, S., et al., 2002, Analysis and Optimization of Solar-Dish/Stirling Engines, *Proc. of Inter. Solar 2002 Conference* [CD-ROM], Reno, Nevada, USA.

[7] Petrescu, S., et al., 1992, The First Law of Thermodynamics for Closed Systems, Considering the Irreversibilities Generated by the Friction Piston-Cylinder, the Throttling of the Working Medium and Finite Speed of the Mechanical Interaction, *Proc. of Inter. Conf. on Efficiency, Costs, Optimization and Simulation of Energy Systems, ECOS'92*, A. Valero, G. Tsatsaronis, eds., Zaragoza, Spain, pp. 33-39.

[8] Petrescu, S., et al., 2003, A Scheme of Computation, Analysis, Design and Optimization of Solar Stirling Engines, *Proc. 16th Int. Conf. on Efficiency, Cost, Optimization, Simulation and Environmental Impact of Energy Systems, ECOS'03*, Copenhagen, Denmark, 1, pp. 1255-1262.

[9] Petrescu, S., and Harman, C., 1994, The Connection between the First and Second Law of Thermodynamics for Processes with Finite Speed. A Direct Method for Approaching and Optimization of Irreversible Processes, Journal of the Heat Transfer of Society of Japan, 33(128), pp. 60-67.

[10] Petrescu, S., et al., 2001, A New Technique for Determining the Coefficient of Regenerative Losses in Stirling Machines, *Proc. Int. Conf. on Efficiency, Costs, Optimization Simulation and Environmental Impact of Energy Systems ECOS'2001*, A. Öztürk and Y. A. Gögüş, eds., Istanbul, Turkey, 1, pp. 377-386.

[11] Petrescu, S., et al., 2003, Application of the Direct Method to Irreversible Stirling Cycles with Finite Speed, International Journal of Energy Research, 26, pp. 589-609.

[12] Petrescu, S., et al., 2000, *Determination of the Pressure Losses in a Stirling Cycle through Use of a PV/Px Diagram*, Proc. Int. Conf. On Efficiency, Costs, Optimization Simulation and Environmental Aspects of Energy Systems ECOS'2000, G.G. Hirs ed., Enschede, Netherlands, pp. 659-670.

[13] Petrescu, S., et al., 2000, A Method for Calculating the Coefficient for the Regenerative Losses in Stirling Machines, *Proc. 5th European Stirling Forum 2000*, Osnabruck, Germany, pp. 121-129, 2000.

[14] Florea, T., Petrescu, S., Florea E., 2000, *Calculation schemes for the study of irreversible processes of the external combustion engines* (Stirling Engines), Leda Press, Constanţa, Romania.

[15] Costea, M., Petrescu, S., Harman, C., 1999, The Effect of Irreversibilities on Solar Stirling Engine Cycle Performance, Energy Conversion & Management, 40, pp. 1723-1731.

[16] Drob, A., 2009, Cogeneration system based on biomass Stirling engine, Technical Report, PU Bucharest, Bucharest.

[17] Costea, M., et al., 1994, Thermal and Dimensional Optimization of a Solar Stirling Engine Cavity Type Receiver, *Proc. Florence World Energy Research Symposium, FLOWERS'94*, E. Carnevale, G. Manfrida, F. Marteli eds., SGEditoriali Padova, Italy, pp. 1075-1082.

[18] Stine, W.B., and Diver, R.B., 1994, A Compendium of Solar Dish Stirling Technology, Sandia Laboratories Report, SAND93-7026 UC-236.

[19] Feidt, M., et al., 2004, *Génie energétique appliqué au solaire. Energie solaire thermique*, Printech, Bucharest.

[20] Danescu, A., Bucurenciu, S., Petrescu, S., 1980, *Use of Solar Energy*, Tehnica Press, Bucharest.

[21] NASA. Relating solar radiation physics to earth & space science concept. Available at:http://education.gsfc.nasa.gov/experimental/all98invProject.Site/Pages/science-briefs/ed-stickler/ed-irradiance.html.

Development of a New Resonance Stirling Engine for Residential CHP-Units

J.P. Budliger[a], R. Schmid[b]
[a] Consultant, CH -1228 Plan-les-Ouates, Switzerland
[b] Rud. Schmid AG, CH-3174 Thörishaus, Switzerland

Abstract: Free piston Stirling engines are ideally suited for the Combined production of Heat and Power in residential homes. Environmental considerations and the raising fuel cost prompted a renewed interest for small CHP-units, heated from outside by continuous combustion with minimal pollutant output. They supply homes with the required heating energy and provide a major share of the domestic electricity needs. Any surplus of electricity produced e.g. during night may also be used to recharge batteries of e.g. hybrid cars, whose market share is expected to raise rapidly. At current fuel prices, these CHP-units will become economically attractive when produced in series.

Keywords: Combined Heat and Power (CHP), Control, Resonance, Stirling

1. Introduction

During the last few decades, remarkable progress has been made in the heating appliance industry. Condensing burner systems reach efficiencies beyond 100% (based on the lower calorific value of the fuel). The size of these units and their cost have been reduced considerably, driven mainly by the highly competitive market situation.

In spite of these very remarkable achievements, it must be recognized that in conventional heating units, the energy released in flames at high temperature is finally used in radiators or for preparing hot sanitary water at merely 40 to 50°C; this downgrading of the heat is a highly irreversible process, involving considerable qualitative losses. To reduce them, the high temperature potential of the combustion products must be used more efficiently.

In **combined heat and power** (CHP) plants, the heat released in the flames at high temperature first serves to drive a thermal engine; the engine waste heat (flue gas and engine cooling water) is released at sufficiently high temperature levels for heating purposes.

Small-scale external combustion engines, i.e. **Stirling engines** appear to be particularly suited for distributed power generation in residential areas. The required long-term operation with minimum demand of maintenance strongly advocates for free-piston solutions. Stringent economic criteria impose products which are suited for industrial mass production. These free piston systems must remain as simple as possible and operate in a stable mode (under full- and part-load conditions) without relying on sophisticated control systems.

In the past decades, different engine configurations were conceived, essentially by highly specialised laboratories. Manufacturers of heating equipment observed these developments for many years, without making any substantial contribution to the basic engine development phase. In the past 2 years, several major European heating equipment suppliers concluded licence agreements for the manufacture of such engines. Since then, hundreds of field test engines were built and their reliability tested. Industrial preoccupations became predominant for achieving long, maintenance-free operating periods of engines which may be produced in series at affordable cost .

This radical change of attitude of the main actors was obviously triggered by the recent, considerable increase of fossil fuel cost, making it mandatory to apply more efficient heating technologies than in the past. With the substantial effort spent for industrialising these products, it is only a matter of time for these products to appear on the market. Unfortunately, the considerable economic pressure associated with this effort hampers the

basic engine development necessary to bring this technology to its full maturity.

In the following, a particular engine concept will be explained, which has been developed by a small team over many years. This independent position makes it possible to assess the basic engine technology proposed by competitors and to point out some of the technical shortcomings, where further conceptual improvements of these engines appear to be mandatory. Some economic considerations may help to better assess the market position of small-scale CHP-units on the future heating equipment market.

2. Single Free-Piston Stirling Engine

A new free-piston Resonance-Stirling concept has been conceived, which is well suited for the above-described purposes. The concept is derived from former work on a Vuilleumier system (an integrated Stirling unit with an engine part driving a heat pump) making use of a resonance tube, which in part was investigated in collaboration with Prof. D. Favrat at EPFL in Lausanne. With the recent development of efficient linear electric generators, engine units producing electricity appear more favourable than Vuilleumier systems.

The proposed engine comprises one single **displacer-power piston**, which is directly coupled with the moving magnets of the linear generator. The displacer part separates the working volume into a hot expansion space and a cold compression space, which communicate one with each other through heater tubes, a regenerator and a cooler (see fig. 1). By the sole piston movement, the pressure of the working gas varies in phase with this movement, what precludes that any work will be produced.

A conveniently shaped and tuned **resonance tube** is appended to the variable compression volume. A standing pressure wave is set up in the tube, with a considerably higher pressure amplitude than the initial wave induced by the piston displacement. Highest pressure amplitudes are set up in the Stirling compartment under resonance conditions; these waves are delayed against the exciting pressure variation by a quarter cycle period. By their action, compression occurs in the Stirling compartments when the cold compression volume is large, expansion when the hot expansion volume is important. The resonance tube exerts a purely mechanical action upon the gas, serving as an **impedance of the oscillating circuit** formed by the Stirling volumes and its piston. The phase of the pressure variation is shifted against the volume variation, in a way that work is produced.

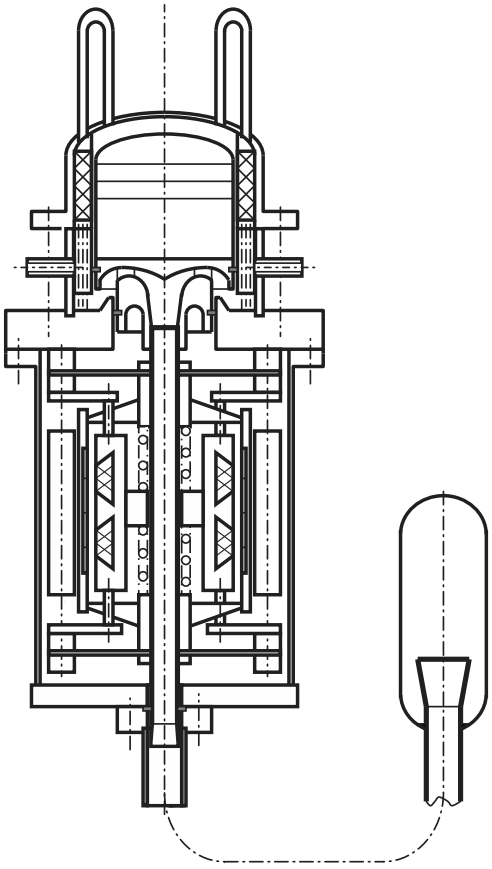

Fig 1. Prototype Stirling Engine *with a single displacer-power piston and a resonance tube leading axially through the electric generator.*

2.1. Free Piston

The free piston is arranged between the hot expansion volume and the cold compression volume. The piston rod section corresponds approximately to half the total piston area, reducing the compression volume and its cyclic variation accordingly to half of the expansion volume. The piston movement thus induces a relatively small periodic pressure change (but which then is augmented by the resonance wave).

The piston is elastically suspended by planar flexure springs, maintaining it precisely centred within its cylinder. Contact-free clearance seals may be used, which are little exposed to wear; reliable operation for long periods with low demand in maintenance may be expected.

A major advantage of the proposed system results from the fact that only one piston needs to be centred relative to its cylindrical housing. This considerably simplifies the manufacture of the units, as well as their accurate assembly.

2.2. Resonance Tube

The tube is dimensioned for its operation at the desired resonance frequency, which also corresponds to the piston frequency. In appropriately shaped tubes (section as a function of the tube length), standing waves with periodic, nearly sinusoidal pressure variations are obtained. The resonance tube losses correspond to flow friction losses of the periodic gas movement within the tube.

The developed concept comprises a single resonance tube passing axially through the linear electric generator. In this way, side forces are minimised and do not impair the dynamic movement of the piston. In addition, this single tube can be bent and arranged within a compact volume.

When exciting a standing pressure wave in a simple tube, lowest resonance frequency is reached when half a wavelength is established over the tube length (velocity nodes at both ends). By appending an appropriately dimensioned Helmholtz volume to the free tube end, its length is further shortened. Also, the system may be operated with a heavier working gas than helium, having a correspondingly lower sound velocity. The optimum working gas needs to be selected as a compromise between the losses in the Stirling compartment and in the tube. Suitable solutions were determined for He/N_2 gas mixtures with molecular masses of between 10 and 16. For an operation at 50Hz frequency, the optimal tube length then lies between 1.50 and 2.00m. These lengths are acceptable when considering that the tube may be placed within standard casing dimensions of the heating equipment.

The use of gas mixtures considerably facilitates the tuning of the system: the tube may be brought to resonance at the selected operating frequency by adjusting the molecular mass of the working gas; the free piston itself may then be tuned by adjusting the gas pressure. Once the system is sealed, it operates at its design frequency, exactly under resonance conditions.

2.3. Electric Linear Generator

A new electric generator has been conceived, which is specifically adapted for the operation with the existing prototype Stirling engine. It consists of a set of electric coils arranged coaxially within a mobile support cylinder, which is equipped with permanent NdFeB – magnets. This cylinder is appended directly upon the displacer-power piston and is guided at both ends by planar flexure bearings. Their restoring force action are further augmented by means of additional mechanical and/or magnetic springs. The electric windings are closely packed and fully embedded within radial stator iron sheets.

Performance measurements were made on a separate test bench, yielding an electric power output of 1500 W at an amplitude of +/- 11 mm, with a measured electric efficiency of between 80 and 83%.

3. Prototype Engine

A first prototype engine was built with a nominal electric power output of 1.5 kW_{EL} at a frequency of 50Hz (see fig. 1). Average gas pressure is 2.5MPa. At nominal stroke of 22mm, the displaced expansion volume

is 220cm^3, the displaced compression volume 115cm^3.

The engine is equipped with a commercially available FLOX-burner of 15kW$_{TH}$ nominal power rating. The reliable operation of this heating source, delivering an exactly adjustable heat output, considerably facilitated the start-up operations. In fact, a smaller burner with only 9kW$_{TH}$ power output would be better suited for the prototype and might be more efficient.

By recirculating flue gas within the combustion chamber, the combustible mixture is diluted and burns completely, without producing any noticeable NO_X-output. A minimal excess air is required and the exhaust gases are cleaner than those produced in standard heating equipments; these burners are particularly well suited for their use in residential areas.

3.1. Experimental results

For starting up the engine, the heater tubes need to be heated above 500°C; the displacer-power piston is then excited electrically and put into a small, oscillating movement, which immediately is enhanced by the onset of the Stirling process. The engine can then be adjusted by varying the working gas pressure and its composition, for an operation at exactly 50 Hz.

The electric power output depends upon the heating power input and the electrically controlled piston amplitude. Nominal power output of 1500 W was achieved with an overall efficiency (electric output/heat input of consumed propane gas) of η_{TOT} =15.5%. A pressure variation up to $\pi = p_{MAX}/ p_{MIN}$ = 1.35 is reached, what corresponds to the design value of the unit. The piston amplitude was +/- 11 mm, which closely meets the analytical predictions.

By reducing fuel gas supply, the electric power output is reduced proportionately, down to about half the nominal power rating. In this range, the heater tube temperatures drop only by 60 to 80°K and the engine efficiency remains virtually constant. The frequency and the piston amplitude, hence the voltage output can be kept constant, making this concept ideally suited also for part-load operation.

The efficiency measured on the basis of the cooling water output amounts to η_W = 22 – 24%, indicating a heater efficiency in the range of η_{HEAT} = 65 – 70%.

3.2. Further envisaged development

The experimental results obtained are highly satisfactory when considering that this assembly was the first power engine built according to the described concept. A number of improvements have been identified, which successively will be incorporated into the system, essentially in view of further augmenting the engine efficiency.:

- the resonance tube will need to be adjusted in view of lowering its associated losses;
- a randomly packed wire regenerator has been used, which should be replaced by a mesh structure, ensuring a more uniform flow distribution, hence an improved thermal performance;
- the existing displacer-power piston is provided with mechanical ring seals, which will need to be replaced by contact-free leakage seals;
- by equipping the unit with an insulating shroud for noise abatement, heat released from the heater head will be recovered and serve to preheat the combustion air.

By adopting these measures, it is expected that the initial objective of building a 1.5kW$_{EL}$ engine with 20 to 22% overall efficiency may be reached. Hereby, the engine must remain as simple as possible. Several machines will then have to be built and fully equipped for performing prolonged field tests under real operating conditions.

3.3. Comparison with competing technologies

In all free piston Stirling engine projects, major emphasis needs to be put on improving the performance figures. Their electric power output, hence their economic value considerably depend on these figures, which still remain well below achievable limits. Furthermore, long-lasting reliable operation, and low manufacturing costs are decisive factors which will determine the commercial success of these units.

Major advantages attributable to our concept may be summarised as follows:

- only 1 mechanical piston is necessary, what considerably reduces the problems associated with contact-free leakage seals of the piston(s);
- the engine can be operated at full load or under part-load conditions, simply by adjusting the fuel supply to the engine. Its operation can be adjusted with great flexibility to the power needs of the dwelling;
- no sophisticated engine control system is required, neither for the start-up phase, nor for maintaining steady-state operation. The engine operation depends on external parameters and is entirely stable.

This latter argument is of major importance, deserving some more detailed explanations:

In conventional free-piston Stirling systems, the engine operation is controlled by means of the linear generator which is coupled to the power piston, as well as by the fuel supply to the burner. The displacer piston movement may only be influenced indirectly by these control functions, hence also the mass flow through the regenerator and the periodic heat exchange between the working gas and the matrix material. The pressure amplitude depends directly upon this heat exchange, what in turn affects the displacer piston movement, an interdependency that tends to an unstable behaviour of the entire system.

Intelligent and rather complex control systems have been conceived [4, 5] which are able to surmount these difficulties. Nevertheless, if laboratory units have been shown to operate in a stable mode, it is supposed that this inherent difficulty strongly hampers the commercialisation of these systems, which will have to operate trouble-free for decades.

In the proposed single-piston engine, the **displacer movement is controlled directly by the associated linear electric generator**. The stability of the periodic process is considerably improved, what simplifies the engine control. This also permits to conceive these units for an operation at higher pressure amplitudes than conventional engines, hence with higher power densities.

The inherent problem of the single-piston units is related with the resonance tube; even if the tube can be bent, the overall packaging volume is larger than for conventional free piston units. In addition, the periodic flow pressure drop in this tube represents a non-negligible performance loss. A major development effort is presently devoted to reduce the drawbacks of the proposed concept.

4. Economic Appreciation

Decentralised CHP-units must comply with many requirements which are listed in the introduction of this paper. Only rather simple concepts with a low demand for maintenance, manufactured in large series at low cost may be sold successfully in the highly competitive heating equipment market.

The energetic benefit of a decentralised CHP can most suitably be appreciated when considering its operation in combination with a heat pump (HP). The CHP and the HP-units normally operate at similar power levels, according to the heat demand of the respective homes. Seasonal electric peak demand of HP can thus be alleviated by supplying electric energy from CHP. The overall savings can then be appreciated on hands of the thermal energy balance of the following scheme:

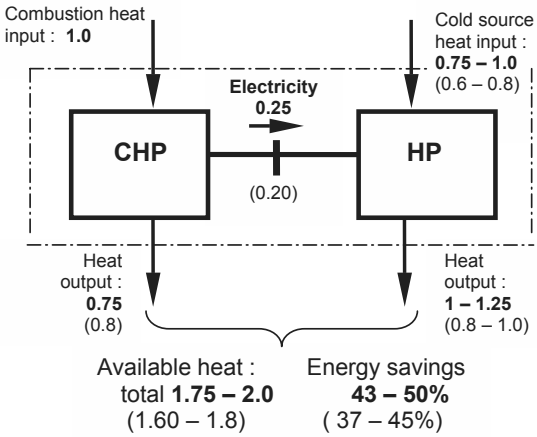

Fig 2. Energy balance of a CHP-unit driving a Heat Pump (HP)

With an assumed electric conversion efficiency of 25%, the combined CHP and HP system produces 1.75 to 2 times more heating energy than released by combustion. The fuel savings are comprised between 42 and 50%, attributable to the CHP as well as to the HP. With an electric efficiency of the CHP-unit of only 20%, the realised energy savings still amounts to 37 - 45% (lower figures of the scheme indicated in brackets).

CHP thus play a complementary role to HP. These units can easily be installed in houses as a retrofit to existing heater systems. As compared to HP, CHP supply higher heating temperatures without reducing efficiency; they are suitable for equipping many existing buildings.

The indicated energy savings become important when considering the threatening shortage of fossil fuel. Also, production of electricity at home (as a by-product of heating) will make it possible to partly refuel hybrid cars. This represents a highly attractive economic perspective, which undoubtedly will strongly promote the introduction of this heating technology.

5. Conclusion

The past century, characterised by an indiscriminate consumption of the fossil fuels, precluded the widespread use of Stirling engines. Their development proves to be demanding, particularly when considering the many requirements imposed by the competition with the traditional heating equipment industry.

Only during the past 5 years, since the Kyoto Agreement came into force, a more serious effort may be observed to conserve energy on a world-wide basis. The enhanced public awareness of threatening climate change effects and of the dwindling fossil fuel reserves provide new opportunities for conceiving improved energy conserving technologies.

The recent doubling of fuel cost within one single year give a considerable incentive for promoting CHP-units for residential homes. The customer is knocking at the doors and the product will be ready in a foreseeable future. It may be expected that within the next few years small CHP-units will replace as retrofit many conventional, fossil-fired heating equipment.

The speed at which these CHP will be introduced on the market will largely depend on the realised energy savings, hence their efficiency, but also on their reliable operation. The potential for future improvements remains considerable and successful products will have to undergo a maturing process. New engine concepts, offering improved performances and good reliability will continue to attract industrial promoters. Qualities like flexible part-load operation, adjustable to the heat and electricity demand of the home, will play an ever growing role.

Scale-up to larger units, which may then be applied in multi-family homes will be the consecutive step of development. This would immediately pave the way for operating these units also with regenerative energies (biomass and solar).

Acknowledgement: The present development has been carried out on behalf of the private Swiss foundation ESMOG. The encouragement received from the members of this foundation and their financial support are highly appreciated.

References

[1] J.P. Budliger, Einfacher Stirling-Motor für die Wärme-Kraft-Kopplung (WKK) in kleinen Wohngebäuden ; European Stirling Forum – Osnabrück, 2000

[2] J.P. Budliger, Supercharged Stirling Engine with one Single Mechanical Piston ; 10th International Stirling Engine Conference (ISEC-10) - Osnabrück, 2001

[3] J.P. Budliger, M.Lindegger, R. Schmid, Prototype Stirling Engine Comprising One Single Free Piston and a Resonance Tube; Intl. Stirling Forum – Osnabrück, 2008

[4] T. H. Lynch, B. Koch, Thermal Cycle Engine Boost Bridge Power Interface (The Boeing Company), Patent No. US 6'871'495 B2

[5] D. Keiter, E. Holliday, Electronic Controller Matching Engine Power to Alternator Power and Maintaining Engine Fequency for a Free-Piston Stirling Engine Driving a Linear Alternator (Sunpower Inc), Patent No. US 2008 / 0122'408 A1

Parametric optimization of an irreversible solar-driven Stirling heat engine with radiation-convection heat losses

*Ruijin Liu , Houcheng Zhang, Jincan Chen, Guoxing Lin**

Department of Physics and Institute of Theoretical Physics and Astrophysics, Xiamen University, Xiamen 361005, P. R. of China

Abstract: An irreversible solar-driven Stirling heat engine system is established, in which not only radiation-convection heat losses from the solar collector to ambience but also the regeneration loss and other irreversibilities of the heat engine cycle are taken into account. Based on thermodynamic analysis and the optimal control theory, the optimum relationship between the overall efficiency of the solar-driven Stirling heat engine system and the operating temperature of the collector is derived and the related performance bounds and design parameters are evaluated and determined. Moreover, the effects of several important parameters including the compositive factor c_1 , the regenerative factor a and the radiation and convection heat loss coefficient ratio ρ on the optimal performance characteristics of the system are investigated in detail. The results obtained here may provide some theoretical bases for the optimal parameter design of solar-driven heat engines.

Keywords: Solar collector, Stirling heat engine, irreversibility, performance optimization.

1. Introduction

Of all the renewable energy sources, solar energy is one of the most abundant energy sources and more and more attentions have been paid to it. A number of novel conceptive designs and apparatus for exploiting and applying solar energy have been investigated from both theory and experiment in recent years. Solar-driven heat engines are one of the most important apparatus which can convert solar energy to work as electricity or heat [1-5]. Some scholars explored the performance characteristics of solar-driven Carnot [6], Brayton [7, 8], Ericsson [9] and Braysson [10, 11] heat engines and employed the radiation heat transfer law to the heat transfer process of the high temperature side. These investigations, which have further included radiation heat losses besides the other irreversibilities in the heat engine cycles, can reveal the effects of multi-irreversibilities on the performance characteristics of the solar-driven heat engines and are closer to the practical solar-driven heat engine systems.

The solar-driven Stirling heat engine cycle is one of the most actual solar-driven heat engine cycles and some performance characteristics have also been investigated by some scholars [12-16]. For example, Chen [13] and Wu [16] studied the effects of imperfect regeneration and heat-transfer irreversibilities on the optimal performance of the solar driven Stirling heat engines. However, the radiation heat loss of the solar collector was not considered in these investigations. In fact, for those solar-driven heat engines or other solar thermal equipments operating at high temperatures [17], it is necessary to consider the radiation heat loss in the investigation of analyzing and evaluating their performance characteristics. Therefore, for the optimal parameter design and performance improvement of the solar-driven Stirling heat engine, it is a significant work to take multi-irreversibilities including the radiation-convection heat losses of the collector into account.

In the present paper, an irreversible solar-driven Stirling heat engine system is modeled, in which multi-irreversibilities including not only the finite-rate heat transfer between the collector and the cyclic working fluid and between the cyclic working fluid and the ambience but also radiation-convection heat losses from the solar collector to the ambience are taken into account. On the basis of thermodynamic analysis and the optimal control theory, the analytical expressions for the overall efficiency of the solar-driven Stirling heat engine system and the operating temperature of the collector are derived and the related performance bounds and design parameters are evaluated and determined. The effects of several important irreversible parameters on the performance

*Corresponding Author: Email: gxlin@xmu.edu.cn Tel.: +86-592-2183936; Fax: +86-592-2189426

characteristics of the system are also investigated in detail.

2. A Stirling heat engine cycle and its mathematical description

It is well known that a Stirling heat engine cycle consists of two isothermal and two constant-volume branches. When the cyclic working fluid is an ideal gas, the amounts of heat Q_1 absorbed from the hot reservoir at temperature T_h and Q_2 released to the heat sink at temperature T_c by the working fluid during the two isothermal processes are, respectively,

$$Q_1 = nRT_1 \ln(V_2 / V_1) \tag{1}$$

$$Q_2 = nRT_2 \ln(V_2 / V_1) \tag{2}$$

where n is the mole number of the working fluid, R is the universal gas constant, T_1 and T_2 are the temperatures of the working fluid in the two isothermal branches, V_1 and V_2 are the volumes of the working fluid along the constant-volume heating and cooling branches, as shown in Fig. 1. It is assumed that heat transfer between the working fluid and the two heat reservoirs obeys Newton's law, so that one has

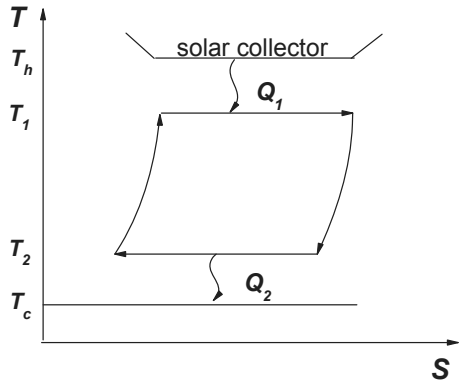

Fig. 1 A solar-driven Stirling heat engine system

$$Q_1 = k_1(T_h - T_1)t_1 \tag{3}$$

$$Q_2 = k_2(T_2 - T_c)t_2 \tag{4}$$

where k_1 and k_2 are, respectively, the thermal conductances between the working fluid and the high and low temperature heat reservoirs, and t_1 and t_2 are the corresponding heat transfer times.

It should be pointed out that the two constant-volume branches are generally used as two regenerative ones and the regeneration is implemented by means of a regenerator. In fact, owing to finite-rate heat transfer, the regenerative loss is inevitable and may be modeled as [13,18]

$$\Delta Q = xnC(T_1 - T_2) \tag{5}$$

where C is the mole heat capacity of the working fluid, x is the fractional deviation from perfect regeneration, and $x = 0$ indicates perfect regeneration.

Owing to the existence of regenerative loss, the net amounts of heat Q_h and Q_c absorbed from the hot reservoir and released to the heat sink per cycle are given by

$$Q_h = Q_1 + \Delta Q \tag{6}$$

$$Q_c = Q_2 + \Delta Q \tag{7}$$

respectively.

For the convenience of calculation, it is assumed that the time spent on the regenerative branches is proportional to that of the isothermal ones, i.e. [13]

$$t_{re} = b(t_1 + t_2) \tag{8}$$

where b is a proportional constant. Thus, the cyclic period

$$t = t_{re} + t_1 + t_2 = (1+b)(t_1 + t_2) \tag{9}$$

From Eqs. (1)-(7) and (9), one can derive the efficiency of the Stirling heat engine

$$\eta_h = \frac{T_1 - T_2}{T_1 + a(T_1 - T_2)} \tag{10}$$

and the average rate of heat supplied by the high temperature reservoir [13]

$$q_h = \frac{Q_h}{t} = \frac{T_1 + a(T_1 - T_2)}{(1+b)[T_1/(k_1(T_h - T_1)) + T_2/(k_2(T_2 - T_c))]} \tag{11}$$

where $a = xC/[R\ln(V_2/V_1)]$ which may be called as the regenerative factor. It may be proven from Eqs. (10) and (11) that for a given q_h, the maximum efficiency of the Stirling heat engine is given by

$$\eta_h = \frac{q_h/k-(1+a)T_h+(2+a)T_c-T_e}{(1+a)[q_h/k-(1+a)T_h+(2+a)T_c-T_e]-2(1+a)T_c} \quad (12)$$

where

$T_e = \sqrt{[(1+a)T_h + aT_c - q_h/k]^2 - 4a(1+a)T_hT_c}$,

$k = \frac{k_1}{(1+b)(1+\beta)^2}$ and $\beta = \sqrt{\frac{k_1}{k_2}}$.

3. The overall efficiency of the solar-driven Stirling heat engine system

A solar-driven Stirling heat engine system consisting of a solar collector and a Stirling heat engine is shown in Fig.1, where the solar collector acts as the high temperature reservoir and supplies thermal flow q_h to the Stirling heat engine. The overall efficiency of the solar-driven Stirling heat engine system

$$\eta = \frac{P}{IA_c} = \frac{q_h}{IA_c}\frac{P}{q_h} = \eta_s\eta_h \quad (14)$$

where $\eta_s = q_h / IA_c$ is the efficiency of the solar collector, I is the solar irradiance, A_c is the aperture area of the collector, and P is the power output of the heat engine.

For a solar collector, when the radiation-convection heat losses from the solar collector to the ambience are considered, the energy balance equation and the efficiency of the collector may be written as [11]

$$q_h = \tau\alpha IA_c - \varepsilon\sigma A_r(T_h^4 - T_c^4) - U_l A_r(T_h - T_c) \quad (15)$$

$$\eta_s = q_h/(IA_c) = \tau\alpha D \quad (16)$$

where $D = 1 - M_2[\rho(T_h^4/T_c^4 - 1) + (T_h/T_c - 1)]$, $\rho = M_1/M_2$, $M_1 = \varepsilon\sigma T_c^4/(\tau\alpha IF)$, $M_2 = U_l T_c/(\tau\alpha IF)$, $F = A_c/A_r$ and A_r are, respectively, the concentration ratio and the absorber area of the collector, $\tau\alpha$ is the effective transmittance-absorbance product, ε is the effective infrared emittance of the absorber plate, σ is the Stefan-Boltzmann constant, and U_l is the convective heat loss coefficient.

Using Eqs (12) and (16), one can obtain the overall efficiency of the solar-driven Stirling heat engine system as follows

$$\eta = \tau\alpha D\frac{c_1D-(1+a)T_h+(2+a)T_c-T_e}{(1+a)[c_1D-(1+a)T_h+(2+a)T_c-T_e]-2(1+a)T_c} \quad (17)$$

where $c_1 = \tau\alpha IA_c/k$, which depends on the heat-transfer coefficients and the other parameters and may be called as a compositive factor.

4. The optimally operating temperature of the solar collector

The efficiency of the solar collector decreases as its operating temperature T_h increases, whereas the efficiency of the Stirling heat engine increases as T_h increases. Therefore, there exists a maximum overall efficiency $\eta_{\max}$ of the solar-driven heat engine system when the operating temperature T_h of the collector attains its optimum value $T_{h,opt}$. Using the extreme condition $d\eta/dT_h = 0$ one can derive the optimally operating temperature of the collector，which is determined by

$$(T_{em}^2 - 2T_cT_{em} - 2T_cc_1D)D' + 2T_cD[T_e' + (1+a)] = 0 \quad (18)$$

where $T_{em} = c_1D - (1+a)T_h + (2+a)T_c - T_e$,

$D' = -4M_1T_h^3/T_c^4 - M_2/T_c$ and

$T_e' = \frac{(1+a)[(1+a)T_h - aT_c - c_1D]}{T_e} - \frac{(1+a)T_h + aT_c - c_1D}{T_e}c_1D'$.

Using Eq. (18), one can, in principle, solve out the optimally operating temperature $T_{h,opt}$ of the collector. Furthermore, substituting $T_{h,opt}$ into Eq.(17), one can attain the maximum overall efficiency $\eta_{\max}$ of the solar-driven Stirling heat engine system. However, Eq.(18) is a transcend equation and it will be dealt with by means of the numerical calculation.

5. Discussion

Equations (17) and (18) are two important analytical expressions of the solar-driven Stirling heat engine system. Based on Eqs. (17) and (18), the effects of the some important irreversible parameters on the performance characteristics of the solar-driven Stirling heat engine system may be analyzed and discussed through the numerical calculation technology.

5.1 Influence of the parameter c_1

Figure 2 shows that the overall efficiency of the solar-driven Stirling heat engine system decreases as the parameter c_1 increases for a set of other given parameters. This is natural, because c_1 is inversely proportional to the equivalent thermal conductance k such that when k decreases, c_1 increases. Thus, the heat supplied to the Stirling heat engine by the collector for a small k or a large c_1 is fewer than that for a large k, so that the overall efficiency of the system becomes smaller. Moreover, it can be seen from Fig.2 that the larger c_1 is, the higher the optimally operating temperature of the collector. In this case, the maximum overall efficiency of the system becomes smaller. For example, when c_1=10，100, 200, and 400, $\eta_{\max} \approx 0.279$, 0.254, 0.229 and 0.188. Furthermore, Fig.3 also shows the variations of $\eta_{\max}$ and $T_{h,opt}$ with the parameter c_1.

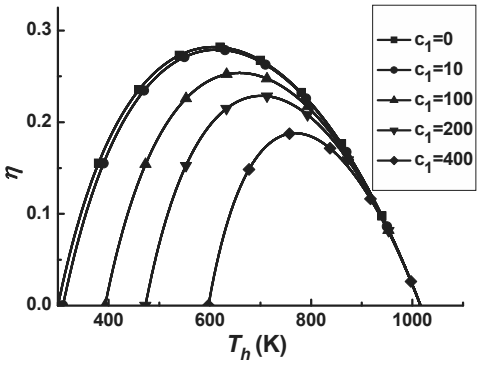

Fig 2 The $\eta \sim T_h$ curves for different c_1, where $T_c = 300K$, a=0.1, M_2=0.2, and $\rho = 0.02$ are chosen

5.2 Influence of the parameter *a*

It can be found from Fig 4 that the maximum overall efficiency of the solar-driven Stirling heat engine system is a monotonically decreasing function of the parameter *a*. The more the heat losses among the cycle processes are, the lower the efficiency η_h of the Stirling heat engine, and this will result in lower overall efficiency of the system. Therefore, it is clear that decreasing the regenerative loss coefficient *x* or the parameter *a* will be beneficial to the performance improvement of the

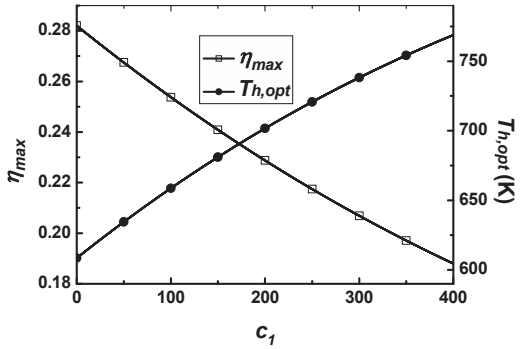

Fig.3 The $\eta_{\max} \sim c_1$ and $T_{h,opt} \sim c_1$ curves, where the values of the related parameters are the same as those used in Fig. 2

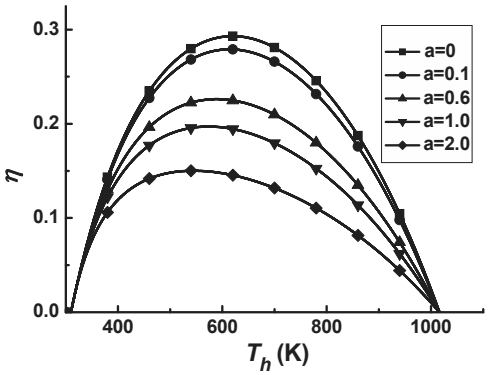

Fig 4 The $\eta \sim T_h$ curves for different a, where $c_1 = 10$ and the values of the related parameters are the same as those used in Fig. 2.

system. As an example, when *a* =2, 1.0, 0.6 and 0.1, $\eta_{\max}$ = 0.150, 0.197, 0.226 and 0.279, and $T_{h,opt}$ = 544K, 572K, 589K and 614K.

5.3. Influence of the parameter ρ

Since the heat loss coefficients of the collector are two important parameters, one should pay more attention to them. Figure 5 shows the effects of the radiation and convection heat loss coefficient ratio ρ on the $\eta \sim T_h$ curves. It can be seen from Fig.5 that for a given M_2, both $\eta_{\max}$ and $T_{h,opt}$ decrease as the parameter ρ increases. For example, when $\rho = 0.001$, 0.005, 0.02, and 0.1, $\eta_{\max} = 0.313$, 0.303, 0.279, and 0.221 for M_2 = 0.2. Moreover, the variations of the maximum overall efficiency $\eta_{\max}$ of the system and the optimally operating temperature $T_{h,opt}$ of the collector with

the parameter ρ are shown in Fig.6. Figure 6 indicates that both $\eta_{\max}$ and $T_{h,opt}$ decrease as the parameter ρ increases.

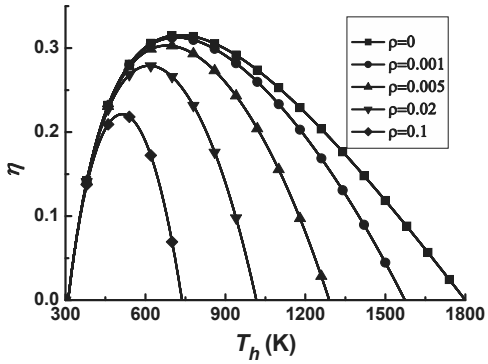

Fig 5 The $\eta \sim T_h$ curves for different ρ , where a=0.1 *and the related parameter values are the same as those used in Fig. 4.*

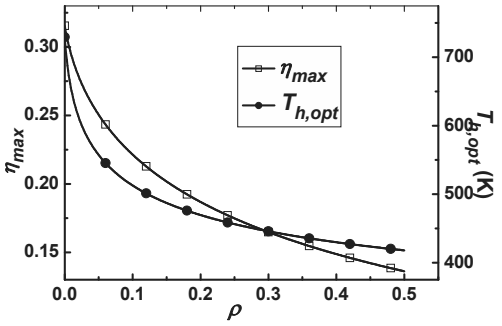

Fig. 6 The $\eta_{\max} \sim \rho$ and $T_{h,opt} \sim \rho$ curves, where a=0.1 *and the values of the related parameters are the same as those used in Fig. 4.*

6. Special cases

1) When $k \to \infty$, $c_1 \to 0$. Eqs (17) and (18) may be simplified as

$$\eta = \tau\alpha D \frac{T_h - T_c}{T_h + a(T_h - T_c)} \tag{19}$$

$$(T_h - T_c)[T_h + a(T_h - T_c)]D' + T_c D = 0 \tag{20}$$

In such a case, the thermal resistance disappears and the corresponding $\eta \sim T_h$ curve with $c_1 = 0$ is shown in Fig 2.

2) When $x \to 0$, $a \to 0$. Eqs.(17)-(18) may be simplified as

$$\eta = \tau\alpha D \frac{c_1 D - T_h + T_c}{c_1 D - T_h} \tag{21}$$

$$(2T_{em}^{*2} - T_c T_{em}^{*} - T_c c_1 D)D' + T_c D(2 - c_1 D) = 0 \tag{22}$$

where $T_{em}^{*} = c_1 D - T_h + T_c$. In this case, there does not exist any regenerative loss in the solar-driven Stirling heat engine and the corresponding $\eta \sim T_h$ curve with *a = 0* is shown in Fig. 4.

7. Conclusions

The irreversible solar-driven Stirling heat engine system is put forward. The overall efficiency η of the system is analyzed and optimized with respect to the operating temperature T_h of the solar collector. The optimal values of some important parameters such as the optimally operating temperature $T_{h,opt}$ of the collector, the maximum overall efficiency $\eta_{\max}$ of the system are determined by a set of characteristic curves. The effects of three parameters c_1, a and ρ related to irreversibility on the optimal performance of the system are analyzed and discussed through the numerical calculation technology. The results obtained are more general than those in literature and may provide some bases for the parameter design and performance improvement of solar-driven heat engines.

ACKNOWLEDGEMENT

This work was supported by the National Natural Science Foundation, P. R. of China (No. 50776074).

Reference

[1] Gordon, M., 1988, On optimized solar-driven heat engines. Solar Energy., 40, pp.457- 461.

[2] Chen, J., 1992, Optimization of a solar-driven heat engine. J. Appl. Phys, 72, pp.3778-3780.

[3] Chen, J., 1996, Thermodynamic analysis of a solar-driven thermoelectric generator. J. Appl. Phys, 79, pp.2717.

[4] Sahin, B., et al., 2006, Thermoeconomic analysis of a solar driven heat engine. Renewable Energy, 31(7), pp.1033-1042.

[5] Salah, M., et al., 1999, Thermodynamic optimization of irreversible solar heat engine. Renewable Energy, 17, pp.183-190.

[6] Sogut, O., and Durmayaz, A., 2005, Performance optimization of a solar-driven heat engine with finite-rate heat transfer. Renewable Energy. 30, pp.1329-1344

[7] Zhang, Y., and Chen, J., 2006, The thermodynamic performance analysis of an irreversible space solar dynamic power Brayton system and its parametric optimum design. J. Solar. Energy Engineering., 128, pp.409-413.

[8] Zhang, Y., et al., 2007, Optimum performance characteristics of an irreversible solar-driven Brayton heat engine at the maximum overall efficiency. Renewable Energy., 32, pp.856-867.

[9] Blank, D., and Wu, C., 1997, Finite-time power limit for solar-radiant Ericsson engines in space applications. Appl. Thermal. Engineering , 18, pp.1347-1357 .

[10] Zheng, S., et al., 2005, Performcnce characteristics of an irreversible solar-driven Braysson heat engine at maximum efficiency. Renewable Energy., 30, pp.601-610.

[11] Wu, L., et al., 2010, Parametric optimization of a solar-driven Braysson heat engine with variable heat capacity of the working fluid and radiation-convection heat losses. Renewable Energy., 35, pp.95-100.

[12] Singh, N., et al, 1997, Effect of Solar collector design parameters on the operation of Stirling power System. Int. J Energy Res., 21, pp.195-200

[13] Chen, J., et al, 1998, Efficiency Bound of a Solar-Driven Stirling Heat Engine System. Int. J Energy Res., 22, pp.805-812

[14] Blank, D., and, Wu, C., 1995, Power optimization of an extra-terrestrial, solar-radiant Stirling heat engine. Energy, 20(6), pp.523-530.

[15] Tlili, I., et al, 2007, Analysis and design consideration of mean temperature differential Stirling engine for solar application. Renewable Energy, 33, pp.1911-1921

[16] Wu, F., et al., 1998, Optimum performance of irreversible Stirling engine with imperfect regeneration. Energy Convers. Mgmt, 39(8), pp.727-732.

[17] Kim, D., et al., 2008, Solar refrigeration options- a state-of-the-art review. Int. J. Refrigeration, 31, pp.3-15.

[18] Howell, R., et al., 1977, Optimum solar collector operation for maximizing cycle work output. Solar. Energy. 19, pp.149–153

Heat Recovery of Exhaust Gas in Automotive Paint Ovens

P. Hanafizadeh[a,b] A. Khaghani[a], H. Shams[a] and M. H. Saidi[a]

[a] *Multiphase Flow Research Group*
Center of Excellence in Energy Conversion
School of Mechanical Engineering
Sharif University of Technology
Tehran, Iran, P.O.BOX: 11155-9567
[b] *Iranian Young Researchers Club*

Abstract: The rising cost of energy and the global warming in recent years have highlighted the need of more advanced systems with higher efficiency and less gas emissions. Consequently, plenty of researches have done on waste heat recovery and renewable sources of energy recently. The target of the present research is feasibility study of heat recovery in automobiles' paint ovens and designing an efficient system to use the lost energy. Research has been carried out on the theory, evaluating the amount of lost and available energy through Thermodynamics and heat transfer principle and choosing applicable design and construction of heat exchanger, especially for their use in ovens for energy recovery, reduction of air pollution and environmental conservation. Experimental measurements were done for data gathering in the case study of ovens in paint shop of Iran Khodro Industrial which is the oldest and biggest automotive corporation in the Middle East. Based on a feasibility study, a system to use this recovered energy was designed. This is then followed by cost analysis of this project which showed economical benefits of the project. The investment return period of the project is also determined.

Keywords: Heat Recovery, Paint Oven, CHP, Exhaust Gas

1. Introduction

The availability of energy plays an important role in the development and prosperity of a nation. In recent years, waste heat recovery and renewable energy sources, are receiving a great deal of attention. To produce heat in industrial processes, fuel and electricity is taking advantage in a plenty amount. Some part of this heat gets out of system as mortality heat and comes into environment. Most of the heat recovery systems transfer the heat from high sources to low ones. The recovered heat may be used for preheating of entering current or used in the HVAC systems. Typical examples of pre heating are combustion air, space heating, or pre-heating boiler feed water or process water. With high temperature heat recovery, a cascade system of waste heat recovery may be practiced to ensure that the maximum amount of heat is recovered at the highest potential. Waste heat can be re-consume for produce electricity and running pumps, fans, and other mechanical equipment.

There are many works on heat recovery in buildings, Fehrm et al. [1] have presented different means of heat recovery from the ventilation system, and discussed the benefit for the environment by using heat pumps for heat recovery from exhaust air in buildings. In their study, on the basis of the measured energy consumption for space heating, ventilation and domestic hot water production, a forced ventilation system featuring a heat pump reduces final energy consumption by 20% and primary energy consumption by 20% when compared installation work is inadequate or the use of heat from the heat recovery system is not given priority. Talom and Beyene [2] modified a three ton absorption chiller and matched it to a 2.8 L V6 internal combustion engine. They prove that the concept is feasible by the experiments which are conducted on the system. The concept could be used for refrigeration and air conditioning of transportation vehicles. El-Baky and Mohame [3] have experimented changing of inlet temperature of fresh air and discussed its results on temperature changes of fresh and return air and heat transfer, also they studied on effects of mass flow rate ratio for both evaporator and condenser sections of heat pipe heat exchanger for air conditioning. Regarding to their results, the enthalpy ratio between the heat recovery and conventional air

mixing is increased with increasing the inlet fresh air temperature and decreased with increasing mass flow rate of return air. Moreover, the heat recovery is increased with increasing inlet fresh air temperature and attained about 85%. Messerer et al. [4] have presented a novel approach for small wood-fired appliances for heat recovery from combustion exhaust. They demonstrate the applicability of specially designed heat exchangers for simultaneous heat recovery and efficient combustion particle deposition. Lui et al. [5] developed a looped separate heat pipe (SHP) as waste heat recovery facility for the air-conditioning exhaust system. A one-dimensional steady-state model was developed to calculate the upper and lower critical values of the SHP operation envelope as a function of the initial filing ratio. Their separate heat pipe heat recovery facility was made of two flat-plate heat exchangers sealed by four copper bars, which could not only enhance the heat exchange rate greatly, but also suppress the reduction of heat recovery efficiency due to compact thermal resistance between fins and tube surface. Furthermore, it also made the course of manufacture simply. Franco and Giannini [6] analyzed the use of a particular kind of compact heat exchanger for heat recovery steam generators(HRGS), their analysis was based on the e-NTU method seems useful in order to optimize both the single HRSG section and a complete HRSG. It was concluded that increasing in HRSG performance can be obtained if the minimization of the total pressure drop on the gas side and the minimization of the weight are considered as design objectives for the two optimization steps with respect to a preliminary design. Cenusa et al. [7] analyzed HRSG performance based on both performance and the capital cost of heat transfer area. Zhang and Zhuang [8] introduced some typical cases of industrial applications which included the equipment for the waste heat recovery and the industrial process equipment. Yang et al. [9] developed a method for using heat pipe heat exchangers for heating applying automotive exhaust gas. Soylemez [10] estimated the optimum heat exchanger area for energy recovery applications. His method claims a feasible solution range not an exact result. The formulation seems to be helpful, especially for industrial applications which have high energy saving potential. Karthikeyan et al [11] have reported some preliminary trends regarding steam generation and work output for an industrial waste heat recovery based on cogeneration system.

The present study indicates a great scope to recover waste heat from various industries ovens and propose a methodology to use this recovered heat in pre-heating air combustion and water consumption. Indeed, this study focuses on paint ovens in an automobile manufacturing.

Generally, paint process in automobile industry has three main stages namely pre-treatment, electro coating and drying [12]. First, the exterior surfaces and the cavities of each body are washed and become ready for painting. Then, during the Electro Deposition Coating (EDC) procedure the car body is dipped into a bath of lacquer and an electric potential between the car (cathode) and an anode is applied. Due to the local electric current density on the car body structure the lacquer adheres on the all internal and external body surfaces. Finally, the surface finishing coats have been applied on the car body. Then after each stage which are mentioned above, the surface of the car body must be dried. Industrial ovens are usually used for this purpose [13]. The paint process and utilization of ovens in this process are depicted schematically in Fig. 1.

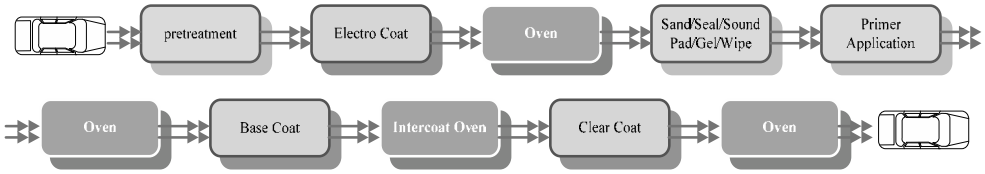

Fig. 1. Schematic diagram of the painting process

It is obvious that a large amount of heat waste in these ovens via exhaust air. Recovery of waste heat from oven exhaust has a direct effect on the efficiency of the paint process in automobile industries. This is reflected by reduction in the fuel consumption, pollutant generation and process cost. So in this research a methodology is proposed which has been carried out on the theory, evaluating the amount of lost and available energy based on Thermodynamics and heat transfer principals and choosing applicable design and construction of heat exchanger, especially for their

use in ovens for energy recovery, reduction of air pollution and environmental conservation.
Based on a feasibility study, an efficient system is

$$\psi = h_{mix} - T_0 s_{mix} \quad (3)$$

designed to use this lost energy. This is then followed by cost analysis of this project which showed economical benefits of the project. The investment return period of the project is also determined.

2. Methodology

Understanding the process is essential for development of Waste Heat Recovery System (WHRS). This can be accomplished by reviewing the process flow sheets, layout diagrams, combustion equation etc. Detail review of these will help in identifying sources and uses of waste heat, upset conditions occurring in the plant due to heat recovery, availability of space and dew point occurring in equipments, such as H_2O dew point.
After identifying source of waste heat and the possible use of it, the selection of suitable heat recovery system and equipments is the next step. Natural gas is used for many industrial purposes, most of them involving combustion and having a heated exhaust stream. The amount of thermal energy remains in that stream varies widely, but probably it has average between 20% and 40% of the thermal energy budget. Combustion equation for theoretic natural gas in this case study which burns with 10% additional air is as below:

$$CH_4 + 2.2O_2 + 8.272N_2 \rightarrow CO_2 + 2H_2O + 0.2O_2 + 8.272N_2 \quad (1)$$

The volume rate and temperature of the discharges are the main effective parameters. A low-volume rate, high-temperature discharge is a more favourable target than a high-volume rate, low-temperature discharge. Not all of the heat is recoverable. Recovering low grade heat discharges less than 120 ℃ is generally not practical with today's technology. Discharges in the 200 to 400℃ range may be near the condensing point of many vapors in the stream. Exhaust discharges above this temperature level are often good candidates for heat recovery using a variety of methods. Thus, the exhaust discharges have a potentiality of producing work. This work ability can be determined by considering of difference of exergy level of exhaust flow in respect to the environmental condition:

$$\text{Obtainable Energy} = \psi_e - \psi_0 \quad (2)$$

where e and o stand for exit and environmental conditions respectively. The exergy of exhaust flow calculated by [14]:
where h, T_0 and s are enthalpy, ambient temperature and entropy respectively. The mix stands for mixture of exhausted combustion products.

h_{mix} and S_{mix} can be computed by following formulas [14]:

$$h_{mix} = \sum y_i h_i \quad (4)$$

$$S_{mix} = \sum y_i S_i \quad (5)$$

In which y_i is mass ratio. Due to the fact that the temperature of combustion products must not be lower than the temperature of its dew point because of distillation H_2O and production of acid, a maximum work ability which is obtainable from exhausted gases is computed by:

$$\text{Maximum Obtainable Energy} = \psi_2 - \psi_{dp} \quad (6)$$

In which ψ_{dp} is the exergy of combustion products in dew point temperature. So the efficiency of 2nd law for exhaust gases can be calculated by [14]:

$$\eta_{2nd\ law} = \frac{\psi_2 - \psi_{dp}}{\psi_2 - \psi_0} \quad (7)$$

Energy of exhaust gases is transferred to inductor liquid with a heat exchanger for the purpose that it uses in an appropriate situation for pre-heating or heating consumable water. Different heat recovery systems can be used like Recuperative and Regenerative heat exchanger. Heat exchangers are so efficient for heat transfer from gas to liquid. Recuperative heat exchangers capture heat from exhaust gases and transfer it to incoming combustion air. They use metallic heat exchange surfaces to capture the heat through radiation and convection. Typical shapes are long concentric lengths of piping with the discharge gas in the inner part, or convective recuperators, with hot gases passing through small pipes in a large shape containing combustion air for pre-heating. A third group is regenerative heat exchanger, using a variety of methods to route the hot gas through a chamber, which is heated and rotated to serve as a route for supply air. In the present study, the specifications of the considered oven in the automobile manufacturing company are summarized in Table1.

Table 1. Paint oven of complement room, Specification of the oven's production

	Mean
% O_2	2.60
ppm CO	221.00
% CO_2	10.43
FT	310.40
ppm NO_X	0.00
ppm SO_2	0.00

Velocity of exhaust gas is measured by Testo 450 portable vane anemometer. In addition, measurement of the air velocity was performed using portable hot wire anemometer with an accuracy of ±0.1 m/s over the measuring range. Moreover, the products' temperature during the curing process was measured through Datapaq logger with an accuracy of ± 0.5°C. Due to the qualification of the present case study, heating the consumption water was found more effective. Because of the fact that it needs less investment, it can be utilized in every season and it has an appropriate efficiency. The results of above explanation for selecting the applicable method for heat recovery are summarized in the below chart.

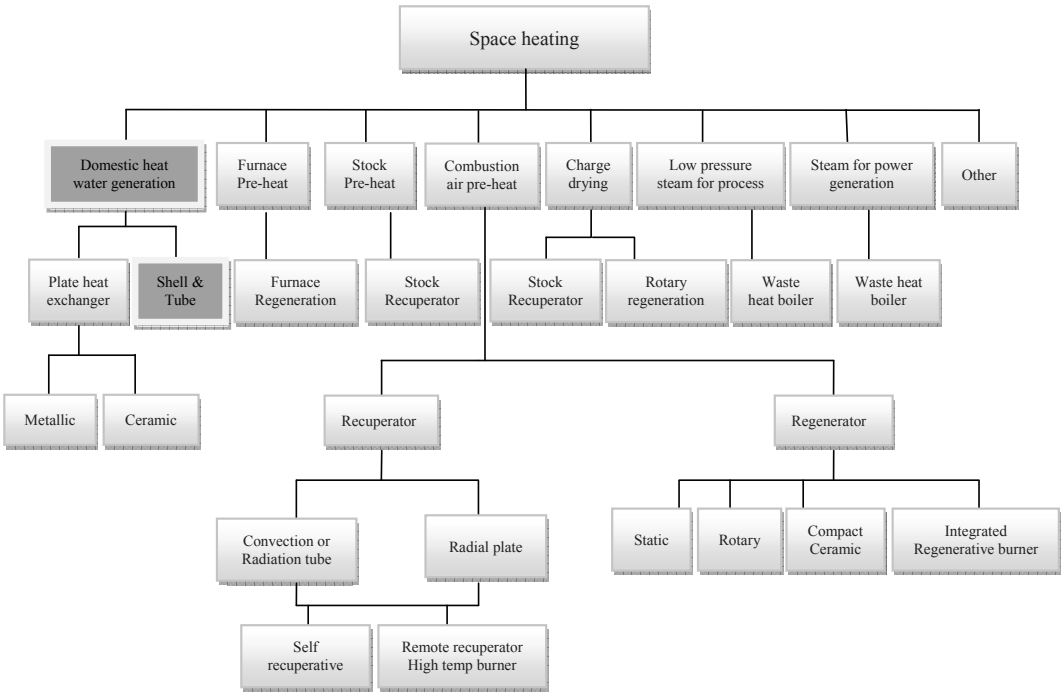

Fig. 2. Selecting appropriate technology for heat recovery

As it can be seen in the chart, shell and tube heat exchanger was selected for heating consumption water. Therefore, the 2nd law efficiency of the heat exchanger can be computed as below [14]:

$$\eta_{\text{2nd law,heat exchanger}} = \frac{(\dot{m}_w\psi_{2w} + \dot{m}_a\psi_{2a})}{(\dot{m}_w\psi_{1w} + \dot{m}_a\psi_{1a})} \quad (8)$$

where, $\psi_{2w}$is the exergy of water after increase in its temperature and $\psi_{1w}$is the exergy of inlet water at environment temperature which is 25 ℃

Design of heat exchanger

Due to the selecting of heat exchanger for heat recovery process, the surface which is needed for heat transfer should be computed. At first heat flow rate for a particular increase in water temperature is calculated by [15]:

$$q_w = \dot{m}_w C_{Pw}(T_{2w} - T_{1w}) \quad (9)$$

In which $\dot{m}_w$ and C_{Pw} are mass flow and special thermal volume of water respectively. Also 2 and 1 are related to the second and first condition of

water. The temperature of exhaust discharge (T_{2m}) can be calculated by below equation [15]:

$$q_{eg} = \dot{m}_{eg} C_{Peg} (T_{2eg} - T_{1eg}) \quad (10)$$

In which eg indicates the exhaust gas.
For computing the surface of heat transfer the below equation is used [15]:

$$q = UA\Delta T_{mean} \quad (11)$$

Where U is the heat transfer coefficient and is defined by [15]:

$$U = \frac{1}{\frac{1}{h_i} + \frac{A_i}{2\pi KL} \ln\left(\frac{r_o}{r_i}\right) + \frac{1}{h_o} \times \frac{A_i}{A_o}} \quad (12)$$

where h_i is convective heat transfer coefficient for water and h_o is convective heat transfer coefficient for discharges and these computed by Nusselt Formula which is $h = \frac{Nu\,K}{D}$.[15]
Also ΔT_{LMTD} is logarithmic mean temperature difference and is defined by [15]:

$$\Delta T_{mean} = LMDT = \left[\frac{\Delta T_a - \Delta T_b}{\ln\left(\frac{\Delta T_a}{\Delta T_b}\right)}\right] = \left[\frac{(T_{2m} - T_{1w}) - (T_{1m} - T_{2w})}{\ln\left(\frac{T_{2m} - T_{1w}}{T_{1m} - T_{2w}}\right)}\right] \quad (13)$$

So the required pipe length in heat exchanger is obtained by $L = \frac{A}{\pi d_i}$

Due to the selection of a shell and tube heat exchanger with fin, specifications of the fin such as thickness (w_o), height (b), inner and outer radius (r_1, r_2) can be obtained from related tables. Moreover, the efficiency of the surface of heat transfer with fin is computed by [15]:

$$\eta_{wo} = 1 - \frac{S_f}{S_t}(1 - \eta_f) \quad (14)$$

Where S_t is external surface of heat transfer and is defined as below [15]:

$$S_t = S_f + S_u \quad (15)$$

Also S_f and S_u are fin surface and tube surface of heat transfer respectively. These are calculated by [15]:

$$S_f = 2\pi r_2 w_o + 2\pi(r_2^2 - r_1^2) \quad (16)$$
$$S_u = 2\pi r_1(\delta - w_o)$$

In addition η_f in equation 16 is fin efficiency and can be obtainable from diagram for disk fin by $mb\ and\ \frac{r_2}{r_1}$ which m is defined as [15]:

$$m = \sqrt{\frac{2h_o}{Kw_o}} \quad (17)$$

So total heat transfer coefficient will be defined as [15]:

$$U = \frac{1}{\frac{1}{h_i} + \frac{A_i}{2\pi KL} \ln\left(\frac{r_o}{r_i}\right) + \frac{1}{h_o \eta_{wo}} \times \frac{A_i}{A_o}} \quad (18)$$

In which A_o and A_i are external and internal surfaces respectively and are calculated by [15]:

$$A_o = S_t \times \frac{L}{\delta} \quad (19)$$
$$A_i = \pi d_i L$$

3. Result and discussion

The oven which is considered is Electro Deposition(ED) paint oven. The specifications of the oven are shown in Table2.

Table 2. Technical specification of ED paint oven

Length(m)	90000
Outer Width(m)	4309
Inner Width(m)	2400
Outer Height(m)	8056
Amount of Exhausting Air(Nm^3/hr)	10000
Total Processing Time(min)	3028
Total Number of Nuzzles	d=60mm (81 units) d=100mm (207 units)

The result of exergy or potentiality of producing work is summarized in Table3.

Table 3. Exergy and efficiency of the heat exchanger

$\psi_2 - \psi_{dp}$ (kJ)	2594.02768
$\psi_2 - \psi_0$ (kJ)	280.90504
$\psi_{2w} - \psi_{1w}$ (kJ)	18553.17
$\eta_{2nd\ law}$	95%
$\eta_{2nd\ law,heat\ exchanger}$	35%

Due to the 10℃ increasing in water temperature, the result of ordinary heat exchanger design is summarized in Table4.

Table 4. Results of $\Delta T_{water} = 10℃$ for ordinary heat exchanger

Q(kW)	29.055
T_{2m}(℃)	266
U($\frac{w}{m^2 ℃}$)	15.457
ΔT_{mean}(℃)	274.11
$A_{heat\ exchanger}$(m^2)	6.825
L(m)	136.83

In this case we have a long heat transfer's length so it cannot be acceptable because of limited area and dramatic decrease in pressure. Thus, the shell and tube heat exchanger which is more efficient was designed for 35℃ temperature increasing of water. The result is shown in Table5. In regards to maintenance heat exchanger better and due to limited area, the whole capacity is divided to the two heat exchangers (8085W). Also 20 tubes with 2.5 meter long and 5/8 inch diameter are considered in each heat exchanger. Therefore, schematic view of the design is as figure2.

Table 5. Results of $\Delta T_{water} = 35℃$ for shell and tube heat exchanger

Q(kW)	101.7
T_{2m}℃	155.25
η_f	0.98
S_f(mm^2)	1988.38
S_u($mm^{2)}$	168.33
η_{wo}	0.9815
U($\frac{w}{m^2 ℃}$)	115.5
ΔT_{mean}℃	194.17
F(R,P)	0.99
$A_{heat\ exchanger}$(m^2)	4.9169
L(m)	98.6

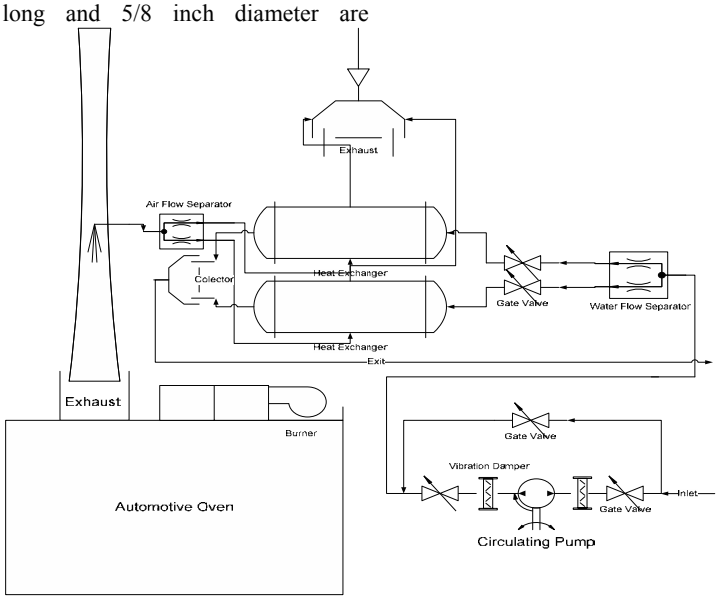

Fig.3. Schematic View of Heat Exchangers Design

By using heat exchanger, the amount of recoverable energy will be 366100kJ/hr. By considering natural gas and oil gas as the most prevalent fuels in ovens and their thermal value, scrounging in fuel consumption will be 9.6154m^3/hr for natural gas which has a direct impression on increasing the efficiency of the oven by 6.1%. The total saving of the fuel is computed for 3,600 work hours in a year. Thus, it is 35096.2 m^3 which is equivalent to 600$ by considering the cost of fuel in Iran. Furthermore, the total executive cost would be 9,600$ regarding to the cost of material and segments in Iran.

4. Conclusion

In this study, waste heat recovery from exhaust gas of automotive paint oven was considered by exergy, thermodynamics and heat transfer analysis. Regarding to the limitation of maximum dew point, the amount of recoverable heat was computed. Also appropriate devices and technology are obtained. Due to the using ovens in

several parts of cars' painting process, the amount of recoverable energy from these ovens is considerable. Therefore, this heat recovery has a myriad of benefits in diverse aspects. As the results of the study, the fallowing remarks can be obtained:

The efficiency of the oven increased dramatically because of the considerable saving in fuel consumption. Consequently, investment on the fuel had a significant decreased. In addition, this waste heat recovery has a great role in declining the cost of pollution since for each m^3 of producing CO_2 about 100$ should be paid**.** It is necessary to evaluate the selected waste heat recovery system on the basis of financial analysis such as investment, depreciation, payback period, rate of return etc. Attending to the total cost of construction and execution for the designed system and the economized costs, payback period will be 16 years in Iran; however, by considering global costs it will be decreased to 2 years. The same analyses are considered for oil gas which is used in cold weather widely as ovens' fuel. The results are summarized in the following Table:

Table6. Results of the study

	Thermal value(Kcal/m^3)	Total Saving (m^3)	Increase in efficiency of the oven (%)	Providence in the cost of fuel($)	Providence in the cost of pollution	Payback period (Iran)	Payback period (World)
Natural gas	9100	35096.2	6.1	600	165	16	2
Gas oil	8800000	36.2926	6.1	740	190	13	1

Acknowledgment

The funding for this research provided by Iran Khodro Company (IKCO) as an internship program jointing with Sharif University of Technology is greatly appreciated. Thanks to Mr. M. Kargar and Mr. S.M. Jamali for his careful review, constructive comments and good suggestions for the manuscript. The authors would like to thank all the members of the Assembly Shop No.2 of IKCO for their contributions to the field test campaign.

Nomenclature

Nomenclature

A	surface area[m^2]
b	fin's height[m]
C_p	special thermal capacity[$\frac{J}{kg\,℃}$]
d	Diameter[m]
h	enthalpy [$\frac{J}{kg}$]
h	convective heat transfer coefficient[$\frac{w}{m^2\,℃}$]
L	Length of heat exchanger[m]
m	Mass[kg]
q	heat transfer rate[w]
r	Radius[m]
S	Entropy[$\frac{J}{℃}$]
s	fin's area[m^2]
T	Temperature[℃]
ΔT_{mean}	logarithmic mean temperature difference[℃]
U	total heat transfer coefficient[$\frac{w}{m^2\,℃}$]
w_0	Fin's thickness[m]
y	mass ratio

Greek symbols

δ	Fin's pitch[m]
η	efficiency
ψ	Exergy[J]

Subscripts

mix	mixture
dp	dew point
e	exit condition
0	environmental condition
w	water
a	air
eg	exhaust gas
i	inner
o	outer
FT	final temperature

References

[1] Fehrm, M., Reiners, W., and Ungemach, M., 2002, Exhaust air heat recovery in buildings, Int. J. Refrigeration, 25, pp. 439–449

[2] Talom, H. L., and Beyene, A., 2009, Heat recovery from automotive engine, App. Thermal Engineering, 29, pp. 439–444

[3] Abd M.A., Baky, E., and Mohamed, M.M., 2007, Heat pipe heat exchanger for heat recovery in air conditioning, App. Thermal Engineering, 27, pp. 795–801.

[4] Messerera, A., Schmatlochb, V., Poschla, U., and Niessner, R., 2007, Combined particle emission reduction and heat recovery from combustion exhaust A novel approach for small wood-fired appliances, Biomass and Bioenergy, 31, pp. 512–521.

[5] Liu, D., Tang, G., Zhao, F., and Wang, H., 2006, Modelling and experimental investigation of looped separate heat pipe as waste heat recovery facility, App. Thermal Engineering, 26, pp. 2433–2441.

[6] Franco, A., Giannini, N., 2005, Optimum thermal design of modular compact heat exchangers structure for heat recovery steam generators, App. Thermal Engineering, 25, pp. 1293–1313.

[7] Cenusa, V., Badea, A., Feidt, M., and Benelmir, R., 2004, Exergetic optimization of the heat recovery steam generators by imposing the total heat transfer area, Int. J. Thermodynamic, 7, pp. 149–156.

[8] Zhang, H., Zhuang, J., 2003, Research, development and industrial application of heat pipe technology in China, App. Thermal Engineering, 23, pp. 1067–1083.

[9] Yang, F., Yuan, X., Lin, G., 2003, Waste heat recovery using heat pipe heat exchanger for heating automobile using exhaust gas, App. Thermal Engineering, 23, pp. 367–372.

[10] Soylemez, M.S., 2000, on the optimum heat exchanger sizing for heat recovery, Energy Conversion & Management, 41, pp. 1419-1427.

[11] Karthikeyan, R., Hussain, M., Reddy, B.V., and Nag, P.K., 1998, Performance simulation of heat recovery steam generators in a cogeneration system, Int. J. Energy Res., 22, pp. 399–410.

[12] Howard, M., 2000, Paint Shop Survey, University of Bath.

[13] Hanafizadeh, P., Sajadi, B., Saidi, M.H., 2009, Innovative Semi Analytical Methodology to Predict automobile body Temperature Distribution in the coat paint ovens, Proceedings of the 2009 ASME Summer Heat Transfer Conference (HT2009), San Francisco, CA, USA.

[14] Sonntag, R., Borgnakke, C., and Van Wylen, G., 2002, Fundamentals of Thermodynamics, John Wily & sons,Inc., Sixth Edition.

[15] Incropera, F.P., and De Witt, D.P., 2002, Introduction to Heat Transfer, John Wily & sons ,Inc., Fourth Edition.

Energy and exergy analysis of an ethanol fueled solid oxide fuel cell power plant.

Yannay Casas[a], Luis E. Arteaga[a], Mayra Morales[a], Elena Rosa[b], Luis M. Peralta[a] and Jo Dewulf[c].

[a]*Chemical Engineering Department. Central University of Las Villas. Road to Camajuaní Km 5.5. Santa Clara, c/p 54830, Villa Clara, Cuba.*
[b]*Applied Chemistry Center, Central University of Las Villas. Road to Camajuaní Km 5.5. Santa Clara, c/p 54830, Villa Clara, Cuba.*
[c]*Research Group ENVOC, Ghent University, Coupure Links 653, 9000 Ghent, Belgium*
Telf: (53) (422)-81164 Fax: (53) (422)-81608

Abstract: A solid oxide fuel cell (SOFC) system integrated with an ethanol steam reforming stage is evaluated considering the first and second laws of thermodynamics. The irreversibility losses distribution and the plant energy and exergy efficiencies are studied under different process conditions (823<T<973K) and water to ethanol molar ratios (5<R_{AE}<6.5). The post combustion of the cell off gases for the heat recovery is also taken into account to maintain the system operation within the auto-sustainability boundaries. An increase of efficiency and irreversibility at the stack is reported when the reactants ratio is increased. The higher losses are placed at the steam reformer (280kW – 350kW) and the cell (400kW – 590kW) due to the combination of the chemical composition and stream conditions on chemical and physical components of the exergy.

Key Words: Exergy Efficiency, Fuel cell, Irreversibility, Steam reforming.

1. Introduction

Fuel cells are considered to be the propulsion system of the near future, since they can produce electricity without polluting the environment, and possess the necessary specific power, power density and durability to replace conventional internal combustion engines from their current applications [1]. In recent years, the solid oxide fuel cell (SOFC) running on pure hydrogen or crude gases has drawn great attention, due to its high efficiency and degree of integration even with turbine cycles [2-4]. SOFCs support internal conversion of light hydrocarbons, alcohols and carbon monoxide without using noble metals as electrodes [1,2,5].

A traditional method to study a power generation system is the energetic analysis applying the first law of thermodynamics; it has been widely used to asses the solid oxide fuel cells. In that paper the effect of the steam reforming kinetic pattern was taken into account and the pinch methodology was applied to minimize the use of utilities. However, it is clear that instead, an exergetic analysis with exergy as the measure of the quality (useful part, transformable to work) of energy can be used to specify design optima which are different from those resulting from the energy conservation law [7].

In this sense Douvartzides et al. [9] developed an energy–exergy analysis in order to optimize the operational conditions of a SOFC power plant, considering only the hydrogen oxidation within the fuel cell, and rejecting the effect of the cell losses, in-situ methane reforming and carbon monoxide conversion. Moreover, Douvartzides et al. [8-9] did not take into account the effect of the kinetic pattern of the ethanol steam reforming (ESR) on syngas composition and instead they use the extent of the reaction (ε). The optimal condition was reached for a SOFC fuel utilization factor of 79.85%, an ethanol conversion of 100%, water to ethanol ratio 3:1 and no energy integration was developed.

The exergy analysis of an integrated internal methane reforming - solid oxide fuel cell - gas turbine (IRSOFC—GT) power generation system was performed by Pegah [10].

Corresponding author: Yannay Casas Ledón email:yannay@uclv.edu.cu

The in-situ partial oxidation of methane and the electrochemical oxidation of hydrogen at the cell anode were taken as main reactions. Fuel cell off gas was used to feed a turbine fulfilling in this way the power requirements for fuel compression. The thermodynamic losses in each unit were calculated and no energy integration strategy was taken into consideration.

The use of renewable fuels coupled to SOFCs have been also reported by Panopoulus et al. [11-12] and Fryda et al. [13] which studied the exergy efficiency of a biomass steam gasification reactor integrated with a high temperature SOFC in a combined heat and power scheme.

In the present paper, the first and second laws of thermodynamics are combined to obtain a system configuration and optimal operational conditions for an external catalytic ethanol steam reformer coupled to a solid oxide fuel cell system. The system combines the renewable character of ethanol with the technical advantages of fuel cells to design a near zero emission system with a high degree of efficiency. On the other hand, a detailed thermodynamic model for the evaluation of the SOFC is provided and a kinetic model is used to asses the conversion of methane within cell anode. The distribution of irreversibility on each device and the whole process are reported joined to the exergy and energy efficiencies. The study starts with an integrated process flow diagram as base case [14] and all the analysis are developed taken into account the effect of the heat exchanger network (HEN) design throw pinch methodology.

The mathematical processing of the models is carried out using the Aspen – Hysys® general purpose modeling-environment.

2. Description of the system

The ethanol steam reformer – solid oxide fuel cell systems are depicted in Fig. 1. The initial fluxes of water and ethanol are pumped into the Mixer where an isothermal mixing takes place at atmospheric conditions (298 K and 1atm). After that, the liquid mixture is vaporized and preheated on devices HEX-1 and HEX-2 prior to the Reactor inlet. The endothermic steam reforming of the ethanol (ΔH = +173.5 kJ/mol) is studied considering a packed bed reactor charged with a Ni/Al hydrotalcite catalyst [15-16] and among the various reaction patterns reported previously [14,16-17] the Lagmuir-Hishelwood kinetic model reported in Arteaga et al. [6,14] is used to describe a six step reaction scheme including the coke deposition on catalyst surface

The mixture leaving the Reactor is then fed into a solid oxide fuel cell module where an air flux (21%O_2, 79%N_2) is used as oxidant which is previously compressed and heated in a Compressor, HEX-3 and HEX-4. The SOFC model is used to study the process and to design various scenarios considering variations of the reformer operational parameters.

Since the λ_{SOFC} ratio of the syngas fed into the anode is higher than two, no carbon deposition problems are supposed to occur on the anode of the SOFC and the in-situ methane reforming; this is studied using a kinetic reactor model which considers the power law pattern with a negative reaction order for water [23]. Moreover, the shift conversion of the carbon monoxide is simulated using a Gibbs reactor model *(equilibrium)*, in this way the offgas composition is calculated rigorously and the energy recuperation in the post-combustor agrees with the real picture of the problem. The fuel utilization factor is defined by (Eq. 1). The heat balance in the cell considers the heat consumed in the methane reforming and the heat produced by the electrochemical reaction and shift conversion.

$$U_f = \frac{\left(f^{in}_{H2} + 4 \cdot X_{CH4} \cdot f^{in}_{CH4} + X_{CO} \cdot f^{in}_{CO} - f^{out}_{H2}\right)}{\left(f^{in}_{H2} + 4 \cdot X_{CH4} \cdot f^{in}_{CH4} + X_{CO} \cdot f^{in}_{CO}\right)} \quad (1)$$

The SOFC exhaust containing H_2, CH_4, O_2, N_2, CO, H_2O, and CO_2 is cooled (to avoid NO_x formation) and burned downstream in the post-combustion system. The post-combustion unit is modeled as an adiabatic conversion reactor *(ConvReact)* and the depleted heat is used to balance the energy requirements in the process.

Corresponding author: Yannay Casas Ledón email:yannay@uclv.edu.cu

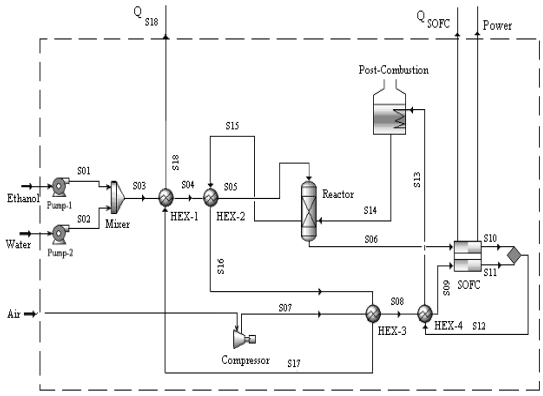

Fig 1. Process flow diagram (PFD).

3. Second Law Analysis

physical and chemical; more precisely, the physical exergy expresses the useful work that a substance can produce when brought reversibly from its state to the "restricted dead state" and it can be written as:

$$e_i^{ph} = \left(H - H_o\right)_i - T_o\left(S - S_o\right)_i \quad (2)$$

Chemical exergy is obtained when the components of the energy carrier are first converted to reference compounds and then diffuse into the environment, which is in reference (dead) state. For a gaseous stream flow, the molar chemical exergy (e_i^{ch}) of all species is given by the (2) Fryda et al. [13]:

$$e_i^{ch} = \sum x_i \cdot e_i^o + RT_o \sum x_i \cdot \ln(x_i) \quad (3)$$

No deviations between real environmental and reference conditions are considered. The standard chemical exergies of all components of each stream represented in the PFD **(**Fig. 1**)** are showed in the Table 1.

Exergy analysis is a thermodynamic method of using the conservation of mass and energy principles together with the Second Law of Thermodynamics for the design and analysis of thermal systems. The purpose of an exergy analysis is generally to identify the location, the source, and magnitude of true thermodynamic inefficiencies in a given process. Exergy is the maximum work that can be produced when a heat or material stream is brought to equilibrium in relation to a reference environment. In this study a temperature of T_o = 298.15 K, pressure P = 1.013 bar and environment composition of 75.67 % N_2, 20.35 %O_2, 0.03 %CO_2, 3.03 % H_2O and 0.92 % Ar are assumed as reference [18].

In the present article the exergy of each material stream is expressed as the sum of two components,

Table1.Standards Chemical Exergy (Stds.Chem.Exergy) of individual species. [26]

Species	**Formula**	**Stds. Chem. Exergy**
Nitrogen	N_2	720
Oxygen	O_2	3970
Water	H_2O_g	$1.171.10^4$
Water	H_2O_l	3120
Carbon Dioxide	CO_2	$2.014.10^4$
Carbon Monoxide	CO	$2.754.10^5$
Argon	Ar	$1.169.10^4$
Ethanol	$C_2H_5OH_g$	$1.371.10^6$
Ethanol	$C_2H_5OH_l$	$1.365.10^6$
Methane	CH_4	$8.365.10^5$
Hydrogen	H_2	$2.385.10^5$
Carbon	C	$4.108.10^5$

Note: All the exergy values are presented in kJ. $Kmol^{-1}$.

An exergy balance for a control volume at steady state is formulated to calculate the exergy destruction (E_{Dest}) of the system at different operational conditions. In the present work all the inlet and outlet streams are considered to determine the irreversibility distribution, which include the sum of matter, energy and power. The mixer, heat exchangers (HEX-1 to HEX-6),

ethanol steam reforming reactor, the SOFC module, the post-combustion unit and the auxiliary equipments (pumps and compressor) are included into the limits of the system (Dashed lines area in Fig. 1). The process global exergy balance, by ignoring the changes in kinetic and potential exergies, is expressed as:

$$E_{irrev} = \left(\sum f_i \cdot e_i\right)_{inlet} - \left(\sum f_i \cdot e_i\right)_{outlet} + \sum_j \left(1 - \frac{T_o}{T_j}\right) Q_j - W \quad (4)$$

Where $E_{irrev}=To*S_{gen}$ (the Gouy -Stodola theorem) represents the rate of exergy destruction into the device due to irreversibilities, e_i is the total exergy of each chemical species i, which is the sum of the physical and chemical exergies.

3.1. Definition of the irreversibilities

Irreversibility at each stage of the process is calculated based on the approaches described previously. The equations for the evaluation of this parameter are present below.

3.1.1 Steam reforming reactor

Exergy destruction of the ESR can be expressed by the following equation.

$$E_{ESR} = \begin{pmatrix} f_{S05} \cdot e_{S05} + f_{S14} \cdot e_{S14} \\ - f_{S06} \cdot e_{S06} - f_{S15} \cdot e_{S15} \end{pmatrix} \quad (5)$$

3.1.2 Heat Exchanger equipment

The exergy balances in all heat exchanger devices can be expressed as follows:

$$E_{HEX\ j} = \left(1 - \frac{T_o}{T_j}\right) Q_j + f\left[\left(e_k^{ph}\right)_{inlet} - \left(e_k^{ph}\right)_{outlet}\right]_{hot} + f\left[\left(e_k^{ph}\right)_{inlet} - \left(e_k^{ph}\right)_{outlet}\right]_{cold} \quad (6)$$

Where j is the heat exchangers and k represent each stream of process (inlet and outlet).

The previous equation is not affected by chemical exergy due to the chemical compositions of the hot and cold inlet streams are constants in the heat exchange equipment.

3.1.3 Solid Oxide Fuel Cell

The chemical transformations into the fuel cell cathode and anode, the dissipated heat to the environment and the power delivered by the electrochemical reaction are considered into the irreversibilities. Then the exergy destruction in the SOFC is calculated as below:

$$E_{SOFC} = -\left(1 - \frac{T_o}{T_{SOFC}}\right) Q_{SOFC} - P_{SOFC} + \sum \left[\left(f_{S09} \cdot e_{S09} - f_{S11} \cdot e_{S11}\right)\right]_{cathode} + \sum \left[\left(f_{S06} \cdot e_{S06} - f_{S10} \cdot e_{S10}\right)\right]_{anode} \quad (7)$$

3.1.4 Compressor

The expressions to determine the compressor irreversibilities are reported by Pegah [10]. It takes into account the compression ratios, polytropic efficiencies and fluid conditions.

$$E_C = f_{air} \cdot R \cdot T_o \left(\frac{1 - \eta_{p,C}}{\eta_{p,C}}\right) \cdot \ln(CPR) \quad (8)$$

3.1.5 Post-Combustion unit

In the after burner the irreversibility is defined considering the chemical and physical components, the losses by heat transfer are zero because the combustor operates adiabatically:

$$E_{PC} = \left(f_{S13} \cdot e_{S13}^{ch} - f_{S14} \cdot e_{S14}^{ch}\right) + \begin{bmatrix} \left(f_{S13} \cdot H_{S13} - f_{S14} \cdot H_{S14}\right) \\ - T_0 \left(f_{S13} \cdot S_{S13} - f_{S14} \cdot S_{S14}\right) \end{bmatrix} \quad (9)$$

4. System energy and exergy efficiencies

Energy efficiency of the whole system (Eq.10) is defined by the ratio between the delivered power and the amount of energy contained in the ethanol molecular structure it is referred to the LHV.

$$\eta_{energy} = \frac{\sum_j W_j}{\left(f^{in} \cdot LHV\right)_{ethanol}} \quad (10)$$

Where $\sum_j W_j$ is the global power generated by the system (work produced – work consumption).

On the other hand, exergy efficiency (Eq.11) is referred to the exergetic potential of the primary fuel (standard exergy of ethanol).

$$\text{exergy} \quad \frac{\sum_j W_j}{f^{in}\ e^{o}_{ethanol}} \tag{11}$$

5. Results and discussion

5.1. Exergy analysis considering operation parameters

An exergy study has been developed in order to simulate the power plant using the Solid Oxide fuel cell technology represented in the Fig. 1. This simulation program is able to calculate the flow rate, temperature, pressure, energy and the exergy content in every stream of inlet and outlet as well as the exergy destruction by irreversibilities of each stage involved in the plant.

The results of the exergy analysis applied to the base case are shown in the Table 2. The conditions selected were $T_{ESR} = T_{SOFC} = 923$ K, $R_{AE} = 6.0$, $U_f = 80$ %, $V_{cell} = 0.64$ V, compressor polytrophic efficiency $_{p,c} + \%\ 0\ _{SOFC} > 2$. Considering the standard chemical potential of ethanol as the inlet flow availability, the irreversibilities represent approximately 66 % of the flow availability, so the exergy efficiency takes a value of 34 %.

Table 2. Base case simulation results.

Cell voltage	Inlet flow availabilit	Stack power	Net power	Energy efficiency	Exergy efficiency
0.6 V	1480 kW	569 kW	502 kW	37.6 %	33.9 %

The effect of the reforming temperature and reactants molar ratio on exergetics efficiency and losses are presented in the Fig. 2 and Fig. 3 respectively.

The fuel cell power and the ethanol flow have a notable influence on the exergy efficiency according to the definition written previously. On the other hand, the cell power is directly proportional to the hydrogen obtained in the reformer. Because of this; the higher hydrogen yield allows the increase of the SOFC power as well as the exergy efficiency. According to the explanation above; the exergy efficiencies are favored by higher reformer temperatures and water to ethanol feed ratios. Exergetic efficiencies reach values ranging from 32 % to 35 % approximately in all analyses; the higher efficiencies are obtained at 973 K and R_{AE} of 6.5.

From an irreversibility point of view, the system studied is not favored by the increase of the reformer operation variables. The lower irreversibility values are obtained at lower temperature and R_{AE}, nevertheless it corresponds to lower exergy efficiency of the process (less than 30%), and so there should always be a balance between system efficiency and system irreversibility.

Further on, it is important to express that the flow diagram is designed on integration principles allowing an optimal use of the hot streams and keeping the design of the plant to operate autonomously, without any interaction between external sources of heat and power (auto-sustainability).

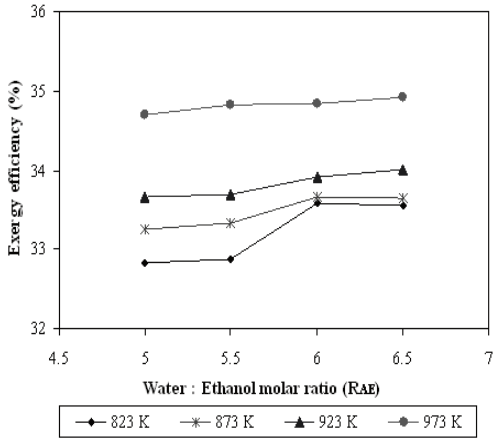

Figure 2. Effect of the reforming temperature and R_{AE} on exergetic efficiency.

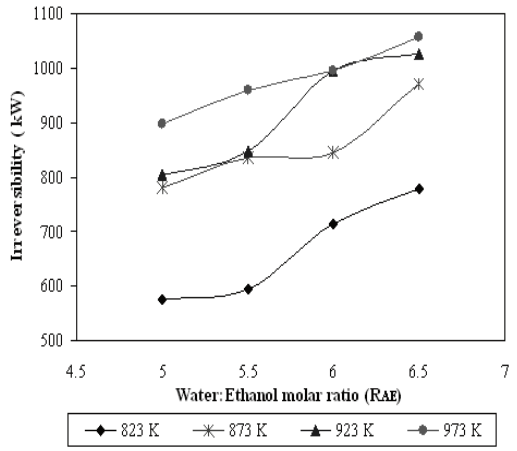

Figure 3. Irreversibilities, varying the reforming temperature and R_{AE}.

The irreversibility of the stages involved in the plant at reforming temperature of 923 K is illustrated in Fig. 4. The total exergy destruction in the system is caused mainly by the SOFC, reformer and post-combustor, which represents more than the 50 % of the inlet flow availability, similar results are reported by Pegah [10]. Changes in the chemical exergies are more relevant than the changes of the physical contributions; this phenomenon is related fundamentally with the chemical reactions extents.

The exergy destruction of the reformer is increased from 276.13 kW to 336.53 kW for feed molar ratios of 5 and 6.5 respectively. That change in performance is due to the increase on the demands of heat in the reformer with R_{AE}, which is caused by the increase of reactions conversion taking place in this stage and the total flow.

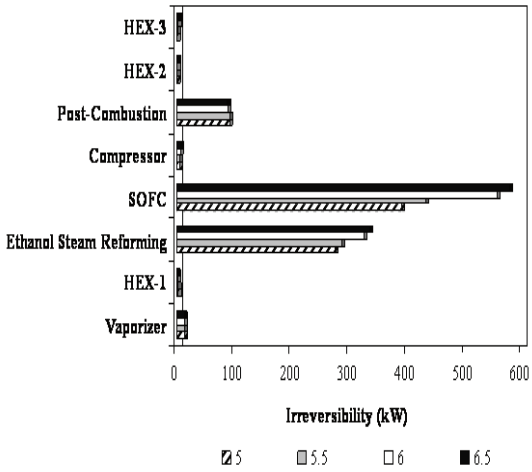

Figure 4. Exergy destruction by irreversibility in cycle stages varying R_{AE}.

In order to investigate the performance of the exergetic losses in the fuel cell, we assumed that the heat rejected by the electrochemical reaction is a waste, because of this; the exergy destructions by heat losses are significant, reaching values of 70% of the exergy destruction of the SOFC for water to ethanol molar ratio of 6.5. The efficient use of wasted heat by the cell in a turbine, heat engines or in a combined cycle can reduce the irreversibilities in this stage and the global system, as well as to improve the exergy and energy efficiencies [19].

The increase of R_{AE} produce a higher hydrogen flow to the fuel cell, converting more chemical energy into electricity, which means more current and power produced. Nevertheless at the same condition, the irreversibility is increased in the fuel cell stack due to the increase of the waste heat and dissipative phenomena (overpotential losses).

The exergy destruction in the post-combustor presents a little decrease for different R_{AE}. Those losses are associated to the irreversibility of the combustion process of H_2, CO and CH_4, the amounts of reactants, the temperature of the combustor and the stoichiometric ratio of the combustion. In this case the amounts of fuels take an important role; especially the energetic content of the inlet stream is reduced with

the increase of the water to ethanol molar ratio, allowing lower losses by the heat transfer.

6. Conclusions

The evaluation presented in this paper allows obtaining a complete idea of the real work delivered by an integrated solid oxide fuel cell and an ethanol steam reforming unit and it relationship with the most relevant operation variables. The effect of water to ethanol ratio and the reforming temperature on the energy and exergy efficiency of the system was also discussed.

The higher exergy efficiencies (35% at 973 K and R_{AE}=6.5) also coincide with higher total irreversibility losses (1050kW) due to the effect of the change in both the chemical and physical components. It was also demonstrated that a balance should be established by the process engineer considering equilibrium between power production and process efficiencies.

Nomenclature

CPR compression ratios

E exergy destruction, kW.

e_i total exergy of each chemical species, kJ/kmol.

e^{ch}_i molar chemical exergy of species, kJ/kmol.

e^{ph}_i molar physical exergy of species, kJ/kmol.

$F^{in}_{ethanol}$ *e*thanol flow feed to the reactor, kmol/s.

H *m*olar absolute enthalpy, kJ/mol.

H_o molar enthalpy at reference state, kJ/mol.

P_{SOFC} cell power output, kW.

Q heat duty of component, kW.

R universal gas constant, J/(K mol).

R_{AE} water/ethanol molar ratio.

S molar absolute entropy, kJ/(mol K).

S_o molar entropy at reference state, kJ/(mol K).

T temperature of component j, K.

T_0 temperature of reference state, 298.15 K.

x *m*ole fraction of species.

Greeks Letters

η_{exergy} exergy efficiency, %.

η_{energy} energy efficiency, %.

Subscripts

C compressor.

ESR reformer.

HEX heat exchanges.

Hot stream of HEX.

Cold stream of HEX.

PC post-combustion.

SOFC solid oxide fuel cell.

i each chemical species of the stream.

j each component of system (mixer, reformer…fuel cell).

k streams of process (inlet and outlet)

S06, S07…S15 streams of the flow diagram

7. References

[1]. Hirschenhofer, J.H., et al., 2006, Fuel Cells Handbook, sixth Ed., EG & G Technical Services, National Energy Technology Laboratory. P.O. Box 880. Morgantown, West Virginia 26507-0880.

[2]. Thorud, B., 2005. Dynamic Modelling and Characterization of a Solid Oxide Fuel Cell Integrated in a Gas Turbine Cycle. Doctoral Thesis. Department of Energy and Process Engineering. Norwegian University of Science and Technology.

[3]. Calise, F., Palomb, A., Vanoli, L., 2006, Design and partial load exergy analysis of hybrid SOFC–GT power plant, Journal of Power Sources, (158), pp. 225 - 244.

[4]. Calise, F., et al., 2006, Simulation and exergy analysis of a hybrid Solid Oxide Fuel Cell (SOFC)–Gas Turbine System, Energy, (31), pp. 3278–3299.

[5]. Ballard., 2007, Case Study - Residential Cogeneration. Groundbreaking Fuel Cell Solution. Ballard Power Systems Inc. 9000 Glenlyon Parkway Burnaby, British Columbia.

[6]. Arteaga-Perez, L.E., et al., 2009, An auto-sustainable solid oxide fuel cell system fueled by bio-ethanol Process simulation and heat exchanger network synthesis, Chemical Engineering Journal, 150, pp. 242–251.

[7]. Hotz, N., Sen, S.M., Poulikakos, D., 2006, Exergy analysis of a solid oxide fuel cell

micropowerplant, J. of Power Sources, 158, pp. 333-347.

[8]. Douvartzides, S,. Coutelieris, F., Tsiakaras, P., 2004, Exergy analysis of a solid oxide fuel cell power plant fed by either ethanol or methane, Journal of Power Sources, 131, pp. 224–230.

[9]. Douvartzides, S., Coutelieris, F., Tsiakaras, P., 2003, On the systematic optimization of ethanol fed SOFC-based electricity generating systems in terms of energy and exergy, Journal of Power Sources, 131, pp. 224–230.

[10]. Pegah, G.B., 2007, Energy and Exergy analysis of internal reforming solid oxide fuel cell- gas turbine hybrid system, International journal of hydrogen energy, 32, pp. 4591-4599.

[11]. Panopoulos, K.D., et al., 2006, High temperature solid oxide fuel cell integrated with novel allothermal biomass gasification Part II, Exergy analysis, Journal of Power Sources, 159, pp. 586–594.

[12]. Panopoulos, K.D., et al., 2006, High temperature solid oxide fuel cell integrated with novel allothermal biomass gasification Part I, Modelling and feasibility study, Journal of Power Sources, 159, pp. 570–585.

[13]. Fryda, L., et al., 2008, Exergetic analysis of solid oxide fuel cell and biomass gasification integration with heat pipe, Energy, 33, pp. 292-299.

[14]. Arteaga, L. E., et al., 2008, Bioethanol steam reforming for ecological syngas and electricity production using a fuel cell SOFC system, Chemical Engineering Journal, 136, pp. 256-266.

[15]. Mas, V., et al., 2008, Ethanol steam reforming using Ni(II)-Al(III) layered double hydroxide as catalyst precursor, Chemical Engineering Journal, 138, pp. 602-607.

[16]. Mas, V., et al., 2008, Ni(II)-Al(III) layered double hydroxide as catalyst precursor for ethanol steam reforming: Activation treatments and kinetic studies, Catalysis Today, 133 (135), pp. 319–323.

[17]. Akande, A., et al., 2006, Kinetic modeling of hydrogen production by the catalytic reforming of crude ethanol over a co-precipitated Ni-Al_2O_3, International Journal of Hydrogen Energy, 31, pp. 1707-1715.

[18]. Kotas, T.J., 1995, The exergy method of thermal plant analysis. Florida: Krieger Publishing Company.

[19]. Hernandez, L., Viatcheslav K.V., 2008, Use of bioethanol for sustainable electrical energy production, Int. J of Hydrogen Energy, in press.

Centrifugal Compressor One-Dimensional Design Calculation and Results Validation

Elkin I. Gutiérrez Velásquez[a], *Marco A. R. Nascimento*[a], *Ruben A. Miranda Carrillo*[a], *Newton R. Moura*[b]

[a] *Universidade Federal de Itajubá, Itajubá, MG, Brasil*

[b] *Petrobras Research and Development Center, Rio de Janeiro, RJ, Brasil*

Abstract: Gas micro turbines have become an efficient form of energy generation which offers several advantages compared with other energy technologies to small scale production. Among these advantages are lower weight and dimensions, fewer moving parts, and heat concentration in a single stream of high temperature which facilitates its installation and its application in the recovery of products that can be used as fuels, such as the combustion of lower calorific value like the biogas. Besides that, the micro turbines have great flexibility and can be applied to different sectors such as micro-generation, transport vehicles, drying processes among many others. The aim of this paper is to present the results obtained by the use of a one-dimensional compressor design tool developed in FORTRAN code, which enables to calculate the main characteristic parameters of a centrifugal compressor. This application is based on non-dimensional parameters. The results obtained were validated with results taken from specialized literature, as well as with results obtained from simulations performed using applications based on CFD techniques. These results show that the developed application delivers results with a very good approximation, at very low computation times and without requiring a high computational cost.

The code was developed as a preliminary tool of design owing to the fact that the commercial codes are blocked and do not permit modify their calculate routines, this prevents the possibility of implement and evaluate any others possibilities, which is of great importance in researching tasks.

Keywords: CFD, centrifugal compressors, gas turbines engines

1. Introduction

In recent years, distributed generation (DG) has received increasing interest due to some advantages such as: improved security of supply, greenhouse gases emission reduction, efficiency gains and greater flexibility in investment [1-3]. The resource conservation and the use of renewable and clean energy sources are some of the alternatives presented to prevent some current environmental problems. Therefore distributed generation systems play an important role as energy sources, not to replace conventional sources of electricity but complementing them.

Among the different types of primary energy sources mostly used are distributed generation fuel cells (chemical energy), small gas turbines and internal combustion engines (heat energy from fossil fuels), photovoltaic cells (solar energy) and wind generators (wind energy) [4-6].

Small gas turbines engines present some advantages over other DG technologies, such as reasonable capital costs, a wide range of power (15-300 kW) [7], operation possibility with different fuels at reasonable efficiency (30 -33% with regenerator) and low levels of emissions [8].

In the development of turbo-machines analytical methods for predicting performance, by means of parametric studies, are used to demonstrate the influence of geometry changes on performance under design and off-design conditions. Computational Fluid Dynamics (CFD) codes are used as reliable design tools for centrifugal compressors avoiding expensive experimental development. The impeller is one of the key components of the industrial centrifugal compressors and turbochargers. The impeller design is critical to the success of a compressor stage design. Basic sizing information to establish the initial parameter scan saves development time for the industrial centrifugal compressor. The diffuser also plays an important role in the compressor operating range once a poorly designed diffuser reduces the compressor operating range and stage efficiency.

This work presents the results of the preliminary compressor design of a simple cycle gas turbine engine obtained with the use of a one-dimensional

FORTRAN code [9]. This permits the calculation of the main characteristics of a centrifugal compressor by means of the application of non-dimensional parameters, with a vast reduction of computational cost. Comparisons are made with full three dimensional CFD analysis and experimental measurement data to validate the results of the developed code. The purpose of this study is to demonstrate that the use of a simple code can produce fast and reliable results in order to avoid large computer running times and storage requirements.

2. Thermal performance analysis

The GE Gate Cycle Enter software 5.51 [10] was used to predict the steady state condition design performance of a simple cycle gas turbine. The aim of this simulation was to obtain the air conditions at the compressor entrance. The simulation scheme used for the simple gas turbine cycle is shown in Fig. 1.

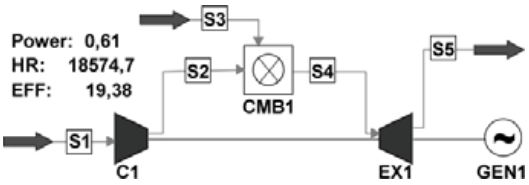

Fig. 1. Scheme used for the simple gas turbine cycle thermal simulation.

The input design parameters used in the GCS simulation are shown in Table 1. These data are based on current technologies for radial turbo-machine. The turbine inlet temperature of 1123K was chosen as this is the maximum temperature put up by the materials for the manufacture of radial turbines, maintaining the mechanical resistance and the useful life without blade cooling [11].

Table 1. Design point input parameters.

Parameter	Value	Units
Ambient temperature	288	K
Ambient pressure	101.32	kPa
Turbine inlet temperature	1123	K
Fuel temperature	288	K
Pressure ratio	4	--
Compressor adiabatic efficiency	80	%
Combustion adiabatic efficiency	99	%
Turbine efficiency	85	%

2.1. Engine design point

The design of a compressor starts with the establishment of the design point obtained by a preliminary simulation of the thermal cycle. The output results of the thermal simulation are shown in Table 2, according to Fig. 1.

Table 2. Thermal simulation results.

Stream	Temperature	Pressure	Flow
S1	288	101.32	4.288
S2	461	405.28	4.288
S3	288	500.00	0.071
S4	1123	397.17	4.395
S5	846	101.32	4.395

3. Compressor design

The objective of the developed centrifugal compressor design code is to find out the basic geometry of a centrifugal compressor from some input data. This information defines the expected performance of the designed compressor.

This work is part of the design of a 600kW simple cycle gas turbine, with annular combustion chamber, so the designed compressor does not have a volute.

A vaned diffuser model with fixed blades in the shape of a circle arc was selected. The mathematical model applied for the calculation was developed by Japikse [12], which allows determining the recovery pressure that can be attained, and the ideal length of the blade, the number and radius of the curvature thereof.

3.1. One-dimensional calculation

In the development of any calculation code that intends to conceive a turbo-machine one must take into account a range of features and/or limitations imposed by the aerodynamic condition, as well as the materials used for such construction.

First, it is necessary to establish the pressure ratio as the design parameter. This and other important input parameters for the one-dimensional code are shown in Table 3. The slip factor of 0.85 is proposed by Dixon [7] as a usual value for centrifugal compressors.

From these variables, the code determines the velocity triangles as a function of the inlet Mach number, and the thermodynamic relations to the entry, after that it determines the velocity triangles in the discharge, and then sets the relative Mach number in the discharge.

Table 3. One-dimensional code input data.

Parameter	Value	Units
Pressure Ratio (PR)	4.0	--
Mass flow rate ($\dot{m}$)	4.28	kg/s
Inlet Pressure (P01)	101.32	kPa
Inlet Temperature (T01)	288	K
Slip Factor (μ)	0.85	--
Impeller Efficiency (η_i)	84%	--
Stage Efficiency (η_s)	80%	--
Inlet Blade Angle (β_1)	-60	deg
Discharge Blade Angle (β_2)	-25	deg
Inlet Absolute Flow Angle (α_1)	0	deg
Discharge Abs. Flow Angle (α_2)	65	deg
Hub/Shroud Radius Ratio (υ)	0.28	--
Impeller Radius Ratio (r_{1s}/r_2)	0.5	--
Diffuser Diameter Ratio (D_5/D_6)	1.35	--
Exit Diffuser Mach Number (M_6)	0.33	--

Once the velocity triangles at the inlet and output are determined, the performance dimensionless parameters calculation is initiated. The code computes the non-dimensional parameters listed in Table 4. Finally the basic dimensions of the compressor are computed. The geometry obtained by the code is shown in Table 5.

Table 4. Non-dimensional parameters [9]

Parameter	Equation	
Incidence factor	$\lambda = \dfrac{\mu}{1-\tan\beta_2 / \tan\alpha_2}$	(1)
Impeller Speed	$\dfrac{U_2}{a_{01}} = \left[\dfrac{(PR)^{\frac{k-1}{k}}-1}{\eta_s \lambda (k-1)}\right]^{1/2}$	(2)
Flow Coefficient	$\varphi = \dfrac{\rho_1}{\rho_{01}}\left(\dfrac{r_{1s}}{r_2}\right)^2 (1-\upsilon^2)\dfrac{C_1}{a_{01}}\dfrac{a_{01}}{U_2}$	(3)
Mass Flow Parameter	$\theta = \varphi \dfrac{U_2}{a_{01}}$	(4)
Blade Loading Coefficient	$\psi = 2\lambda\eta_s$	(5)
Specific Speed	$N_s = \dfrac{(\pi\varphi)^{\frac{1}{2}}}{\left(\dfrac{\psi}{2}\right)^{\frac{3}{4}}}$	(6)
Power Coefficient	$\dot{W}_{ND} = \psi\theta\left(\dfrac{U_2}{a_{01}}\right)^2$	(7)

The results obtained were compared with experimental measurements. The differences obtained between the computed and the measurement data are shown in Table 6. The measurements were made by Krain [7] and the results calculated were determined by the one-dimensional code. Table 6 shows that these differences are reasonably small. The greatest differences show deviation below 4%. No information related to other parameters is presented once the author does not report any additional information.

Table 5. Basic compressor geometry

Parameter	Value	Units
Impeller		
Shroud radius	95.25	mm
Hub radius	26.67	mm
Inlet area	26270	mm^2
Discharge radius	190.51	mm
Blade height	10.84	mm
Axial length	95,25	mm
Discharge area	12970	mm^2
Blades number	19	----
Diffuser		
Inlet radius	209.56	mm
Discharge area	14270	mm^2
Discharge radius	282.90	mm
Blade length	143.00	mm
Blade spacing	93.55	mm
Blades number	19	----

Table 6. Basic impeller geometry

Parameter	Experiment	Code	Dev [%]
Hub Radius	35.4	35.5	0.28
Shroud Radius	91.7	92.0	0.36
Exit Radius	200.0	200.9	0.44
Rotation [rpm]	22360	22839	2.14
Exit Absolute Mach	0.96	0.92	3.89
Tangential Velocity	468.3	480.5	2.60

3.2. CFD simulation

A numerical CFD modeling was performed using ANSYS CFX® three-dimensional code [8], this applies the Finite Volume Method (FVM) technique to solve the Navier-Stokes equations. The CFD modeling was performed based on the values presented in Table 1.

The physic domain was conformed for two passages one for the rotor and another for stator.

The modeled domain of the whole stage was dissected by hexahedron structural multi-block grid topology. H-topology was used in the inlet, outlet and main flow passage domains. H grid used, provided good resolution at the leading and

trailing edge. The grids are refined at the near-wall, end wall, leading edge, and trailing edge of both the rotor and diffuser.

Preliminary simulations showed that the impeller inlet area could to restrict the required air flow, so it was build the geometry of the impeller with 10 passages; each passage of the rotor is composted for a blade and a splitter. The splitter has a 30% reduction by the leading edge. The computational mesh for both rotor and diffuser is shown in Fig. 2. The Fig. 2(a) show the rotor mesh composed of 79552 nodes and 69800 elements.

For stator a single blade passage was modeled. The blade is located in the center of the domain and nodes are buried in the width of the blade to improve resolution of the leading and trailing edges, and to reduce grid skewness in these regions. The computational mesh, shown in Fig. 2(b) consists of 103114 nodes and 92244 elements.

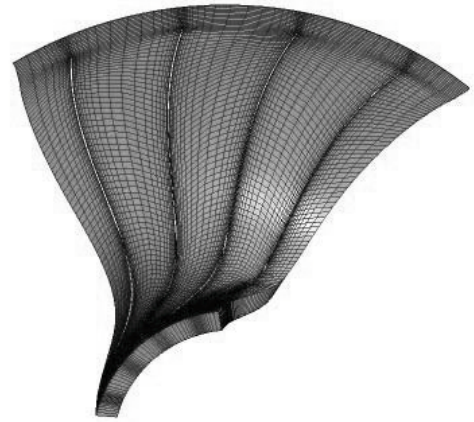

(a)

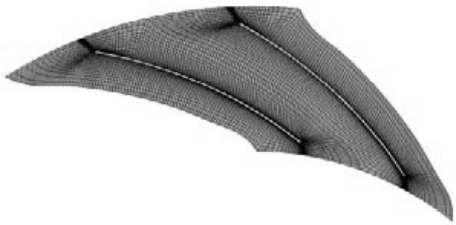

(b)

Fig. 2. Mesh section at 50% span: a) Rotor, b) Diffuser

The characteristics of the mesh generated for both the impeller and the diffuser are shown in Table 7. The dimensions used for the generation of the mesh required for the CFD simulation, were obtained from the data produced by the one-dimensional code. Fig. 3 shows the configuration of the geometry achieved for both the impeller and the diffuser.

Table 7. Mesh characteristics

Domain	Nodes	Elements
Impeller - R1	79 552	69 800
Diffuser - S1	103 114	92 244
All Domains	182 666	162 044

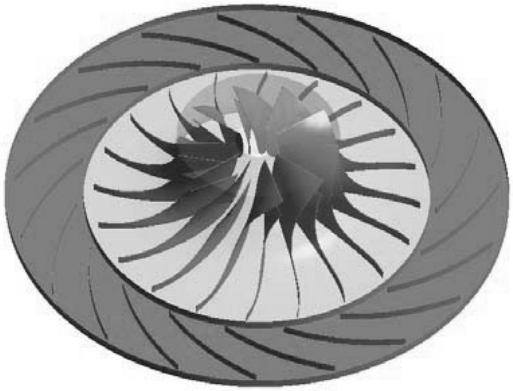

Fig. 3. CFD assemble impeller-diffuser.

A rotational domain with an angular velocity of 25149 rpm and a stationary domain for both the impeller and the diffuser respectively were used. A reference pressure of 101.32 kPa was setting up. The option for the heat transfer was Total Energy, which includes the high-speed energy effects. The turbulence model used was the k-ω based Shear-Stress-Transport (SST) model, whose superior performance has been demonstrated in several validation studies [9-11].

The rotor-stator interface was connected by a general grid connection interface using the Stage Frame Change Model.

The boundary conditions used was total pressure at inlet and static pressure at outlet. This combination was chosen in order to determine the system mass flow as part of the solution. Both boundary conditions at inlet and outlet were configured with subsonic flow regime. The relative pressure at inlet was set up in 0 kPa. The inlet total temperature was 288 K. The relative pressure at outlet was set up in 274.52 kPa. A summary of the main parameters used in the simulation is shown in Table 8.

Table 8. Boundary Parameters

Parameter	Value
Inlet	
Domain	R1
Flow direction	Normal to Boundary Condition
Flow regime	Subsonic
Heat transfer	Stat. frame total temp.
Stat. frame total temp.	288 [K]
Mass and momentum	Stat. Frame Total Pressure
Relative pressure	0 [kPa]
Turbulence:	Medium Intensity and Eddy Viscosity Ratio
Outlet	
Domain	S1
Flow regime	Subsonic
Mass and momentum	Average static pressure
Pressure profile blend	0.05
Relative pressure	274.52 [kPa]
Wall	
Domain	R1, S1
Location	Hub, Shroud, Blade
Heat transfer	Adiabatic
Mass and momentum	No slip wall
Wall roughness	Smooth wall
Interface	
Domain interface	R1 to S1
Interface type	Fluid-Fluid
Frame change	Stage
Mesh connection	General Grid Interface

Fig. 4 shows the compressor performance curve to the design speed achieved by CFD analysis; the design point for the projected one-dimensional code is also plotted.

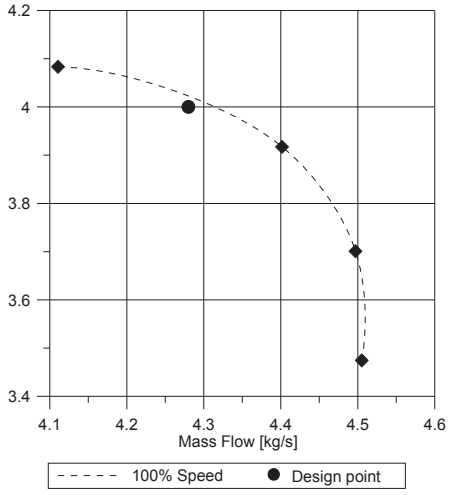

Fig. 4. CFD velocity curve of the centrifugal compressor at 100% speed

A comparison between the results obtained by the one-dimensional code and the CFD simulation is shown in Table 9.

Table 9. 1-D and CFD comparison results

		Parameter	CFD	Code	Dev [%]
Stage Performance		Mass flow rate	4,11	4.28	4.12
		Input power	780,4	752.2	3.61
		TPR	4,08	4.23	3.69
		TTR	1,69	1.61	4.72
		ηi	74,58	80.00	7.27
Impeller	Inlet	Static Pressure	89.84	89.84	0.00
		Total Pressure	101.3	101.3	0.00
		Static temperature	278.3	278.3	0.00
		Total temperature	288.1	288.0	0.03
		Absolute Mach	0.41	0.42	0.93
		Tangential velocity	228.6	250.9	9.75
		Absolute velocity	138.5	144.8	4.58
	Outlet	Static pressure	280.0	232.4	17.0
		Total pressure	512.4	429.0	16.3
		Static temperature	402.7	388.6	3.50
		Total temperature	486.6	463.0	4.87
		Absolute Mach	0.93	0.98	4.69
		Relative Mach	0.58	0.56	2.83
		Absolute velocity	377.2	386.5	2.48
Diffuser	Inlet	Absolute velocity	380.6	349.5	8.18
		Absolute Mach	0.94	0.88	6.32
		Flow angle	26.36	24.32	8.37
	Outlet	Absolute velocity	144.7	142.3	1.67
		Absolute mach	0.33	0.33	1.12
		Flow angle	33.78	35.19	4.01
		Static pressure	375.8	375.8	0.00
		Total pressure	413.6	405.3	2.07
		Static temperature	467.3	453.1	3.13
		Total temperature	486.1	463.0	4.99

4. Assessment of results

The one-dimensional code developed permits the calculation of the basic dimensions, the velocity triangles at the inlet and outlet, and the operating conditions of the two components, the impeller and the diffuser. The set of results obtained by this code was compared with both experimental measurements and CFD simulation. Results show that the discrepancies obtained are significantly lower, being those lesser than 4% when compared with experimental data, and lesser than 5%, in most parameters evaluated for comparison with the results obtained by CFD simulation. In the latter case, the greatest differences are found in the

output impeller pressure, which differs around 17%. Although these variations are significant these could be substantially reduced considering the calculation the different kind of compressor losses which is part of future work. Another reason for this difference is because the code developed ignores the effect of impeller-diffuser interface, and the area near at the interface impeller-diffuser is a highly unstable area.

The computational cost represents a significant difference; because the computational time required for the one-dimensional code is lesser than two seconds and the computational time spent for each simulation of the whole impeller-diffuser is about 10 hours. However, the aim of this paper is not to replace the use of CFD, but rather to serve as a tool to facilitate the design work, helping to define appropriate geometries that can subsequently be validated by CFD applications

Conclusions

The application of non-dimensional parameters, applied to the design of centrifugal compressors, facilitates the design tasks, generating reliable results in significantly less computation time.

The developed one-dimensional code constitutes a practical and reliable preliminary design tool for determining the basic configuration of centrifugal compressors.

The code was validated by means of values obtained through experimental measurements and through simulations based on CFD techniques and the results have shown good approximation.

The main contribution of this paper is to demonstrate that by the use of a simple code it is feasible to obtain fairly close results in comparison with those which can be obtained by laborious iterative processes such as those developed through the analysis using CFD techniques.

Nomenclature

A area, m^2
a speed of sound, m/s^2
b blade height, mm
C absolute velocity, m/s
CFD computational Fluid Dynamics
D diameter, m
DG distributed generation
GCS gate Cycle Software
k specific heat ratio
M mach number
$\dot{m}$ mass flow rate, kg/s
N_s specific speed
p pressure, kPa
P power, kW
PR pressure ratio
R gas constant, J/(kg k)
r radius, mm
T temperature, K
TPR total pressure ratio
TTR total temperature ratio
U tangential velocity, m/s
V relative velocity, m/s
FVM finite volume elements

Greek symbols

α flow angle
β blade angle
ϕ flow coefficient
η efficiency
λ incidence factor
μ slip factor
θ mass flow parameter
ρ density
υ hub/Shroud Radius Ratio
ψ blade loading coefficient

Subscripts and superscripts

0 Stagnation
1 Impeller inlet
2 Impeller discharge
5 Diffuser inlet
6 Diffuser exit
h Hub
i Impeller, input
m Meridian component
s Shroud, stage

References

[1] Chicco G, Mancarella P. Distributed multi-generation: A comprehensive view. Renewable and Sustainable Energy Reviews, Elsevier 2009;13:535–51.

[2] Pepermans G, Driesen J, Haeseldonckx D, Belmansc R, D'haeseleer W. Distributed generation: definition, benefits and issues. Energy Policy, Elsevier 2005;33:787–98.

[3] Strachan N, Farrell A. Emissions from distributed vs. centralized generation: The importance of system performance. Energy Policy 2006;34(17):2677-89.

[4] Borbely A-M, Kreider JF. Distributed Generation. The Power Paradigm for the New Millennium Florida, USA; 2001.

[5] Zobaa AF, Cecati CA. Comprehensive Review on Distributed Power Generation. International Symposium on Power Electronics, Electrical Drives, Automation and Motion 2006.

[6] El-Khattam W, Salama MMA. Distributed Generation Technologies, Definitions and Benefits. Electric Power System Research Elsevier 2004.

[7] Nascimento MAR, Venturini OJ, Lora ES, Sierra GA, Rodrigues LO, Carvalho HM, Moura NR. Cycle selection and compressor design of 600kw simple cycle gas turbine engine. ASME Turbo Expo 2008 2008.

[8] Silva Lora E, Nascimento MAR. Geração Termelétrica, Planejamento, projeto e operação. 2004.

[9] Compaq Computer Corporation. Compaq Visual Fortran. 2000.

[10] Energy Services. GATE CYCLE 5.51. 2005.

[11] Oliveira LM, Nascimento MAR, Menon GJ. The thermal impact of using syngas as fuel in the regenerator of regenerative gas turbine engine. Proceedings of ASME Turbo Expo 2009: Power for Land, Sea and Air 2009.

[12] Japikse D, Baines N. Diffuser Design Technology. Concepts ETI Inc, Vermont, USA 1998.

[13] Dixon SL. Fluid Mechanics and thermodynamics of turbo machinery. Elsevier 2003.

[14] Krain H. Test Case 2: Centrifugal Impeller, DLR. In: Group ETS, editor. Seminar and Workshop on 3D Turbo machinery Prediction II. Val d'Isère, France; 1994.

[15] Ansys inc. ANSYS CFX 12.0. 2009.

[16] Bardina JE, Huang PG, Coakley TJ. Turbulence Modeling Validation Testing and Development. NASA Technical Memorandum 110446 1997.

[17] Bardina JE, Huang PG, Coakley TJ. Turbulence Modeling Validation. AIAA Paper 97-2121 1997.

[18] Alencar HS, Nascimento MAR, Villanova H. Estudo Numérico termo-aerodinâmico para Câmaras de Combustão para Turbinas a Gás: Aplicação ao Caso da Micro turbina. Itajubá - Brasil: Universidade Federal de Itajubá - UNIFEI; 2007.

[19] Whitfield A, Baines NC. Design of radial turbo machines. Longman Scientific & technical; 1990.

Acknowledgments: The authors wish to thank the Petrobras Research and Development Center (CENPES), the Coordination of Improvement of Higher Education (CAPES), the National Council of Technological and Scientific Development (CNPq), and the Foundation for Research Support of Minas Gerais (FAPEMIG) for their collaboration and support in the development of this work..

CFD Simulation of Spray Ignition and Combustion in Like Diesel Conditions

Alvaro Delgado Mejía[a], Elkin I. Gutiérrez Velásquez[b], Luis Hernàndez Ariano[a]

[a] *Universidad de Antioquia, Medellín, Colombia*
[b] *Universidade Federal de Itajubá, Itajubá, MG, Brasil*

Abstract: A Numerical simulation of ignition and combustion process of n-heptane sprays, at like diesel engine conditions, were made using the OpenFOAM CFD (Computational Fluid Dynamics) code. The combustion chamber consisted in a cubic shaped mesh where an Eulerian – Lagrangian approach was carried out for the computations. In the study, a gas reaction scheme involving 56 species and 300 reactions was employed, other parameters such pressure injection, orifice diameter or injection rate were typical for a diesel engine, whereas parameters like ignition delay, flame lift-off and combustion temperature were considered in the analysis. The results were validated with some experimental data reported by Sandia National Laboratories, on a high pressure and high temperature constant volume vessel. The simulations indicate that CFD codes are a suitable tool for spray ignition, combustion, and even harmful emissions studies, although is evident a strong grid dependence.

Keywords: CFD, combustion, diesel, spray.

1. Introduction

Nowadays the manufacturers of internal combustion engines are facing a serious challenge with the emission restrictions, and for this reason it has been necessary to improve the mixture formation and combustion processes in order to reduce engine raw emissions and to optimize its performance and emission characteristics. For that reason, simulation of such processes are becoming more and more important in contrast to experimentation, because of their lower cost and the flexibility in changing operational conditions and because it allows to calculate the temporal and spatial behavior of main variables of the process. For this purpose, they have to be predictive in terms of combustion description and pollutant emissions. Nevertheless, the success of any simulation lays on the predictive capabilities and the reliability of the models adopted for the treatment of governing processes, these models including cavitation, fuel spray and break-up, auto-ignition, turbulent combustion and pollutant chemistry models [1]. In diesel engine combustion, these processes have a very complex heterogeneous as well as transient nature, which results in a big challenge to deal with.

2. Computational model

The simulation was carried out in a cubic shaped combustion chamber, Fig. 1, with the same dimensions of the Sandia constant volume vessel [2], and validated with the data currently available on its website, including reacting and non-reacting sprays in a constant volume chamber, at conditions that span or exceed those typically experienced in a diesel engine.

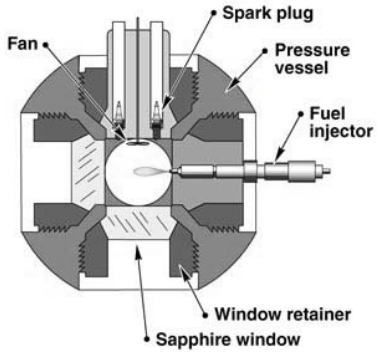

Fig. 1, Schematic cross - section view of the experimental combustion chamber [2]

The corresponding mesh model used for this study consisted of a 108 mm side cubic box, with approximately 250,000 cells. A previous study of

Corresponding Author: Alvaro Delgado Mejía, Email: adelgado@udea.edu.co

grid dependence was carried out, in order to determine the appropriated mesh size. Thus, four grids with 200,000 cells, 225,000 cells, 250,000 cells and 300,000 cells were simulated with a reactions scheme involving just one reaction and five species. The analysis allowed to conclude that from 250,000 cells, the results was practically the same, and for that reason that was the mesh density selected.

The conditions in which simulations were performed are listed in Table 1, and try to be representative of an ordinary diesel engine:

Table 1. Simulation parameters.

Parameter	Values	Units
Ambient O_2 concentration	21	%
Ambient gas temperature	800, 900, 1000	K
Ambient gas pressure	3.4, 3.8, 4.25	MPa
Ambient gas density	14.8	kg/m^3
Injector Orifice diameter	0.1	mm
Injection pressure	150	MPa
Fuel	n-heptane	----
Fuel temperature	373	K

Both, ambient temperature and injection pressure are feasible for a turbocharged diesel engine with a compression ratio about 18.

2.1. The CFD code

OpenFoam is a free, open source CFD software package to deal with complex fluid flows involving chemical reactions, turbulence and heat transfer. It has been written in the object oriented C++ programming language and uses finite volume numerics to solve systems of partial differential equations on any 3D unstructured mesh of polyhedral cells. The fluid flow solvers are developed within a robust, implicit, pressure-velocity, iterative solution framework, although alternative techniques are applied to other continuum mechanics solvers. Domain decomposition parallelism is fundamental to the design of OpenFOAM and integrated at a low level so that solvers can generally be developed without the need for any 'parallel-specific' coding [3]. For this work, the simulation was based on the case *aachenbomb* which is computed with the *dieselFoam* solver.

2.2. Model formulation

In diesel engines, both mixture formation and combustion process are simultaneous and with a strong dependence and interaction with each other, being the liquid atomization, the collision ant the secondary break up of fuel droplets, the energy, mass and momentum exchange, the most influencing phenomena. At the same time several chemical reactions take place allowing the auto ignition, the burnout of the premixed phase and the posterior diffusion combustion. Even with the best computational tools, the modeling of these processes is a demanding task.

Following a methodology where the numerical simulation of flow and mixture formation is a combination of the Eulerian approach for the gas-phase and the Lagrangian description for the droplet-phase, some submodels for the spray atomization and break up, droplet collision and evaporation, turbulence, ignition and combustion were implemented.

2.2.1 Spray

As In CFD simulation of diesel combustion, the predictive capabilities of the spray model play an important role, the spray model employed in this work was the wave break up model, proposed by Reitz [4-6] and has been widely applied in primary as well as in secondary break up models [7]. This model is based in the assumption that the growing of the instabilities of Kelvin – Helmoltz over the surface of a cylindrical liquid jet that penetrates into a stationary gas, is linear.

2.2.2 Auto ignition

In explosions of hydrogen and hydrocarbons – air mixtures, it has been observed that temperature increase take place after a certain induction time or ignition delay time, characterized for radical – chain explosions which are extremely temperature dependent [8].

The model adopted for simulating the auto ignition process was one of the most widely used, the so called Shell Model, developed originally by Halstead et al [9] in order to predict knock in spark ignition engines, but later adjusted and applied to modeling diesel ignition, as described in [10, 11]. The Shell ignition model involves eight reaction steps between five species that represents a virtual mechanism that attempts to reflect the actual ignition behavior of hydrocarbon air mixtures, including multistage ignition and cool flames. This model has been largely used in diesel fuel ignition

simulation by several authors [12-15] and even lately applied with soybean biodiesel blends [16].

2.2.3 Turbulence

There are numerous models formulated to describe the turbulent combustion, each one based on its own assumptions and leading to different levels of complexity and CPU time consumptions. Based on the RNG k–ε model, modified for consider the effect of compressibility and the interaction with the spray, and assuming a fast chemistry, the flame surface density model is able to provide accurate results for CPU times compatible with industrial applications.

2.2.4 Combustion

An appropriated combustion model must be capable to solve the flow equations and model the chemical reactions involved, requiring a coupling between CFD solver and the chemistry of the process. Thus, the mesh density and the level of detail for the chemistry scheme determine the CPU time consumption.

Such interactions were modeled by means of the Chalmers PaSR (partially stirred reactor model) model [17] which is based in the concept that each computational cell can be divided into a reacting zone, and a non reacting zone; the former is treated like a perfect stirred reactor, in which all present species are homogeneously mixed and reacted. After reactions, the species are assumed to be mixed due to turbulence for the mixing time τ_{mix} being this the final concentration in the entire and partially stirred cell. The chemical source term, f_m, in the species transport equation is approximated by [17]:

$$\frac{\partial \rho_m}{\partial t} + \nabla \cdot (\rho_m \mathrm{u}) = \nabla \cdot \left[\rho D \nabla \left(\frac{\rho_m}{\rho} \right) \right] + f_m + \dot{\rho}_m^s \delta_{ml} \quad (1)$$

Where ρ_m is the mass density of species m, ρ the total gaseous mass density, **u** the gas velocity, f_m is the Chemical source/sink term, and ρ_m^s the source due to evaporation of the liquid, although in this work only single component fuel were considered.

$$f_m = \kappa \frac{d[product]}{dt} = \kappa \left(-k_f [fuel]^c [oxididizer]^d \right) \quad (2)$$

Here, k_f is the forward reaction coefficient, calculated by means of an Arrhenius expression, c and d forward reaction order and κ is the reaction rate multiplier, defined as:

$$k_f = A T^b \exp\left(\frac{-E_a}{RT} \right) \quad (3)$$

$$\kappa = \frac{\tau_{chem}}{\tau_{mix} + \tau_{chem}} \quad (4)$$

Where A is the pre exponential factor, b temperature exponent, E_a activation energy, R the ideal gas constant, T the temperature, τ_{chem} is the chemical time, proportional to the inverse of k_f, τ_{mix} is the mixing time which is calculated according to:

$$\tau_{mix} = C_{mix} \frac{k}{\varepsilon} \quad (5)$$

Where C_{mix} is a model constant varying between 0.001 – 0.3, depending on the flow; k the turbulent kinetic energy and ε is the turbulent kinetic energy dissipation rate. In the present work the CFD solver assumes the Taylor timescales with C_{mix} = 0.03.

Additionally, for the simulations, a gas phase reaction scheme including 56 species and 300 reactions was considered.

3. Results and discussion

Next, the results of the CFD simulation are presented, first for the ignition and then for the lift-off and temperature evolution inside the vessel, compared in any case with the measurements.

3.1. Ignition

There are several criteria used to measure and define the ignition delay of sprays injected into high pressure, high temperature, and constant volume vessels, depending on which variables are chosen to model it, but the most common are the pressure rise, the temperature rise and the burnt fuel associated to ignition. Fig. 2 to 4 shows the CFD results for the pressure rise, compared with the corresponding experimental measurements, for the case in which ambient temperature vary from 800 to 1000 K and injection pressure is 150 bar.

After the injection there is a slight fall in the pressure and temperature inside the vessel, due mainly to the evaporation, but in a short interval of time, in the order of 1 ms, occurs a sudden increase due to the chemical reactions and allowing the auto ignition to take place. It is usual to assume that when such increase is positive, or

about 10 kPa, then ignition has occurred. In this context, it seems that the CFD simulations match very well the experimental delay time reported for the same conditions, as can be seen in Fig. 5, where the results of simulations and the corresponding measured data are summarized for all the cases studied.

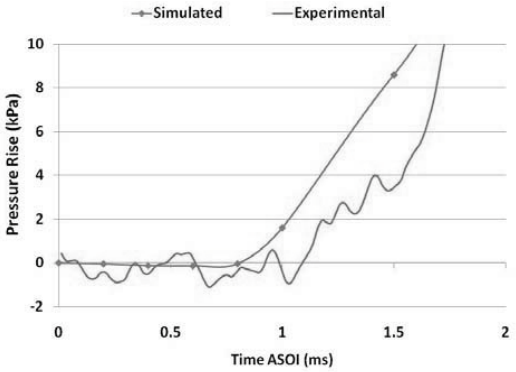

Fig. 2. Ambient pressure rise inside the vessel, for ambient temperature of 800 K

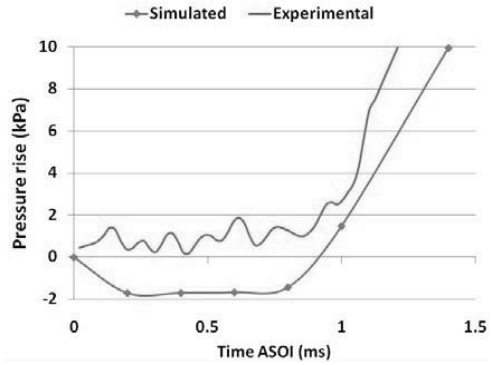

Fig. 3. Ambient pressure rise inside the vessel, for ambient temperature of 900 K

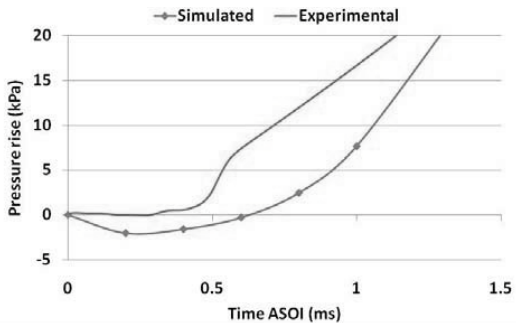

Fig. 4. Ambient pressure rise inside the vessel, for ambient temperature of 1000 K

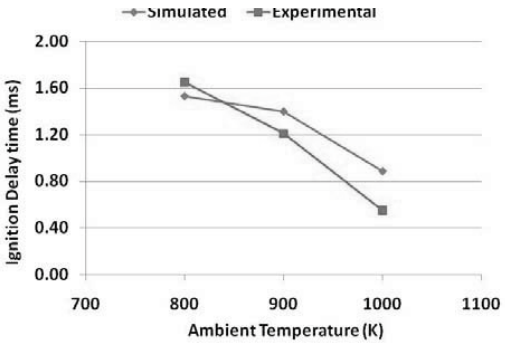

Fig. 5. Ignition Delay time for the simulation and the experimental results.

3.2. Flame lift – off length

When the vaporized fuel is mixed with air due to the effects of turbulence, then ignition occurs and the flame front develops, resulting in a flame lift-off or a separation from the injection location.

In the case of lift-off length, for the simulation conditions, the experimental results reported are in a good agreement. Understanding the lift-off as the axial distance from injector to location of high-temperature reaction, then from the simulation it can be established that this is achieved when OH concentration is significant, because it exists as an equilibrium product in regions of high temperature and results from chemical reactions in near-stoichiometric, high-heat-release regions [18]. Figure 6 shows the CFD result for the OH concentration in the interval from 2 to 2.4 ms, which gives a lift-off about 50 mm.

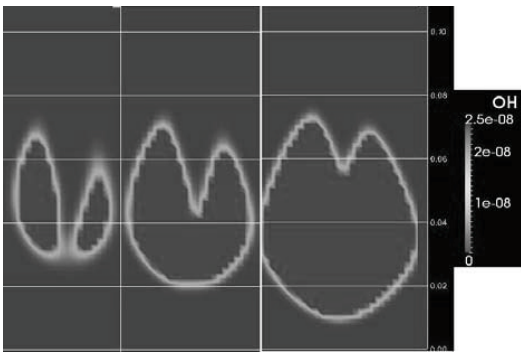

Fig. 6. Flame lift-off CFD simulation (ambient pressure = 800 K, injection pressure = 150 bar), based in the OH concentration.

In Fig 7, a comparison between CFD simulation and experimental data is presented, and it is clear

the good approximation of the CFD results compared with the experimental, despite of the limited gas phase reaction scheme used.

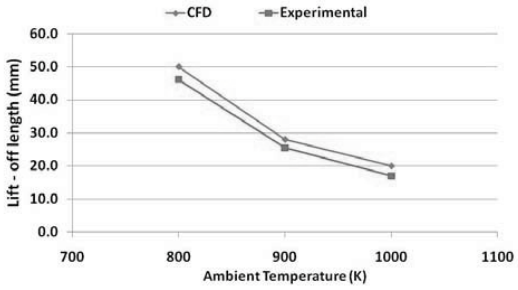

Fig. 7. Flame lift – off length for the simulation and the experimental results.

3.3. Temperature Evolution

A way to visualize flame formation and development is by means of the temporal temperature evolution, which is presented in Fig. 8, compared with the corresponding view of the chamber. It can be seen the great influence of turbulence on the flame propagation.

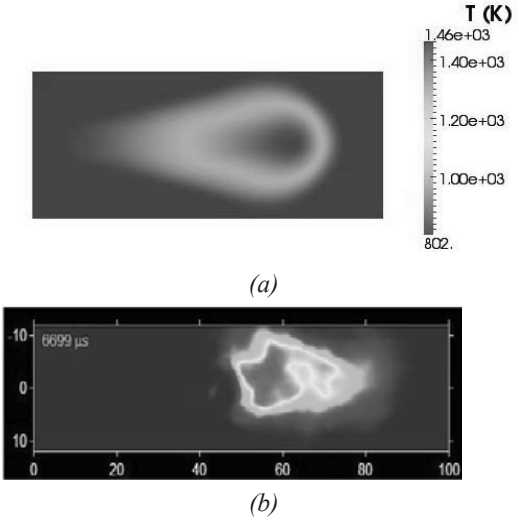

(a)

(b)

Fig. 8. Temperature profile for ambient temperature at 900 K: a) simulation (up in t = 6 ms), b) experimental (down in t = 6.7 ms)

4. Conclusions

Ignition and combustion process of n-heptane sprays, at like diesel engine conditions were simulated in the OpenFoam CFD code. The work focused in to determine the convenience of the models employed for the simulation, especially with the ignition and flame lift-off.

Although the results of the CFD simulation give coherent values, it is observed a little difference with measurement data, represented in a under prediction for both, ignition delay time and flame lift – off, by the simulation.

As many other works concerning combustion simulation, the modeling of turbulence is a serious challenge that must be improved.

It is necessary to perform additional simulations to establish a clear tendency about the ignition and flame lift-off phenomena, in order to establish a dependency with the injector orifice diameter or the injection pressure, for example.

Although a more detailed gas phase reaction scheme involving more species and reactions could give better results, the increase in computation time would be greater for just one processor.

Nevertheless, not only OpenFoam, but any CFD code, demonstrate the capabilities to simulate the combustion process.

References

[1] Shui L., et al. Validation and modification of wave spray model for diesel combustion simulation. Fuel 87 (2008) 3420–3427.

[2] Sandia National Laboratories. Engine Combustion Network (share.sandia.gov/ecn).

[3] OpenFoam User Guide. Version 1.6, March 2006.

[4] Reitz R.D. Modelling Atomization Process in High Pressure Vaporizing Sprays. Atomization and Spray Technology, Vol 3:309-337, 1987.

[5] Reitz R. D., Bracco F. V. Mechanism of Atomization of Liquid Jets. The Physics of Fluid, Vol 25, p1730-1742, 1982.

[6] Reitz R. D., Diwakar R. Effect of Drop Breakup on Fuel Sprays. SAE Paper 860469.

[7] Stiesch G. Modelling Engine Spray and Combustion Processes. Springer, Hannover, 2003.

[8] Warnatz J., Maas U., Dibble R. Combustion, physical and chemical fundamentals, modelling and simulation, experiments pollutant formation. Springer, 4th edition. Berlin, 2006.

[9] Halstead M., et al. The Autoignition of Hydrocarbon Fuels at High Temperature and Pressures – Fitting of a Mathematical Model. Combust Flame, Vol 30, pp 45-60, 1977.

[10] Kong S. C., et al. The Development and Application of a Diesel Ignition and Combustion Model for Multidimensional Engine Simulations. SAE Paper 950278.

[11] Sazhina E.M, et al. A Detailed Modelling of the Spray Ignition Process in Diesel Engines. Combust Sci and Tech, vol 160, pp 317-344, 2000.

[12] Theobald M.A., Cheng W.K. A Numerical Study of Diesel Ignition. Journal of the ASME. 87-FE-2, 1987.

[13] Griend V.L., et al. Modeling Combustion of Alternate Fuels in a DI Diesel Engine Using KIVA. Transactions of the ASAE 33(2):342-350. 1990.

[14] Kong, S.C., Reitz R.D. Multidimensional Modeling of Diesel Ignition and Combustion Using a Multi step Kinetics Model. Journal of Engineering for Gas Turbines and Power, 115:781-789, 1993.

[15] Hamosfakidis, C., Reitz R.D. Optimization of a hydrocarbon fuel ignition model for two single component surrogates of diesel fuel. Combustion and Flame. 132:433-450. 2003.

[16] Yuan W., et al. Computational Study of Biodiesel Ignition in a Direct Injection Engine. ASAE Meeting Presentation. Paper Number: 036035.

[17] Nordin N. Complex Chemistry Modelling of Diesel Spray Combustion. Doctoral Thesis, Chalmers University of Technology, Goteborg, 2001.

[18] Siebers D., Higgins B. Flame Lift-Off on Direct-Injection Diesel Sprays Under Quiescent Conditions. SAE Technical Paper 2001-01-0530.

Energy and Exergy Analysis of a residential SOFC-GT/Absorption Chiller system

Mehdi Hosseini, Masoud Ziabasharhagh

Porous Media Laboratory, Faculty of Mechanical Engineering, K.N. Toosi University of Technology, Tehran, Iran

Abstract: One of the greatest challenges in today's developing world is to develop efficient and low cost systems as well as low gas emission to supply energy demand of residential areas. It is very convenient to introduce a system, which has the ability to supply electricity and cooling demand of a building. Although, there are some well-developed combined heat and power (CHP) systems, e.g. gas turbine CHP, there is an increasing trend to use fuel cells as the main part of CHP systems, especially for residential applications. On the other hand Absorption Chillers have the ability to supply cooling demand using low grade waste heat. Thus, fuel cells are combined with absorption chillers, as CHP systems, to produce electricity and cooling load of a building or a residential area. In this paper, a parametric study of a Solid Oxide Fuel Cell/ Gas Turbine/CHP system is performed to investigate the effect of some major design and operational parameters on the system performance. Moreover, the effects of SOFC stack temperature, compressor pressure ratio, and absorption chiller design parameters on the first and second laws of thermodynamics are investigated. Results show that SOFC Stack Temperature has a significant and direct effect on the CHP system overall efficiencies. Moreover, compression pressure ratio increases net power output, but the overall efficiency of the system decreases.

Keywords: Solid oxide fuel cell, hybrid CHP system, absorption chiller, energy and exergy analysis.

1. Introduction

Energy management and reducing carbon dioxide emission rate are two major concerns in today developing world. A great portion of world's energy consumption is produced by power generation for residential areas, which also release a substantial amount of carbon dioxide into the atmosphere. Many researchers and energy engineers are working on developing new electricity generation systems with high efficiency and low emission characteristics. Among them Solid Oxide Fuel Cell (SOFC) seems to have a great chance in dominating the world's future power generation market. SOFCs generate electricity based on electrochemical reactions, and have the capability to use a diverse range of fuels, e.g. natural gas, ethanol, biogas, pure hydrogen, etc. Moreover, SOFCs' outlet gas temperature is high enough to be used in a hybrid or combined cycle to produce more power or heat energy. Indeed, SOFCs' stack outlet temperature is typically about 1000 ˚C. Therefore, in many manufactured plants, the SOFC flue gas enters to a micro gas turbine (MGT) to generate electricity. Many researchers work on SOFC-MGT systems to study the hybrid system performance under different operational conditions. Chan et.al [1] presented a model for simple SOFC-Gas Turbine hybrid systems. They studied the effect of operating pressure and SOFC fuel consumption on the performance of the components and overall systems. Motahar and Alemrajabi [2] performed an exergy analysis for a SOFC and steam injected gas turbine hybrid power system. Hot gas turbine exhaust gases is directed to a heat recovery steam generator to produce steam and inject it into the gas turbine. Exergy values and efficiencies are calculated for each component. The components with the highest proportion of irreversibility in the hybrid system are identified and compared. A parametric study is also performed for different values of compression pressure ratio, current density and pinch point temperature difference in the heat recovery steam generator. Thermo-Economic optimization of a Solid Oxide Fuel Cell, Gas Turbine hybrid system by Autissier [3] is another example of previous works on SOFC-GT modeling. In this paper, a systematic method to select a design according to user specifications is presented. The optimization is based on the multi-objective approach, and a thermo-economic approach is then used to compute the integrated system performances, size, and cost. Besides the researches on Solid Oxide Fuel Cell-Gas Turbine hybrid systems, some researchers have worked on

Corresponding Author: Mehdi Hosseini, Email: Mehdi.m.hosseini@gmail.com

the integration of SOFC in a combined heat and power (CHP) system. This CHP system provides heat and power for a consumer simultaneously. Akkaya [4] et al. performed an analysis of SOFC-GT/CHP systems based on exergy analysis. Detailed exergy calculation for each component and investigating the performance response of the system to the design and operation parameters are among the main parts of the work. Their model consists of a SOFC module, a gas turbine, and a heat recovery steam generator (HRSG) which provides steam for the CHP consumer. Hawkes [5] et al. studied SOFC micro CHP systems to provide electricity and heat for a residential area. Different heat demand profiles for a typical UK residential dwelling are considered along with a detailed model of SOFC based micro-CHP technical characteristics. Economic and environmental outcomes are modeled for each heat demand profile.

The SOFC-CHP addresses a high efficiency system that reduces heat loss and carbon emission to the atmosphere. It also eliminates the consumer dependence on the electricity grid. The development of such systems relies vigorously on the solid oxide fuel cell development both from engineering and economical aspects. In addition, the exact behavior of SOFCs in a CHP system should be addressed. This requires studying different configurations and possibilities for using fuel cells in a combined heat and power system. Velumani [6] et al. proposed a hybrid SOFC/micro gas turbine/ Absorption Chiller in order to provide electricity and cooling demand of a residential area. They proposed a model to provide up to 230 kWe and 55 kW cooling media for a building and the hybrid CHP system parameters were determined. However, the effect of SOFC/GT/Absorption design and operation parameters on the system performance has not been carrying out. In this paper, a detailed thermodynamic analysis is performed for a SOFC/MGT/Absorption Chiller system to investigate its performance behavior. Therefore, the effect of SOFC inlet air pressure (compressor pressure), SOFC stack temperature and absorption chiller design parameters are investigated.

2. SOFC/Micro GT/Absorption chiller hybrid CHP system

The SOFC/MGT schematic is shown in Fig. 1. The SOFC module is fed by natural gas (CH_4) and serves the main power generation system. CH_4 is reformed to hydrogen and carbon dioxide in the anode side of the SOFC. The produced hydrogen then goes to an electrochemical reaction with oxygen ions in the anode. This electrochemical reaction forms electrons, which serve as the electricity in an external circuit.

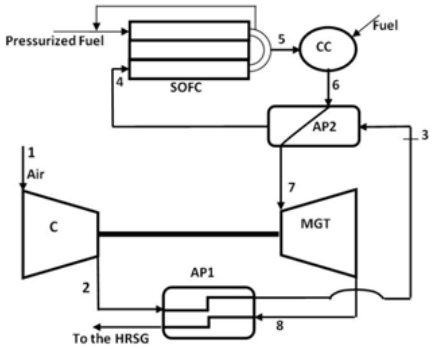

Fig.1. SOFC/micro gas turbine flow diagram

The oxygen ions are formed in the cathode side of the fuel cell. In SOFCs ambient air serves as oxygen source. The product gases leave anode at a temperature about 1000 ˚C, and are fed to the combustion chamber, where they go through a combustion process with the cathode excess air. To control the micro gas turbine inlet temperature, a precise amount of fuel is fed to the combustion chamber, too. The combustion gases then enter the micro gas turbine and perform work. Gas turbine flue gas still has a lot of energy to be recovered, since its temperature is somehow 600 ˚C. Therefore, the MGT flue gas is used to preheat the SOFC inlet air, and to produce saturated steam in the HRSG. The HRSG outlet steam enters the Absorption Chiller in order to provide space cooling.

Absorption cooling is a well-known technology that utilizes low value heat for chilled water production. In absorption chillers the refrigerant is water and the working fluid is usually Lithium Bromide water solution, therefore; there is no environmental concern about releasing CFCs to the atmosphere. Absorption chillers are manufactured in single, double, and triple effect configurations. The single effect absorption chiller schematic is shown in Fig. 2. In the evaporator (9-10), water evaporates in low pressure environment and takes heat from chilled water in heat exchange pipe. In the absorber, LiBr solution absorbs steam

coming from the evaporator. The absorption yields the condensation heat and dilutes the solution. So, the absorber is cooled by cooling water, and its solution (1) is pumped up (2) to the heat exchanger and then to the generator (3). In the generator, the solution is heated by heating steam from HRSG so that the solution boils to remove some of its water (7). Then the solution becomes concentrated and returns to the absorber (4). In the condenser, the steam from the generator is condensed to water (8), so the latent heat is released. The condenser is cooled by cooling water.

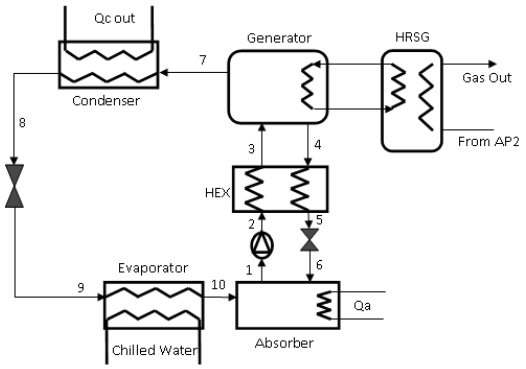

Fig.2. Absorption chiller schematic

2. Thermodynamic modeling

The analysis is performed based on the first and second law steady-state analysis. The detailed thermodynamic model is based on the works by [1], [2], [4], and [7]. A brief review of the SOFC/MGT/Absorption Chiller is presented here.

2.1. SOFC

Thermodynamic modeling of solid oxide fuel cell is a well-performed scientific procedure.

The electrochemical reactions in the SOFC are as follow:

Reforming:

$$CH_4 + H_2O \rightarrow CO + 3H_2 \quad (1)$$

Shifting:

$$CO + H_2O \leftrightarrow H_2 + CO_2 \quad (2)$$

Overall anode-cathode reaction:

$$H_2 + \frac{1}{2}O_2 \rightarrow H_2O \quad (3)$$

Cell voltage is modeled according to Eq. 4:

$$V_c = V_N - (V_{ohm} - V_{act} - V_{conc}) \quad (4)$$

In Eq. 4, VN is the Nernst Voltage, and is related to reacting components' Gibbs free energy, and their partial pressure. The second term on the right hand side of Eq. 4 in the parentheses is the sum of voltage losses in the fuel cell due to irreversibilities comprising Ohmic, Activation, and Concentration polarizations, respectively.

The equilibrium constants of reforming and shifting reactions are temperature dependent and can be obtained from the following equations [1-2, 4]:

$$log\ K_P = AT^4 + BT^3 + CT^2 + DT + E \quad (5)$$

The constants in Eq. 5 are listed in Table. 1

Table 1: Values of equilibrium constants of reforming and shifting processes

	Reforming	Shifting
A	-2.63121×10^{-11}	5.47301×10^{-12}
B	1.24065×10^{-7}	-2.57479×10^{-8}
C	-2.25232×10^{-4}	4.63742×10^{-5}
D	1.95028×10^{-1}	-3.91500×10^{-2}
E	-6.61395×10^{1}	1.32097×10^{1}

When the temperature is known, the equilibrium constants can be calculated from Eq. 5, and the reactant molar components are determined by solving Eqs. 6-7:

$$K_{pr} = \frac{P_{H_2}^3 P_{CO}}{P_{CH_4} P_{H_2O}} \quad (6)$$

$$K_{ps} = \frac{P_{H_2} P_{CO_2}}{P_{CO_2} P_{H_2O}} \quad (7)$$

SOFCs are manufactured in stacks, and each stack is made of series of single cells. The cell's specifications are based on the Siemens Tubular Solid Oxide Fuel Cells with 834 cm^2 active area, and up to 0.35 A/cm^2 current density.

The SOFC power output is:

$$W_{SOFC} = i \times V_c \times N_{SOFC} \times A \quad (8)$$

Having known the electrochemical reacting molar components, one can calculate SOFC power and outlet gas composition. Therefore, the composition of the SOFC stack flue gas which enters the combustion chamber of the gas turbine is precisely determined. As shown in Fig.1 a part of anode gases is re-circulated for methane reforming.

2.2. Micro Gas Turbine

Thermodynamic modeling of MGT and air compressor is related to compressor pressure ratio, and MGT and compressor isentropic efficiencies.

Air compressor outlet temperature

$$T_{oc} = T_{ic}\left\{1+\frac{1}{\eta_c}\left(rc^{\frac{\gamma_a-1}{\gamma_a}}-1\right)\right\} \quad (9)$$

Micro gas turbine outlet temperature

$$T_{oMGT} = T_{TIT}\left\{1-\eta_{MGT}\left(1-\left[\frac{P_{in}}{P_{out}}\right]^{\frac{\gamma_g-1}{\gamma_g}}\right)\right\} \quad (10)$$

In the combustion chamber, the fuel cell stack flue gas and supplementary fuel react. Molar flow rate of gases at the outlet at the specified MGT inlet temperature can be determined using the combustion energy balance.

Finally, the SOFC-MGT net power output is calculated:

$$W_{net} = W_{SOFC} \times \eta_{conv} + W_{MGT} - W_c - W_{FuelC} \quad (11)$$

In which η_{conv} is DC/AC power converter.

2.3. Absorption chiller

Gas turbine outlet flue gas enters the heat recovery steam generator, and saturated steam is produced. The produced steam mass flow rate depends on the flue gas temperature and mass flow rate, and the HRSG pressure. The thermodynamic model for absorption chiller is based on the model presented by Sencan [7].

In modeling the SOFC-MGT, the thermodynamic reference state is ambient air at T=35˚C and 1 bar atmospheric pressure for summer seasons, and T=10˚C for winter seasons. The reference state for LiBr solution in the absorption chiller is pure water at T=35˚C.

3. SOFC/MGT/Absorption chiller performance Analysis

Knowing how the design and operation parameters affect the SOFC/MGT/Absorption chiller CHP system is important in development and implementation of the systems in the residential areas.

To study such behaviors a computer code is developed based on the mathematical model as mentioned briefly in the previous sections. The basic input data to the computer code are presented in table 2. As these data determine the hybrid CHP system performance specifications, one can study the performance changes by changing any of them. It has much more sense to only study the effect of some major parameters like compressor pressure ration, SOFC stake temperature, MGT inlet temperature (TIT), and absorption design parameters, e.g. LiBr solution concentration and generator temperature.

Table 2: the simulation input data

SOFC	
Air Compressor Polytropic Efficiency	87%
Fuel Compressor Isentropic Efficiency	87%
Stack Outlet Temperature, ˚C	1000
Activation Area, cm^2	834
Cell Current Density, A/cm^2	0.35
Fuel Utilization	0.85
Compressor Pressure Ratio, rc	8
AP1 outlet temperature (Point 3), ˚C	527
Micro Gas Turbine	
MGT isentropic efficiency	0.83
TIT, ˚C	1127.15
Heat Recovery Steam Generator	
Pinch Point temperature difference	10
Absorption Chiller	
Generator Temperature, T_4	90
Evaporator Temperature	8
Weak Solution Concentration, x_3	56
Strong Solution Concentration, x_4	60
Weak solution temperature, T_3	60

3.1. Effect of Compressor Pressure Ratio

The effect of compressor pressure ratio on the system performance is presented here. Figure 3 shows that SOFC output power increases with pressure ratio. In order to maintain pressure balance in the SOFC stack, the pressure at both anode and cathode sides must be equal. Therefore; by increasing SOFC inlet air pressure the pressure of the inlet fuel must be increased, too. Since fuel cell voltage increases with fuel pressure [8] any increase in the compressor pressure ratio results in increase in the SOFC stack power output.

It is a familiar trend in gas turbines that the turbine power has a maximum amount while increasing the pressure ratio. Also, Fig. 5 shows that the system net power output has a maximum value. This occurs because of the GT behavior. Now the effect of pressure ratio on the overall hybrid CHP system and absorption chiller cooling load is studied. Fuel cell operational pressure has a great influence on the voltage losses, which cause the stack to heat up.

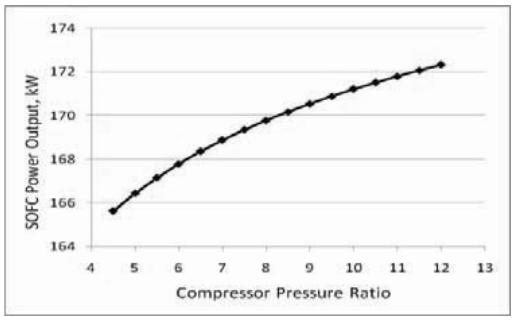

Fig.3. Effect of compressor pressure ratio on the SOFC power output

Micro turbine power output changes due to changes in the pressure ratio, and is illustrated in Fig. 4.

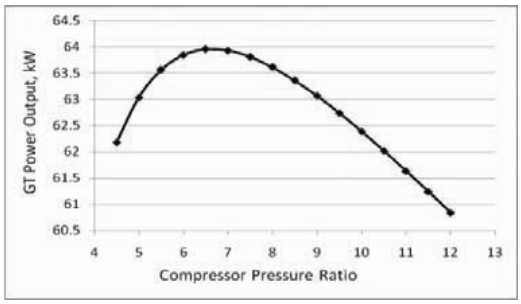

Fig.4. Effect of compressor pressure ratio on the MGT power output

In order to cool down the SOFC stack and control its temperature, excess air is provided, acting as cooling media. Increasing the stack pressure, results in less voltage overpotentials [9], therefore; the required excess air flow rate decreases. This is shown in Fig. 6. Since the inlet fuel mass flow rate to the fuel cell is constant, the stack outlet flow decreases. This leads to lower GT flue gas, and lower HRSG input energy. Therefore, the HRSG product steam decreases, which means less input energy to the generator of the absorption chiller.

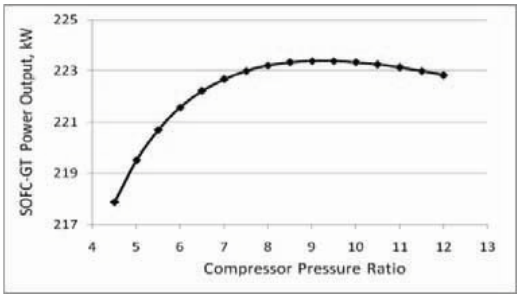

Fig.5. Effect of compressor pressure ratio on the SOFC/MGT power output

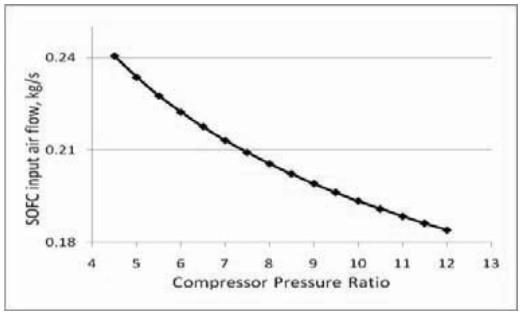

Fig.6. Effect of compressor pressure ratio on the SOFC inlet air

The COP of a single effect absorption chiller depends only on the evaporator and generator energy loads, and is constant since the generator and the evaporator temperatures are assumed to be constant. Therefore as the generator inlet energy decreases the evaporator cooling loads decreases in the same manner (Fig. 7).

The SOFC/MGT/Absorption Chiller first and second laws efficiencies are calculated according to the system net power output, absorption chiller cooling load, and hybrid system fuel consumption. This is formulated in equations 12 and 13.

In which Ex_{eva} is exergy value of the absorption chiller evaporator. The product of the chiller is

cooling, and its exergy is obtained according to equation 14:

The efficiencies are calculated based on fuel lower heating value (LHV) and for methane LHV=50050 kJ/kg.

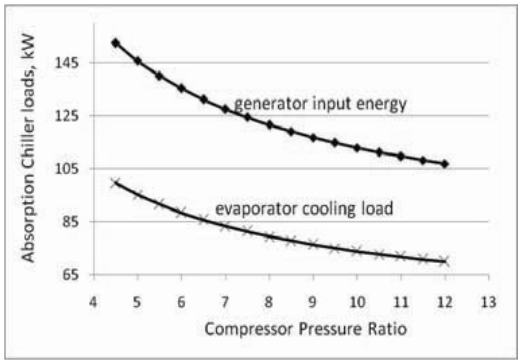

Fig.7. Effect of compressor pressure ratio on the absorption chiller generator and evaporator loads

Since there is a slight change in the system net = Ơ = 63 C 3 1 3 1 3 change significantly (Fig. 8). The decrease in the first law efficiency is due to the significant decrease in the absorption chiller cooling load. The exergy efficiency increase is due to the decrease in fuel cell air flow, which has led to the decrease in mass flows in the other components, e.g. GT and HRSG. A parameter that affects exergy efficiency is exergy destruction. Indeed by decreasing exergy destruction, the system exergy efficiency is increased. In a hybrid system, usually the most amount of exergy destruction is in processes which correspond to chemical reactions like in combustion chambers. Lower flow rate of chemical reactants (fuel + air) results in lower value of exergy destruction in the system.

3.2. Effect of SOFC Stack Temperature

The SOFC stack temperature increases the net power output as is shown in Fig. 9. Temperature has direct effect on SOFC voltage output. Thus, temperature increment causes increase in voltage, and this results in generation of more heat in the SOFC stack. To prevent the stack to heat up, the amount of the excess air to the system must be increased. Therefore, the system air flow rate is increased due to the increase in stack temperature. It also increases the required air flow rate to the stack. Therefore, absorption chiller cooling load increases due to the increased inlet steam to the generator. These changes result in increase in first and second laws efficiencies, Fig. 10.

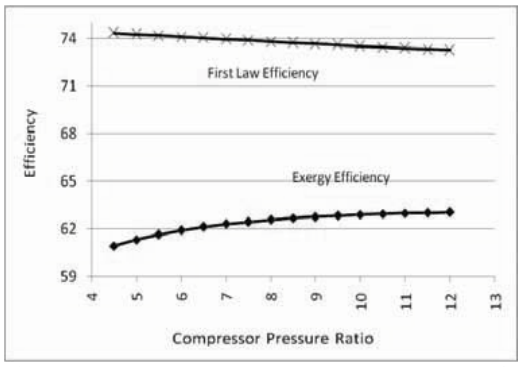

Fig.8. Effect of compressor pressure ratio on the SOFC/MGT/Absorption Chiller efficiencies

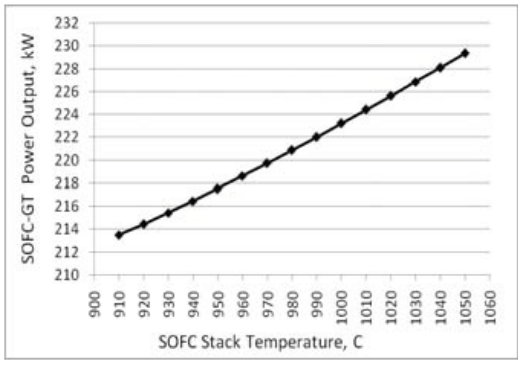

Fig.9. Effect of SOFC stack temperature on the net power output

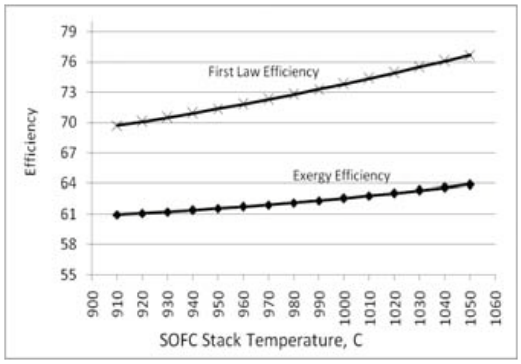

Fig.10. Effect of SOFC stack temperature on the overall efficiencies

3.3. Effect of Absorption Chiller Design Parameters

In a residential area, a great portion of energy consumption is for cooling, and it is of the hybrid CHP duty to provide such a demand. The single effect absorption chiller that is modeled in this paper supplies only a part of the cooling demand, since it only uses the recovered heat from the SOFC/MGT power system. Thus it is the 3 3 163 C 3 3 3 63 0 = chiller design parameters, so that maximum cooling load will be achieved. This will definitely increases the hybrid CHP efficiency, and reduces the global pollution by avoiding the need for fuel to provide cooling.

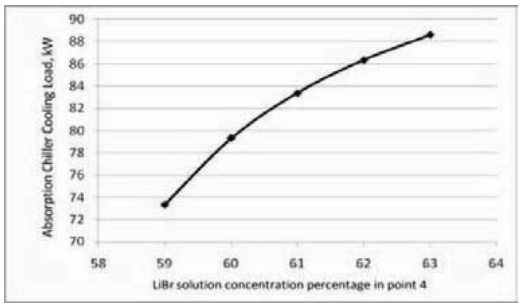

Fig.11. Effect of the LiBr solution concentration at generator outlet on the evaporator cooling effect, x_3=56%

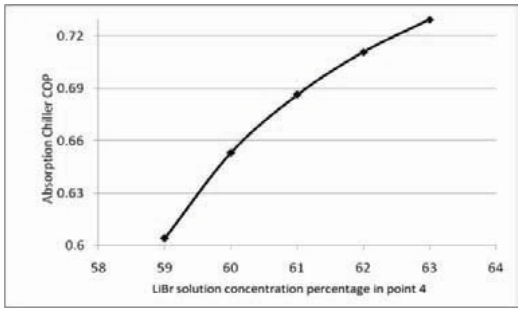

Fig.12. Effect of the LiBr solution concentration at generator outlet on the chiller COP, x_3=56%

Absorption chillers use the concentration changes between the generator and the absorber instead of a compressor, which is used in compression chillers. The concentration difference in the system affects the chiller performance and chilled water production rate. Figure 11 shows that by increasing the Lithium Bromide solution concentration difference (x_4-x_3) the evaporator cooling load increases. As the generator input energy is constant, the chiller Coefficient of Performance increases, too (Fig. 12).

It seems that increasing the difference between the LiBr solution concentrations entering and exiting the generator increases the chiller COP, but further increase results in salt crystallization, which prevents the system from proper working. The prescribe trend increases the first law efficiency as in Fig. 13.

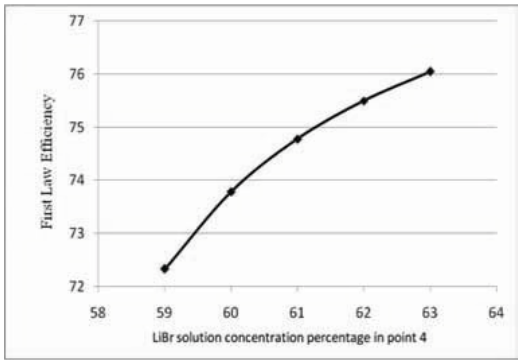

Fig. 13: Effect of the LiBr solution concentration at generator outlet on the overall system first law efficiency, x3=56%

4. Conclusion

In this paper and energy and exergy balance of a hybrid CHP system was performed. The system consists of a solid oxide fuel cell, a micro gas turbine, and a single effect absorption chiller. The SOFC/MGT provides electricity for a residential area, and the absorption chiller is used to provide a portion of its cooling demand. The analysis showed that air compressor pressure ratio increases the SOFC/MGT net power output, while the absorption chiller cooling load decreases. The decrease is due to the decrease in the overall gas flow in the micro turbine and in the heat recovery steam generator. However, exergy efficiency increases because of the decrease in the system overall gas flow.

In addition, the SOFC stack temperature has a favorable effect on the system performance, with increasing net power output, cooling provision, and system efficiencies.

In the last section the effect of the Lithium Bromide concentration in the absorption chiller on the cooling provision of the evaporator was investigated.

The results here indicate that for choosing the proper system design points, one should perform economical analysis for the hybrid system. Moreover, exergo-economic multi-objective optimization is required.

Nomenclature

V	fuel cell voltage, (V)
K	reaction equilibrium constant
T	temperature, K
T_0	environment temperature = 308, K
P	pressure, bar
W	work, kW
i	fuel cell current density, A/cm^2
N	number of cells in the SOFC stack
A	cell active area, cm2
$AP1$	air pre-heater No. 1
$AP2$	air pre-heater No. 2
rc	compressor pressure ratio
MGT	micro gas turbine
Ex	exergy value, kW
CC	combustion chamber

Greek symbols

η	efficiency
γ	specific heat capacities ratio

Subscripts

c	compressor
MGT	micro gas turbine
$SOFC$	solid oxide fuel cell
TIT	turbine inlet temperature
oMGT	micro gas turbine outlet
FuelC	fuel compressor
a	air
g	gas
oc	compressor outlet
ic	compressor inlet
in	turbine inlet
out	turbine outlet
FL	first law
SL	second law
eva	evaporator

References

[1]. Chan S.H., Ho H.K., Tia Y., 2002, Modelling of simple hybrid solid oxide fuel cell and gas turbine power plant, Journal of Power Sources, 109, pp. 111-120.

[2]. Motahar S., Alemrajabi A. A., 2009, Exergy based performance analysis of a solid oxide fuel cell and steam injected gas turbine hybrid power system, International Journal of Hydrogen Energy, 34(5), pp. 2396-2407

[3]. Autissier N. et al., 2007, Thermo-Economic Optimization of a Solid Oxide Fuel Cell, Gas Turbine Hybrid System, Journal of Fuel Cell Science and Technology, 4, pp. 123.

[4]. Akkaya A. V. et al., 2008, An analysis of SOFC/GT CHP system based on exergetic performance criteria, International Journal of Hydrogen Energy, 33, pp. 2566-2577.

[5]. Hawkes A.D. et al., 2007, Solid oxide fuel cell micro combined heat and power system operating strategy: Options for provision of residential space and water heating, 164, pp. 260-271.

[6]. Velumani S. et al., 2009, Proposal of a hybrid CHP system: SOFC/microturbine/absorption chiller, Int. J of Energy Research, pp.

[7]. Sencan A. et al., Exergy analysis of lithium bromide/water absorption systems, 30, pp. 645-657.

[8]. James Larminie, Andrew Dicks, 2003, Fuel Cell Systems Explained, 2nd edition, John Wiley & Sons Ltd, England, chapter 7.

[9]. Mark C. Williams, 2004, Fuel Cell handbook, 7th edition, DOE, Chapter 7.

Using Exergetic Analysis to Assess Environmental Impact of Diesel Spilled In Soil

S.E. Díaz-Méndez [a], A. Hernández-Guerrero [b], J.M. Rodríguez-Lelis [c]

[a] *Department of Mechanical Engineering, Autonomous University of Carmen, Calle 56 # 4, C.P. 24180, Ciudad del Carmen, Campeche, Mexico.*
[b] *Mechanical Engineering Department, University of Guanajuato, Apartado Postal 215A, C.P. 36730, Salamanca, Guanajuato, Mexico.*
[c] *Mechanical Engineering Department, National Center for Research and Technical Development (CENIDET), Interior Internado Palmira S/N, C.P. 62490, Cuernavaca, Morelos, Mexico.*

Abstract: Gauging accurately the impact of society on the environment has become one of the most important goals around the world. A number of attempts can be found in the literature where a set of indicators to assess and manage the beneficial and detrimental effects of human activities on air, water, land, energy use, and waste production are proposed; these attempts are aimed to measure its progress and set targets for future legislation, control and economic policies on human activities.}A general environmental impact indicator, as those authors describe, should be based on quantitative terms to enable to estimate the harmful effects of industrial operations. Exergetic analysis, specially exergy destruction or lost work is a concept that contains the elements that permit its use as a measure of reduction and excessive consumption of resources. The environmental impact index, proposed EII_{LW}, has the capability to identify sustainability and how far is the ecosystem from this condition. Low and high limits could be set, where the system can operate sustainably, and setting these as a base line, and the larger the environmental impact index, the closest to destruction the system will be. An application of the environmental impact index to diesel spilled in soil and how it affects the plant growth rate is showed. The results confirm a separation from the base line, and it defines the amount of exergy that can not be stored by the plant.

Keywords: Environment Impact Index, Lost Work, Exergy Destruction.

1. Introduction

When the human being interacts with its environment, by sending or extracting materials to or from ecosystems, he tends to break the equilibrium that exist between the flows of mass and energy in the ecosystem (it happens when there is overflowing or over extracting of goods and reducing the ability of the ecosystem to transform those goods, impeding to continue the sustainable cycle). As the ecosystem reduces its capacity to transform energy and mass, humans will experience the same unavailability, caused by the consumption of those goods that he throws or overexploits.

In this sense, gauging accurately the impact from society on the environment has become one of the most important goals around the world. A number of attempts, that trying to use the concept of exergy, can be found in the literature where a set of indicators to assess and manage the beneficial and detrimental effects of human activities on air, water, land, energy use, and waste production are proposed [1-10]. These indicators are aimed to evaluate its progress and set targets for future legislation, control and economic policies on human activities. Among of them, Rosen [1] has mentioned that the exergy, in the unrestricted waste emissions, has the potential to impact on the environment. His proposal is based on the fact that there is disequilibrium between the elements of the emissions and the elements in the environment. Also, Sciubba [11] has mentioned that the accepted meta-paradigm for the assessment of the state of the environment is: (a) environmental scientists, engineers, physicists, chemists and biologists have the role of defining, troubleshooting and calibrating a proper set of "decision parameters", called ecological indicators (EI); and (b) National & International Agencies use these EI in their evaluations.

Thus a general environmental impact indicator should be based on quantitative terms, able to estimate the harmful effects of industrial operations. Exergy destruction or lost work is a

concept that contains the elements that permits measure of reduction and excessive consumption of resources. Also, it quote the following that has been observed and described by Jorgensen [12]: an ecosystem takes up all matter (nutrients) necessary for it from its environment; it gets free energy from solar energy and organic food, and returns matter producing entropy. In the process, organisms permanently dissipate the energy in order to maintain their structures (which might be called dissipative), to develop and to evolve. Hence, the access to free energy is a central problem of existence for any living organism.

The struggle for life is first of all a struggle for free energy. Thus, it may be argued, that if the ecosystem is represented by a thermodynamic system, the same principles apply, and the difference to other studies is based on how the available energy and entropy is evaluated, and if they are chemical, magnetical, a heat sink or a source, etc. Thus, in this work the concept of exergy is used (mainly exergy destruction or lost work) as the capability to identify sustainability and how far is the ecosystem from this condition. Low and high limits could be set, where the system can operate sustainably, and setting these as a base line, and the larger the environmental impact index, the closest to destruction the system will be. On the other hand, the same separation from the base line defines the amount of exergy required to revert the contamination plus the amount of exergy required from the same irreversibilities of the reversion process. In this work a simple study of exergy destruction or lost work was carried out; diesel representing oil was spilled in soil to see how it affects the plant growth, then the exergy that can not be stored by the same plant is analyzed.

2. Soil polluted with diesel affecting plant growth rate

A plant was contaminated with diesel, and then the effect on the plant growth rate was appreciated qualitatively as shown in Figure 1. The soil was polluted with 25 ml of diesel and another plant was used as a control, the soil around it without diesel; both plants received 30 ml of water each day during three months. It can be appreciated that one plant is smaller than the other one, because it was affected by the diesel. The plant polluted with diesel will be mentioned as *Polluted Plant*, the other one as *Control Plant* to avoid confusion.

Figure 1. Left, Control Plant, and Right, Polluted Plant with 15 ml of diesel.

Then the plants, one at a time, were introduced in an small cubic chamber of 0.027 m^3, made with polystyrene to simulate an adiabatic chamber; a common incandescent light bulb of 1 W was used as a light source to provide energy to the plant, it was controlled to offer only 0.0155 W; a thermocouple was used to measure the temperature of the air inside the chamber, and it was registered every twenty minutes. Also the temperature of the air was registered without the plant in the chamber.

The initial temperature of the air inside the chamber in each test was 27 °C. The results of the final stable temperature inside the chamber are shown in Table 1.

Table 1. Final stable temperature inside the chamber.

Test	Final Temperature, °C	Final Temperature, K
Without Plant	31	301.15
With Polluted Plant	30	302.15
With Control Plant	29	302.15

Temperatures registered every 20 min for each test is shown in Figure 2. It necessary to say that the thermocouple was not connected to a reader card device, it was connected direct to a multimeter device and this only displays integer numbers.

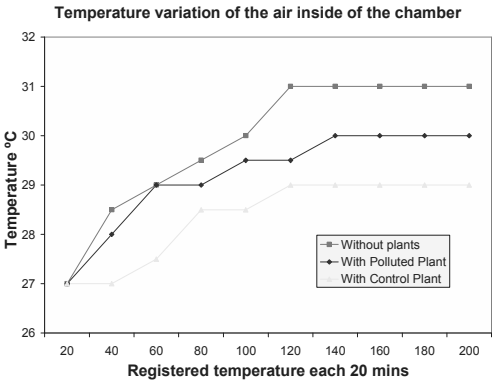

Figure 2. Variation of the air temperature inside the chamber as a function of time

3. Exergy destruction or lost work variation

The following thermodynamics equations [13] are used to calculate the lost work or the exergy that is not used by the plant, and that it is absorbed by the air inside the chamber:

$$\dot{W}_{lost} = T_0 \dot{S}_{gen} = \dot{W}_{rev} \quad \dot{W}_{actual} \tag{1}$$

When all the reversible work is not used, it becomes lost work; and it corresponds to the first test, when there are not plants inside the chamber, all the electrical work provided by incandescent light bulb passes direct to the air; in other words, this electrical work is fully converted in to lost work, it can be represented as follow:

$$\dot{W}_{lost} = T_0 \dot{S}_{gen} = \dot{W}_{rev} = \dot{W}_{electrical} \tag{2}$$

The lost work that is not used by the plant and passes to air (for the Polluted Plant and Control Plant tests) are evaluated using the entropy balance equation for an adiabatic closed system:

$$\dot{W}_{lost} = T_0 \frac{dS_{cv}}{dt} = T_0 \dot{S}_{gen} \tag{3}$$

The entropy variation in the volume control, dS_{cv}, is evaluated using an ideal gas equation as follow:

$$dS_{cv} = m(S_2 - S_1) = m \quad c_v \ln \frac{T_{final}}{T_{initial}} + R \ln \frac{V_{final}}{V_{initial}} \tag{4}$$

Where c_v the is specific heat at constant volume, taken as 0.718 kJ/kg.K. If there is not variation of the chamber, then:

$$dS_{cv} = m(S_2 - S_1) = m \quad c_v \ln \frac{T_{final}}{T_{initial}} \tag{5}$$

The mass of the air is estimated as follow:

$$m = \rho V \tag{6}$$

Where ρ is the density of the air, 1.2 kg/m^3 and V is the volume of the chamber, the mass was estimated as 0.0324 kg. The lost work for each test is evaluated as:

$$\dot{W}_{lost} = T_0 \frac{dS_{cv}}{dt} = T_0 \frac{m(S_2 - S_1)}{dt} \tag{7}$$

$$\dot{W}_{lost} = T_0 \frac{m \quad c_v \ln \frac{T_{final}}{T_{initial}}}{dt} \tag{7a}$$

Using equation (7) for the Control Plant test the lost work is:

$$\dot{W}_{lost}_{\ Control\ Plant} = (300K) \frac{1.2kg \quad (0.718kJ/kg.K) \ln \frac{302.15K}{300.15K}}{6000s}$$

$$\dot{W}_{lost}_{\ Control\ Plant} = 0.00773W$$

Using the same Equation (7), the lost work for the Polluted Plant test is:

$$\dot{W}_{lost}_{\ Polluted\ Plant} = (300K) \frac{1.2kg \quad (0.718kJ/kg.K) \ln \frac{303.15K}{300.15K}}{6000s}$$

$$\dot{W}_{lost}_{\ Polluted\ Plant} = 0.01157W$$

Also, using Equation (7) the lost work when there is not plant in the chamber is estimated as:

$$\dot{W}_{lost}_{\ Without\ Plant} = (300K) \frac{1.2kg \quad (0.718kJ/kg.K) \ln \frac{304.15K}{300.15K}}{6000s}$$

$$\dot{W}_{lost}_{\ Without\ Plant} = 0.01545W$$

Summary of this lost work calculation are shown in Table 2.

Table 2. Lost work as a function of the final stable temperature inside the chamber.

Test	Final Temperature, °C	Final Temperature, K	Lost Work
Without Plant	31	301.15	0.01545
With Polluted Plant	30	302.15	0.01157
With Control Plant	29	302.15	0.00773

In the next section is shown how to use the lost work as environmental impact index o indicator, also a brief discussion is exposed.

4. Exergy destruction or lost work as an environmental impact indicator

In the present section, the core part of this work, an environmental indicator that uses the concept of exergy destruction or lost work is introduced. When an ecosystem is in equilibrium, as already described, the use of the resources is maximized, and the exergy destruction is maintained to a minimum. This is a desirable state that hopefully can be found in some virgin areas of the earth. In an ideal world, this state offers an opportunity to draw a base o reference line from where its evolution can be followed. Then the sum of all the contributions of lost work, as described by Equation (3), of all the subsystems of the ecosystem, will be equal or greater than this base line, in such a way that:

$$\sum_i T_0 \dot{S}_g \Big|_{\substack{sphere,i \\ alterated\ state}} \geq \sum_i T_0 \dot{S}_g \Big|_{\substack{sphere,i \\ pristine\ state}} \quad (8)$$

or

$$\sum_i \dot{W}_{lost} \Big|_{\substack{sphere,i \\ alterated\ state}} \geq \sum_i \dot{W}_{lost} \Big|_{\substack{sphere,i \\ pristine\ state}} \quad (8a)$$

Here sphere,i represents each of the parts that compose an ecosystem; water, soil, air, organisms and human beings, also can represent the energy from the sun.

In addition, the purpose of this section is to show how the environmental impact index is interpreted, only the sphere that represents the organisms or the biosphere is taken into account, the other spheres are omitted, but this does not mean that can not be obtained its environmental impact index, i.e. the diesel that is thrown by the society to the soil has useful energy or the evaporation, dissipation or absorption of the diesel are processes needed to restore the environment to its pristine state that also it use an amount of useful energy, and these can be taken into account and they can be added to the sum of all the contributions of lost work. In this work cost are not taken into account.

Bearing in mind that the exergy destruction or lost work is the main variable affecting the capacity of a subsystem to carry out work, then the relationship of the evolution for two given states in time can be constructed, such that:

$$EII_{LW,sphere} = 100 \bullet \frac{\sum_i T_0 \dot{S}_g \Big|_{\substack{sphere,i \\ Alterated\ state}} - \sum_i T_0 \dot{S}_g \Big|_{\substack{sphere,i \\ Pristine\ state}}}{\sum_i T_0 \dot{S}_g \Big|_{\substack{sphere,i \\ Pristine\ state}}} \quad (9)$$

or

$$EII_{LW,sphere} = 100 \bullet \frac{\sum_i \dot{W}_{lost} \Big|_{\substack{sphere,i \\ Alterated\ state}} - \sum_i \dot{W}_{lost} \Big|_{\substack{sphere,i \\ Pristine\ state}}}{\sum_i \dot{W}_{lost} \Big|_{\substack{sphere,i \\ Pristine\ state}}} \quad (9a)$$

Where the ratio EII_{LW} will be now referred as the environmental impact index. The behavior of equation (9) or (9a) may be explained as follows:

- EIILW ≈ 0, it is when the base-line or natural conditions, do not change with time in the ecosystem.
- EIILW < 0, it is when the ecosystem carries a condition that can revert previous effects, in such a way that the quantity of lost work or the entropy generation is minimal.
- EIILW > 0, is the case when the ecosystem carries a condition of existence of loss work, and can not be reverted.

If the Control Plant state is taken as the pristine state or base line state as 0.00773 W, then a quantities deviation from this state can be obtained. First, using equation (9) the pristine state is evaluated versus the same pristine state, it is:

$$EII_{LW,biosphere} = \frac{0.00773W - 0.00773W}{0.00773W} = 0$$

This result is in accordance with an ecosystem that does not have change time. When a damage or change occurs, then:

$$EII_{LW,biosphere} = \frac{0.01157W - 0.00773W}{0.00773W} = 49.68 \approx 50$$

And when plants do not exist, the value of the indicator is:

$$EII_{LW,biosphere} = \frac{0.01545W - 0.00773W}{0.00773W} = 99.98 \approx 100.00$$

In Table 3 the results of the value of EII_{LW} for the biosphere are summarized.

Table 3. EII_{LW} for pristine and altered states of the biosphere.

Test	Lost Work	EII_{LW}	State
Without Plant	0.01545	100	
With Polluted Plant	0.01157	50	Altered State
With Control Plant	0.00773	0	Pristine State

When the Control Plant was in the chamber, the lost work was 0.00773 W, and it does not vary with the time, then the index EII_{LW} took a value of zero. But, when the Polluted Plant was in the chamber, simulating an altered state or ecosystem, the lost work increases to 0.01157 W, and the index EII_{LW} took a value greater than 0, it is 50, indicating that the ecosystem is throwing 50 % of useful energy, due to the diesel spilled in the soil, also this value represents how many times the human being is deviating an ecosystem from its base line or pristine state. When there is not plant in the chamber, all the useful energy is wasted, for this reason the index EII_{LW} took a values greater than 0, it is 100, no energy is used by the plant.

5. Conclusion

A study of the impact over an energy system (organisms or biosphere sphere) due to an environment impact by diesel spilled in the soil from human activities (society sphere) was carried out in the present work. When the proposed environmental impact index, EII_{LW}, took values above 0, see Table 3, there was an alteration of the base-line state of the environment, resulting in an inefficient use of resources. The values of EII_{LW} must be close to 0 when there is no change in the environment, as shown in the same Table 3. Thus the lost work in all the parts of an ecosystem can be used as a measure of the reduction and excessive consumption of the resources when human activity is out of control. This work confirms those results.

Thus, the environmental impact index lost work (Exergy Destruction) presented in this work, can be a useful tool for assessing the environmental impacts of emissions of materials from the society into the environment. This index can be used to analyze thoroughly the waste of resources in the activities of the society. An important addition that this method offers is the advantage to establish quantitative and qualitative guidelines for savings and efficient use of natural resources. Also as a consequence, one can wonder how many times the human being is deviating an ecosystem from sustainability.

The example presented in this work is a good approximation to compute the environmental impact with an exergy-based method; it was applied to simple part or sphere of an ecosystem, the biosphere, the different interaction that it could have with other parts or sphere are not taken into account. To have better approximation about the lost work in the entire ecosystem, it is necessary to complete the model with some information about the elements, it is important to know how elements can move by different paths inside the parts or spheres of the ecosystem and this way predict much better the behavior and tendencies of the ecosystem. Thus, there is still much to be done to clearly identify all necessary indexes that will account for all type of situations, ecosystem, and cost.

References

[1]. Rosen, M.A., Ao, Y., (2008a) “Using exergy to assess air pollution levels from a smokestack – Part 1: Methodology”, Int. J. Exergy, Vol. 5, Issues 4, pp. 375-387.

[2]. Rosen, M.A., Ao, Y., (2008b) “Using exergy to assess air pollution levels from a smokestack – Part 2: illustration and methodology extension”, Int. J. Exergy, Vol. 5, Issues 4, pp. 388-399.

[3]. Sciubba, E., "Exergy as a direct measure of environmental impact", In Proceedings of the IMECE ASME WAM '99 (International Mechanical Engineering Congress and Exposition), Nashville, TN, 1999.

[4]. Sciubba, E., "Exergy Destruction as an Ecological Indicator: Merits and Limits", Panel ECOS 2006, Crete, Greece, 2006.

[5]. Seager, T.P., Theis, T.L., (2002), "Exergetic pollution potential: Estimating the revocability of chemical pollution", Exergy an International Journal, Volume 2, pp. 273-282.

[6]. Seager, T.P., Theis, T.L., (2003), "A thermodynamic basis for evaluating environmental policy trade-offs", Journal Clean Technologies and Environmental Policy, Volume 4, pp. 217-226.

[7]. Stavropoulos, G.G. and Skodras, G., (2003), "The Use of Exergy for Evaluating Environmental Impact of Processes", OPET Network.

[8]. Torres, C., Valero, A., Rangel, V., Zaleta, A., (2008), "On the cost formation process of the residues", Energy, Vol. 33, Issue 2, pp. 144-152.

[9]. Valero, A., (2006), "Exergy accounting: Capabilities and drawbacks", Energy, Vol. 31, Issue 1, pp. 164-180.

[10]. Yang, L. et al., (2006), "Exergy analysis on eco-industrial systems", Science in China: Series B Chemistry, Volume 49, Issues 3, pp. 281-288.

[11]. Sciubba, E., Bastianoni, S., and Tiezzi, E., Exergy and extended exergy accounting of very large complex systems with an application to the province of Siena, Italy", Journal of Environmental Management, Volume 86, Issue 2, pp. 372-382, 2008.

[12]. Jorgensen, S. E. and Svirezhev Y. M., (2004), "Towards a Thermodynamic Theory for Ecological Systems", Elsevier.

[13]. Bejan, A., Tsatsaronis, G., and Moran, M., (1997), "Thermal design and optimization", John Wiley and Sons Inc. New York.

Premature Deterioration of Blades in an Axial Flow Turbocompressor due to the Fogging System Operation, and its Re-design Solution

Zaleta-Aguilar A,. Olivares-Arriaga A., Ayala A., Rangel-Hernández V. H, Belman- J.M.

Department of Mechanical Engineering, University of Guanajuato

Salamanca – Valle de Sgo. Km. 3.5 + 1.8, Salamanca, Guanajuato. C.P. 36885. Mexico.

Abstract: The fogging systems have been used for the last decades to mainly increase the power of the gas turbines in regions where the environment temperature is high with respect to the ISO conditions. The fundamental principle of the fogging systems is to reduce the dry-bulb temperature by saturating the air with spray water until the wet-bulb temperature is reached, so the air mass flow rate and the power output are increased. Nevertheless, in order to obtain an optimal operation of the fogging system it is necessary: a) to install sprays that allow to obtain diameters of water´s drops in the rank of 5 to 40 microns, b) to have enough time of residence in the admission duct to evaporate water, without inertial effects that promote condensation, and c) to have an optimal control with respect to the environmental conditions and power demand to avoid an excess of water.

In this paper, it is demonstrated by means of a thermodynamic analysis and a numerical simulation (by Computational Fluid Dynamic -CFD), how a wrong installation of the fogging system can create condensation of water into the admission duct of a gas turbine, causing damage in the flow path of the compressor. This is because water in liquid conditions can produce erosion, vortex and vibrations in the blades of the turbocompressor. A numerical simulation (by Computational Fluid Dynamic -CFD) was performed for an actual turbogas and focused mainly on finding the trajectories that the particles of water followed, to see their density-distribution in the admission duct. In order to generate the model, an actual geometry was taken from and admission duct of an actual turbogas power station. The results revealed that the actual erosion of the gas turbine blade was due to the particles of condensed water from the fogging system. So a re-design of the sprays position, and logical of control was proposed, in order to avoid excess of water consumption, internal decay of the turbine, and impact on power availability.

Keywords: Fogging system, Premature deterioration, Blades, CFD.

1. Introduction

In México, the regulation of the electrical demand at rush hours, as well as in other countries, has required to rely on open turbogas or combined cycle power plants so as to regulate in a faster way the electrical generation. Nevertheless, because of the weather conditions in some countries as well as in Mexico it has been seen that that the electrical power decreases down to 20% of nominal power at standard conditions, since the power depends strongly upon the air mass flow entering the compressor and this on the environmental conditions. . In a case of a turbomachine, wherein its power is linked directly to its volumetric flow rate, it is convenient to have a more dense air so as to increase the mass flow rate. Several authors [1,2] report that by each degree Celsius the power may fall between 0.5 to 0.9 percent (by each degree Fahrenheit 0.3 to 0.5 %). The pressure has also an effect upon the power of the gas turbines, although not on their efficiency. That is, when the pressure falls, so does the density of the air, therefore the amount of inlet air mass flow decreases.

In this framework, the most common systems used to reduce the environmental effect are: a) *The direct evaporative cooler*. This system reduces the temperature of the air by evaporating the water. The cooling is achieved by getting the air through a filter in which water is drained off. Because of the low relative humidity of the ambient, part of the liquid water evaporates. The energy necessary to evaporate the water comes from the air and, therefore, this is cooled. An evaporative cooler can

increase the relative humidity up to 85 percent [1] b) *The Fogging System*. This system works similarly to the evaporative cooler but instead of using a humid filter fog, nozzles are used to operate pressures between 1000 and 3000 psig. Such pressure produces billions of water´s drops with a diameter of roughly 5 to 40 microns [1]. This system raises the relative humidity to a 100 percent. Its operation is generally controlled by a Programmable Logic Controller (PLC) which receives signals of temperature and relative humidity before the fogging system and carries out the proper operation to control the necessary water flow by means of a bank of pumps. c) *The wet compression*. The humid compression includes an atomizing and spraying system, modifications in the logical operation of the gas turbine as well as additional changes in some components so as to make them safer and more reliable. So, because of the combined effect between the evaporative cooling and the intercooling system of the first stages of the compressor d) *Mechanical refrigeration*. In this system the air temperature can be as low as desired, no matter what the weather conditions are. However, it has the disadvantages of being installed at high costs and having a considerable electrical consumption of ancillary equipments.

2. Fundamentals of the fogging system

In order to compress the air, the compressor requires roughly a 66 percent of the total power generated by the turbine. From an energy balance of the compressor, it yields,

$$W_c = \frac{c_p T_1 \left[\left(\frac{P_2}{P_1} \right)^{\frac{\gamma-1}{\gamma}} - 1 \right]}{\eta_c} \qquad (1)$$

Upon examination of Eq. (1), it is observed that the work depends on the air temperature at the entrance of the compressor. Therefore, if the air temperature increases, then the power consumed by the compressor will be greater.

The power output is smaller when the temperature increases since the power used to compress the air is greater whereas the power generated by the turbine falls, Fig. 1. Therefore it is important to reduce the power loss by decreasing the dry-bulb temperature until the wet-bulb temperature is achieved (100% relative humidity). Under certain circumstances, it is possible to reduce the temperature down to 20 ºC.

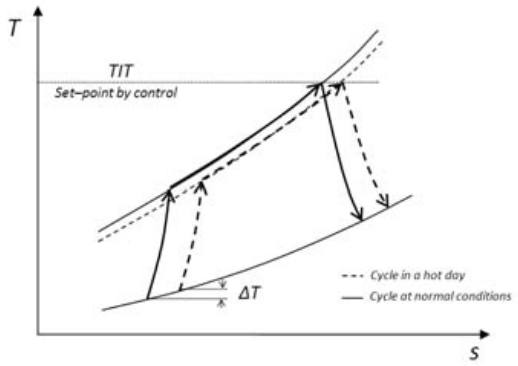

Fig. 1. Diagram T – s, at normal conditions and at a hot day with fogging system.

Besides, it is also necessary to do a heat transfer analysis between the microscopic drops of water (less than 20 microns) and the air so as to assure a considerable residence time in the admission duct to get the evaporation. If an excess of water were present in the fogging system or the evaporation of the water was not achieved, then water drops would appear in the first stages of the compressor and, as a consequence, this may erode the blades and cause irreversible damages.

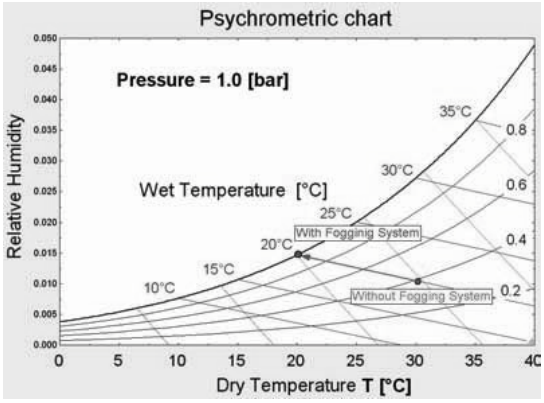

Fig. 2. Psychrometric chart showing fog system effect. Ref [7]

The operation point with and without fogging system can be plotted on a professional psychrometric chart, see Fig. 2. The fogging system causes a change in the dry bulb temperature so that wet-bulb conditions are achieved and, therefore, saturated air is present.

3. Gas turbine selection

The turbine analyzed herein is a Westinghouse model W-501D24. In particular, such turbine was considered because in a previous maintenance it was found that the low-pressure compressor blades had already incrustations as well as premature damages. Besides, it had been recently fitted with a fogging system. The gas turbine is comprised of a multi-stage axial flow compressor (as many as 19 stages) and only one admission of IGV, a 4-stages expansion turbine and a radial combustion chamber. In addition it has a fogging system for recovering of power.

4. Analysis of the problem

This analysis relates to study the phenomenon that originated the premature damage of the blades. In order to do so, a methodology was set up, which consisted of:

a) Visual Inspection and Historical Data Recall

b) Thermodynamic Analysis of the Compressor

c) Fluid dynamic Analysis

d) Chemical Analysis

Which are defined as:

Visual Inspection and Historical Data Recall. A technical visit to the plant was carried out in order to take evidence of the gas turbine components that presented damage because of premature aging. Data from the gas turbine monitoring system as well as from the operation personnel was collected.
Thermodynamic analysis of the compressor, calculation of the properties was performed stage by stage in the compressor. The analysis was set up in the Engineering Equation Solver (EES software). One of the advantages of using this software is that it has properties for the wet air. Hence the effect of the fogging system on the thermodynamic properties of the air is considered to be a mixture of air and steam.
c) *Fluid dynamic analysis.* A CFD model for studying the fluid dynamic of the gas turbine was prepared. The aim was to find the trajectories of the water as well as their density in the admission duct assembly.
e) *Chemical analysis*, incrustation samples were taken from the compressor´s bladesMetallographic tests were made.

4.1. Visual inspection

Upon visual inspection, it was observed that the blades of the low pressure stages had a premature damage at the flow inlet profile because of erosion and some uncovered loosening of material on the surface of the moving blades outlet. Besides some scratch from a solid or liquid particle of the air was seen on the gas turbine blade. Fig. 3 shows a blade from the first stage. Also, it can be seen the scratches due to the high-density particles flowing on the surface.

Fig. 3. Compressor´s Blade damage (1st stage)

On the other hand, Figure 4 shows one blade of each rotor stage of the 19 stages of the Turbocompressor. There it is observed that scratches are no longer visible from the 7th to 19th stage. Hence it is inferred that liquid (water) suddenly evaporates.

Fig. 4. Compressor´s Blade damage (all stages) due to a bad fogging System Operation.

4.2. Thermodynamic analysis

It was inferred from analysis of the centrifugal trajectories of the drops that they had been introduced by the air flow. In addition, blades revealed unreasonable rugosity which strongly supported the hypothesis of particle infiltrations and undue erosion because of the liquid particles present in the compressor.

Accordingly, in order to find the thermodynamic conditions (pressure and temperature) of the water, a thermodynamic analysis was carried out, see results on Fig 5. The analysis was made in EES (Engineering Equation Solver) software and the boundary conditions (inlet and outlet pressure and temperature) were taken from instrumentation data own the plant. There it can be observed that the water temperature is lower than the saturation temperature up to stage 7. This observation coincides with the phenomenon presented on Fig 4, since only erosion trajectories are seen on the former stages

By the same token, the cause of the sub- cooled water may well be due to a over saturation of water in the spray nozzles.

	1 $kAire_{etapa,i}$	2 $p_{etapa,i}$	3 $T_{etapa,i}$	4 $T_{sat,i}$ [C]
[1]	1.3970725	0.9034	36.4	96.79
[2]	1.3969910	1.034	50.49	100.5
[3]	1.3968374	1.184	65.22	104.4
[4]	1.3965563	1.355	80.62	108.3
[5]	1.3961030	1.551	96.7	112.4
[6]	1.3954419	1.776	113.5	116.5
[7]	1.3945485	2.033	131	120.7
[8]	1.3933995	2.327	149.3	125.1
[9]	1.3919922	2.664	168.4	129.5
[10]	1.3903240	3.049	188.2	134.1
[11]	1.3884016	3.49	208.9	138.8
[12]	1.3862377	3.995	230.4	143.6
[13]	1.3838501	4.573	252.8	148.5
[14]	1.3812602	5.235	276	153.6
[15]	1.3784925	5.993	300.1	158.8
[16]	1.3755725	6.86	325.2	164.1
[17]	1.3725269	7.853	351.2	169.7
[18]	1.3693818	8.989	378.2	175.3
[19]	1.3661626	10.29	406.1	181.1

Fig.5. Inter-stage Compressor properties conditions.

Therefore, in order to find the correct amount of water required b the fogging system to saturate the air a psychrometric analysis was undertaken.

The chart plotted in Fig. 6 represents the relation between the volumetric water flow rate and the environment temperature (dry bulb) necessary to get a relative humidity of 100%. The colored lines represent different relative humidity. In particular, for a given relative humidity of 20% and a temperature of 34.5°C, it is necessary a volumetric flow rate of only 8 m^3/h. It is important to mention that these conditions are the most critical for the fogging system. In view of the fact, it is concluded that the flow of water supplied to the fogging system is higher than the necessary since plant reports account for a flow of 13 m^3/h. This bad operation causes that air is over saturated and hence water condenses.

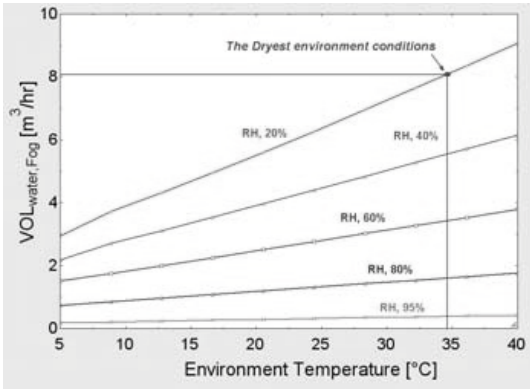

Fig.6. Volumetric Flux vs. Dry Temperature with different relative humid

4.3. Fluid Dynamic analysis

With the aim of yielding a computational model and representing the physical phenomenon of the fogging system. Measurements of the compressor admission duct were taken physically in-situ from the turbine.

In order to represent the hydrodynamic phenomenon of the fogging system, it was made a computational model using Fluent®. The boundary conditions are listed in the Table 1.

Table 1. Boundary Conditions for the modeling.

Boundary Conditions		
Mass Flow Rate	313.58	kg/s
Inlet Absolute Pressure	97.95	kPa
Inlet Air Temperature	300	K
Turbulent Intensity	5	%
Outlet Absolute Pressure	79.34	kPa
Turbulent Intensity	5	%
Injection for fogging system		
Velocity Magnitude	21.57	m/s
Cone Angle	30	°
Radius	0.0130937	m
Mass Flow Rate/injection	0.0036897	kg/s
Size drop (diameter)	13	µm

The figure 7 shows the arrangement of nozzles of the fogging system, they are set after the filters.

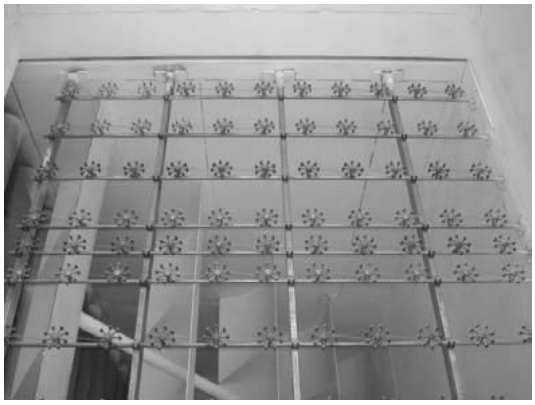

Fig.7. Adjustment of the fog nozzles

Figure 8 shows the computational domain for the fogging system model. The mesh generated to realize the modeling consisted of 536.034 cells, this density of mesh required a time of solution of approximately 2 hours in each case using a 4 GB RAM, 2.2 GHz duo processor computer. This mesh is comprised largely of tetrahedrons and triangular prisms.

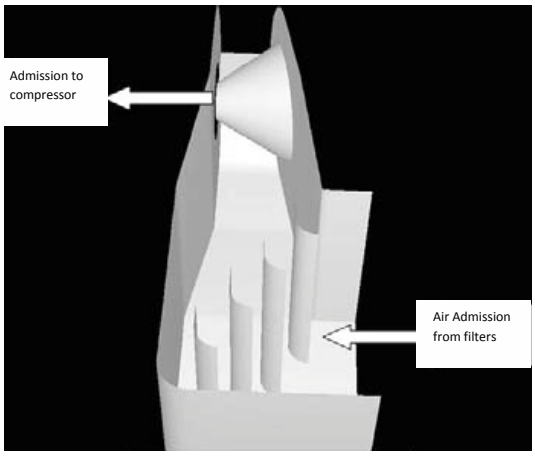

Fig.8. Computational Domain of Air Admission.

Fig 10 shows the air trajectory from the filters inlet down to the admission of the inlet guide valves of the compressor. This simulation was done with air only so as to validate the results with the design data. There it is observed well defined and aligned trajectory lines. Just before the IGV's inlet, they change their trajectories by the effect of the baffle plates and low speed, thereby taking the direction towards the compressor´s admission. The flow pattern occurs in accordance to geometry, amount of mass flow rate and pressure gradients.

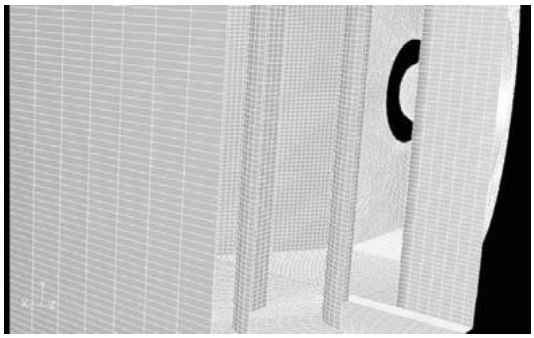

Fig.9.Mesh Generated

The concentration density of water drops due to the injection of water within the computational domain for different sectors can be seen from Fig. 11 to 13. There, no uniformity of the water-drop trajectories is observed, it can be dangerous because it can produce more vibration than under normal conditions, and on the other hand, it can be assume that water-drops can cause erosion in the blades as it was showed in the figure 3. Also, in some regions, the high density of water-drops can impact in the over saturated air.

Accordingly, it is observed the heterogeneity in the distribution of the water drops, which, in accordance to theory, halts the evaporation of water during its passage from the injection to the entrance to the compressor.

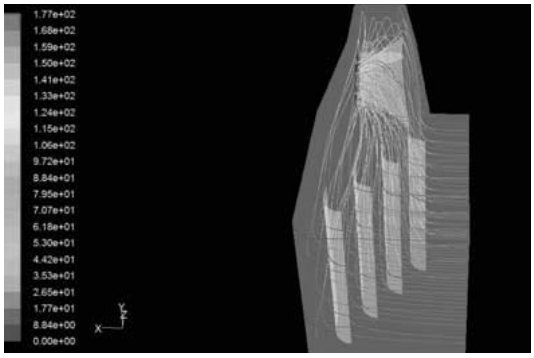

Fig.10. Air path lines (velocity in m/s)

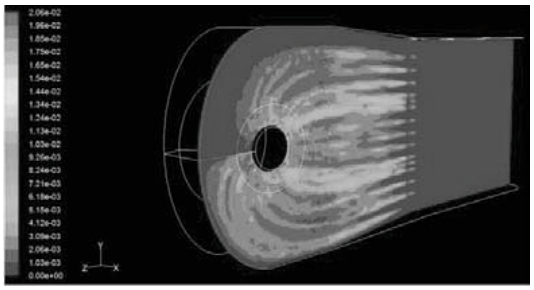

Fig.11.Density-distribution of droplets (plane 1)

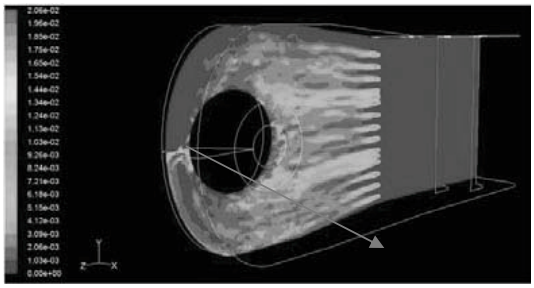

Fig.12. Density-distribution of droplets (plane 2)

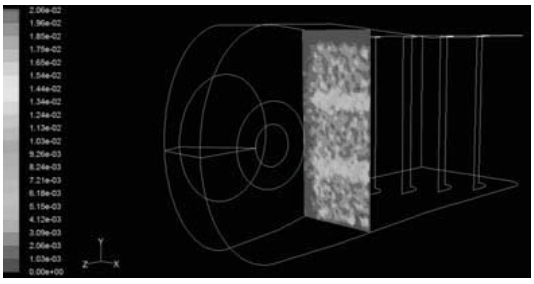

Fig.13. Water Drops Concentrations at plane 3.

On the other hand, according with the thermodynamic analysis if the amount of water that is being supplied by the pumps is higher than the necessary, then some water drops will remain liquid thereby eroding the blades in the first stages of the compressor. So it is recommended to reduce the amount of water provided for the fogging system and redesign a better adjustment of the fog nozzles. This new design would cause a proper evaporation of the water drops before entering the compressor and thus avoiding damages in the compressor. The fogging systems have been widely accepted in the last decade, and related literature can be found elsewhere.

4.4. Chemical analysis of the incrustations

In order to carry out this analysis, two samples were taken from different surface areas of the blades, where incrustations were present. Then as a classification basis the samples were labeled, Fig 3, as A (red) and B (yellow). The samples were analyzed by a an Inel Diffractometer equipped with an x-ray tube and a 30 kVa, 30 mA copper anode.

For sample A, the results were the following:

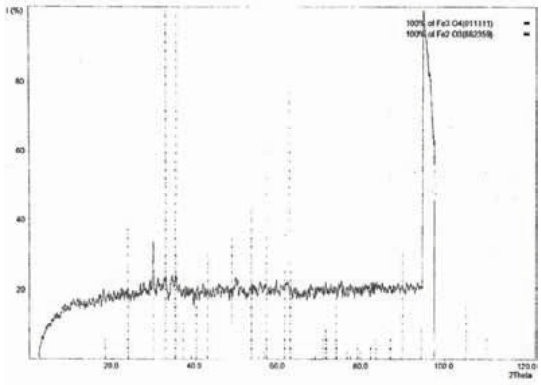

Fig.14. Diffractogram of the sample "A"

Figure 14, shows the crystalline phases of Hematite, Fe2O3, and Magnetite, Fe2O4, the sample A was put under a magnetic field and a phenomenon of ferromagnetism was present.

For sample "B", the results were as follows: It was found the presence of Iron Sulfide (yellow aspect). In order to determine the likely nature of the fracture, a tiny surface of the deteriorated blade was polished, see Figure. 15.

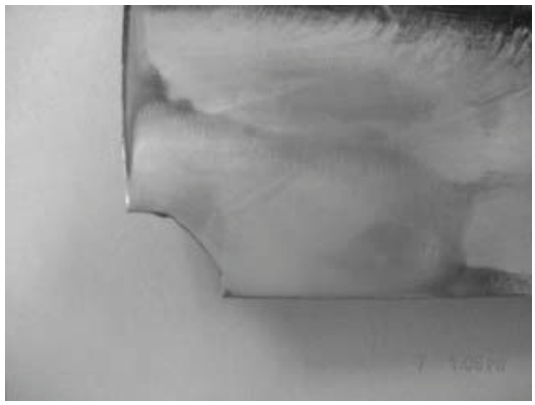

Fig.15. Tip fracture of a blade damaged.

Afterwards, so as to bring to view the grain border of the polished surface, this was attacked with a 3 % Nital solution: 1 – 5 ml Nitric acid, and 100 ml of ethanol during 20min; then it was attacked with

an acid solution, 70% of FeCl3; the chemically attacked sample was then analyzed in 2000Zeiss metallographic microscope. Refer to Fig 16 and 17.

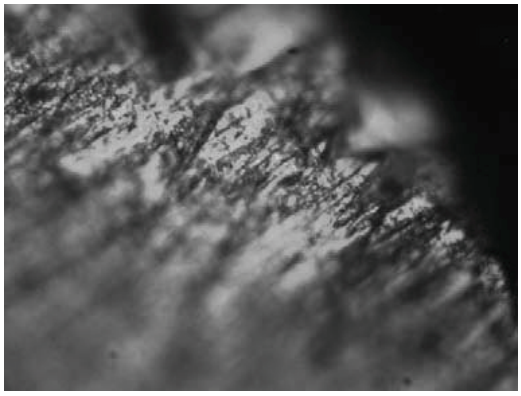

Fig.16. Lateral Amplified vision of the Tip fracture of a blade damaged

Analysis of Results

Results from the X-ray diffraction analysis show that in surfaces where the patina is present a part of the iron has been oxidized thereby yielding oxides. On the other hand, the chemical analysis of sample B demonstrated that the blade surface had been polluted with sulphur as traces of iron sulfide were found. The cause of such pollution in the compressor has to do with the environment surrounding the turbogas since the water of used in the fogging system holds low pollution levels.

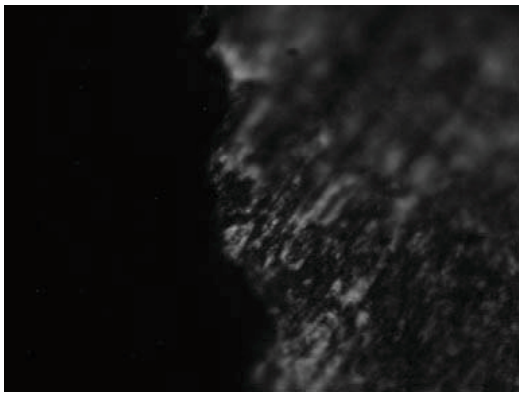

Fig.17. Frontal Amplified vision of the Tip fracture of a blade damaged

In regard to the fracture, the metallographic analysis revealed an intergranular fracture. So it is concluded that such fracture belong to the fragile type because of the crystallization of the base material caused probably by the environment pollutants.

5. Conclusions

Upon the thermodynamic analysis it was proven the presence of water drops through stages 1 to 7. In particular, water drops caused a premature damage on the blade surface; this was because of the combined effect between the humidity and the presence of sulphur in the environment.

As well, in order to rule out the possibility that the processed water had a high mineral content, an analysis was carried out. From the analysis it was determined that the water was supplied from an inverse osmosis treatment plant, so it was impossible that the root of the problem was this.

Besides, it was found that the sulphur source was due to the industries located nearby to the power plant. The corrosive environment, because of the presence of NOx and SOx, caused the blade oxidation as well as it was found traces of iron sulphur which made the crystal to be crystallized. Such chemical attack modified the structure of the blades which originated the fracture of the material at the outlet of the blade.

Consequently, it has been proposed to take up an adjustment in the control system in order to avoid the over saturation due to excess of water. Likewise, it has been recommended to install a drainage in the admission duct since there will always be condensed water in the duct.

For the fluid dynamic analysis, it was found that the distance and amount of water were not the appropriate, hence a proposal for redesigning the fog nozzles and the amount of water.

Finally, the combination of fundamental physical laws with advanced analysis tools allows to properly identifying the root causes of real problems. However, this search of root causes depends strongly on the skill of the engineer.

Nomenclature

C_p constant pressure specific heat, J/(kg K)
P pressure, kPa
T temperature, K
W compressor work, MJ

Greek symbols
γ specific heat ratio

η efficiency

Subscripts and superscripts
1 inlet compressor
2 outlet compressor
c compressor

References

[1]. Meher C. B., Mee T. R. 2000, Inlet Fogging of Gas Turbine Engines Part A: Theory, Psychrometrics and Fog Generation, Proceedings of ASME Turbo Expo 2000, paper no. 2000-GT-307.

[2]. Mustapha C., Cyrus B, 2002, Inlet Fogging Of Gas Turbine Engines - Part B: Fog Droplet Sizing Analysis, Nozzle Types, Measurement And Testing, Amsterdam, The Netherlands, Proceedings of ASME Turbo Expo 2002.

[3]. Hsiao-Wei D. Chiang, Pai-Yi Wang, Hsin-Lung Lee, 2008, Power Augmentation Study Of An Existing Combined Cycle Power Plant By Overspray Inlet Fogging, Proceedings of ASME Turbo Expo 2008, June 9-13, 2008, Berlin, Germany

[4]. Mustapha C., Cyrus B, Gas Turbine Power Augmentation — Parametric Study Relating To Fog Droplet Size And Its Influence On Evaporative Efficiency, Proceedings of ASME Turbo Expo 2008, June 9-13, 2008, Berlin, Germany

[5]. Jobaidur R. Khan and Ting Wang, Simulation Of Inlet Fogging And Wet-Compression In A Single Stage Compressor Including Erosion Analysis, Proceedings of ASME Turbo Expo 2008, June 9-13, 2008, Berlin, Germany.

[6]. Mustapha C. Cyrus B. Thomas M., Inlet Fogging of Gas Turbine Engines Part C: Fog Behavior in Inlet Ducts, CFD analysis and wind Tunnel Experiments, Proceedings of ASME Turbo Expo 2002, June 3 – 6, 2002, Amsterdam The Netherlands.

[7]. EES, Engineering Equation Solver, 2003, Software Package, Professional version 6.804, F-chart Software.

AUTHOR'S INDEX

Acevedo Galicia, Luis E. (4-211)
Achaichia, Abdennacer (3-19)
Adi, Lifshitz (2-135)
Agathou, Maria S. (4-383)
Ahmadi, Pouria (4-203)
Altamirano-Cabrera, Juan-Carlos (3-347)
Alterio, V. (5-339)
Alvaro Delgado, Mejía (5-405)
Ameri, Mohammad (4-203, 5-17)
Amidpour, Majid (1-213, 1-321, 1-449, 1-465, 2-447, 4-193, 4-255, 4-469)
Amrollahi, Zeinab (4-133)
Anastasovski, Aleksandar (1-121)
Andrade Torres, Ednildo (4-339)
Andrés Silva Ortiz, Pablo (4-9)
Angrisani, Giovanni (5-157)
Angulo-Brown, F. (3-503, 4-421, 5-253, 5-293)
Araújo, Maria Elieneide (3-447)
Arcioni, Livia (3-83)
Aretakis, N. (4-123)
Arias-Hernandez, L.A. (3-503, 4-421)
Armas, Juan Carlos (3-487)
Arribas, Juan José (4-439)
Arteaga, Luis E. (5-389)
Arvani, Ata (1-449)
Asakuma, Yusuke (2-525)
Assad, Paulo Celso Xavier (2-501)
Atakan, Burak (3-27, 5-317)
Atong, Duangduen (2-531)
Augsburger, Germain (2-345, 2-353)
Aumann, Richard (3-59)
Ayala, A. (5-425)
Azizi Yeganeh, Amirmahyar (1-321)
Babac, Gulru (3-455)
Babaie, Meisam (1-241)
Baccino, Giorgia (4-185)
Badea, Nicolae (5-173, 5-353)
Bailey, Margaret (5-181)
Baker, Derek (3-331)
Balanuța, Ciprian (5-173)
Balli, M. (3-115)
Bandeira Santos, Alex Álisson (4-339)
Bandyopadhyay, Santanu (5-111)
Banerjee, Rangan (5-111)
Barbosa, João Roberto (4-35)
Barbouchi, Sami (3-405)
Bardow, André (4-219, 4-241)
Barmparitsas, Nikolaos (3-397)
Barquín Gil, Julián (4-447)
Barranco-Jiménez, M. A. (3-503, 5-253, 5-293)
Bartela, Łukasz (4-1, 4-27, 4-99)
Barzotti, Maria Chiara (3-83)
Bassano, Claudia (2-233)
Bauer, Christian (1-357)
Bayod-Rujula, Angel A. (2-485)
Becker, Helen (4-91)
Bédécarrats, Jean-Pierre (2-145, 2-217, 3-67, 5-125)
Begg, S.M. (1-113)
Behbahaninia, Ali (4-255)
Belman-Flores, J.M. (4-165, 5-425)
Bělohradský, P. (4-347)
Benali, Marzouk (2-11)
Benali, Tahar (1-107)
Benjumea, Pedro (2-1)
Benvenuti, Cristoforo (2-429, 2-495)
Berger, Roland (4-367)
Beritault, David (2-217)
Berntsson, Thore (1-233, 4-51)
Besson, C. (3-115)
Bettocchi, Roberto (3-355)
Beyene, A. (2-413)
Bin Omar, Mohd Nazri (4-317)
Bladimir, Ramos-Alvarado (3-279)
Blanco-Marigorta, Ana-Maria (1-337)
Bohn, D. (2-371)
Bojarski, A.D. (4-411)
Bolland, Olav (4-133)
Bonafin, J. (5-73)
Bongs, Constanze (1-9)
Bonhote, Ph. (3-115)
Bonvin, Dominique (5-141)
Bornatico, R. (3-221)
Bory, D. (4-279)
Boschiero do Espirito Santo, Denilson (5-233)
Boudehenn, François (3-421)
Boukis, I. (2-277)
Boutin, Olivier (4-295)
Boyano, Alicia (1-337)
Bram, S. (1-481)
Brandon, Nigel (5-9)
Brillet, Christophe (5-125)
Brkic, Dejan (4-325)
Brown, Andrew P. (3-19)
Brum (3-99, 3-467)
Bruno, Joan Carles (2-293)
Brus, G. (2-207)
Buchgeister, J. (1-305)
Buczyński, Rafał (4-375)
Budliger, J.P. (5-369)
Budnik, Michał (4-43)
Bunin, Gene A. (5-141)
Buoro, Dario (1-397)
Burbano, Juan Carlos (1-53)
Cadorin, Margherita (2-153, 5-309)
Calise, Francesco (3-213, 5-149)
Campisi, Anthony (4-19)
Cano-Andrade, Sergio (3-339)
Capobianchi, Paolo (5-103)
Caprara, Claudio (3-355)
Carassai, Anna (1-17)
Cardona, F. (5-339)
Carnevale, Ennio (5-45)
Carrasquer, Beatriz (1-179)
Carré, Jean-Baptiste (3-75)
Carvalho, Monica (1-71)
Casarsa, Luca (4-357)
Casas, Yannay (5-389)
Castaing-Lasvignottes, Jean (3-67)

Catapano, Francesco (5-201)
Cazacu, Nelu (5-173)
Chamorro, César R. (1-431)
Champier, Daniel (2-145, 5-125)
Changenet, C. (3-263)
Chaouki, J. (2-505)
Charitos, Alexander (2-167)
Chavez-Rodriguez, Mauro Francisco (2-109, 2-259)
Chen, Hui (1-457)
Chen, Zhen (2-387)
Chourpouliadis, Christos (2-317)
Christidis, Andreas (3-371)
Chritensen, Rolf (3-291)
Cirez-Oto, Fernando (2-485)
Cisotto, Andrea (2-405)
Clemente, Stefano (3-9)
Clodic, Denis (1-137, 3-189)
Coince, Anne-Sophie (3-405)
Connors, Stephen (2-327)
Coppens, Marc-Olivier (5-259)
Coronas, Alberto (2-293)
Corrêa da Silva, Rodrigo (4-271)
Corti, Andrea (5-45)
Costea, M. (5-361)
Cullen, Barry (5-243)
Cuvilliez, Anne-Laure (2-311)
Cvetković, Svetislav (1-121)
Czarnowska, Lucyna (4-287)
Dahlquist, E. (2-83)
Dai, Wei (3-493)
Dalla Vedova, Matteo (4-185)
Dashtbani, J. (1-523)
De Lima, Rosiane C. (4-149)
de Oliveira Júnior, Silvio (1-53, 2-1)
De Pascale, Andrea (4-357)
De Paula Perreira, Pedro Alfonso (4-339)
De Petris, Marco (5-133)
De Ruyck, J. (1-481)
De Sousa Barbosa, Erilson (3-447)
Declaye, S. (3-379)
Deiana, Paolo (2-233)
Demierre, Jonathan (3-91, 3-317)
Dentice d'Accadia, M. (3-213)
Descoins, Nicolas (1-187)
Desideri, Umberto (3-83)
Dewulf, Jo (4-227, 5-389)
Diaz-Méndez, S.E. (5-419)
Djemaa, A. (4-279)
Dobre, C. (5-361)
Dobrovicescu, A. (5-361)
Dolatshahi, Amirali (2-447)
Domigan, Whitney (5-181)
Domingos, Tiago (1-345)
Dos Santos, Rogério R. (4-149)
Doukelis, Aggelos (3-397)
Dubey, Maneesh (3-205, 3-253)
Dubuis, Matthias (1-389)
Duhot, G. (3-263)
Dumbliauskaite, Monika (4-91)
Dutra, Kaio Hemerson (3-447)
Egli, Armin (1-129)
El-Nashar, A.M. (1-205)
Eleftheriadis, Eirinaios (3-397)
Elizalde-Blancas, F. (5-267)
Erlach, Berit (2-45)
Ertesvåg, Ivar S. (4-133)
Escobar Palacio, José (1-63, 2-249)
Evola, Gianpiero (3-421)
Facchinetti, Emanuele (5-1)
Fagerlund, Johan (4-67, 4-77, 4-459)
Fallahi, H.R. (1-523)
Fallahsohi, H. (3-263)
Fält, Martin (3-413)
Faucherand, Rémy (4-295)
Favrat, Daniel (1-97, 1-263, 2-345, 2-353, 3-1, 3-75, 3-91, 3-317, 5-1, 5-301)
Fazlollahi, Samira (4-447)
Federley, Jaana (1-1, 4-141)
Feidt, Michel (1-27, 5-243, 5-361)
Fen, He (2-77)
Feng, Jie (2-387)
Ferrão, Paulo C. (2-189, 2-327, 3-363, 4-83)
Ferrasse, Jean-Henri (4-295)
Ferruzzi, Gabriele (5-149)
Fiaschi, Daniele (2-135, 3-229)
Fink, Mathias (4-367)
Firat, Coskun (1-439, 2-413)
Fisk, David (3-167, 3-175)
Flores Arteaga, Johnathan (5-233)
Fodor, Zsófia (2-285)
Fogelholm, Carl-Johan (2-101)
Forchelet, J. (3-115)
François, Grégory (5-141)
Frangopoulos, Christos A. (4-287)
Fuentes, Alejandro (3-339)
Fukui, Keisuke (2-525)
Galashev, A.E. (1-171)
Gambarotta, Agostino (3-35, 3-43)
Gandier, J. A. (2-197)
Gando-Ferreira, Licinio M. (4-459)
García-Castillo, L. M (3-481)
García, Araceli (2-473)
Garrison, Jared (2-335)
Gassner, Martin (1-249, 2-27, 2-35, 2-269, 2-311)
Gerbelová, H. (4-83)
Gerber, Léda (2-269, 2-459)
Gewald, Daniela (5-63)
Ghanbarzadeh, S. (1-489)
Gholampour, P. (1-489)
Ghorbani, Sanubar (3-429)
Giannakopoulos, Dionysios (3-397)
Gibout, Stéphane (3-67)
Gil de Moya, Cristina (2-101)
Gnanapragasam, N.V. (2-225)
González Alriols, María (2-473)
Görling, Martin (2-119)
Górski, Jan (1-409)
Grieu, Stéphane (3-197)
Grigoriadis, Th. (4-107)
Grill, Andreas (3-59)
Grillo Reno, Maria Luiza (4-9)
Grunewald, Peter (3-397)
Guevara Carazas, Fernando J. (2-93)
Guizzi, Giuseppe Leo (5-325)

Güray, Bora Şekip (3-331)
Gutiérrez Velásquez, Elkin I. (5-85, 5-397, 5-405)
Gutiérrez-González, A. P (3-481)
Guzzella, L. (3-221)
Haghtalab, Ali (4-427)
Haji Abedin, Ali (3-107)
Haldi, Pierre-André (1-263)
Hamedi, M. H. (4-193)
Hammond, G.P. (4-395)
Hanafizadeh, P. (1-489, 5-381)
Harkin, Trent (4-59)
Hasanzadeh, Kazem (1-449, 1-465, 4-255)
Haseli, Y. (1-37)
Hashizume, Takumi (5-301)
Hawthorne, Craig (2-167)
He, Fen (1-255)
He, Wei (4-303)
Henchoz, S. (3-91)
Henggeler Antunes, Carlos (1-329)
Henning, Hans-Martin (1-9)
Hernàndez Ariano, Luis (5-405)
Hernández-Figueroa M.A. (1-89)
Hernández-Guerrero, A. (1-421, 5-267, 5-419)
Heyen, Georges (4-235)
Hita, A. (4-279)
Hoadley, Andrew (4-19, 4-59, 4-311)
Hoban, Michael (2-459)
Hobbs, Benjamin F. (3-339)
Holda, Adam (1-499)
Holmberg, Henrik (4-141)
Hong, Hui (2-363)
Hongguang, Jin (2-363)
Hooper, Barry (4-59)
Horta Nogeira, Luiz A. (4-35)
Hossam-Eldin, A. (1-205)
Hosseini, Mehdi (5-411)
Houcheng, Zhang (5-375)
Hountalas, D.T. (5-53)
Howlett, R.J. (1-113)
Iluk, Tomasz (2-513)
Iman shayan, S. (3-271)
Imperato, Raffaele (1-145, 1-161)
Ioakimidis, Christos S. (2-189, 4-83)
Ioannou, Eleni (2-317)
Irrazabal Bohorquez, Washington Orlando (4-35)
Ismaiel, A. (1-205)
Ito, Koichi (5-301)
Jahanshahi Anbuhi, Sana (4-427)
Janach, Walter E. (5-119)
Janusz-Szymańska, Katarzyna (4-99)
Jaubert, Jean Noël (1-107)
Jin, Hongguang (2-467)
Jincan, Chen (5-375)
Jones, R. A. (2-197)
Jönsson, Johanna (4-51)
Juárez-Robles, D. (5-267)
Jung, Johannes (4-241)
Junlobol, Kitisak (1-473)
Kakaras, Emmanuel (2-277, 3-397)
Kakatsiou, K. (3-475)
Kalfas, Anestis I. (2-317)
Kalliakoudi, K.P (3-237)
Kang, Wang (4-227)
Kangwanpongpan, Tanin (4-271)
Kapasakis, P. (4-123)
Karellas, Sotirios (2-277, 3-291, 3-397)
Karimi, Mohammad (4-203)
Karlsson, Magnus (4-263)
Katsirou, Vassiliki (2-317)
Kawanami, Osamu (2-525)
Keirstead, James (3-167, 3-175)
Kermes, V. (4-347)
Khaghani, A. (5-381)
Khoshgoftar, L. (4-193)
Khoshgoftarmanesh, M.H. (4-193, 4-469)
Kim, Y. M. (3-1)
Kimijima, S. (2-207)
Kirova-Yordanova, Zornitza (1-45)
Kirschbaum, Stefan (4-219)
Kjelstrup, Signe (4-303, 4-333, 5-259)
Klemeš, Jiří Jaromír (2-285)
Knecht, W. (5-53)
Koch, Christoph (3-371)
Koch, Sebastien (5-125)
Kohl, Thomas (2-101)
Kolenda, Zygmunt (1-499)
Komatsu, Y. (2-207)
König, Nikolaus (5-63)
Koras, Andreas (2-317)
Koronaki, I.P (3-237, 3-439, 3-475)
Koroneos, C. (4-107)
Kosmadakis, G.M. (5-191)
Kosmidou, M. (4-107)
Kotowicz, Janusz (2-513, 4-1, 4-27, 4-99)
Kousksou, Tarik (2-145, 3-67, 5-125)
Krautz, Hans Joachim (4-271)
Krewinkel, R. (2-371)
Krummenacher, Pierre (1-97)
Kupper, Christian (5-133)
Kuramochi, Hidetoshi (2-525)
Kyritsis, Dimitrios C. (4-383)
Labidi, Jalel (2-473)
Ladino-Luna, Delfino (3-499)
Lai, T.M. (1-365)
Lam, H.K. (1-365)
Lampinen, Markku (1-1)
Lapido, Margarita (3-487)
Latkowski, Jacek (1-499)
Laurenczy, Gábor (3-137)
Lavoie, J.M. (2-505)
Lazzaretto, Andrea (1-223, 2-175, 2-301)
Le Pierrès, Nolwenn (3-421)
Leal, Elisângela Martins (5-285)
Lee, S.H. (1-113)
Lee, S.T. (3-1)
Lefevre, Sébastien (4-295)
Leibundgut, Hansjürg (3-245)
Lemort, V. (3-379)
Leonardi, Daniela (3-83)
Leonardo, Marraccini (3-161)
Leontaritis, Aris (3-291)
Lestienne, Remi (1-187)
Li, Peiwen (3-279)
Li, Zheng (1-255, 2-77, 2-387)

Ligeret, C. (3-263)
Lin-shi, X. (3-263)
Lin, Guoxing (3-123, 5-375)
Lior, Noam (2-395)
Liszka, Marcin (2-69, 4-43)
Liu, Pei (1-255)
Llano-Ponte, Rodrigo (2-473)
Llera, Rocío (4-439)
Lo Prete, Chiara (3-339)
Lo, W.C. (1-365)
Lombardi, Lidia (5-45)
Lora, Electo E. S. (2-249)
Lorente-Lafuente, Ana M. (2-485)
Lott, Melissa C. (1-533)
Lozano, Miguel A. (1-71)
Luo, Ercang (3-493)
Luterbacher, Jeremy S. (2-311)
Macêdo, Emanuel N. (2-127)
Maeda, Kouji (2-525)
Mahmed, C. (3-115)
Manente, Giovanni (2-301)
Manfrida, Giampaolo (2-135, 2-161, 3-153, 3-161)
Manjula, Antony (4-19)
Manno, Michele (5-325)
Maranzana, M. (2-495)
Marcinichen, Jackson Braz (3-309)
Marco, Coviello (2-161)
Mardan, Nawzad (4-263)
Maréchal, François (1-187, 1-249, 1-389, 2-19, 2-27, 2-35, 2-269, 2-311, 2-459, 4-91, 5-1, 5-301)
Mariaca, Cristina (2-395)
Marinova, Mariya (2-241)
Martelli, Roberta (3-355)
Martha de Souza, Gilberto F. (2-93)
Martin, Andrew (2-353)
Martin, M. Carmen (1-431)
Martínez-Patiño J. (1-89)
Martínez, Amaya (1-179, 1-195)
Martins, Márcio F. (2-127)
Martins, Matthieu (2-421, 2-479, 3-51)
Masi, Massimo (5-225)
Mateos-Espejel, Enrique (2-241)
Mathioudakis, K. (4-123)
Matsuo, Keigo (5-301)
Matuszek, Katarzyna (2-513)
Mauran, Sylvain (2-421, 2-479, 3-51, 3-131)
Mazet, Nathalie (3-131, 3-183)
McGovern, Jim (5-243)
Medina Flores, J.M. (4-165)
Meggers, Forrest (3-245)
Melo, M. (4-83)
Mendes da Silva, Julio (1-63, 1-381)
Menezes Leal Junior, Amauri (2-519)
Merola, Simona Silvia (5-209)
Micheli, Diego (3-9, 4-357)
Mili, Lamine (3-339)
Minarelli, Francesca (3-355)
Minghua, Wang (1-255)
Miranda Carrillo, Ruben A. (5-85, 5-397)
Mirzaparikhany, Sanaz (1-511)
Misra, R.D. (3-205, 3-253)
Molinari, Rodolfo (2-93)
Mondéjar, Maria E. (1-431)
Mondot, Michèle (3-67)
Moorhouse, David J. (4-177)
Morales, Mayra (5-389)
Morandin, Matteo (2-175)
Moreira, Hugo L. (1-63, 5-217)
Morini, Mirko (2-153, 3-355)
Morosuk, Tatiana (1-17, 1-337, 4-317)
Motevallian, Seyed Javad (4-469)
Moulod, Mohammad (5-17)
Moura, Newton R. (5-397)
Moutinho, Alexandra (3-323)
Murr, Rabih (1-137, 3-189)
Nag, PK (3-205, 3-253)
Nakajo, Arata (5-141)
Naqvi, M. (2-83)
Nascimento, Marco A. R. (5-85, 5-397)
Naw, Rolanda (4-317)
Nduagu, Experience (4-67, 4-77, 4-459)
Nebra de Perez, Silvia Azucena (2-109, 4-157)
Nema, Archana (3-205)
Neveu, Pierre (3-183)
Ni, Weidou (2-387)
Nikulshin, Vladimir (3-461)
Nóbrega, Carlos (3-99, 3-467)
Nogueira Assad, Marta Maria (2-501)
Nolte, V. (2-371)
Norman, J.B. (4-395)
Normann, Cathernie S. (3-339)
Novinzadeh, Alireza (1-241)
Nowak, Grzegorz (2-69)
Nukulkit, Sira (1-153, 1-473)
Olivares-Arriaga, A. (5-425)
Oliveira Jr, Silvio (1-381)
Oliveira, Carla (1-329)
Olmos-Mata, David (3-405)
Olsen, Don (1-129)
Orsini, Giuseppe (1-275)
Osvaldo, José Ventrini (4-9)
Öztürk, Z. Fatih (1-505)
Pacelli, Simone (5-103)
Pacheco-Ibarra, J. Jesús (3-389, 4-165)
Padula, Stefano (3-153)
Páez-Hernández, Ricardo (3-499)
Palacios-Bereche, Reynaldo (2-109)
Palombo, A. (3-213)
Panjeshahi, M.H. (1-523, 3-271)
Panopoulos, K.D. (2-277)
Panousis, G. (2-277)
Papadakis, G. (3-379)
Papillon, Philippe (3-421)
Pappa, Konstantina (3-397)
Pariotis, E.G. (5-191)
Paris, Jean (2-11, 2-19, 2-241, 2-505)
Pauletta, S. (2-495)
Pavlas, Martin (2-61)
Pellegrini, Luiz Felipe (1-53)
Peralta, Luis M. (5-389)
Perander, Jorma (4-115)
Pereira, Gonçalo (3-323)
Pérez-Fortes, Mar (4-411)
Pérez-Raya, I. (5-267)

Pérez, Carlos (3-487)
Périn-Levasseur, Zoé (2-11, 2-19)
Petrakopoulou, Fontina (1-17)
Petre, C. (5-361)
Petrescu, Stoian (5-243, 5-361)
Pfeifer, Peter (5-259)
Pfeiffer, M. (3-221)
Pharoah, John (5-259)
Piacentino, Antonio (1-145, 1-161, 5-339)
Picón-Núñez, M. (1-89)
Pierandrei, Giovanni (3-145)
Pignolet, Pascal (2-145, 5-125)
Pina, André (3-323, 3-363, 4-83)
Pinamonti, P. (5-73)
Pinelli, Michele (2-153, 3-355)
Placé, S. (3-263)
Poboss, Norman (2-167)
Polit, Monique (3-197)
Popela, Pavel (2-61)
Pottel, Lothar (3-371)
Pratt, David M. (4-177)
Ptasinski, Krzysztof J. (2-69)
Puig-Arnavat, Maria (2-293)
Puigjaner, L. (4-411)
Quijera, José Antonio (2-473)
Quoc Tuan, Tran (3-197)
Quoilin, S. (3-379)
Rabczak, Sławomir (1-409)
Radu, Robert (4-357)
Rajput, SPS (3-253)
Rakhmanova, O.R. (1-171)
Rakopoulos, C.D. (5-191)
Ramalho, Ruben (1-345)
Rangel-Hernández, V. H (1-421, 3-481, 4-165, 5-425)
Rašković, Predrag (1-121)
Reddy, B.V. (2-225)
Reini, Mauro (1-397, 3-9, 5-73)
Renaud, Blaise (1-97)
Renó, Maria L. G. (2-249)
Reza Farmani, Mohammad (1-241)
Ribeiro, Geraldo L.S. (4-149)
Ricci, Giuseppe (2-233)
Riehl, Roger (2-519)
Ritter, Volker (3-245)
Rivaletto, M. (2-145)
Rivero, R (1-81)
Rivier, Michel (2-217)
Rodrigues dos Santos, Rogerio (5-285)
Rodríguez-Lelis, J.M. (5-419)
Rogdakis, E. (3-475)
Rojas, Jaime (4-249)
Rojczyk, Marek (3-301)
Romão, Inês (4-67, 4-77, 4-459)
Roque Díaz, P. (1-481)
Rosa, Elena (5-389)
Roselli, Carlo (5-157)
Rosen, Marc A. (2-225, 3-107)
Røsjorde, Audun (4-303)
Rossi, Nicola (2-301)
Roth, Stefan (1-357)
Roumeliotis, I. (4-123)
Rubio Rodríguez, M. A. (1-481)
Rubio-Jimenez, C.A. (1-421)
Rubio-Maya, Carlos (3-389, 4-165)
Rueangul, Noppanat (1-153)
Ruggero Spina, Pier (2-153, 5-309)
Ruijin, Liu (5-375)
Ruohonen, Pekka (4-141)
Ruzinov, Vladimir (2-429)
Sabev Varbanov, Petar (2-285)
Saccomani, Renan Heck (4-157)
Sagia, Z. (3-439)
Sahoo, Lalit Kumar (5-111)
Saidi, M.H. (1-489, 5-381)
Sainlez, Matthieu (4-235)
Salehi, Gholam Reza (1-321, 1-449, 1-465, 4-255)
Samsatli, Nouri (3-167, 3-175)
Sanchez Cifuentes, Augusto (4-211)
Sanchez-Salas, N. (5-253, 5-293)
Santoro, Michele (5-103)
Santos, José (1-63, 1-81, 1-381, 2-249, 5-217)
Sari, Osman (3-115)
Sasso, Maurizio (5-157)
Sayyaad, Hoseyn (1-241)
Scarpete, Dan (5-165, 5-353)
Sceia, André (3-347)
Scheffknecht, Günter (2-167, 4-367)
Schenler, Warren (1-357, 5-95)
Schiffmann, Jürg (3-75)
Schmid, R. (5-369)
Schuster, Andreas (3-59, 3-291, 5-63)
Schuster, Anja (2-167, 4-367)
Sciacovelli, Adriano (5-33)
Sciubba, Enrico (1-275, 3-145)
Segovia, José J. (1-431)
Sementa, Paolo (5-201, 5-209)
Serra, Luis M. (1-71, 1-89)
Shah, Nilay (3-167, 3-175, 5-9)
Shah, Nipen M. (4-311)
Shaho, Youyuan (2-467)
Shams, H. (1-489, 5-381)
Shamsaei, Yousef (1-321)
Shin, D.G. (3-1)
Siddiqi, M. Aslam (3-27)
Siemanond, Kitipat (1-153, 1-473)
Silva Lora, Electo Eduardo (4-9)
Silva-Martinez, J.J. (4-421)
Silva, Carlos (2-327, 3-323, 3-363)
Sisman, Altug (1-415, 1-439, 1-505, 3-455)
Skorek-Osikowska, Anna (4-1, 4-27)
Sobolewski, Aleksander (2-513)
Sorbi, Nicola (3-83)
Sosa-Arnao, Juan Harold (4-157)
Spelling, James (2-353)
Spliethoff, Hartmut (3-59, 5-63)
Srathongniam, Suppanit (1-473)
Sricharoenchaikul, Viboon (2-531)
Sriprapakhan, Preecha (2-453)
Ståle Ertesvåg, Ivar (4-303)
Stanek, Wojciech (1-373, 3-301)
Stegou-Sagia, A. (3-439)
Stehlík, Petr (2-61)
Stenhede, Claes (3-291)
Stephane, Deleris (1-187)

Stitou, Driss (2-421, 2-479, 3-51, 3-131, 3-183)
Stoppato, Anna (2-405)
Stouffs, Pascal (2-379)
Stougie, Lydia (2-441)
Strub, Françoise (2-145, 2-217)
Sui, Jun (2-467)
Suomalainen, Kiti (2-327)
Svensson, Elin (1-233)
Swiecki, Karolina (2-167)
Szczygieł, Ireneusz (3-301)
Szlęk, Andrzej (4-375)
Szmyd, J.S. (2-207)
Taccani, Rodolfo (3-9, 5-277)
Tahouni, N. (3-271)
Tani, Filippo (1-263)
Tantakitti, Chutchawan (2-453)
Tchanche, Bertrand F. (3-379)
Tezel, F. H. (2-197)
Thibault, J. (2-197)
Thome, John Richard (3-309)
Tippayawong, Nakorn (2-55)
Tirca – Dragomirescu, G. (5-361)
To, W.M. (1-365)
Tock, Laurence (2-35)
Toffolo, Andrea (1-223, 2-175, 2-301)
Tondeur, Daniel (1-107)
Tornatore, Cinzia (5-209)
Torres-Cuadra, César (1-283, 3-389)
Toti, Francesco (5-133)
Touré, Abdou (2-379)
Touš, Michal (2-61)
Tremuli, P. (5-73)
Tsatsaronis, George (1-17, 1-337, 2-45, 3-371, 4-317)
Tsikonis, Leonidas (5-141)
Uche-Marcuello, Javier (1-179, 1-195, 3-389, 4-439)
Usón, Sergio (1-283, 4-439)
Uzuneanu, Krisztina (5-165, 5-353)
Vaglieco, Bianca Maria (5-201)
Vahdat Azad, Abazar (1-213)
Vaja, Iacopo (3-35, 3-43)
Valdivia, Yarelis (3-487)
Valero, Alicia (1-283, 1-291, 4-439)
Valero, Antonio (1-179, 1-195, 1-283, 1-291)
Van der Ham, L.V. (4-333)
Van der Kooi, Hedzer J. (2-441)
Van der Vorst, Geert (4-227)
Van Giang, Tran (3-197)
Van Langenhove, Herman (4-227)
Van Oijen, J.A. (1-37)
Vanoli, Laura (5-149)
Varma, PVKK (2-505)
Veca, Elisabetta (2-233)
Velásquez Arredondo, Héctor Iván (2-1)
Velo, E. (4-411)
Venturini, Mauro (3-355, 5-309)
Venturini, Osvaldo J. (2-249)
Verda, Vittorio (1-89, 4-185, 5-33)
Verma, V. K. (1-481)
Viand, Alain (4-295)
Vieillard, Philippe (1-291)
Vieira da Silva, Maria Eugênia (3-447)
Vielle, Marc (3-347)
Villamañán, Miguel A. (1-431)
Villamañán, Rosa M. (1-431)
Vlad, Ciprian (5-173)
Vogel, Frédéric (2-27)
Voldsund, Mari (4-303)
Voll, Philip (4-219)
von Spakovsky, Michael R. (1-223, 3-339)
Voncilă, Ion (5-173)
Wakui, Tetsuya (5-25)
Walker, Larry P. (2-311)
Wang, Chuan (4-115)
Wang, Zhe (2-77)
Webber, Michael (1-533, 2-335)
Weber, Céline (3-167, 3-175)
Weber, Roman (4-375)
Wegele, Johannes (3-317)
Weidmann, Nicolas (3-347)
Wellig, Beat (1-129)
Westermark, Mats (2-119)
Wilhelm, Erik (5-95)
Witzig, A. (3-221)
Wogan, David M. (1-533)
Wohlgemuth, Volker (1-71)
Wongsiriamnuay, Thanasit (2-55)
Wuillemin, Zacharie (5-141)
Wuilloud, Eric (2-435)
Xiao, Feng (1-457)
Xiaoxi, Yang (2-467)
Xue, Yali (2-77)
Yan, J. (2-83)
Yang, Minlin (2-467)
Yang, Zhiwei (2-77)
Yari, Mortaza (1-511, 3-429)
Yfantis, E. A. (4-123)
Yokoyama, Ryohei (5-25)
Yoshida, Shu (5-301)
Yoshiharu, Amano (5-301)
Yu, Bo (3-493)
Zaleta-Aguilar, A. (3-481, 4-165, 5-425)
Zannis, T.C. (5-53)
Zanoni, Marco A. B. (2-127)
Zarin, Arash (3-429)
Zehnder, Michele (3-75)
Zevenhoven, Ron (3-413, 4-67, 4-77, 4-459)
Zhang, Chuanqiang (2-363)
Zhang, Houcheng (3-123)
Zhang, Jiansheng (2-77)
Zhang, Jianyun (2-387)
Zhao, Yingru (5-9)
Zhelev, Toshko (4-249)
Ziabasharhagh, Masoud (5-411)
Zieba, Mariusz (4-367)
Ziębik, Andrzej (1-313, 4-43, 4-403)
Zoughaib, Assaad (1-137, 3-189)
Zuliani, Nicola (5-277)
Zuñiga-Cerroblanco, J.L. (1-421)
Zuwala, Jaroslaw (1-313)
Zyhowski, Gary J. (3-19)

KEYWORD'S INDEX

Absorber (4-427)
Absorption (3-429, 4-133, 5-173)
Absorption Chiller (3-213, 5-233, 5-411)
Absorption Ejecto-Compression Chiller (1-53)
Active Magnetic Refrigeration (3-115)
Adsorption (2-197, 3-447)
Advanced Exergetic Analysis (1-17, 1-337, 4-317)
Air-Conditioning (3-475)
Air-Water Heat Pump (3-75, 3-405)
Airlift System (1-489)
All-Electric (5-95)
Allocation (1-71)
Aluminium Sector (4-279)
Ammonia (1-45)
Anaerobic Digestion (3-355)
Applied Fuel Cell Modeling (5-141)
Area Targeting (1-523)
Aspen Plus (4-27)
Atomization (4-347)
Autothermal Thermophilic Aerobic Digestion (ATAD) (4-249)
Autothermal Gasification (2-277)
Availability (1-489)
Back-Up Power (3-197)
Bagasse (2-249)
Basic Oxygen Furnace (4-439)
Batch Process (1-97)
Batteries (5-119)
Bean (2-453)
Bejan Number (1-421)
Bellman-Zadeh Approach (1-241)
Bio-Butanol (4-383)
Bio-Methanol (2-119)
Biocoal (2-45)
Biodiesel (2-525, 2-531)
Biofuels (1-249, 2-1, 2-27, 2-35, 2-189, 2-269, 2-311, 2-395)
Biogas (1-431, 5-45)
Biogas Reforming (2-207)
Biomass (2-1, 2-35, 2-45, 2-55, 2-69, 2-119, 2-167, 2-189, 2-225, 2-293, 2-405, 2-513, 2-519, 3-355, 4-157, 5-353)
Biomass Co-Firing (1-313, 2-61)
Biomass Power Generation (2-467)
Biomass Stove (2-145, 2-217)
Biomass-To-Liquid Systems (2-101)
Biorefinery (2-11, 2-19, 2-241)
Bitumen (2-495)
Black Liquor Gasification (2-83)
Blades (5-425)
Boiler (4-157, 5-309)
Booster (3-75)
Bottom-Up (4-279)
Bottoming Cycle (3-19, 5-73)
Bouduard Reaction (2-233)
Brewery (4-91)
Bromine Ions (1-171)
Building (3-83)
Building Application (5-339)
Building Energy Consumption (3-237)
Building Energy Requirements (3-237)
Building Heat Loss (3-229)
Building’S Thermal Behavior (3-405)
Buildings (3-245)
Combined Heat and Power systems (CHP) (1-27, 5-381)
Calculation Methods (4-325)
Carbon Capture (4-59)
Carbon Capture Sequestration (CCS) (4-9, 4-19, 4-51, 4-83, 4-99, 4-107)
Carbonate (4-59)
Carnot Cycle (3-51)
Cascade Refrigeration Machine (4-317)
Catalysis In Water (3-137)
Catalyst Saving (5-259)
Centrifugal Compressor (3-145, 5-397)
Chemical Exergy (1-195, 5-317)
Chemical Looping Combustion (2-225)
Chemicals (4-227)
Chlorine Electrolysis (4-241)
Chromosome (1-321)
City Layout (3-175)
Classical Thermosize Power Cycles (3-455)
Classroom Technology (1-533)
Clausius Rankine Cycle (5-63)
Climate Policy (3-347)
Co-Firing (2-69)

CO_2 (2-233, 4-427)
CO_2 Capture (2-167, 4-67, 4-77, 4-133)
CO_2 Compression (4-43)
CO_2 Emissions (2-83, 3-397)
CO_2 Mineralisation (4-67, 4-77)
CO_2 Reduction (3-137)
CO_2 Separation (2-225, 5-1)
Coal (2-225, 4-9)
Coal Gasification (2-233, 4-27)
Coal-Derived Synthetic Natural Gas (2-387)
Coefficient Of Performance (3-475)
Cogeneration (1-241, 1-313, 1-397, 2-293, 2-405, 3-51, 4-35, 4-157, 5-25, 5-181, 5-233, 5-309, 5-325)
Cogeneration System (5-339)
Combined Cooling, Heating and Power (CCHP) (5-173)
Combined Cycle Power Plant (1-17)
Combined Cycles (2-353, 4-149, 5-63, 5-243)
Combined Heat (1-89, 1-357, 3-153, 3-161, 3-167, 3-371, 5-157, 5-165, 5-369)
Combined Heat and Power (CHP) (1-113, 3-27, 4-43, 4-255,5-411)
Combustion (3-355, 4-375, 5-405)
Combustion Plant (2-61)
Combustion Simulation (4-357)
Combustor Model (4-357)
Complex Energy System (1-223, 3-331)
Compressed Air Energy Storage (2-335)
Compression (5-173)
Computational Fluid Dynamics (CFD) (3-145, 3-279, 3-301, 4-271, 5-397, 5-405, 5-425, 5-191)
Concentrated Pv Systems (2-413)
Concentrated Solar Thermal Power Plant (2-363)
Condenser Product (1-381)
Condensing Heater (3-317)
Condition Number (1-449)
Conical Nozzle (5-125)
Constraint Adaptation (5-141)
Constructal (5-267)
Control (4-185, 5-369)
Control Strategy (5-285)
Control System Regulation (4-165)
Conventional Exergetic Analysis (1-17, 1-337)
Cooling Cycle (3-309)
Cost (1-63)
Cost Of Electricity (4-287)
Cost Reduction (2-413)
Coupled Power-Refrigeration Cycle (3-205)
Crevices (5-191)
Critical Flow Function (1-409)
Cryogenic Process (1-81)
Culm (5-181)
Cumulative Exergy Consumption (1-275)
Cumulative Exergy Extracted Out Of The Natural Environment (Ceene) (4-227)
Data Center (5-325)
Data Mining (4-235)
Decomposition (4-395)
Dehumidification (3-467)
Demand Side Management (3-363)
Density Distribution (1-439)
Density Measurements (1-431)
Desiccant (3-467, 5-157)
Desiccant cooling (3-475)
Desiccant wheels (3-475)
Design (3-371, 4-177)
Design Of Experiments (3-405)
Development Of Southern Countries (2-217)
Diagnosis (4-123, 4-211)
Diesel (5-53, 5-405)
Diffusional Losses (5-259)
Dispatchable Power (2-335)
Dissipative Component (1-381)
Distillation (1-449, 1-465, 4-255, 4-333)
Distributed Domestic Generation (2-153)
Distributed Generation (3-355, 5-309)
District Energy System (3-175)
District Heating (3-189, 3-371, 5-325)
District Heating Network (1-397)
District Heating System (4-403)
DNA (1-321)
Domestic Heater (3-229)
Double-Flash (2-161)
Dry Reforming (2-207)
Dryer (2-127, 2-217)
Dual Fluidized Bed Gasifier (2-167)
Dual Fuel Engines (5-73)
Dual Fuel SI Engine (5-225)

Dual-Gas Source (1-255)
Dump Truck (5-111)
Dynamic Demand Response (3-363)
Dynamic Heat Source (3-59)
Dynamic Models (3-35, 3-43, 3-421)
Dynamic Optimization (4-249)
Dynamic Simulation (3-213)
Dysfunctions (4-211)
Ecologic Analysis (4-1)
Economic Optimization (3-379)
Economic Profitability (2-153)
Economics (2-189, 3-339)
Economy-Energy-Environment Interactions (1-329)
Ecosenseweb (4-287)
Effective Temperature (4-141)
Efficiency (1-63, 3-499, 4-157, 4-395)
Effluents (2-259)
Electric (5-165)
Electric Motors (5-119)
Electrical Load (5-17)
Electricity Generation (5-119)
Electricity Generation & Consumption (1-365)
Electricity Market (4-447)
Electricity Production (2-441)
Electricity Sector (3-331)
Electrochemical Power (5-285)
Electrostatic Potential (2-525)
Emissions (1-45)
Energetic Efficiency (1-187, 4-295)
Energy (1-213, 2-225, 2-473, 3-253, 3-389, 4-35, 4-279, 4-395, 5-411)
Energy Analysis (2-241, 3-107, 3-331)
Energy Conversion (2-19)
Energy Crops (3-355)
Energy Density (5-285)
Energy Efficiency (1-1, 2-19, 3-245, 4-249, 4-263, 4-303, 5-259, 5-325)
Energy Impacts (2-11)
Energy Integration (1-249)
Energy Management (3-197)
Energy Modeling (3-323)
Energy Performance (5-111)
Energy Performance Of Residential Buildings (5-309)
Energy Planning (3-323, 3-363)
Energy Prediction (2-317)
Energy Route (1-481)
Energy Saving (1-107, 1-145, 1-457, 2-19, 3-263)
Energy Storage (2-335)
Energy Supply System (5-301)
Energy Sustainability (1-481)
Energy System (1-481, 1-533, 2-459, 4-83)
Energy System Evaluation (2-101)
Energy Tariffs (5-309)
Engine (5-233)
Enthalpy (1-291)
Enthalpy Recovery (3-467)
Entropic Maps (3-145)
Entropy (1-1, 1-9,1-421)
Entropy Generation (1-489, 1-499, 3-145, 5-33)
Environment Impact Index (5-419)
Environmental Aspects (1-241)
Environmental Assessment (1-345)
Environmental Certification (3-83)
Environmental Loads (1-71)
Environmental Taxation (3-347)
Environomic Optimization (2-269)
Equipartition Of Entropy Production (5-259)
Ericsson Engine (2-379)
Erosion (4-123)
Ethanol (1-249, 2-93, 2-109, 2-197, 2-241, 2-395, 5-201)
Evacuated Collectors (3-213)
Evaporative Cooling (1-9, 3-475)
Evolutionary Algorithm (1-97, 4-193)
Exergetic Analysis (4-317)
Exergetic Cost (2-259, 4-211)
Exergoeconomic (1-53, 1-81, 1-255, 4-193, 5-217)
Exergoenvironmental (1-305, 2-249)
Exergy (1-9, 1-81, 1-137, 1-249, 1-283, 1-291, 1-373, 2-161, 2-441, 2-473, 3-107, 3-183, 3-245, 3-253, 3-301, 3-339, 3-481, 3-487, 4-177, 4-227, 4-295, 5-181, 5-217)
Exergy Analysis (1-45, 1-107, 1-489, 2-1, 2-447, 2-447, 3-331, 4-133, 4-203, 4-303, 4-439, 4-459, 5-411)
Exergy Approach (1-179)
Exergy Components (1-63)
Exergy Cost (3-67, 3-487)
Exergy Cost Theory (3-389)
Exergy Destruction (1-17, 3-253, 3-429, 5-419)

Exergy Efficiency (1-263,3-429, 5-389)
Exergy Life-Cycle (1-275, 1-481)
Exergy Losses (1-499, 3-27, 4-141)
Exergy Maximization (2-479)
Exergy Of Water (1-195)
Exhaust Gas (5-381)
Exhaust Heat Recovery (5-53)
Expanders (3-153, 3-161)
Experimental Design (4-295)
Experimental Results (2-379, 3-421)
External Environmental Cost (4-287)
External Heat Supply Reciprocating Engine (2-379)
External Heat Transfer Control (2-127)
External Irreversibilities (5-361)
Externalities (4-287)
Fermentation (2-197)
Ferromagnetic Material (3-123)
Figure Of Merit (3-503, 4-421)
Filtering Maps (4-165)
Final and Useful energy (2-435)
Finite Speed Processes (5-361)
Finite Time Thermodynamics (5-253)
Fire-Tube Boiler (2-371)
Fischer-Tropsch (2-189)
Fixed Bed (2-55, 4-375)
Flameless Combustion (4-367)
Floor Heating (3-229)
Flow Distribution (3-279)
Flow Rate Equation (4-325)
Fog (4-203)
Fogging System (5-425)
Food Industry (1-97)
Forest Biorefinery (1-233)
Formic Acid (3-137)
Fossil Fuels (5-353)
Fouling (4-123)
Frozen Shrimp (2-453)
Fuel Cell (5-17, 5-95, 5-149, 5-173, 5-339, 5-389)
Fuel Cell Performance (5-267)
Fuel Consumption (5-209)
Fuel Cycle (1-275)
Fuel Impact (4-211)
Fuel Reactor Simulation (2-225)
Fuel-Nox (4-367)
Full-Working Condition (2-77)
Fuzzy Decision Making (1-241)
Gas Bearings (3-91)
Gas Recovery (4-439)
Gas Turbine (4-1, 4-123, 4-203, 5-1, 5-9)
Gas Turbines Engines (5-397)
Gas-Solid Carbonation (4-67, 4-77)
Gaseous LPG Injection (5-225)
Gasoline Direct Injection (GDI) (5-201)
Gasification (2-55, 2-69, 2-119, 2-293, 2-513, 2-519, 2-531, 3-355, 4-9)
Gasifier (2-77, 2-513, 4-9, 4-27)
Generating Electricity System (5-353)
Generation III & IV Reactors (1-263)
Generation Technologies (1-345)
Generator Absorber Exchange (GAX) (3-429)
Genetic Algorithm (1-321, 4-311)
Geographical Information Systems (Gis) (3-355)
Geothermal (2-459)
Geothermal Energy (3-19)
Geothermal Power (2-161)
Geothermal Sources (2-301)
Getter Pumping (2-429)
Gibbs Free Energy (1-291)
Gibbs Systems Dynamics (2-421)
Glycerol (2-531)
Gouy-Stodola Law (4-141)
Graphical Exergy Analysis (2-363)
Greece (4-107)
Greenhouse Gases Emission (1-365, 4-279)
Grid Connected (2-485)
H-S Model (1-63)
Heat Exchange Coefficients (3-291)
Heat Exchanger (2-217, 3-301, 3-317)
Heat Exchanger Network (1-129, 1-145, 1-321, 1-457, 1-523, 2-285)
Heat Exchanger Network Design (1-153)
Heat Exchanger Network Retrofit (1-473)
Heat Integration (1-97, 1-465, 4-255)
Heat Pump (1-137, 3-75, 3-189, 3-229, 3-245, 3-317, 3-397)
Heat Recovery (5-381)
Heat Recovery Network (1-161)
Heat Sinks (1-421, 3-279)
Heat Storage (1-97, 3-371)

Heat Transfer (4-333, 5-191)
Heat Transfer Feasibility (1-223)
Heat Transportation Over Long Distance (3-183)
Heat-Following MicroCHP (2-153)
Heating (3-67)
Heating System (3-461)
Heliostat Field (2-345)
Heuristics (5-95)
HFC-245fa (3-19)
High Performance (3-245)
High Pressure H2 Generation (3-137)
High Speed (3-91)
High Temperature Pem Fuel Cells (5-277)
High-Efficiency Cogeneration (4-403)
Hot Air Engine (2-379)
Hybrid (3-429, 5-95)
Hybrid Cycle (2-119, 5-1)
Hybrid Energy Management (1-113)
Hybrid Hvac (5-157)
Hybrid Modeling (3-347)
Hybrid System (5-9)
Hydraulic Pipeline Systems (4-325)
Hydraulic Turbomachinery (5-133)
Hydrogen (2-167, 2-225, 5-325)
Hydrogen Energy System (2-225)
Hydrogen Production (1-337)
Hydrogen Storage (3-137)
Hydrogenation (3-137)
Hydrolysis (2-1)
Hydrothermal Carbonisation (2-45)
Hydrothermal Gasification (2-27)
IGCC Power Plants (4-411)
Induced Effects (4-165)
Industrial Ecology (1-283)
Industrial Energy Efficiency (4-241)
Industrial Energy Systems (4-219)
Industrial Metabolism (4-227)
Industry (4-395)
Industry Model (4-279)
Influence Of Incentives (2-405)
Infrared (1-171)
Inlet Air Cooling (4-203)
Integrated Catalysis (1-255)
Integrated Gasification Combined Cycle (Igcc) (4-9)
Integrated Thermal System (5-233)
Intelligent Systems (1-113)
Intensity (4-395)
Internal (5-361)
Internal Combustion Engine (5-45, 5-63, 5-119, 5-217)
Inverted Brayton-Joule (5-1)
Investigatory Installation (2-513)
Investment Payback Period (5-309)
Investment Planning (1-233)
Investments (4-263)
Iron Oxide (2-225)
Irreversibility (1-81, 3-499, 5-293, 5-375, 5-389)
Irreversible Heat Engines (5-253)
Irreversible Thermodynamics (3-503, 4-333, 4-421)
Iterative Procedures (5-233)
Joule Cycle Engine (2-379)
Ketone-Benzol Dewaxing Process (1-457)
Kinetic Modeling (4-427)
Knudsen Number (1-511)
Kraft Process (2-241)
Kraft Pulping (2-11)
Kraft Recovery Boiler (4-235)
Laminar Boundary Layer (1-511)
Landfill Gas (5-45)
Large Power Units (2-69)
Law-Of-The-Wall (5-191)
Led (2-501)
Lennard-Jones Potential (1-439)
Life Cycle Analysis (1-357, 1-365, 1-481, 2-249, 2-269, 2-311, 2-485, 3-83, 4-411)
Life Cycle Assessment (1-345)
Life Cycle Impact Assessment (1-305)
Lignin Extraction (2-11)
Lignite (4-19)
Lignite Power Plant (4-107)
Lignocellulosic Biomass (2-473)
Lignocellulosic Ethanol (2-311)
Liquefaction (4-317)
Liquid Fuels From Renewable Sources (4-347)
Liquid Piston (3-51)
Liquid Wastes (4-347)
Liquified Natural Gas (LNG) (2-447, 4-317)

Liquified Natural Gas (LNG) Evaporation (2-441)
Liquified Petroleum Gas (LPG) (5-225)
Lithium Cells (5-103)
Load Management (3-405)
Local Manufacture (2-217)
Lock-In Situations (1-233)
Lost Work (5-419)
Low Exergy (3-245)
Low Mach Number (5-125)
Magnetic Refrigerating System (3-115)
Magnetocaloric Effect (3-115)
Malfunctions (4-211)
Manufacturing (4-395)
Mass Transfer (1-89, 4-333)
Mathematical Programming (1-473)
Maximum Power (3-499)
Media (4-203)
Membrane Reformer (5-325)
Membrane Separation (4-99)
Methane/Steam Reforming (2-207)
Methanol (2-249)
Micro Gas Turbine (5-103)
Micro-CHP (5-157, 5-309)
Micro-Cogeneration (2-379)
Micro-Evaporator (3-309)
Micro–Polygeneration (3-481)
Micro/Nano Heat Engines (3-455)
Microgrids (3-339)
Microprocessor (3-309)
MILP (4-263, 4-447)
Mimosa (2-55)
Mineral Carbonation (4-459)
Minerals (1-291)
Minimization (1-499)
Minimized Total Cost (4-469)
Mixed Refrigerants (2-447, 4-311)
Mixed-Integer Program (3-371)
Modelica (2-371)
Modeling (1-187, 2-293, 4-83, 4-411)
Moist Air (1-9)
Molten Carbonate Fuel Cell (5-33)
Monetary Cost (3-487)
Monoethanolamine Absorption (MEA) (4-107,4-427)
Motoring (5-191)
Multi-Component Distillation (1-107)
Multi-Criteria Decision Analysis (Mcda) (1-357, 5-95)
Multi-Objective Linear Programming (1-329)
Multi-Objective Optimisation (2-269, 2-353, 2-459, 4-59)
Multi-Objective Particle Swarm Optimization (1-241)
Multi-Period (2-459)
Multi-Sectoral Models (1-329)
Multi-Stage Optimization (5-301)
Multi-Stream Heat Exchangers (3-271)
Multidisciplinary Education (1-533)
Multifunctional Heat Pump (3-67)
Multiphase Flow (1-489)
Multipurpose Process (3-51)
Nano Scale Diffusion (1-505)
Nant De Drance Project (2-435)
Natural Gas (1-81, 4-339)
Natural Gas Combustion (3-317)
Natural Gas Distribution Systems (4-325)
Network (3-175)
NGCC Power Plants (4-411)
Ni/SDC Catalyst (2-207)
Nitric Acid (1-45)
Nitrogen (1-431)
Nitrogen Fertilizers (1-45)
Non-Endoreversible (3-499)
Non-Equilibrium (3-503, 4-421)
Non-Linear Programming (2-61)
Non-Premixed Flames (4-383)
Non-Renewable Resources Depletion (1-373)
Northern Regions (3-413)
Northwestern European Electricity Market (3-339)
Nuclear Energy (1-263)
Nuclear Exergy (1-275)
Nuclear Fuel Cycle (1-263)
Numerical Meanline Investigations (5-85)
Numerical Modelling (4-27)
Numerical Simulation (5-125)
Numerical Simulations (4-375)
Off-Design (2-135)
Off-Grid (3-153, 3-161)
Off-Grid Wind Power (2-387)
Office Building (5-301)

Oil Platform (4-303)
Oil-Free (3-91)
Opencast Mine (5-111)
Operational Planning (5-25)
Operational Requirements (1-345)
Optical Diagnostics (5-209)
Optical Fibers (2-413)
Optical Measurements (5-201)
Optimal Control (4-149)
Optimal Fuel Cell Performance (5-141)
Optimal Process Scale (2-269)
Optimal Sizing (5-25)
Optimal Temperature (2-479)
Optimisation (1-27, 1-37, 1-161, 1-187, 1-213, 1-389, 1-397, 2-27, 2-61, 3-167, 3-271, 3-301, 3-371, 3-461, 4-193, 4-263, 4-469, 5-17, 5-33, 5-111, 5-293, 5-361)
Optimization Of System (3-115)
Optimization Under Uncertainty (1-233)
Optimum Performance (3-123)
Optimum Pressure Ratio (1-37)
Organic Rankine Cycle (2-135, 2-301, 2-405, 3-9, 3-19, 3-27, 3-35, 3-43, 3-59, 3-91, 3-153, 3-161, 3-205, 3-291, 3-317, 3-379, 4-115, 5-45, 5-63, 5-73)
Organosolv (2-473)
Otto Cycle (5-243)
Overall Cop (3-205)
Overall Cycle (3-253)
Overlap Reactions (2-127)
Oxy-Fuel Combustion (4-271)
Oxyfuel (4-19)
Oxygen Enhanced Combustion (OEC) (4-339)
Oxygen Staged (2-77)
Ozone (1-171)
Packed Beds (3-99)
Paint Oven (5-381)
Paper (2-11, 2-19)
Paper Industry (4-51)
Paper Machine (1-1)
Particle Swarm Optimization (3-221)
Payback Time (2-485)
Peak Electrical Demand (3-405)
PEMFC (5-325)
Performance Characteristics Of Energy Conversion Systems (3-503, 4-421)
Performance Optimization (5-375)
Performance Prediction (5-85)
Primary Energy Saving (PES) (4-403)
Petroleum Coke (4-9)
Phase Change (3-99)
Photovoltaics (2-485)
Physical Hydronomics (1-179)
Pinch (1-137, 2-447)
Pinch Analysis (1-121, 1-129, 1-145, 1-161, 1-473, 2-175, 4-91, 4-459)
Pinch Technology (1-213, 1-457, 1-523)
Pipeline Networks (4-325)
Plant-Wide (1-187)
Plastics (4-227)
Plate-And-Fin Heat Exchangers (3-271)
Plate-Fin Heat Exchanger (1-523)
Polarization Curves (5-267)
Pollutants (1-45)
Pollutants Emission (5-209)
Pollution (3-339)
Pollution Abatement (4-287)
Polygeneration (1-255, 2-119, 3-389, 5-149, 5-157, 5-317)
Polysun (3-221)
Portugal (4-83)
Post-Combustion Co2 Removal (4-43)
Power (3-153, 3-161, 3-167, 5-157, 5-165, 5-267)
Power (Chp) (5-369)
Power Density (5-285)
Power Generation (1-357, 4-149, 5-125)
Power Interchange (5-25)
Power Losses (4-141)
Power Plants (3-371)
Power Station (4-403)
Power Systems (1-345)
Predictive Control (3-263)
Premature Deterioration (5-425)
Pressure Drop (3-271)
Pressure Drop Consideration (1-523)
Pretreatment (2-311)
Primary (2-435)
Primary Energy Efficiency (2-101)
Primary Energy Factor (2-101)
Prime Mover (5-165)

Process Design (1-255, 1-389, 2-27, 2-35, 2-269, 2-459)
Process Energy Efficiency (4-77)
Process Heat (2-495)
Process Integration (1-1, 1-89, 1-121, 1-129, 1-233, 1-249, 2-27, 2-35, 2-285, 4-51, 4-91)
Process Optimization (1-129)
Process Simulation (1-107, 2-473)
Production Decision Model (4-447)
Programme Of Measures (1-179)
Propane (2-447)
Pulp (2-11, 2-19, 4-51)
Pulp Mill (2-83)
Pulverized Coal Power Plant (4-287)
Pumped Storage (2-435)
Pumping Power (1-213)
Pyrolysis (2-127)
Quantum Potential (1-505)
Quantum Size Effects (1-415, 1-439, 1-505)
Quantum Surface Energy (1-415)
Quasi-Stationary Simulation (4-219)
R-245Ca (3-205)
R134A (3-317)
Radial Compressor (3-317)
Radial Inflow Rotor (5-85)
Radial Turbine (3-317)
Radiant Panels (3-229)
Radiation Modeling (4-271)
Radiative Cooling (3-413)
Radiators (3-229)
Raman Spectra (1-171)
Random Forests (4-235)
Rankine Cycle (2-277, 2-371, 3-27)
Real- Time Optimization (5-141)
Receiver Design (5-361)
Rectangular Microchannels (1-421)
Refrigerant (1-137)
Refrigerant Flow Measurements (1-409)
Refrigerating System (3-263)
Refrigerator (3-447, 3-493)
Refuse-Derived Fuels (RDF) (2-277)
Regenerative Gas Turbine Cycle (1-37)
Regenerator Losses (5-361)
Relaxation (1-161)
Reliability Simulation (2-93)
Renewable Energy (2-55, 2-335, 3-197)
Renewable Energy Conversion (2-459, 2-269)
Renewable Resource Variability (2-327)
Renewables (2-285)
Renewal Planning (5-301)
Repowering (4-1, 4-35)
Residential (3-347, 5-165)
Residential Heating (3-91)
Residential Sector (3-397)
Residues Allocation (1-381)
Resonance (5-369)
Restaurant Waste (2-467)
Retrofit (1-153, 1-161)
Robot Path Planning (5-285)
Roller Mill (2-93)
Scenarios (4-279)
Scroll Compressor (3-9, 3-75)
Scroll Expander (3-9)
Second Law (1-511)
Second Law Analysis (4-141)
Second Law Efficiency (1-37, 3-253)
Seebeck Cells (2-145)
Selection Criteria (1-137)
Sell-And-Tube Heat Exchanger (1-523)
Sensitivity Analysis (3-439)
Sequence (1-449, 1-465, 4-255)
Sequential Simulation (4-427)
Series Hybrid Vehicle (5-103)
Simulated Annealing (3-271)
Simulation (1-113, 2-459, 2-519, 3-35, 3-43, 4-123, 4-469, 5-233)
Simulation Code (3-309)
Simulation Model (2-77, 5-277)
Simultaneous Heat (1-89)
Single (3-309)
Single Sinker Densimeter (1-431)
Single-Flash (2-161)
Single-Stage (3-75)
Singular Value (1-449)
Slip-Flow (1-511)
SNG (1-249)
SOFC (5-25)
SOFC Load Tracking (5-141)
SOFC Operation (5-141)

Software (1-129, 5-233)
Software Umberto (1-71)
Solar (2-353, 5-353)
Solar Air-Conditioning (3-131)
Solar Collector (2-479, 3-131, 3-439, 5-375)
Solar Combisystem (3-221)
Solar Cooling (2-421)
Solar Energy (2-467, 3-213, 3-447, 5-149)
Solar Energy Conversion (2-379, 2-413)
Solar Heating (3-439)
Solar Radiation Spectrum (2-501)
Solar Simulator (2-501)
Solar Stirling Engine (5-361)
Solar Thermal Energy Conversion (2-135, 3-153, 3-161)
Solar Thermal Panel (2-429, 2-495)
Solar Thermal Power Plant (2-371)
Solar Tower Thermal Power Plants (2-345)
Solar-Driven Heat Engine (5-293)
Solar-Powered Absorption Chiller (3-421)
Solid Oxide Fuel Cell (5-1, 5-9, 5-411)
Solid/Gas Sorption (3-131)
Soot (4-339)
Spark Ignition Small Engine (5-209)
Specific Fuel Consumption (5-111)
Spray (5-405)
Stability (2-387)
Staged Process (4-67)
Standardized Liquid Fuels (4-347)
Steady-State (1-187)
Steam (2-109)
Steam Gasification (2-167)
Steam Methane Reforming (SMR) (1-337, 5-277, 5-389)
Steam Network (4-469)
Steam Power Plant (4-193)
Steam Production (4-235)
Steelmaking (4-459)
Steelworks (4-115)
Stirling (5-369)
Stirling Cycle (5-243)
Stirling Engine (5-353)
Stirling Heat Engine (5-375)
Stirling Refrigeration Cycle (3-123)
Storage (4-67, 4-77)
Storage Tank (2-495, 3-439)
Strained Flames (4-383)
Structural Theory Of Thermoeconomics (3-67)
Sugar (2-109)
Sugarcane (2-395)
Sun Tracking System (2-485)
Supercritical (2-135, 3-291)
Supercritical Coal-Fired Power Plant (4-1)
Supercritical Evaporator (3-91, 3-317)
Supercritical Power Plant (4-99)
Sustainability (1-373, 1-533, 2-109, 2-241, 2-441, 3-83, 3-339)
Sustainability Assessment (1-357)
Sustainable Development (1-313)
Syngas Combustion (4-357)
Syngas Production (2-519)
Synthesis (2-175)
Synthesis/Design Optimization (1-223, 2-301)
Synthetic Natural Gas (2-83, 2-269)
T – H -Diagram (3-27)
Tar (2-167)
Techno-Economical Analysis (3-189)
Technology Assessment (4-241)
Technology Pathways (4-51)
Temperature Glide (1-137)
Temperature Jump (1-511)
Thermal (2-353)
Thermal Conversion (2-531)
Thermal Efficiency (3-27, 5-165)
Thermal Energy (2-145)
Thermal Energy Storage (2-335, 3-107)
Thermal Gains (3-237)
Thermal Integration (3-189)
Thermal Load (5-17)
Thermal Management (4-177)
Thermal Penalty Factors (1-145)
Thermal Pinch (1-89)
Thermal Radiation (4-339)
Thermal Storage (2-453, 3-99)
Thermally Driven Heat Pump (3-91)
Thermo-Ecological Cost (1-373, 3-301)
Thermo-Economic Function (3-123)
Thermo-Economic Modeling (2-35)
Thermo-Economic Optimisation (2-345, 4-91)

Thermo-Economics (2-353)
Thermo-Hydraulic Process (2-421)
Thermoacoustic (3-493)
Thermochemical Energy Storage (3-107)
Thermochemical Process (3-183)
Thermochemical Reactor (3-131)
Thermodynamic Inefficiencies (1-17)
Thermodynamic Optimisation (5-9, 5-243)
Thermodynamic Properties (1-439)
Thermodynamics (1-27)
Thermodynamics At Nano Scale (1-415)
Thermoecological Cost (1-313)
Thermoeconomic (1-63, 1-241, 1-283, 1-381, 1-397, 2-259, 3-389, 3-461, 3-481, 4-35, 4-185, 4-211, 5-217)
Thermoeconomic Performance (5-293)
Thermoeconomics Optimization (5-253)
Thermoelectric Generator (5-125)
Thermoelectric Power Generator (2-145)
Thermoelectricity (2-145)
Thermogravimetric Analysis (2-233)
Thermophotovoltaic (TPV) (2-153)
Thermopower (4-219)
Thermosize Effects (3-455)
Times (3-323)
Times Modeling (3-363)
Top-Energy (4-219)
Topology (1-145)
Torque Converter (5-133)
Total Annual Cost (TAC) (1-465, 4-255)
Tower Receiver (2-363)
Transesterification Reaction (2-525)
Transient Analysis (4-185)
Transport (3-347)
Transport Distance Influence (2-101)
Transportation (5-95)
Traveling Wave (3-493)
Trigeneration (1-53, 1-71, 5-233)
Turbine (5-317)
Turbocompounding (5-53)
Two-Phase (3-309)
Two-Stage (3-75)
Ultra-Micro-Turbogas Compressor (UMTG) (3-145)
Uncertainty (1-389)
Uncertainty Handling (1-329)
Underfloor Systems (3-439)
Unit Commitment (3-371, 4-447)
Uranium (1-275)
Urban Driving Cycles (5-103)
Urban Energy Systems (3-167)
Urea (1-45)
Utility Vehicles (3-59)
Utilization Factor (3-237)
Vacuum (2-429)
Variable-Speed Compressor (3-263)
Varying Supply & Demand (2-285)
Ventilation (3-67)
Venturi Nozzles (1-409)
Vinasse (2-259)
Virtual Power Plant (3-197)
Wasp Model (2-317)
Waste Heat (4-43)
Waste Heat Recovery (3-59, 3-379, 4-115)
Waste Heat Utilization (2-467)
Waste Treatment (1-283)
Wastewater Treatment (1-187, 4-249)
Water (2-109, 3-389)
Water Cluster (1-171)
Water Distribution Networks (1-213)
Water Electrolysis (2-387)
Water Framework Directive (1-179)
Water Potential (1-195)
Weibull Distribution (2-317)
Welfare Economics (3-347)
Wet Air Oxidation (4-295)
Wind Energy (2-317)
Wind Power (1-345)
Wind Scenario Generation (2-327)
Working Fluid (3-379)
Yeast & Ethyl Alcohol Plant (1-121)

ecos 2010

SPONSORS

ÉCOLE POLYTECHNIQUE FÉDÉRALE DE LAUSANNE

Schweizerische Eidgenossenschaft
Confédération suisse
Confederazione Svizzera
Confederaziun svizra

Office fédéral de l'énergie OFEN

INSTITUTIONAL PARTNERS

Lausanne

canton de vaud
LIBERTÉ ET PATRIE

TECHNICAL PARTNERS

ALPIQ

ecleer

HOLDI GAZ

BG
Ingénieurs Conseils
Ingenieure & Berater
Consulting Engineers

SUPPORTING ORGANIZATION

ASME
SETTING THE STANDARD

International centre for applied thermodynamics
ICAT
1997